Fluid flow paths in sedimentary basins: implications for exploration in challenging geological environments

Chantelle Roelofse

Submitted in partial fulfilment of the requirements for the degree of PhD

Cardiff University

School of Earth and Environmental Sciences

August 2020

Dedicated to my dad, Hendrik Roelofse.

It’s that rocky mentality,

that life is going to beat you down,

but it’s about how many times

you get back up……

……You’ve got to be naive enough to start

and stubborn enough to finish.

(Bear Grylls)

Abstract

Seismic interpretation and attribute analysis of three-dimensional seismic data often reveals focused fluid flow features such as pockmarks, mud volcanoes, hydrothermal vent complexes and amplitude anomalies. This thesis analyses three distinct data volumes from the Jæren High (Central North Sea), East Breaks area (northern Gulf of Mexico Basin), and Vøring Basin (mid-Norwegian margin), where fluid flow features are observed. The three study areas reveal a variety of these features across a range of depths and associated structures within sedimentary basins, from salt walls and pods, to salt minibasins and magmatic sill complexes. Thus, this thesis aims to improve our understanding of fluid migration in sedimentary basins and discuss the impact of the results on the hydrocarbon industry.

A comprehensive seismic and borehole dataset from the Jæren High is used to investigate the distribution and timing of buried pipes and pockmarks, which reveal seal breach across salt welds and Mesozoic strata. A semi-automated method in ArcGIS is used to map and characterise 196 depressions in three seismic surfaces. Depressions range in width from 225 m to 842 m and in vertical relief from 14 m to 178 m, scales that are comparable with the literature but that expand the limited evidence of large, 'mega' pockmarks, particularly in buried strata at the depth of prolific hydrocarbon reservoirs. It is shown that Upper Cretaceous depressions are likely to be drape features and pockmarks formed during the Upper Jurassic and Lower Cretaceous. Burial history modelling reveals gas maturity in Carboniferous strata, which may have sourced the observed pockmarks. High-amplitude anomalies within- and outside of pipes suggest further fluid seepage across salt welds, a character increasing the risk of seal breaching on the Jæren High if this structure is considered as a carbon capture and storage site.

Data from the East Breaks area of the northern Gulf of Mexico Basin are used to analyse the morphology and distribution of 720 pockmarks and 62 mud volcanoes on the sea floor, correlating these with underlying structures and source intervals in a major salt province. Salt diapirs and associated crestal faults are the main fluid focusing pathways, whilst high-amplitude anomalies in salt minibasins may indicate gas pockets or hydrocarbons that have not leaked to the sea floor. The relationship between the depth of fluid source and size of pockmarks and mud volcanoes is deemed complex, in contrast to the expected correlation between increasing pockmark size and depth of source. In fact, the shallow plumbing system in East Breaks is dominated by pockmarks, whilst mud volcanoes are sourced from the deeper parts of the salt minibasins.

The influence of magmatic sills, dykes and hydrothermal vent complexes on fluid migration is explored in the Modgunn Arch dataset from the southern Vøring Basin, Norwegian Sea. A total of 85 buried hydrothermal vent complexes are mapped, from which three examples of stacked vent complexes are identified, indicating important reactivation of existing conduits. Amplitude anomalies in younger strata suggest later-stage fluid seepage across hydrothermal vent complexes, highlighting the importance of magmatic structures in controlling fluid migration pathways. Larger vents tend to be fed by deeper sills, while a greater proportion of the larger vents are associated with amplitude anomalies.

In conclusion, the presence of pipes, conduits and faults weaken or strengthen the host rock, depending on the *in-situ* stress states and cementation of these pathways. This will impact the degree of overpressure increase required for modern day reactivation of these pathways. As a result, this thesis explores the complexity of focused fluid migration pathways through sedimentary basins with the aim of understanding the importance of subtle features on seismic data as recurrent fluid flow paths. These are important considerations when exploring in challenging geological environments such as salt-rich and magmatic basins, as well as when identifying sites suitable for carbon capture and storage.

Author note and status of publications

The results chapters presented in this thesis have been prepared as scientific papers for publication in international journals. Their present status is as follows:

Chapter 4 has been published as Roelofse, C., Alves, T. M., & Gafeira, J. (2020). Structural controls on shallow fluid flow and associated pockmark fields in the East Breaks area, northern Gulf of Mexico. *Marine and Petroleum Geology*, *112* (104074).

Chapter 5 has been published as Roelofse, C., Alves, T. M., Gafeira, J., & Omosanya, O. (2019). An integrated geological and GIS-based method to assess caprock risk in mature basins proposed for carbon capture and storage. *International Journal of Greenhouse Gas Control*, *80*, 103–122.

Chapter 6 has been accepted for publishing in the journal *Basin Research*, titled: Reutilisation of hydrothermal vent complexes for focused fluid flow on continental margins (Modgunn Arch, Norwegian Sea).

Although the articles are jointly co-authored with the project supervisors, the work presented in the publications is that of the lead author, Chantelle Roelofse. Editorial work was provided by the project supervisors in accordance with a normal thesis chapter.

Acknowledgements

I would like to express my gratitude to all the people who have contributed to this thesis and my PhD journey.

I want to thank Tiago Alves (Cardiff, first supervisor) for all his knowledge, guidance, and support throughout the PhD, for all the editorial work and for always being on hand to ask questions and discuss ideas. Thank you for encouraging me to take time off and for generally being a fantastic supervisor and mentor, I couldn't have done it without you.

Thank you also to Joana Gafeira (BGS, second supervisor) for your patience in introducing me to ArcGIS and the workings of the BGS Mapping Toolbox, as well as editorial work and answering my queries. To my pastoral supervisor, Emma McKinley – I am so grateful for all your advice, support and of course, Costa trips. Thank you for being there for me and helping to clear my head.

The work in this thesis was conducted as part of the Natural Environment Research Council (NERC) Centre for Doctoral Training (CDT) in Oil and Gas, under its Exploration in Challenging Geological Environments research theme. It is sponsored by Cardiff University and the British Geological Survey (BGS) via the British University Funding Initiative (BUFI), whose support is gratefully acknowledged. The work has been undertaken in the 3D Seismic Laboratory in the School of Earth and Environmental Sciences, for which Cardiff University is thanked for its ongoing support of the lab and facilities. We are grateful to PGS, the Norwegian University of Science and Technology (NTNU), the Norwegian Petroleum Directorate (NPD) and Diskos, and the United States Geological Survey (USGS) for access to 3D seismic data volumes and permission to publish results from these data volumes, as well as the BGS and NPD for access to well data. We also acknowledge the Bureau of Ocean Energy Management (BOEM) for developing the Northern Gulf of Mexico Deepwater Bathymetry Grid and Seafloor Anomalies and making them publicly available for use. We also acknowledge Schlumberger (for Petrel® and Petromod®) and ESRI (for ArcGIS) for providing academic licences to Cardiff's 3D Seismic Lab. The British Geological Survey (BGS) is also thanked for the provision of the Seabed Mapping Toolbox. Furthermore, the editors and reviewers (N. Wildgust, S. Müller, M. Zecchin, D. Dunlap, M. Ireland, A. Rotevatn, B. Manton, D. Jerram and S. Planke) are thanked for their constructive comments on published manuscripts.

I am fortunate to have been a part of the NERC CDT and had access to industry-standard training alongside the PhD research and I am very grateful to John Underhill, Lorna Morrow and Anna Clark for all the hard work they have put in to the CDT. I have met fantastic people on courses and field trips and would like to acknowledge Laura-Jane Fyfe in particular, for being an incredible friend and support throughout the past 4 years.

I would like to thank my fellow 3D Seismic labbers, past and present – in particular, Nick, Nathalia, Roberto, Lilly and Cerys – for all the coffee breaks, crossword puzzles, interesting lunchtime discussions, annual multicultural Christmas lunch, and general humour to keep us going. Special thanks also to Gwen Pettigrew for her help in the lab, always being up for a chat and for getting the lab up and running after lockdown – just in time for me to finish my thesis.

Outside of the lab, I want to thank Sarah for always being supportive, available for a tea break and for being an all-round awesome friend. I am also so grateful for my girlies of 21RS: Silvia, Gwawr, and Muireann. I moved into a spare room for a year, but instead I moved out of a home after four years. I am so thankful for your friendships, for what you have done to help me through my PhD journey and for putting up with me through a couple of months of lock down whilst I finished my thesis – the impromptu dancing kept me sane!

I want to thank my family for their unending support and encouragement. This PhD journey has been my greatest challenge and the thesis itself a side-show to what I have experienced and learnt these past 4 years. Words cannot describe how much I miss you dad, Hendrik, I think of you every day, thank you that you always believed in me, whatever the goal. I am so grateful to you mum, Estelle, for your support and help to persevere as always, but especially for unexpectedly being my pandemic lockdown buddy for 3 months. Thank you for the homecooked food, morning coffees, creative and fun lockdown activities (only when I wasn't working of course) and for still loving me afterwards despite me going crazy writing up the thesis! Dankie vir alles wat julle vir my gedoen het en dat julle my altyd ondersteun sodat ek my mik punte kan bereik. Ek sal altyd dankbaar wees vir die opofferings wat julle gemaak het, ek is so lief vir julle. Dankie vir die geloof wat julle my gegee het.

Above all, thank you God for always walking with me, footprints in the sand; and for being my strength when I felt weak, my rest when I couldn't sleep, my joy, my everything.

Table of Contents

List of Figures

List of Tables

List of Equations

CHAPTER ONE

Introduction and Literature Review

1 Introduction and Literature Review

1.1 Rationale and research aims

1.1.1 Rationale

Focused fluid flow through sedimentary basins is recorded at multiple depths, from seafloor features that chiefly reflect the escape of biogenic and diagenetic fluids, to larger and deeper subsurface conduits for thermogenic fluid and magma (e.g. Judd and Hovland, 2007; Moss and Cartwright, 2010; Planke et al., 2005; Szpak et al., 2015). With the advent of three-dimensional (3D) seismic data and the development of acquisition and advanced processing techniques, fluid escape features previously missed in seismic data can now be imaged clearly and with greater accuracy. This is mainly due to enhanced seismic resolution and the ability to image vertical features in 3D, as well as improved imaging around and below salt. When recognised in 3D seismic data, fluid flow features may represent palaeo- or modern paths for fluids on their way from source to reservoir (secondary migration), or leakage pathways from a reservoir to a shallower reservoir or the surface (tertiary migration). Their presence is key to the recognition of hydraulically active areas and petroleum systems, describing migration pathways and associated geohazards, as seismic is often the first or sole data type available to discern whether a geographical area is worth exploring (Andresen, 2012; Hovland et al., 2002).

As technological developments allow exploration wells to be drilled in deeper water and in deeper rock formations, they become more expensive and the detailed assessment of leakage risk is crucial to avoid dry wells. In the past decade, the average exploration well on the UK continental shelf, in water depths of roughly 100 meters, cost somewhere between £25 and £40 million (The Oil and Gas Authority, 2018). As a comparison, the average deepwater exploration well in the Gulf of Mexico, in water depths in the order of 1000 meters, costs between US $75 and US $120 million (Amado, 2013). Therefore, the accurate interpretation of fluid flow features can help to save millions in time and infrastructure. In particular, deepwater regions of the Gulf of Mexico, the North Atlantic margin, and basins offshore Brazil and West Africa, to name a few, are highly prospective regions in which exploration is likely to increase (Pettingill and Weimer, 2002). Such passive margin settings, as well as failed rift basins (e.g. the North Sea) often contain salt or magmatic intrusions, which act as fluid focusing structures (Holford et al., 2017; Judd and Hovland, 2007). Therefore, determining the relative timing of fluid flow

and the formation of these structures, as well as their spatial relationships, is vital for exploring in these challenging geological environments and is applicable to continental margins across the world.

Higher quality seismic datasets have the potential to rejuvenate exploration in mature basins, such as the North Sea, where smaller or deeper targets have been missed. In such basins, infrastructure may already be in place or nearby and extension to new, smaller targets (so-called satellite fields) is financially beneficial. Furthermore, the identification of leakage pathways is important when assessing potential carbon capture and storage sites, which may also typically be located in mature basins such as the North Sea due to the abundance of well data, established reservoir models and understanding of seals able to hold hydrocarbons in place over geological time. Carbon capture and storage has been identified as a necessity in the energy transition if the energy industry is to continue producing the required hydrocarbons for a growing human population and simultaneously reduce greenhouse gas emissions.

Pockmarks are depressions indicative of focused fluid escape on the sea floor, and were first discovered using side-scan sonar data by King and MacLean (1970) (Section 1.2.2). Pockmarks are often present in large numbers in pockmark fields, hence mapping them manually can become a laborious task, with human error distorting the results when characterising their morphologies. Hence, Gafeira et al. (2012; 2018) developed a coded script used in GIS (Geographic Information Systems) that semi-automatically identifies, maps and characterises the morphology of bathymetric depressions. This script was first applied to multibeam echosounder bathymetric data (Gafeira et al., 2012) and subsequently to recent and buried pockmarks in 3D seismic data (Geldof et al., 2014), as explained further in Chapter 3. This novel mapping script allows the rapid and consistent mapping and characterization of pockmarks, from which statistical analyses may be performed, with the aim to reduce errors and increase accuracy when analysing large datasets. The identification and analysis of such features is used to determine the sources of fluid, fluid pathways and their terminus, as well as the timing of fluid flow in the sedimentary basin. This knowledge is used to understand the hydrocarbon plumbing system and is integrated into basin analysis and modelling (Andresen, 2012).

1.1.2 Aims of the research

This research will help to improve understanding of the physical processes behind the breaching of seal units and the escape of hydrocarbons from structural traps and reservoirs. In this thesis,

3D seismic data is used to investigate palaeo-fluid flow features rooted in a sedimentary basement (Jæren High, Central North Sea), recent fluid flow features above large salt diapirs (East Breaks, Gulf of Mexico), and fluid flow associated with buried hydrothermal vent complexes (Modgunn Arch, mid-Norwegian margin). The three case studies are used to explore how the morphological attributes of pockmarks and other fluid flow features change with depth in a sedimentary basin, spanning deeper to shallower stratigraphic units, from which their significance in controlling fluid flow pathways in the past and at present day is discussed. The analyses were used to answer the following research hypotheses:

- **Salt welds are key seal bypass pathways on the Jæren High in the Central North Sea – see Chapter 4.** If true, fluid flow features will be located stratigraphically above salt welds, consequently reducing the trap integrity at the Top Rotliegend Group level. If false, fluid flow features will not be spatially associated with salt welds.
- **Salt diapirs and crestal faults promote tertiary fluid migration in the East Breaks area of the Gulf of Mexico – see Chapter 5.** If true, pockmarks and mud volcanoes will be concentrated above salt diapirs and crestal faults which alludes to the location of deeper hydrocarbon-bearing reservoirs, whilst traps in salt minibasins are not leaking or do not contain hydrocarbon-bearing reservoirs. If false, pockmarks and mud volcanoes will not be concentrated above salt diapirs and crestal faults, and fluid flow is more widespread, spanning the centre of adjacent salt minibasins and areas not recording significant halokinesis.
- **The size of fluid flow features can be used as a proxy to predict the depth of a leaking reservoir or a sill – see Chapters 5 and 6.** If true, the size of pockmarks, mud volcanoes or hydrothermal vent complexes will increase with the depth of fluid source. If false, there will not be a correlation between the size of features and the depth of source; these features cannot be used as a predictive tool, only as an indicator of fluid escape.
- **Focused fluid flow features are preferential leakage pathways long after their initial formation – see Chapters 4, 5, 6 and 7.** If true, amplitude anomalies suggesting fluid presence are spatially associated with or above the fluid flow features, and these features will be prone to reactivation. If false, amplitude anomalies are not spatially restricted to the fluid flow features, these features represent one-off events that do not influence fluid flow after their formation. In addition, amplitude anomalies are laterally extensive and are more likely due to lithological changes.

- **The BGS Seabed Mapping Toolbox is an effective mechanism to map and interpret large pockmark fields on the sea floor and on buried surfaces in 3D seismic data – see Chapters 4 and 5.** If true, the pockmarks identified by the Tool will match up with the original surfaces in 3D seismic data, without excluding clearly visible pockmarks or including high numbers of seismic artefacts. If false, pockmarks will be mapped incorrectly or excluded; therefore the Tool is not a time-efficient method to interpret pockmark fields.

Chapter-specific research aims are outlined in each results chapter (4, 5, 6).

The following section encompasses a literature review of the key topics studied in this thesis, detailing several fluid flow features – their appearance in seismic data and how they formed; fault mechanics and rock failure (specifically related to the discussion in Chapter 7), and the formation of salt structures, relevant to the results shown in Chapters 4 and 5.

1.2 Fluid flow features

Fluid flow features have been classified according to their geometry, lithology, and the type of impact they impose on the surrounding sediment (e.g. Cartwright et al., 2007; Huuse et al., 2010; Løseth, et al., 2009). Another approach is to classify them according to the formation mechanism: a) subsurface sediment remobilization; b) vertically focused fluid flow; and c) laterally extensive fluid flow (Andresen, 2012). Subsurface sediment remobilization includes sand injectites and mud volcano systems (e.g. Hansen et al., 2005; Huuse and Mickelson, 2004). Vertically focused fluid flow features include pockmarks, gas chimneys, pipes and methane derived authigenic carbonates (e.g. Hovland et al., 2005; Løseth et al., 2009; Pilcher and Argent, 2007). Examples of laterally extensive fluid flow features include bottom simulating reflectors (BSRs), free gas zones and hydrocarbon related diagenetic zones (Andresen, 2012). A summary of the main, relevant fluid flow features in this thesis is presented below, with particular focus on pipes and pockmarks.

1.2.1 Pipes

Fluid pipes are imaged in seismic data as vertical to sub-vertical zones of reduced reflection continuity that have a columnar geometry in 3D (Cartwright and Santamarina, 2015; Løseth et al., 2011). As a result of this vertical structure, they are often difficult to image in seismic data. Pipes are only imaged when the diameter of the pipe is of the order of the horizontal resolution limit (Brown, 2003) and may be under-represented, as their presence in seismic is also dependent on the inherent limits of vertical seismic resolution. The imaging accuracy decreases with increasing depth along the pipes, and with decreasing pipe width (Løseth et al., 2011). Fluid pipes vary in diameter from 10s to 100s of metres and are generally 100s of metres in height, although pipes greater than 1000 m in height have been recorded offshore Nigeria, by Løseth et al., (2011). The lateral margins are often well imaged and can be identified in 3D seismic data using time slices and seismic volume attributes such as coherency or variance (Cartwright and Santamarina, 2015).

When pipes have been imaged internally, they are often shown to have offset reflections relative to the host succession; deformed or attenuated reflections that may be upward convex or concave, or often enhanced amplitude reflections within the vertical zone – this may reflect gas, fluid or cementation within the pipe itself (Cartwright and Santamarina, 2015; Løseth et al., 2011; Maia et al., 2016). Seismic or gas chimneys are similar to pipes in that they are

vertically elongate structures with chaotic interior reflections associated with gas leakage, but are generally much broader in cross section (Heggland, 1998).

Models of pipe formation consider fluid escape along a fracture network, or 'fracture mesh' (Sibson, 2000, 2003). When pore-fluid pressure increases sufficiently to overcome the overburden pressure, the overburden is hydraulically fractured, and permeable pathways are created for fluids to migrate through (Fig. 1.1 in Cartwright et al., 2007). In Rhodes, Greece, outcrop analogues of pipes also suggest that intense fracturing occurred during the formation of a pipe and that the pipe interior consists of brecciated seal facies with variable fracture intensity (Cartwright et al., 2007; Løseth et al., 2011). The stress states and 'fracture mesh' are explained in more detail in Section 1.3.

Pipes often terminate in a pockmark indicating recent fluid flow (or a buried/paleo-pockmark, indicating past fluid flow), the timing of which is marked by the reflection within which the pockmark is found (Judd and Hovland, 2007). If a porous medium is reached before the surface, the fluids may dissipate into the strata and form a seepage pipe rather than a blow-out pipe (Cartwright et al., 2007). Some pipes terminate in vertically stacked, high-amplitude anomalies, which may be evidence of prolonged low flux of fluids after the main pipe formation event (Cartwright and Santamarina, 2015). Cartwright et al. (2007) categorised pipes into four groups: dissolution, hydrothermal, blowout and seepage pipes. The pipes investigated in this thesis are blowout pipes (Chapters 4, 5), hereafter referred to as pipes, whilst hydrothermal pipes (Chapter 6) are hereafter referred to as hydrothermal conduits (see Section 1.2.4).

1.2.2 Pockmarks

King and MacLean (1970) were the first to introduce the term 'pockmark' to describe small 'blips' on echo sounder records observed on the continental shelf of Nova Scotia, Canada. Pockmarks have since been discovered in areas where fluid flow is focused and fluid escape is from low-permeability, fine-grained surficial sediments (Hovland et al., 2002; Hovland and Judd, 1988). Pockmarks are defined as shallow depressions on the seabed, generally circular to elliptical in shape, with diameters ranging from a few metres to up to 300 m and from 1 m to 80 m in depth (Gay et al., 2006; Hovland and Judd, 1988).

The traditional conceptual model for pockmark formation was proposed by Hovland and Judd (1988) where thermogenic gas generated at depth migrates upwards and accumulates in near-seafloor sediments, a phenomenon generating domes on the sea floor

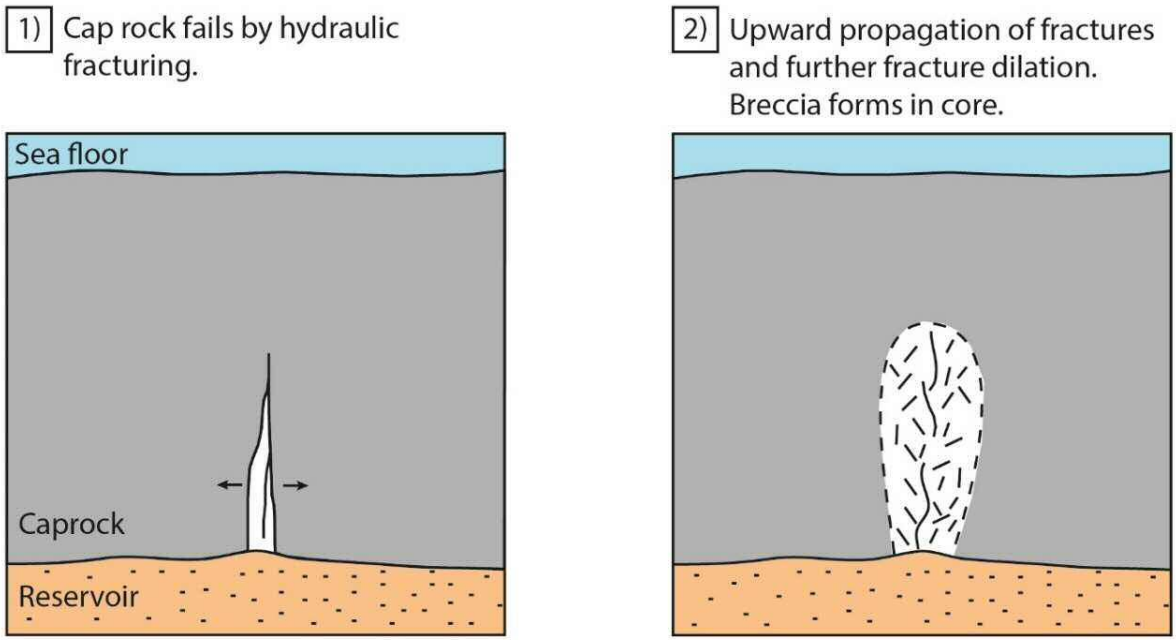

Fig. 1.1. Model showing pipe and pockmark development, from 1 to 3, based on existing models for diatreme formation and b
Modified after Cartwright et al. (2007).

(Judd and Hovland, 2007). Small tension fractures on these domes allow gas to escape, which, when gas velocity is large enough, leads to dome collapse and fluidization of the seafloor, lifting sediment into the water column as a gas-sediment plume, thus producing a pockmark (Stewart, 1999b). Once the pockmark is produced, there is an established fluid flow pathway to the surface through which continued low level flux can occur, or the pockmark may be reactivated by another pulse of gas (Cathles et al., 2010). An adaptation to the traditional model for pockmark formation is suggested by Cathles et al., (2010), to account for the fluid type, amount, saturation and periodicity of fluid expulsion. Cathles et al. (2010) proposed that "a capillary seal traps gas beneath a fine-grained sediment layer…and gas accumulates until its pressure is sufficient for gas to invade the seal. The seal then fails completely, releasing a large fraction of the accumulated gas into an upward-propagating gas chimney, which displaces water like a piston as it rises. Near the sea floor, the water flow causes the sediments to become "quick" (i.e. liquefied), in the sense that grain-to-grain contact is lost and the grains are suspended dynamically by the upward flow. The quickened sediment is removed by ocean-bottom currents, and a pockmark is formed." (Fig. 1.2). In this model, gas is the major fluid type. As mentioned in 1.2.1, it is also considered that the capillary seal is hydraulically fractured, and fluids escape along a fracture network to the surface.

When interpreting pockmark morphology, V-shaped depressions generally represent erosion from a point source due to fluid escape during the initial stage of pockmark development (Masoumi et al., 2014) (Fig. 1.3). This initial shape can be modified into a U-shape by processes that led to erosion of the pockmark walls, such as slumping or current scouring (Betzler et al., 2011; Dimitrov and Dontcheva, 1994). If depressions are not traditionally pockmarks, but instead are craters, these may have formed by collapse and have U-shaped rather than V-shaped morphologies. Pockmarks are typically circular in plan view, but can be elongate or eccentric, particularly if affected by bottom-currents. If a directional trend in the long axis of pockmarks exists, this may be used to make inferences of palaeo-bottom currents (Geldof et al., 2014).

The 'root' zone of a pipe is considered to be the source of the fluid, but this is often poorly imaged, particularly at depth (Cartwright and Santamarina, 2015). However, spatial analysis shows that the distribution of pipes and pockmarks are often controlled by underlying structures that focus fluids towards a point or area, from which the pipes form (e.g. Hovland et al., 2002). Pockmarks have been found vertically clustered above the margins of salt domes (de Mahiques et al., 2017; Schmuck and Paull, 1993; Taylor et al., 2000); in linear trails above

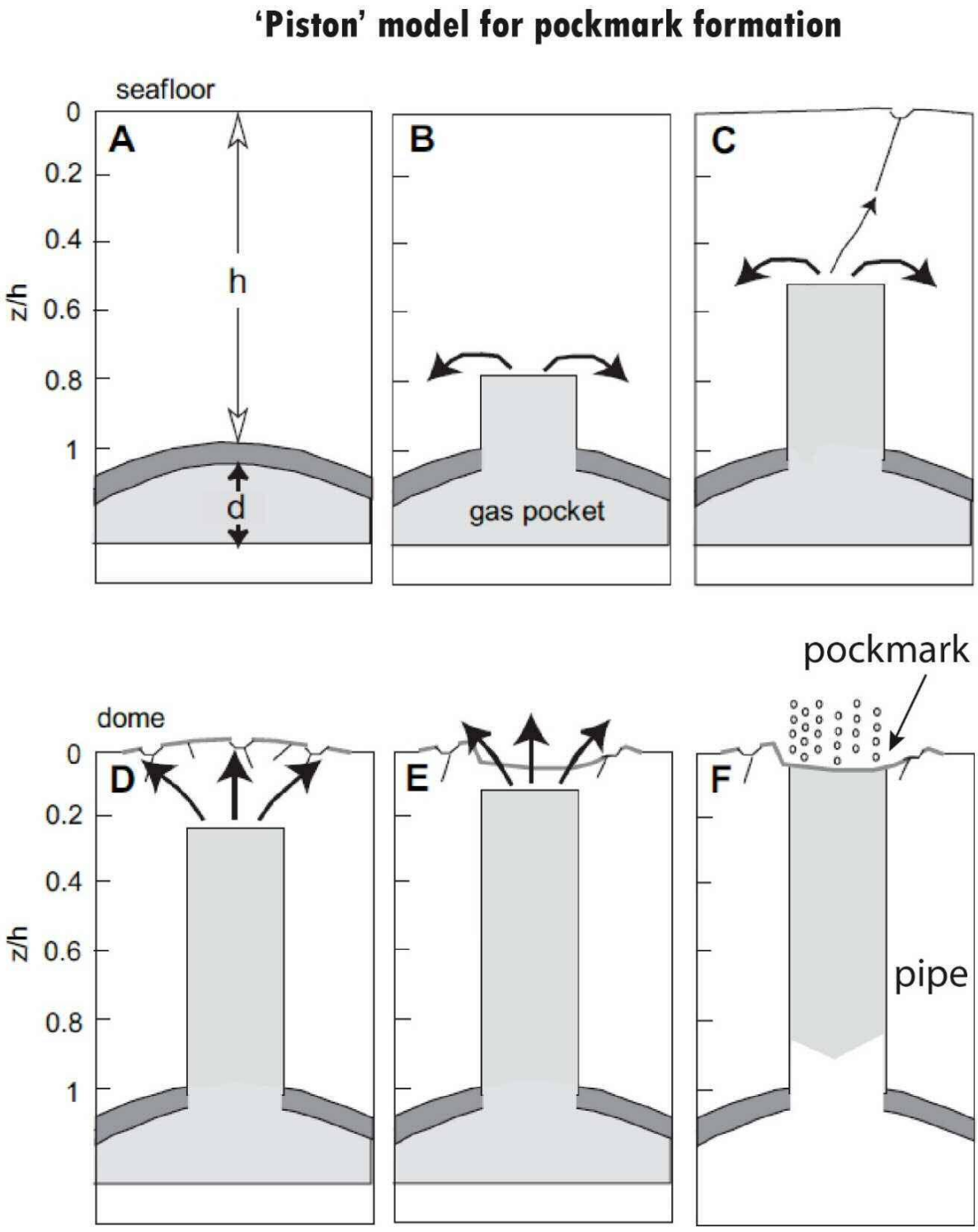

Fig. 1.2. Schematic model of the formation of a gas chimney towards the sea floor. A) Gas is trapped below an anticline of a fine-grained sediment (dark grey), which forms a capillary seal. B) When the gas accumulates to a thickness d, the seal fails, and gas is released into a chimney. Water is displaced as the chimney moves upward. Water movement is indicated by arrows, and water-saturated areas are white. C) The surface deforms and the first pockmarks start to form. D) Sediment deformation above the chimney becomes more severe and pockmark formation becomes more frequent. E) The pockmarks merge into a large pockmark with dimensions similar to the gas chimney. F) when the chimney reaches the surface the gas pocket quickly drains. After this, the water is drawn by capillary forces back into the fine layers of the failed portion of the seal and it is healed. Gas may accumulate below it again, and the gas chimney formation process may be repeated. After Cathles et al. (2010).

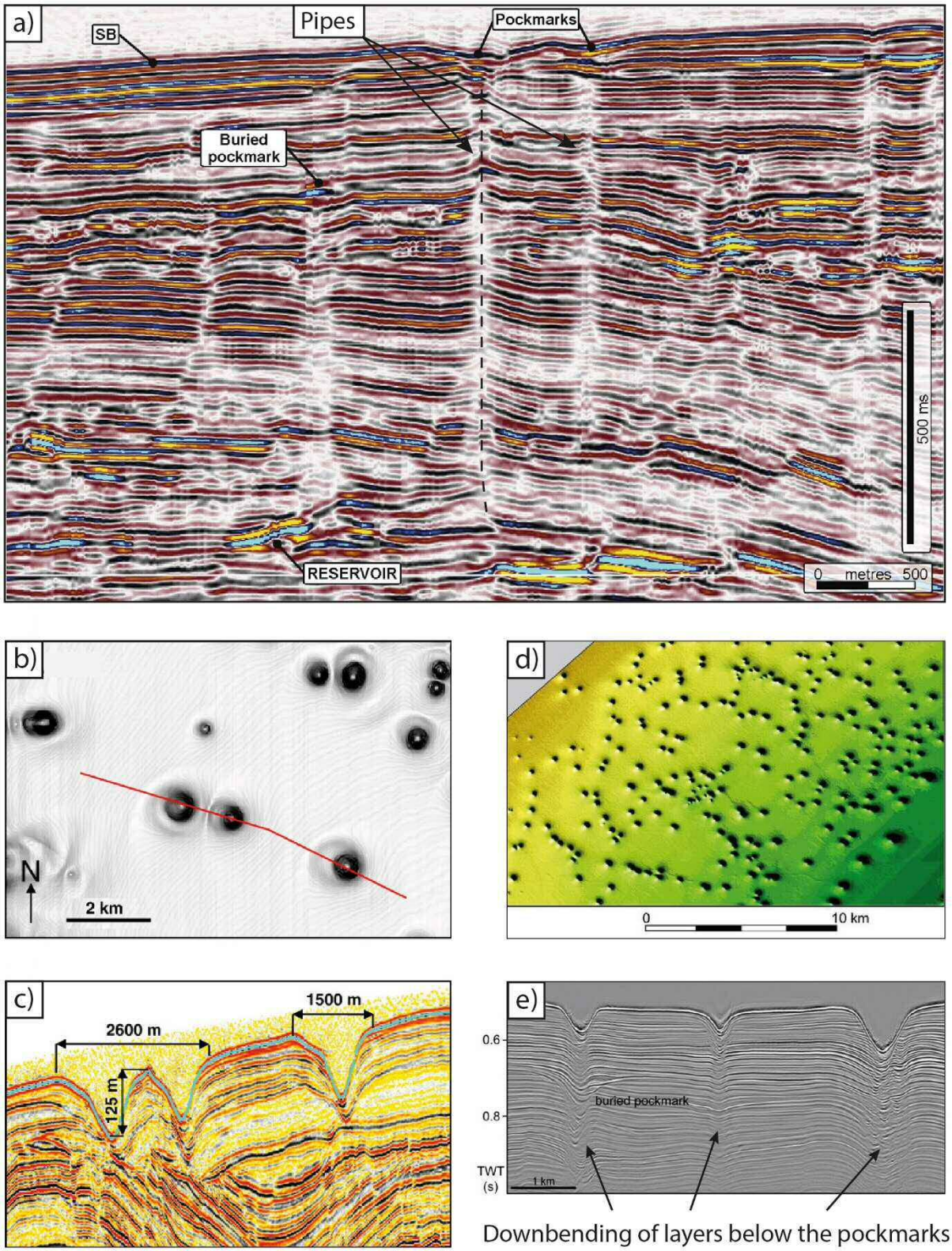

Fig. 1.3. Examples of pipes and pockmarks. a) Buried and recent pockmarks with underlying pipes, offshore Nigeria, after Løseth et al. (2011). b) Dip map of pockmarks on the West African margin, offshore Gabon, with c) a seismic cross section through three pockmarks, after Pilcher and Argent (2007). d) Map view of a pockmark field in the Santos Basin, offshore Brazil, after de Mahiques et al. (2017). e) Seismic section through pockmarks in the Maldives carbonate platform after Betzler et al. (2011).

faults and faulted anticlines (Dimitrov and Woodside, 2003; Eichhubl et al., 2000; Ward et al., 2016); clustered above lithological structures such as karsts (Howarth and Alves, 2016) and sand injectites (Huuse et al., 2010); and forming polygonal patterns, for example, when fed by deeper polygonal fault systems (Gay et al., 2006; Maia et al., 2016).

Pockmarks are imaged in 3D seismic data; however, higher-resolution (~metre scale) imaging methods such as multibeam echosounders and sidescan sonar can image the seabed as well as the water column, which often show gas bubbles immediately above pockmarks, indicating active gas seepage (Judd and Hovland, 2007). Understanding pockmarks and their distribution is important for: characterising slope and seabed instability when placing infrastructure; assessing environmental impacts due to methane release from dissociation of gas hydrates or biogenic gas; identifying local ecology and habitats; and, if the gas is thermogenic, pockmarks indicate an active petroleum system where hydrocarbons leak to the surface (e.g. de Mahiques et al., 2017; Judd and Hovland, 2007). Buried pockmarks detected in seismic data indicate an episode of focused fluid flow in the past (Fig. 1.3a, e).

1.2.3 Mud volcanoes

Mud volcanoes are positive, often conical and crater-shaped fluid escape features on the sea floor that chiefly comprise mud and other sediments. They may reach several hundreds of metres in height and a few kilometres in diameter (Judd and Hovland, 2007). They periodically or continuously vent liquid mud, water and hydrocarbon products, forming in thick sedimentary basins where significant overpressures build at great depths – often due to rapid sedimentary loading and hydrocarbon generation (Mazzini, 2009). These phenomena result in density inversion and the upward mobilisation of deep mudstones and accompanying fluids (Brown, 1990; Milkov, 2000; Judd and Hovland, 2007). Therefore, mud volcanoes are important indicators of deep plumbing systems in a sedimentary basin. Fig. 1.4a summarises the formation of a mud volcano, while Fig. 1.4b shows examples of recent and buried mud volcanoes in seismic data, where chaotic seismic chimneys connect the mud volcanos to the deeper parts of the basin.

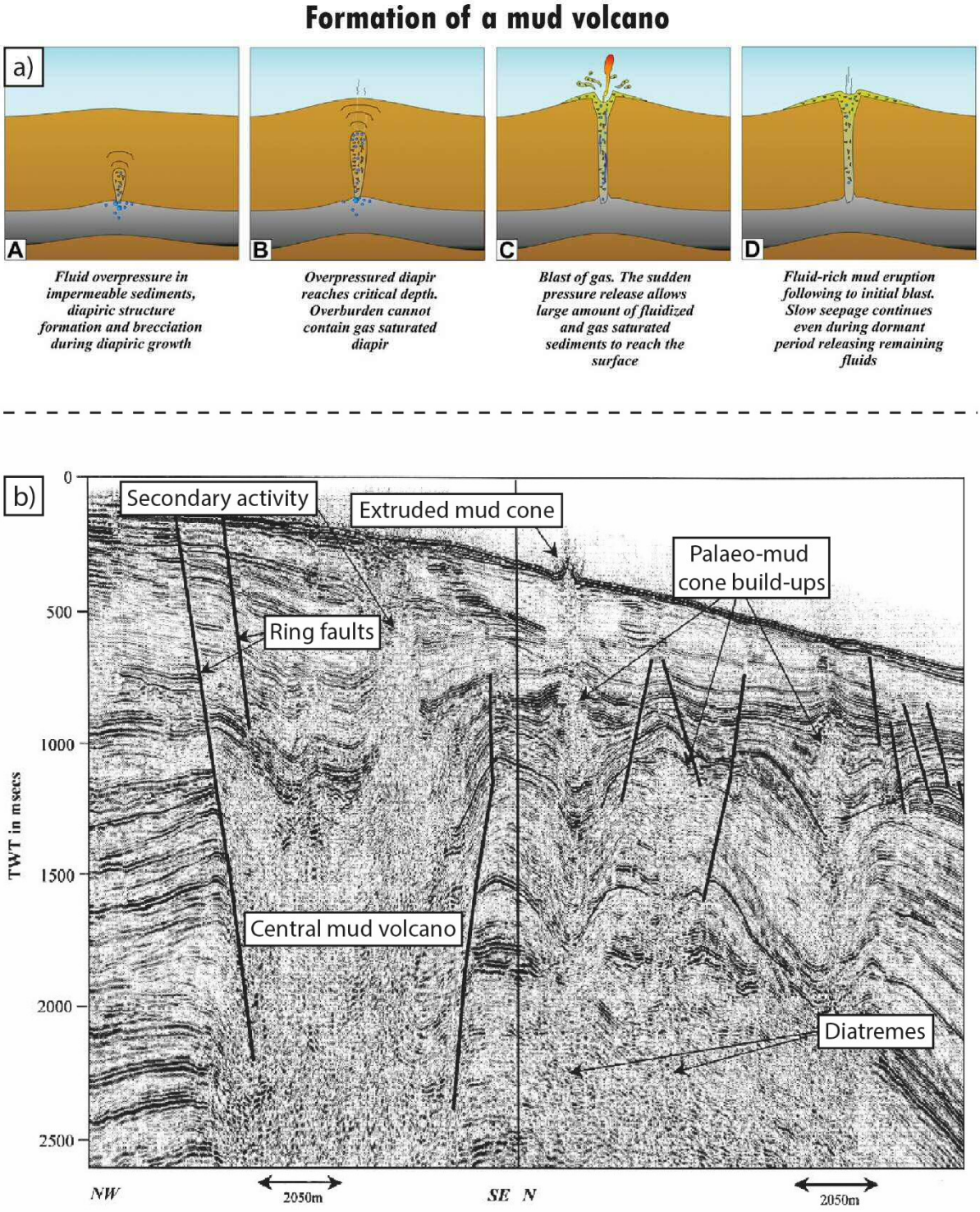

Fig. 1.4. a) Schematic representation of the formation of a mud volcano, from A to D, after Mazzini (2009). b) Seismic cross section example of extruded and buried mud volcanoes after Fowler et al. (2000).

1.2.4 Hydrothermal vent complexes

Hydrothermal vent complexes (HTVCs) are large fluid escape structures that form in volcanic sedimentary basins during the intrusion of magmatic sills (Omosanya et al., 2018; Svensen et al., 2003; Svensen et al., 2006). When sills intrude into sedimentary rocks, the surrounding strata is rapidly heated and pore waters boil to form gas and expand. This expansion, combined with the intrusion of magma and any other associated hydrothermal fluids, increases pore fluid pressures, causing the sudden overpressuring and fracturing of the surrounding rocks (Jamtveit et al., 2004; Omosanya et al., 2018). If sufficient overpressure is achieved, a fracture network extends vertically and fluids migrate rapidly to erupt at the sea floor, forming HTVCs. This fracture network, the hydrothermal conduit, connects the intruding sill to the sea floor. Conduits are imaged as pipe-like, vertical zones of low amplitude with chaotic interior reflections, terminating as dome, eye-shaped or crater morphologies at their summits with diameters ranging between 0.5 – 11 km (Hansen, 2006; Planke et al., 2005) (Fig. 1.5). Crater and eye-shaped structures are created by the excavation of sedimentary material in the eruptive process. After the main fluid escape event, it is thought that low-level fluid seepage into the infilling sedimentary strata maintains higher-than-average pore fluid pressures, inhibiting compaction to the degree of the surrounding sediments. This results in the formation of ‘eye-shaped’ HTVCs (Kjoberg et al., 2017). Dome HTVCs are considered to be akin to mud volcanoes, such that large volumes of fluidized mud and sediment erupt onto the sea floor to form conical, dome-shaped structures. The close relationship between HTVCs and underlying sills has allowed the estimation of the timing of sill intrusion based on the stratigraphic position of the upper terminations of the HTVCs (Hansen, 2006; Planke et al., 2005).

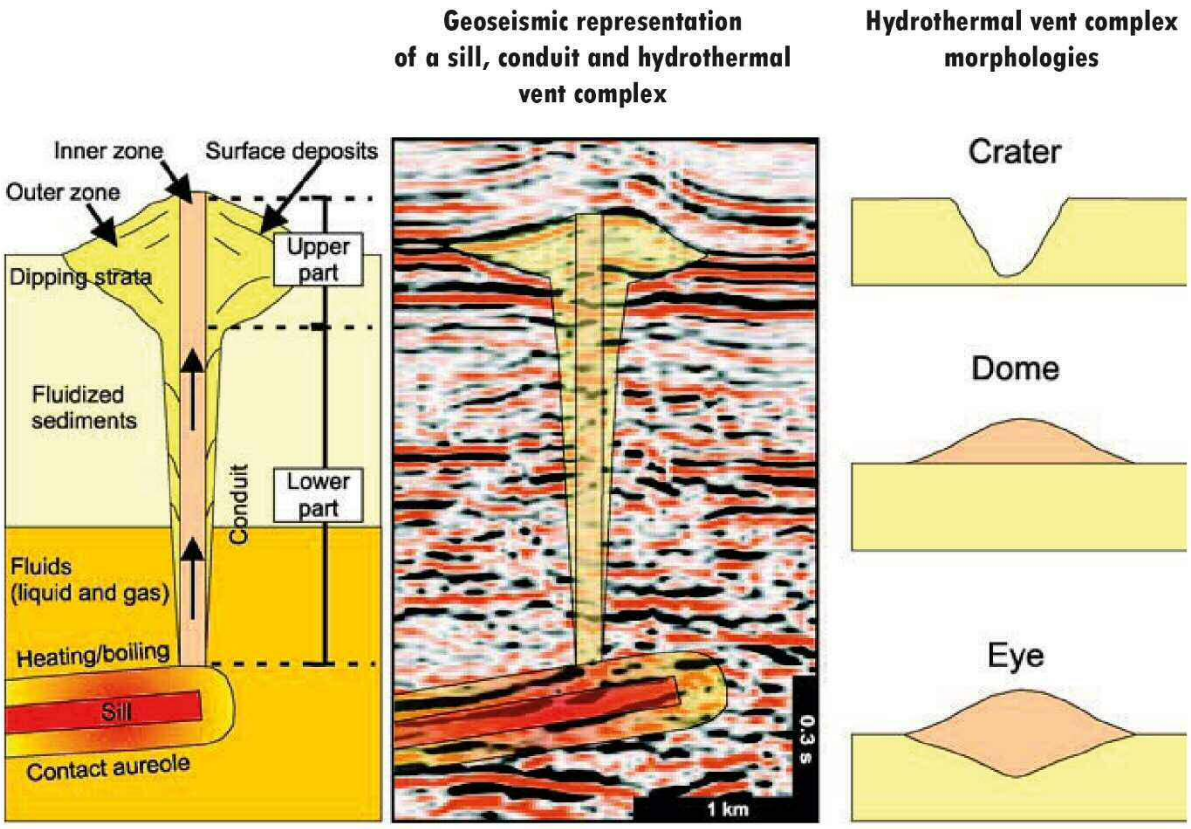

Fig. 1.5. Schematic and seismic example of a hydrothermal vent complex. The upper part of the complex is crater, dome or eye-shaped and is connected to the termination of a sill by a cylindrical conduit zone with disturbed seismic data in the lower part. Modified after Planke et al. (2005).

1.2.5 Direct hydrocarbon indicators

A range of amplitude anomalies in seismic data can indicate the presence of fluids or fluid contacts. Direct hydrocarbon indicators (DHIs) are acoustic manifestations of hydrocarbons within the sedimentary succession, which appear as local amplitude anomalies. These include polarity reversals, flat spots (fluid contacts), bright- and dim spots (Løseth et al., 2009) (Fig. 1.6). A polarity reversal is a phase shift of 180° along a continuous reflection. A flat spot is a relatively flat seismic reflection which cross-cuts dipping stratigraphic reflections, representing a fluid contact, but these can be difficult to identify if the host stratigraphy is parallel to the fluid contact. Bright spots are local increases in amplitude along a reflection, whilst dim spots are local decreases in amplitude. Soft bright spots close to the surface may indicate shallow gas, which may be biogenic or thermogenic. Flags – either vertically along faults, or stacked brightening of reflectors - may indicate fluid columns. Amplitude anomalies often represent the presence of fluids, but may also be a sign of, for example, cemented zones, overpressured sands, local lithological changes, or sedimentary disruption by a previous phase of fluid flow; hence, they must be interpreted with caution (Andresen et al., 2011).

1.2.6 Gas hydrates and free gas zones

Gas hydrates are crystalline, ice-like compounds composed of water and gas, where gas molecules are trapped within a framework of hydrogen-bonded water molecules (Judd and Hovland, 2007). The gas mainly consists of methane, with trace amounts of light hydrocarbons, carbon dioxide, nitrogen and hydrogen sulphide (Judd and Hovland, 2007). In the Gulf of Mexico, gas hydrates can form from biogenic or thermogenic gas under high pressure and low temperature conditions, therefore typically close to the sea floor and at water depths of at least 300-600 m (Hutchinson et al., 2011). Given that the temperature of sedimentary basins increases with depth, gas hydrates are typically only stable in the uppermost 100-200 metres below the sea floor.

Due to the niche environmental conditions required to keep gas hydrates in a solid stable state, slight changes in pressure or temperature result in dissociation of gas hydrates into free gas. Pockmark fields are often found to be related to shallow gas produced in this way (Judd and Hovland, 1992; Rollet et al., 2009). If gas hydrates are laterally extensive, they can also form a shallow seal, such that free gas accumulates immediately below (Fig. 1.7). In seismic data, a reduction in the p-wave velocity in the transition from gas hydrates in sediments to shallow gas or water in the pore spaces below results in a ‘soft’ seismic reflection – a ‘bottom simulating reflector’ (BSR) – which mimics the seafloor horizon,

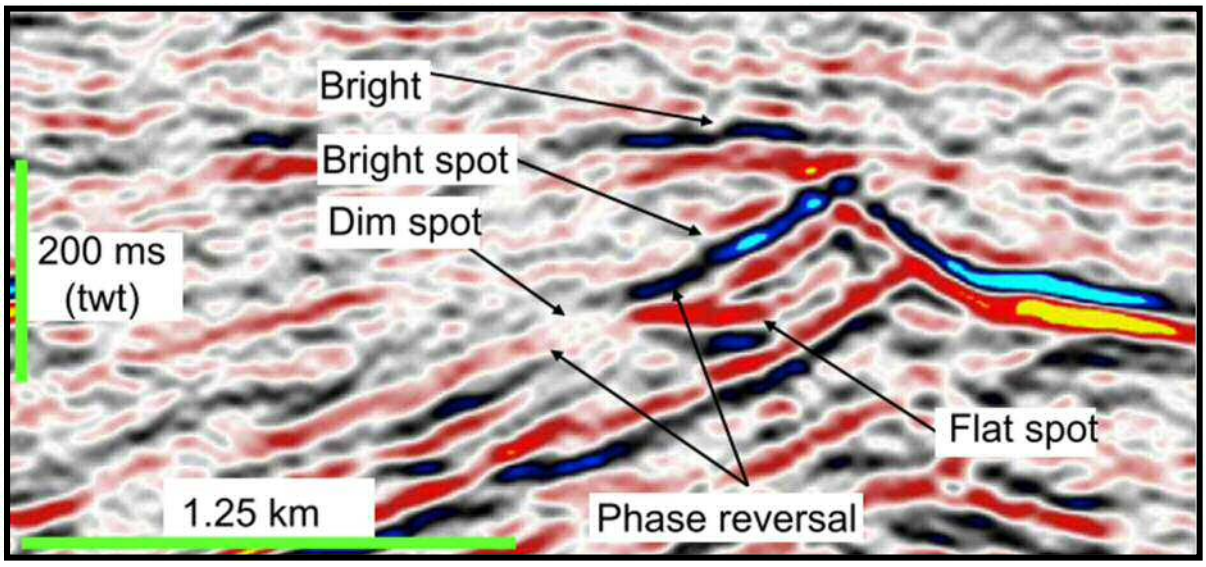

Fig. 1.6. Summary of direct hydrocarbon indicators: a bright spot, dim spot, flat spot and polarity/phase reversal. After Løseth et al. (2009).

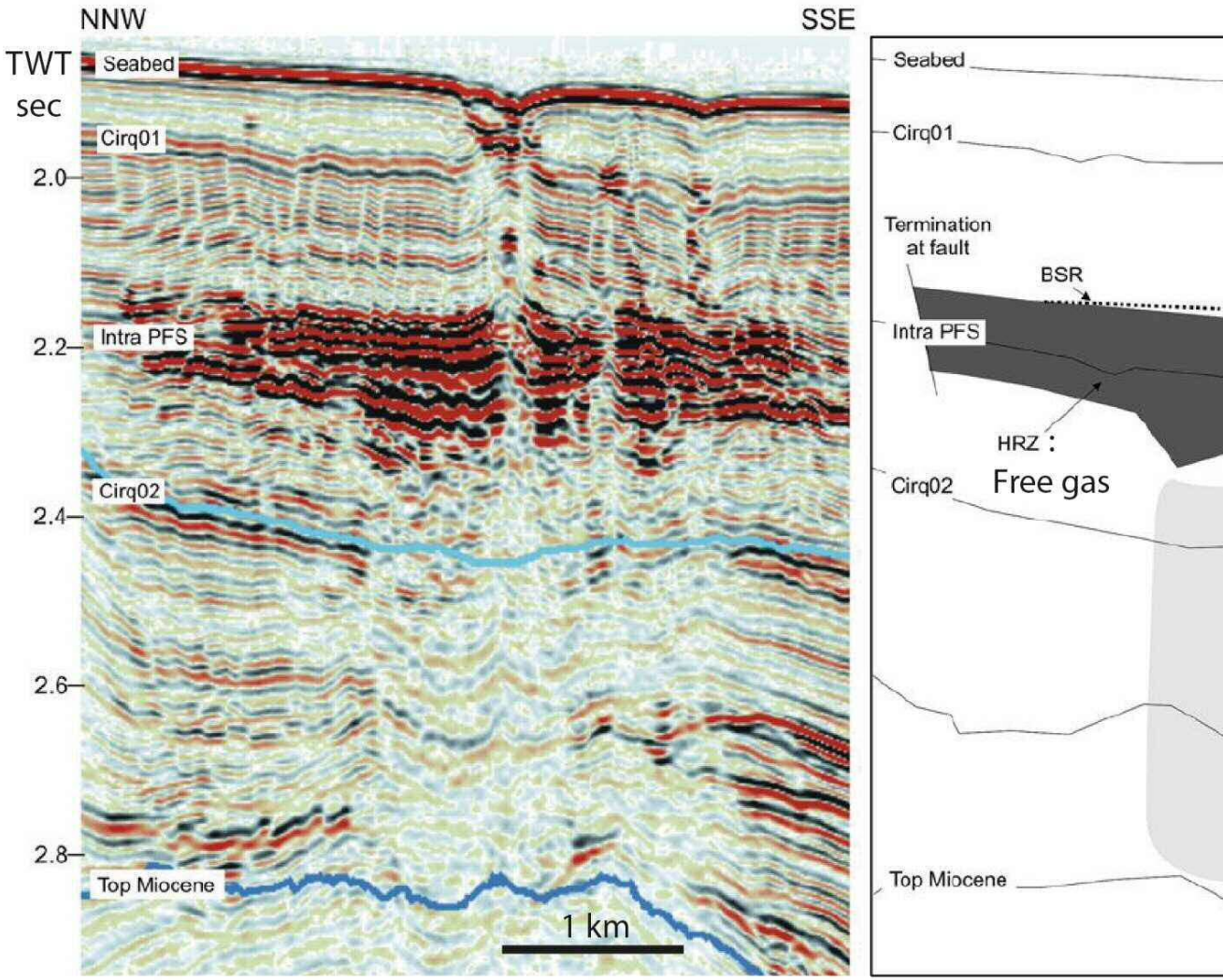

Fig. 1.7. Seismic example (left) and sketch (right) of a bottom simulating reflector (BSR) corresponding to the ba
Lower Congo Basin, offshore Angola. The high reflectivity zone (HRZ) below the BSR was interpreted to indicate
Huuse, 2011).

often cutting across strata reflections (Jackson, 2004).

1.2.7 Diagenetic fronts: Opal A-CT transition

The Opal A-CT transition occurs during early diagenesis in sediments that are mainly composed of diatom frustules and radiolarian tests, such as deep-marine mudstones. The form of silica is Opal A, which, during diagenesis, is dissolved and reprecipitated as Opal-CT, and with further burial, as quartz (Berndt et al., 2004; Davies and Cartwright, 2002; Neagu et al., 2010). The resulting strata containing recrystalised Opal-CT has a greater impedance contrast and results in a high-amplitude, hard seismic reflection that is generally parallel to the sea floor reflection and often cross-cuts host seismic reflections (Fig. 1.8a) (Neagu et al., 2010).

1.2.8 Polygonal fault systems

Polygonal fault systems are networks of non-tectonic normal faults, often tier-bound, that are formed during the rapid burial and compaction of thick mudstone units (Cartwright, 2011; Cartwright and Dewhurst, 1998). Theories explaining their formation include dewatering and volumetric contraction of overpressured clay-rich layers, or diagenesis of clay-rich sediments which leads to shear failure under low confining stresses (Cartwright, 2011). Polygonal faults are so called due to their polygonal distribution in plan view, and may act as fluid migration pathways, as evidenced by pockmarks located stratigraphically above the triple-junction of polygonal faults (Gay et al., 2004). Alternatively, as polygonal faults are predominantly found in shale units, these may still be sealing (Cartwright et al., 2007). Polygonal faults have also been observed in areas with diagenetic boundaries such as the Opal A-CT boundary (Fig. 1.8b, c).

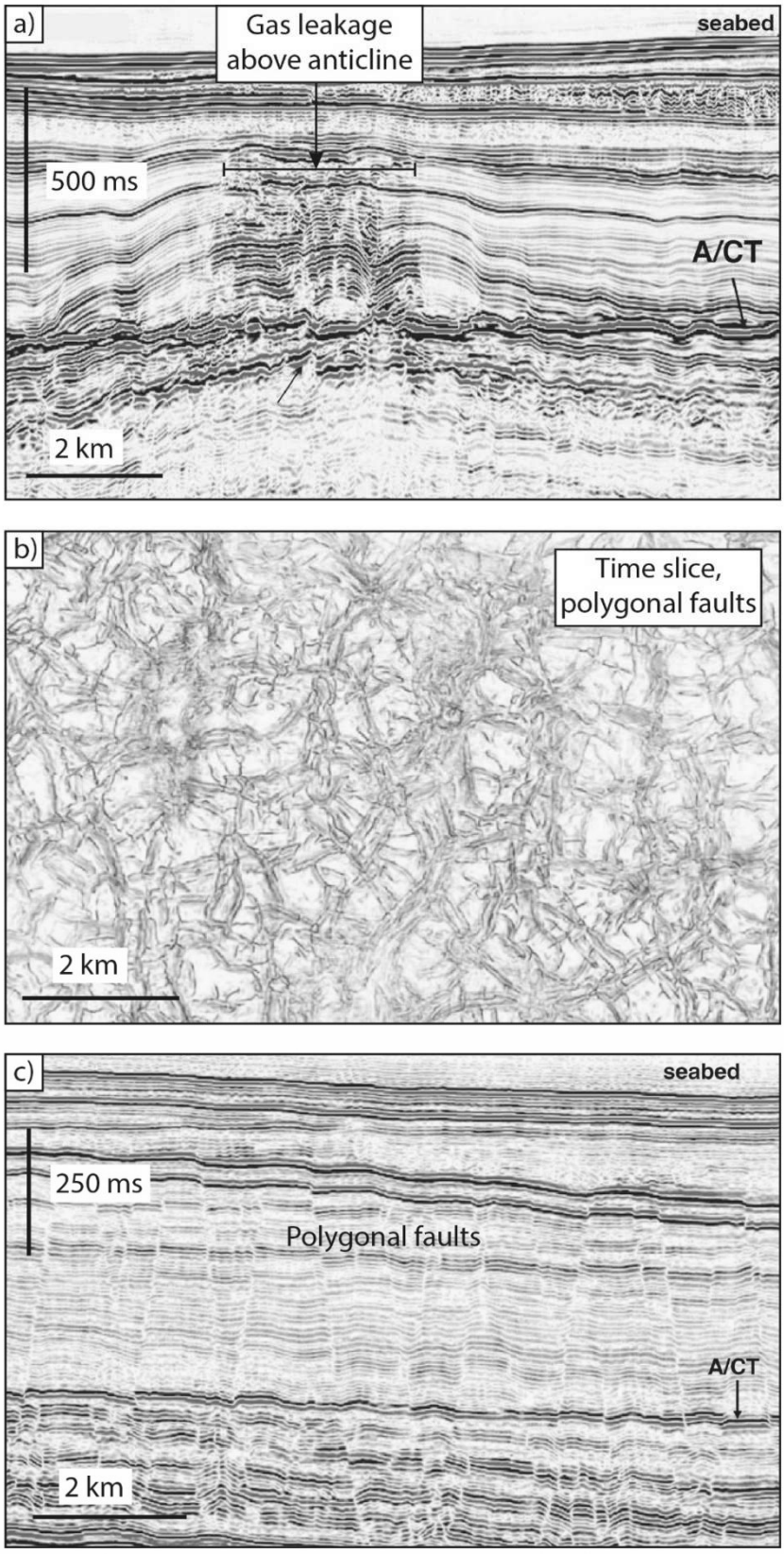

Fig. 1.8. a) Seismic profile example of an Opal A-CT phase boundary, cross-cutting seismic reflections across a large anticlinal trap with extensive gas leakage. b) Time slice showing the plan-view of polygonal faults. c) Seismic profile showing polygonal faults and an Opal A-CT phase boundary from offshore mid-Norway. After Cartwright et al., (2007).

1.3 Stress states and overpressure in rocks

In this section, a brief overview of stress states, brittle rock failure and overpressure is given, as the focused fluid escape which forms features including pipes, pockmarks, mud volcanoes and hydrothermal vent complexes described in the previous section is related to overpressure build up and fracturing of the overburden.

1.3.1 Brittle rock failure and Mohr circles

Anderson (1905) described how faults or fractures will form in relation to the orientations of three perpendicular principal stresses, where one stress is vertical (σ_v) and the other two are horizontal ($\sigma_H > \sigma_h$). Three basic cases were presented: normal faulting occurs when the vertical stress is greater than both of the principal horizontal stresses; reverse faulting occurs when both the maximum and minimum principal horizontal stresses are greater than the vertical stress; and strike slip faulting occurs when the maximum horizontal stress is greater than the vertical stress, which is greater than the minimum horizontal stress. Fig. 1.9 shows these three stress regimes schematically. Yet, it is rare for these end members to exist. Rather, a combination of strike-slip and normal or reverse faulting actually occurs, known as oblique slip. When $\sigma_v = \sigma_H > \sigma_h$, normal-oblique slip occurs, whereas when $\sigma_H > \sigma_v = \sigma_h$, reverse-oblique slip occurs (Bott, 1959). Oblique-slip faulting therefore has a component of dip-slip and strike-slip movement; oblique-slip faulting typically occurs when existing faults are reactivated, especially when these faults have been rotated since initial formation (Bott, 1959).

During burial, the magnitude of vertical stress, or average lithostatic pressure , will increase according to Equation 1.1:

Equation 1.1

where ρ is the density of the rock, g is gravitational acceleration and h is the height, or thickness of the overburden (Jaeger and Cook, 1979). The lithostatic pressure is for a completely solid rock and does not account for pore space filled with fluids. Hydrostatic pressure is the pressure of a column of water, and the pore fluid in a rock is at hydrostatic pressure if it is connected to the surface by a network of interconnected pores. As a rock compacts, pores become smaller and fluid is squeezed out, however, if fluids are unable to escape or the rate of compaction surpasses the rate of fluid escape, the pore-fluid pressure will increase above hydrostatic levels – this is known as overpressure (Osborne and Swarbrick, 1997).

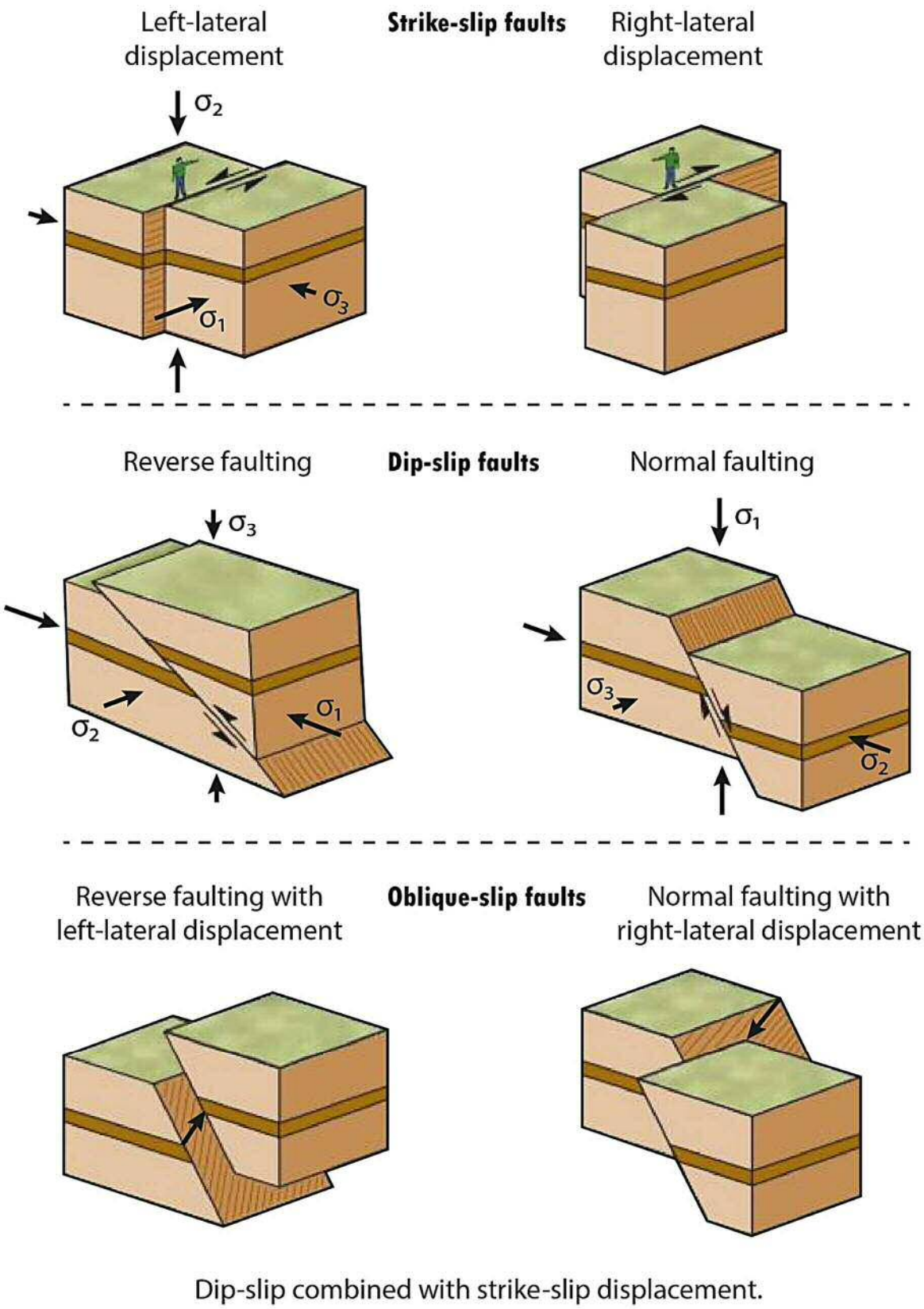

Fig. 1.9. Anderson fault types: strike-slip, normal and reverse faulting, as well as oblique-slip faults. For normal faults, the greatest principal compressive stress is vertical; for strike-slip, vertical stress is intermediate, and for reverse faults, vertical stress is the minimum principal compressive stress. Modified after Marshak (2016).

Hence, the formation pressure, which takes into account this pore-fluid pressure, generally lies in between the hydrostatic and lithostatic pressure gradients on a pressure-depth plot (Fig. 1.10). The pore-fluid pressure ( ) is the pressure exerted by the pore fluids in between the grains of rock: the greater the pore-fluid pressure, the greater the amount of overburden weight that is supported by the fluids, thus the effective vertical stress (decreases and rock failure occurs at a lower effective stress than the average lithostatic stress (Equation 1.2) (Osborne and Swarbrick, 1997; Swarbrick et al., 2005).

Equation 1.2

Failure of a fault depends on the coefficient of friction along the fault (μ), the tensile strength of the rock (T), the shear stress (τ), maximum and minimum stresses (σ_1 and σ_3, respectively), the angle (θ) between the normal of the fault plane and σ_1, and finally, the pore-fluid pressure, P_f. Mohr circles show graphically the scenario for when a rock 'fails' along a fault of a given angle δ to the vertical (i.e. 90-θ) (Fig. 1.11). The greater the differential stress – the difference between maximum and minimum compressive stresses – the larger the Mohr circle (Streit and Hillis, 2004). For a fault to form and slip, the shear stress must be greater than the frictional resistance to shear, in addition to the cohesive strength of the rock, C (Morris et al., 2016). The stress conditions required for shear failure are given by the linear Coulomb failure envelope (Equation 1.3) (Jaeger et al., 2007):

Equation 1.3

where σ_n is the normal stress experienced on the slip surface. Jaeger and Cook (1979) determined that the coefficient of internal friction generally lies between 0.5 and 1.0 (Sibson, 1998). The condition for formation of tensile fractures is given by the parabolic Griffith failure criterion, normalized here to tensile strength, T (Griffith, 1924):

Equation 1.4

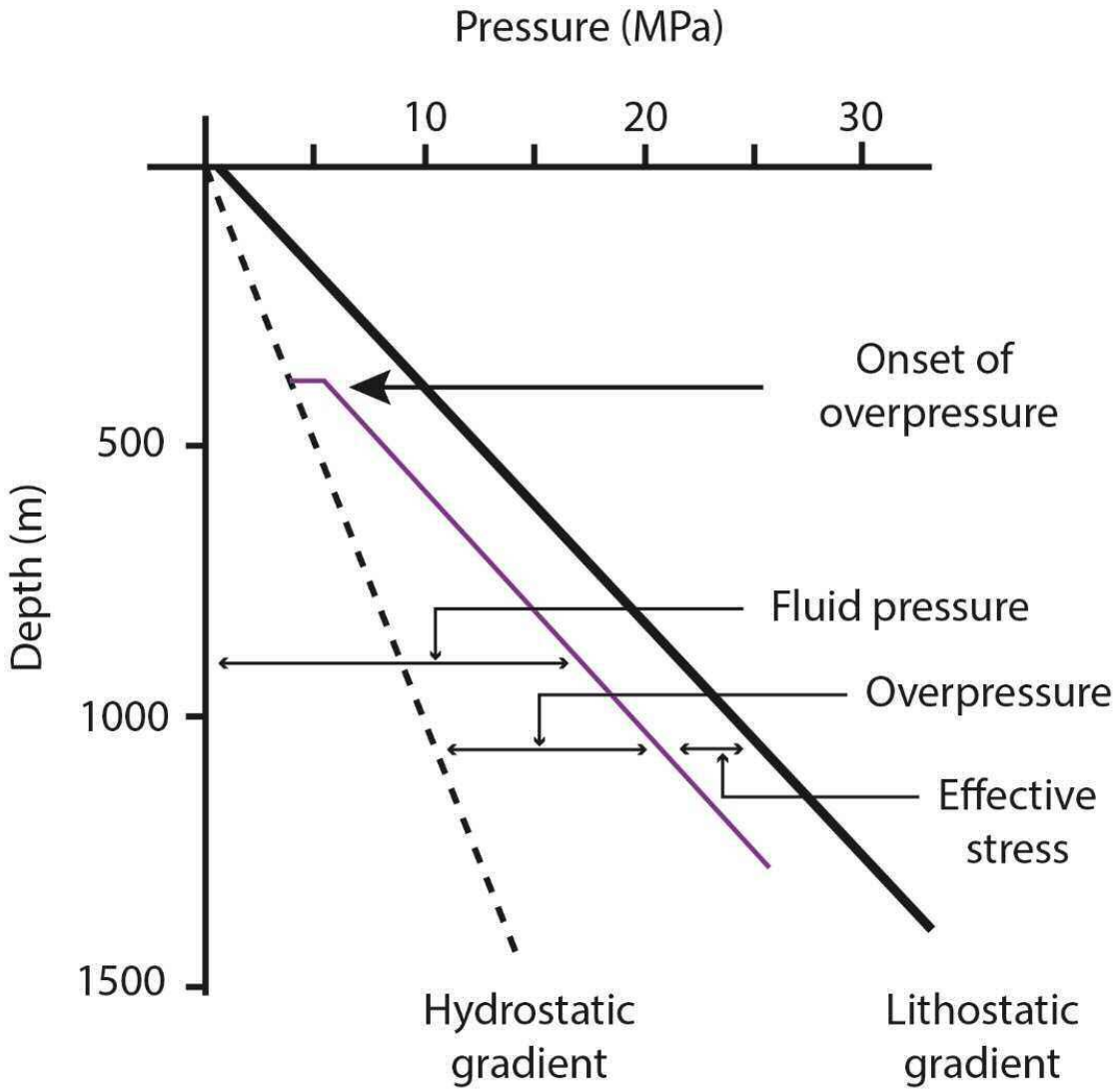

Fig. 1.10. Pressure-depth plot showing the lithostatic and hydrostatic pressure gradients and hypothetical pore-fluid pressure with depth. As the pore-fluid pressure increases above hydrostatic pressure, the formation is said to be overpressured. Modified from Jolly and Lonergan (2002).

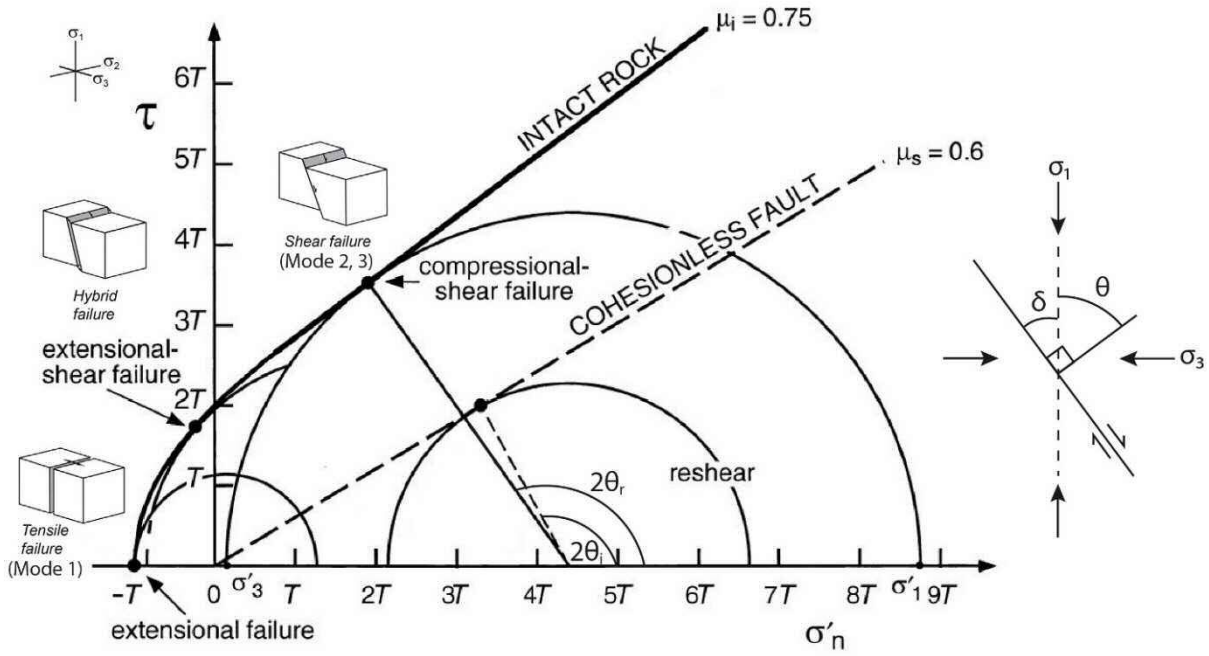

Fig. 1.11. Generic Mohr diagram illustrating the composite Coulomb-Griffith failure envelope for an intact rock, normalized to tensile strength, T and with a coefficient of internal friction, $\mu_i = 0.75$ in the compressional field. A reshear failure envelope for cohesionless faults with $\mu_s = 0.6$ is also indicated. Two examples of Mohr circles are shown for different failure modes of an intact rock, or re-shear of an optimally oriented existing fault. Modified after Sibson (1998) and Ferrill et al. (2017).

Equation 1.4 predicts that shear strength is when effective normal stress is zero. When pore fluid pressures increase, the Mohr circle shifts to the left and failure occurs when the Mohr circle crosses the combined Coulomb-Griffith failure envelope. According to Andersonian stress states, in a homogeneous crust with typical values of internal friction, faults develop at ~ 30° to σ_1; hence, end-member normal faults should dip at ~60°, thrust faults at ~30° and strike-slip faults at ~90° to the horizontal (Sibson, 1985).

The type of brittle failure that occurs in a rock depends on the local stress regime (Fig. 1.11). When the differential stress is greater than 5.66 times the tensile strength of the rock and the Mohr circle crosses the failure envelope in the compressional field (where effective normal stress is greater than zero), compressional shear failure will occur (Sibson, 1998, 2000). Where differential stress is less than four (4) times the tensile strength, extensional (tensile) failure occurs, and if differential stress is between four (4) and 5.66 times the tensile strength, extensional-shear failure occurs (Sibson, 1998, 2000). Tensile fracturing, that is, opening of a fracture in the direction perpendicular to the maximum stress, is also known as 'mode 1 failure', whilst shear failure parallel to the plane of the fracture can occur in-plane or out-of-plane (e.g. Ferrill and Morris, 2003; Hancock, 1985; Kettermann and Urai, 2015) (failure modes 2 and 3, respectively, Fig. 1.11).

Although, it is often the case that mixed-mode failure occurs regardless of the stress regime, particularly on a micro-scale. Hill (1977) and Sibson (1996, 2000) described a 'fracture mesh' within a top seal, which forms in response to the infiltration of pressurised fluids into stressed heterogeneous crust and results in a range of brittle structures that are differently oriented and become interlinked into a mesh-like structure (Fig. 1.12a). The overall stress regime will impact the orientation of the fracture mesh, but ultimately, a combination of extensional and shear failure may occur within the fracture mesh (Fig. 1.12b). These mesh structures act as high permeability pathways for fluid flow (Sibson, 1998).

1.3.2 Mechanisms generating overpressure

Osborne and Swarbrick (1997) summarised the mechanisms which generate overpressure in sedimentary rocks. They comprise: increase of compressive stress; changes in the volume of the pore fluid or rock matrix; and fluid migration or buoyancy. An increase in compressive stress occurs as sediments are buried. When the rate of pore-fluid expulsion is slower than the rate of burial, this results in disequilibrium compaction and overpressure increases, particularly in low-permeability sediments (Swarbrick and Osborne, 1998). In addition, disequilibrium compaction occurs when there is a difference in the rate of fluid escape

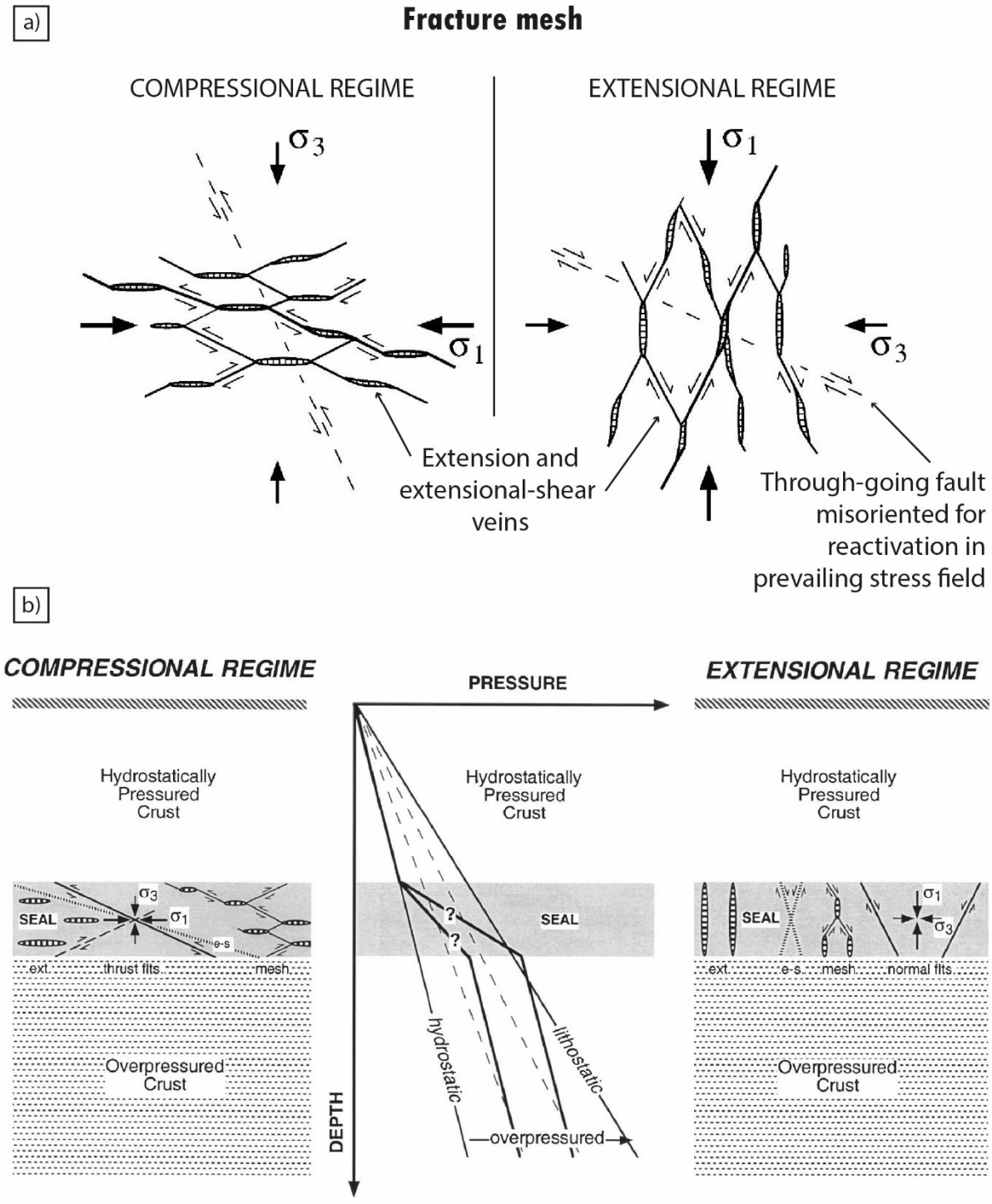

Fig. 1.12. a) Schematic representation of fault-fracture meshes in compressional and extensional regimes. Modified after Hill (1977) and Sibson (2000). b) Hypothetical pressure-depth plot across a seal (centre), showing that brittle faults, fractures and fracture mesh structures in both compressional and extensional regimes provide potential fluid leakage pathways across a low-permeability seal (ext = hydraulic extension fracture; e-s = extensional-shear fracture; flts = faults). Modified after Sibson (2003).

and, therefore, compaction between two rocks; for example when sandstone units are encased in mudstones and pore fluids in the sand are unable to escape through the shales, the sandstones become overpressured (Osborne and Swarbrick, 1997). Yardley and Swarbrick (2000) also demonstrated that overpressures can be transferred laterally along slightly inclined reservoirs, such as to structural crests.

Fluid-expansion mechanisms include the maturation of kerogen to gas, the release of water during clay diagenesis (e.g., during smectite to illite transformation), and the expansion of fluids due to higher temperatures (Barker, 1990; Perry and Hower, 1972; Tingay et al., 2007). Furthermore, heating of mudstones can lead to clay mineral dehydration, releasing H_2O, and organic matter breaks down to CO_2 and CH_4, contributing to overpressure generation if the fluids are unable to escape through the pore network (Svensen et al., 2004; Aarnes, et al., 2011; Kjoberg et al., 2017). Diagenesis also increases the rock matrix volume, for example, during early burial of biosiliceous sediments, Opal-A converts to Opal-CT, which results in a decrease in porosity as the crystal structure of Opal-CT takes up more pore space than Opal-A, resulting in an increase in overpressure (Chaika and Dvorkin, 2000; Neagu et al., 2010).

1.4 Salt tectonics

1.4.1 Salt structures in sedimentary basins

Large salt structures and associated faults are considered key fluid-focusing structures in salt basins. Jackson and Hudec (2017) discussed at least five (5) lines of evidence which suggest that the flanks of salt structures can act as fluid migration conduits: i) fluid-escape features such as pockmarks on the sea floor above diapirs; ii) shallow-gas anomalies clustered in stratigraphy above diapirs; iii) pore-fluid geochemical anomalies near diapirs; iv) patterns of cementation near diapirs, and v) hydrocarbon distribution adjacent to salt bodies. Salt diapirism may occur by extension, erosion, or uplift of the overburden, or by overthrusting of the salt. Once salt reaches the surface, it can continue rising by passive diapirism, where the diapir grows as sediments accumulate around it (Hudec and Jackson, 2007). Salt thickness is a key control on the structural style (Fig. 1.13) and whether the overburden is decoupled from the basement or not.

Salt diapirs form effective fluid-flow pathways because rising diapirs lift, rotate, fold and fracture rocks above and adjacent to the salt. Connected fractures provide vertical fluid migration pathways, whilst rotation of reservoirs can create high-relief hydrocarbon traps and,

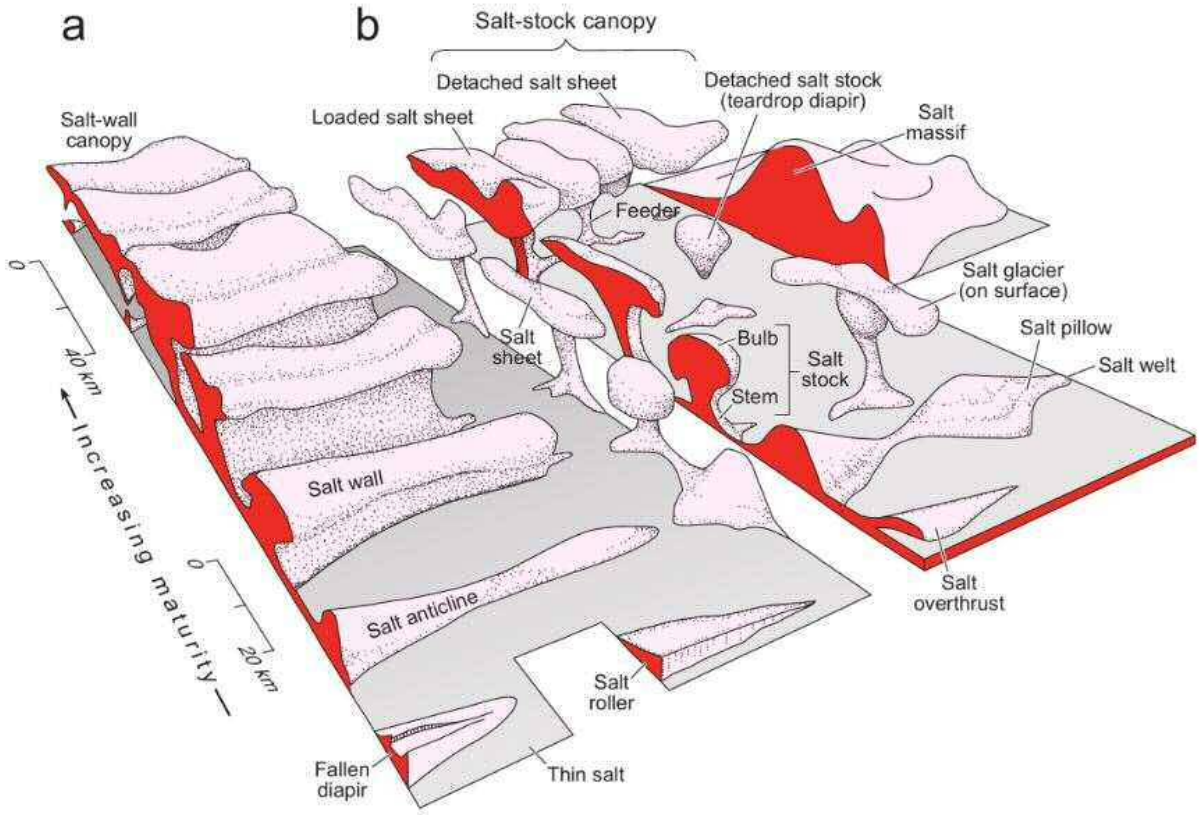

Fig. 1.13. Schematic illustration of different sizes and shapes of salt structures. (a) "Elongated structures rising from line sources. (b) structures rising from point sources". After Jackson and Talbot (1991) and Jackson and Hudec (2017).

if fluids become sufficiently overpressured, seal breach occurs (Jackson and Hudec, 2017). Meanwhile, rock salt itself is generally impermeable and will act as a seal if there is a sufficient trap. In addition, radial and crestal faults typically located above the crests of salt structures may act as fluid-flow pathways towards the surface (Mattos et al., 2016; Stewart, 2006) (Fig. 1.14). These extensional faults are susceptible to reactivation and associated fluid migration when there is further salt movement or salt dissolution, as seen in the Espìrito Santo Basin offshore Brazil, and in the Barents Sea offshore Norway, respectively (Mattos and Alves, 2018; Mattos et al., 2016).

There have been numerous studies on the mechanisms of initiating salt tectonics. Jackson and Vendeville (1994) noted that "several processes have been invoked to initiate salt tectonics: erosional unloading, sedimentary differential loading, large-scale thermal convection of salt, local heat sources such as intrusions, gravity gliding and spreading, sub-salt deformation, and thin-skinned extension and contraction". These mechanisms were reviewed by Jackson and Talbot (1986) and more recently by Hudec and Jackson (2007). They deduced that the primary driving force for salt tectonics is differential loading, which may be generated by gravitational forces, whilst buoyancy due to density differences between salt and the overburden is a secondary force and subordinate to gravity. Salt buoyancy is relatively localised and tends to be restricted to the very deepest parts of the basin, such as in the northern Gulf of Mexico Basin, whilst the relatively thinner salt on platform areas such as the Jæren High – compared to the graben centres in the North Sea – would not promote the growth of tall diapirs (Bishop et al., 1995). The most common structures seen on the Jæren High are salt -walls, -welds, -pillows, and on the edges of East Central Graben, salt diapirs. Meanwhile, the continental slope of the northern Gulf of Mexico contains salt -sheets, -diapirs and -welds, with salt-wall canopies and detached salt structures in deeper parts of the basin.

1.4.2 Regional tilt and gravity sliding

Koyi et al. (1993) stated that a ductile layer, such as salt, can decouple the cover from the basement, allowing for differential thick- and thin-skinned stress states and deformation, whilst some stress can be taken up in the ductile layer itself. In areas where salt is thin or absent, basement structure plays an important role in controlling the structural style of the overlying sediments, as the salt does not decouple the cover from the basement (Penge et al., 1993).

Stewart (2007) summarised the main driving mechanisms of salt tectonics, which

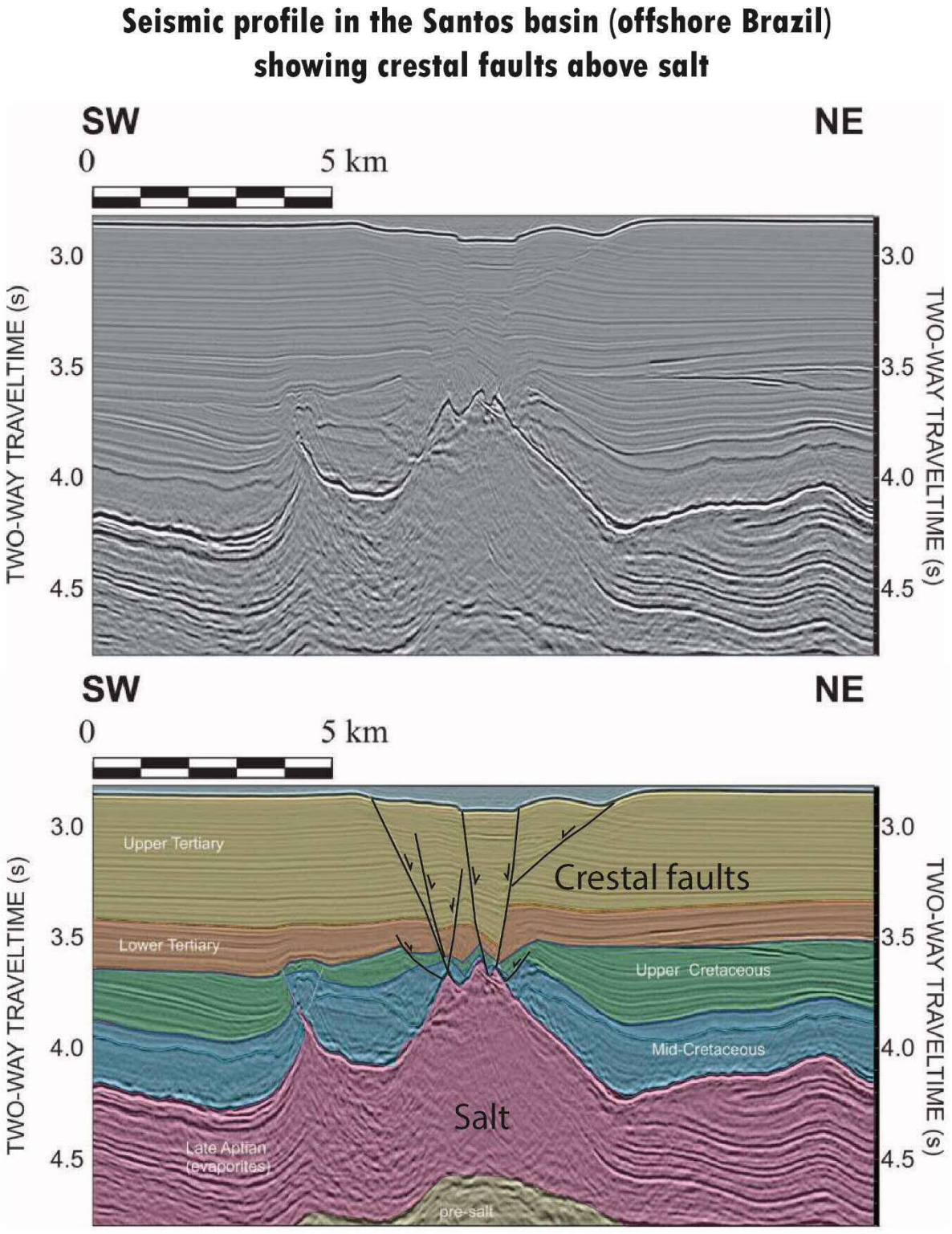

Fig. 1.14. Uninterpreted and interpreted seismic section in the Santos Basin of Aptian evaporites, with extensional crestal faults in the overburden. Modified after Varela and Mohriak (2013).

include regional tilt and associated gravity gliding and gravity spreading. Gravity gliding and spreading are two basic types of deformation driven by near-field stresses (Morley et al., 2011). Gravity gliding is typically associated with passive margins such as the Gulf of Mexico, where an area of up-dip extension is linked with down-dip contractional toe region via a detachment layer (Morley et al., 2011). Thin-skinned gravity slip due to regional tilt leads to elongate, linear salt withdrawal basins (described below, Jackson and Vendeville, 1994; Vendeville and Jackson, 1992), such as those seen in East Breaks, Gulf of Mexico.

Although the North Sea is not a passive margin setting, there is still evidence of tilting from faulting and rotation of major basement fault blocks, initiating gravity-driven, thin-skinned slip of the cover (Jackson and McKenzie, 1983; Stewart et al., 1997).

1.4.3 Salt minibasins, salt welds and turtle-anticline structures

Salt withdrawal basins refer to sediment-filled areas subsiding within a salt body (Hudec et al., 2009; Jackson and Talbot, 1991). Other names have been used to describe these features including 'rim synclines' (Koyi, 1994), 'salt minibasins' (Hudec et al., 2009) and 'pods' (Hodgson et al., 1992). As mentioned above, active tectonics, gravity tectonics, deposition and loading of sediments with greater density than salt, will cause salt to start moving laterally and eventually vertically to form salt walls and salt diapirs, depending on how much salt is available (Hudec and Jackson, 2007; Hudec et al., 2009; Rowan and Weimer, 1998). Salt minibasins are evident in between these salt walls and diapirs, and are found across the world in salt provinces, including the Gulf of Mexico (Worrall and Snelson, 1989), Central North Sea (Stewart and Clark, 1999), Campos and Santos Basins (Demercian et al., 1993), to name a few.

If sufficient sedimentation and loading of salt minibasins and concurrent salt withdrawal occurs, a salt weld may be formed at the base of the salt minibasin. A salt weld is the contact of two sedimentary units that were previously separated by salt (Jackson and Cramez, 1989). Salt welds form through salt withdrawal or salt reduction, which involves a decrease in the cross-sectional area of salt over time (Jackson and Cramez, 1989). Salt reduction can either occur through dissolution, or by flow out of the plane of section, often by faulting.

Wagner and Jackson (2011) used analytical and numerical models to investigate how salt moves by viscous flow during welding. They concluded that where salt flow is restricted, such as beneath a broad, prograding sediment wedge, up to ~50 m of salt can remain in an incomplete weld. Two factors resist salt flow: the strength of overburden and boundary drag along edges of salt body (Hudec and Jackson, 2007). Where salt flow is unrestricted such as beneath a subsiding minibasin, viscous flow can remove almost all salt, leaving as little as 1 m.

This means that for a complete weld to form, the remaining salt must be dissolved (Wagner and Jackson, 2011).

From their terminology, primary welds are those at the autochthonous level (Fig. 1.15). These are not directly associated with faults and more closely resemble those seen on the Jæren High, in the Central North Sea. Meanwhile, secondary welds may occur, for example below detached salt sheets or diapirs, such that rocks which were previously laterally separated by salt, are now close or adjacent to each other – these have been interpreted in the Gulf of Mexico Basin (Jackson and Cramez, 1989).

Salt welds are important in hydrocarbon provinces as they can act as fluid flow pathways from pre-salt source rocks or reservoirs to post-salt reservoirs – several discoveries in the Gulf of Mexico Basin, Campos Basin and offshore Angola rely on migration across welds (Rowan, 2002; Wagner and Jackson, 2011). Plio-Pleistocene reservoirs contain hydrocarbons sourced from sub-weld Mesozoic source rocks in the northern Gulf of Mexico (e.g. McBride et al., 1998). Targeting shallow reservoirs makes drilling for hydrocarbons more economic and reduces risk. Shallower wells are cheaper to drill, and drilling through thick salt layers such as those seen offshore Brazil is associated with high costs and risk, in terms of wellbore stability through the salt (Weijermars et al., 2014), and risk of encountering overpressured carbonates and dolomite stringers within the salt (pers comm., Alves 2017). Salt welds can be detrimental to hydrocarbon provinces if hydrocarbons leak from a deeper reservoir to the surface and potential hydrocarbon fields are lost. However, other exploration targets, for example, below allochthonous salt in the Gulf of Mexico (e.g., Kaskida, Keathley Canyon Block 292/291), rely on welds to seal (Wagner and Jackson, 2011).

Rowan (2002) discussed the factors which control whether or not welds seal, which include: the nature and shape of the weld; lithology and geometry of the units either side of the weld; the presence or absence of weld-parallel slip; and the timing of weld formation with respect to hydrocarbon expulsion and migration. Timing is a key factor: if there is still salt below the minibasin when hydrocarbons migrate, they are likely to be sealed and continue to move up-dip, and the future welds are not breached. This also allows hydrocarbons to accumulate in a sub-salt closure and build up high pore fluid pressures, which may exceed the fracture gradient of the overburden and cause expulsion of hydrocarbons across the weld, once it has formed (Finkbeiner et al., 2001). Another problem is the ability to image a salt weld – there may still be an effective seal present below the limit of seismic resolution. Due to the variety of sub- and supra-weld hydrocarbon discoveries, each case should be examined individually.

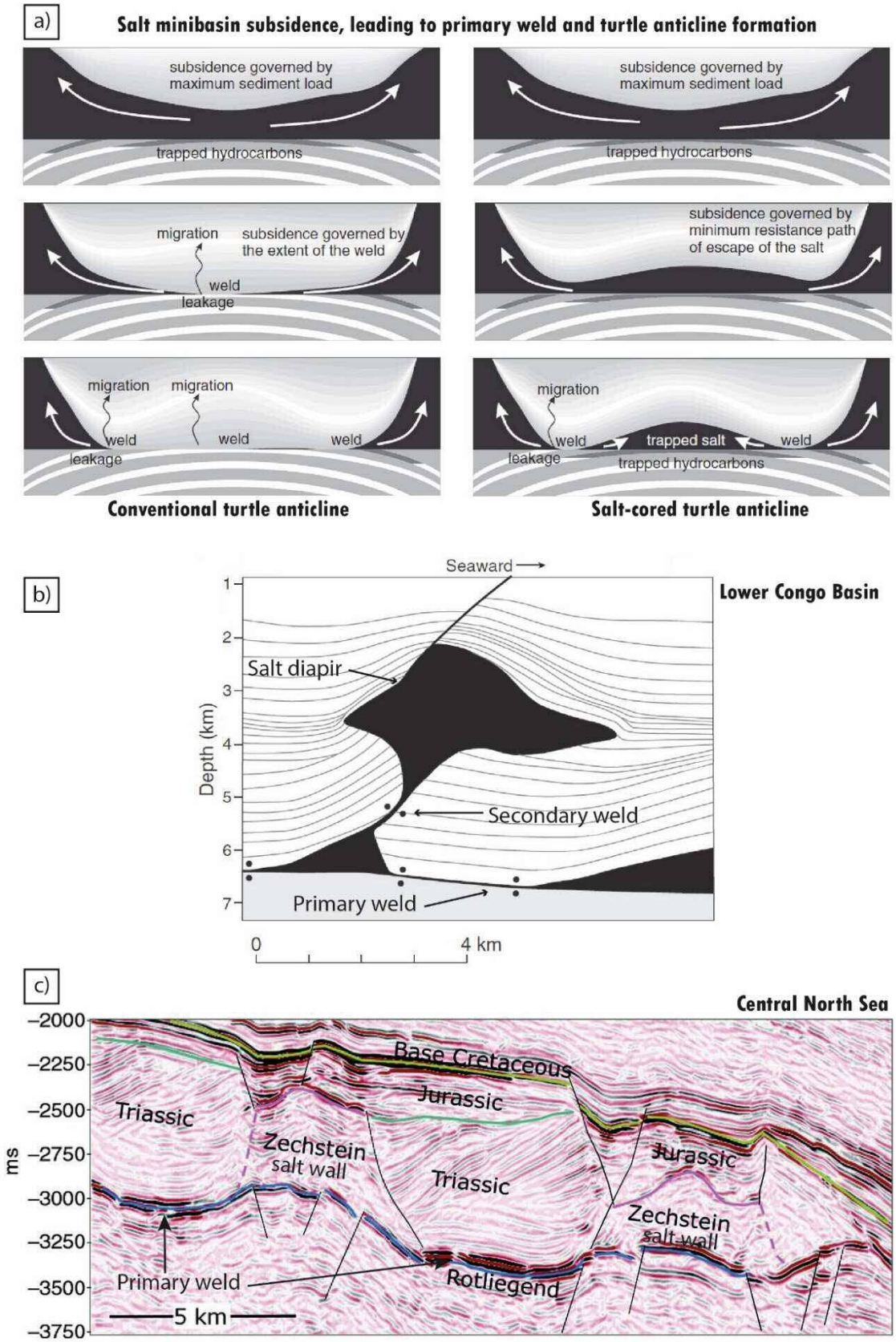

Fig. 1.15. a) Structure and evolution of conventional turtle anticlines (left) and salt-cored turtle anticlines (right). Welds and migration pathways are labelled. After Peel (2014). b) Example of a secondary salt weld produced by lateral shortening of a diapir of Aptian salt, Lower Congo Basin. Modified after Jackson et al. (2008) and Wagner and Jackson (2011). c) Interpreted seismic section showing primary salt welds beneath Triassic minibasins adjacent to Zechstein salt walls in the Central North Sea. Modified after Karlo et al. (2014).

Turtle-anticline structures are associated with salt welds and form as a result of salt evacuation in minibasin provinces. Peel (2014) described the formation of salt withdrawal minibasins. When a weld forms, or salt no longer evacuates from the centre of a minibasin, the minibasin centre stops subsiding and subsidence shifts towards the its flanks, until that part ceases to subside as the weld expands, and so the process continues until salt has evacuated into the adjacent salt wall/diapir. The structure of the minibasin becomes inverted, creating a turtle anticline. Crestal faulting is often associated over the core of the growing turtle.

When determining the relative timing of turtle anticline- and salt weld formation, Peel (2014) showed that for narrow minibasins, welding and turtle inversion can be synchronous, whilst for wider minibasins, the onset of inversion occurs before weld formation – the time difference between inversion and welding increases with increasing width of the minibasin. Narrower basins tend to weld under the central axis, whilst wider minibasins can weld under minibasin flanks, as a lens of salt can become trapped beneath the central core of the turtle anticline (Fig. 1.15a). In terms of assessing hydrocarbon leakage pathways – a trapped salt lens may prevent migration to supra-salt reservoirs, trapping hydrocarbons in sub-salt reservoirs, whilst migration occurs across nearby salt welds (Peel, 2014).

1.5 Thesis layout

This thesis is split into eight chapters. Chapter 1 provides an overview of the thesis and summarises previous literature on fluid flow features and salt tectonics in sedimentary basins. The geological settings of the three study areas are summarised in Chapter 2, including the petroleum systems in each study area. The 3D seismic datasets and main methodologies used are described in detail in Chapter 3, followed by the results of the studies in Chapters 4, 5 and 6. The relationship between buried pockmarks, pipes, amplitude anomalies in Mesozoic stratigraphy and salt welds in the Central North Sea are investigated in Chapter 4. Chapter 5 investigates the correlation between modern pockmarks and mud volcanoes and structure on the slope of the northern Gulf of Mexico Basin. In contrast to Chapters 4 and 5, Chapter 6 investigates intermediate-depth magmatic and associated fluid flow features in the Norwegian Sea. The results are gathered in Chapter 7 to compare and contrast fluid flow pathways in these settings and discuss their implications for reactivation and seal breaching in modern times. The final conclusions are provided in Chapter 8

CHAPTER TWO

Geological settings of the Central North Sea basin, northern Gulf of Mexico basin and mid-Norwegian margin

2 Geological Settings

2.1 Introduction

This chapter reviews the geological settings for the three study areas of the thesis. Each section will describe the location and summarise the structural and stratigraphic evolutions of the basin, focusing on the petroleum systems of each study area.

2.2 Central North Sea Basin

2.2.1 Location of the study area

The Jæren High is a tilted basement fault block forming the eastern shoulder of the East Central Graben, Central North Sea (Fig. 2.1). The study area is located on the Jæren High across Norwegian blocks 7/1; 7/2; 7/4; 7/5; 7/6; 7/7; 7/8; 7/9 and UK block 23. The structural evolution of the Central North Sea is described below.

2.2.2 Structural and stratigraphic evolution of the Central North Sea Basin

2.2.2.1 Paleozoic

The Central Graben forms one of three rift arms of Triassic-Jurassic age, centred 50 km northwest of the Jæren High (Zanella and Coward, 2003). During the Carboniferous, widespread peat, fluvial-deltaic sand and mud, were deposited across a broad plain extending south from the Caledonian Highlands of Scotland and Norway towards the Variscan foreland basin (Glennie and Underhill, 1998). The peat deposits converted to coal during subsequent burial. The Variscan Orogeny followed, which originated the east-west trending Northern and Southern Permian Basins chiefly filled by desert sand and muds of the Rotliegend Group (Glennie, 1998). During the late Permian- earliest Triassic, extension and subsidence of the Permian basins outpaced sedimentation, resulting in sea-level rise and deposition of the evaporitic Zechstein Group of the North Sea (Underhill, 2003) (Fig. 2.2).

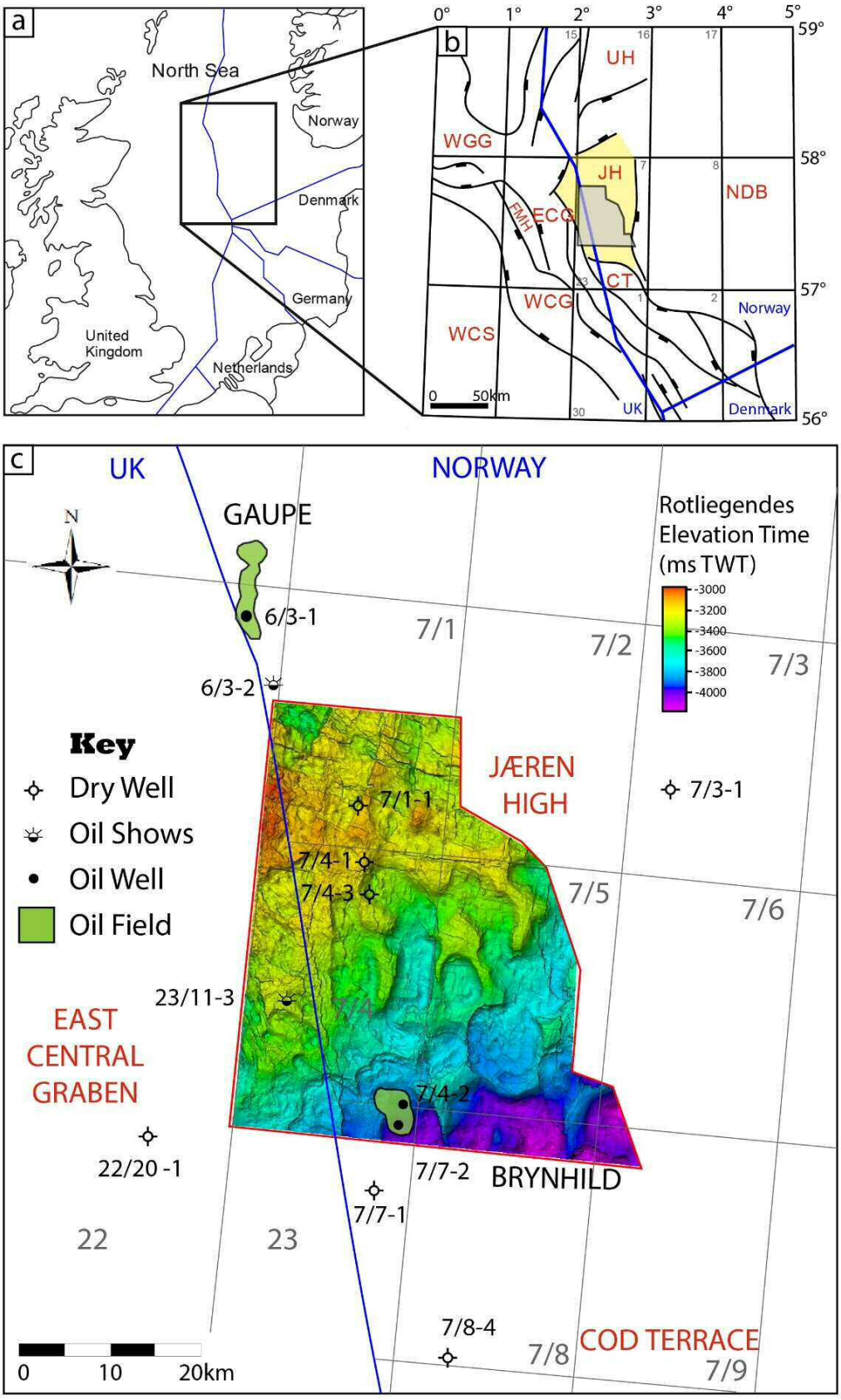

Fig. 2.1. a) Map of North Sea. b) Main faults and structural elements near study area (denoted by the grey polygon); UH = Utsira High; WGG = Witch Ground Graben; FMH = Forties-Montrose High; WCS = West Central Shelf; WCG = West Central Graben; ECG = East Central Graben; CT = Cod Terrace; JH = Jæren High (yellow-shaded area); NDB = Norwegian-Danish Basin. Structure was generated from maps by the Norwegian Petroleum Directorate. c) Two-way-time elevation surface of the Top Rotliegendes. Key exploration wells and fields are labelled.

2.2.2.2 Mesozoic

The region returned to a continental setting in the Triassic, a period characterised by active extension (rifting) in semi-arid, intra-continental basins, and halokinesis in areas with thick salt deposits (Goldsmith et al., 2003). The style of halokinesis on the Jæren High is described by Penge et al. (1993) and Alves and Elliott (2014) as *rift-raft tectonics,* whilst Hodgson et al. (1992) and Høiland et al. (1993) describe it as a 'pod-interpod' model of halokinesis in the study area. Subsiding Triassic minibasins (pods) and adjacent salt walls formed as a result of *rift-rafting*, some of which are 2.3 km high. A positive feedback mechanism ensued until Triassic pods became grounded on the Permian sandstones, forming salt welds. In some cases, the pods were inverted into turtle anticline structures (Karlo et al., 2014). Importantly, grounding of Triassic pods over the Permian strata may have occurred as early as the Middle-Late Triassic on the Jæren High (Smith et al., 1993).

2.2.2.3 Rift-raft tectonics vs. the podology model

Two contrasting models have been proposed to explain the structural relationship seen in seismic data between salt walls and Mesozoic sediment packages on the Jæren High, which are summarised below.

Penge et al. (1993, 1999) developed the rift-raft model to explain the relationship between Mesozoic sediment packages and Zechstein salt in the adjacent East Central Graben. In this model, 'rafts' are described as discrete blocks of thick, undeformed Triassic sedimentary rocks separated from each other by zones of intense faulting, where the interval thins over an elevated salt wall (Penge et al., 1993). The rafts generally overlie salt, although some may ground onto the underlying Rotliegendes, where sufficient salt evacuation has taken place to form a salt weld (Goldsmith et al., 2003). Such a model invokes regional extension following Triassic deposition as the driving mechanism for deformation, thereby implying that salt movement was a passive (rather than active) process, and helped accommodating regional, layer-parallel extension in overlying Triassic brittle rocks (Penge et al., 1993).

The model of Penge (1993; 1999) has been questioned by diverse authors; for example, Spencer (Statoil, Stavanger, Norway) mentioned that "to the east [of the Central North Sea], in the Jæren High area, intra-Triassic halokinesis accompanied sediment deposition in basins, as demonstrated by the presence of cross-cutting seismic reflectors within the Triassic sequences" – see Høiland et al. (1993). It is possible that more than one evolutionary model is viable for the Jæren High considering the lateral variability in structural styles recorded there.

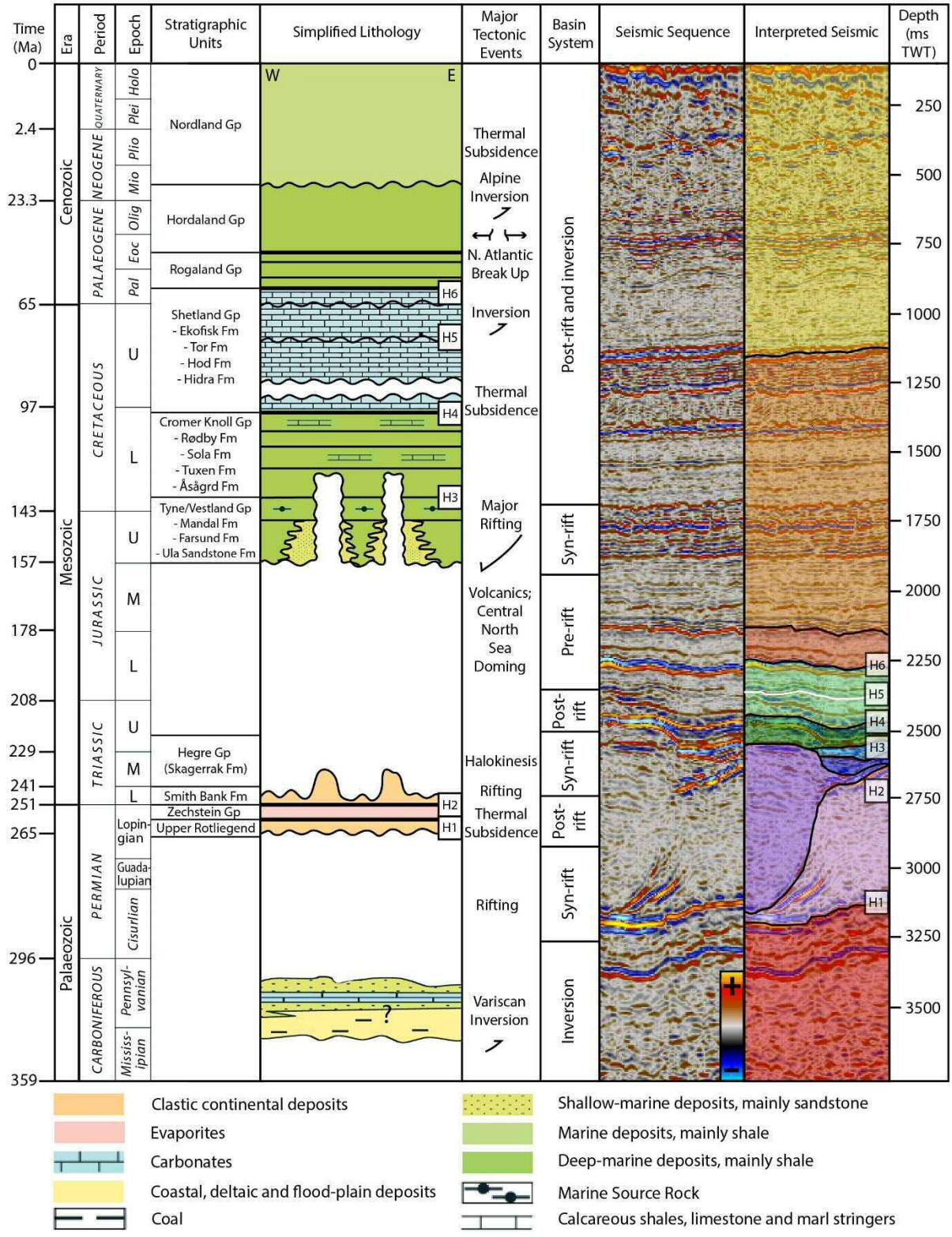

Fig. 2.2. Stratigraphic framework of the Jæren High. Seismically mapped horizons are denoted as H1 – H6. Representative seismic interpretation is shown on the right. Modified after the Norwegian North Sea Lithostratigraphic Chart from the Norwegian Petroleum Directorate.

Equally, the quality of the seismic data previously used is much poorer than the seismic interpreted in this thesis, and interpretations and models are subject to change with improved imaging.

Penge et al. (1999) also emphasised the importance of regional tilting and resultant gravity gliding (Stewart, 2007; Vendeville and Jackson, 1992) in controlling the Mesozoic structure, as well as sedimentary thickness and competence, and salt thickness. Penge et al. (1999) classified the Jæren High as an area with gentle dip and slow strain rate with thick salt, above which predominantly shales of the Smith Bank Formation were deposited which behave in a semi-brittle fashion compared to the more brittle nature of the overlying Skagerrak sandstones. The resulting morphology may appear closer to a pod-interpod-like structure. Bishop et al. (1995) suggested that regional structural dips of 1-3° predominated during the Triassic-Early Cretaceous on the West Central Shelf of the Central North Sea, dip values that are sufficient to allow gravity spreading above a salt layer (Cobbold and Szatmari, 1991; Wu et al., 1990). These dip values are inferred to have been similar to those recorded in the Jæren High area, during the same time period.

The *rift-raft* structural evolution model implies that extension occurred after the deposition of Triassic units, and that salt movement passively responded to extension rather than being active during the Triassic. However, it is widely accepted by several authors that salt mobilization occurred as early as the mid-Triassic, as proved by the syn-tectonic deposition of the Smith Bank and Skagerrak Formations (Hodgson et al., 1992; Smith et al., 1993; Stewart and Clark, 1999; Stewart and Coward, 1995). This alternative evolutionary model is manifested on seismic data as onlapping, diverging and cross-cutting reflectors within the Triassic sediment 'pods' (Høiland et al., 1993).

Hodgson et al., (1992) and Smith et al., (1993) invoked the 'pod-interpod' model to explain many Mesozoic-Permian salt structures in the Central North Sea, including those on the Jæren High. Such a model was later supported by Karlo et al., (2014). In the 'pod-interpod' model, deposition and loading of Triassic continental sediments onto Zechstein salt eventually lead to salt-sediment density inversion at the base of sediment pods, subsequently driving the process of salt withdrawal from minibasins to form adjacent salt walls (Hodgson et al., 1992). Once the sediment pods were grounded and formed salt welds on the Rotliegendes, Triassic minibasin formation and salt wall growth ceased. This process was enhanced by gravitational sliding on a regionally tilted surface and, as such, may have started forming the Jæren High at this time, promoting the dominant north-south orientation of salt walls and intervening depocentres observed at present (Hodgson et al., 1992).

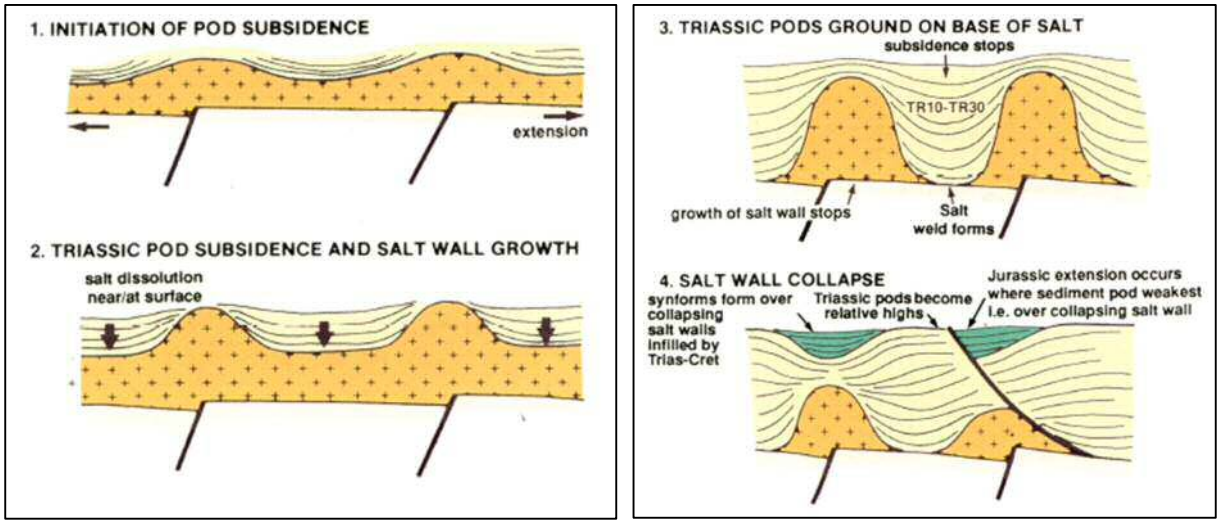

Fig. 2.3. Triassic ‘podology’ model, after Hodgson et al. (1992) and Smith et al. (1993).

It is believed that the grounding of sediment pods occurred as early as the middle-late Triassic in areas such as the Jæren High (Smith et al., 1993).

During the Jurassic, differential erosion and salt dissolution caused partial collapse of the salt walls, creating topographic lows that became infilled with Late Jurassic sediments, whilst the Triassic sediment pods formed 'arches' or relative topographic highs until the Early Cretaceous (Høiland et al., 1993). In some cases, supra-salt minibasins were also fault-bounded due to Jurassic extension, particularly where faults were decoupled from the basement due to the salt décollement (Stewart, 1999a). The thickness of the salt controlled both the maximum thickness of the sediment pods and the wavelength of the salt walls (Hodgson et al., 1992). Fig. 2.3 illustrates the evolution of salt walls and sediment pods.

2.2.2.4 Jurassic to Recent

During the Jurassic and Cretaceous, a mantle hot-spot known as the 'North Sea Dome' was present in the region (Underhill and Partington, 1993). This thermal dome caused regional uplift across the Jæren High and promoted erosion of Mesozoic sequences down to Lower Jurassic and Upper Triassic strata (Erratt et al., 1999). Subsequent collapse of the thermal dome marked the onset of Late Jurassic deposition, commencing at the farthest reaches of the grabens and younging towards the centre (Rattey and Hayward, 1993).

By Late Jurassic time, rifting and transgression outpaced sediment supply to promote the deposition of shallow marine sands and deep-marine shales. This occurred initially in isolated, supra-salt minibasins; then homogeneously across the deepest parts of the Jæren High (Høiland et al., 1993). Consequently, Upper Jurassic units on the Jæren High range in thickness from 0 m to 200 m, whilst in the adjacent East Central Graben they can be up to 1000 m thick (Fraser et al., 2002).

As active rifting propagated towards the North Atlantic, thermal subsidence in the Lower Cretaceous resulted in the drowning of the North Sea rift and widespread deposition of marine sequences of marls, limestones and carbonates (Cromer Knoll Group; Copestake et al., 2003). Clastic units were reintroduced into the basin in the Paleocene (Ahmadi et al., 2003), leading to the deposition of >2 km of strata and the (deep) burial of older rift-related sequences.

2.2.3 Petroleum systems of the Central North Sea

A petroleum system includes the geological elements and processes required for source rock maturation, petroleum generation, subsequent migration and accumulation of hydrocarbons (Magoon, 1989; Magoon and Dow, 1994; McBride et al., 1998).

Relatively few wells have been drilled on the Jæren High compared with the adjacent Central Graben, of which only two (2) penetrate pre-salt strata. The stratigraphy and petroleum systems elements of the Jæren High are summarised in this thesis using the Norwegian North Sea nomenclature from previous studies; they describe the stratigraphy based on borehole data or, instead, by integrating seismic with potential field datasets to infer the presence of stratigraphic units of certain ages (Milton-Worssell et al., 2010).

The main petroleum plays in the Central North Sea revolve around a Jurassic source rock and younger reservoirs and seals. However, the principal petroleum play of the Southern North Sea, sourced by Carboniferous coal measures beneath Rotliegendes sands and Zechstein salt, may also be present in the Central North Sea.

2.2.3.1 Carboniferous source rock

The source rock of the many gas fields in the Southern North Sea consists of the widely distributed Westphalian coal measures (Leeder and Hardman, 1990; Ziegler, 1990). It is thought that the Westphalian Coal Measures were eroded from the Jæren High and only a few of the Visean Coal Measures have been preserved in this area (Milton-Worssell et al., 2010). However, as no wells have penetrated these Visean strata, uncertainty still exists about the presence of coal measures right below the Jæren High.

The main reservoir unit in the Jæren High occurs within the Permian Rotliegend Group, the ‘Rotliegend Leman Sandstone Formation’ (Rhys, 1974), which primarily consists of cross-bedded, dune sandstones deposited in an aeolian environment with interbedded wadi deposits (Glennie, 1998). This reservoir is located at the top of rifted basement rocks, above which the Zechstein Group was deposited to form a competent seal. The Zechstein Group consists of six sedimentary cycles (Z1-Z6) that reflect deposition in response to alternating marine transgression (and water recharge) of the Permian Basin, and subsequent regression (and evaporation) of confined sub-basins. These six sedimentary cycles consist of carbonates, dolomites, anhydrites and halite respectively from the basin margin to the basin centre (Underhill, 2003).

2.2.3.2 Jurassic source rocks

The dominant source rock in the Central North Sea is the Kimmeridge Clay Formation (Kubala et al., 2003). In the Norwegian sector of the North Sea it is called the Mandal Formation and is made of organic-rich marine shales formed during a widespread marine transgression in the Late Jurassic. Burial history models indicate that the Kimmeridge Clay Formation became oil mature during the Late Cretaceous in the East Central Graben and has been gas- and gas-condensate mature since the Oligocene (Kubala et al., 2003). There is no evidence of Lower or Middle Jurassic units in the wells drilled on the Jæren High, although there may be Middle Jurassic fluvial-coastal-plain coal measures (Bryne Formation) in the adjacent Norwegian-Danish Basin or the Central Graben (Fig. 2.1b). Oil and gas fields sourced from Jurassic sources have been found in Mesozoic and Cenozoic reservoirs throughout the North Sea.

2.2.3.3 Triassic reservoirs

The Triassic was dominated by the deposition of terrestrial sandstones and shales, in a semi-arid environment. Syn-sedimentary deposition affected facies distribution due to Zechstein evaporite mobility (Underhill, 2003), with Triassic units forming large pods between growing salt walls. The Smith Bank Formation was deposited during the Early Triassic and consists predominantly of lacustrine shales – the most common Triassic unit seen on the Jæren High. The Skagerrak Formation (Middle-Late Triassic) is relatively poorly documented on the Jæren High, although it may be present at the tops of the Triassic pods. The Skagerrak Formation consists of interbedded fluvial sandstones, floodplain and lacustrine facies. Fluvial sandstones such as those in the Jasmine field have been found to be productive reservoirs in the Central Graben over tilted fault blocks (Archer et al., 2009).

2.2.3.4 Jurassic-Cenozoic reservoirs

Hydrocarbon fields have been discovered in a range of syn- to post-rift reservoirs in the North Sea. The Elgin-Franklin Fields (Lasocki et al., 1999) are examples of where Middle-Upper Jurassic fluvial sandstones are the main reservoirs. Although these may be compartmentalised by floodplain mudstone facies, they prove to be prolific hydrocarbon-bearing sandstones, as seen for example in the billion-barrel Brent Field, trapped by faults in tilted half grabens (Struijk and Green, 1991; Underhill, 1998). Upper Jurassic shallow marine sandstones such as those within the Ula Sandstone Formation are more laterally extensive and are exploited in the Ula Field (Stewart, 1993).

Further drowning of the rift led to the widespread deposition of limestones and chalk in the North Sea. Due to the complex poro-perm properties of carbonates, where tight, these rocks can act as seals, whilst where fractured, carbonates have shown to be prolific reservoirs, such as the Ekofisk Field in the Norwegian sector of the North Sea (Sulak, 1991). Hydrocarbons have been produced from fractured chalk in the Ekofisk- and Tor Formations since 1971, which are separated by a tight carbonate zone (Hermansen et al., 2000).

The reintroduction of deep-marine clastic sedimentation to the North Sea Basin provided additional reservoir facies in Cenozoic strata. Paleocene to Eocene-age turbidites also contain billion-barrel hydrocarbon fields, such as the Forties Field in the North Sea (Hill and Wood, 1980). Turbidite sandstones may be sealed by deep-marine shales in stratigraphic traps, or trapped in anticlines above salt diapirs or in tilted beds juxtaposed against salt diapirs, such as the turbidites of the Pierce Field in the Central North Sea (Birch and Haynes, 2003).

The large variety of stratigraphic units proved to be reservoirs which flow during hydrocarbon production are also potential targets for future carbon capture and storage projects.

2.3 Northern Gulf of Mexico Basin

2.3.1 Location of the study area

The East Breaks area is located within the uppermost continental slope of the northern Gulf of Mexico Basin, 230 km southeast of Houston, Texas (Fig. 2.4). This location marks the start of the renowned salt minibasin province of the Gulf of Mexico. The structural evolution of the Gulf of Mexico Basin is described below.

2.3.2 Structural and stratigraphic framework of the northern Gulf of Mexico

2.3.2.1 Mesozoic evolution

The northwest Gulf of Mexico is dominated by systematic, thermally driven subsidence overprinted by eustatic base-level changes (Watts, 1982; Galloway, 1989). Its generalised stratigraphy is summarised in Fig. 2.5 and Fig. 2.6. In the Late Triassic, the North American plate rifted from Pangaea and a series of grabens and half-grabens were formed, filled

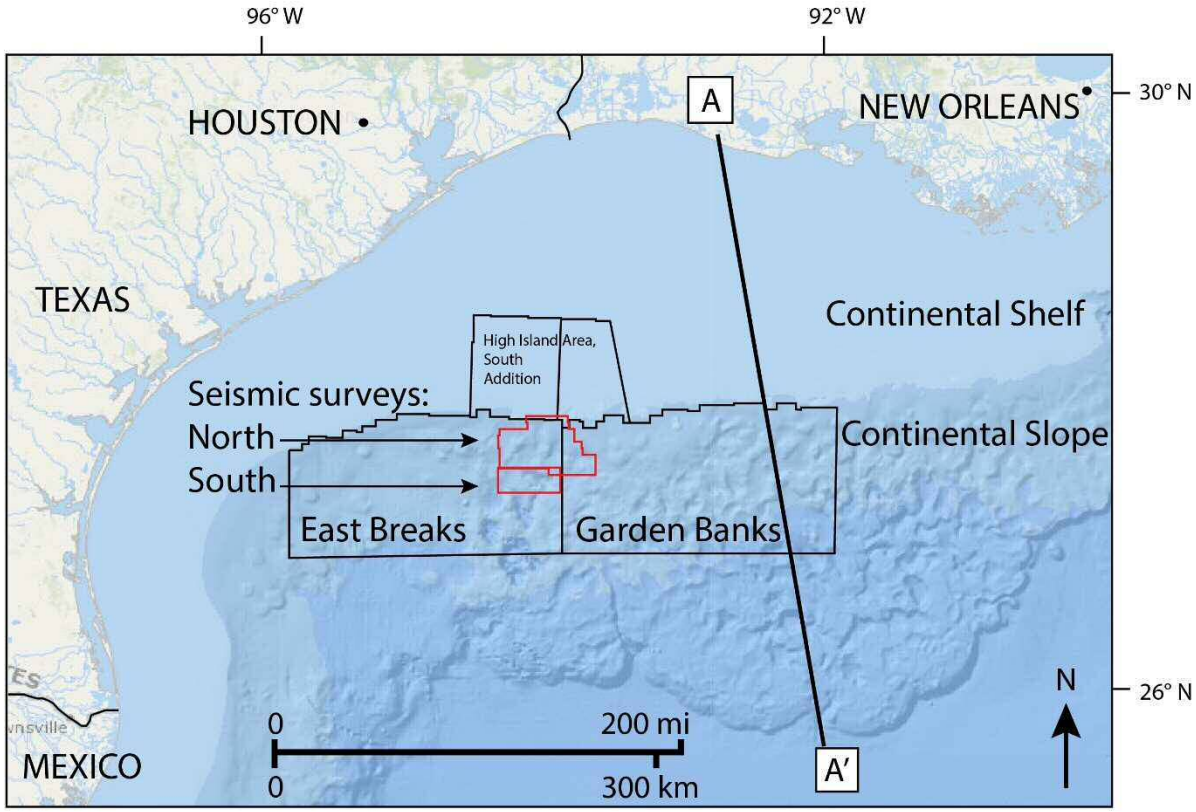

Fig. 2.4. Location map of the study area in the Gulf of Mexico. The two interpreted 3D seismic surveys are outlined in red in the north-eastern corner of East Breaks, northern Gulf of Mexico. The regional line A-A′ is shown in Fig. 2.5.

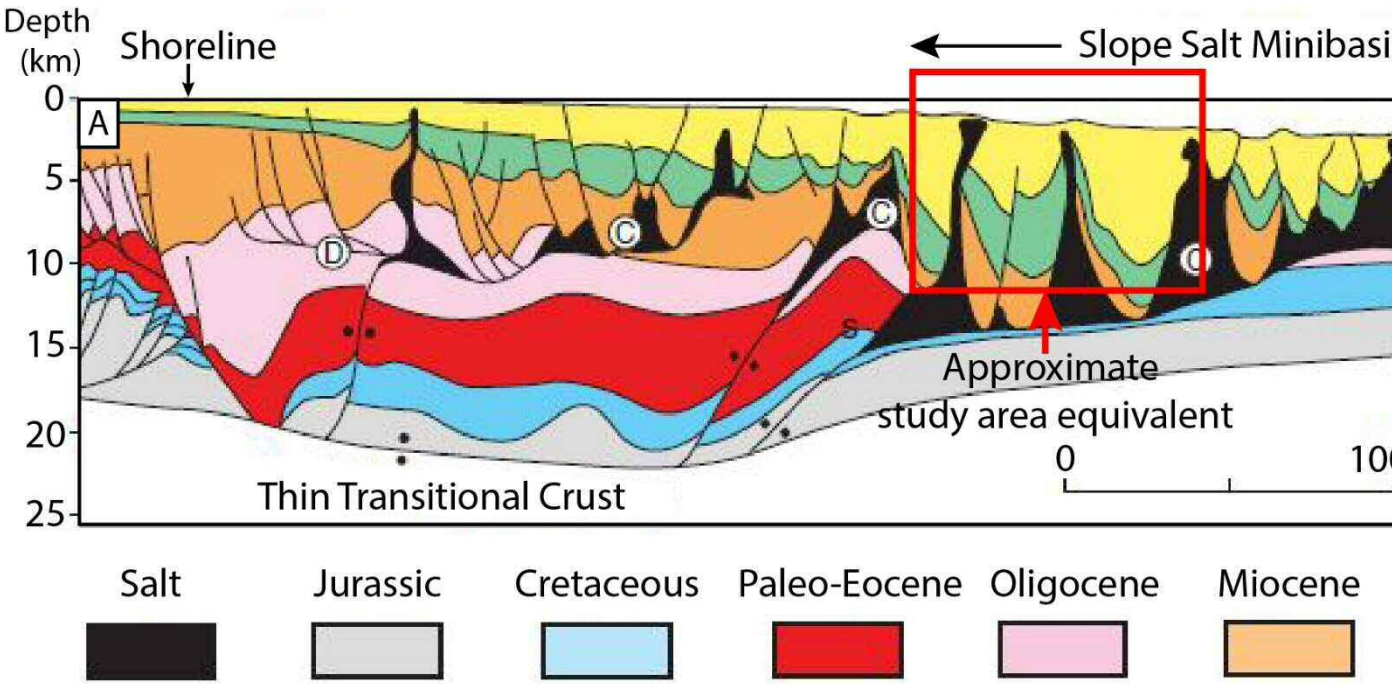

Fig. 2.5. Regional seismic line across the northern Gulf of Mexico. The red box indicates the approximate location of the study area, in Fig. 2.4. Modified from Galloway et al. (2008).

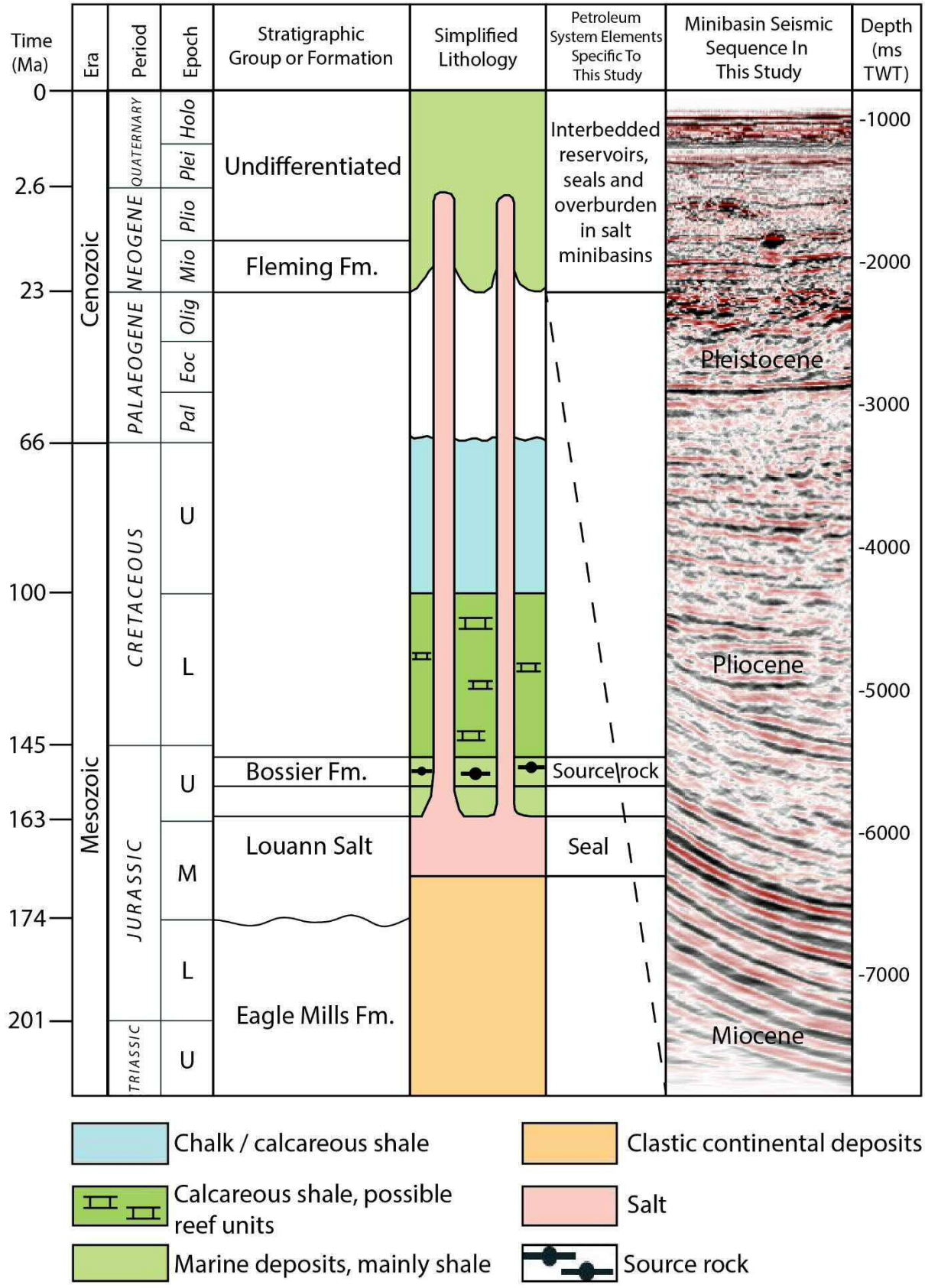

Fig. 2.6. Mesosoic-Cenozoic stratigraphic section of the East Breaks area of the northern Gulf of Mexico coastal plain, with petroleum system elements specific to this study indicated in the figure. Modified from Hackley and Ewing (2010) and Mello and Karner (1996).

with continental red beds and volcanic rocks, known collectively as the Eagle Mills Formation (Salvador, 1987). Deposition of sedimentary units in a coastal plain to shoreface environment followed during an Early Jurassic transgression (Hudec et al., 2013). By the Middle Jurassic, initial connection to the Pacific Ocean formed a semi-restricted basin in which the Louann salt was deposited (Fig. 2.7a). Hudec et al. (2013) estimated that 3 - 4 km of salt was deposited in as little as 2 Ma, after assuming similar depositional rates to thick salt basins in the Mediterranean Sea (Krijgsman et al., 1999) and southeast Brazil (Pietzsch et al., 2018).

Further rifting and extension of the continental crust led to continental breakup, the formation of oceanic crust, and ultimately seafloor spreading during the Late Jurassic, separating the Louann salt basin from the southern Campeche salt basin in Mexico (Bird et al., 2005) (Fig. 2.7c). Post-rift thermal subsidence resulted in the relative deepening of the basin as the connection with the North Atlantic Ocean was being established. This resulted in the widespread deposition of organic-rich, deep-marine shales during the latest Jurassic (Tithonian) (Hood et al., 2002), one of the major source rock intervals in the Gulf of Mexico Basin. Seafloor spreading ended by the earliest Cretaceous (c. 140 Ma), marking the start of the passive-margin phase. This passive-margin structure remained inherent to the Gulf of Mexico Basin until the present day. In contrast to the Jurassic, slow rates of clastic sediment influx generated a largely carbonate depositional system during the Cretaceous (Galloway, 1989).

2.3.2.2 Cenozoic evolution and salt tectonics

During the Paleogene, the Laramide inversion caused uplift of the Sierra Madre Occidental in Mexico and renewed uplift of the Rocky Mountains in North America, phenomena that resulted in the introduction of large volumes of clastics in the Gulf of Mexico via the Rio Grande and Houston Delta Systems (Galloway et al., 2000).

The deposition of thick (8 – 14 km) deep-marine units in the northwest Gulf of Mexico caused flexural loading and gradual steepening at the base of the Louann salt, initiating widespread gravitational tectonics and salt mobility in the region (Galloway, 1989). This led to the development of large-scale structures including salt canopies, allochthonous salt sheets, salt diapirs and salt welds, in between salt minibasin depocenters (e.g. McBride et al., 1998; Rowan et al., 1999). Such salt structures deformed the palaeo-seafloor bathymetry and continue to do so at present, spatially controlling the deposition of younger sediments (Fig. 2.8). Simultaneously, deep burial of the Jurassic (Tithonian) source rock resulted in hydrocarbon generation (Hood et al., 2002).

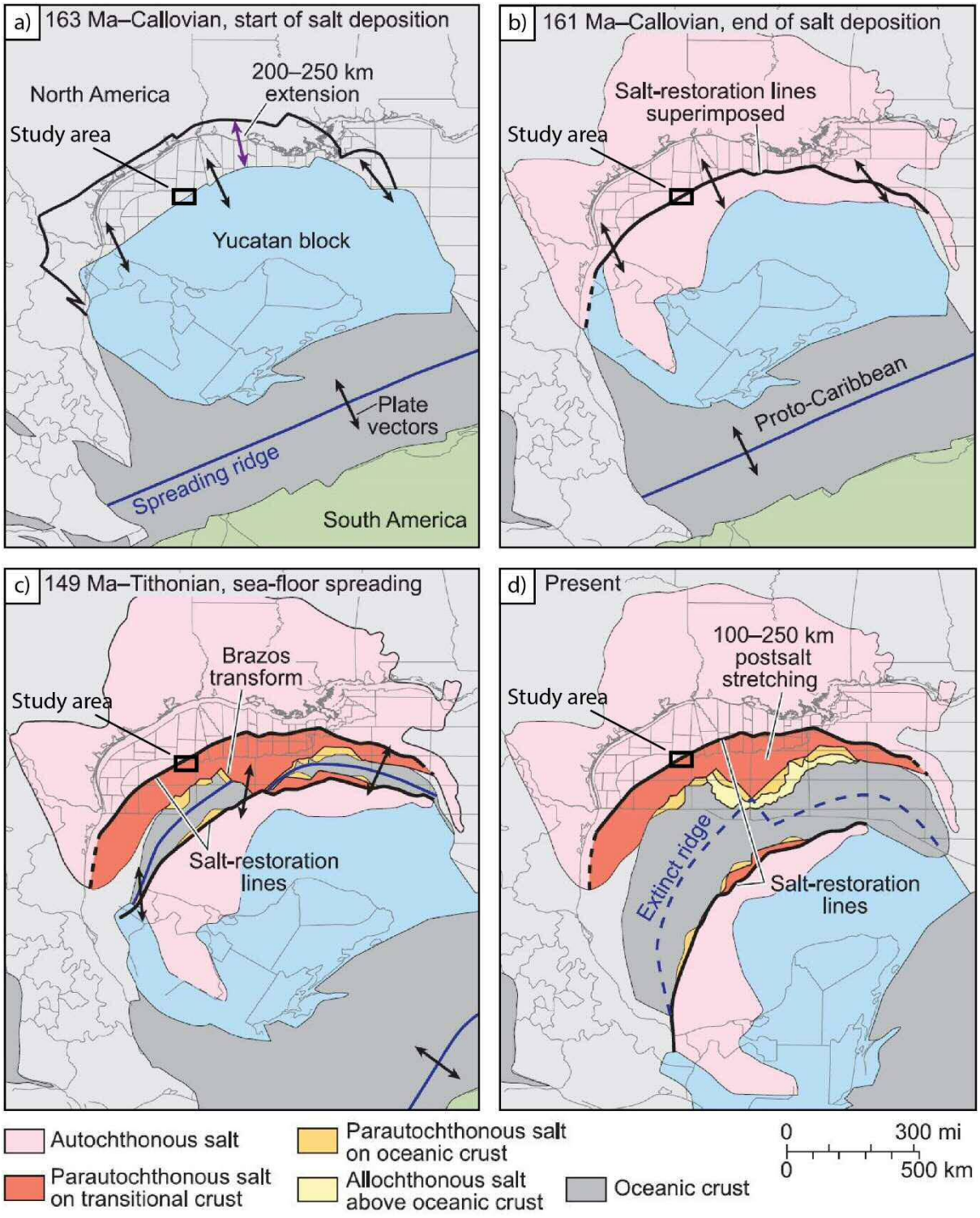

Fig. 2.7. Palaeogeographic reconstruction of the Gulf of Mexico Basin; a) 163 Ma – Start of salt deposition in the Callovian; b) 161 Ma – Callovian, end of salt deposition; c) 149 Ma – Tithonian, seafloor spreading; d) Present day, with study area labelled. Modified from Hudec et al. (2013).

During the Cenozoic, the continental shelf of the Gulf of Mexico prograded ~290 km southwards and accumulated up to 18 genetic sequences (Feng, 1995). These sequences consist of deep-water turbidites confined within canyons, salt minibasins, or sediment deposited as submarine fans on the basin floor. The turbidite intervals, comprising prolific hydrocarbon reservoirs, are intercalated with condensed deep-marine hemipelagic mud, biogenic oozes and reworked transgressive/retrogressive slope facies that form local seal units (Galloway et al., 2000).

2.3.3 Petroleum systems of the northwest Gulf of Mexico

The prolific petroleum prospectivity of the northern Gulf of Mexico Basin owes itself to the occurrence of widespread Upper Jurassic to Lower Cretaceous source rocks, which are buried so deeply that only 26 wells have penetrated them. Nevertheless, the importance of these source rocks is clear at a regional scale as over 226 oil and gas fields and discoveries are located in the northern deep-water (i.e., >457 m water depth) Gulf of Mexico (Weimer et al., 2017). The northern Gulf of Mexico is a vast basin, therefore the focus here is on the north-western East Breaks area.

Two of the major source rocks were deposited during the Oxfordian and Tithonian as organic-rich deep-marine shales (Weimer et al., 2017). The extensive salt seal, the Louann Salt, was deposited at the end of the Middle Jurassic (Callovian-Oxfordian) and became mobile from as early as the Kimmeridgian in the northwest Gulf of Mexico. Allochthonous salt layers and diapirs resulting from salt tectonics controlled the subsequent Cenozoic deposition, forming a variety of hydrocarbon traps (Jackson and Talbot, 1986, 1991; Talbot, 1993).

Reservoirs consist mainly of single to multi-storey, deep-sea channel-fill sands, fans and turbidites ranging in age from Miocene to Pleistocene, sealed by hemipelagic mudstones. These reservoirs are typically located in salt minibasins towards the flanks of salt diapirs (Weimer et al., 2017). Rapid deposition and loading led to overpressured sandstones, which, combined with a low geothermal gradient, inhibited significant chemical and mechanical compaction, resulting in sandstone reservoirs of good quality (McBride et al., 1998). The most common traps in the deep-water northern Gulf of Mexico Basin are three-way closures against a fault or salt flank, and stratigraphic traps. An example of a producing field in East Breaks is called ‘SW Horseshoe’, where hydrocarbons are produced from a late Pliocene sandstone reservoir in a 3-way closure with a fault-bounded trap (Weimer et al., 2017).

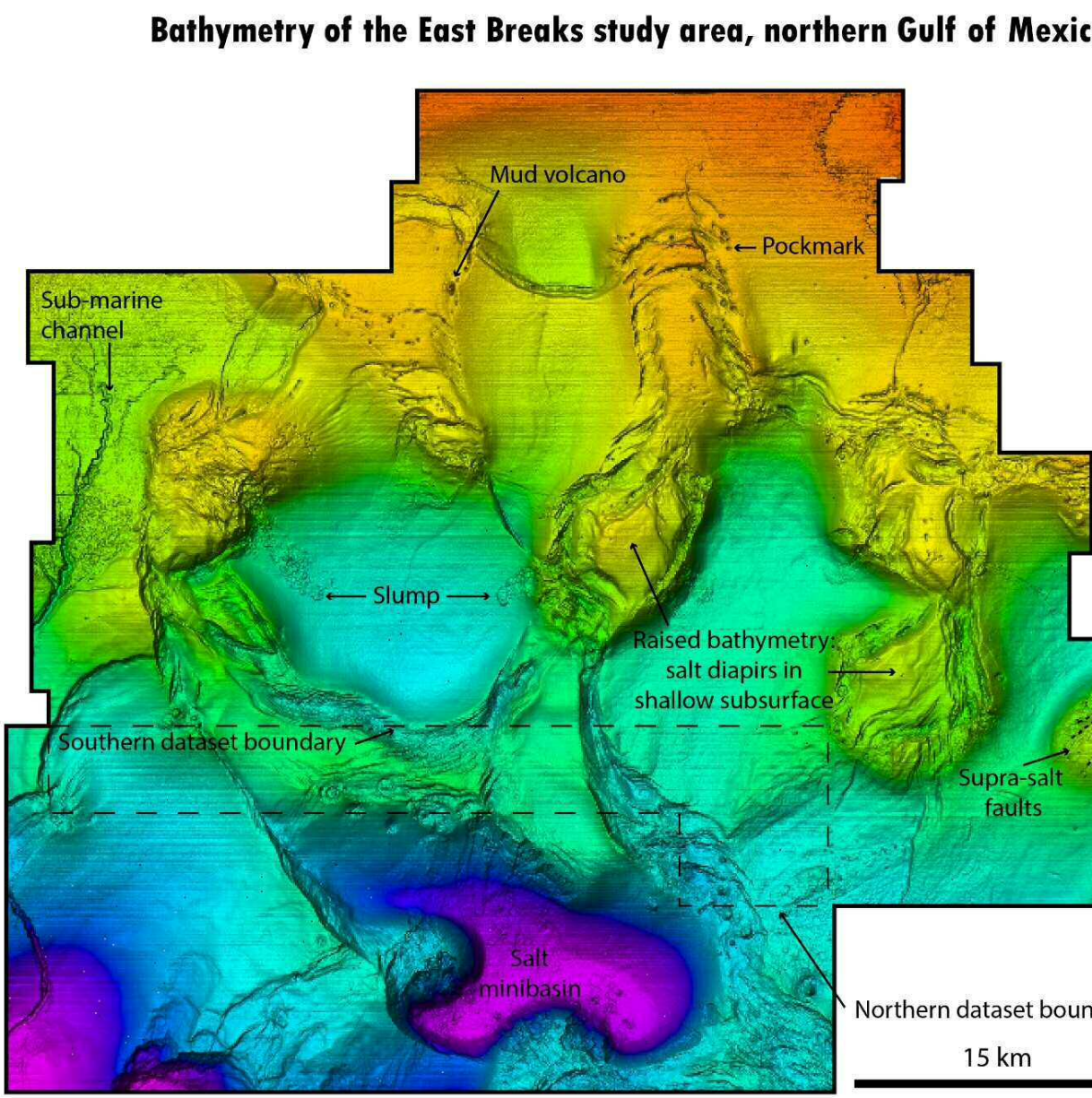

Fig. 2.8. Bathymetric map highlighting main seafloor features in the East Breaks area including pockmarks, mud volcanoes, fa

2.4 Mid-Norwegian Margin

2.4.1 Location of the study area

The Modgunn Arch is a N-S trending Tertiary dome located at the border between the Vøring and Møre Basins on the mid-Norwegian margin, ~370 km west of Trondheim (Fig. 2.9). The study area is on the southern Modgunn Arch, showing ample evidence of magmatic activity in the early Cenozoic, in the form of sills and hydrothermal vent complexes. The structural and stratigraphic evolution of the southern Modgunn Arch is summarised below.

2.4.2 Tectonic evolution of the Modgunn Arch

The Norwegian margin has undergone several phases of extension and compression since the late Paleozoic. Prior to this, orogenic events such as the Caledonian Orogeny established the NE-SW structural trend of the Vøring and Møre Basins in the Norwegian Sea (Doré et al., 1997). The Vøring and Møre Basins are Cretaceous in age and were predominantly filled by marine sediment. The basins are 400-500 km long and separated by the Jan Mayen Corridor, an extension of the Jan Mayan Fracture Zone (Brekke et al., 1999).

Three main phases of rifting formed the mid-Norwegian margin: 1) Permian to Early Triassic, 2) Late Jurassic to Early Cretaceous, and 3) Late Cretaceous to Paleocene (Gómez and Vergés 2005). In the study area, the Late Cretaceous – Paleogene continental rifting was accompanied by widespread magmatic intrusion of sills and associated hydrothermal vent complexes into thick Cretaceous strata (Omosanya et al., 2018; Planke et al., 2005; Svensen et al., 2003). The intrusions are directly linked to continental breakup and oceanic crust formation between Norway and Greenland at ~55 Ma, around the Paleocene-Eocene boundary (Lundin and Doré, 2002). After continental breakup, a combination of mid-Cenozoic compressional doming, basin inversion along the Jan Mayen Corridor, and local differential compaction, resulted in the formation of the Modgunn Arch as observed at present, which is roughly oriented north-northwest to south-southeast (Brekke, 2000; Gómez and Vergés, 2005). Using stratigraphic relationships, Brekke (2000) suggested that the Modgunn Arch was formed in the Middle Miocene synchronously with the neighbouring Helland-Hansen Arch. The Plio-Pleistocene records widespread glaciation and subsequent progradation of clastic sediments along the mid-Norwegian margin (Hjelstuen et al., 1999). Several submarine landslides occurred across the Norwegian margin in response to glacial advance and retreat.

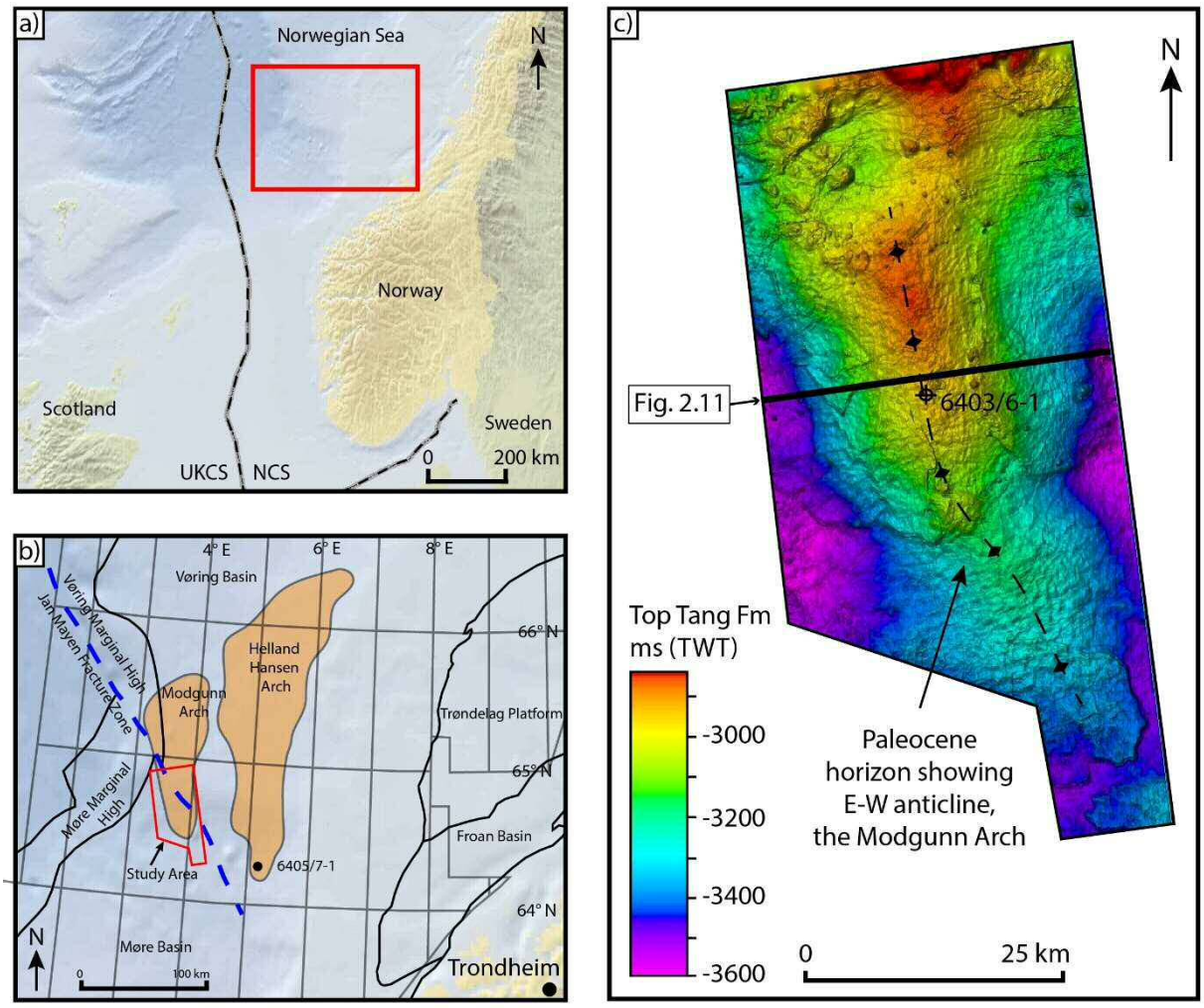

Fig. 2.9. a) Map of the Norwegian Sea. b) Location of study area of the Modgunn Arch and main structural elements of the Vøring and Møre Basins. c) Paleocene-age Top Tang Formation horizon showing the anticline-structure, with the location of well 6403/6-1. An E-W seismic profile across the crest of the Arch is shown in Fig. 2.11.

In the southern part of the Modgunn Arch, Song et al. (2020) correlated the location of recent submarine slides to the distribution of underlying faults and suggested that fluid migration along these faults weakened the overlying strata, leading to slope instability over the arch.

2.4.3 Stratigraphy of the Modgunn Arch

In this work, stratigraphic data for the Vøring and Møre basins are based on the Norwegian Petroleum Directorate (NPD) lithostratigraphic chart from 2015 (Fig. 2.10). Lithostratigraphic information specific to the study area is provided by the Edvarda well, 6403/6-1. This exploration well reached a depth of 4120 m, penetrating the Quarternary Naust Formation near the sea floor to terminate in the Lysing Formation, part of the Upper Cretaceous Cromer Knoll Group (Dalland et al., 1988) (Fig. 2.10).

The Lysing Formation consists of white-grey sandstones deposited by deep-marine fans. Overlying the Lysing Formation are the Kvitnos, Nise and Springar Formations, making up the Shetland Group (Upper Cretaceous). The three latter formations consist of calcareous claystones interbedded with minor carbonates and sandstone stringers, reflecting deposition in open marine environments (Dalland et al., 1988). The Nise Formation contains a greater proportion of sand when compared to the rest of Upper Cretaceous strata, consisting of interbedded sandstones, siltstones and shales (NPD Factpages, Dalland et al., 1988). An unconformity separates Cretaceous strata from the Paleocene Rogaland Group, which was also deposited in a deep-marine environment. The Tang and Tare Formations consist of claystones with minor sandstone and limestone, whilst the overlying Tare Formation contains variable amounts of volcanic tuffs. Tuff content increases towards the base of the unit, reflecting high volcanic output during this time (Kjoberg et al., 2017; Schmiedel et al., 2017). The Tare Formation is equivalent to the Balder Formation in the North Sea (Dalland et al., 1988; Deegan and Scull, 1977).

The deep-marine, claystone-dominated Brygge Formation of the Hordaland Group overlies the Rogaland Group and was deposited during the Early Eocene to Early Miocene (Fig. 2.10). The Kai Formation of the Nordland Group (Early Miocene to Late Pliocene) contains alternating claystone, siltstone and sandstone with limestone stringers, all deposited in a marine environment (Dalland et al., 1988). In contrast, a thick, prograding clastic wedge was deposited across the mid-Norwegian margin from the Late Pliocene to Early Pleistocene as a result of the Northern Hemisphere glaciation and tectonic uplift of Fennoscandia (Gómez and Vergés, 2005; Hjelstuen, et al., 1999). This unit is present on the Modgunn Arch as the 40-m thick Naust Formation.

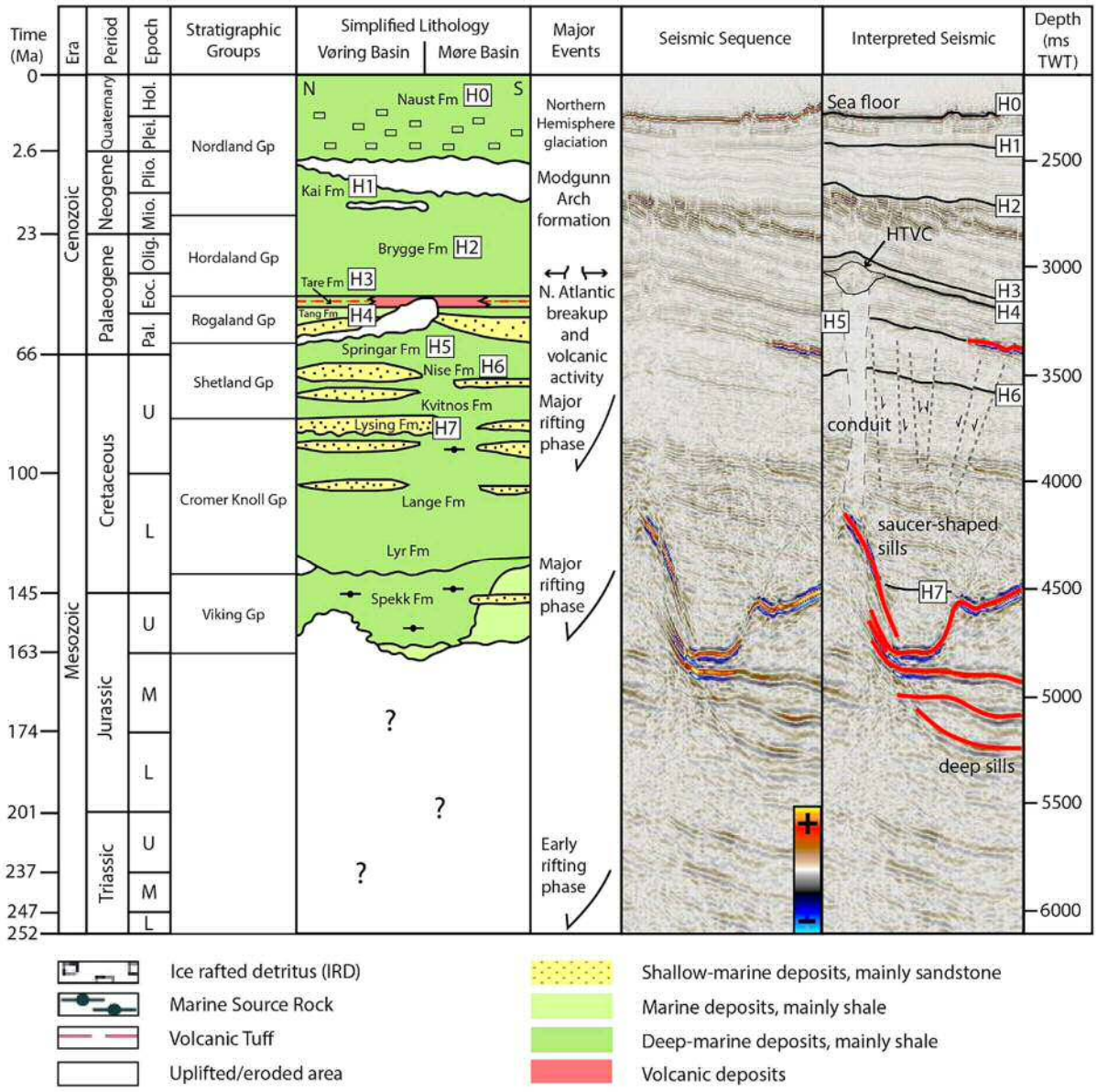

Fig. 2.10. Stratigraphic framework of the Modgunn Arch, Norwegian Margin. Representative seismic interpretation is shown on the right, with seismic horizons labelled H1-H7. Modified after "The 2014 NPD lithostratigraphic charts" (2014). HTVC = hydrothermal vent complex.

On the Modgunn Arch per se, the presence of igneous rocks is confirmed by a 1-m thick sill unit encountered in well 6403/6-1 (Manton, 2015). Magmatic intrusions are evident throughout the Cretaceous and Paleocene strata as positive high-amplitude, saucer-shaped and planar-transgressive seismic reflections cross-cutting host strata (Fig. 2.11).

2.4.4 Petroleum systems of the Vøring and Møre Basins

Brekke et al. (1999) summarised the hydrocarbon potential of the Vøring and Møre Basins. They noted that the main uncertainty for prospectivity in the two basins is the distribution and maturity of organic-rich source rocks, although a regional transgression during the Late Jurassic resulted in the deposition of a source rock akin to the Kimmeridge Clay Formation (Underhill, 1998). Cretaceous sandstones with reservoir potential are considered to be present, but may not be laterally extensive (Brekke et al., 1999). Yet, if charged by a Cretaceous source rock, these reservoirs could form a promising play, particularly if located within anticlinal or fault traps such as on the Modgunn Arch (Brekke et al., 1999).

A successful Paleocene play consisting of an early Paleocene sandstone reservoir, a Tertiary domal trap and an unknown thermogenic source is present towards the Trøndelag Platform area of the Møre Basin (Brekke et al., 1999). The Paleocene play can also be present elsewhere on the Norwegian margin, but requires either hydrocarbon migration from Cretaceous source rocks or re-migration from older source intervals (Brekke et al., 1999). No hydrocarbon fields have been discovered to date on the Modgunn Arch and the presence of volcanics makes the study area difficult to explore; the high chance of drilling into volcanic rocks turns the prospect economically costly and technically challenging.

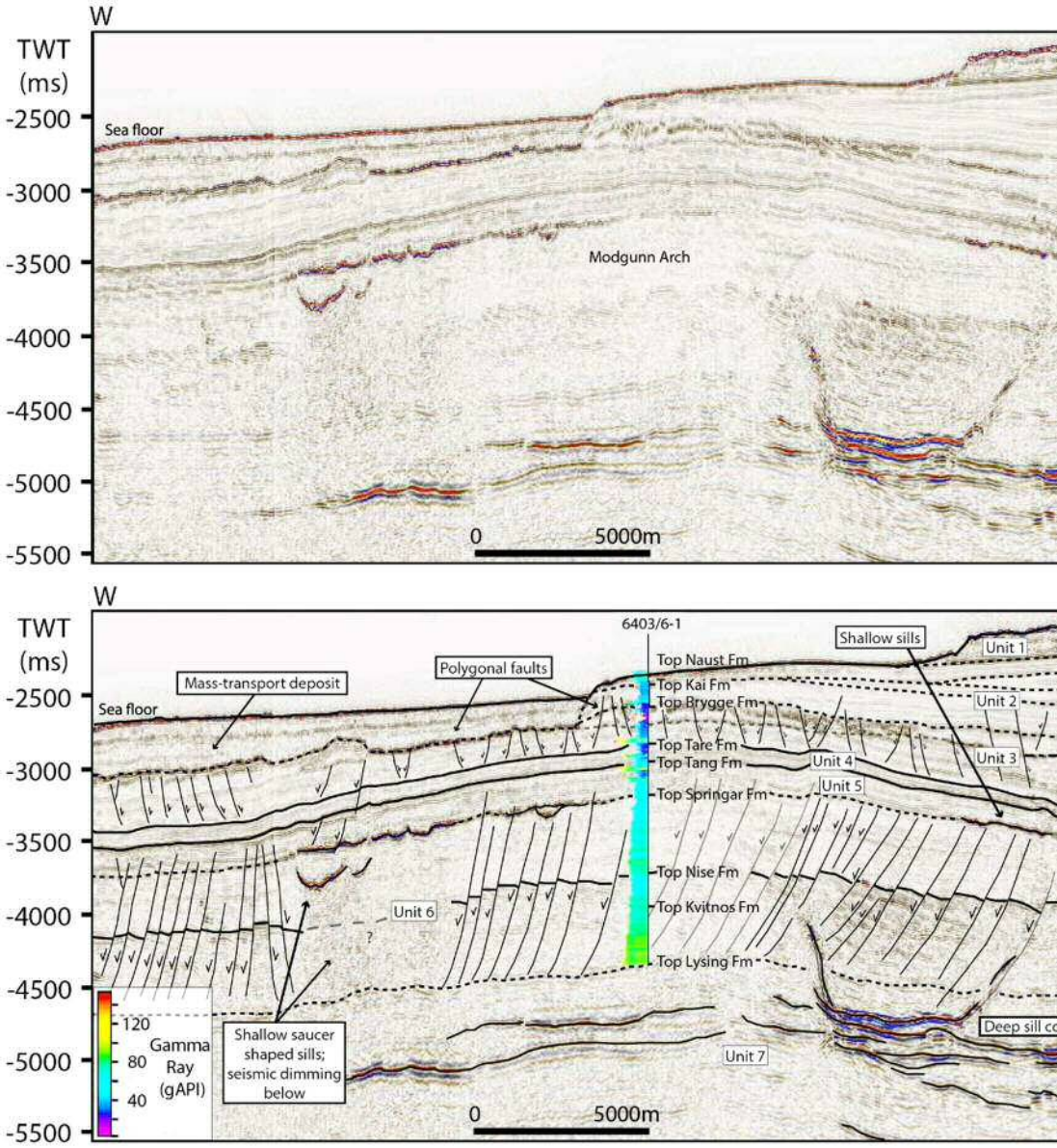

Fig. 2.11. a) Uninterpreted and b) interpreted representative seismic profile E-W across the Modgunn Arch showing well 64 labelled well tops. Seismic units 1 – 7 and seismic horizons H0 – H7 are labelled in the figure. Location of seismic profile

CHAPTER THREE

Data and Methods

3 Data and Methodology

3.1 Introduction

This thesis makes use of three-dimensional (3D) seismic volumes to interpret subsurface geological structures and fluid flow features. The interpreted seismic volumes were shot for hydrocarbon exploration and are being used for research in Cardiff University's 3D Seismic Lab. This chapter provides an overview of how seismic data is acquired, processed and interpreted, as well as details on the seismic datasets used. Seismic interpretation methodology is summarised in 3.4 and the Seabed Mapping Tool created by the British Geological Survey is described in 1.1. Specific methods used for each dataset are covered in Chapters 4, 5 and 6.

3.2 Seismic data

Three-dimensional (3D) seismic data and interpretation is one of the most significant advances in the hydrocarbon industry and plays a fundamental role in both exploration and production (Sheriff and Geldart, 1995). Seismic data is used by geologists to visualise and interpret subsurface geology, from which they can create conceptual structural models and understand the geological processes and history of the study area (Cartwright, 2007). 3D Seismic data allows for far more detailed visualization and characterization of subsurface geometries, with greater resolution compared with 2D seismic data, where the latter only provides a cross-sectional view (Biondi, 2006).

3.2.1 Acquisition of seismic reflection data

Acquisition of seismic data in exploration involves artificially creating sound waves, called seismic waves, which travel through the subsurface, are reflected from different layers of rock and detected and recorded at the surface (Fig. 3.1). During offshore seismic acquisition, a seismic survey vessel tows streamers – often up to 12 km in length – across the sea. An air gun or water gun array is activated from the vessel, creating a bubble pulse which forms acoustic energy of a given wavelength and frequency (Bacon et al., 2007). This energy travels as compressional waves (P-waves) through the water into the subsurface and undergoes a combination of reflection and refraction: the relative amounts of energy that are absorbed, reflected and refracted depends on the physical properties of the rock and the heterogeneities in the subsurface (Kearey et al., 2002) (Fig. 3.2). Some energy is reflected to the surface, which

is recorded by hydrophones attached to the streamers at the sea surface. The survey vessel tracks backwards and forwards to create a three-dimensional grid, where inlines are in the direction of the boat movement, crosslines are perpendicular to inlines and typical trace spacing varies from 12.5 to 50 m (Brown, 2004; Yilmaz, 2001). In essence, seismic data visually represents the time taken for the acoustic wave to travel from the source (airgun) down to a given geological boundary and back (Bacon et al., 2007). The depth (or z-axis) is measured as two-way time (TWT), in seconds or milliseconds.

When a P-wave propagates through the subsurface and encounters a change in the physical properties of the rock with depth, the incident P-wave partitions into a reflected wave and a transmitted wave (Fig. 3.2) (Sheriff and Geldart, 1995; Gluyas and Swarbrick, 2013). The reflected wave is detected at the surface which manifests in seismic data as a seismic reflection. The magnitude of seismic waves reflected depends on the velocity and density contrast between two rocks. The velocity of a seismic wave through a rock unit varies according to physical rock properties such as composition, texture, porosity, fluid content and elastic modulus (Kearey et al., 2002). P-wave velocity (V_p) is dependent on density (ρ), bulk compressibility (K) and the shear modulus (μ) of the rock (Equation 3.1).

$$\frac{\quad}{\quad}$$

Equation 3.1

Acoustic impedance is the product of the P-wave velocity and density of the rock layer (Equation 3.2).

Equation 3.2

The reflection coefficient, R, is used to quantify the effect that acoustic impedance has on the reflected wave propagation when a P-wave interacts with a geological interface (Equation 3.3). The greater the contrast in acoustic impedance between two layers, the greater the reflection coefficient and the higher the amplitude of the resulting seismic reflection (Kearey et al., 2002). The numbers 1 and 2 represent the upper and lower rock units across a boundary, respectively.

Equation 3.3

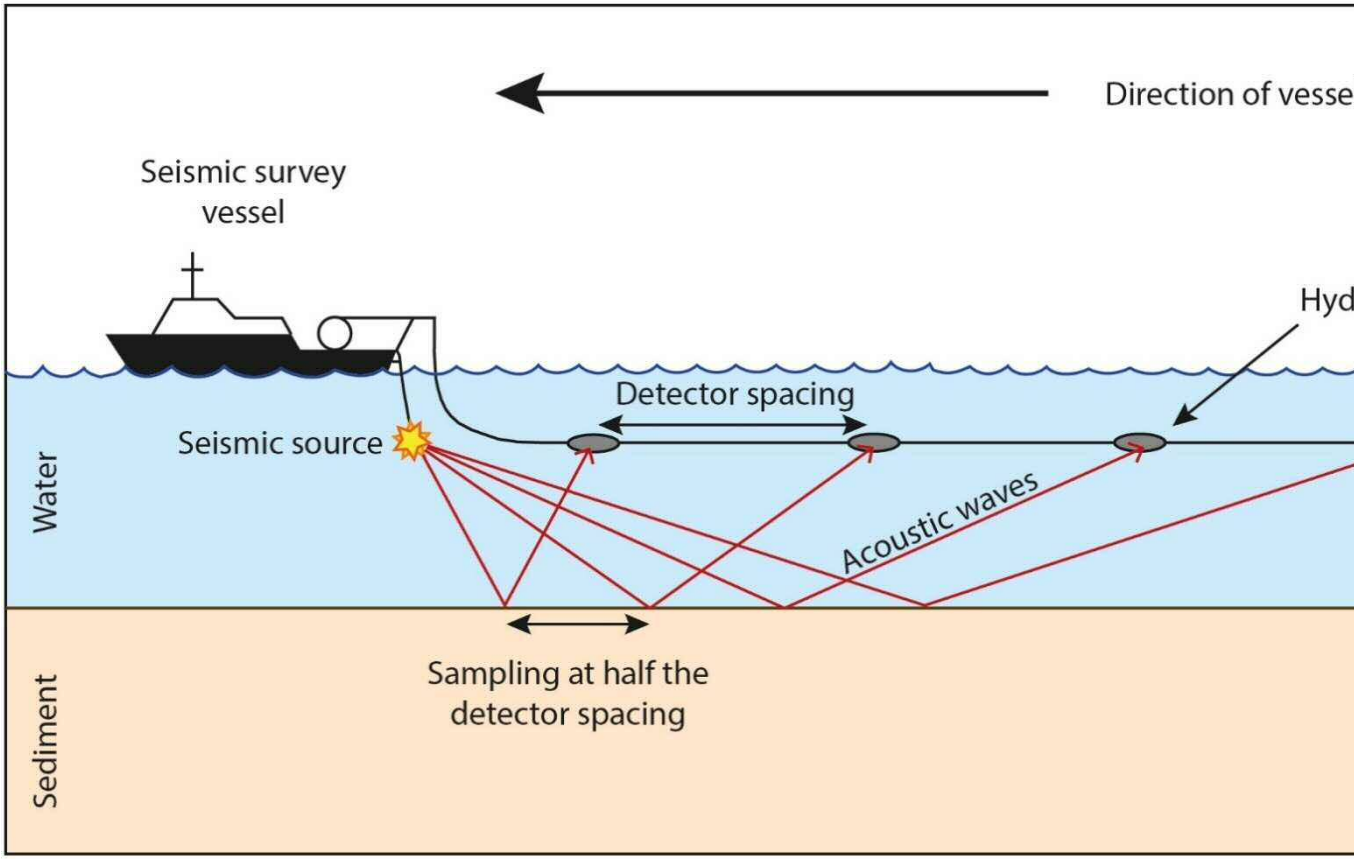

Fig. 3.1. Simplified schematic of the basic principles of offshore seismic acquisition. A seismic survey vessel tows a seism
compressional P-waves travel through the water to sediment layers and reflect to the sea floor, where they are detected at hydr

For example, the amplitude of a seismic reflection from a sandstone-salt contact will be greater than that from a mudstone-sandstone contact, as the change in P-wave velocity is greater for the former. Seismic velocity generally increases with depth as rocks are buried and more compacted, whilst the presence of fluids such as oil and gas decrease the velocity of the host rock strata and in some cases result in local amplitude anomalies (Gluyas and Swarbrick, 2013).

The inverse of the reflection coefficient is the transmission coefficient (T), which represents the measure of the effect that acoustic impedance has on propagation of the transmitted wave (Equation 3.4) (Kearey et al., 2013; Veeken, 2006).

$$T = 1 - R$$

Equation 3.4

The relative amplitudes of the reflected and transmitted waves also depend on the angle of incidence at which the P-wave comes into contact with a geological boundary (Fig. 3.2) (Gluyas and Swarbrick, 2013). The transmitted wave continues to propagate through the subsurface until it reaches another boundary with an acoustic impedance contrast, where the process of P-wave partitioning is repeated (Bacon et al., 2007; Gluyas and Swarbrick, 2013). For this reason, the energy and therefore amplitude of the reflected waves decreases with depth.

Seismic data are displayed as sinusoidal transverse waves, or wavelets, with two-way time increasing from the top of the display downwards (Gluyas and Swarbrick, 2013). The peaks and troughs of wavelets have amplitudes proportional to the reflection coefficient of a geological boundary; an increase in acoustic impedance with depth results in a positive amplitude (peak), whilst a decrease in acoustic impedance with depth results in a negative amplitude (trough) (Sheriff and Geldart, 1995). The wavelets are typically displayed in discrete colours, such as the 'SEG (Society of Exploration Geophysicists) normal polarity classification' (Brown, 2004). In Chapter 5, black indicates a peak and red indicates a trough, whilst in Chapters 4 and 6, a more detailed colour bar was used, grading from yellow to red (very positive to positive), through white (zero-crossing), to blue and cyan (negative to very negative), as shown in Fig. 3.3. Gradational colour schemes can help to highlight amplitude anomalies such as dim or bright spots which would have been overlooked if the colour scheme was purely black and white.

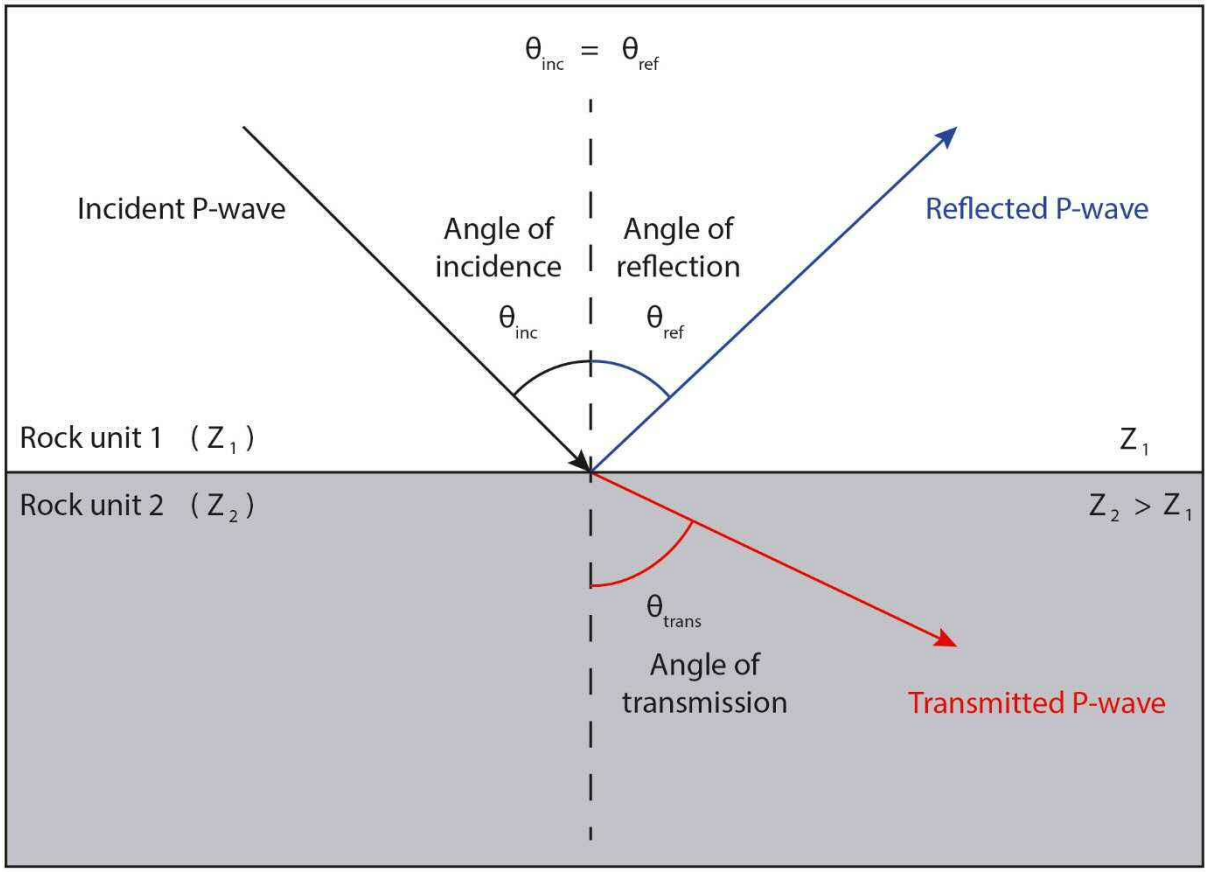

Fig. 3.2. Diagram showing the reflection and transmission of a P-wave as it encounters a rock surface with an acoustic impedance contrast. Some energy of the P-wave is reflected in Rock unit 1, whilst some is transmitted through Rock unit 2 below. The angle of incidence equals the angle of reflection, whilst the angle of the transmitted wave depends on the rock type of Rock unit 2. Modified from Veeken (2006) and Kearey et al. (2002).

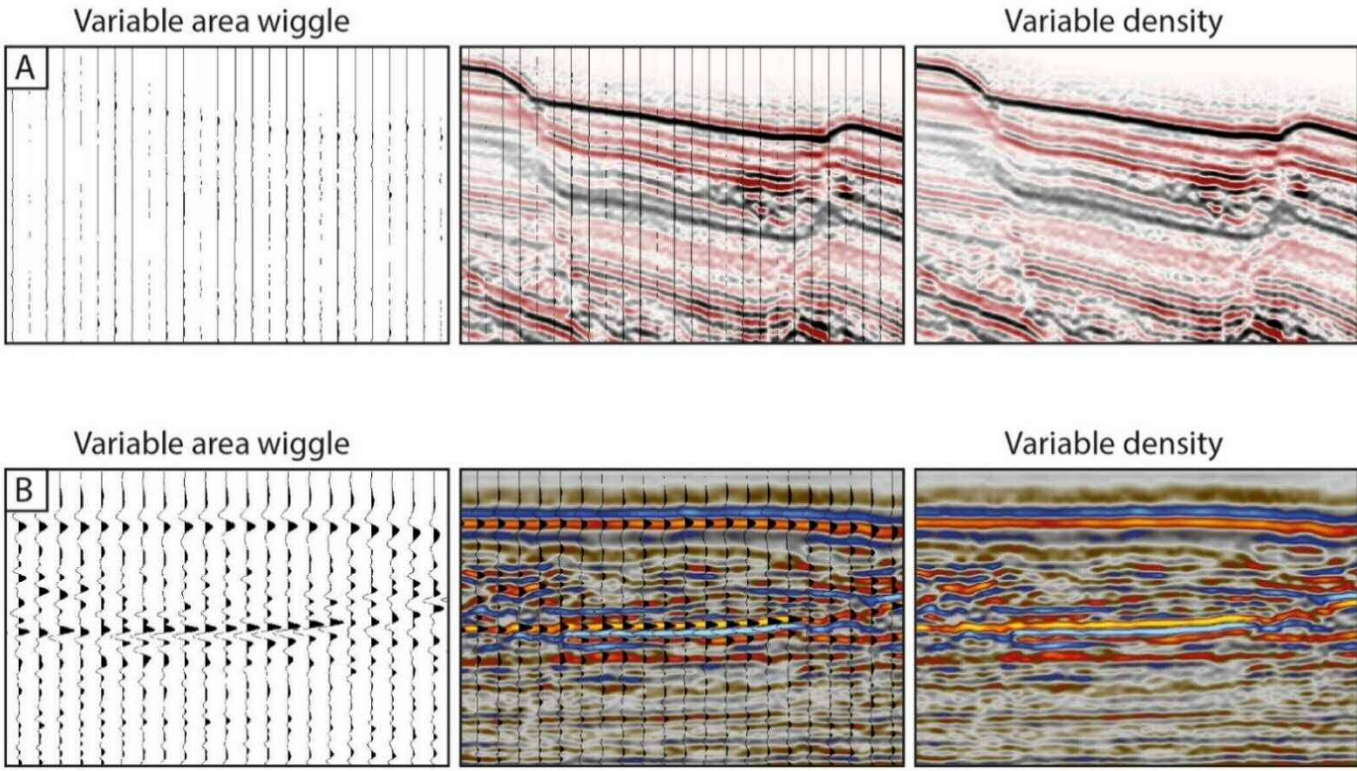

Fig. 3.3. Example of seismic data displayed as variable area wiggle and how it is converted into variable density using differen
used in Chapter 5 for the East Breaks dataset; whereas b) shows a yellow-white-cyan colour bar which is used in Chapters 4
datasets, respectively.

Seismic data can be presented as maximum, minimum or zero-phase. Zero-phase data means that the wavelet is symmetrical about a point of zero amplitude, the 'zero-crossing' (Evans, 1997) (Fig. 3.3). The three seismic datasets used in this thesis are processed in zero-phase, therefore the centre of the wavelet and resulting seismic reflection coincides with a geological interface.

3.2.2 Seismic resolution

Seismic resolution is a key parameter used as a measure of quality of the seismic data. It controls the spacing at which it is possible to detect and resolve two individual geological features, both vertically and horizontally, and controls what the interpreter is able to visualise (Brown, 2004; Kearey et al., 2002).

3.2.2.1 Vertical resolution

The vertical resolution of a seismic dataset is determined by the seismic source signal and the wavelength of the seismic waves passing through the Earth (Bacon et al., 2007). The wavelength (λ) of a seismic wave is a function of velocity (v) and frequency (f) (Brown, 2004):

–

Equation 3.5

The tuning thickness is the limit of vertical seismic resolution – it is the bed thickness where two horizon events become indistinguishable and are resolved as one reflector (Badley, 1985). The maximum vertical resolution possible is between ¼ and 1/8 of the dominant wavelength of the reflected pulse (Sheriff and Geldart, 1995) and is calculated as follows (Equation 3.6):

– ———————

Equation 3.6

where λ is the wavelength and f_{max} is the maximum frequency of the interval, and interval velocity is the time it takes for the seismic wave to propagate through the rock interval of interest. The minimum threshold for detecting a geological feature is considered to be as small

as λ/30 (Yilmaz, 2001). Frequency refers to the number of full seismic wave cycles that pass through a fixed point in a given unit of time, for example, per second. Higher frequencies are absorbed as the waves travel deeper into the subsurface; and increased compaction and diagenesis also increase the seismic wave velocity with depth, which leads to an increase in wavelength: for these reasons, vertical resolution decreases with depth (Brown, 2004; Kearey et al., 2002).

It is possible to improve vertical resolution using deconvolution during seismic processing (Kearey et al., 2002). Deconvolution aims to recover high frequencies by shortening the pulse length using inverse filtering, often with an anti-aliasing filter (Kearey et al., 2013; Veeken, 2006). In shallow seismic surveys, seismic resolution is typically much higher, even to centimetre-scale, as higher frequencies are used at a trade-off with depth of penetration, therefore these are less useful for hydrocarbon exploration (Veeken, 2006). Nevertheless, shallow seismic surveys are useful for assessing the presence of shallow gas hazards and seabed instability, which are important factors to consider when laying subsea infrastructure or drilling wells (Judd and Hovland, 2007).

3.2.2.2 Horizontal resolution

Horizontal resolution is controlled by two main factors: the detector spacing and the Fresnel zone (Kearey et al., 2002). For a flat-lying horizontal reflector, the horizontal resolution is at least half the detector spacing, therefore decreasing the detector spacing improves horizontal resolution. A seismic signal can be thought of as an infinite number of rays of energy which reflect off an interface, where the recorded signal results from interference of a group of backscattered rays in a circular area called the Fresnel Zone (Bacon et al., 2007). The section of the reflector from which energy is returned to the receiver within half a wavelength of the initial reflected arrival is the Fresnel zone, as this interferes constructively to build up the reflected signal (Kearey et al., 2002). The width of the Fresnel zone represents the absolute limit of horizontal resolution (Fig. 3.4). The width (w) of the Fresnel zone is related to the dominant wavelength (λ) of the source signal and the reflector depth (z) as follows:

Equation 3.7

As with vertical resolution, the horizontal resolution decreases with depth as the seismic wavelength increases. Bin spacing refers to the horizontal dimensions of the ‘bins’ or cells,

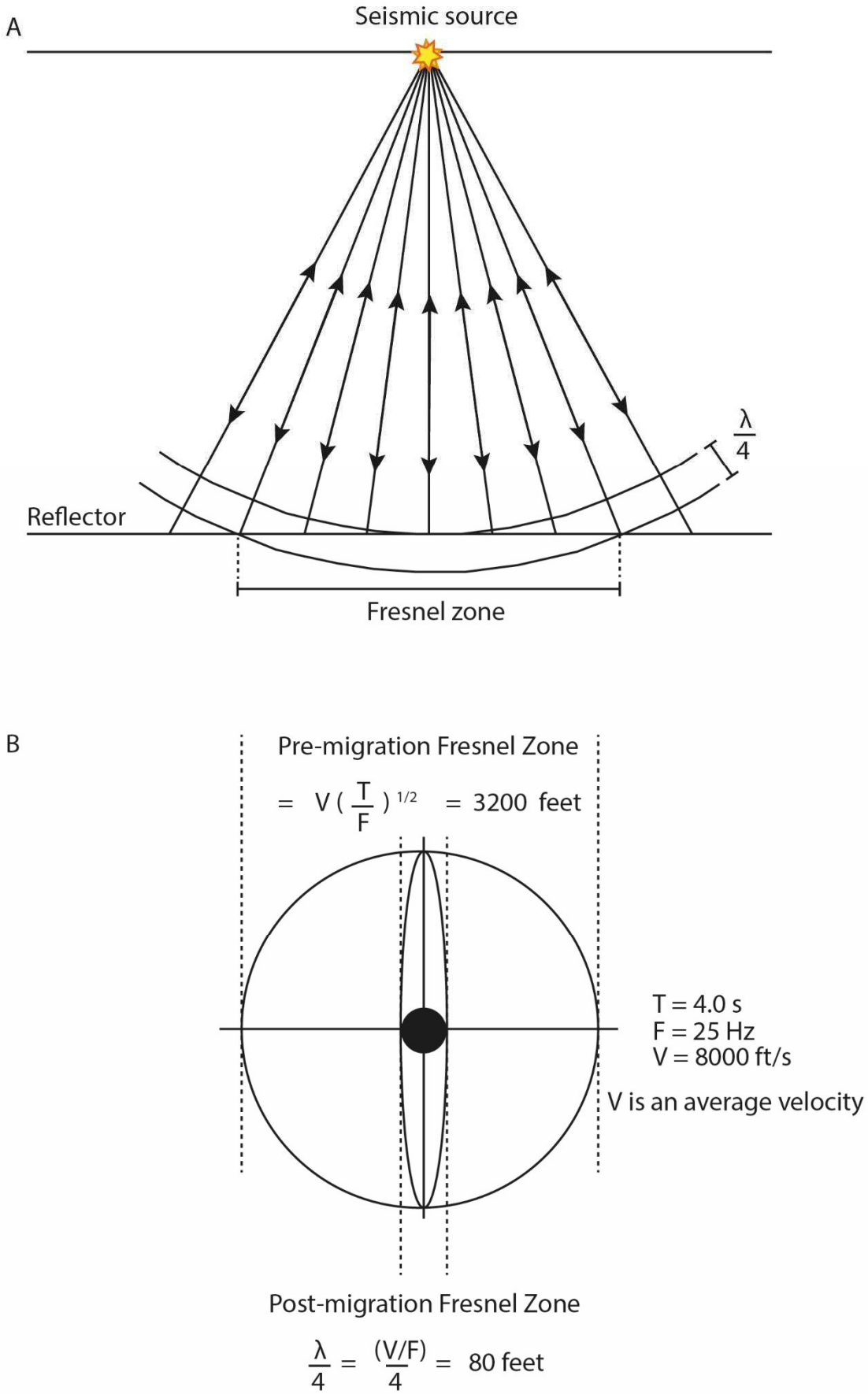

Fig. 3.4. a) A simplified scenario of a flat reflector where the energy returns to the source (therefore receiver), modified from Kearey et al. (2002). The Fresnel Zone is the horizontal region of the reflector where all the energy is returned within half a wavelength of the initial reflected arrival (Kearey et al., 2002). The energy from within this zone contributes constructively to the seismic signal at this point in space. b) Schematic showing the reduction of the Fresnel Zone after migration to λ/4, with values provided as an example. Modified from Brown (2004).

within which seismic reflections are stacked/grouped to represent one reflection. This is usually half the receiver spacing and can be considered to approximate the horizontal resolution of the data.

Seismic processing is required to turn 'raw data' into a 3D seismic volume for interpretation. The collection of raw seismic data that falls in the same area, the common midpoint (CMP) gather, is stacked to create a CMP stack which will improve the signal-to-noise ratio (Kearey et al., 2002). Following this, the stacked data is migrated, which involves repositioning out of plane reflections due to dipping beds, focusing the energy that is spread over a Fresnel Zone and collapsing diffraction patterns produced by single point reflectors and faulted beds (Bacon et al., 2007; Kearey et al., 2002). The seismic data is also subjected to frequency filtering, which removes frequencies that are only attributed to noise in the seismic section; the resulting migrated seismic data therefore has reduced noise and increased horizontal resolution (Kearey et al., 2002).

3.3 3D Seismic datasets in this study

This thesis focuses on three study areas, from the Central North Sea, the Gulf of Mexico and the Norwegian Sea. The details of the three, 3D seismic datasets used are provided below.

3.3.1 Jæren High, Central North Sea

The 3D seismic reflection data covers an area of 2400 km^2 across the Jæren High and was interpreted on Schlumberger's Petrel® software. It was provided by PGS (Petroleum Geo-Services) and processed in zero phase, SEG (positive) standard polarity, such that an increase in acoustic impedance with depth manifests as a peak, which is coloured red, whilst a trough is negative and blue (Fig. 2.2, Fig. 3.3b). Bin spacing is 50 x 50 m and the vertical sampling rate is 4 ms two-way-time (TWT). Tuning thickness and lateral resolution of the Mesozoic section is 50 m.

3.3.2 East Breaks, Gulf of Mexico

Two 3D seismic reflection surveys were interpreted in the East Breaks region, in the upper slope of the northern Gulf of Mexico Basin (Fig. 2.3). The surveys have been provided by the United States Geological Survey (USGS). No well logs were available in the study area. Nevertheless, detailed stratigraphic descriptions are provided by Beaubouef and Friedmann (2000), whose study area overlaps with the westernmost part of this survey (Fig. 5.1).

3.3.2.1 East Breaks seismic survey 1 (North)

The northern survey B-32-91-TX covers an area of 2031 km^2 and was acquired in 1991 by Calibre Seismic Company. The survey was processed in zero-phase, SEG positive standard polarity such that an increase in acoustic impedance with depth manifests as a peak and is coloured black, whilst a trough is coloured red (Fig. 3.3a, Fig. 5.2). Bin spacing is 20 x 25 m and the vertical sampling rate is 4 ms (TWT). The dominant frequency is 50 Hz and the tuning thickness (λ/4) at the seafloor is 8 m, with a vertical limit of detectability (λ/30) of 1 m.

3.3.2.2 East Breaks seismic survey 2 (South)

The southern dataset was acquired in 1989 by Shell Offshore Inc., covers an area of 835 km^2 and was processed in zero-phase, SEG negative standard polarity – as this is the opposite to the northern dataset, the colour bar was flipped so that the datasets visually match. A trough is coloured black and represents an increase in acoustic impedance with depth. Bin spacing is decimated to 100 x 100 ft with a vertical sample rate of 4 ms TWT. The dominant frequency is 35 Hz; tuning thickness at the seafloor is 11 m and the vertical limit of detectability (λ/30) is 1.3 m. Water depth ranges from 85 m – 1395 m, deepening to the south (Fig. 2.8).

3.3.3 Norwegian Sea

The final 3D seismic reflection survey is located offshore mid-Norway, on the Modgunn Arch (Fig. 2.9). The survey MC3DMGS2002 covers an area of 2635 km^2 and was acquired in 2002 by PGS. The survey was processed in zero-phase, European polarity such that an increase in acoustic impedance with depth is shown as a red positive peak, whilst troughs are coloured blue (Fig. 2.10, Fig. 3.3b). Inlines and crosslines are oriented NNW and WSW respectively, processed to a bin spacing of 12.5 m. The seismic cube is presented in two-way-time (TWT) with a vertical sampling rate of 4 ms TWT. Well 6403/6-1 was drilled in the centre of the Modgunn Arch in 2002; well-seismic correlations indicate that the vertical seismic resolution is ~8 m in the Brygge to Naust Formations (Upper Eocene to Quaternary in age). Vertical seismic resolution approaches 17 m in the Tare and Tang Formations (Paleocene to Upper Eocene); 29 m in the Springar Formation and 36-40 m in strata spanning the Nise to Top Lysing Formations (Upper Cretaceous in age).

3.4 Seismic interpretation

The main method used for analysis in this thesis is seismic interpretation, which was undertaken using Schlumberger's Petrel® 2017, 2018 and 2019, in the 3D Seismic Lab at Cardiff University.

3.4.1 Horizon mapping

Stratigraphic data from wells for Chapters 4 and 6 were tied to the seismic volumes to help identify key stratigraphic units and the corresponding seismic reflections were mapped using the horizon interpretation tool. Initially, manual seismic interpretation was undertaken in grids of every 50 inlines and crosslines, with more detailed interpretation in areas of increasing complexity, up to every inline and crossline where necessary. Following this, the 3D 'autotracking' interpretation tool was used to fill in the interpreted grid, where the tool identifies seismic reflections with similar amplitudes and phase (Fig. 3.5) (Hart, 1999). In complex areas, where the autotracker does not find similar seismic reflections, the tool stops interpreting and further manual quality control is required.

Surfaces were created from the interpreted horizons using the 'Make Surface' Tool in Petrel®, from which attributes could be extracted, isopach maps generated and fluid flow features were mapped, as described in Section 1.1. Fig. 3.6 shows an example from Chapter 4 of how key structural maps relate to the seismic section.

3.4.2 Time-depth conversions

The vertical scale of seismic data is usually presented in two-way time. However, it is useful for interpretation to convert the dataset into metres depth, using Equation 3.8:

$$\frac{\quad}{\quad} \quad \frac{\quad}{\quad}$$

Equation 3.8

where D is the depth, TWT is two-way time in milliseconds which is converted into one-way time by dividing by two, and v is the seismic velocity in metres per second, for the given interval. The value is divided by 1000 to convert milliseconds into seconds, such that the output depth is in metres. Depth conversion was carried out in Chapters 4 and 5 in order to apply the Seabed Mapping Toolbox to the structural maps (see section 3.5). In Chapter 5, the average seismic velocity of water was used as only the seabed was depth converted and no wells were available. In Chapter 4, the key horizons corresponding to the stratigraphic horizons in the wells

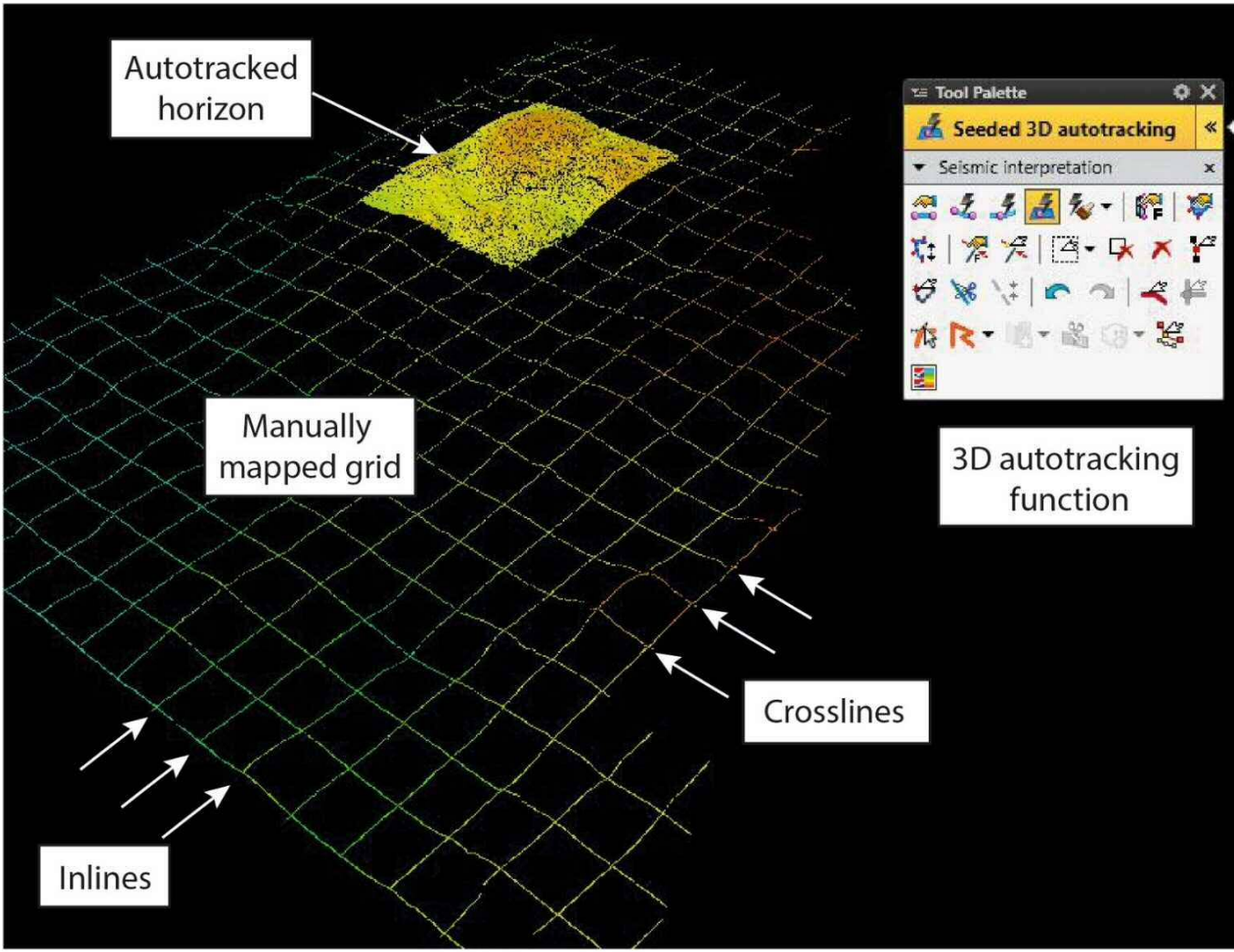

Fig. 3.5. 3D window showing the process of seismic interpretation of a horizon in Petrel® along inlines and crosslines in a gr
function.

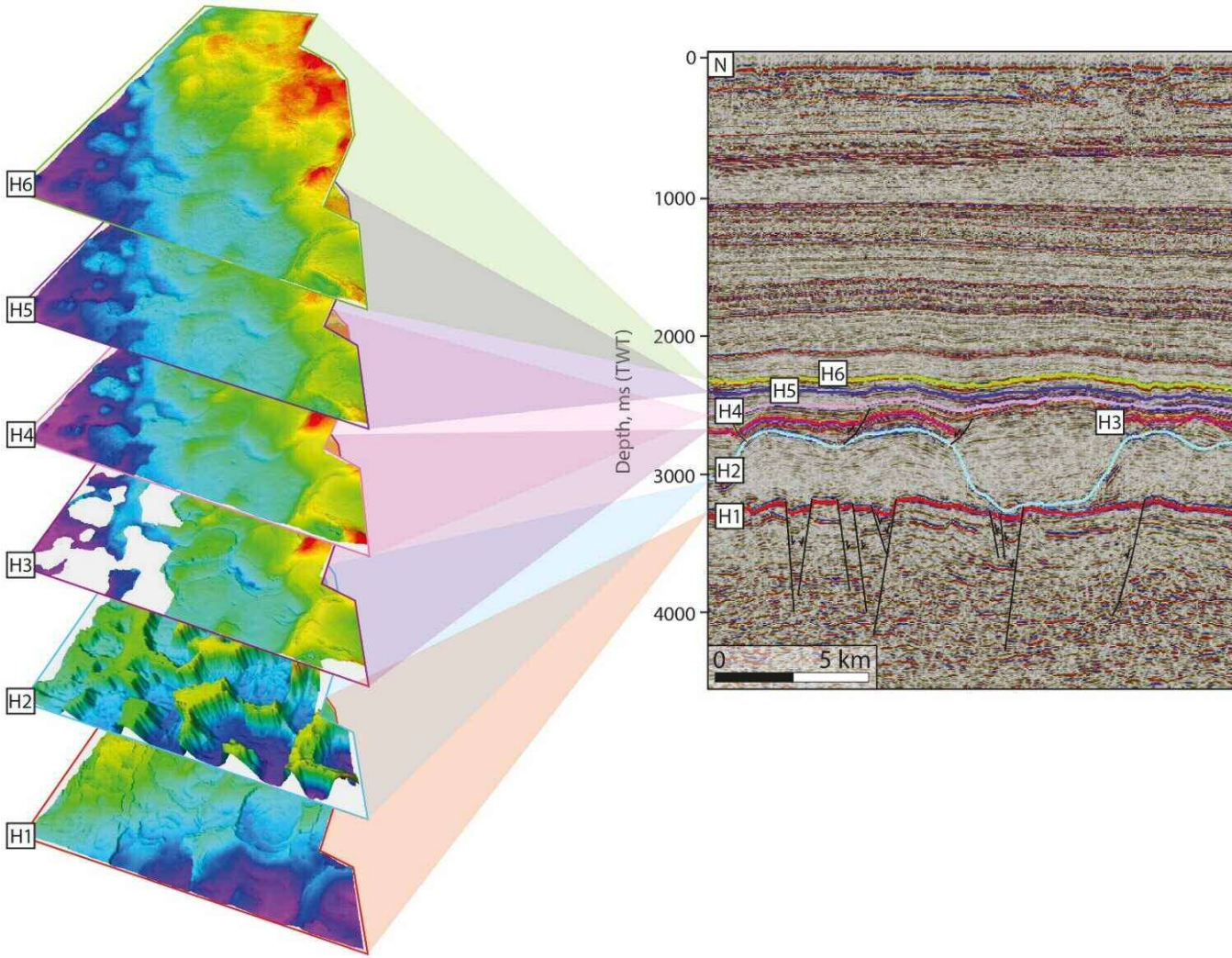

Fig. 3.6. Example of how six (6) interpreted structural maps relate to a seismic line, using seismic data from the Jæren Hig

true vertical depth.

Base – Horizon or constant	Interval velocity, m/s	Interval the velocity represents
Seabed	1450	Seawater
Top Hordaland Group	1700	Shallow mudstone-dominant units, Nordland Group
Top Chalk	2200	Hordaland Group siliciclastics
Top Cromer Knoll Group	4600	Chalk Group
Top Zechstein Salt	3600	Average of Cromer Knoll Group marls and Triassic sands/shales
Top Rotliegend Group	4650	Zechstein Salt
Base of dataset	4450	Rotliegend Group sandstones

Table 3.1. Velocity model in Petrel used for depth conversion of the Jæren High seismic dataset in Chapter 4.

3.4.3 Seismic attribute analyses

Volume and surface seismic attributes are used to better visualise and constrain fluid flow features in three dimensions in the seismic data. A large variety of seismic attributes are available in Petrel®; in this thesis variance, RMS amplitude, maximum magnitude, dip and dip azimuth were used and are described below.

Amplitude (Fig. 3.7a): amplitude is a widely used attribute as it is a measure of the largest displacement of a wavelet from the base to its crest, recorded as either positive (maximum) or negative (minimum) (Fig. 3.3). The amplitude varies in accordance with acoustic impedance across a geological interface, which can change due to (e.g.) lithology, porosity, thickness changes and fluid content (Brown, 2004). Amplitude is the default setting of a seismic section, from which other seismic attributes can be extracted.

Isochron (Fig. 3.7c): also known as thickness maps, these record the time difference between two given horizons or surfaces. This was key in this thesis for showing where there are thick salt walls versus salt welds in Chapter 4.

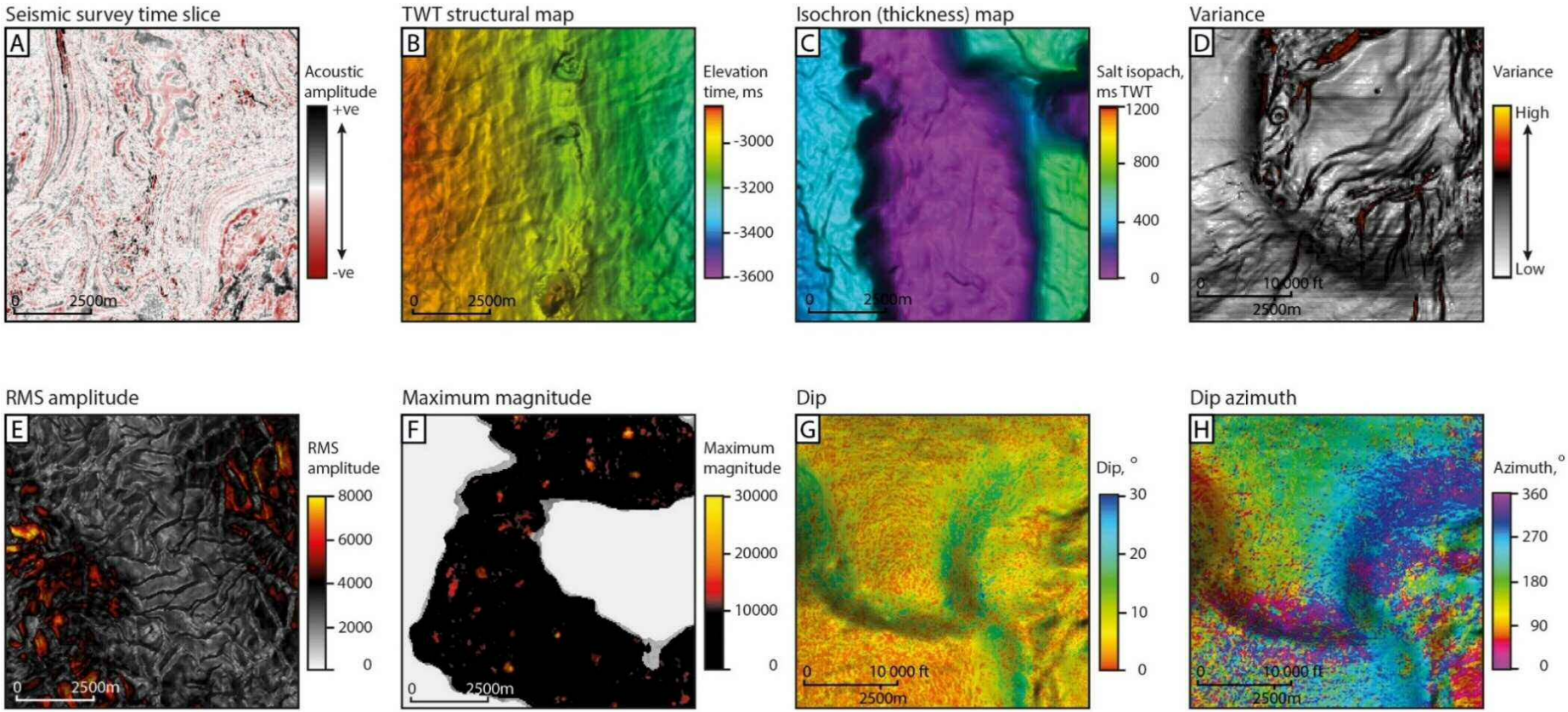

Fig. 3.7. Examples of different structural maps and seismic attributes used in the interpretation of the 3D seismic data volumes in this thesis: a) a time slice with original acoustic amplitude; b) a two-way time structural map; c) an isochron (thickness) map; d) variance; e) root-mean-square amplitude; f) maximum magnitude; g) dip and h) dip azimuth.

Variance (or coherence) (Fig. 3.7d): variance is a measure of the waveform similarity, recording how similar a given trace is to its neighbouring trace. Similar traces are mapped as low variance values, while discontinuities have high variance values (Brown, 2004). The variance attribute highlights irregularities such as faults, depressions, chaotic pipe interiors and salt walls.

Root-mean-square (RMS) amplitude (Fig. 3.7e): RMS amplitude takes the average squared amplitudes for a defined interval (Brown, 2004). This allows the interpreter to identify both high- and low-amplitude anomalies which, in this thesis, are considered to be evidence of fluid flow.

Maximum magnitude (Fig. 3.7f): the maximum positive or negative seismic amplitude value was extracted between two horizons or within a time window (Omosanya and Alves, 2013; Marfurt and Alves, 2014). This was used to highlight any high-amplitude anomalies irrespective of whether they are peaks or troughs, in Chapter 4.

Consistent Dip: the seismic volume attribute 'Consistent Dip' was applied in Chapter 5, from which 'Dip' (Fig. 3.7g) and 'Dip Azimuth'(Fig. 3.7h) seismic volumes were created. These attributes were extracted to surfaces to show areas of greater dip and – opposite to dip azimuth – the up-dip fluid migration pathways from deeper to shallower strata.

3.5 Seabed Mapping Toolbox

An ArcGIS-based Toolbox developed by the British Geological Survey – the BGS Seabed Mapping Toolbox (De Clippele et al., 2017; Gafeira et al., 2018) – was used to semi-automatically map confined depressions within a horizon and extract morphological characteristics including Vertical Relief, Width, Length and Width:Length Ratio. Manual interpretation of confined features – particularly when the morphology of the features is to be analysed – is subject to human error and is very time-consuming. Therefore, a semi-automated mapping approach is beneficial for mapping large datasets in the most accurate and time-efficient way possible, with the aim of reducing errors and maintaining consistency across a dataset.

The Toolbox is used for initial automatic mapping; however, manual interpretation is required to quality-control the output. In 2012, Gafeira et al. created and used a python script for semi-automated mapping of confined features to delineate pockmarks (negative features) in multibeam echosounder data. The Seabed Mapping Toolbox was thus adapted and developed from the initial script and has also been applied to mapping coral mounds (positive features) on

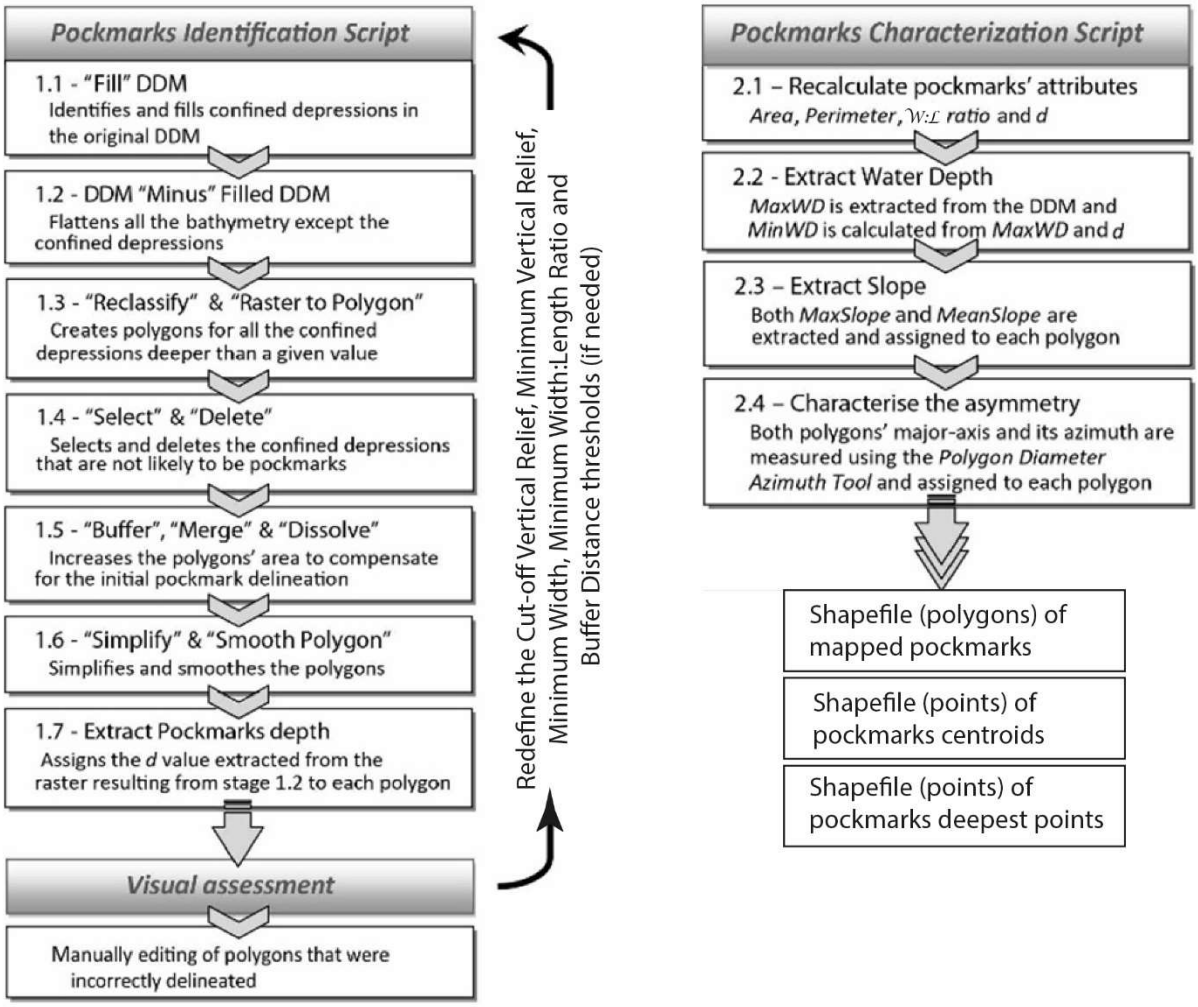

Fig. 3.8. Pockmark Identification (a) and Characterization (b) Script methodology workflows, modified after Gafeira et al., (2012). DDM = digital depth model.

bathymetric data (De Clippele et al., 2017). The script was used once to map pockmarks in 3D seismic data (Geldof et al., 2014), but only at the seabed and a second horizon (H1) around 150 ms TWT below the seabed, therefore its applicability in 3D seismic data was still to be tested.

The BGS Seabed Mapping Toolbox consists of four main Tools: 1) Bathymetric-based Feature Delineation Tool; 2) Bathymetric Positioning Index (BPI) based Delineation Tool; 3) Feature Short Description Tool; and 4) Feature Full Description Tool. Each Tool requires certain parameters set by the user, which will be used as minimum thresholds. A further toolset in the Toolbox is called 'Upstream Tools', where two standard ArcGIS tools are available (Create Fishnet and Focal Statistics), as well as a BGS-developed tool called Filter-based Clip.

3.5.1 Bathymetric-based Feature Delineation Tool

A summary of the Bathymetric-based Feature Delineation Tool used in Chapters 4 and 5 is as follows (Fig. 3.8):

The ASCII text file of the surface mapped in Petrel® is uploaded into ArcGIS as a points file, displaying x-y data and depth. The points are converted into a raster file using the 'Raster from Points' Toolbox, resulting in a digital depth model (DDM). The following description is for depressions but can be inverted for positive features.

1.1: The 'Fill' tool is applied to mimic 'filling' the depressions with (eg) water. This process aims to remove the effects of topography, as the depth of the depression is dependent on the height of the nearest neighbour depression. This process redefines the lowest elevation on the rim of a sink depression, that is, the 'overflow' point.

1.2: The original DDM is subtracted from the 'Fill' DDM, to result in having only depressions within a flat reference surface.

1.3: The raster is 'Reclassified', where the minimum and maximum depth values are stated, such that artefacts or larger structures are removed. The newly reclassified raster is then converted into a polygon.

1.4: Small irregularities and artefacts may still be present but can be delineated and removed.

A degree of manual editing is involved, hence the 'semi-automated' approach of mapping features – the remaining depressions considered to be true features can be manually edited to resemble depression shapes, particularly if the shapes are spurious or unrealistic. It is not possible to accurately determine the shapes of depressions smaller than 3 grid cells, thus these are removed.

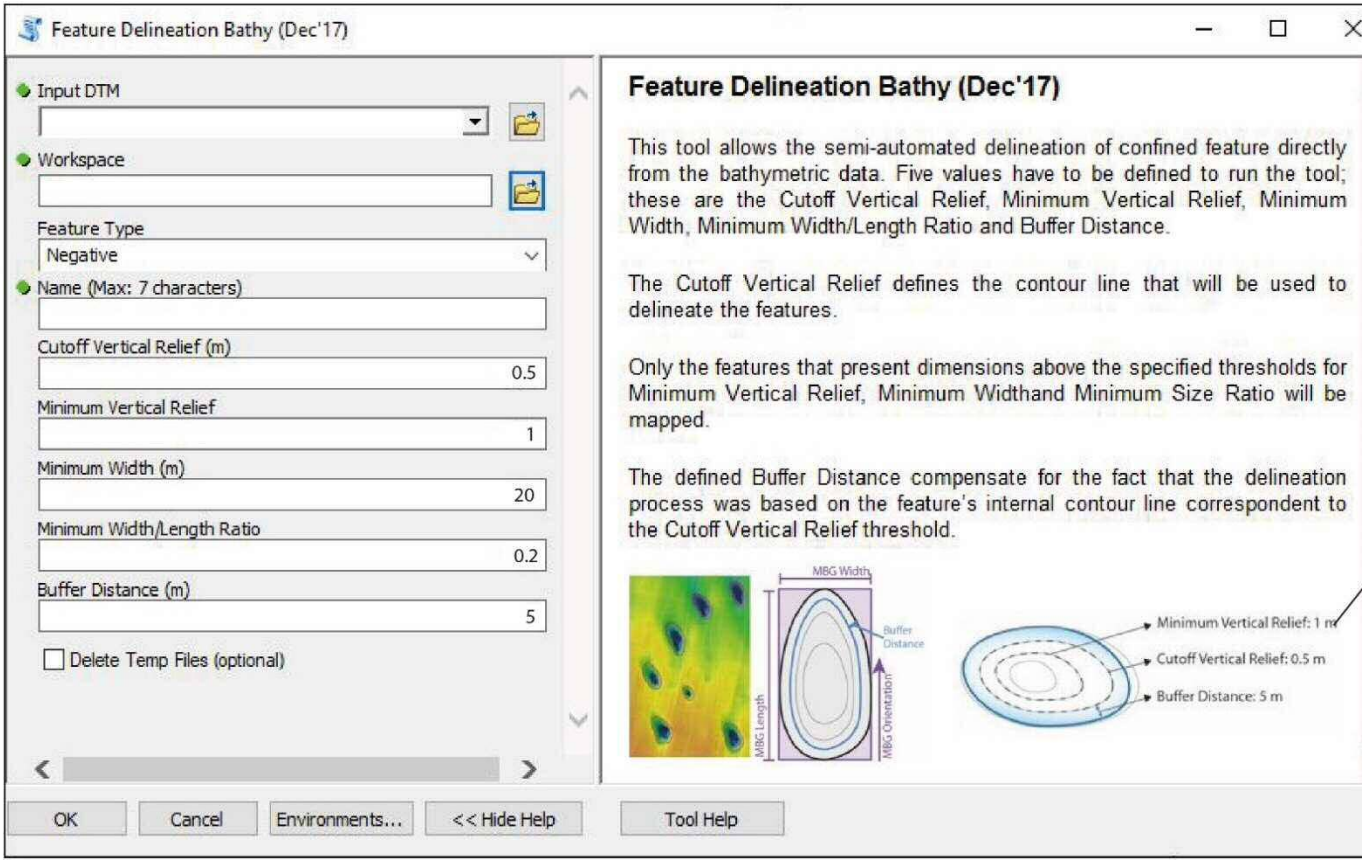

Fig. 3.9. Input parameters for Bathymetric-based Feature Delineation Tool from ArcGIS. DTM = digital terrain model, as a ra
Petrel®.

1.5: The next step is to add a 'buffer', which expands the current polygon borders, to ensure the full extent of the depression has been included to the rim, to compensate for the fact that the delineation process was based on the internal contour line corresponding to the cutoff vertical relief threshold. Following the buffer, the new buffer polygons are 'merged' by applying a 'spatial join', and 'dissolved' to create a new polygon shapefile.

1.6: The new shapefile can be simplified and smoothed, to remove any remaining artefacts.

1.7: The depth value of each depression is extracted, using the 'Extract by mask', 'Raster to point' and 'Spatial Join' tools.

At this point, the final result of the first script is achieved – a shapefile which delineates the mapped features with an attribute table summarising the area (in square metres); perimeter (in metres) and depth (in metres) of each depression.

The mapping thresholds are described in Gafeira et al. (2018) which include *Minimum Vertical Relief, Minimum Area* and *Minimum Width:Length Ratio*. The '*Minimum Area'* has been changed to '*Minimum Width'* in this thesis (Fig. 3.9). The *Minimum Width* must be defined by the width of at least 2 pixels to represent a geometrical shape. The *Cutoff Vertical Relief* marks where the initial internal contour line is marked, whilst the *Buffer Distance* expands the polygon borders to include the full extent of the depression to the rim.

The width of the mapped features was defined using the ArcGIS minimum bounding geometry function. This function computes a rectangle defining the smallest width enclosing the delineated features, which is used to infer eccentricity and ellipse axes lengths (Geldof et al., 2014). In order to obtain the morphological characteristics of depressions, interpreted surfaces had to first be converted from two-way time to the depth domain. Interval velocities were obtained from wells or estimated for seawater and used to depth convert the interpreted seismic volume in Petrel®.

The final delineation should be assessed visually, by overlaying the resulting shapefile over the original surface and determining whether further manual editing is required, or if thresholds need to be adjusted. Gafeira et al. (2012) noted that if the appropriate threshold values are used, the number of polygons that require manual editing should not exceed 10% of the total number of pockmarks delineated by the tool.

3.5.2 Feature Short Description Tool

As some of the pockmarks have been manually edited, the Feature Short Description Tool is applied to recalculate the Area, Perimeter, Width, Length and depression Depth values for each feature (Fig. 3.10). In order to recalculate the deepest value within each new

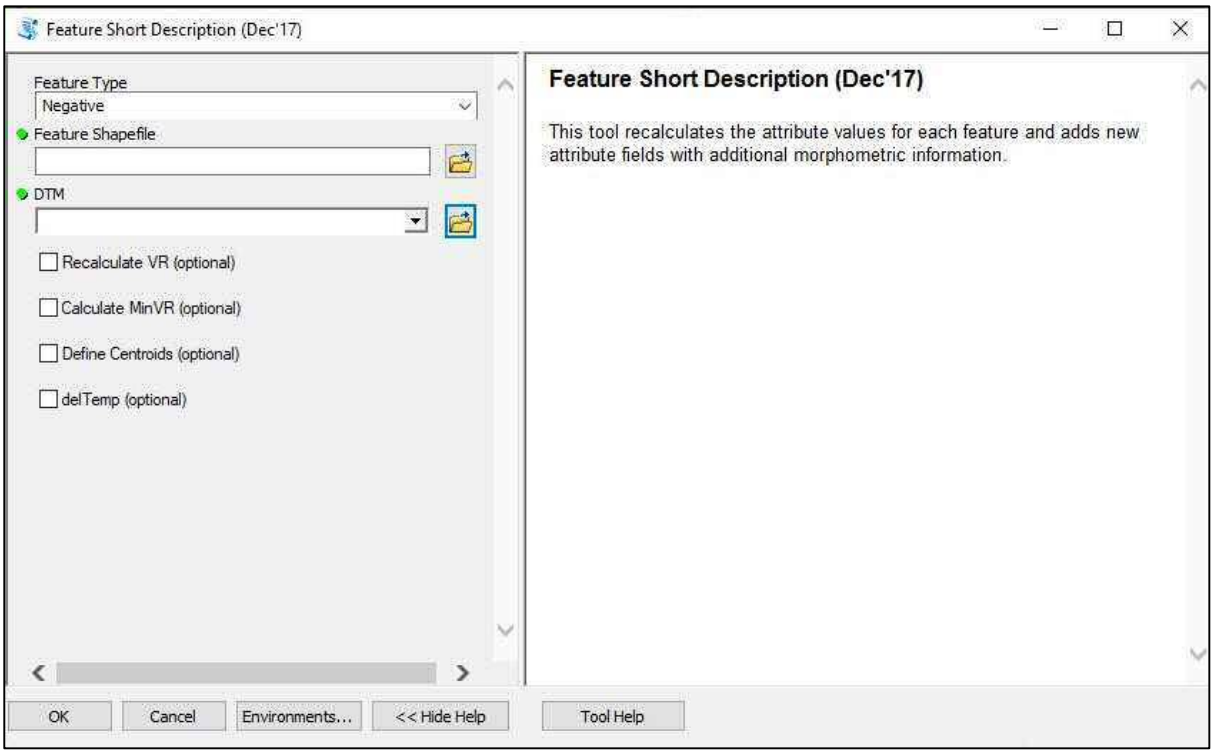

Fig. 3.10. Inputs for Feature Short Description Tool in ArcGIS. Feature shapefile is the resultant polygon shapefile from the Feature Delineation Tool; DTM is the digital terrain model – the original depth raster. VR = vertical relief.

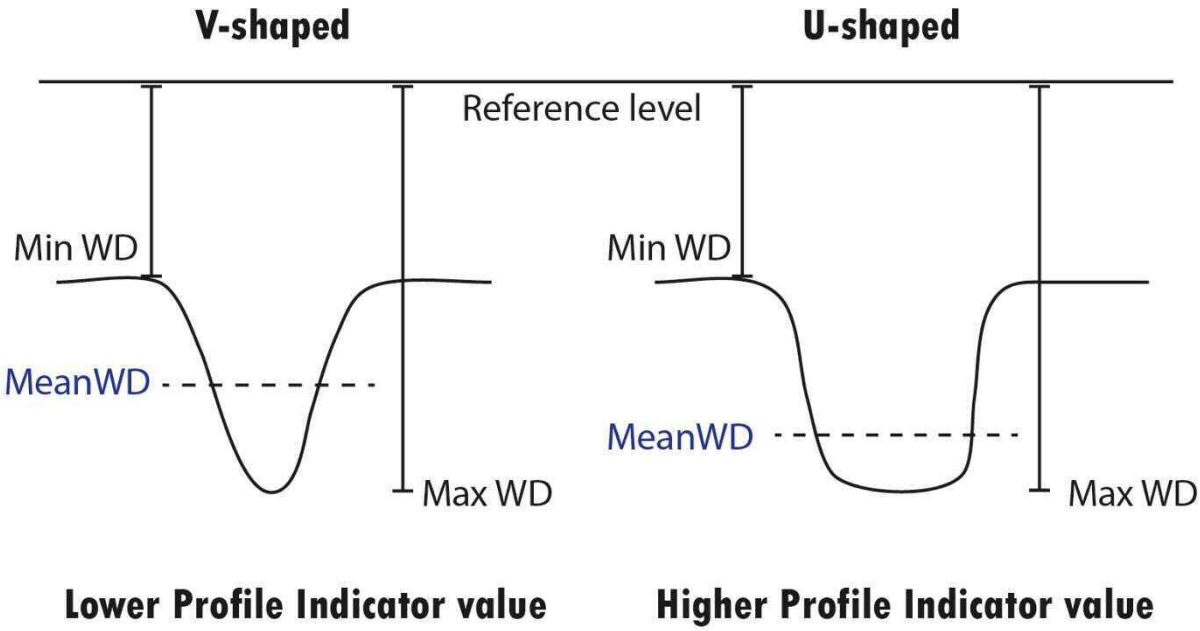

Fig. 3.11. Schematic of V- and U-shaped pockmark profiles, showing how the mean water depth (MeanWD) changes and affects the Profile Indicator value. Modified after Gafeira et al., (2018).

depression, the 'depth of water' needs to be defined, from which the minimum water depth – the rim of the depression, and maximum water depth – the deepest point in the depression – are calculated. By subtracting the two depths, the result is the vertical relief of the depression – the maximum depth of the depression. Once the new depth is known, the maximum- and minimum slope for each depression can be calculated.

Another aspect of morphology that can be assessed is whether the depressions are more V-shaped or U-shaped – this may reflect a single venting point (V-shaped), versus a potential collapse feature or wider venting area (U-shaped). This can be assessed by calculating the profile indicator: the ratio between the vertical relief and mean water depth (Equation 3.9), such that if the mean is closer to the base of the depression (higher ratio), the morphology is more U-shaped. If the ratio is closer to 1:2 (0.5), it is likely to be more V-shaped (Fig. 3.11).

Equation 3.9

After using the two Tools mentioned above, the following shapefiles are output:

- A polygon shapefile that outlines the depressions.
- A point shapefile that delineates the centroids of the depressions.
- A point shapefile that shows the position of the deepest point within the depressions.

The polygon shapefiles are imported back into Petrel to compare with and relate to the seismic data in three dimensions, to analyse the spatial relationship with structures below and across the study area.

3.5.3 Bathymetric Positioning Index (BPI) Tool

In some cases, the raster is reclassified into a BPI map, where absolute values of a parameter are used to define features. For example, instead of a change in depth, the Tool records a change in value of a seismic attribute such as amplitude, above a given threshold (Fig. 3.12). This was applied in Chapter 4 to map high-amplitude anomalies within Triassic pods to compare spatially with overlying mapped depressions.

The final output of the Tools includes a table of morphological attributes for the shapefile, from which statistical analyses can be made and compared within and across datasets. Table 3.2 summarises the main attributes and what they represent. Further attributes can be added manually, such as the presence or absence of amplitude anomalies (Chapter 4), measuring the depth of source, or comments on the underlying structure (Chapter 5). During data analysis for Chapter 5, ArcGIS often froze or crashed due to the size of the dataset. The dataset was clipped into smaller blocks, the Tool run individually on each block, and the resulting shapefiles merged into one file.

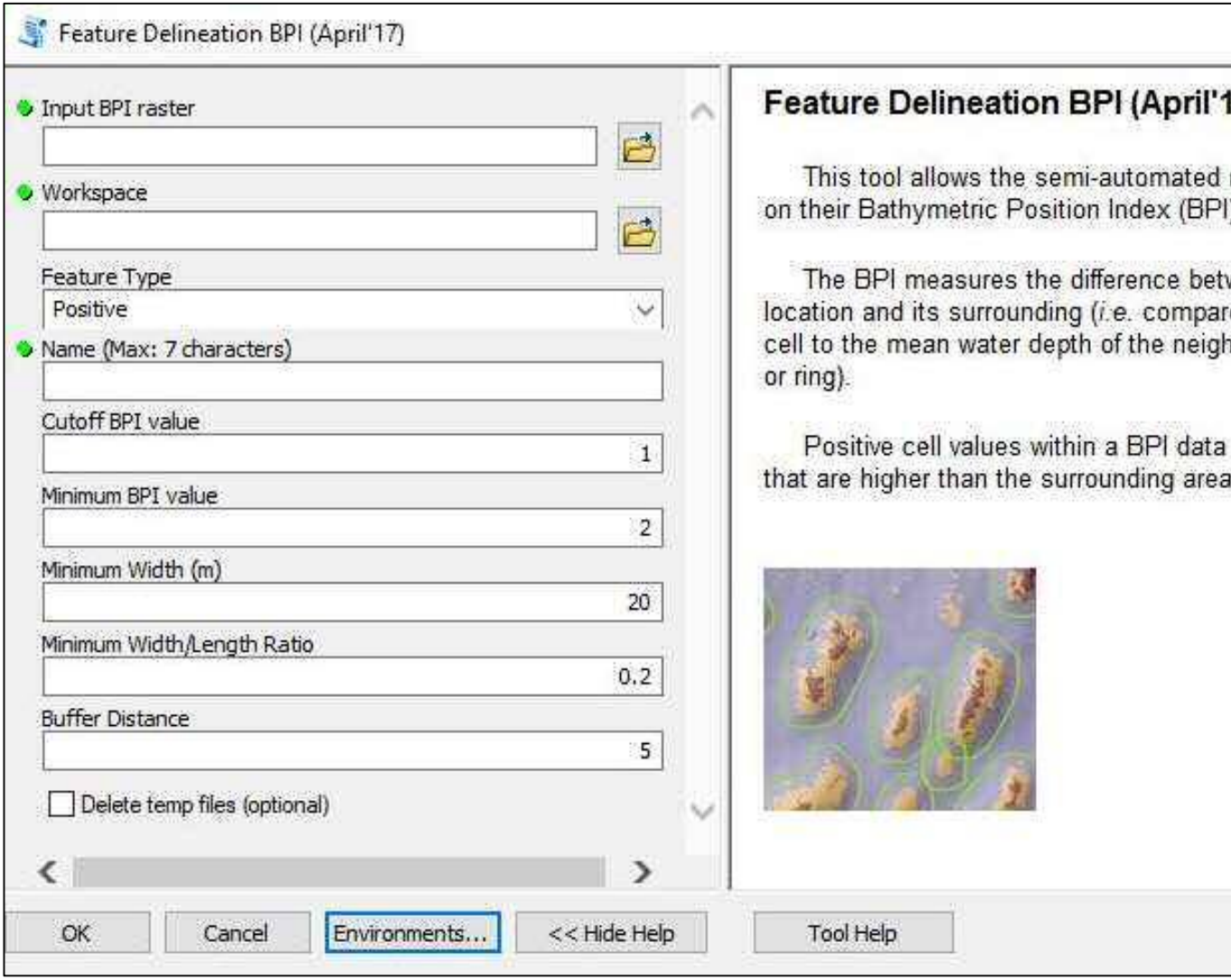

Fig. 3.12. Input parameters for Bathymetric Position Index (BPI) Feature Delineation Tool in ArcGIS. BPI values in Chapter and buffer distance are in meters.

Attributes	What the attribute represents
Area	Area of each polygon feature in square metres
Perimeter	The perimeter of each polygon feature in metres
MBG_Width MBW_Length MBG_Orient	Describes the dimensions and orientation of the Minimum Bounding Geometry (MBG) rectangle that contains each delineated feature (using the option of "rectangle by width")
MBG_W_L	Describes the aspect ratio of the MBG's resulting rectangles (i.e. length of the shorter side, MBG_Width, divided by the length of the longer side, MBG_Length). This value can be used as a proxy to the feature aspect ratio and to infer the feature eccentricity
MinWD and MaxWD	The maximum water depth to minimum water depth capture the feature water depth range
MeanWD and StDevWD	The mean water depth and standard deviation of water depth describe the distribution of water depth values
MaxVR	The maximum vertical relief values are defined by subtracting the maximum water depth from minimum water depth
MinVR	The minimum vertical relief correspond to the vertical relief between the deepest and shallowest point of the feature and the last confined contour line within the delineated feature
PI (Profile Indicator)	The profile indicator is the ratio (MinWD – MeanWD / MinWD – MaxWD). It can be used to assess whether the feature is more V-shaped or U-shaped
Max Slope	The maximum slope is measured as the maximum change in value of a cell with its eight closest neighbours, in degrees to the horizontal
Mean Slope	The mean slope is the average change in value of a cell with its eight closest neighbours, in degrees to the horizontal

Table 3.2. Table summarising the main attributes that result from applying tools from the BGS Seabed Mapping Toolbox.

3.6 Statistical analyses

Statistical data was computed based on the results of the BGS Seabed Mapping Toolbox. Box plots were plotted to show the ranges of individual morphological attributes to describe and compare across different categories, whilst scatter graphs were plotted to determine any correlations between morphological attributes.

Percentages of pockmarks, mud volcanoes and amplitude anomalies were calculated in different structural settings to describe the spatial distribution of these features. Spatial analysis of clustering was computed using the 'Next Nearest Neighbour Index (Rn)' (Equation 3.10), a first order statistic which determines whether the points (e.g. pockmarks) are clustered (Rn < 1), random (Rn = 1) or dispersed (Rn > 1) (Clark and Evans, 1954; Mitchell, 2005):

Equation 3.10

where (Obs) is the mean observed nearest neighbour distance, n is the number of pockmarks and a is the aerial extent of pockmark coverage in the study area. This statistical parameter was calculated using the 'Average Nearest Neighbour' Tool in ArcGIS. In addition, the Average Nearest Neighbour Tool calculates a Z-score and p-value, for statistical significance. For example in Fig. 3.13, when the Z-score is less than -2.58, there is less than 1% likelihood that a clustered pattern is a result of random chance.

Further methods and parameters specific to the three datasets are described in Chapters 4, 5 and 6.

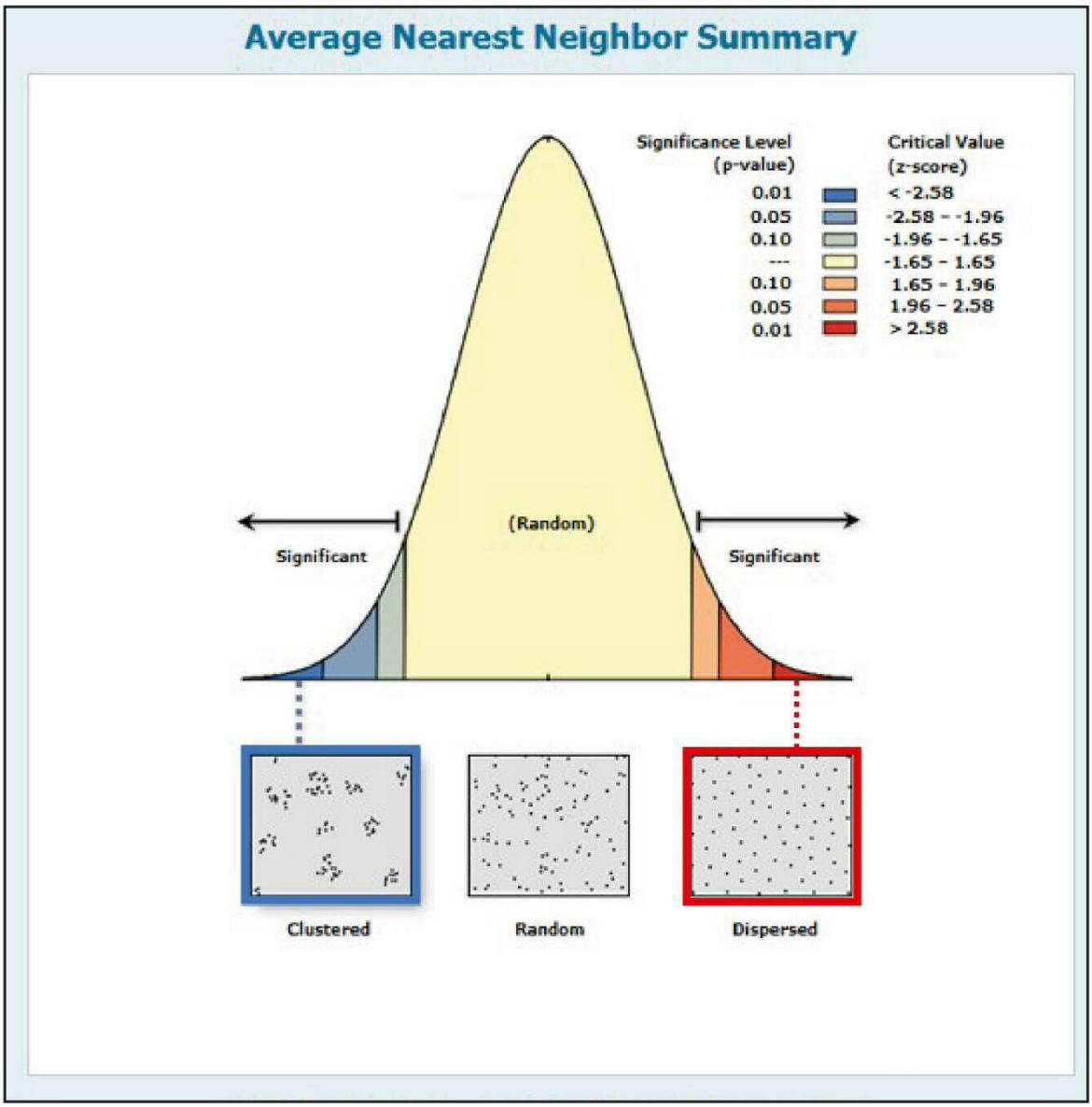

Fig. 3.13. Average Nearest Neighbour normal distribution schematic plot showing a range of Z-score values for clustered, random and dispersed spatial distribution of points. Adapted from ArcGIS.

CHAPTER FOUR

Large pipes in the Norwegian Central North Sea: A case for important fluid bypass through early Mesozoic successions

4 Fluid flow across salt welds

4.1 Abstract

The subsurface injection of carbon dioxide (CO_2) comprises a technique to enhance oil recovery and, consequently, the economic value of depleting oil and gas fields. It complements carbon capture and storage, which is a key technology to mitigate greenhouse gas emissions. In this work, an integrated method developed by the British Geological Survey and Cardiff University used high-resolution 3D reflection seismic and borehole data from the Jæren High to analyse potential seal breaches and fluid flow paths in a frontier area of the North Sea, ultimately assessing the risk of a possible carbon capture and storage site. The spatial analysis of subsurface fluid flow features was integrated with borehole and geochemical data to model the burial and thermal history of potential storage sites, at the same time estimating the timing of fluid expulsion. On seismic reflection data, fluid pipes connect reservoir intervals of different ages; spatial analyses thus reveal clusters of fluid flow features above strata grounded onto deep reservoir intervals. The integrated method shows that gas matured from Visean coals to migrate up-dip during the Triassic-Jurassic into lower sandstone reservoirs in the Rotliegend Group. The containing seal interval above the Rotliegend Group was breached once sufficiently large volumes of gas generated high overpressures in the reservoir. Some of these fluid flow features may still be active pathways, as indicated by bright amplitude anomalies within the pipes. This study shows how integrated analyses may enhance understanding of fluid-flow pathways and tertiary migration, de-risking prospective sites for carbon capture and storage.

4.2 Introduction

Enhanced hydrocarbon recovery techniques are critical for extracting maximum volumes of hydrocarbons from mature fields. They involve thermal, chemical, and gas-injection techniques, one of which comprises the injection of CO_2-enriched solutions in reservoirs approaching depletion (Thomas, 2008). In parallel, Carbon Capture and Storage (CCS) is itself regarded as important as a technique to mitigate CO_2 emissions. This forms a positive feedback in the energy industry as mature basins such as the North Sea comprise viable targets for CCS, at the same time benefiting from a vast database of seismic, well and dynamic production data.

In the North Sea, depleted gas fields have been assessed for combined enhanced oil and gas recovery and CCS, e.g. the Bunter Sandstone in the Southern North Sea (Agada et al., 2017; Williams et al., 2013), and the P18-4 Gas Field offshore The Netherlands (Arts et al., 2012). The Utsira Sands, located within the overburden of the Sleipner Gas Field (Norwegian North Sea) have been successful in storing CO_2 for more than 20 years, while natural gas is being produced from nearby fields (Eiken et al., 2011). Depleted hydrocarbon fields are particularly important for the implementation of CCS as they can successfully store large volumes of CO_2 as demonstrated by their natural containment of hydrocarbons over geological timescales. In addition, potential CO_2 storage sites may occur adjacently to known producing fields. One of such cases is the regionally extensive Permian Rotliegend Group, which is a saline aquifer in areas where hydrocarbons are not found in economic volumes (Wilkinson et al., 2013). Notwithstanding the latter examples, the injection of CO_2 for combined enhanced hydrocarbon recovery and CCS requires a detailed understanding of geological risks and uncertainties prior to the implementation of such techniques, namely the recognition of potential fluid flow paths through caprocks and the sealing capacity in target storage areas. Previous studies predicting the migration of injected gas plumes have indicated that CO_2 can migrate for large distances; for example, uncontained CO_2 plumes can reach nearby wells and create risks in terms of well integrity and gas management in many an oil and gas field (Li et al., 2018).

The study area is located on the Jæren High basement structure; this is a relatively underexplored part of the Norwegian Central North Sea and extends into the UK sector, in which wells target Paleocene successions near large salt diapirs on the eastern margin of the East Central Graben (Fig. 2.1, Fig. 4.1). In contrast, wells in the Norwegian North Sea penetrate Triassic strata and the Upper Permian Zechstein Group (Fig. 4.3). Two oil fields

have so far been discovered on the Jæren High; the Gaupe Field to the north of the study area and the Brynhild Field to the south (Fig. 4.1c). Both contain Upper Jurassic reservoirs above broad, developed salt walls. In the study area, pipes and associated depressions are imaged on 3D seismic reflection data within the Mesozoic succession of the Jæren High. These features are likely associated with fluid flow and rooted in deep Paleozoic strata. Hence, this setting contrasts with salt injection features (Clark et al., 1999) and other documented pipes in the North Sea, which typically originate from Cenozoic strata (e.g. Berndt et al., 2003) or are located above salt diapirs (de Mahiques et al., 2017; Salisbury, 1990). The fluid flow features at the upper terminations of pipes are termed depressions to begin with; the interpretation of these features is made by studying their morphology and formation mechanisms. Hence, the aims of this chapter are to:

a) Analyse the spatial distribution of buried depressions and pipes using an integration of geographic information systems (GIS), seismic and well modelling, using the example of the Jæren High.
b) Determine the timing of fluid flow across the Mesozoic succession of the Jæren High.
c) Relate the presence of fluid flow features to the local and regional geological settings of the UK and Norwegian North Sea.
d) Discuss the implications of seal bypass and associated risks to CCS based on the method presented here.

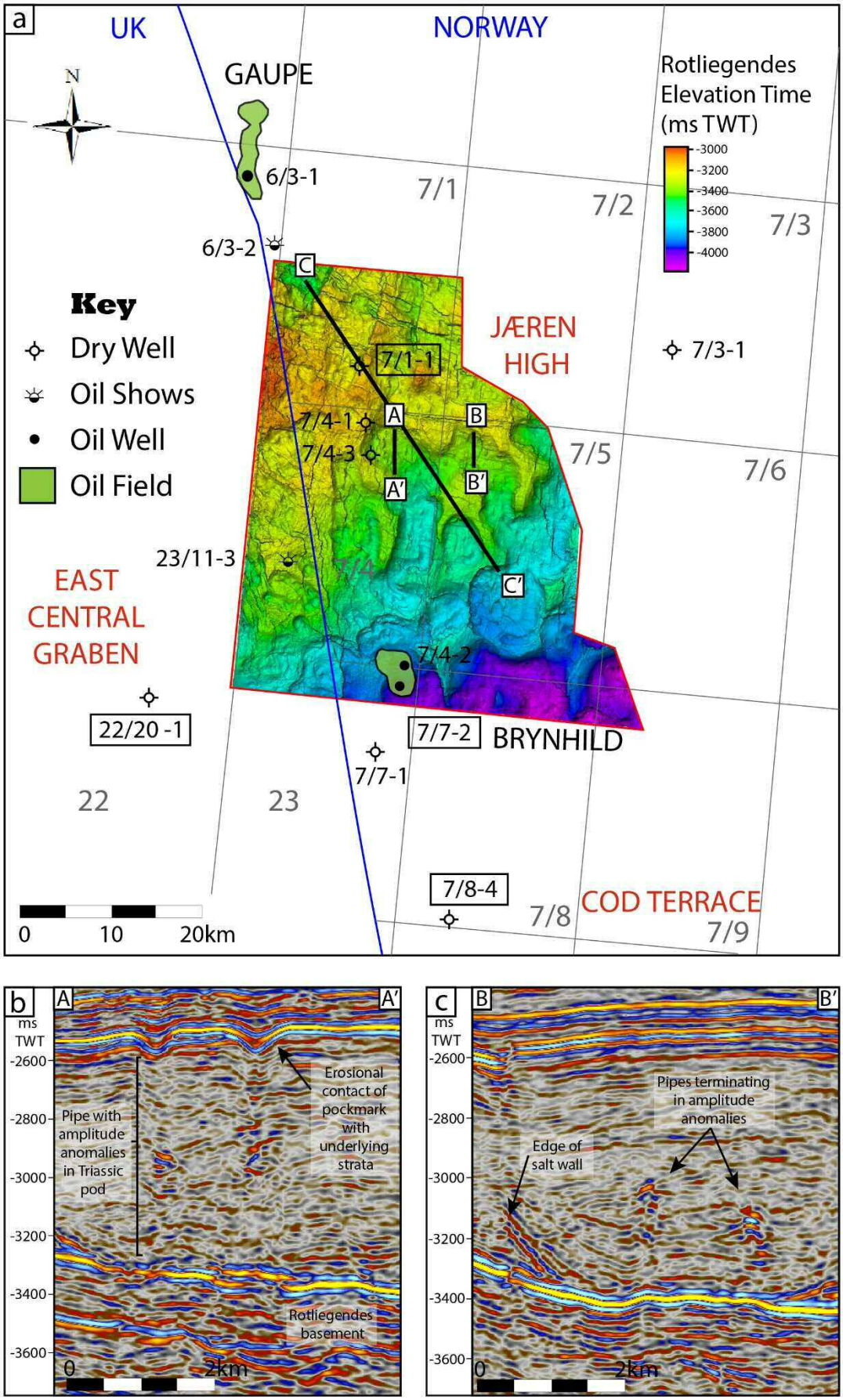

Fig. 4.1. a) Two-way-time elevation surface of the Top Rotliegend Group. Key wells and fields are labelled; wells in boxes are used for burial history modelling in Fig. 4.12. Seismic line C-C' is shown in Fig. 4.4. b) Seismic example of a pipe terminating in a pockmark. c) Seismic example of a pipe terminating in a high-amplitude anomaly.

4.3 Chapter specific data and methods

4.3.1 Seismic interpretation

The interpreted 3D seismic reflection data was acquired across the Jæren High in the Central North Sea. For a full description of the data resolution, see section 3.3.1. The focus of this study is the Mesozoic section, from 2 to 4.3 seconds two-way travel time (TWT). Fig. 4.1 shows the two-way time elevation surface map of the Top Rotliegendes with relevant wells and seismic lines.

Wireline logs and reports of twelve exploration wells were used, of which two were provided by the British Geological Survey for the UK sector. Detailed well information including composite logs, well reports and geochemical reports of the remaining ten wells were obtained from the Norwegian Petroleum Directorate (NPD) online database.

The adopted methodology is summarised in Fig. 4.2. Six horizons (H1 to H6) were mapped on seismic data to highlight the pod-interpod structure of the Mesozoic succession and the associated distribution of buried depressions (Fig. 4.3, Fig. 4.5, Fig. 4.6 and Fig. 4.7). Five wells were tied to the seismic data to correlate horizons and constrain the local stratigraphy; three of these wells are shown in Fig. 4.3 (wells 6/3-2, 7/1-1 and 7/7-2). Isopach maps were generated from interpreted surfaces to highlight lateral thickness changes and the distribution of salt walls and welds.

The seismic Variance attribute was used to highlight irregularities such as faults, pockmarks, and salt. Maximum Magnitude maps were extracted between the interpreted Mesozoic surfaces to determine whether any high-amplitude anomalies were prevalent – possibly representing fluid pockets or cemented units – and if there is any spatial significance to them (Fig. 4.4). However, not all the high-amplitude anomalies in the Triassic pods were extracted initially, as they have similar or lower amplitudes to high-amplitude strata in the Skagerrak Formation, where this latter is present immediately below horizon H4 (i.e. from the Top Cromer Knoll Group to – 150 ms TWT; Fig. 4.4 and Fig. 4.9). Equally, the extent of any high-amplitude anomalies observed immediately below the pockmarks cannot be mapped clearly if they are of similar amplitude to the more continuous seismic reflections in the Skagerrak Formation. To overcome these limitations, the anomalies within 150 ms TWT below horizon H4 (Top Cromer Knoll Group) were interpreted manually on Petrel®, and their presence was assigned to the attribute tables of depressions that coincide with seismic anomalies (Table 4.3, Appendix B).

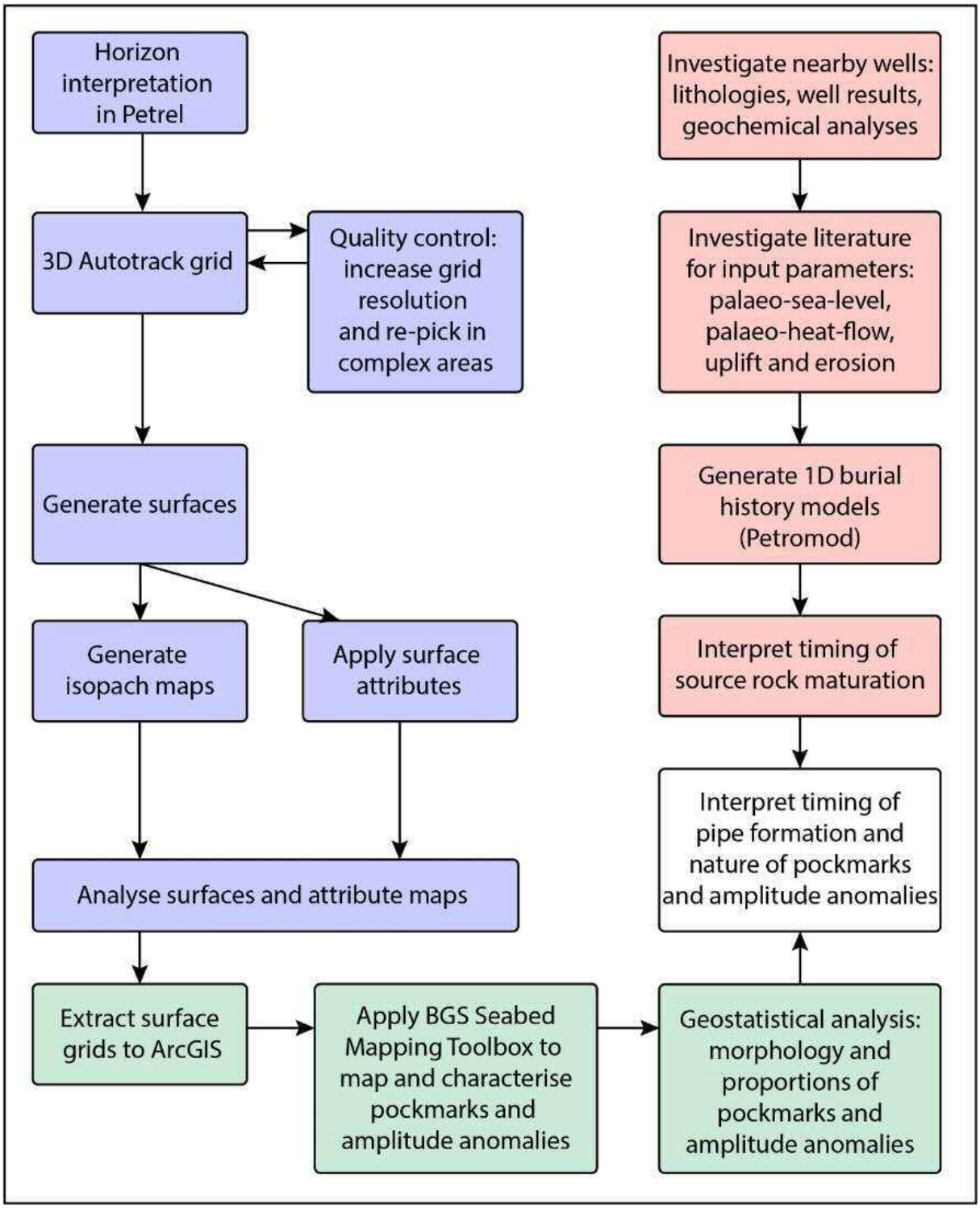

Fig. 4.2. Flow chart summarising the methodology used in this Chapter. Three different types of software were used, Petrel® for seismic interpretation (blue boxes), ArcGIS® for mapping pockmarks and anomalies (green boxes), as well as spatial and morphological analysis of mapped features, and Petromod® for the maturation modelling of key wells (red boxes).

Secondly, the window for Maximum Magnitude extraction was reduced to between 150 ms TWT below the Top Cromer Knoll Group (horizon H4), and 50 ms TWT above the Top Salt horizon H2, thus reducing any spurious results due to human error when mapping the Top Salt Horizon (Fig. 4.4). The resulting Maximum Magnitude surface was then exported to ArcGIS and the high-amplitude anomalies were identified using the Seabed Mapping Toolbox: the BPI Tool. The minimum and cutoff BPI was an amplitude of 12000, minimum width was 50 m (horizontal resolution), minimum width:length ratio was 0.2 and a buffer distance of 5 m was chosen. Ultimately, significant quality control was undertaken, including comparing with seismic profiles, as anomalies do not have to be circular to semi-circular like depressions.

Three seismic surfaces containing circular depressions were exported from Petrel into ArcGIS® version 10.1: a) the Top Mandal Formation (H3), b) the Top Cromer Knoll Group (H4), and c) the Intra-Chalk horizon (H5) (Fig. 4.3). The Seabed Mapping Toolbox was used to map and characterise the depressions from these three horizons. The Toolbox mapping thresholds described in Gafeira et al. (2012) were adapted for this dataset (Table 4.1).

Input Parameters	Values
Cutoff vertical relief	7 m
Minimum vertical relief	25 m
Minimum width	100 m
Minimum width:length ratio	0.2
Buffer distance	100 m

Table 4.1. Input parameters for the Seabed Mapping Toolbox. Cutoff vertical relief and buffer distance were chosen by trial and error. Minimum vertical relief was defined as 25 m, half of the vertical resolution. Minimum width must be defined by at least two pixels, and horizontal resolution is 50 m, therefore minimum width is 100 m. Minimum width:length ratio was 0.2, as used in Gafeira et al. (2012).

The morphological characteristics of the mapped depressions are compared with the published data to interpret possible mechanisms for their formation. The Width and Width:Length Ratio of the acoustic anomalies, as well as the pipe height, were assigned to the ArcGIS' attribute table describing the depressions. Spatial analysis was conducted visually by overlaying the delineated depressions and anomalies above the salt isopach surface. Statistical analysis included generating box plots to visualize the ranges of pipe heights and morphological attributes including Vertical Relief, Width, and Width:Length ratio. Scatter graphs were generated to compare the Vertical Relief and Width of depressions in the same spatial locations but different horizons.

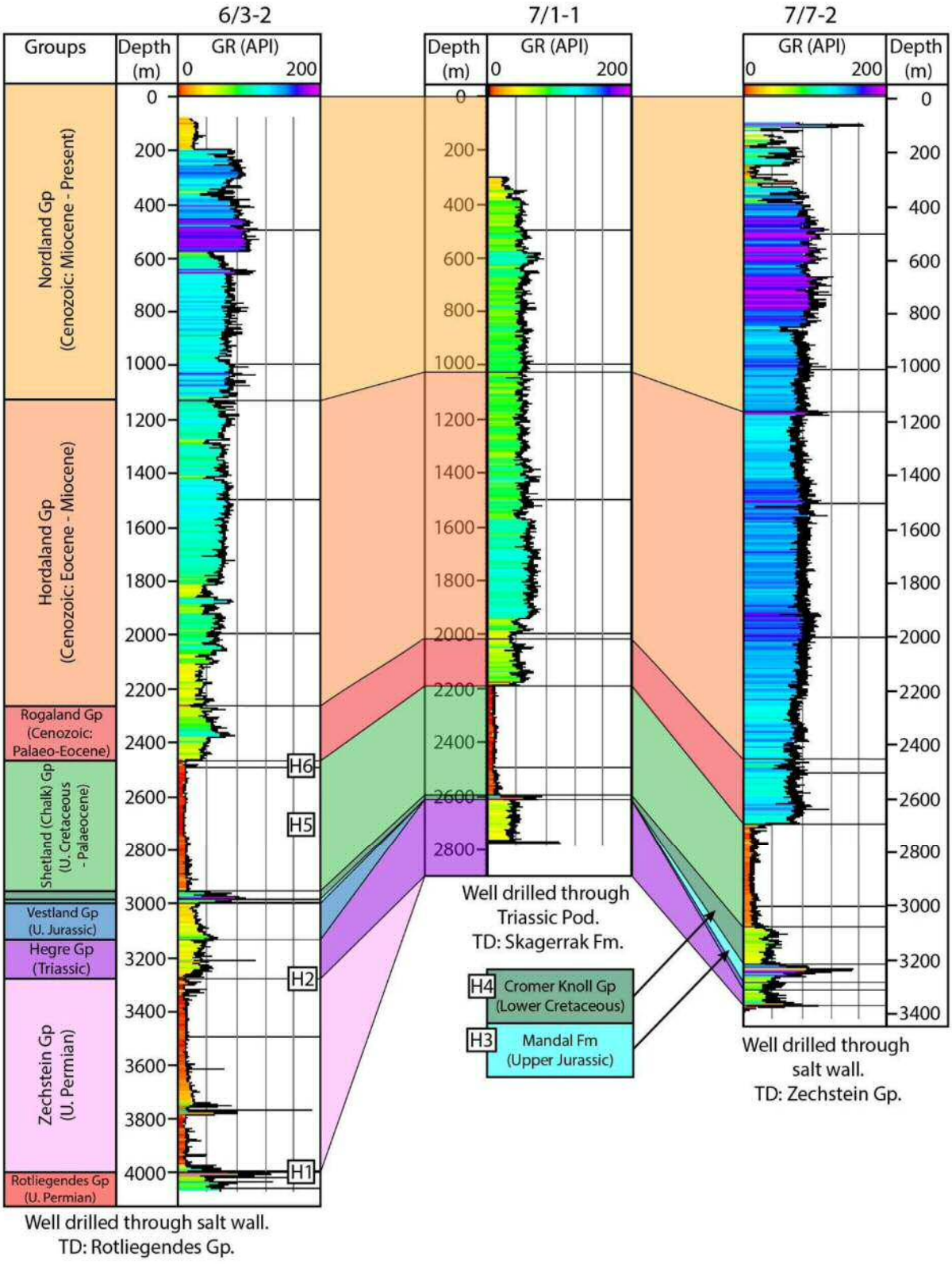

Fig. 4.3. Well correlation panel using gamma ray logs, from the north-west (6/3-2) to south-east (7/7-2), through salt walls and a Triassic pod. The seismic horizons mapped in this work are named H1 to H6.

4.3.2 Petromod Modelling of Burial History

Schlumberger's Petromod® was used to generate simplified, 1D burial history plots for four wells on and close to the Jæren High (Fig. 4.1). Model inputs including sub-surface lithologies, thicknesses, ages and bottom-hole temperatures were derived from well reports from the NPD website database. The magnitude and timing of tectonic uplift events, as well as a palaeo-sea level curve, were obtained from the literature (e.g. Monaghan et al., 2017; Underhill and Partington, 1993; Ziegler, 1992). The thermal history used was taken from Frederiksen et al. (2001). Although the thermal history in this latter work is characteristic of strata further to the south of the Jæren High, it was considered as representing the regional heat flow values for the study area. Model parameters are summarised in Appendix A.

The thickness of strata not penetrated by wells, such as Zechstein, Rotliegendes and Carboniferous strata, are estimated from the depth-converted seismic volume and using interval velocities from exploration wells 7/3-1 and 6/3-2. The interpretations in Milton-Worssell et al. (2010) also provided valid constraints on the thickness of Paleozoic strata.

Pepper and Corvit (1995) ran a series of experiments to redefine the hydrocarbon generation windows for different organofacies, from marine shale source rocks to terrestrial, humic coal source rocks. They concluded that for humic coals such as the Westphalian in the Southern North Sea, the gas generation window ranges from 175°C to 220°C to generate between 10% and 90% of the potential gas in Paleozoic source rocks. The oil generation window for a marine shale source such as the Kimmeridge Clay Formation (UK equivalent of the Mandal Formation in the Norwegian North Sea) ranges from 105°C to 145°C, and its gas generation window varies from 145°C to 210°C. These isotherm thresholds for the two source rocks are labelled on the resulting burial history models and were used to interpret the timing of source rock maturation on and close to the Jæren High. Geochemical well reports from the NPD website were investigated to summarise the hydrocarbon findings of each well.

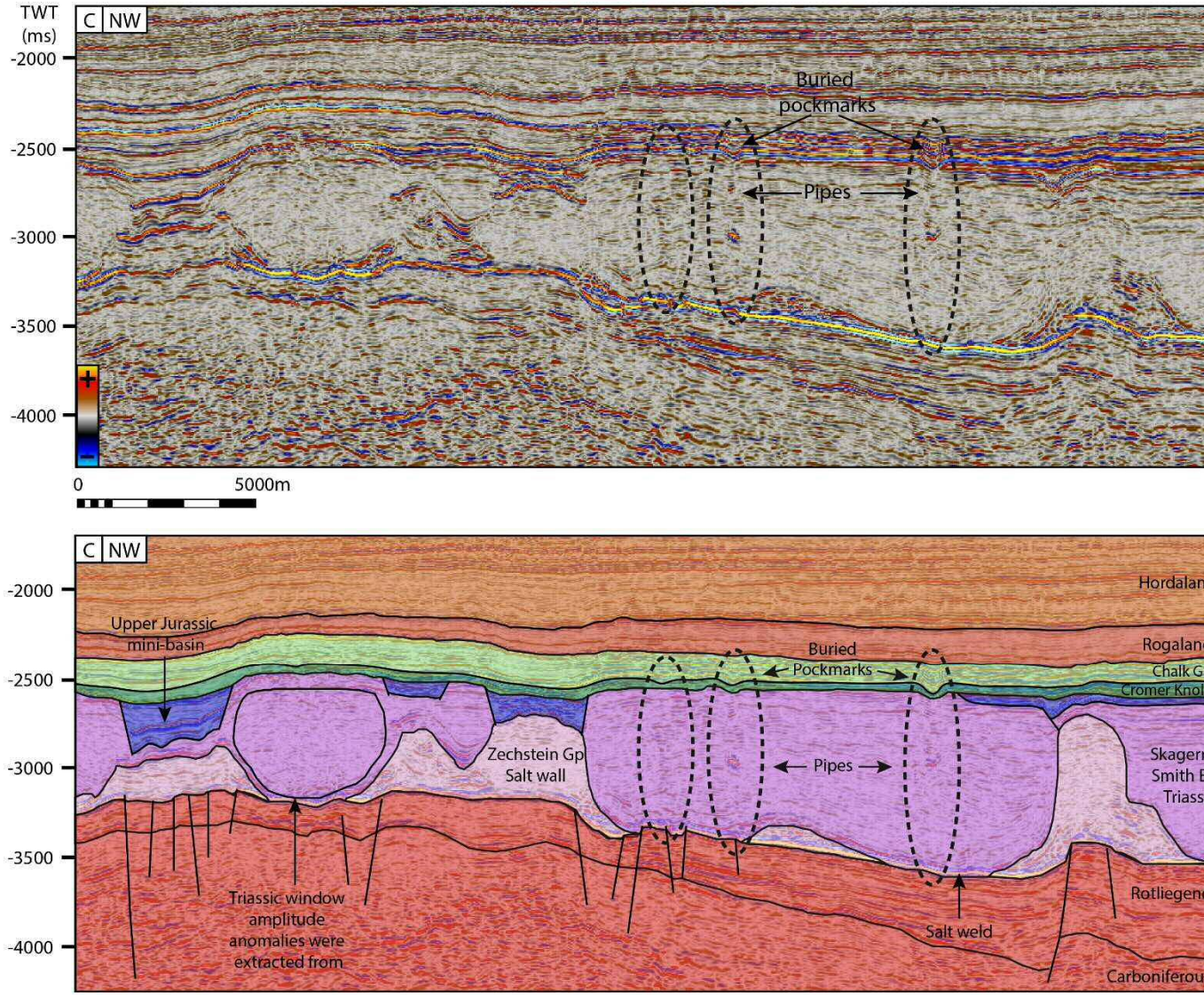

Fig. 4.4. Regional seismic line between -1800 ms TWT and -4200 ms TWT, from northwest to southeast, showing the key fe
basement, salt walls and grounded sediment pods crosscut by vertical pipes that terminate in buried pockmarks. The Triassic w
of high-amplitude anomalies is also highlighted.

4.4 Seismic Stratigraphy

4.4.1 Carboniferous/Devonian units

Pre-salt units are poorly resolved, consisting of mostly chaotic seismic reflections. Some continuous reflections and faults are evident. The units dip to the southeast, pinching out towards the crest of the Jæren high to the northwest.

4.4.2 Horizon 1 – Top Rotliegend Group (Late Permian)

The top of the Rotliegendes is marked by a bright hard seismic reflection below which sub-parallel, continuous reflections are observed. No wells penetrate Carboniferous strata, so it is unclear as to the true depth extent of the Rotliegend Group.

Small 'ridges' are seen in map view on the surface of the Rotliegend Group within the salt weld zones, which may be imaging artefacts, or a consequence of disruption due to fluid flow related to overlying pipes. The Rotliegend Group was coupled with the top of the basement during the main rifting episode and is tilted to the SE.

4.4.3 Horizon 2 – Top Zechstein Group (latest Permian)

The top of the Zechstein Group is marked by a bright 'hard' seismic reflection. Where the contact is near vertical imaging is poor and the contact is inferred. The Zechstein Group is preferentially located on relative basement highs, and form salt walls with a predominant N-S trend and minor E-W trend, with intervening salt welds (Fig. 4.5b). The thickness of the Zechstein Group was calculated using an interval velocity of 4650 m/s from well 6/3-2, and is shown to vary from 0 m to ~2300 m, thickening south-eastwards.

The interior of some salt walls consists of poorly imaged, low amplitude, chaotic, discontinuous seismic reflections. In contrast, more extensive salt walls contain continuous, horizontal reflections, similar to the overlying clastic units, and could be mistaken as such. However, well calibration confirms the presence of the Zechstein Group.

4.4.4 Smith Bank – Skagerrak Formation (Triassic)

The Triassic units are found in large pods between salt walls. Seismic reflections are of low amplitude due to the inherent homogeneity of the silt- and mudstones that predominate

within this unit. Where the Triassic strata are well imaged, a combination of diverging and parallel internal reflections is observed, with onlap both within the pods and onto the adjacent salt walls. Strata downlap onto the Rotliegend Group is common where turtle-back anticlines have formed, indicating grounding of sediment pods and salt weld formation as early as the Triassic. Thin Triassic units have been identified above some salt walls in wells 6/3-2 (145 m) and 7/7-2 (45 m), but may not be present everywhere. Narrow, chaotic pipes cross cut the Triassic pods, but are poorly imaged due to the semi-transparent nature of the Triassic strata, apart from occasional amplitude anomalies. The top Triassic does not show a clear seismic reflection and it was not interpreted.

4.4.5 Horizon 3 – Top Mandal Formation (Late Jurassic)

The Lower-Middle Jurassic is assumed to be absent across the Jæren High as it has not been crossed by any wells – the area was emergent during the Early Jurassic doming of the North Sea. The Upper Jurassic has a limited distribution, being absent above most of the Triassic pods and present directly above salt walls – the thickest section encountered is 157m in well 6/3-2.

The Mandal Formation manifests as a high-amplitude seismic reflection that is characteristic of a 'hot shale', just as the Kimmeridge Clay Formation, its UK equivalent. The Mandal Formation is also clearly marked by a sharp peak in gamma ray curves (Fig. 4.3). Towards the east of the study area, where the Mandal Formation is interpreted to occur above the Triassic pods, some depressions are seen, with pipes imaged below.

4.4.6 Horizon 4 – Cromer Knoll Group (Early Cretaceous)

The Base Cretaceous Unconformity lies across the Triassic pods and Upper Jurassic above salt walls. The Top Cromer Knoll Group (hereafter, CKG) is also an unconformity representing the top of either the Rødby, Sola, Tuxen or the Åsgard Formations. The CKG comprises continuous, gently undulating internal seismic reflections. The top of this Group marks the transition from marls to the Chalk Group, and manifests as a bright hard seismic reflection, draping the full extent of the Triassic-Jurassic pods and interpods. This surface is shown to be covered in large circular depressions (Fig. 4.6b).

4.4.7 Horizon 5 – Intra-Chalk Group (Late Cretaceous)

This horizon is an intra-Chalk unconformity, possibly corresponding to the Top Hod Formation. It varies greatly in amplitude, but is largely continuous, draping the underlying topography. In some cases, the surface contains depressions above those seen in the Cromer Knoll Group.

4.4.8 Horizon 6 – Top Chalk Group (Late Cretaceous – Early Paleocene)

The Top Chalk is another bright, continuous seismic reflection, marking the transition from Cretaceous-Paleocene Chalk to Tertiary clastics. Internal seismic reflections in the Chalk Group are generally parallel to sub-parallel and of low amplitude. Some faults appear to cut the Chalk Group, whilst no depressions are interpreted inside this unit.

4.4.9 Top Sele Formation (Paleocene)

The Paleocene unit contains mostly low amplitude, parallel to sub-parallel internal reflections representing hemipelagic mudstones onlapping onto basin highs. The Sele Formation is cut by high angle, high density polygonal faults that extend into younger strata.

4.4.10 Hordaland and Nordland Groups (Paleocene – Recent)

The Hordaland and Nordland Groups, from Eocene to present, consist of parallel, continuous reflections, with occasional, weakly sub-parallel and onlapping seismic reflections, demonstrating the largely hemipelagic nature of their strata.

The seismic-stratigraphy of the study area is summarised in Table 4.2 and the stratigraphic framework is shown in Fig. 2.2.

Age of Base	Stratigraphic Units	Thickness (m)	Seismic Units	Seismically Mapped Horizon Number	Lithologica
Paleocene	Nordland Group Hordaland Group Rogaland Group	1800 - 2600			Hemipelagic thin sand bo
Upper-Lower Cretaceous	Chalk Group	300 - 500	Top Chalk Group	H6 H5	Chalk limes Chalk limes
Lower Cretaceous	Cromer Knoll Group	20 - 250	Top Cromer Knoll	H4	Calcareous c
Upper Jurassic	Mandal Formation Ula Formation	0 - 200	Top Mandal Formation	H3	Predominan shales (Man The Ula For marine sand
Uppermost Permian	Skagerrak Formation Smith Bank Formation	0 - 2300			Skagerrak F and mudston Smith Bank and floodpla siltstone uni
Upper Permian	Zechstein Group	0 - 2300	Top Zechstein Group	H2	Evaporite su halite, anhy stringers.
Permian	Rotliegend Group	200 - 500	Top Rotliegend Group	H1	Red, aeolian interbedded, facies.
Upper Devonian	Carboniferous units	1000 +			A mixture o and mudston

Table 4.2. Summary of the stratigraphy of the Jæren High and seismic units mapped.

4.5 Seismic interpretation

The results of the detailed mapping undertaken in this Chapter are illustrated in Fig. 4.5, Fig. 4.6, and Fig. 4.7, where key features are highlighted for each interpreted horizon. Rotliegendes strata dip to the southeast and contain an array of faults that is oriented predominantly N-S and E-W. Relatively shallower sections of the basement are likely due to a combination of basement faulting and velocity pull-up below thick salt walls (Fig. 4.5a, b). The salt walls are approximately oriented N-S, increasing in thickness to the southeast, separated by Triassic pods where salt is thin or absent. The Upper Jurassic Mandal Formation is absent updip over the pods but present in supra-salt minibasins (Fig. 4.4 and Fig. 4.6a), whilst overlying Cretaceous sediments are present across the study area and become shallower to the east, opposite to the Rotliegendes (Fig. 4.6b). This suggests tilting of the basement and erosion or non-deposition of the Mandal Formation during the Jurassic, followed by subsidence of the Jæren High in the Upper Jurassic to Cretaceous, as the North Sea rift was 'drowned', centred on the grabens west of the study area. Pockmarks are observed at the Top of the Mandal Formation, at the Top of the Cromer Knoll Group and within the Chalk Group, whilst being absent at Top Chalk level, a character suggesting that fluid venting had ended by this time (Fig. 4.7a,b). The non-uniform structure of the Top Chalk horizon implies that the underlying salt-pod structures placed controls on the distribution of sedimentation until at least the Upper Cretaceous.

The results of semi-automatic mapping and characterisation of the depressions in three surfaces – Top Mandal Formation (H3), Top Cromer Knoll Group (H4) and Intra-Chalk (H5) – as well as high-amplitude anomalies in Triassic strata, are summarised below.

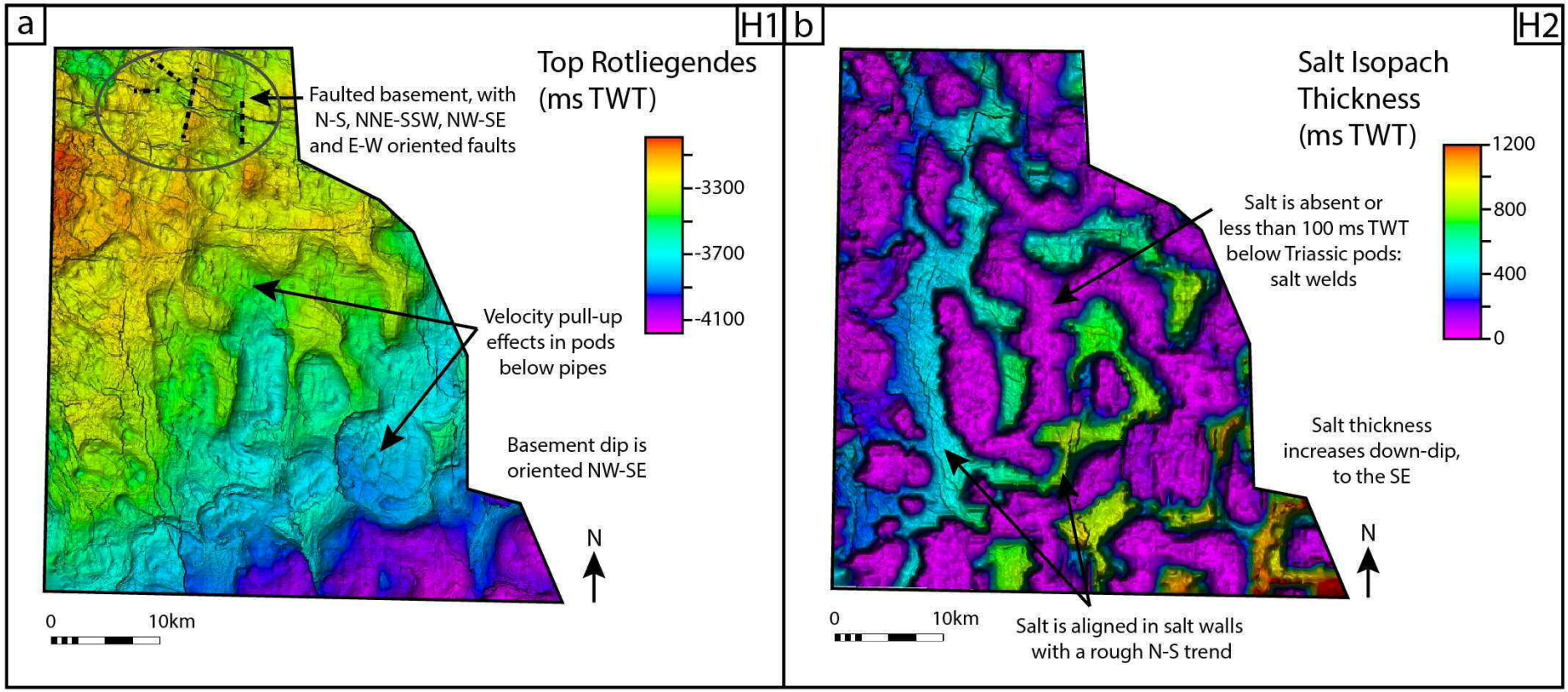

Fig. 4.5. a) Time-structural map for the Top Rotliegendes (horizon H1). b) Two-way time salt isopach map showing salt walls. Salt welds are observed where salt is absent or below 100 ms TWT.

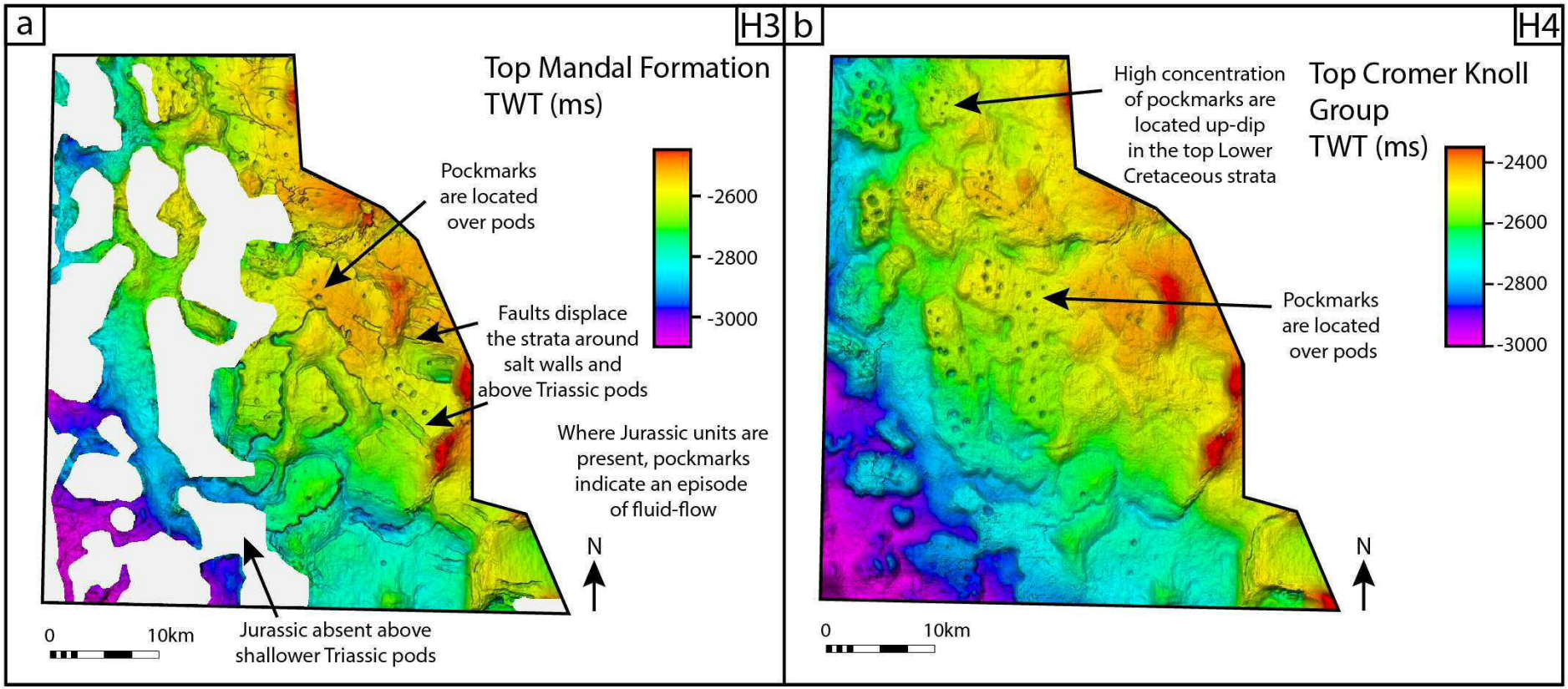

Fig. 4.6. a) Time-structural map for the Top Mandal Formation (horizon H3). b) Time-structural map for the Top Cromer Knoll Group (horizon H4).

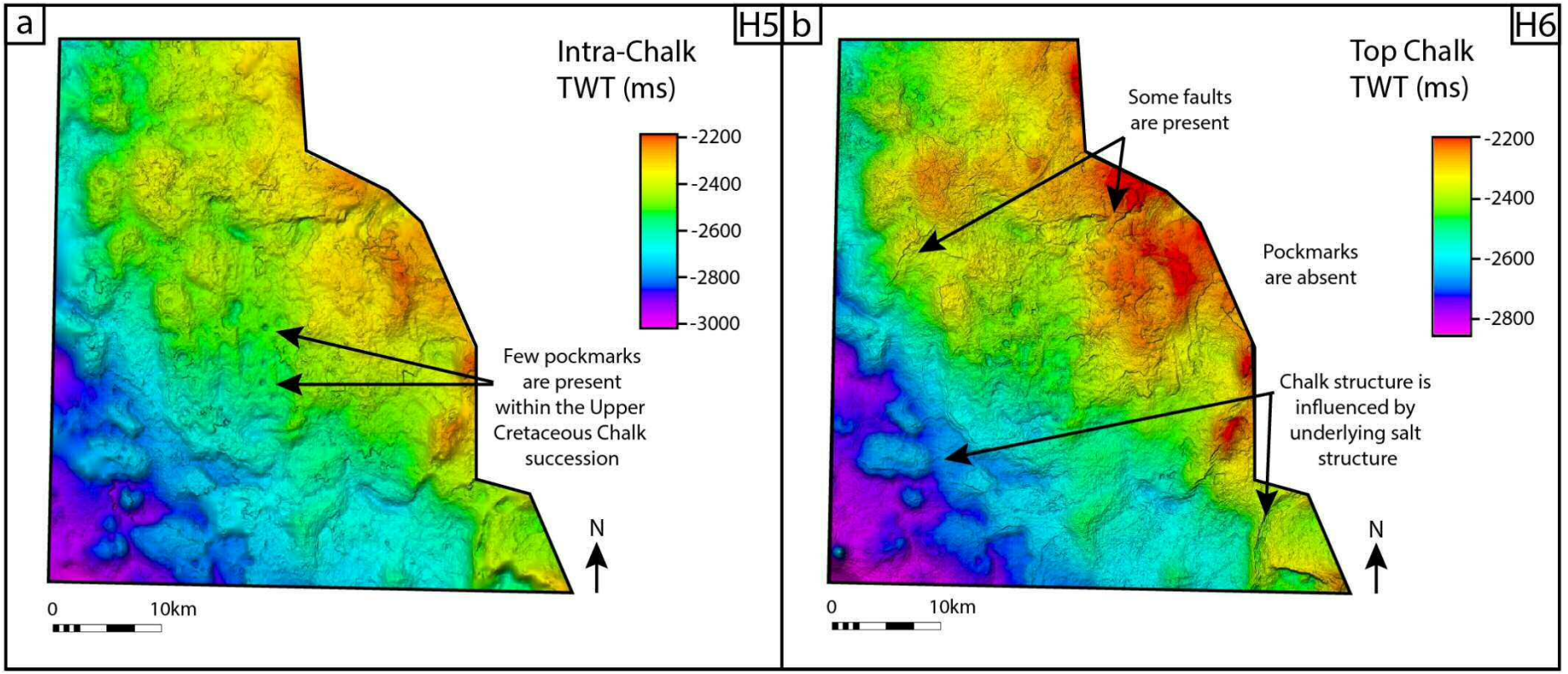

Fig. 4.7. a) Time-structural map for the Intra-Chalk Group horizon H5. b) Time-structural map for the Top Chalk Group (horizon H6).

Table 4.3 summarises the relationship among pipes, depressions and seismic anomalies. High-amplitude anomalies are found throughout the study area immediately below depressions and in pipes within the multiple Triassic pods interpreted in the study area. No amplitude anomalies were found above the depressions in the Chalk Group, revealing that gas has not migrated upwards to reach these strata – there are no interpreted gas pockets in the Chalk Group. The depth of the anomalies is variable and does not appear to correlate with any specific stratigraphic layer. Fig. 4.9 shows examples of the different anomalies and depressions on the seismic data; in particular, Fig. 4.9a shows that the Top Zechstein salt (horizon H2) was deformed (inflected up) vertically, a likely result of fluids below the salt breaching the seal and migrating upwards with relatively high pressures.

Horizon/ zone	No. depressions/ anomalies	As % of mapped depressions	No. of pipes which terminate at that level	As % of total pipes	No. anomalies in pod - of pipes that terminate at that level	As % of pipes that terminate at that level	No. anomalies below depression	As % of depressions at that level	No. of soft anomalies
Intra-Chalk	36	18.4%	0	0.0%	0	0.0%	0	0.0%	0
Cromer Knoll Group	113	57.7%	103/321	32.1%	87/103	84.5%	14/113	12.4%	0
Mandal Formation	47	24.0%	40/321	12.5%	30/40	75.0%	3/47	6.4%	0
Subtotal: depressions	196	100.0%	143	44.5%	117/143	81.8%	17/196	8.7%	0
High-Amplitude Anomalies in Pods	295		178	55.5%	178	100.0%			23
Total	491		321	100.0%					23

Table 4.3. Summary of the number of depressions and anomalies mapped in different seismic-stratigraphic horizons H3 to H5.

Of the 295 mapped amplitude anomalies, 55.5% are not shown to be connected to a depression in younger strata (e.g., Fig. 4.9b). Discrete high-amplitude anomalies are prevalent in the study area (74.6%), while the remaining 25.4% are stacked in pipe columns. The majority of depressions (81.8%) have an associated high-amplitude anomaly within the pipe. All these are positive (hard) anomalies and may indicate cemented pipes, carbonate nodules, or possibly sandstone bodies within a largely mudstone succession.

Twenty-three of the anomalies not associated with a depression are negative (soft) – they may indicate isolated gas pockets as the presence of gas in sediments reduces the average seismic velocity and density of an interval, and can manifest as a negative seismic reflection (Andresen et al., 2011). Of the 113 depressions observed in horizon H4 (Top Cromer Knoll Group), only 12.4% are interpreted to exhibit high-amplitude anomalies directly below the depressions. These could represent cemented zones or carbonate nodules that formed just below the surface once the pipe and depression were established. Pipes range in height from 660 m to 2280 m, with 50% of the pipes ranging between 1100 m and 1500 m (Fig. 4.10). Blow-out pipes of similar dimensions have been recorded offshore Nigeria (Løseth et al., 2011). The three levels of depressions mapped in this work suggest that fluid flow occurred during the Upper Jurassic, Lower Cretaceous and early Upper Cretaceous, with the main episode coinciding with the end of the Lower Cretaceous (H4).

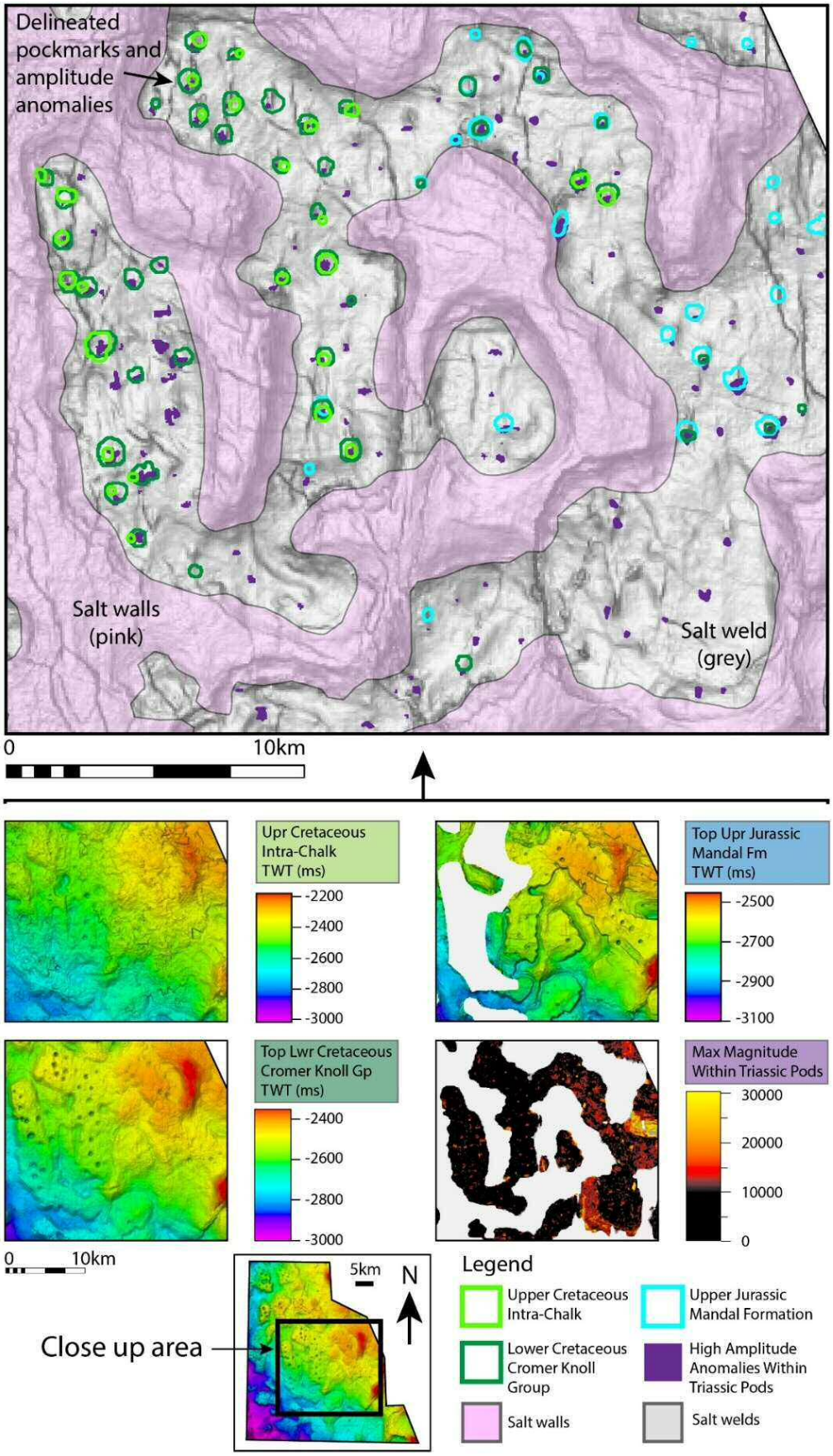

Fig. 4.8. Depressions and amplitude anomalies delineated in ArcGIS®. Open polygons denote mapped depressions, closed purple polygons denote mapped amplitude anomalies. The basemap shows the Variance attribute from the Top of the Rotliegend Group (Horizon 1), highlighting the presence of multiple basement faults (dark grey). It is clear from superimposing the mapped polygons with the salt that depressions and anomalies are only distributed within the Triassic pods.

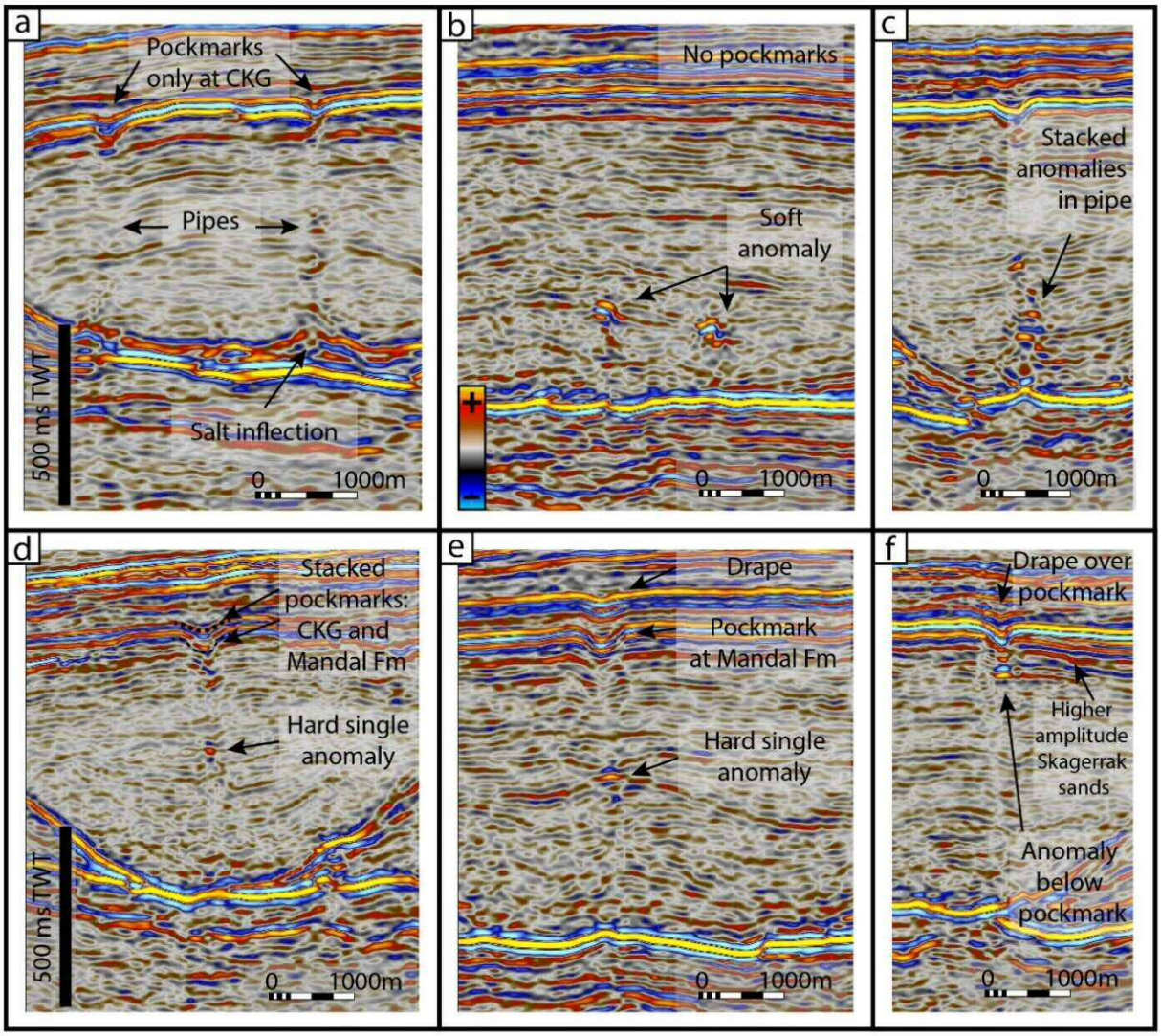

Fig. 4.9. Seismic examples of pipes, pockmarks and amplitude anomalies. The horizontal scale and polarity are the same across all the figures. a) Pipes terminating in pockmarks at the top of the Cromer Knoll Group (CKG), with salt inflections indicating a breach in the seal. b) Soft amplitude anomalies with no shallower pockmarks, possible gas pockets. c) Stacked amplitude anomalies in a pipe. d) A single hard amplitude anomaly in a pipe, with stacked pockmarks at the Top CKG and Mandal Formation horizons indicating multiple episodes of fluid flow. e) A pockmark at the Top Mandal Formation horizon, with the Cromer Knoll Group horizon 'draping' over it. f) An amplitude anomaly immediately below the pockmark and higher amplitude continuous reflections of the Skagerrak Formation.

4.7 Morphological analysis

Fig. 4.10 displays the ranges of the morphological characteristics of depressions in the form of box plots. Table 4.4 summarises these plots numerically.

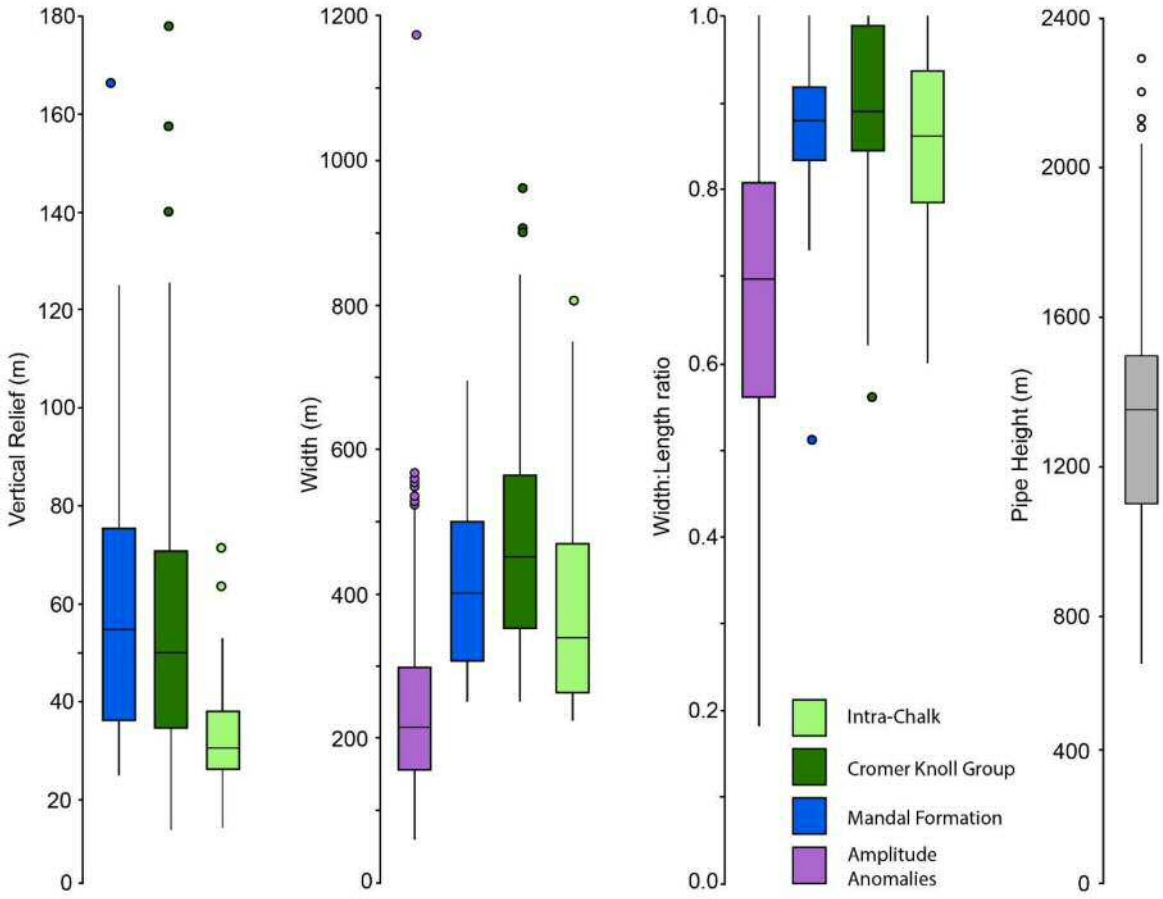

Fig. 4.10. Box plots summarising key morphological attributes of depressions and amplitude anomalies, from left to right: width, width:length ratio – a proxy for eccentricity, vertical relief and pipe height. Attribute ranges are consistently similar for the Mandal Formation and Cromer Knoll Group depressions, whilst those of the Intra-Chalk are generally smaller in width and vertical relief. Pipe heights vary according to the Triassic pod isopach, which increases down-dip on the Jæren High.

The Vertical Relief value describes the vertical fall from the rim of the depression to its deepest point. Vertical Relief ranges from 15 m to 178 m. The Intra-Chalk depressions have the smallest range of values, from 15 m to 71 m, with a median value of 30.5 m. These values are much smaller than those in the CKG and Mandal Formation, which have similar interquartile ranges – from 35 m to 75 m, and medians of 50 and 55 m, respectively (Fig. 4.10).

The width of the depressions ranges from 225 m to 842 m, with a median value of 450 m. The width of the anomalies ranges from 60 m to 575 m, with an outlier at 1170 m. The median width is 220 m, almost half of that of the depressions (Fig. 4.10).

Aspect ratio (width:length) is a proxy for eccentricity and ranges from 0.6 to 1.0 for all the depressions, with a median ratio of 0.88 (Fig. 4.10). These values reflect low eccentricity, or high sphericity. In contrast, the width:length ratios of amplitude anomalies range from 0.18 to 1.0, with a median of 0.70. This reflects the highly irregular nature of the amplitude anomalies.

Their width and vertical relief were compared for depressions coinciding vertically at different levels. The plots in Fig. 4.11a and Fig. 4.11c show that the width and vertical relief of depressions in the Cromer Knoll Group are always greater than those at the Intra-Chalk horizon H5, as all the points plot below the y=x line. All the Intra-Chalk depressions coincide with underlying depressions at horizon H4 (Top Cromer Knoll Group). The width and vertical relief are also greater for the majority of the Mandal Formation depressions when compared to depressions at the Top of the Cromer Knoll Group (Fig. 4.11b and Fig. 4.11d).

From these results it is interpreted that the depressions at Intra-Chalk level may not be real pockmarks, and are instead ‘drape features’ across the underlying pockmarks at Top Cromer Knoll Group level – the Intra-Chalk unit drapes over the underlying topography and is not formed by further fluid flow from below – and likewise for the Cromer Knoll Group depressions over the Mandal Formation pockmarks. Based on the graphs and manual investigation in Petrel, it is suggested that ten of the depressions in the Cromer Knoll Group, overlying depressions in the Mandal Formation, are drape features, whilst the remaining seven depressions are associated with stacked pockmarks that indicate multiple episodes of fluid flow through the same pipe(s).

The total number of interpreted pipes is 321: the sum of the pipes which terminate at the Mandal Formation (12.5%), the Cromer Knoll Group (32.0%) and the anomalies without shallower depressions (55.5%). The fact that over half of the interpreted pipes are not connected to palaeo-pockmarks suggests that active seal breaching and leakage could be occurring across the salt welds.

Horizon/zone	Width (m)			Width:Length ratio		
	min	max	median	min	max	median
Intra Chalk	225	805	338	0.6	1	0.86
Cromer Knoll Group	250	842	452	0.62	1	0.89
Mandal Formation	250	695	401	0.73	1	0.88
Amplitude Anomalies in Pods	60	575	220	0.18	1	0.70

Table 4.4. The minimum, maximum and median values of three morphological parameters of the depressions and amplitude an
and Vertical Relief.

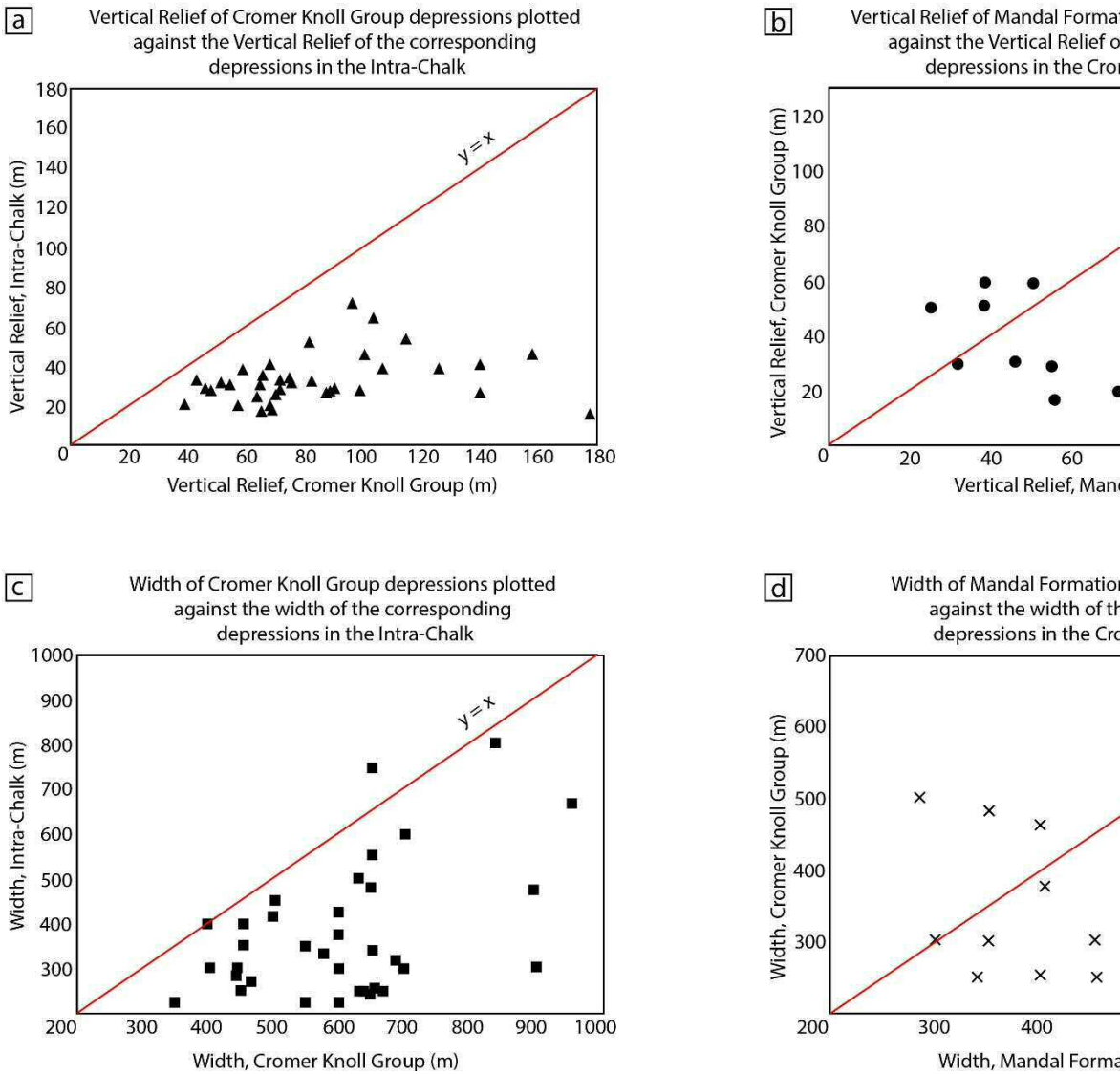

Fig. 4.11. Scatter graphs comparing the Vertical Relief and Width of the Upper and Lower Cretaceous depressions, and Lower C for the same locations. Red lines mark y = x, where the Vertical Reliefs and Widths are equal. Graphs a) and c) show that th Knoll Group are always larger than the corresponding Intra-Chalk depressions, as the points plot below the y = x line. Grap Formation depressions are larger than the corresponding Cromer Knoll Group depressions, with only five exceptions.

gas throughout the Mesozoic. These rocks have been buried to depths over 6 km and are presently overmature (Fig. 4.12).

The Carboniferous on the Jæren High ranges from 4 to 6 km depth and is interpreted to have entered the peak gas generation window during the Oligocene, remaining there to the present day. Fig. 4.12d shows the dramatic cooling effect of the thick salt due to its high thermal conductivity compared with clastic sediments, as the two modelled wells in a salt wall (7/7-2) and Triassic pod (7/1-1) show very different thermal histories. As heat flow has regional sources, it is likely that the thermal model from 7/7-2 is more representative of the Jæren High. However, it is also possible that some gas was generated on the Jæren High earlier in its history, possibly during Upper Jurassic-Lower Cretaceous rifting.

It is also clear that the Upper Jurassic Mandal Formation reached the gas generation window during the Oligocene in the East Central Graben, whereas on the Cod Terrace it only reached similar conditions during the Quaternary. Whilst it could be possible for gas to migrate along the graben-bounding fault to the Jæren High in the Cenozoic, large salt diapirs extending from the basement up to the Cenozoic units line up on the graben margin, likely preventing migration across to the Jæren High. This is also proved by the presence of Paleogene sand plays above salt diapirs in the UKCS, such as the Lomond and Pierce gas fields, sourced by gas from the Kimmeridge Clay/Mandal Formation buried in the East Central Graben. Therefore, it is unlikely that the gas forming the pipes was sourced from the Upper Jurassic Mandal Formation.

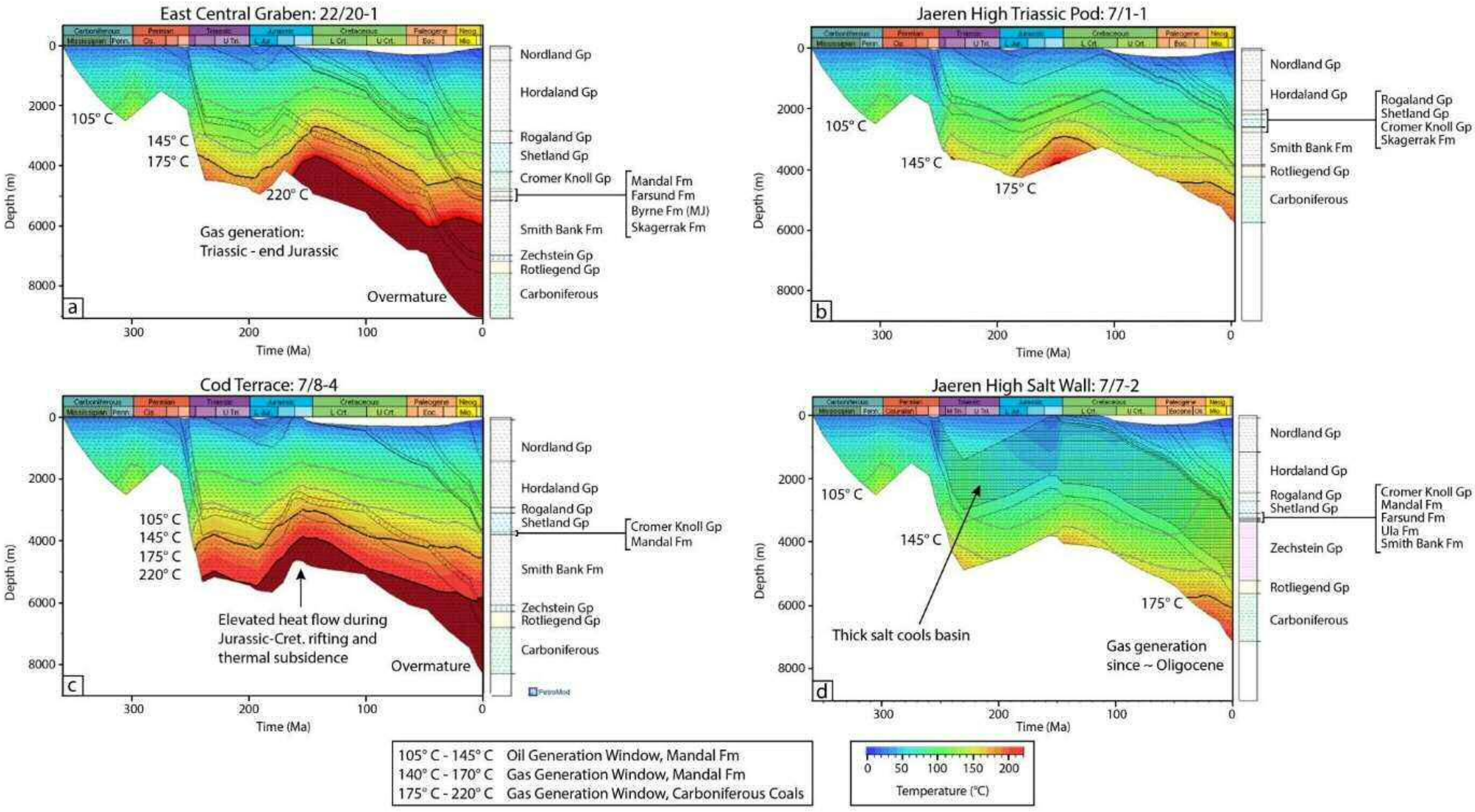

Fig. 4.12. Results of the burial history modelling from four wells in the Central North Sea, locations labelled in Fig. 4.1. The Carboniferous strata in the East Central Graben (a) and Cod Terrace (c) became gas mature for coals in the Triassic, and overmature from the Cretaceous to present. Some gas may have been produced on the Jæren High during the Late Jurassic (b), but more likely from the Oligocene to Recent, depending on the regional cooling impact of the salt. It is interpreted that long-distance migration in the Mesozoic sourced the pipes at that time, with local maturation and migration occurring at present.

4.9 Geochemical evidence

Findings from key wells on the Jæren High are summarised in Table 4.5. Most of the wells drilled on the Jæren High are located above salt walls, targeting the Jurassic and Triassic sandstone units. Those that found oil were sourced from the Upper Jurassic Mandal Formation. Only three wells were drilled into the Triassic pods. The wells terminate within the upper 300 m of the Skagerrak and Smith Bank Formation, 7/1- 1, 7/4-3, and 7/7-1, all of which were dry and with no gas shows.

Well 7/1-1 was drilled adjacent to a depression in the Cromer Knoll Group, with a high-amplitude anomaly below it, but no gas shows were recorded. The maximum methane recorded was 0.37% in the top of the Upper Cretaceous Chalk, with average values remaining well below 0.1% throughout the Chalk and into the Triassic. Cores were also taken in the Chalk, which were proved to be tight. Stylolites are common, which when fractured along these lines of weakness were seen to have very thin bands of black, shale-like impurities that do not fluoresce under UV light. The Chalk Group did not contain any oil stains or visible porosity.

Well	Objective(s)	Salt Wall or Triassic Pod; Formation TD	Findings
6/3-1 Gaupe Field	Primary – Jurassic and Triassic sandstones; Secondary – Paleocene sandstones and Late Cretaceous porous/fractured chalk	Salt Wall; TD Skagerrak Fm.	72 m oil and gas condensate column discovered within Jurassic and Triassic reservoirs. Paleocene sandstones absent. Logs suggested hydrocarbons in the Chalk, but flow tests were negative; proved a tight formation.
6/3-2	Primary – Jurassic and Triassic sandstones; Secondary – Cretaceous chalk and Rotliegendes sandstones	Salt Wall; TD Rotliegend Gp.	Oil shows, but no moveable hydrocarbons within the Chalk, Ula or Skagerrak sands. Poor reservoir quality in the Chalk, <0.02 mD permeability. Rotliegendes were water saturated without trace of hydrocarbons.
7/3-1	All horizons down to Permian Rotliegendes	Salt Wall; TD Carboniferous	Triassic and Early Jurassic units missing. No spores – for maturity assessment – observed in samples of Rotliegendes or Carboniferous. 8 m of Carboniferous drilled, no hydrocarbon source potential. Dry well.
7/1-1	Triassic Skagerrak Fm.	Triassic Pod; TD 147 m into Skagerrak Fm.	Jurassic units absent. Dry well.
7/4-1	Upper Jurassic sandstones	Salt Wall; TD Zechstein Gp.	17 m Ula Fm. penetrated, no hydrocarbons. Triassic-Middle Jurassic absent. Dry well.
7/4-3	Primary – Triassic Skagerrak Fm. Secondary – Late Cretaceous-Paleocene Ekofisk and Tor Fms.	Triassic Pod; TD 267 m into Smith Bank Fm.	No Skagerrak sandstones, only Smith Bank floodplain mudstones. Jurassic absent. Dry well.
7/7-2 Brynhild Field	Upper Jurassic sandstones	Salt Wall; TD Zechstein Gp.	19.5 m oil column discovered within the Ula Fm. Sandstones. No gas cap. 40 m of Smith Bank Fm. present. Good oil shows in Mandal Fm. – excellent oil prone source rock and oil window maturity.
7/4-2 Brynhild Field	Primary – appraise well 7/7-2. Secondary – Triassic Smith Bank Fm.	Salt Wall; TD Zechstein Gp.	Shows in Ula Fm. and 4 m of Skagerrak Fm. No shows in underlying Triassic – Skagerrak and Smith Bank Fm. present.
7/7-1	Primary – Triassic sandstones Secondary – Paleocene sandstones	Triassic Pod; TD 212 m into Smith Bank Fm.	Paleocene sandstones pinch out in blocks 7/4 and 7/7. No Skagerrak Fm. Dry well.
23/11-3	Upper Jurassic sandstones	Salt Wall; TD Smith Bank Fm.	Oil shows. No Skagerrak Fm. Abandoned as a dry well.

Table 4.5. Summary of the objectives, drilling location with respect to salt walls or Triassic pods, and results of the key wells on the Jæren High. Data has been summarised from the Norwegian Petroleum Directorate web pages.

4.10 Discussion

4.10.1 A model for fluid migration and caprock breaching on the Jæren High

Detailed investigation of fluid flow features combined with burial history modelling allows for the description of the fluid migration history of the Jæren High, adding to the geological history described by Høiland et al. (1993). Fig. 4.13 summarises the history of fluid flow on the Jæren High.

Imaged pipes are shown to be rooted in the Permian Rotliegendes and cut through the Triassic succession, across salt welds. Previous studies state that salt welds formed as early as the Mid-Late Triassic due to sediment loading and salt evacuation (Høiland et al., 1993). The geometry of Triassic pods on the Jæren High supports this statement. Seismic reflections in the Smith Bank Formation bend down onto the Rotliegend Group and salt wall edges, forming turtle anticlines, a character indicating grounding of sediment pods (e.g. Karlo et al., 2014), whilst the younger Triassic reflections level out and become parallel towards the top of the pods (Fig. 4.13).

Pipes terminate in the form of depressions within the Mandal Formation (Upper Jurassic) and Cromer Knoll Group (Lower Cretaceous) and are interpreted to form pockmarks at this level. The build-up of excessive gas and fluid within the Rotliegend Group caused high overpressures to develop. Once the capillary entry pressure of the overlying seal was exceeded, gas and fluid migrated across salt welds and through the Triassic mudstone succession by hydrofracturing, forming pipes that terminated at the palaeo-seafloor as those described in Moss and Cartwright (2010). Sediment is removed into the water column, leaving behind a depression known as a pockmark. Therefore, the timing of tertiary fluid migration is indicated by the level of the pockmark; the pipes terminate in pockmarks formed during the Upper Jurassic-Lower Cretaceous. The migration of gas could have occurred over years to centuries or more (Cathles et al., 2010). The term ‘craters’ may be a more apt name for these features, owing to their large sizes, as modern, recorded pockmarks are typically up to 300 m wide and range in vertical relief between 1 m and 80 m deep (Hovland and Judd, 1988; Gay et al., 2006). Large pockmarks have nonetheless been described on the Scotian Shelf as typically measuring 10-700 m in diameter and being 1-45 m deep (Hovland et al, 2002).

It is possible for pipes to form due to rapid compaction and dewatering of mudstones (Berndt et al., 2003). However, the pipes identified on the Jæren High are rooted in Rotliegendes strata and, in most cases, generate local folds (inflections) within the salt (Fig.

4.9a). This indicates a breach in the seal and fluid bypass through the salt welds, supporting the interpretation of gas and fluid expulsion from depth. This interpretation also relates to giant pockmarks found at the top of Lower Cretaceous Marl in the Lower Saxony Basin of the Netherlands (Strozyk et al., 2018). Strozyk and co-authors interpreted that gas sourced from Carboniferous coals migrated across salt welds into shallower Cretaceous strata, forming giant pockmarks.

Results show that 28.0% of the pipes with depressions formed during the Upper Jurassic, whilst the main period of fluid flow on the Jæren High occurred during the Lower Cretaceous, as 72.0% of the pockmarks terminate at this level. The pipes forming stacked pockmarks may have been active throughout this time, whilst those generating discrete pockmarks were plugged and cemented at an early stage (e.g. Hovland et al., 2005; Andresen et al., 2011). Thirty-six depressions were mapped at the Intra-Chalk level. However, morphological analysis shows that the Intra-Chalk depressions are always associated with corresponding depressions at the Top Cromer Knoll Group, H4, the latter of which are consistently greater in width and vertical relief. This led to the interpretation that the depressions at Intra-Chalk level are drape features due to differential compaction. Still, it is possible that low-level seepage occurred after the initial formation of the pockmarks. Not all the depressions show these 'drape' features, perhaps due to laterally varying lithology in the overlying Chalk Group, or due to thickness variations and different degrees of differential compaction.

Although the pipes are interpreted to be sourced from Rotliegendes strata, the gas is likely to have been expelled from deeper (Carboniferous) coals. The burial history plot for the Jæren High shows that Carboniferous strata did not reach sufficiently high temperatures to enter the gas maturation window during the Mesozoic (Fig. 4.12b, d). However, investigation of nearby potential source kitchens showed that the Carboniferous entered the gas maturation window during the Triassic, remaining there throughout the Mesozoic (Fig. 4.12a and Fig. 4.12c). Hence, the interpretation is that gas could have been sourced to the west of the Jæren High in the East Central Graben, migrating vertically along the graben-bounding fault. Importantly, the presence of pipes and pockmarks up to 40 km away from this fault, down-dip of the Jæren High, suggests that large volumes of gas accumulated there and putatively sourced gas to the study area from the southeast, i.e. from the Cod Terrace region in Norwegian waters. These two source kitchens, exceeding 6 km depth, are presently overmature.

4.10.2 Data limitations and the importance of understanding leakage risks

Morphological analyses have been undertaken to describe the pockmarks and discern their formation mechanisms. However, it became apparent that due to the resolution of the data and the scale of variation of the morphological characteristics, only a few basic parameters were viable for analysis, e.g. width, vertical relief and eccentricity. Small-scale changes in slope and roughness may give insight into whether the depressions are pockmarks, sinkholes or hypogenic collapse structures, but these variations are not resolved on the interpreted seismic volume. However, as the depressions are situated within the marine shales of the Mandal Formation, and marls of the Cromer Knoll Group, it is not possible for the depressions to be hypogenic karst structures. Furthermore, compaction and burial will have removed or distorted morphological features that would be clear at the seabed or shallow subsurface. This could impact interpretations as the depressions within the Chalk Group, considered to be 'drape' features, can actually represent fluid flow, but are smaller due to the differing lithology of the Chalk Group compared to the Cromer Knoll Group and Mandal Formation.

Xia and Wilkinson (2017) summarised the geological reasons for exploration failure in boreholes drilled on the UK Continental Shelf. They noted that 6% of the wells failed due to poor caprock sealing, 6% due to incorrect trap depth prediction, and 21% due to incorrect prediction of trap geometry and extent. This emphasizes the importance of analysing fluid migration and leakage across broad regions of sedimentary basins.

In this work, the 'hard' anomalies are interpreted to be cemented zones or carbonate concretions. Only 13% of the anomalies that are not connected to pockmarks are 'soft' – if these represent pockets of gas, then it is possible that leakage is occurring at present, an unfavourable setting when assessing sites for CO_2 injection. Fluid flow pipes are actively bypassing salt welds and the overlying mudstone successions, despite thicknesses of up to ~2200 m. Thickness is one of the four seal risk factors described by Downey (1984) together with capillary entry pressures, lateral lithological variations and variable degrees of fracturing. A thicker seal unit is considered to be more effective, but is still dependent on the height of the fluid column and resulting build-up of pore-pressure. On the Jæren High, with seal thickness ranging from 650 to 2200 m, the seal was still breached (Fig. 4.9).

In summary, the method presented here is important for predicting the mechanisms behind pipe formation and whether gas can be trapped in the pipe itself. It also helps discerning if the pipes are active and gas is migrating towards a shallower reservoir, or even leaking towards the surface. If depressions were mainly found within the Chalk Group, then these could have been collapse structures formed due to hypogenic fluid migration when the Chalk Group

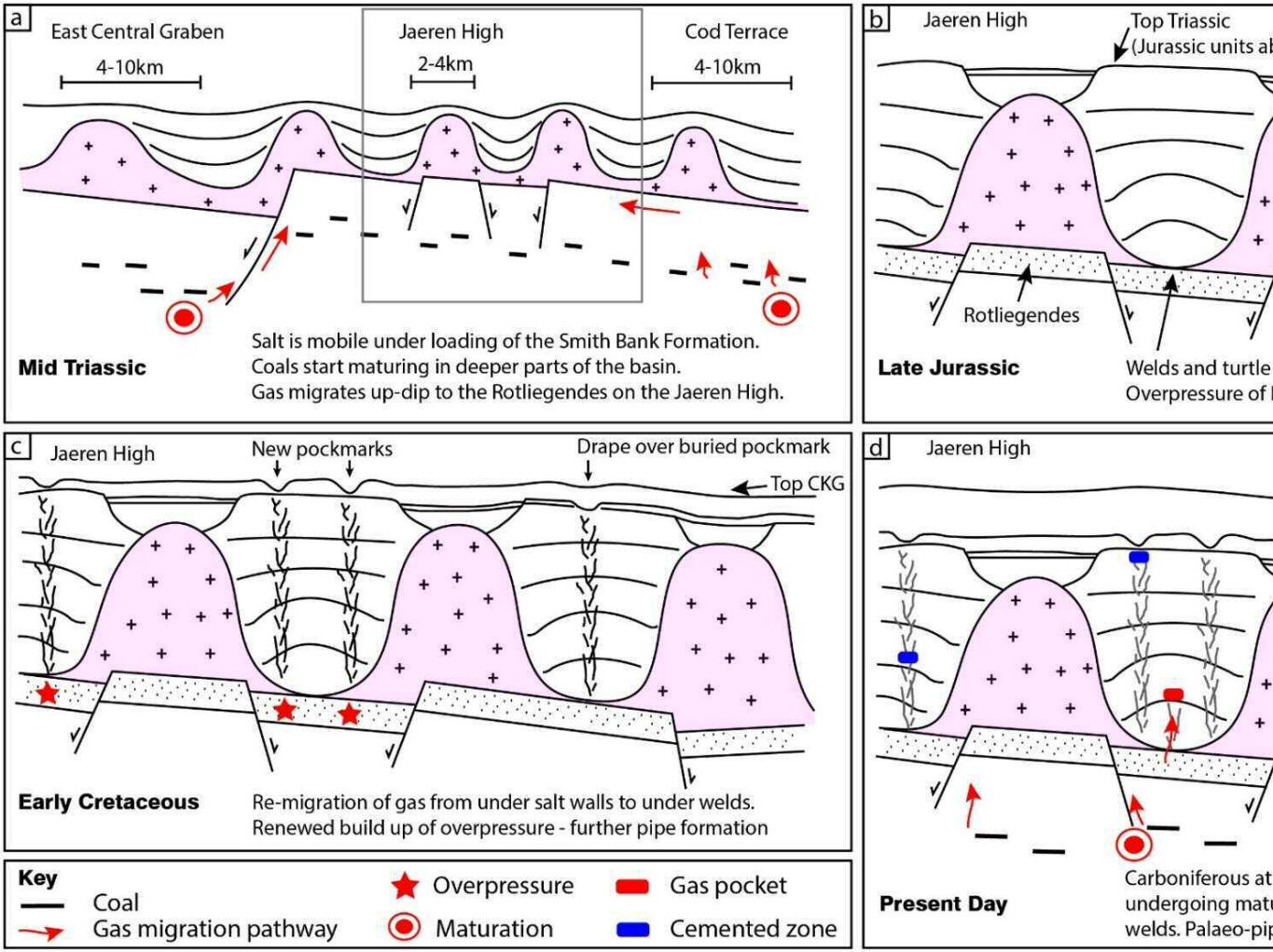

Fig. 4.13. Summary of the fluid migration evolution of the Jæren High, from a) to d). a) Shows a regional schematic, modified fro the Jæren High only, marked in a grey box in a). Gas pockets (red) and cemented zones (blue) are interpreted from 'soft' and 'ha migration pathways. CGK – Cromer Knoll Group.

was buried, as opposed to fluids venting onto the sea floor (Masoumi et al., 2014). However, the depressions are found within the marls and shales, rebuking such an interpretation. Exploration wells consistently found tight limestones with very low gas concentrations in the Chalk Group, so it is unlikely that gas has accumulated at this level, and that the pipes are active at present.

4.11 Chapter specific summary

This study shows how a novel integrated method using GIS, borehole geochemical and 3D seismic data can be used to better visualise and model fluid flow features that have previously been overlooked, or unresolved. Understanding the timing of tertiary fluid migration and the locations of fluid flow pathways is important for assessing and managing the risk of fluid escape for both hydrocarbon exploration and carbon capture and storage. The results of this work can be summarised as follows:

a) In the study area, large vertical fluid pipes sourced in the Permian Rotliegend Group cut across 600 to 2300 m of Triassic mudstones, across salt minibasins, or pods. These pipes terminate as pockmarks in the Upper Jurassic Mandal Formation and Lower Cretaceous Cromer Knoll Group. This indicates the timeframe of vertically focused fluid expulsion and the potential for fluids to leak from these established pipes.
b) As the pockmarks range from 250 to 842 m in width and 14 to 178 m in vertical extent, they reflect the transport of extremely large volumes of fluid, which were required to form features of this scale. The gas migrated into the Mesozoic strata sequence sourced from the East Central Graben to the west, and Cod Terrace to the southeast.
c) Long-distance vertical and up-dip migration occurred towards the Jæren High, until pore-fluid pressures were sufficiently high to breach the Smith Bank Mudstone Formation seal.
d) Thus, high-amplitude anomalies represent both cemented pipes and potential gas pockets, whose presence indicates increased risk as a potential flow pathway. These are crucial data to determining where active leakage is occurring at present, and whether a site will be suitable for containment and geological storage of carbon dioxide.

CHAPTER FIVE

Structural controls on fluid flow in the East Breaks area, northern Gulf of Mexico

5 Fluid flow in a salt minibasin province

5.1 Abstract

Three-dimensional (3D) seismic data, combined with semi-automated mapping methods in ArcGIS, were used to analyse the morphology and distribution of 720 pockmarks and 62 mud volcanoes in the northern Gulf of Mexico. The relationship amongst salt bodies, faults and the distribution of pockmarks and mud volcanoes stresses the significance of these structures in focusing fluid flow on continental margins. The pockmarks were classified according to their structural setting and depth of source and correlated with seep data from the Bureau of Ocean Energy Management (BOEM). Key findings include: a) half of the pockmarks are located within faults rooted on the top of salt diapirs, whilst 96% of the pockmarks are associated with salt diapirs – emphasising the importance of salt and crestal faults in focusing fluid flow to the sea floor; b) diffusion flow through the salt minibasins is evident due to the presence of soft amplitude anomalies (indicating fluids) and pockmarks located far from salt or faults; c) oil and gas are actively leaking to the sea floor; d) a higher density of fluid flow features are found in areas with steeper minibasin dips and greater catchment areas. While no correlation is clear between the morphological attributes and depth of source, the shallow plumbing system is dominated by pockmarks whereas mud volcanoes are sourced from the deeper parts of the salt minibasins. In summary, this study uses a novel approach to analyse the plumbing system in a salt-rich basin based on the recognition of surface fluid flow features. The importance of characterising the fluid flow features and associated structures to reduce risk and uncertainty is stressed in terms of both shallow gas hazards and hydrocarbon leakage from deeper reservoirs.

5.2 Introduction

In the last two decades, much research has focused on the formation of pockmarks and pipes, as well as their spatial relationship with underlying structures. These include buried turbiditic channels, salt diapirs and polygonal faults (Gay et al., 2003; Andresen et al., 2008; Maia et al., 2016). Pockmarks comprise engineering challenges and hazards for seafloor infrastructure and

exploration drilling (Judd and Hovland, 2007). Many studied pockmark fields have been found to be related to shallow gas, particularly when this is produced by methane hydrates that are dissociated by pressure or temperature changes (Judd and Hovland, 1992; Rollet et al., 2009). Evidence for shallow gas in seismic data may include acoustic haze or dimming, enhanced seismic reflections (or bright spots), and phase reversals, to name a few (Judd and Hovland, 1992). In contrast, mud volcanoes are positive fluid escape features on the sea floor, which periodically or continuously vent liquid mud, water and hydrocarbon products and form in thick sedimentary basins with high overpressures (Mazzini, 2009). The upward mobilization of deep mudstones and fluids means that mud volcanoes are important indicators of the deep plumbing system in a sedimentary basin.

The Northern (US) Gulf of Mexico is a mature, hydrocarbon-rich basin with over 53,000 wells drilled along the continental margin into deeper waters (400-7000ft) (Kaiser, 2018). Oil slicks and gas plumes have been detected in the study area (East Breaks) amongst fields of pockmarks and mud volcanoes, indicating an active hydrocarbon plumbing system. However, the study area contains few wells and no producing fields have been discovered to date (Fig. 5.1). As shown by Xia and Wilkinson (2017), seal failure and leakage from reservoirs (tertiary migration) can lead to losses in the economic value of hydrocarbon prospects; these economic risks need to be fully accounted for in successful hydrocarbon field cases, thereby highlighting the importance of identifying indicators of hydrocarbon leakage. Against such a background, the aims of this chapter are as follows:

- Characterise the morphology and distribution of pockmarks and mud volcanoes and relate to the structures at depth;
- Describe the plumbing system of East Breaks and discuss the implications for hydrocarbon trapping and leakage in this case study for exploration in salt basins;
- Conclude whether the interpreted fluid flow features can be used as a predictive tool for the depth of hydrocarbon source intervals.

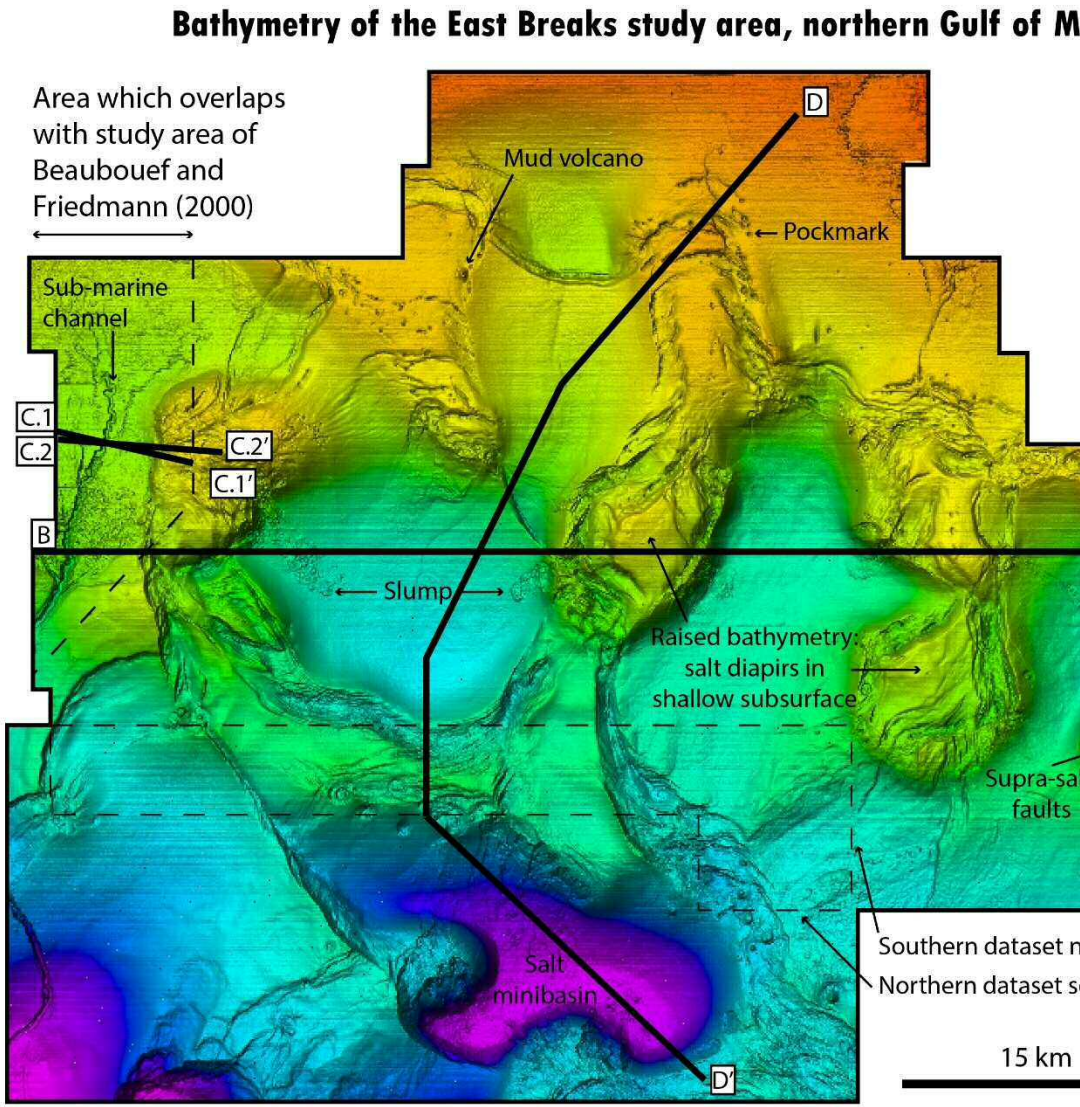

Fig. 5.1. Bathymetric map highlighting main seafloor features in the study area of the Gulf of Mexico (East Breaks) includ slumps and channels. Seismic line B-B' is shown in Fig. 5.2; lines C.1-C.1' and C.2-C.2' are shown in Fig. 5.4; line D-D' is here, but a regional line representative of the structure of the northern Gulf of Mexico Basin, in Fig. 2.5.

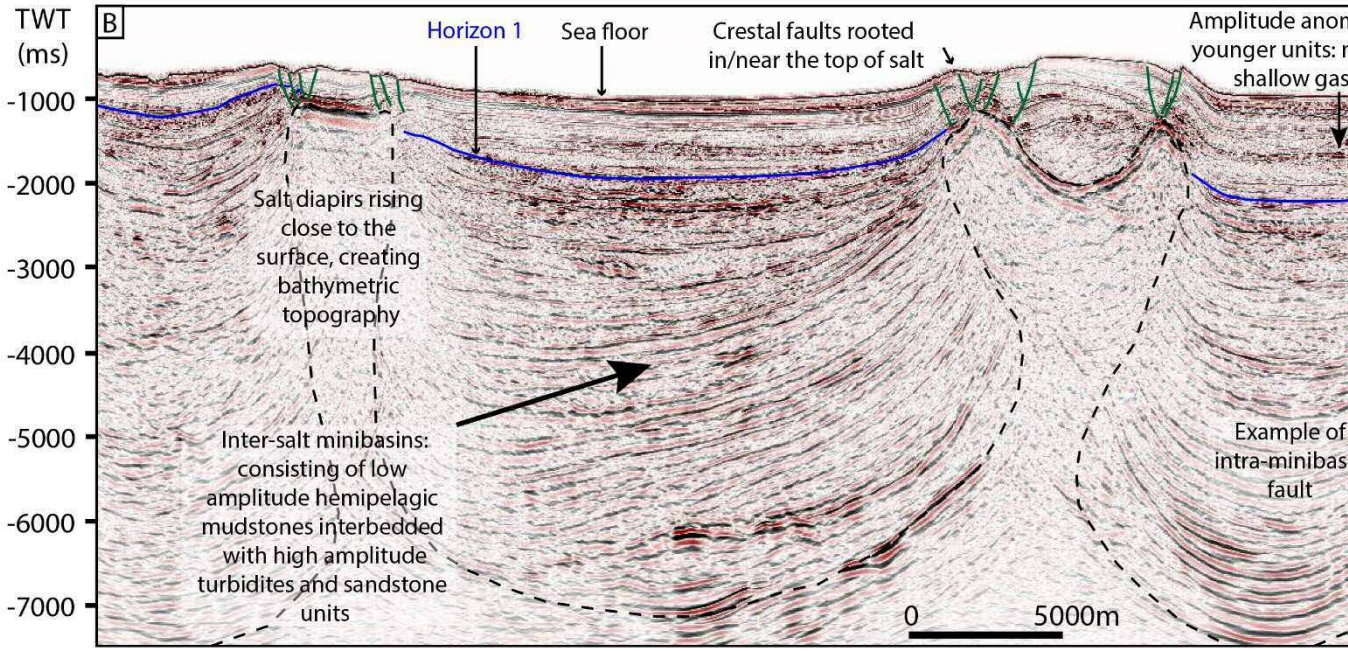

Fig. 5.2. Representative E-W seismic line through the salt minibasins and salt diapirs, highlighting the main structure of the st
Fig. 5.1.

bathymetric map of the northern Gulf of Mexico and interpreted several seafloor anomalies such as pockmarks, oil slicks and seismic amplitude anomalies. These anomalies are available in the form of Geographic Information System (GIS) shapefiles (Kramer and Shedd, 2017). The anomalies were imported into Petrel and compared with fluid flow features and deeper structures identified in the seismic data. The methodology adopted in this work is summarised in Fig. 5.3.

5.3.1 Seismic interpretation

Two seismic horizons were mapped, the sea floor and 'Horizon 1', which is the deepest and most continuous reflector that could be traced across the investigated salt minibasins (Fig. 5.2). The seismic volume attribute Variance was used to highlight irregularities such as faults, pockmarks, and salt bodies. The seismic volume attribute 'Consistent Dip' was applied, from which Dip and Dip Azimuth seismic volumes were created. These attributes were extracted at the sea floor and Horizon 1 in the salt minibasins to determine the areas of greater dip and the migration pathways from minibasins to supra-salt strata – these pathways are in the opposite direction to Dip Azimuth, as fluids migrate up dip. Seismic artefacts such as acquisition footprints have been accounted for during quality control to ensure that interpretations represented true geology (Marfurt and Alves, 2014).

5.3.2 ArcGIS semi-automated mapping and characterisation

The mapped seafloor surface from the 3D seismic data was converted from the time to depth domain using a water velocity of 1500 m/s and exported from Petrel into ArcGIS 10.7. The Seabed Mapping Toolbox (Gafeira, et al., 2012; Gafeira et al., 2018), was used to semi-automatically map the confined depressions (pockmarks) on the sea floor and extract

Input Parameters	Values
Cutoff vertical relief	2 m
Minimum vertical relief	5 m
Minimum width	20 m
Minimum width:length ratio	0.2
Buffer distance	10 m

Table 5.1 Summary of the input parameters used for the Seabed Mapping Toolbox in ArcGIS. Parameters were chosen, after trial and error, to be above the vertical resolution limit of detectability to keep the number of artefacts mapped and number of missed pockmarks to a minimum. Minimum width equals the minimum horizontal bin spacing, whilst the width:length ratio is adopted from Gafeira et al. (2012). Buffer distance extends the polygon compensating for the fact that the vertical relief threshold cuts the uppermost part of each pockmark and was chosen to be half of the minimum width (Geldof et al., 2014).

Although the Seabed Mapping Toolbox can also trace positive features, the mud volcanoes were manually mapped as the Toolbox processing time was deemed too long, in the order of hours, compared to less than an hour to map manually. In addition, many positive structures such as fault scarps were found to be incorrectly mapped as mud volcanoes. A subset of the Toolbox called 'Short Description Tool' was run for the mud volcanoes to calculate their morphological attributes, namely width and vertical relief (Fig. 5.8, Fig. 5.15, Fig. 5.16, Appendix D).

Seismic resolution is a key consideration when interpreting fluid flow features such as pockmarks and pipes. The resolution is very high near the sea floor (~8 m tuning thickness, ~1 m detectability), though in other basins in the world ROV/multibeam data have revealed pockmark fields at sub-metre scale (Hasiotis et al., 1996; Moss et al., 2012). It is possible that much smaller pockmarks do exist in the study area as these are not always resolved in seismic data. Also, the Seabed Mapping Toolbox identified pockmarks that were not mapped by the BOEM, which illustrates how easy it is to miss pockmarks.

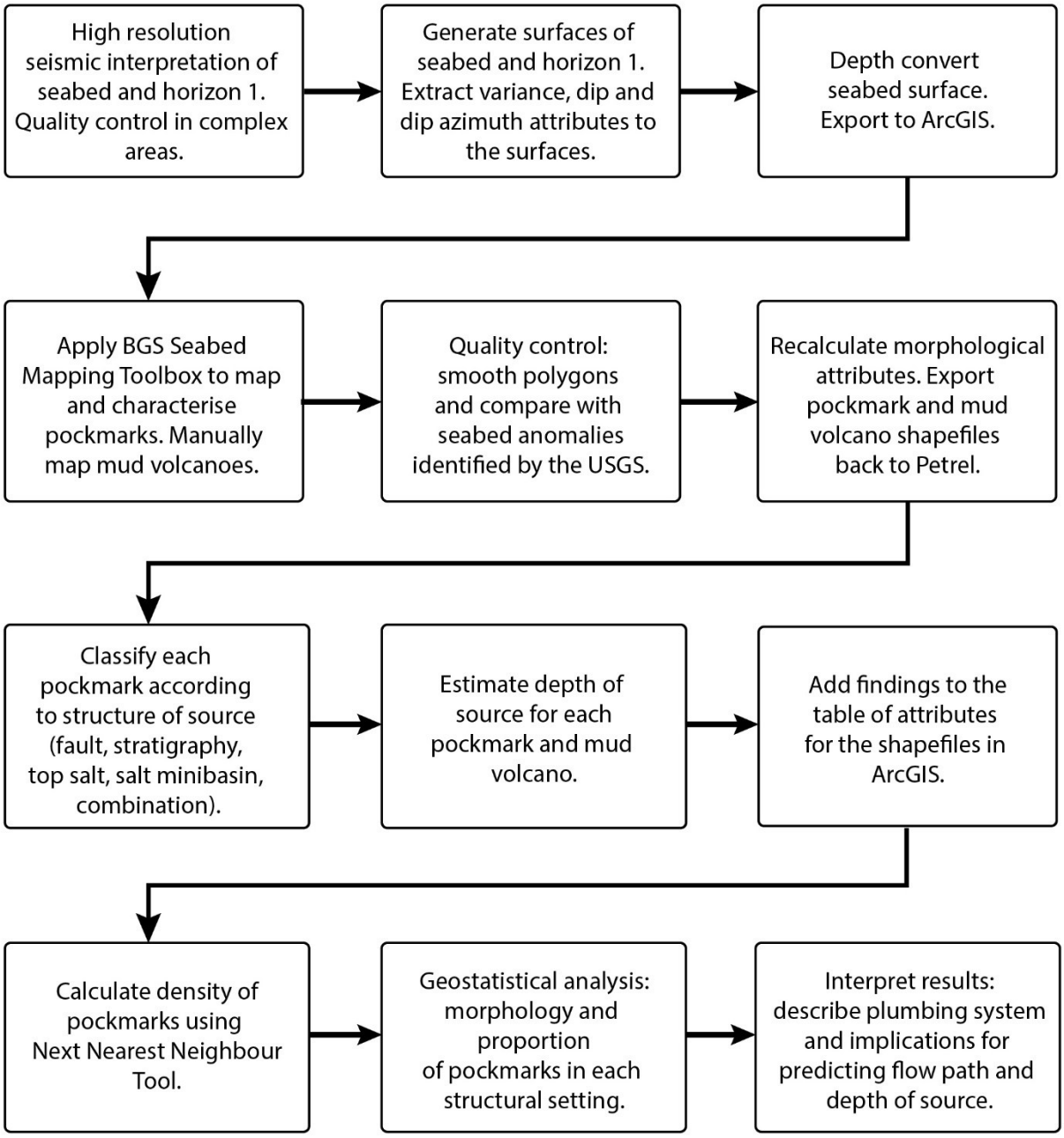

Fig. 5.3. Workflow of methods and interpretation steps followed in this Chapter. An integration of Petrel (for seismic interpretation) and ArcGIS (for mapping anomalies and spatial analysis) was used.

5.3.3 Structural relationship and depth prediction

The pockmark and mud volcano shapefiles were exported into Petrel® to identify the underlying structures in the seismic profiles and manually estimate the depth of source for each fluid-flow feature to the interpreted structure, in milliseconds (TWT). The depth of source of pockmarks was estimated to the nearest 50 ms TWT, whilst the depth of source of the mud volcanoes was estimated to the nearest 100 ms TWT, which was noted as a minimum depth due to the attenuation of seismic with depth combined with large seismic chimneys immediately below the mud volcanoes. Pockmarks were classified into groups according to their main source in the seismic cross-sections below and these classifications were added to the table of pockmark attributes.

Due to the quality of the seismic data, particularly around salt, it is not always clear to see where a pipe would extend to, or be sourced from. Equally, it is not always clear what the source of a pockmark is – a pipe is not always imaged, particularly when it is sub-seismic in scale or no longer active. This was particularly true in the studied salt minibasins where the depth of source is difficult to predict and may be underestimated. Seismic chimneys are only present below the areas identified by the BOEM to be actively leaking gas, as well as below mud volcanoes. Such processes may be occurring over a greater area, and not only focused in a pipe.

5.3.4 Spatial analysis and geostatistics

The spatial distribution of pockmarks and mud volcanoes was investigated to better understand the relationship between fluid escape at the sea floor and structures at depth. Spatial analysis was conducted visually by overlaying the delineated pockmarks and mud volcanoes with the seafloor anomalies interpreted by the BOEM. The ‘Point Density’ Tool in ArcGIS was used to calculate the density of pockmarks per km^2, and results were plotted on a variance map of the sea floor (Fig. 5.12).

Statistical data was computed based on the morphological results by plotting box plots, calculating percentages of pockmarks in different settings and cross-plotting morphological attributes.

The ‘Next Nearest Neighbour Index (Rn)’ (Equation 3.10) was calculated to determine whether the points (pockmarks) are clustered ($Rn < 1$), random ($Rn = 1$) or dispersed ($Rn > 1$) (Clark and Evans, 1954; Mitchell, 2005). The aerial extent of pockmark coverage in the study area was determined by subtracting the area with no pockmarks per km^2 from the total study area.

5.4 Seismic stratigraphy

The seismic stratigraphy of the study area is summarised in Fig. 5.4**.** The Jurassic Louann salt forms irregular-shaped, diapiric structures with chaotic internal seismic character that extend vertically from the bottom of the survey towards the sea floor between discrete minibasins. The strata in the deepest parts of the minibasins are generally characterised by low amplitude, continuous seismic reflections that are upturned towards the edges of the minibasins by the Louann salt. These units represent Mio-Pliocene deep-marine siliciclastics, most likely hemipelagic mudstones (Galloway, 2008). Wedge geometries with onlap and infill are apparent down to 6 s TWT, a consequence of the different growth rates across distinct salt diapirs, indicating that salt has been mobile since at least the Miocene. However, the seismic quality decreases considerably with depth due to the high absorption of acoustic energy by the Louann salt (Fig. 5.2; Fig. 5.6).

Seismic facies interpretations are correlated with those of Prather et al. (1998) and Beaubouef and Friedmann (2000). The study area of Beaubouef and Friedmann (2000) overlaps this study area by ~8 km on its western edge and was, therefore, deemed a reliable reference given the absence of available well data. The authors describe these minibasins as being filled rapidly with pronounced stratigraphic cyclicity, especially during the late Pleistocene.

Three key seismic facies filling salt minibasins were identified by Beaubouef and Friedmann (2000) within the initial 1s TWT below the sea floor, corresponding to the late Pleistocene (Fig. 5.4). Facies one (1) consist of low amplitude, chaotic seismic reflections, which are interpreted as mud-rich slumps, slides and debris flows of mass-transport complexes (MTCs). Facies two (2) exhibits high amplitude and continuous seismic reflections, with onlapping geometries, local erosional surfaces, and fan-shaped or distributary map patterns. These are interpreted to be sediment gravity flows, which are collectively called ‘distributary channel-lobe complexes’ (DLCs) and are considered to be the richest in sand with the greatest reservoir potential (Beaubouef and Friedmann, 2000). Facies three (3) consist of thin, highly continuous seismic units interpreted to represent hemipelagic mudstones deposited during periods of abandonment and sediment starvation – also called hemipelagic drape complexes (DCs) (Beaubouef and Friedmann, 2000). In Fig. 5.4, this is labelled four (4), to be consistent with Beaubouef and Friedmann (2000). All these slope depositional systems were abandoned and draped by a condensed interval of hemipelagic mud during the Holocene transgression and the present-day sea-level highstand.

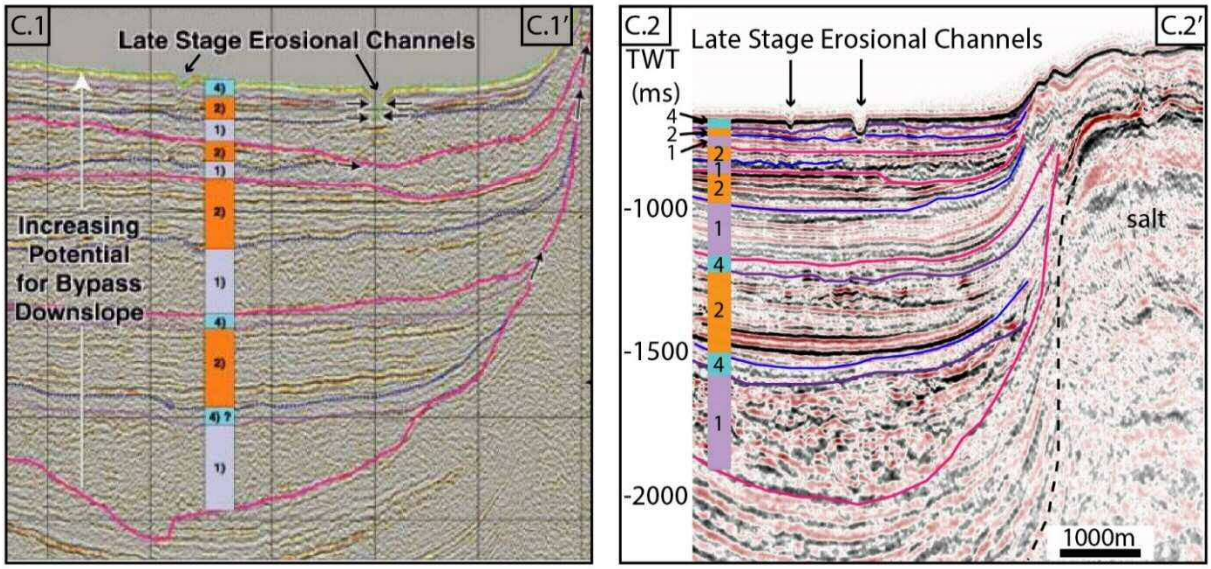

Fig. 5.4. Comparison of the 2D seismic line given by Beaubouef and Friedmann (2000) (C.1-C.1') and the approximate equivalent line in the seismic survey available for this study with the best match (C.2-C.2'). Location is shown in Fig. 5.1. Although some differences may be present, overall features are clear: generally chaotic facies (seismic facies type one) correspond to mass transport complexes (MTCs); higher amplitude regular facies (seismic facies type two) are 'DLCs' - distributary channel-lobe complexes ; whilst lower amplitude continuous facies (seismic facies type four) are 'DCs' – hemipelagic drape complexes. Seismic facies type three is omitted here for consistency, because in the study by Beaubouef and Friedmann (2000), it represents a different facies that is not apparent in this part of the basin.

5.5 Seismic interpretation of fluid flow features

5.5.1 Seismic interpretation of amplitude anomalies

Seismic interpretation of the sea floor revealed deformed bathymetry containing pockmarks, fault scarps, mud volcanoes and sediment slumps (Fig. 5.1; Fig. 5.5). These features are confirmed by previous work done by the BOEM and their classification of seafloor anomalies.

Fig. 5.6 shows seismic-based evidence of high-amplitude anomalies within the salt minibasins – often high-amplitude reflections within normal reflections. These are typically associated with higher reflectivity and/or chaotic seismic units (e.g. MTCs) as well as some examples of channel-shaped bright spots in seismic section. Pockmarks are not associated with most of these anomalies. Rare cases of polarity reversal and flat spots have also been found within the sediments in the minibasins, which are interpreted to indicate fluid contacts – likely gas-on-water (Fig. 5.6a, Fig. 5.6c).

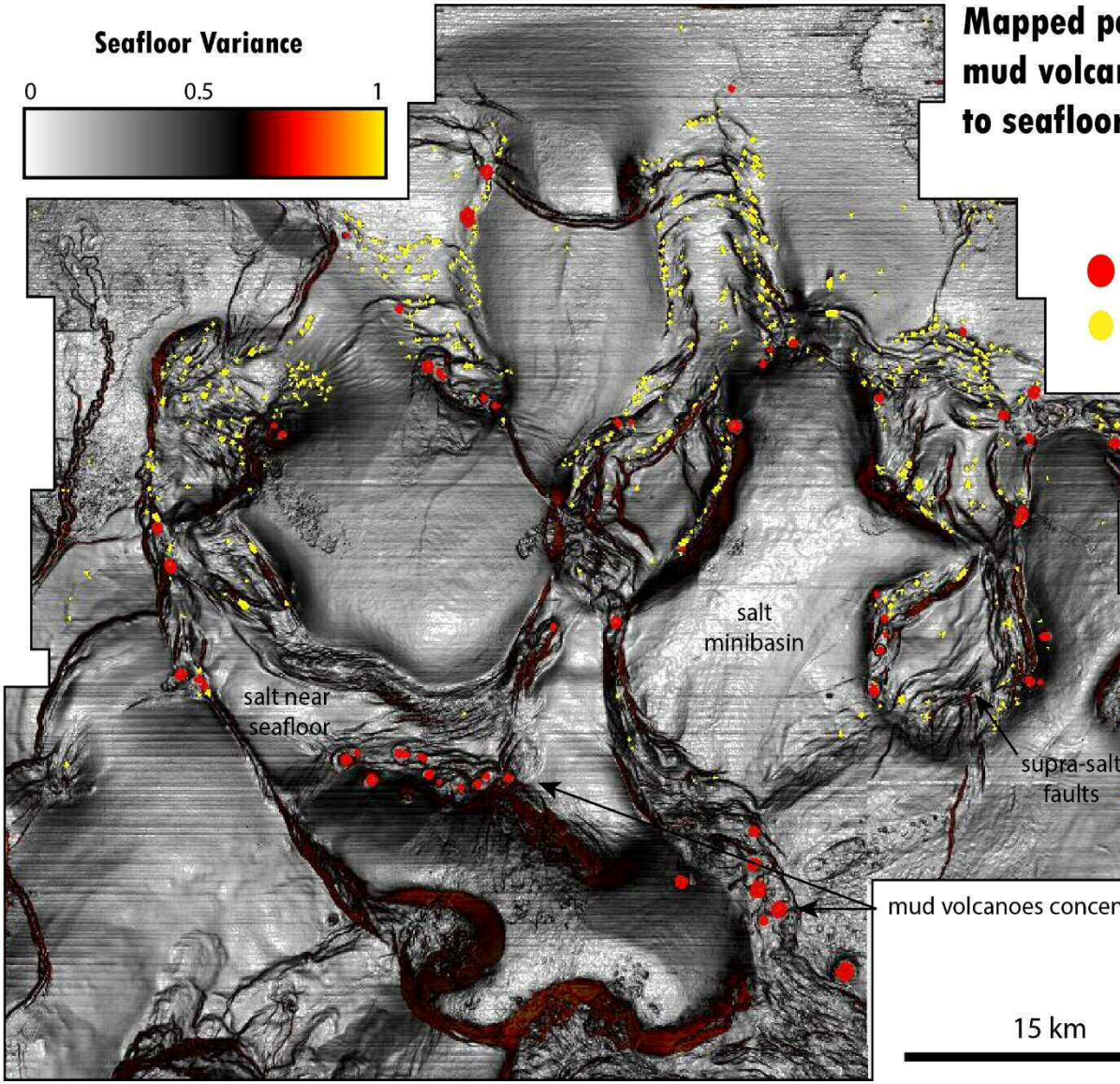

Fig. 5.5. Seafloor variance map which emphasizes seafloor structure, in particular faults; salt minibasins; salt diapirs close to t
and 62 mud volcanoes (red) mapped using ArcGIS in this study. Pockmarks and mud volcanoes are focused above and along
faults meet the sea floor.

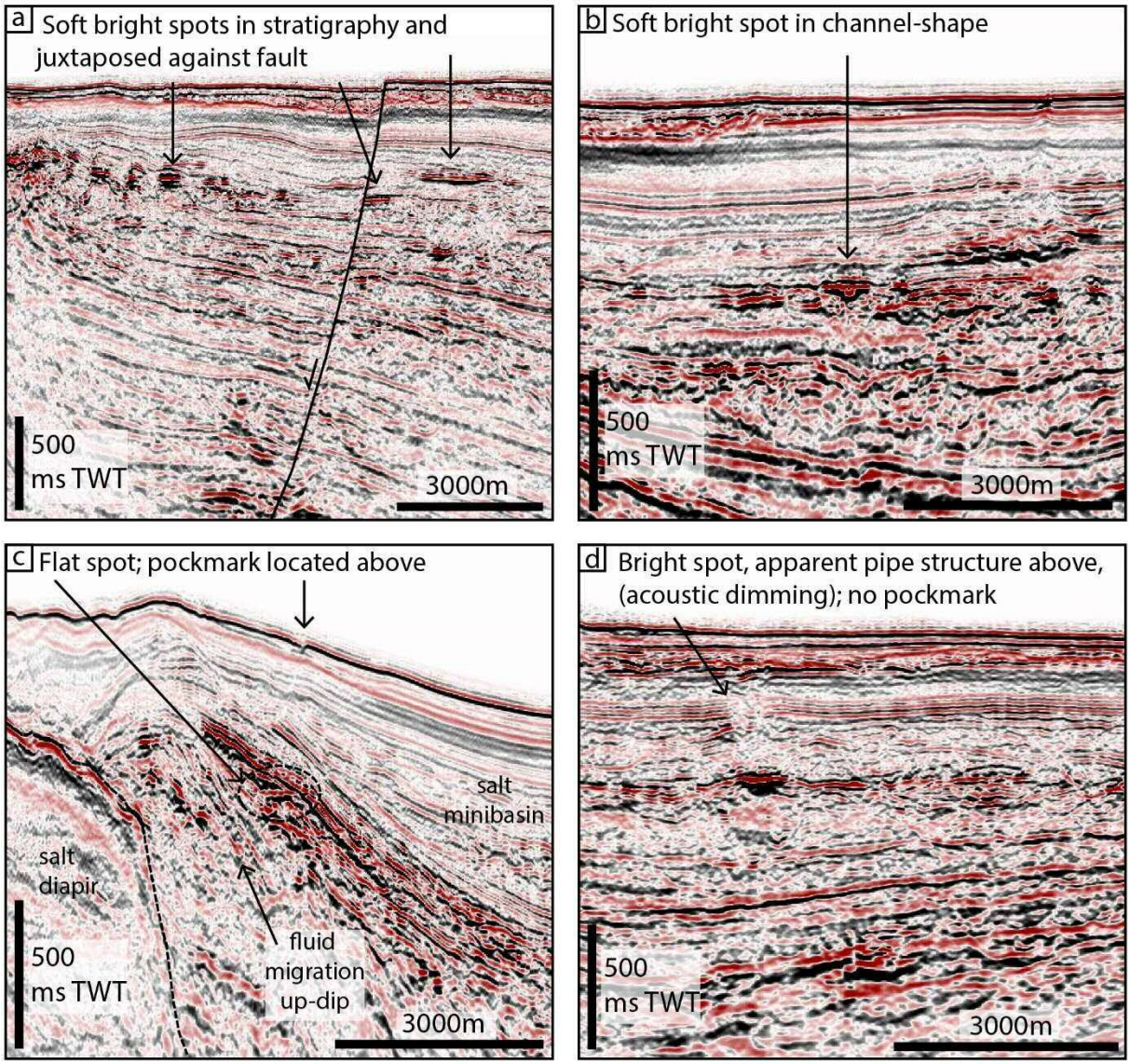

Fig. 5.6. Examples of the different amplitude anomalies in the salt minibasins: a) soft bright spots in stratigraphy and bright spot juxtaposed against fault; b) soft bright spot in channel-shape; c) flat spot, with pockmark located above, revealing a possible association; d) bright spot with acoustic dimming above but no visible pockmark.

5.5.2 Interpretation of mud volcanoes

A total of 62 circular-shaped seafloor mounds were manually mapped. At least 12 mounds are interpreted to be mud volcanoes according to the BOEM data, whilst the others have seismic characteristics including a vertical seismic chimney below the anomalously high-amplitude sea floor and cone-like seafloor structure (Fig. 5.7). Matching the descriptions of other authors (e.g. Brown, 1990; Chen et al., 2015), these mounds are therefore interpreted as mud volcanoes. The mud volcanoes are larger than the pockmarks, with widths ranging from 135 - 725 m (Fig. 5.8). The BOEM identified at least 12 mounds to be actively leaking hydrocarbons and brine.

The mud volcanoes are found along the edges of salt diapirs across the study area, whilst 19 cluster in the southern part of the study area, where very few pockmarks have been identified. In some cases, mud volcanoes appear to be sourced from the top of salt (source depth from 400 – 1000 ms TWT). In general, seismic chimneys appear to extend from at least 600 - 2000 ms TWT below mean sea level, into the bottom of the minibasins.

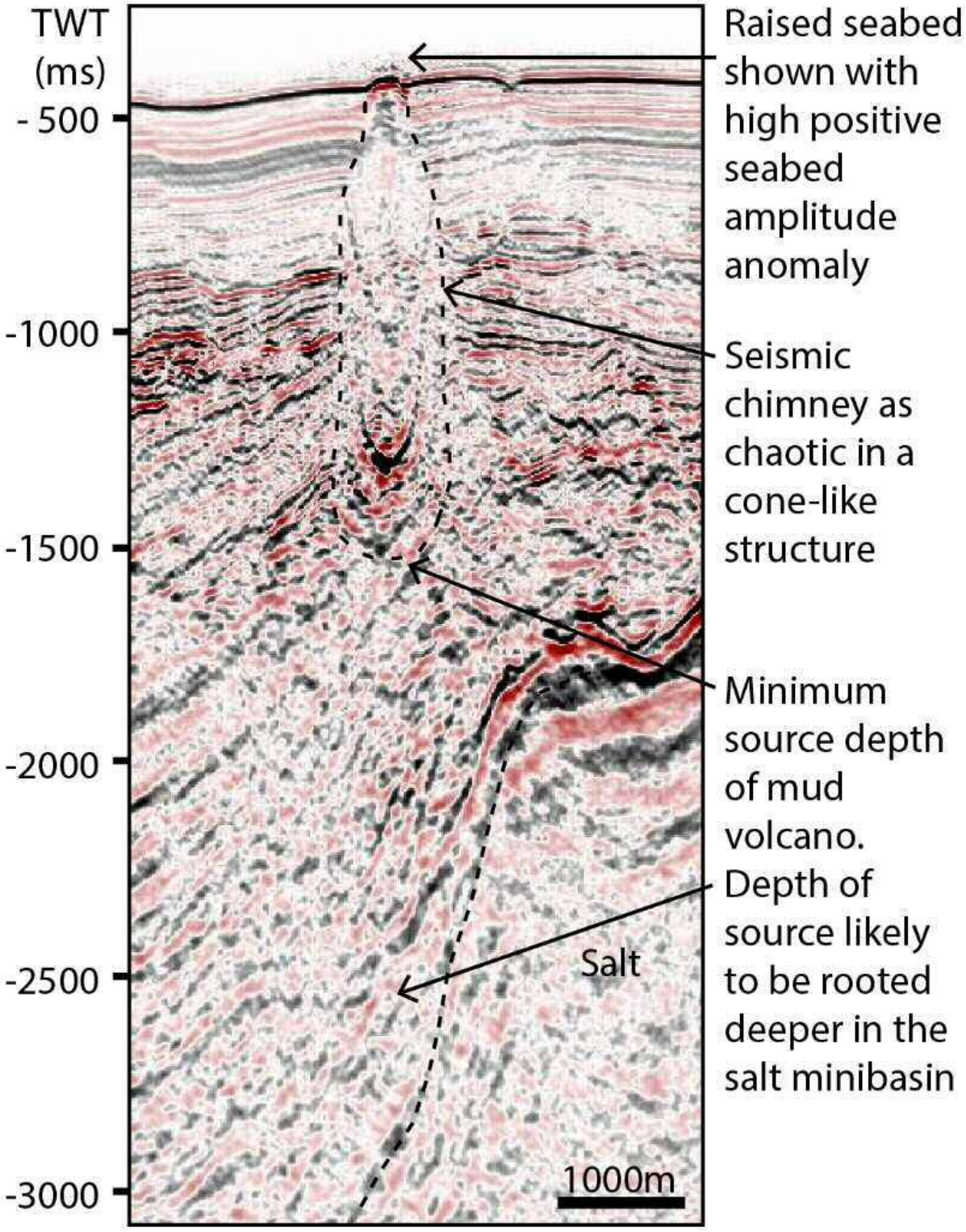

Fig. 5.7. Example of a near-seafloor structure interpreted to be a mud volcano: large seismic chimney, high positive amplitude at the sea floor, raised seafloor bathymetry. Depth of source interpreted is a minimum, as the chaotic and poorly resolved seismic at depth makes it difficult to interpret the true depth of source.

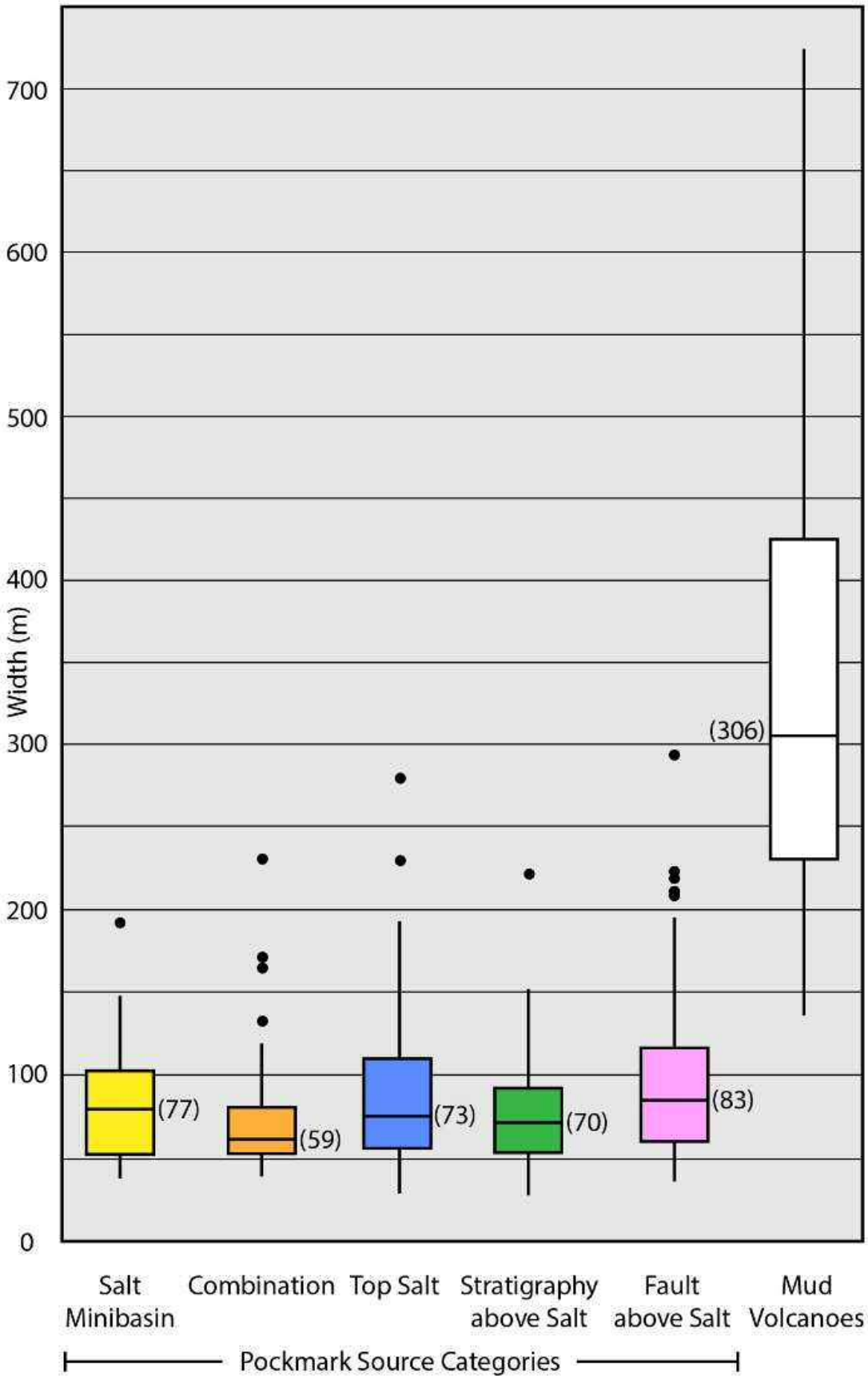

Fig. 5.8. Box plot showing the widths of the pockmarks across the different source categories and mud-volcano widths. The mud volcanoes are on average 3-4 times larger than pockmarks in the study area. Black dots are outliers, and median values are labelled.

5.5.3 Dip and dip azimuth of the salt minibasins

Dip and dip azimuth maps show the degree and direction of dip (respectively) of the sea floor and Horizon 1 at depth (Fig. 5.9, Fig. 5.10). The dips of the minibasin stratigraphy adjacent to the salt structures increase considerably with depth due to the diapiric nature of the salt, causing the bedding to be upturned at the edges of salt to 10° - 30° (Fig. 5.9a, Fig. 5.10a). Azimuths of the sea floor and Horizon 1 are predominantly to the south, between 150° - 225°. The direction of along-horizon migration is opposite to azimuth, therefore the regional migration is predominantly to the north, with locally south-migrating pathways. The presence of pockmarks decreases towards the south, perhaps reflecting the regional migration to the north invoked here, whilst mud volcanoes are present across the study area but concentrated in the south. The minibasins become deeper and edges are steeper in the south of the study area (Fig. 5.11), which coincides with the cluster of 19 mud volcanoes shown in Fig. 5.12.

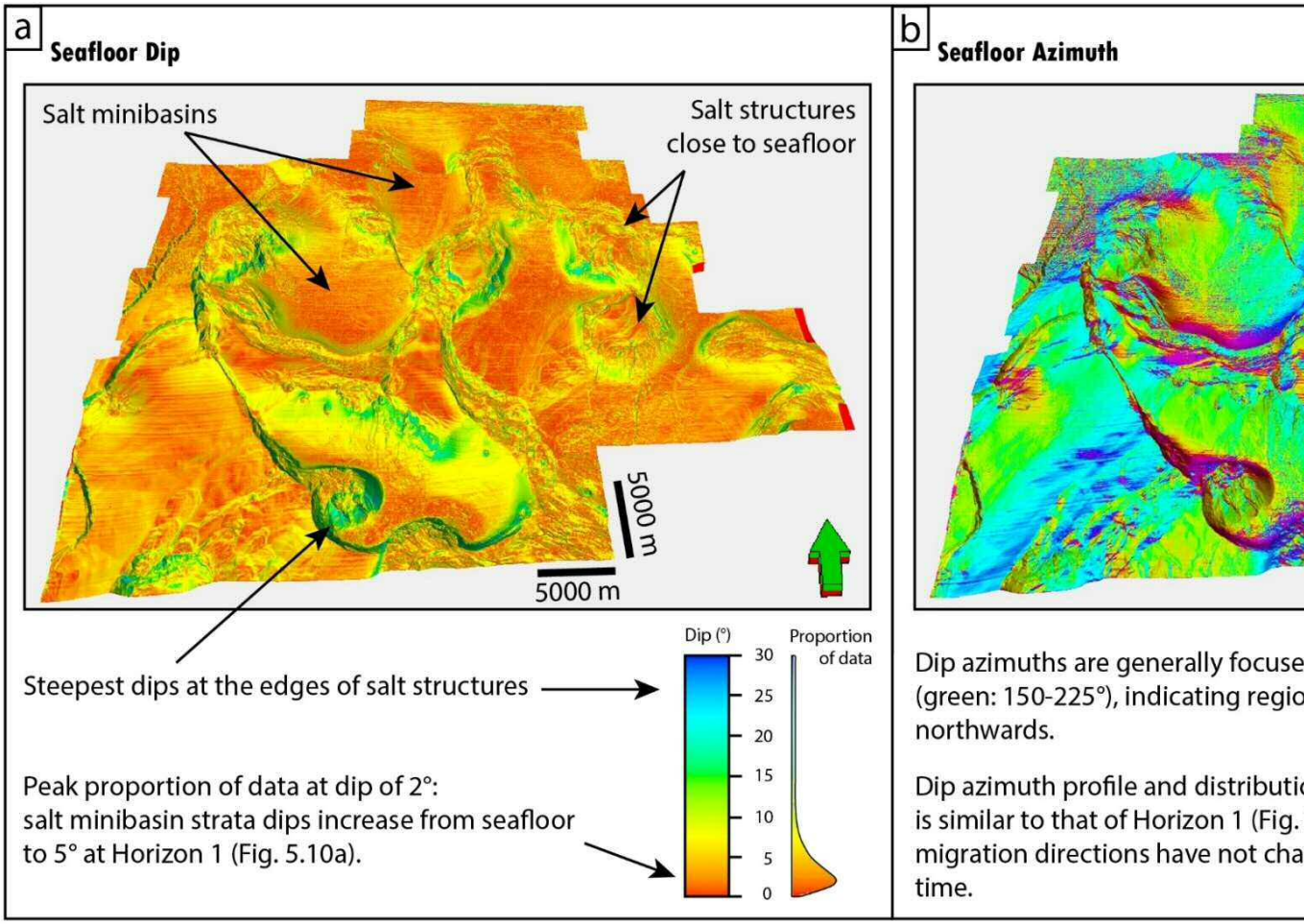

Fig. 5.9. a) Seafloor dip map showing small dips in the minibasins, increasing in steepness towards the edges of salt stru predominantly southwards-dipping sea floor. Fig. 5.9 is represented in 3D. See Fig. 5.5 for locations of mud volcanoes and poc for comparison with Horizon 1.

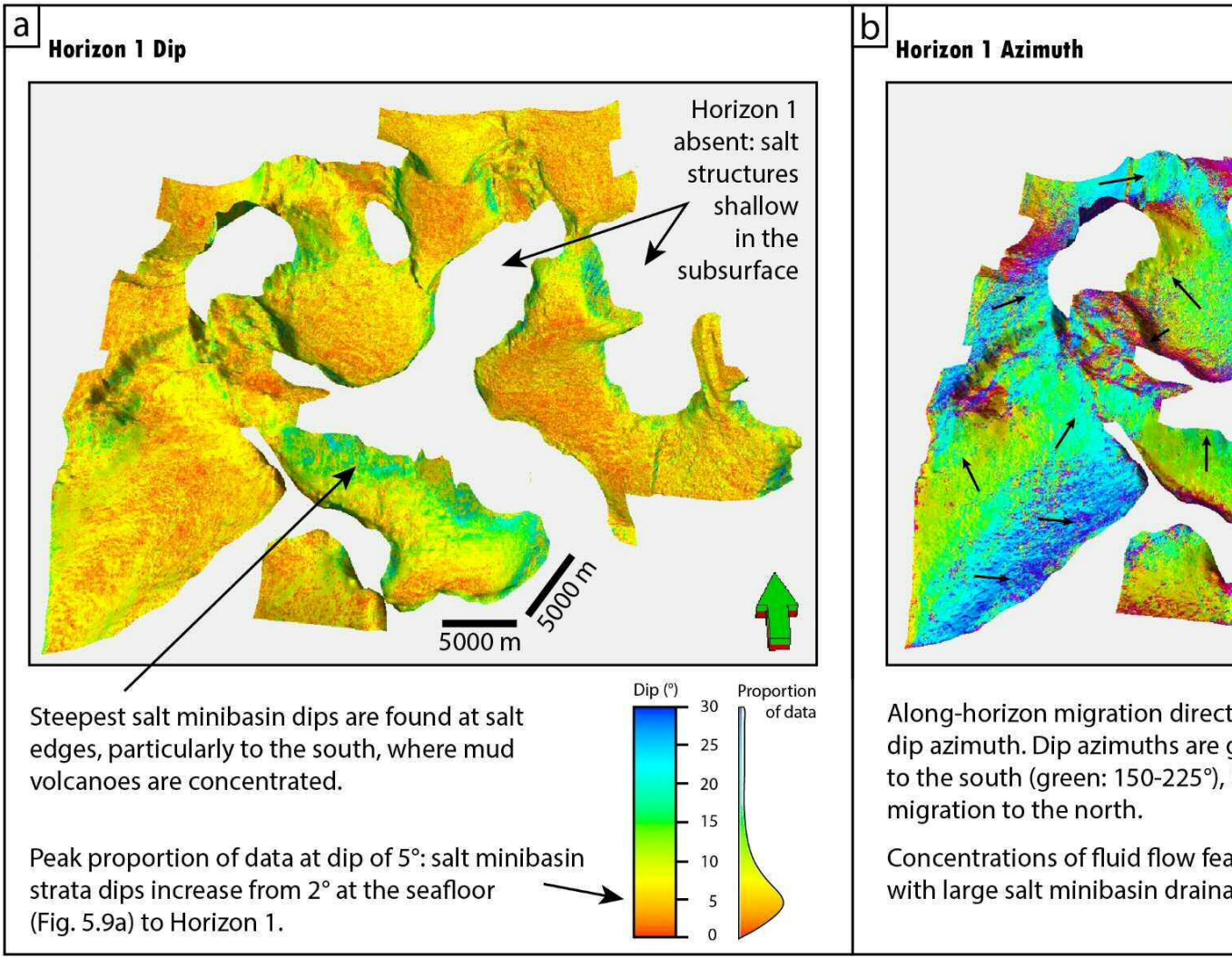

Fig. 5.10. a) Horizon 1 dip map with dips steeper than those at the sea floor; b) Horizon 1 dip azimuth map. Direction of f azimuth, therefore regional northern migration is evident, indicated by arrows. Fig. 5.10 is represented in 3D. See Fig. 5.5 relative to sea floor in 2D. See Fig. 5.9 for comparison with sea floor.

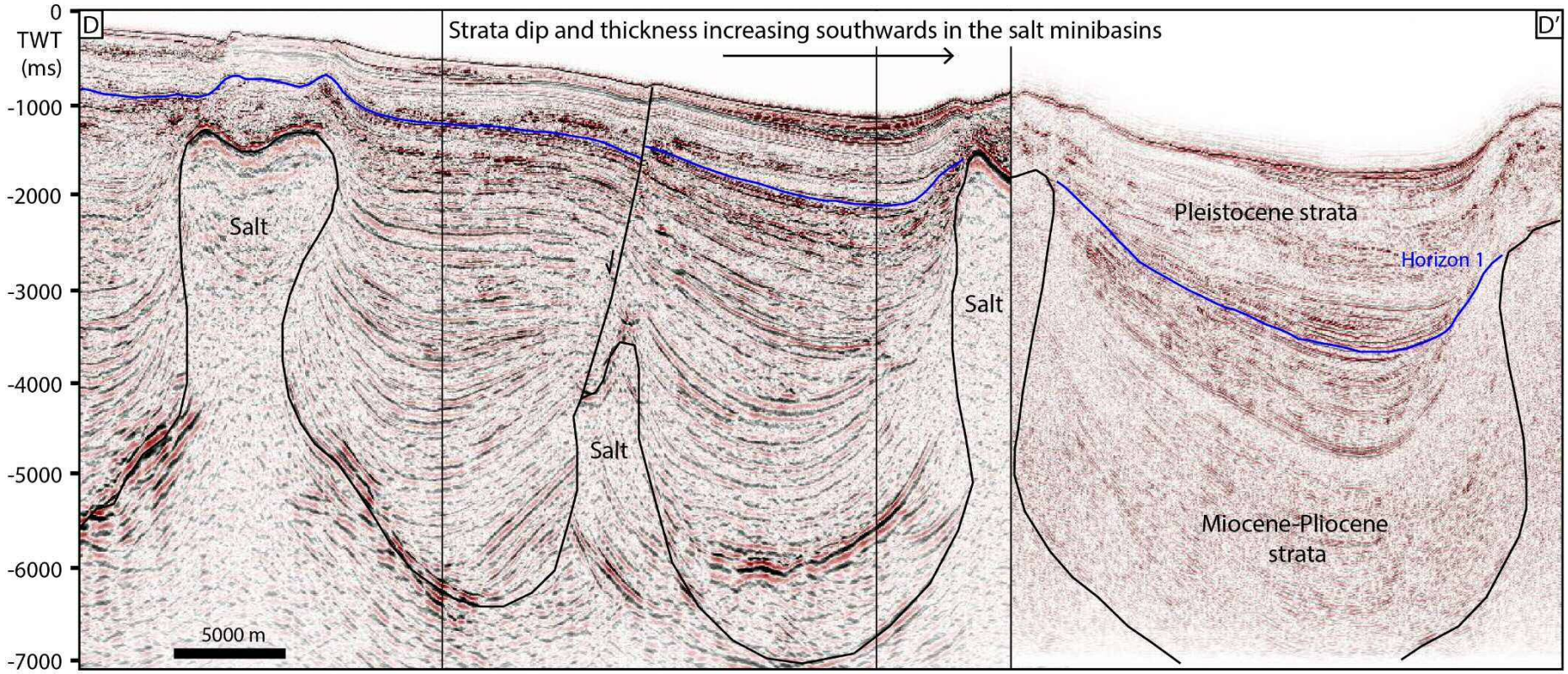

Fig. 5.11. Composite seismic line through the salt minibasins in the study area, from north to south, showing increasing thickness and dip of salt minibasin stratigraphy to the south. Location of line is shown in Fig. 5.1.

pockmarks appear clustered. This is validated statistically by the Next Nearest Neighbour ratio (Rn). The observed mean distance between any two pockmarks is 470 m and Rn = 0.56 with a Z-score of -22.6, meaning there is less than 1% likelihood that this clustered pattern is the result of a random process. These values illustrate two key points: a) that the pockmarks are clustered in small focal areas relative to the size of the study area, and b) these densities are low compared with data from other sedimentary basins (Table 5.2).

Several near-seafloor anomalies are depicted in the BOEM data (Table 5.3; Fig. 5.13). As with the mapped pockmarks, these anomalies occur near faults and above the salt structures, indicating focused fluid pathways in these areas. The presence of natural gas plumes and oil slicks confirms that hydrocarbons are leaking to the sea floor, as opposed to being overpressured brines or biogenic gas. Gas plumes are associated with pockmarks, indicating that these are active, established pathways of hydrocarbons to the sea floor (Fig. 5.13). The high- and low near seafloor amplitude anomalies representing possible oil leakage points are located where faults meet the sea floor, suggesting that these are the main leakage pathways for oil.

Paper	Density: /km^2	Width (m)	Vertical Relief (m)	Location
Moss et al. 2012	100 - 600	16	0.5	Rosetta Region, Eastern Slope, Western Nile Deep Sea Fan
Tasianas et al. 2018	n/a (elliptical pockmarks) 600 – 700 (unit pockmarks)	Up to 300 Up to 20	Up to 12 Up to 1	Snøvit Area, Hammerfest Basin, SW Barents Sea
Hasiotis et al. 1996	80 - 150	25 - 250	0.5 - 15	Gulf of Patras, northern Peleponnese, Greece
Judd and Hovland, 2007	10 - 40	50 - 150	1 - 3	Witch Ground Basin, North Sea
Judd and Hovland, 2007	Up to 160	20 - 200	1 - 35	Gulf of Maine, USA
This chapter: pockmarks	*0 - 15*	*20 – 400*	*1 - 41*	*East Breaks, northern Gulf of Mexico, USA*
This chapter: mud volcanoes	*0 - 2*	*135 - 725*	*2 - 55*	*East Breaks, northern Gulf of Mexico, USA*

Table 5.2. Examples of the density of pockmarks per km^2, average width and vertical relief of pockmarks from other papers and this dataset.

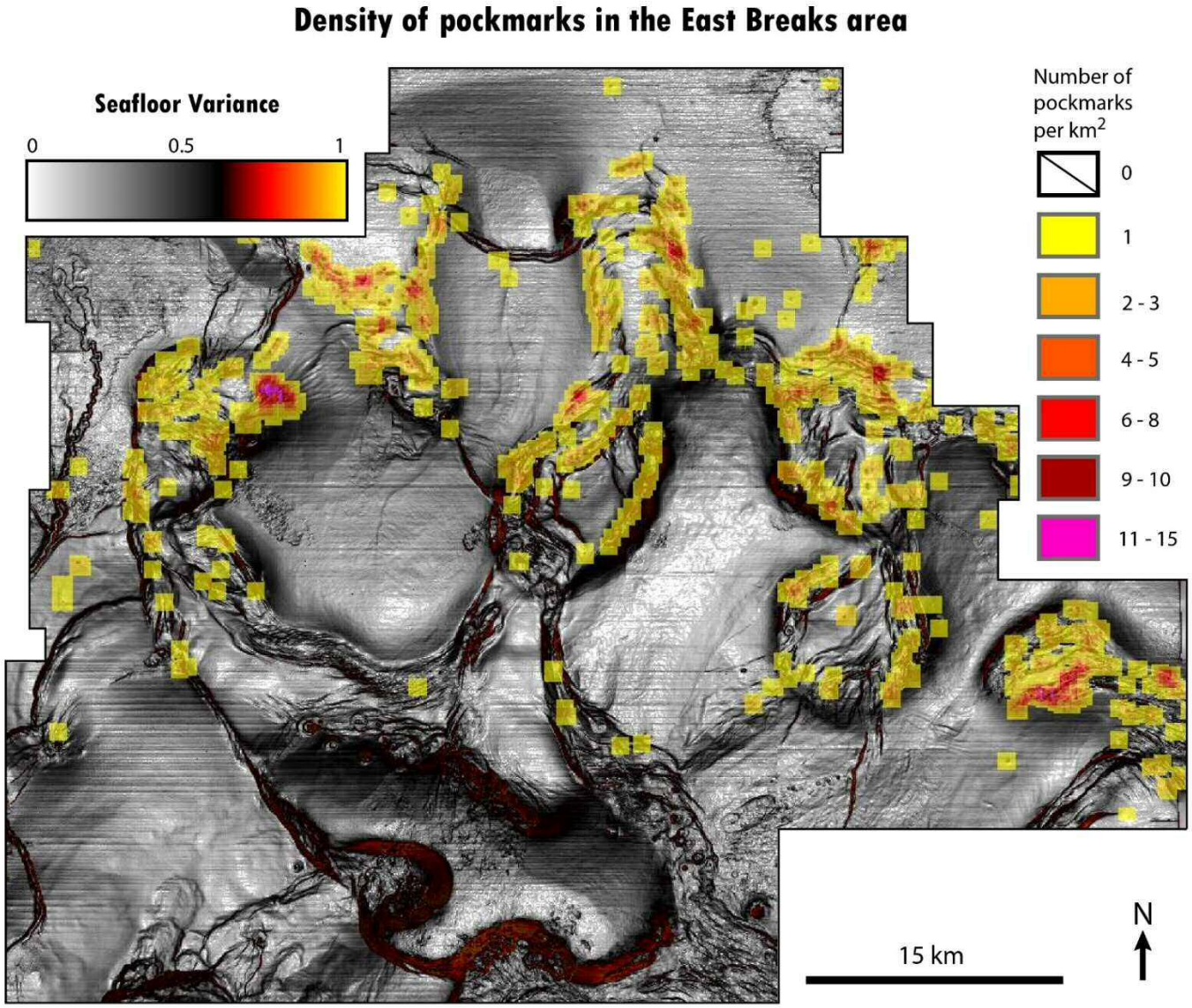

Fig. 5.12. Seafloor variance map, overlain with the density of pockmarks, ranging from 0 to 15 per km^2. Pockmarks are concentrated along faults above areas of raised topography, coinciding with shallow salt structures below. Pockmarks are mostly absent in the southern part of the study area, where mud volcanoes predominate.

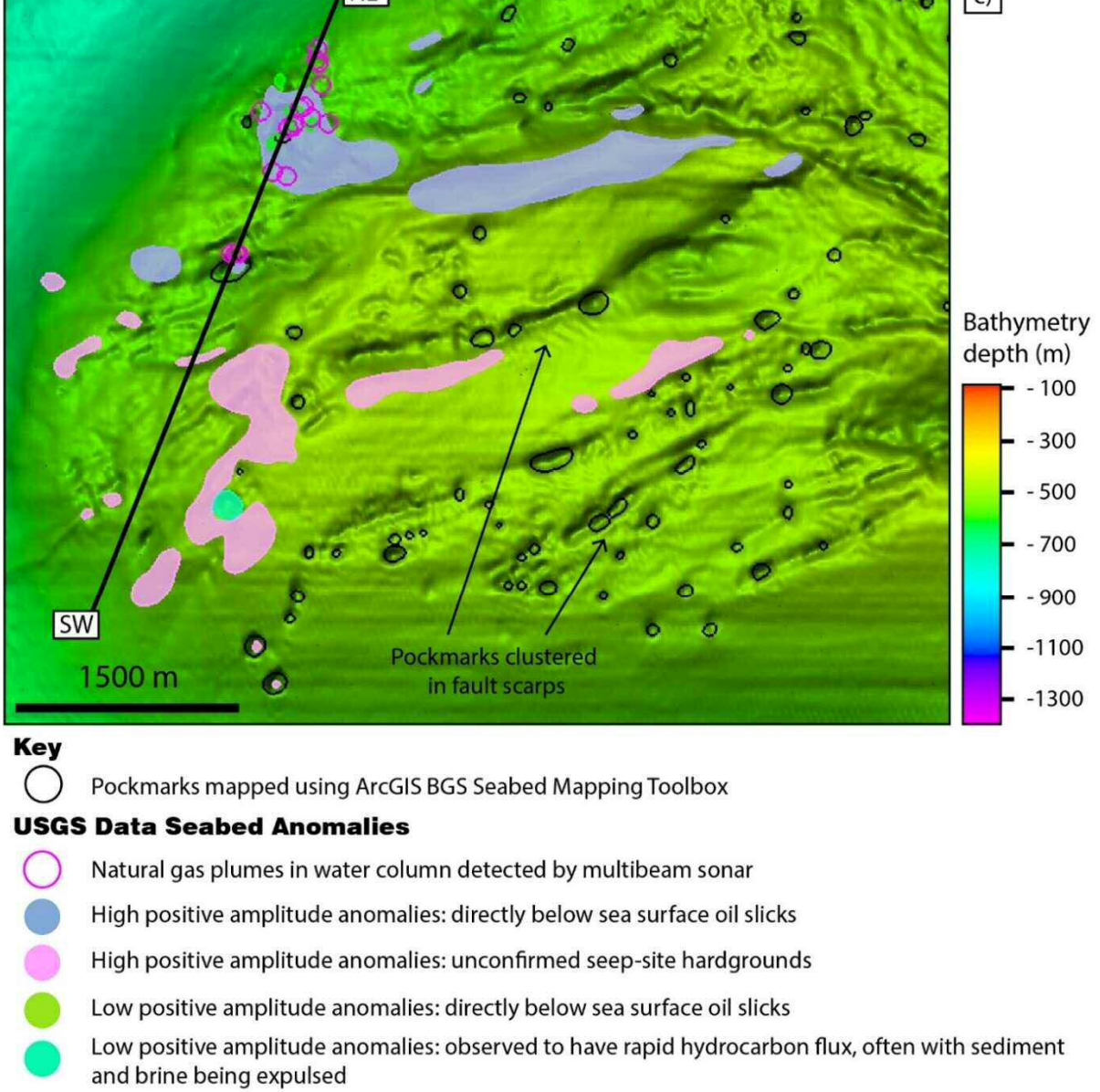

Key

Pockmarks mapped using ArcGIS BGS Seabed Mapping Toolbox

USGS Data Seabed Anomalies

Natural gas plumes in water column detected by multibeam sonar

High positive amplitude anomalies: directly below sea surface oil slicks

High positive amplitude anomalies: unconfirmed seep-site hardgrounds

Low positive amplitude anomalies: directly below sea surface oil slicks

Low positive amplitude anomalies: observed to have rapid hydrocarbon flux, often with sediment and brine being expulsed

Fig. 5.13. a) Map of study area showing the zoomed-in area of c). b) NE-SW seismic section showing a gas chimney above a salt diapir, location indicated in c). c) Zoomed-in example of the concentration of seafloor amplitude anomalies (identified by the BOEM) near faults and pockmarks. Natural gas plumes are also shown to be concentrated in these areas which correspond to chaotic seismic chimneys immediately below in the seismic. The seismic chimneys may represent active gas migration or scattering of energy if hardgrounds had formed at the sea floor above.

Pockmarks	explosive gas expulsion. Few pockmarks have visible active migration pathways on vertical seismic profiles, but most appear to be dormant and without discernible active migration. Rapid expulsion is interpreted to be exclusively gas and appear to be purely destructive due to the removal of sediment. No sediment, brine, or oil expulsion has been observed during direct observations.	447 mapped by the BOEM.
Mud Volcanoes	Cones of sediment typically on low slopes that are built at high flux sites that do not exhibit high positive amplitude response. The rate of flux at the expulsion sites is too rapid for bacterial consumption of the hydrocarbons to convert them to authigenic carbonate hardgrounds, thus sessile chemosynthetic organisms and corals are usually not found on these features. These are unconfirmed by direct observation.	Twelve mapped by the BOEM.
Positive seep anomalies	High, positive seafloor amplitude anomalies interpreted in seismic, which have not yet been confirmed as seep-site hardgrounds.	309, irregularly shaped polygons mapped by the BOEM, typically along faults or near pockmark locations.
Positive seep anomalies – possible oil	High, positive seafloor amplitude anomalies interpreted in seismic, located directly below sea surface oil slicks, or within one water depth's distance. Not directly observed to be seeping oil, but possible oil seeps due to proximity to oil slicks.	Sixteen (16) were mapped by the BOEM, located along faults above salt.
Negative seep anomalies	Anomalously low, positive seafloor amplitude anomalies interpreted in seismic. The most active of this type show a phase reversal – a negative amplitude response of the sea floor – these areas have been observed to have rapid hydrocarbon flux, often with sediment and brine being expulsed in conjunction with the hydrocarbons.	56 were mapped by the BOEM and are all located above salt structures.
Negative seep anomalies – possible oil	Low positive / negative seafloor amplitude anomalies interpreted in seismic, located either directly below sea-surface oil slicks or within one water depth's distance. Not directly observed to be seeping oil, but possible oil seeps due to proximity to oil slicks.	Ten polygons were mapped by the BOEM, in four clusters. Two clusters are in the same area as a gas plume and 'seep anomaly positives – possible oil'.

Table 5.3. Summary of the main seep anomalies detected and mapped by the BOEM, and the descriptions given.

Pockmarks were classified into five (5) different settings that correlate with the type of source at depth: a) stratigraphic carrier beds located above the salt diapirs, indicated by an amplitude anomaly or pinch-out of beds along a structure such as an anticline; b) pockmarks sourced directly from the top of salt; c) pockmarks located within a fault scarp at the surface, whereby the fault is rooted in a carrier bed above salt, or on the top of a salt diapir; and d) pockmarks sourced from carrier beds in adjacent salt minibasins (Table 5.4). The fifth group of pockmarks accounts for those generated by a combination of sources; in some areas of the dataset it is difficult to interpret the underlying structure. For instance, inlines may show no shallow salt and the pockmarks appear to occur in salt minibasins, whilst salt is well imaged in adjacent crosslines. Fig. 5.14 shows examples in seismic of pockmarks from each of these settings. Approximately 96% of pockmarks are associated with salt diapirs at depth, with sources predicting to be top salt (17%), stratigraphic units above the salt (21%), or supra-salt faults (49%). The pockmarks located within fault scarps at the sea floor are not associated with vertical pipes, indicating that fluid flow occurred along the fault plane. This flow was still focused and with a degree of explosiveness as surface material within the fault scarp was excavated to form distinct pockmarks on the sea floor.

The pockmarks located within the minibasins (4%) are interpreted to have been sourced from high amplitude anomalies in the shallow stratigraphy (Fig. 5.14d).

	Pockmark source categories					**Mud volcanoes**
	Minibasin	Combination	Top Salt	Stratigraphy above salt	Faults above salt	
Number of pockmarks or mud volcanoes	31	61	124	154	350	62
% of total pockmarks	4	9	17	21	49	n/a

Table 5.4. Summary of the pockmark source categories, the number of pockmarks found in each category and the number of mud volcanoes in the study area.

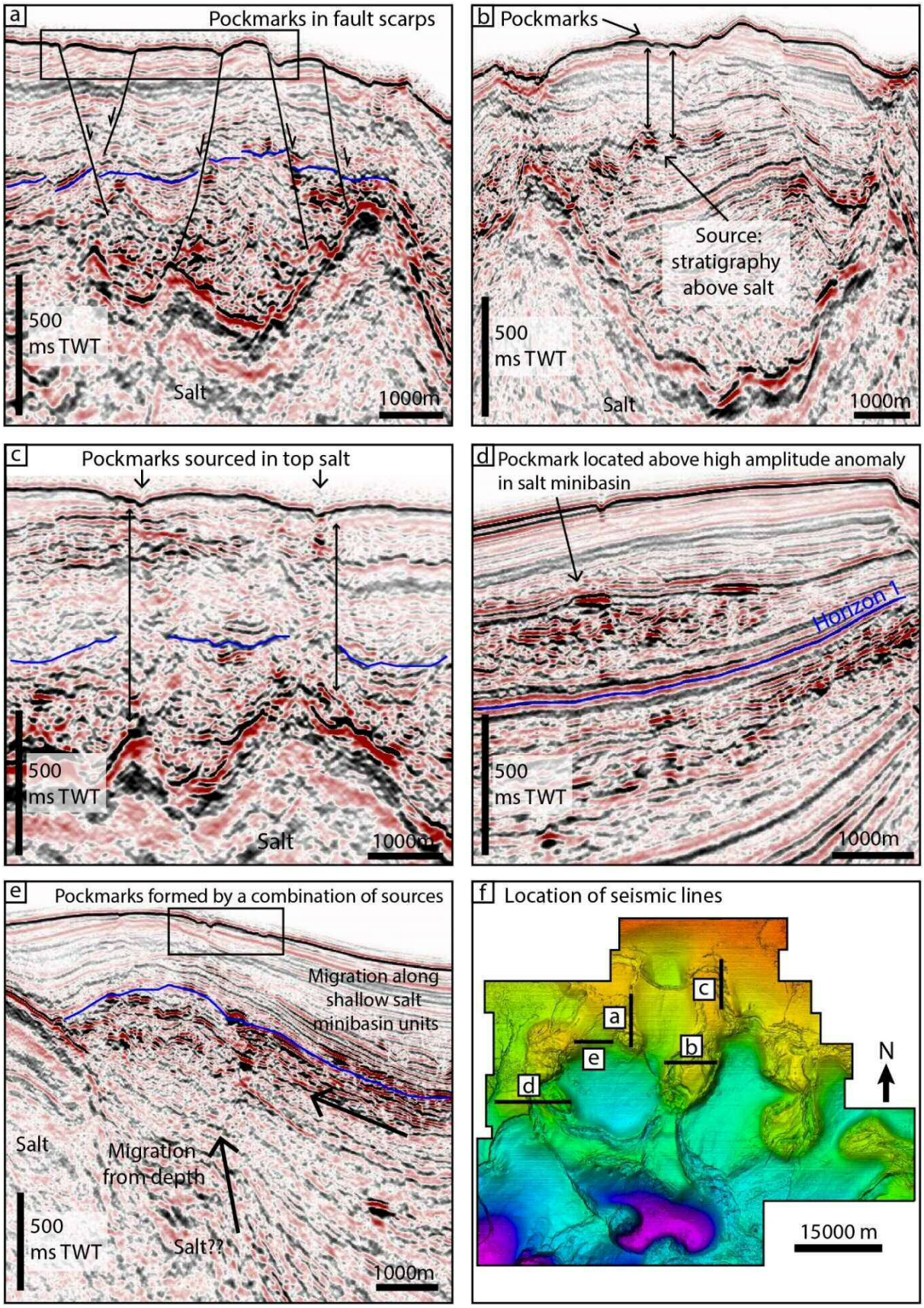

Fig. 5.14. Seismic examples of the five (5) different source categories: a) pockmarks located in fault scarps; b) pockmarks that appear to be sourced in stratigraphy above salt; c) pockmarks sourced from top salt; d) pockmarks located in salt minibasins sourced from amplitude anomalies; e) pockmarks whose source is difficult to interpret, or may be sourced from a combination of fluids from depth and from shallower salt minibasin units. Fig. 5.14f) shows the locations of the seismic sections. Horizon 1 is labelled in blue and is absent in Fig. 5.14b).

5.7 Source depth and morphological analysis of pockmarks

Box plots were generated for the estimated depth of source for the pockmarks in each pockmark source category (Fig. 5.15). The plot shows a range of depths from 100 - 1750 ms TWT, with the data clustered between 400 – 800 ms TWT. The depths of source are not clearly distinct across different structures, and given that most of the pockmarks are associated with top salt, the depth is a function of the growth of the salt diapir to the sea floor.

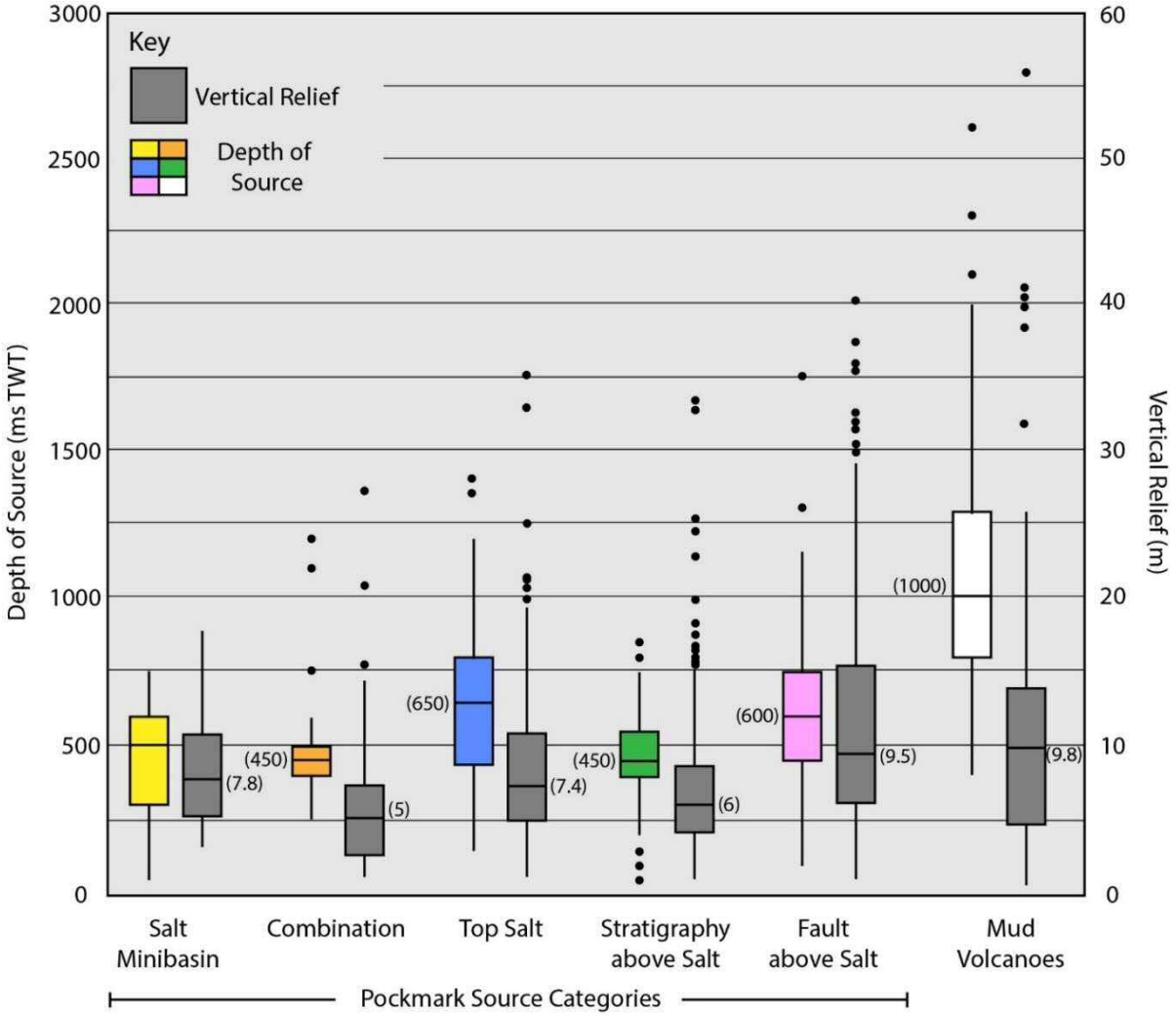

Fig. 5.15. Box plots showing the ranges of source depths (coloured boxes) and vertical relief (grey boxes) – negative for the pockmarks, positive for the mud volcanoes – across the different source categories. Graph shows generally similar sizes of the fluid flow features, whilst source depth is on average much deeper for the mud volcanoes compared with the pockmarks. Median values are labelled on the graph. Colours correspond to the different source categories labelled in the x-axis and match those in Fig. 5.8 and Fig. 5.17.

Vertical relief ranges from 1 m to 41 m whilst width ranges from 20 m to 400 m, similarly to normal pockmarks measured in other parts of the world (Table 5.2). Fig. 5.15 also illustrates the distribution of vertical relief across the structures, which all seem to cluster between 3 – 15 m. The median value for fault-sourced pockmarks is slightly greater (9.5 m) than for the other categories (5-7.5 m), and the range of data and maximum values for salt-related pockmarks are greater than for those in the minibasins. However, morphology of pockmarks does not clearly correlate to the structural sources.

Pockmark and mud volcano width was plotted against depth of source (Fig. 5.16). Pockmark widths are clustered below 200 m across the range of depths, from 50 – 1200 ms TWT. In this study, depth of source does not directly control the size of the pockmark, as shown by the horizontal trendline. In contrast, there is a trend of increasing width of mud volcanoes with increasing depth.

Pockmark eccentricity is represented by the width:length ratio: the greater the ratio, the more spherical the pockmark (Fig. 5.17). The mean width:length ratio is 0.79, however the majority of the data lies above this value, indicating high sphericity across the structures which suggests that pockmarks have not been deformed by bottom currents or side collapse (Judd and Hovland, 2007) and are assumed to be very recent features. There is a greater range of width:length ratio for the pockmarks found in fault scarps. Highly eccentric pockmarks (width:length ratios down to 0.25) elongated parallel to the strike of faults further supports the interpretation that fluids are utilising the faults as flow pathways to the surface.

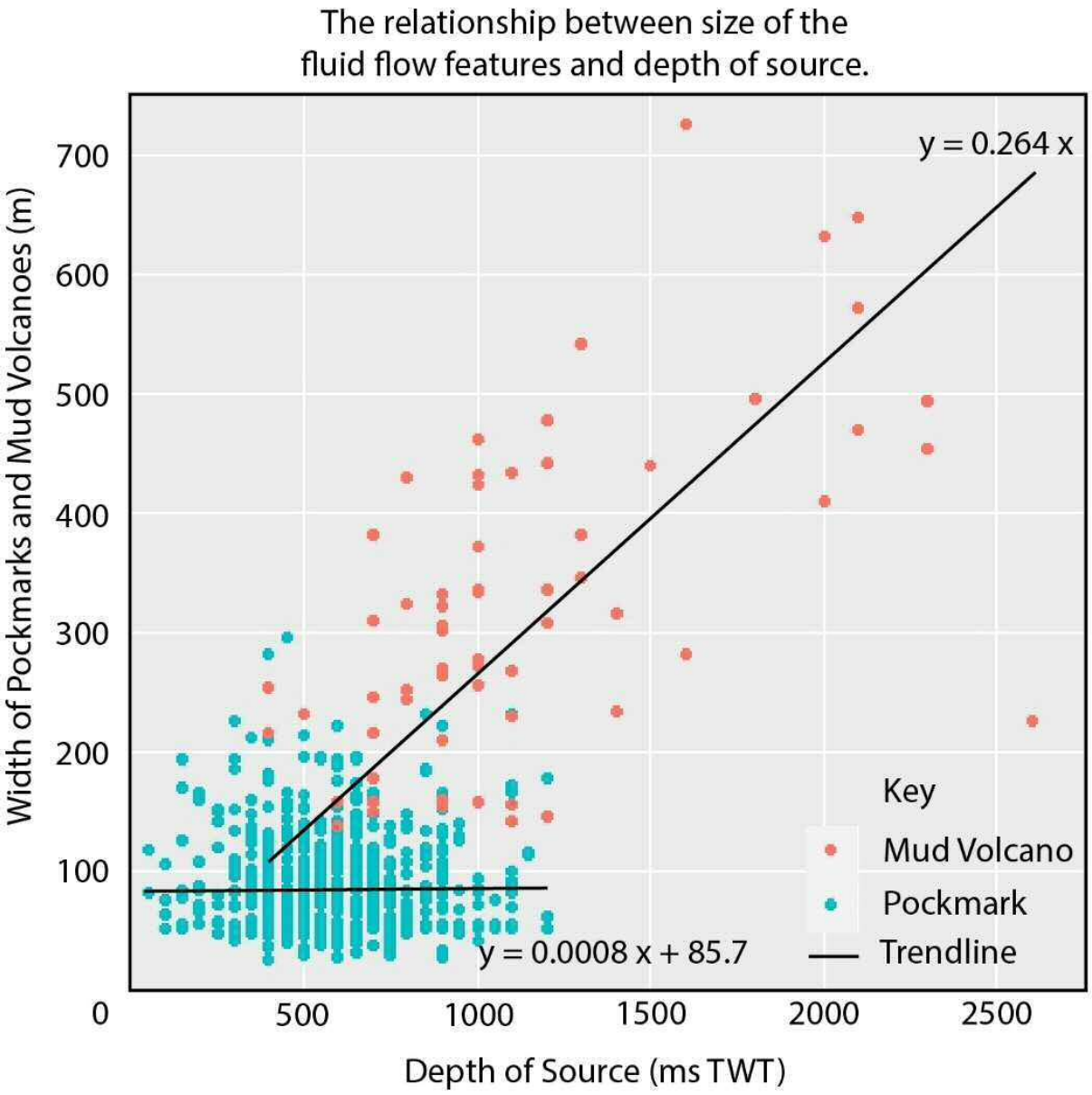

Fig. 5.16. Scatter graph of the width of pockmarks (blue) and mud volcanoes (red) plotted against source depth. A general positive trend is seen for the mud volcanoes, whilst no trend is evident for the pockmarks. The pockmarks are generally small and sourced in shallow strata, whilst mud volcanoes are larger and sourced from deeper parts of the salt minibasins.

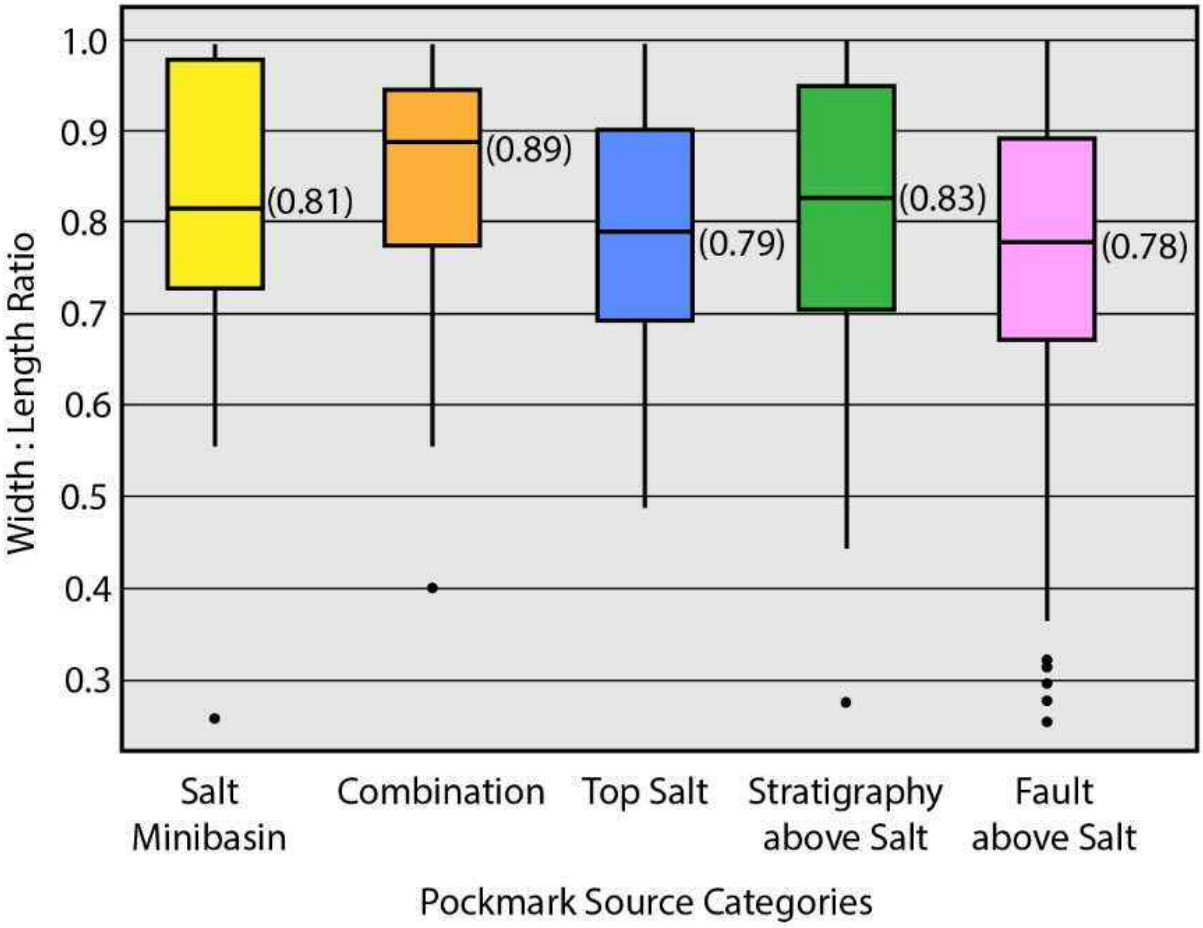

Fig. 5.17. Box plot showing the width:length ratios of the pockmarks across the different source categories. Lower w:l ratios correspond to greater eccentricity values. Most of the values lie between 0.7 and 1.0, whilst pockmarks associated with faults have slightly lower w:l ratios. Median values are labelled.

5.8 Discussion

5.8.1 Hydrocarbon plumbing systems at East Breaks

The results of the seismic and GIS mapping show that the pockmarks are concentrated above salt diapirs, whilst mud volcanoes are located at edges of salt or at fault intersections. Statistical and spatial analysis confirmed that the salt diapirs are the dominant structures for focusing fluids from depth, with supra-salt faults including crestal, roller and ramp faults (Rowan et al., 1999) as pathways for fluids to the surface.

Due to the deep burial of source rocks in the Gulf of Mexico, few source rocks have been penetrated during drilling on the continental slope. The petroleum systems of the field 'East Breaks 160-161' has been described (Armentrout, 1999); however, the critical moment is related to a source rock predicted to be within the Miocene strata (Dow et al., 1990). The Miocene source rocks would not yet have produced large volumes of gas or gas condensate, which may explain the lack of evaporative hydrocarbons in the produced crudes at the field 'East Breaks 160-161', compared to the majority of fields in the northern Gulf of Mexico (Thompson et al., 1990). Gross et al. (1995) noted that the potential source rock occurs within the Upper Jurassic (Tithonian) and for this to be plausible, generation must have been delayed until very recently. Alternatively, hydrocarbons from the Tithonian source migrated to primary reservoirs during the early Cenozoic and to secondary reservoirs and the sea floor over the course of the last 1 Ma after salt welds formed, which provided the fluid bypass pathway (McBride et al., 1998).

The uppermost 1.0 s TWT of sediment are considered to be Pleistocene to Recent in age – Beaubouef and Friedmann (2000) proposed that the deposition of these units occurred within the latest Pleistocene, over approximately 100 kyr, highlighting the rapid deposition and fill of the minibasins. This also implies that fluid flow features are modern, less than 100 kyr and fluid migration occurred rapidly. Many are active at present, as the BOEM data notes the presence of ascending gas within the water column, clustered around pockmarks (Fig. 5.13). Oil slicks and gas plumes confirm that the pockmarks are not simply a result of rapid compaction and dewatering of sediments.

Two main fluid flow mechanisms are invoked in this work (Fig. 5.18). Primarily, sub-salt hydrocarbons migrated across salt welds and into minibasin stratigraphy. Migration occurred along salt, or along carrier beds which are tilted up towards the salt diapir walls. The fluids meet the sediment-salt interface and are diverted up the flow path of least resistance,

along the salt surface by boundary flow (Jackson and Hudec, 2017). Fluids flow vertically and horizontally across the top of diapirs. Here, they continue to flow vertically to the surface along faults – in which case, pipes are not seen. Alternatively, fluids concentrate in shallow reservoirs, accumulating in volume until the pore volume pressure exceeds overburden pressure and a fracture network forms to the surface, forming a pipe which terminates in a pockmark at the sea floor. Sediments under tension such as those above salt diapirs provide migration pathways for pipes to form (Judd and Hovland, 2007). It is interpreted that pipes formed from the salt diapir flanks, the tops of salt diapirs, and from carrier beds above the salt. It is also possible that hydrocarbons were escaping to the sea floor much earlier than the last few thousand years, but without the formation of pockmarks. Judd and Hovland (2007) noted that a stable sea floor with no large-scale active erosion or deposition is required for pockmarks to form, and up until the Holocene transgression, this study area was experiencing very high rates of deposition, evidenced by the thick Pleistocene sediments.

Secondly, diffusive fluid flow may also have occurred vertically across the strata within the minibasins – or along deep-seated faults within minibasins (Fig. 5.2). Hydrocarbons could accumulate in sand-rich zones within mass transport complexes. Bright spots throughout the minibasins indicate the abundance of shallow gas pockets. These may be hydrocarbons found in stratigraphic traps, particularly buried channels (Fig. 5.6b). Fig. 5.6c shows one of a few examples of interpreted flat spots – a fluid contact, which suggests the presence of hydrocarbons as shallow as 1 s TWT below the sea floor within the minibasins. The shallow strata are also tilted due to the ongoing salt movement, so hydrocarbons could be migrating laterally up-dip towards the salt flanks near the surface. Alternatively, the bright spots may be a result of biogenic gas, which is also prolific in the Gulf of Mexico due to high total organic carbon input and high sedimentation rates, particularly in the salt minibasins (Boswell et al., 2012; Hutchinson et al., 2011). In the Gulf of Mexico, gas hydrates can form from biogenic or thermogenic gas under high pressure and low temperature conditions, therefore typically close to the sea floor and at water depths of at least 300-600 m (Hutchinson et al., 2011). If gas hydrates are present in the study area, they could be acting as seals in the salt minibasins (Speight, 2011) as few pockmarks (4% of total mapped) are clearly observed here. In such a case, biogenic or thermogenic gas could accumulate below gas hydrates and migrate up-dip towards the salt diapirs and source the pockmarks.

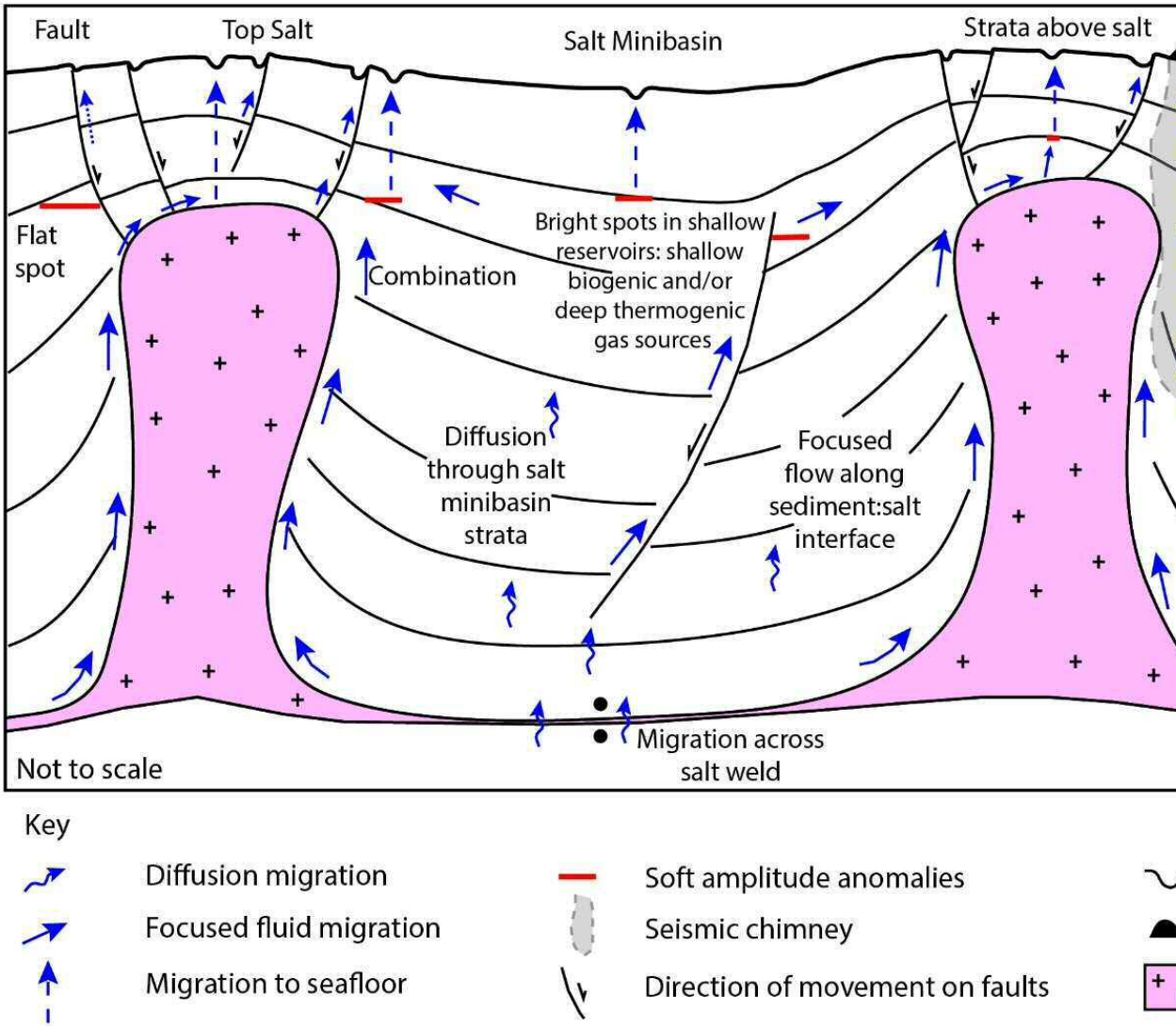

Fig. 5.18. Schematic summary of the plumbing system within the north-eastern region of East Breaks salt minibasin province, n
indicate the variety of migration pathways shown: across salt welds, through minibasin strata, along the sediment-salt interfa
sea floor. Pockmarks are formed from shallow accumulations of gas, whilst seismic chimneys below mud volcanoes extend to
much deeper sources.

5.8.2 Relationship amongst pockmarks, mud volcanoes, underlying structures and depth of source

No clear correlation is seen between the size or morphology of pockmarks and structures or depth of source. It was hypothesized that larger pockmarks would have deeper sources, as greater overpressure is required to produce a larger explosive force that excavates more material at the sea floor. Maia (2017) showed that, in an extensive study of pockmarks in the Lower Congo Basin, there is a positive correlation between depth of the fluid source interval and pockmark size. Nevertheless, there are several factors that can influence the size of the pockmarks in the East Breaks study area, the combination of which may have resulted in a non-descript relationship between pockmark size and depth of source or structural source type.

The size of pockmarks depends partly on the volume of gas that has accumulated – the larger the volume, the greater the overpressure and explosive force to form the pockmark. A shallower source can still produce a large pockmark if sufficient volume of gas is expelled. For a pockmark to have formed from a deeper source, a higher gas pressure (volume) is required to overcome the higher overburden pressure. Energy dissipates as fluids migrate vertically (particularly if more porous media are encountered and gas migrates laterally), and in such a case, gas may not reach the surface (Fig. 5.6d). However, fluid volume increases due to gas expansion and exsolution as it rises, causing the upward buoyancy force to increase also and generally still form a pockmark (Judd and Hovland, 2007).

This particular study does not establish a clear correlation between the depth of the reservoir hosting fluids which formed the pockmarks, and pockmark morphology. In most cases, the source of the pockmarks was considered to be an amplitude anomaly in sub-surface strata, the crest of an anticline, or the top of salt. However, as the seismic profiles beneath the mud volcanoes all appeared to show seismic chimneys extending vertically deeper than the top of the salt diapirs (on the flanks), it is expected that the mud volcanoes reflect much deeper fluid flow, potentially sourced at several kilometres depth. The mud volcanoes are substantially larger seafloor features compared to the pockmarks, where each one formed from a larger catchment area at depth compared to the pockmarks in the shallow subsurface. Huge overpressures are required to form the mud volcanoes, as well as mobilizing mud potentially from a few kilometres' depth, to the sea floor. This was likely supported by the combination of rapid loading of the minibasins and hydrocarbon (particularly gas) migration within these overpressured and therefore lower density mud units (Judd and Hovland, 2007).

It is apparent that the mud volcanoes are sourced from much deeper in the minibasins, particularly in areas where the minibasins are thicker – towards the south of the study area – which coincide with steeper dipping, deep minibasin strata hydraulically feeding these seafloor

features. In contrast, pockmarks reflect the shallow plumbing system. Despite their relatively smaller size compared with the mud volcanoes, these are still large pockmarks compared to those mapped in other basins (Table 5.2) and represent significant volumes of shallow fluid escape to the sea floor.

5.8.3 Implications for hydrocarbon storage and leakage risk in East Breaks

The high proportion of pockmarks associated with the salt diapirs suggests that the primary fluid bypass features are the salt diapirs and overlying faults. The dynamic nature of the salt deforms the overlying sedimentary units by faulting, and these faults are utilised by fluids as effective flow pathways from top salt to the sea floor. It is likely that large volumes of hydrocarbons have already leaked to the sea floor during the Cenozoic. The base of salt is also not imaged, indicating a very deep (> 8 s TWT) source of salt – how much more can the salt diapirs grow towards the surface? Weijermars et al. (2014) stated that salt may be moving up to 100 mm/yr in the Gulf of Mexico, which confirms how mobile the salt is at present day and poses further risk for drilling in close proximity to – or through salt, as exploration wells are deformed, can fracture and fail.

Despite the small number of pockmarks in the minibasins, fluids migrated across the minibasin strata or along intra-minibasin faults to shallower units. Even though the high abundance of direct hydrocarbon indicators and absence of overlying pockmarks alludes to the potential of shallow hydrocarbon accumulations, it should be remembered that anomalies such as bright spots may arise as a result of gas saturations from only a few percent to complete gas saturation (Conn and Arthur, 1990; Judd and Hovland, 1992) and must be interpreted with caution. Even if these are not viable exploration accumulations, the presence of shallow gas presents another drilling hazard.

The varying quality of the data made it difficult to interpret the underlying structures in several regions, increasing the exploration risk. The source category ‘combination’ took this uncertainty into consideration. In some areas, the seismic inline showed no salt, whilst the cross-line appeared to show underlying salt. This also alluded to the likelihood of dual-fluid sources into the same shallow reservoir: both from the deeper parts of the minibasins and from shallower, gently dipping strata.

There is clearly an active petroleum system, but how much has leaked already, the location and depth of the main reservoirs remains uncertain. The poor sub-salt data quality makes it difficult to predict where hydrocarbon accumulations may be below the flanks of the diapirs, if at all, but must not be ruled out, as several hydrocarbon fields in the world have been

discovered in these settings. Examples include the Auger field in the Gulf of Mexico (Hearon et al., 2014) and the Merganser field in the Central North Sea (Charles and Ryzhikov, 2015). The surveys used in this study were acquired in 1991, therefore re-processing of the data, or availability of newly acquired data at the present day will prove invaluable for imaging sub-salt, characterising the structures and revealing possible hydrocarbon traps.

5.9 Chapter specific summary

In this chapter, three-dimensional seismic data, combined with semi-automated mapping methods in ArcGIS were used to analyse the morphology and distribution of 720 pockmarks and 62 mud volcanoes in the northern Gulf of Mexico. Mapping and characterising the pockmarks and mud volcanoes has allowed a detailed analysis and description of the key leakage pathways in the East Breaks area of the northern Gulf of Mexico, and is expected to be applicable to other study areas in the Gulf of Mexico as well as other salt basins around the world. The main conclusions are as follows:

- Salt diapir edges and crestal faults are the dominant focused fluid flow pathways to the surface – supported by the evidence of 96% of the pockmarks being located above the salt diapirs.
- Diffusive fluid flow also occurred through the minibasin to shallower units, and focused fluid flow along intra-minibasin faults. Gas has accumulated in reservoirs consisting mainly of mass transport complexes, from which fluid flow was also diverted sub-vertically towards the structural highs created by the growing salt diapirs.
- Key seal bypass elements in this setting are supra-salt normal faults associated with extension above growing salt diapirs, vertical pipes and the resulting pockmarks at the sea floor. Hydrocarbon leakage is active at present day.
- Mud volcanoes are sourced from the deepest parts of the minibasins, whilst pockmarks represent the shallow plumbing system. Larger fluid flow features are associated with greater minibasin catchment area and dip.
- The semi-automated mapping method increases accuracy and reduces the time spent characterising shallow fluid-flow systems.

CHAPTER SIX

Reutilisation of hydrothermal vent complexes for focused fluid flow on the Modgunn Arch (mid-Norwegian margin)

6 Reutilisation of hydrothermal vent complexes for focused fluid flow

6.1 Abstract

Conventional three-dimensional (3D) seismic data reveal abundant igneous activity on the Modgunn Arch, mid-Norwegian margin. Magmatic sills and associated hydrothermal vent complexes located at various depths prove the repeated utilisation of Paleocene-Eocene magmatic conduits. In total, 125 sills and 85 hydrothermal vent complexes were mapped, with vent complexes ranging in diameter from 300-3100 m and sills from 0.5-50 km. Three examples of stacked vent complexes are presented, revealing large eruptions of hydrothermal fluids vertically through the same conduit, from sills to the palaeo-sea floor. The vent complexes are found throughout Paleocene strata (66 - 56 Ma), whilst at least ten (10) vents were active during the Eocene. This study emphasises the importance of characterising ancient magmatic structures, as hydrothermal conduits and vent structures were, and may still be, reutilised as preferential fluid flow pathways to shallower strata. A minimum of four (4) phases of hydrothermal vent complex formation are inferred. Cretaceous faults are both bypassed and used for magma and fluid flow. The reutilisation of magmatic structures here described may bring to light previously overlooked plays and renew interest in exploring magma-rich continental margins.

6.2 Introduction

Magmatic activity in sedimentary basins has a critical impact on all five elements of a petroleum system: maturation of source rocks, fluid migration, reservoir rocks, seals and traps (Rohrman, 2007; Holford et al., 2012; Senger et al., 2017). For example, magmatic intrusions in the Faroe-Shetland Basin acted as both barriers and carriers for hydrocarbons and other fluid; as crystalline intrusions may inhibit fluid flow and compartmentalise reservoir and source rocks (Senger et al., 2017). Conversely, fractured intrusions facilitate migration to shallow reservoirs (Rateau et al. 2013). Iyer et al. (2017) modelled the temperature profile around magma intrusions in the Harstad Basin, offshore Norway, and demonstrated that source rocks can be

overcooked in their vicinity. Conversely, source rocks considered to be too shallow for maturation may be heated into the oil window to produce hydrocarbons, but typically only in close proximity to the intrusions and for a limited time period during their cooling stages (Stagpoole and Funnell, 2001).

It is clear from the words above that magmatic activity adds much uncertainty and complexity to potential petroleum plays. Yet, large hydrocarbon fields may be discovered when magmatic elements work in favour of petroleum systems, such as the Rosebank Field, and Laggan and Tormore Fields in the Faroe-Shetland Basin (Duncan et al., 2009; Schofield et al., 2017). Even when hydrocarbon potential has been hampered, hot intrusive rocks elevate the local geothermal gradient, turning an otherwise unprospective area into one posed for the development of geothermal energy (Bischoff et al., 2019). Areas currently exploited for geothermal energy are related to young igneous systems, Quaternary volcanism and shallow (<6 km) magmatic intrusions, as in the case of Iceland (Stimac et al., 2015). Other regions with elevated geothermal gradients, possibly due to a thinned crust inherited from continental rifting (e.g. North Sea), are becoming increasingly important. Elgin and Franklin are examples of high pressure, high temperature hydrocarbon fields in the North Sea from which heat could be used to generate electricity on oil and gas platforms (Lockett, 2018).

Hydrothermal vent complexes (HTVCs) formed due to the expulsion of gases and fluidised material are associated with the emplacement of igneous intrusions in sedimentary basins (Svensen et al., 2003; Svensen et al., 2006; Kjoberg et al., 2017; Reynolds, et al., 2017; Omosanya et al., 2018). Supra-sill strata are often fractured at the tips of magmatic sill complexes due to the build-up of overpressure associated with the release of fluids and gases within metamorphic aureoles (Jamtveit et al., 2004; Omosanya et al., 2018). Fluids migrate towards the sea floor through fractured conduits to form HTVCs. These typically occur in basins that experience crustal extension with considerable magmatic input, e.g. the Karoo Basin in South Africa (Svensen et al., 2006), magma-rich continental margins such as the Bass Basin offshore Australia (Holford, et al., 2017), or the Vøring and Møre Basins offshore mid-Norway (Skogseid et al., 1992; Planke et al., 2005). Hence, rift basins and resulting continental margins are commonly categorised as magma-rich or magma-poor, with magma-rich margins being associated with: a) higher spreading rates than their magma-poor counterparts, and b) large volumes of syn-rift igneous rocks (White and McKenzie, 1989; Franke, 2013). Large Igneous Provinces (LIPs) such as the North Atlantic Igneous Province, form in such magma-rich continental margins (Bryan and Ernst, 2008).

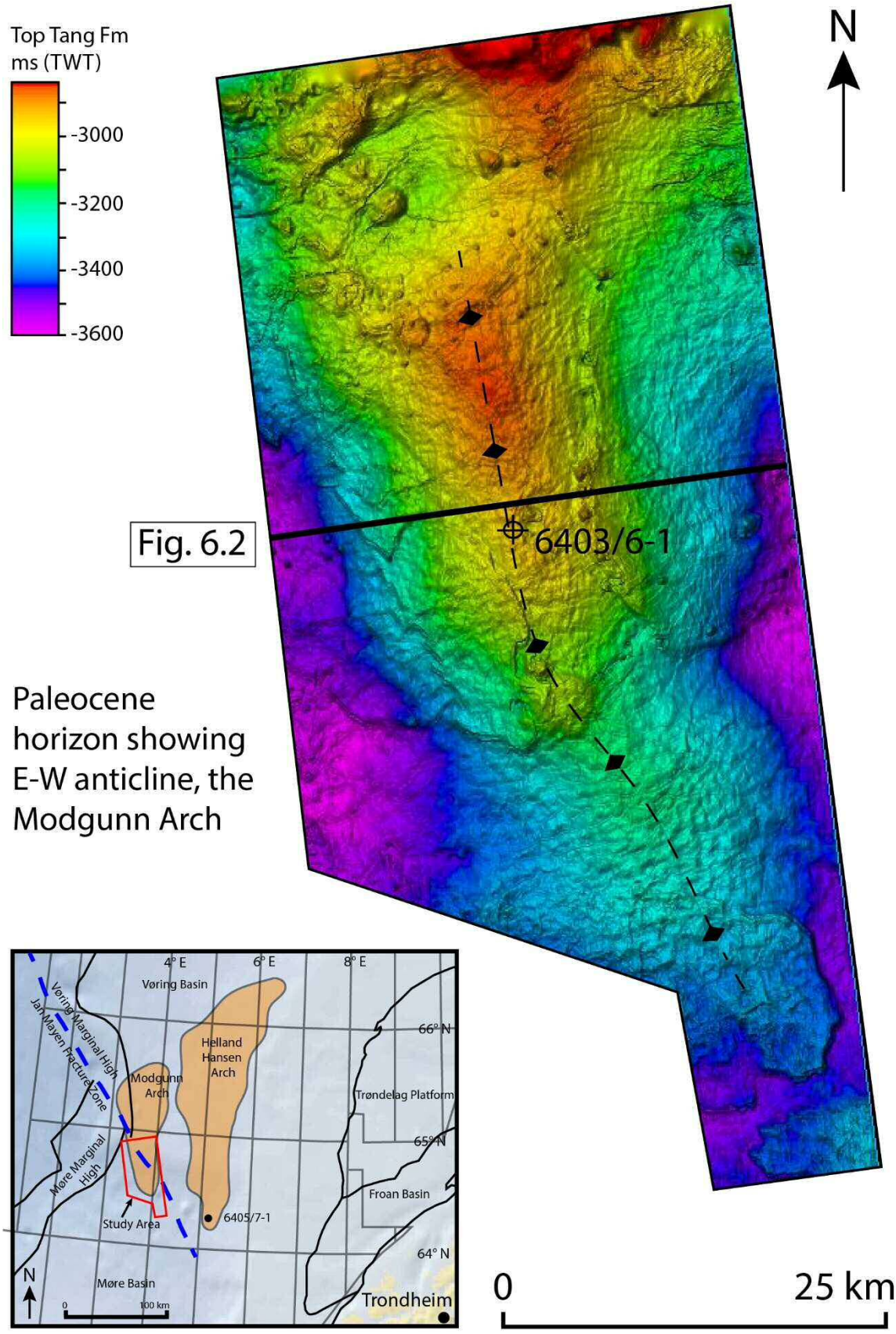

Fig. 6.1. Map of the Paleocene-age, Top Tang Formation, showing the E-W trending anticline: the Modgunn Arch, with the location of the seismic profile in Fig. 6.2 labelled.

This study focuses on the southern part of the Modgunn Arch, a N-S trending Paleogene dome in the southern Vøring Basin with ample evidence of magmatic activity during the early Cenozoic (Manton, 2015; Miles and Cartwright, 2010) (Fig. 2.9, Fig. 6.1). Sills are imaged in seismic reflection data as saucer-shaped or sheet-like, high-amplitude reflections that cross-cut the host-rock strata, caused by an increase in acoustic impedance with depth (Hansen and Cartwright, 2006) (Fig. 2.10, Fig. 2.11). In comparison, hydrothermal vent complexes are imaged as pipe-like, vertical zones of low amplitude and chaotic reflections in the conduits, terminating as dome, eye-shaped or crater morphologies at their summits (Hansen, 2006; Omosanya et al., 2018) (Fig. 1.5). Based on the stratigraphic position of upper terminations in the HTVCs, Hansen (2006) and Planke et al. (2005) used the close relationship between the latter vent complexes and underlying sills to estimate the timing of sill intrusion. They considered the North Atlantic Volcanic Province in the Vøring and Møre Basins to have been emplaced from the Paleocene to Eocene; the volcanic gases subsequently released from the HTVCs during this time are considered to be the cause of the major climate change event known as the Paleocene-Eocene Thermal Maximum (Aarnes et al., 2015).

Radiometric dating of sills to estimate the duration of intrusions can be somewhat erroneous due to subsequent alteration processes of intruded magma and to the poor sampling usually provided by exploration boreholes (Gibb and Kanaris-Sotiriou, 1988). Knowing this, Hansen and Cartwright (2006) used post-intrusion sediment distribution and onlap relationships in seismic data to calculate the timing of sill intrusions. Hansen (2006) stated that the formation of HTVCs occurs within the time it takes for an intrusion to cool, with very thick (>300 m) sills solidifying within 10 ka (Jaeger, 1958). This timeframe is much faster than the resolution obtained from seismic interpretation, which Hansen (2006) demonstrated to have a minimum uncertainty of >100 ka. In a subsequent study, Svensen et al. (2010) dated the Pb-U ages in zircons from two mafic sills in well 6607/5-2, to 55.6 +/- 0.3 Ma and 56.3 +/- 0.4 Ma, which proved to be more precise than previous methods of dating sills using K-Ar (Gibb and Kanaris-Sotiriou, 1988). In addition, Hafeez et al. (2017) used Ar-Ar dating on igneous samples offshore mid-Norway, which yielded dates of 57-58 Ma.

The properties of the acquired seismic signal make it impossible to obtain absolute ages for discrete distinct intrusive events based solely on seismic data, as slightly diachronous HTVCs may share the same basal and upper vent boundaries. Nevertheless, the relative timing of HTVCs and their intrusions can be inferred when using relatively high-quality seismic data to image different stratigraphic levels, as demonstrated in this paper. As core and physical rock samples from sills are not commonly collected by wells, seismic relationships are still a useful tool for assessing the relative timing of intrusions. For instance, Holford et al. (2017) and

Svensen et al. (2003) presented examples of HTVCs focusing fluid migration to shallower units in the Bass and Vøring Basins, respectively, long after the intrusions happened. Against such a background, the research questions of this chapter are as follows:

a) How many distinct magmatic events are recorded on the Modgunn Arch, and how extensive are these events on a magma-rich margin such as offshore mid-Norway?
b) Are hydrothermal vent complexes fed by specific types and depths of sills?
c) What are the implications of reutilising magma migration pathways on the local petroleum systems, at the scale of a hydrocarbon- or geothermal prospect?

6.3 Chapter specific data and methods

The interpreted 3D seismic reflection survey was acquired offshore mid-Norway, on the southern part of the Modgunn Arch (Fig. 2.9, Fig. 6.1). For a full description of the data resolution, see section 3.3.3. One exploration well was used to tie horizons and ages to the seismic data (Fig. 6.2). Well 6403/6-1 was drilled in 2006 in the centre of the Modgunn Arch to test for hydrocarbons in the Upper Cretaceous (Campanian) Nise and Lysing Formations, as well as putative reservoirs in Paleocene and Maastrichtian strata (Factpage 6403/6-1, 2008). Although traces of migrated hydrocarbons were interpreted from post-well geochemical analyses in side-wall cores from the uppermost Nise Formation, there were no hydrocarbon shows in the Nise or Lysing Formations. Sandstones were tight and the well was abandoned (Factpage 6403/6-1, 2008).

6.3.1 Seismic interpretation of horizons and sills

High-resolution seismic mapping of 125 magmatic sills and three (3) key seismic horizons tied to well 6403/6-1 was completed: the Top Tare Formation, Top Tang Formation and Top Nise Formation (Fig. 6.2, Fig. 6.3). The quality of the Top Nise Formation seismic reflection varied considerably throughout the study area due to seismic dimming by overlying sills. In these areas, the Nise Formation is assumed to be present but it was not seismically interpreted (Fig. 6.3c). Thickness variations occur in the Tare Formation due to differential compaction over intrusion-related structures (Kjoberg et al., 2017; Song et al., 2020).

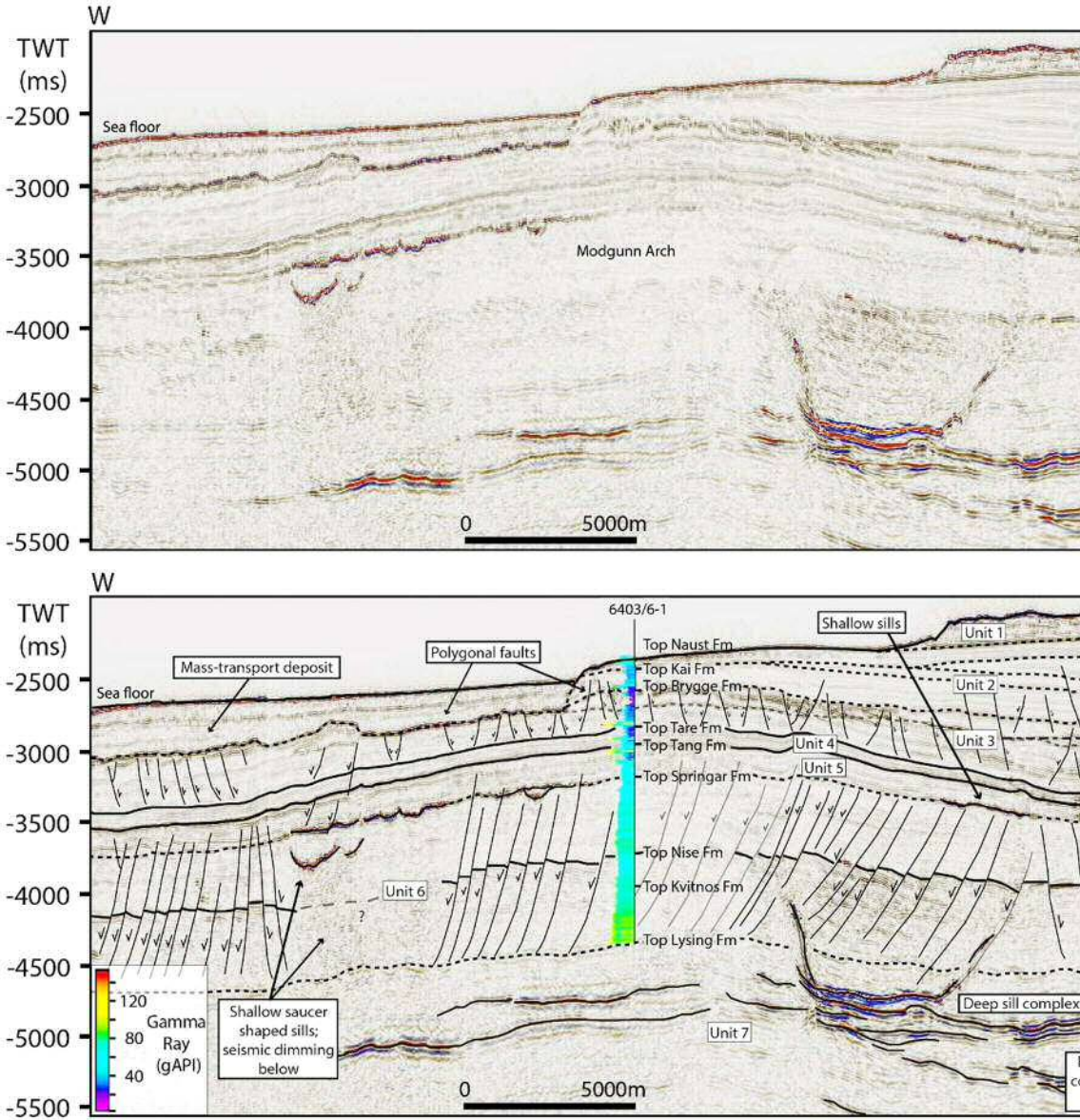

Fig. 6.2. E-W seismic profile across the southern Modgunn Arch, a) uninterpreted, b) interpreted, with seismic units and hori

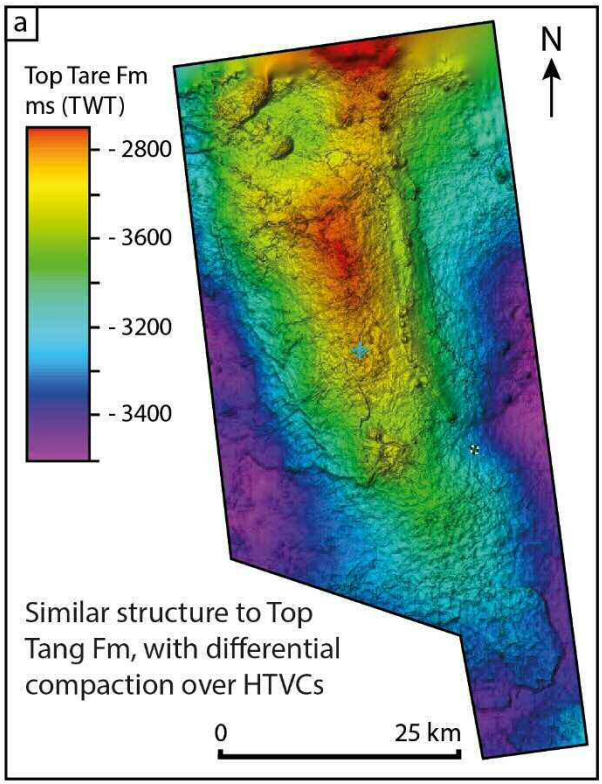

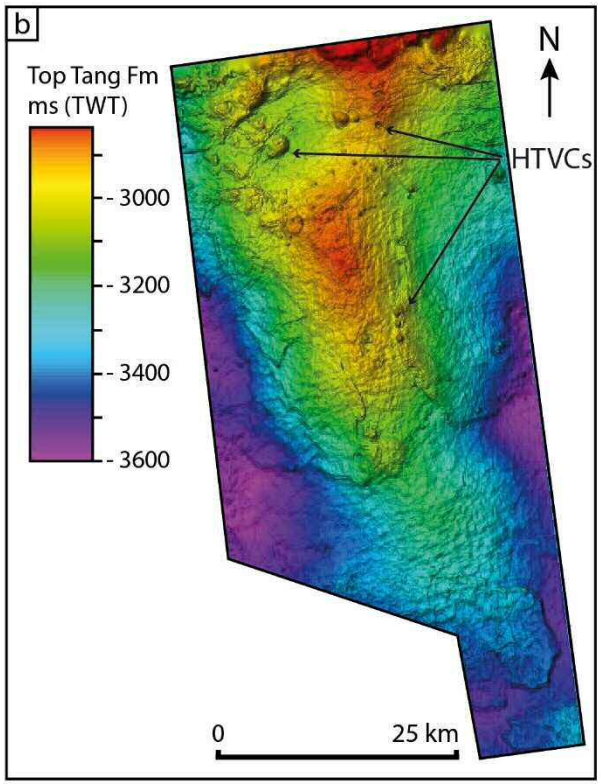

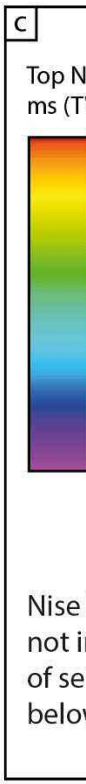

Fig. 6.3. Seismic surfaces of the three mapped horizons: a) Top Tare Formation (H3), b) Top Tang Formation (H4), and c) Top

interpreted in 2D seismic sections using both manual and 2D-autotracking picking tools in a 5x5 inline and crossline grid, after which polygons were drawn in map view around each sill, and corresponding surfaces were generated. Each sill was classified into one of three categories according to their relative depth of emplacement: a) shallow sills within the lowermost Tang and Springar Formations, b) medium-depth sills within the Nise and Kvitnos Formations and c) deep sills in the Lysing Formation and deeper strata. Based on well 6403/6-1, shallow sills occur at depths between 2400 and 3048 m, medium-depth sills occur at depths between 3048 and 4018 m, and the deepest sills are below 4018 m. Well 6403/6-1 was drilled right in the centre of the southern part of the Modgunn Arch, so these depths increase to the east, west and south along the flanks of the arch as the strata have been folded after sills were intruded.

Schofield et al. (2017) showed that as many as 88% of the sills penetrated by wells in the Faroe-Shetland Basin were less than 40 m in thickness; therefore, although 125 sills were mapped in this study area, it is expected that more sills exist well below the seismic resolution of the interpreted 3D volume i.e. the sills are tuned reflections. Also, the convoluted nature of sill intrusions hinders the identification of discrete sills in parts of the study area. However, the presence of a dense population of sill complexes is clear in seismic data (Fig. 6.2).

6.3.2 Seismic interpretation of hydrothermal vents

Hydrothermal vent complexes were identified in seismic data as vertical zones of low amplitude and chaotic reflections in the conduits terminating close to the Top Tang Formation, forming ‘crater’, ‘dome’ and ‘eye-shaped’ vents. The interior of the vents varies between chaotic seismic reflections and clear reflections that terminate within the vents. These morphologies were used to classify the HTVCs following the methodology in Planke et al. (2005) and Hansen (2006) (Fig. 6.7 and Fig. 6.8). Due to the variation in depth of the vents, a regional ‘top vent’ or ‘base vent’ horizon was not interpreted, but the tops and bases of the vents

(2012) by measuring the number of seismic reflections from the base vent horizon above or below the Top Tang Formation, and their distribution was plotted on a bar plot across four (4) sectors of the Modgunn Arch (Fig. 6.9). In this method, the presence of high-amplitude anomalies or seismic dimming in the strata overlying the HTVCs was plotted relative to the Top Tare Formation, as they possibly indicate later stages of fluid flow. Sills were plotted relative to the Nise and Lysing Formations. However, as the seismic reflectivity of host strata diminishes with depth, the approximate thickness of the sill complex or thickness of the strata crossed by a sill is represented in ms TWT instead of the number of seismic reflections as in Alves (2012). This thickness is measured to the nearest 50 ms TWT. As the interpretation of sill complexes is limited by seismic resolution, the thicknesses are not assumed to be accurate, but relative across the study area. A summary of the HTVCs and sills interpreted in this chapter is provided in Appendix E.

The root-mean-square (RMS) amplitude attribute was extracted in a 100 ms TWT window across the Nise Formation horizon to reveal amplitude anomalies that may correspond to fluid flow.

6.3.3 Spatial analysis and geostatistics

The spatial distribution of HTVCs was investigated visually by relating them to their source sills across four sectors, as described above. The HTVC polygons were exported from Petrel into ArcGIS, and the ArcGIS Tool, 'Point Density' was used to calculate the density of HTVCs per 10 km^2 in the study area.

The 'Next Nearest Neighbour Index (Rn)' (Equation 3.10) was calculated to determine whether the points (HTVCs) are clustered ($Rn < 1$), random ($Rn = 1$) or dispersed ($Rn > 1$) (Clark and Evans, 1954).

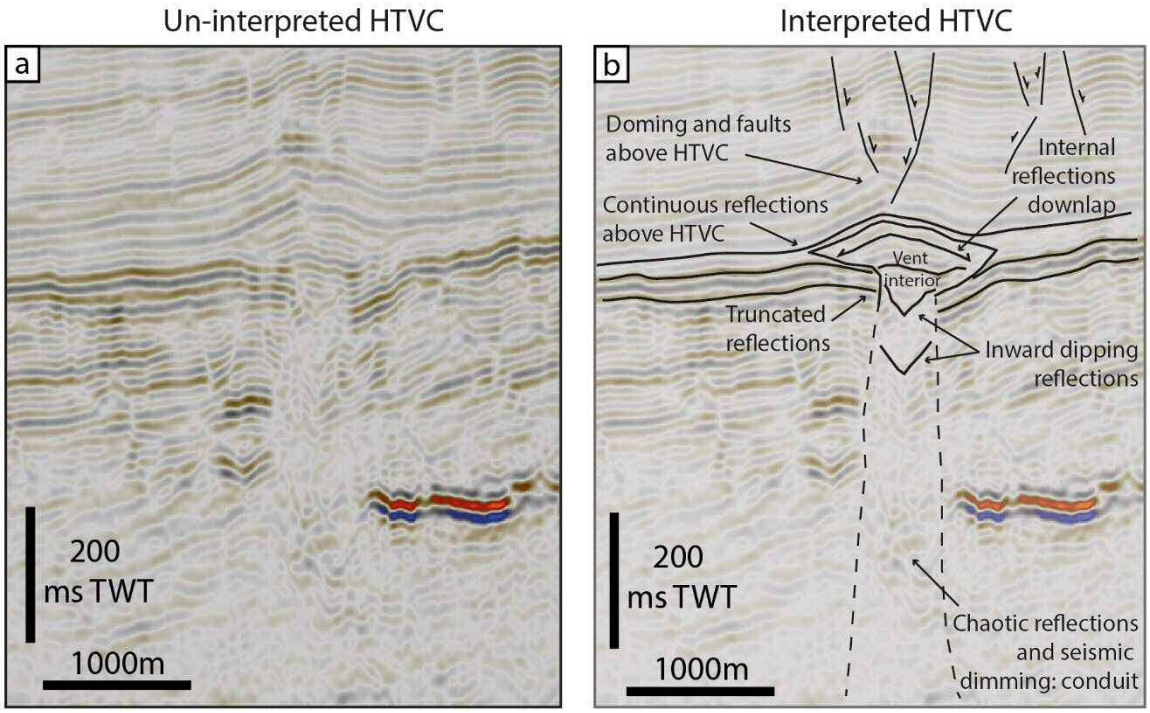

Fig. 6.4. Example of an un-interpreted (a) and interpreted (b) hydrothermal vent complex, highlighting seismic reflection characteristics. Further examples of the different vent types are given in Fig. 6.7.

6.4 Seismic stratigraphy

The study area comprises seven (7) seismic-stratigraphic units (Fig. 6.2; Table 6.1). The horizons delineating main stratigraphic units (and their relative ages) are determined from the stratigraphic tops in well 6403/6-1. Unit 1 consists of chaotic internal strata bound by an irregular sea floor and a relatively planar base (H1), suggesting the presence of a mass-transport deposit. Unit 2 (bounded by horizons H1 and H2) consists of the Kai Formation and forms a wedge of planar strata with internal onlapping geometries displaced by a shallow tier of faults that extend down to Unit 3. Unit 3 (bounded by horizons H2 and H3) correlates with the Brygge Formation and is faulted, showing multiple local onlap and truncation geometries, with laterally discontinuous amplitudes ranging from seismic dimming to high-amplitude, positive anomalies, in places associated with underlying faults or HTVCs. A positive amplitude seismic reflection cross-cuts this unit in the northeast of the study area, corresponding to a 'fossil' Opal A-CT phase boundary (Brekke et al., 1999). Unit 4 (bounded by horizons H3 and H4) correlates with the Tare Formation and consists mostly of planar seismic reflections with local high-amplitude anomalies, onlap and thickness changes above HTVCs. Horizon H3 (Top Tare Formation) is a positive, medium-amplitude seismic reflection, whilst horizon H4 (Top Tang Formation) comprises a positive, high-amplitude seismic reflection that shows slight lateral variations in amplitude as this reflection is an unconformity. Both horizons were seismically mapped across the study area.

Unit 5, spanning from H4 to H5, consists of planar seismic reflections with occasional onlapping relationships. It contains HTVCs with chaotic internal seismic characters, whilst external seismic reflections either onlap onto the HTVCs or are truncated against them (Fig. 6.7). Below HTVCs, and at the base of this unit, are locally very high amplitude, positive seismic reflections corresponding to igneous intrusions. These are typically saucer-shaped but also planar transgressive and layer-parallel (Planke et al. 2005).

Unit 6 (bounded by horizons H5 and H7) and Unit 7 (below horizon H7) are mostly seismically transparent, but large faults at least 1 s TWT in height offset them. Horizon H6 (Top Nise Formation) is a densely faulted, negative seismic reflection. Its amplitude is low, but still relatively high compared to the surrounding stratigraphy; it was therefore possible to map this horizon across the study area, except in areas where seismic dimming prevented a reliable interpretation. Igneous intrusions are present, are characteristically saucer-shaped in Unit 6, whilst those in Unit 7 have planar transgressive or layer-parallel geometries (Fig. 6.2).

Seismic Units	Age of base	TWT Thickness (ms)	Internal character, geometry, and terminations	Probable lithology (Dalland et al., 1988)	Seismic horizons
1	Pliocene	0-200	Chaotic internal strata, bound by an irregular sea floor and relatively planar base	Mass-transport deposit	H0-H1
2	Miocene	0-250	Wedge of planar strata with internal onlapping geometries; displaced by a shallow tier of faults which also extend to Unit 3	Deep-marine shale, with minor siltstones, sandstones and limestone stringers	H1-H2
3	Mid-Eocene	150-400	Faulted by polygonal faults; unit contains abundant local onlap and truncation geometries, with discontinuous amplitudes ranging from seismic dimming to high amplitude, positive anomalies, often in association with underlying faults or HTVCs. Contains a positive amplitude seismic reflection which crosscuts this unit in the northeast of the study area	Deep-marine shales; Positive amplitude seismic reflection which crosscuts stratigraphy corresponds to a 'fossil' Opal-A-CT phase boundary (Brekke et al., 1999)	H2-H3
4	Late-Paleocene	50-100	Mostly planar seismic reflections, with local high-amplitude anomalies and onlap and thickness changes above HTVCs	Deep-marine shales, possibly with variable amounts of volcanic material such as tuff	H3-H4
5	Early-Paleocene	100-200	Mostly planar seismic reflections, with occasional onlap. Unit 5 contains HTVCs typically with chaotic internal seismic character, whilst external seismic reflections either onlap onto the HTVCs or are truncated against them, where they are erosional. High amplitude, planar transgressive, layer-parallel and saucer-shaped reflections are present at the base of this unit	Deep-marine shales; with minor sandstones and limestones. HTVCs consisting of remobilised mudstones and possibly magmatic material. High-amplitude reflections at the base are sills and flows	H4-H5
6	Upper Cretaceous	1000-1500	Mostly seismically transparent, with heavily faulted planar strata. Faults at least 1 s TWT displace this unit. High amplitude, mostly saucer-shaped reflections cross-cutting host strata are also present	Deep-marine calcareous shales, interbedded with minor carbonates and sandstone stringers. Saucer-shaped igneous intrusions cross-cut host stratigraphy	H5-H7
7	Lower Cretaceous - Late Jurassic?	>2000	Mostly seismically transparent, with large faults displacing the poorly resolved strata. High-amplitude planar transgressive or layer-parallel reflections are evident	Marine shales, with interbedded submarine fan deposits. Deep sill complexes are present	H7 and deeper

Table 6.1. Summary of the seismic stratigraphy of the Modgunn Arch.

6.5 Seismic interpretation of magmatic fluid flow features

6.5.1 Morphology and density of hydrothermal vent complexes

The HTVCs are circular to oval-shaped in plan view and their average diameter ranges from 300-3100 m (Fig. 6.6), whilst the approximate height of the HTVCs range between 27 and 374 m. These scales are similar to those interpreted offshore Greenland and elsewhere offshore Norway, along the North Atlantic margin (Table 6.2).

Paper	Diameter, m	Height, m	Location
Planke et al. (2005)	400 – 11 000	30 - 450	Vøring and Møre Basins, offshore Norway, regional study
Reynolds et al. (2017)	700 – 11 000	36 - 504	Danmarkshavn and Thetis Basins, offshore NE Greenland
Omosanya et al. (2020)	516 - 3945	77 - 600	Vøring Basin, offshore Norway
This chapter	300 - 3100	27 - 374	Modgunn Arch, south Vøring Basin, offshore Norway

Table 6.2. Published ranges of diameter and height of hydrothermal vent complexes along the North Atlantic margin, with data added from this chapter.

The craters are generally wider than the domes and eye-shaped HTVCs, recording a median diameter of 1104 m, compared to 682 m and 700 m for domes and eye-shaped vents, respectively. Of the 85 hydrothermal vent complexes mapped in the study area, 17 are craters, 21 are domes and 47 are eye-shaped vents. These HTVCs are distributed across the Modgunn Arch directly above the tips of stratigraphically deeper source sills (Fig. 6.5). The density of HTVCs ranges from 0 to 14 per 10 km^2, with the greatest concentration in the north to northeast of the study area. A nearest neighbour ratio of 0.75 suggests a clustered pattern of HTVCs; a Z-score of -4.45 and p=0.000008 indicates that there is a less than 1% likelihood that this clustered pattern could be the result of random chance.

Out of 125 mapped sills, 27 sills (22%) feed shallower HTVCs. The source sills range in diameter from 1-50 km, i.e. the presence of HTVCs does not appear to be dependent on the size of the sills. Of the 27 source sills four (4) are shallow sills, 13 are medium-depth sills, and 10 are deep-seated sills. All of the sills are associated with five (5) or fewer HTVCs, apart from two sills on the eastern flank of the Modgunn Arch where a large deep sill extending for at least 50 km in a N-S direction appears to feed 20 HTVCs along its rim (Sill A). Another discrete sill

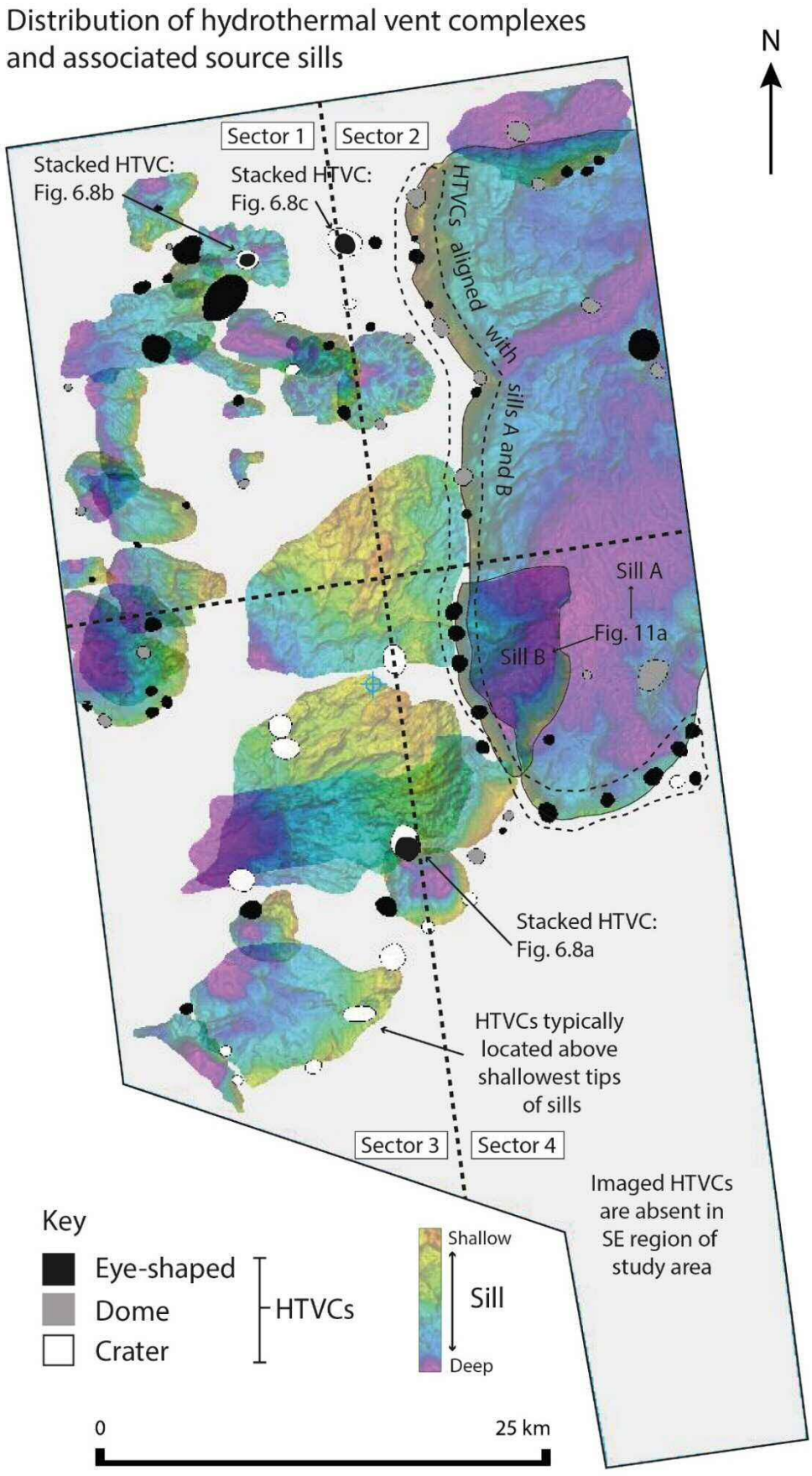

Fig. 6.5. Map showing the distribution of 85 hydrothermal vent complexes, coloured by structure, and the 27 source sills mapped in this work. In the study area, 20 HTVCs are aligned with the 50 km N-trending sill on the eastern flank of the Modgunn Arch. The four sectors shown in Fig. 6.9 are labelled on the map.

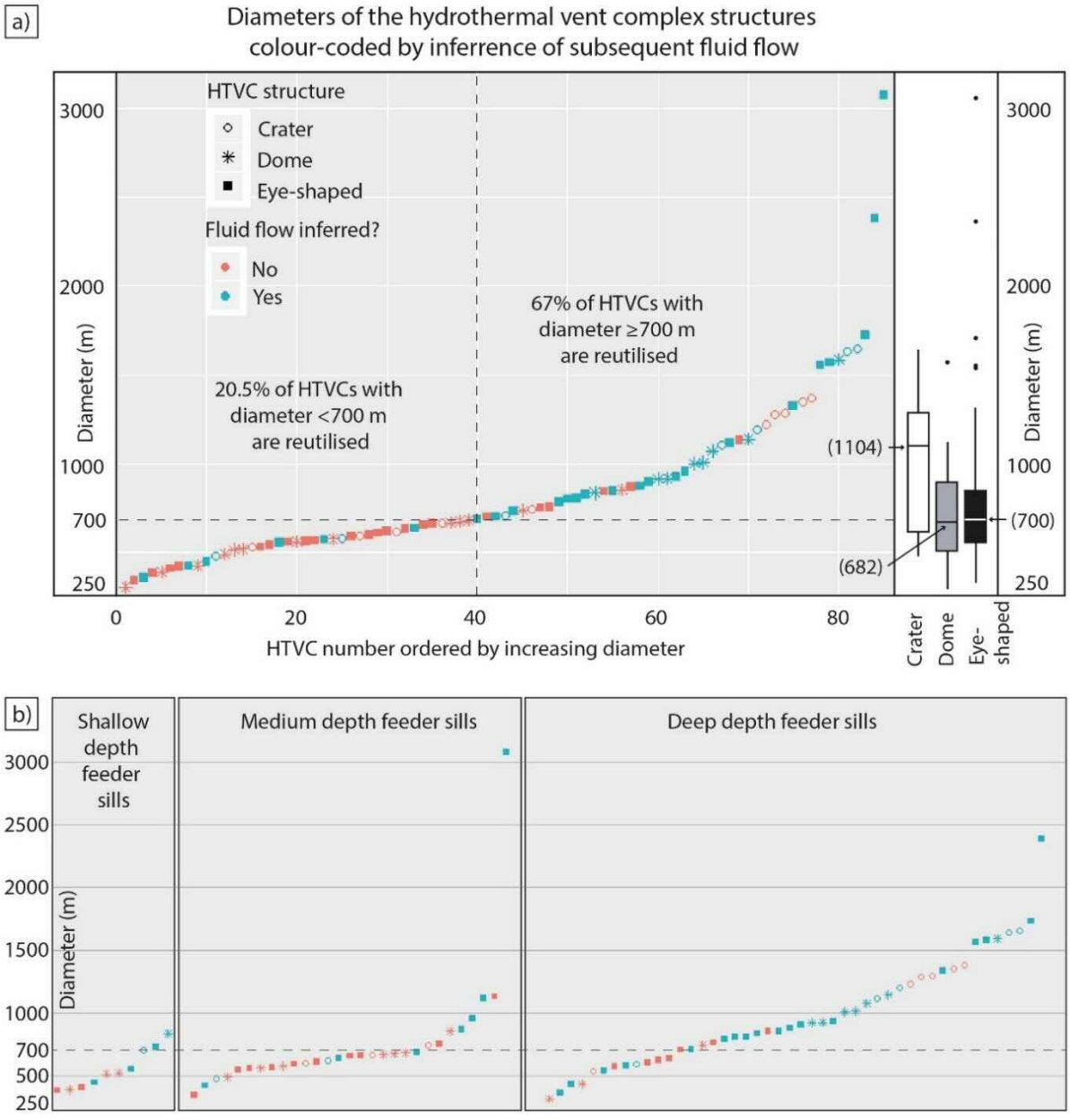

Fig. 6.6. a) Graphic representation of the range of the diameter of HTVCs, ordered by increasing diameter (scatter plot) and by structure (box plots). The colours represented in the scatter graph reflect the positive (or negative) inference of subsequent fluid flow from amplitude anomalies above HTVCs. The box plots show the range in the diameter of HTVCs, with median values in brackets. The plots show that craters are on average larger features compared to the domes and eye-shaped HTVCs. Generally, the larger HTVCs are reutilised by fluid. b) Diameter of HTVCs divided into three groups according to the depth of the feeder sill feeding the HTVC: shallow, medium, and deep depth, with the same symbol key as a).

(Sill B) on the eastern flank feeds seven (7) HTVCs (Fig. 6.5). These sills are interpreted to be spatially coincident with a deep crustal fault, which was likely the source for the sill complex and magmatic fluids.

6.5.2 Distribution of hydrothermal vent complexes and associated seismic anomalies

Fig. 6.7 and Fig. 6.8 show examples of different structures and levels of HTVCs in seismic section. The spatial and temporal distribution of HTVCs across four sectors of the Modgunn Arch is shown by the bar plots in Fig. 6.9. The locations of amplitude anomalies, seismic dimming and the relative depths of underlying source sills are also indicated.

Sector 1, in the northwest of the study area, comprises 20 HTVCs located below the Top Tang Formation. There are three (3) columns of seismic dimming above eye structures; one column from Top Tare upwards through the Brygge Formation and above a high-amplitude anomaly within the Tare Formation, one column from Top Tang to Top Tare Formation, and the third column from the Top Tare Formation upwards through the Brygge Formation. High-amplitude anomalies are present above six (6) HTVCs, which are fed by sills occurring at unequal depths in Cretaceous strata. There is one example of a deeply buried crater with an overlying eye structure (Fig. 6.8b), interpreted to indicate reutilisation of an existing hydrothermal conduit by overpressured hydrothermal fluids to form another HTVC.

Of the 24 HTVCs interpreted in Sector 2, in the northeast of the study area, all but four (4) are associated with the Top Tang Formation, with eye-shaped HTVCs and dome structures distributed above and below the Top Tang Formation. There are high-amplitude anomalies in the Brygge formation above eleven (11) HTVCs, and all of these HTVCs are fed from deep-seated sills. The seismic amplitude of the Brygge formation shows great lateral variation, and is in places typically not associated with HTVCs. This means such amplitude anomalies could be lithological or due to shallow fluid processes. However, Fig. 6.7c clearly shows an example of a soft, bright spot within the Brygge Formation, laterally-restricted and located directly above an HTVC, interpreted to represent a gas pocket. This gas could have been fed from the pre-Cenozoic strata. This high-amplitude anomaly was interpreted and RMS amplitude extracted to show its limited lateral extent in plan view (Fig. 6.10a, b). In addition, RMS amplitude was extracted between the Top Tare Formation (H3) and 100 ms TWT above H3, to show in plan-view examples of where high-amplitude anomalies are located immediately above HTVCs (Fig. 6.10c).

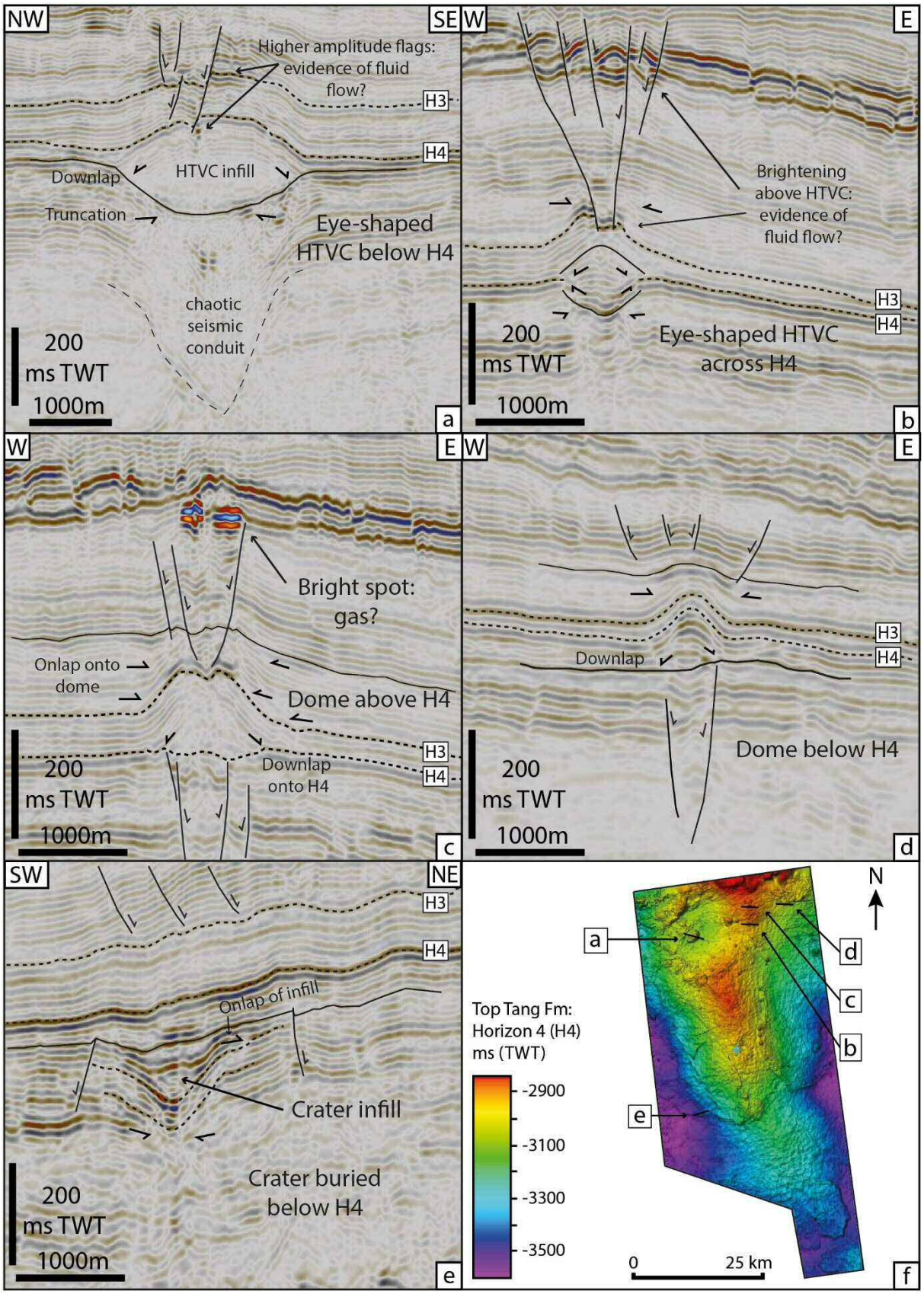

Fig. 6.7. Examples of the different structural types of HTVCs relative to Horizon 4 (Top Tang Formation): a) eye-shaped below H4; b) eye-shaped across H4; c) dome above H4; d) dome below H4; e) crater below H4; f) Time-structure map of the Top Tang Formation with locations of the HTVCs shown in a) to e).

There is one example of stacked HTVCs whereby an eye-shaped HTVC is positioned within and just above a deeper crater structure (Fig. 6.8c). It is suggested that this hydrothermal conduit has been reutilised just after the crater was filled such that the uppermost crater fill was eroded during the formation of the overlying eye-shaped HTVC. No clearly resolved sill was interpreted as the source of this stacked HTVC and two nearby HTVCs, whilst seismic dimming and distortion is clear in a narrow, vertical pipe-like manner to the deeper parts of the basin (Fig. 6.7c). It is possible that these are vertical dykes feeding the HTVCs, as opposed to sills. Dykes appear in seismic section as narrow, sub-vertical columns of chaotic or low amplitude seismic character, which may be traced in plan view as linear features (Thomson, 2007).

Sector 3, in the southwest of the study area, comprises craters located between two (2) and six (6) seismic reflections below the Top Tang Formation. Conversely, the eye-shaped HTVCs are closely associated with the Top Tang Formation, occurring either immediately below, or crossing into the Tare Formation. Despite being associated with the Top Tang Formation, the two domes show different timings of formation; the larger dome was formed during the deposition of the Tang Formation (e.g. Fig. 6.7d), whereas the smaller dome formed on top of the Top Tang Formation during the deposition of the Tare Formation (e.g. Fig. 6.7c). The plot in Fig. 6.9 shows HTVCs at various seismic reflections below the Top Tang Formation, indicating several phases of magmatic activity and formation of HTVCs from the Paleocene to early Eocene. There is also evidence of one hydrothermal conduit terminating in a crater and overlying eye-shaped HTVC, a character suggesting that the hydrothermal conduit generating the crater was reutilised to form the eye structure above (Fig. 6.8a). Two HTVCs show seismic dimming in the Tare and Brygge Formations, which may be indicative of gas escape in the past. There are also three high-amplitude anomalies within the Tare and Brygge Formations, which may indicate gas pockets at present day.

Sector 4, in the southeastern part of the study area, reveals HTVCs that are more closely related to the Top Tang Formation. Eight (8) eye structures and six (6) domes were formed at the very top of the Tang Formation, whilst four (4) craters are found within the Tang Formation per se. Eleven (11) HTVCs are associated with high-amplitude anomalies in the Tare and lowermost Brygge Formations, whilst three (3) eye structures are associated with high-amplitude anomalies at the Top Tare and base Brygge Formations. Seismic dimming is observed in the overlying Brygge Formation. All HTVCs with high-amplitude anomalies were fed from deep-seated sills (Fig. 6.9).

From the 85 HTVCs mapped in this work, 82 comprise hydrothermal conduits - three conduits terminate in stacked pairs of HTVCs and two of these pairs also show amplitude brightening in the Brygge Formation (Fig. 6.8b, c), interpreted to indicate subsequent fluid flow.

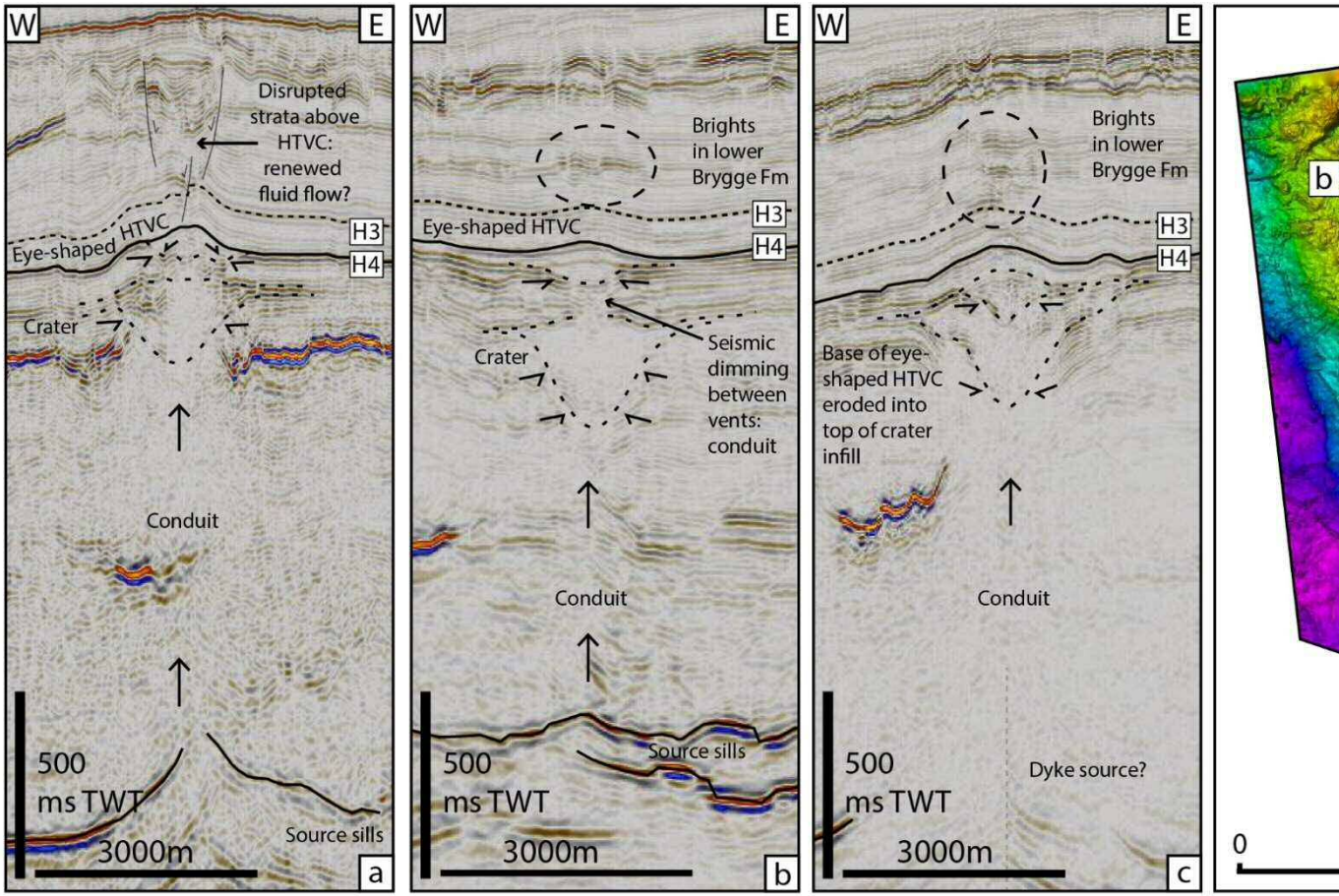

Fig. 6.8. Seismic examples of stacked HTVCs and those with overlying high amplitude anomalies. a) Crater HTVC located s
Formation, with an eye-shaped HTVC above at the Top Tang Formation horizon. Seismic dimming is observed through the HTV
renewed fluid flow. b) Crater HTVC located 12 seismic reflections below the Top Tang Formation, with an eye-shaped HTVC l
in the overlying strata suggest later fluid migration. c) Crater HTVC located four (4) seismic reflections below the Top Tang F
of the crater fill, indicating a second phase of HTVC formation immediately after the crater was filled. It is interpreted that the la
seismic disruptions indicate that a vertical dyke fed the HTVCs. d) Top Tang Formation with locations of seismic examples.

Combining the number of high-amplitude anomalies and seismic dimming above HTVCs gives a total of 35 hydrothermal conduits (43%) that are interpreted to have focused fluid flow after their initial formation. The eastern flank of the arch (the northeast and southeast sectors) contains 22 examples of HTVCs with overlying amplitude anomalies, where all 22 HTVCs were originally fed from deep-seated sills. The western flank of the arch (the northwest and southwest sectors) contains 13 examples of which six (6) HTVCs were originally fed from medium-depth sills. It is interpreted that the majority of renewed fluid flow originates from the depths of the deepest sills in the basin (or even from deeper, lower-crust sources) on the eastern flank of the Modgunn Arch, an area coinciding with a large arch-bounding fault associated with several deep-seated sills. The deepest sills feed 51 HTVC conduits, medium sills feed 25 and shallow sills feed five (5) of the HTVC conduits, whilst dykes feed three (3) HTVC conduits. All of the HTVCs associated with Sill A (20 HTVCs) and Sill B (7 HTVCs) are located at the Top Tang horizon, whilst a few of the other sills which feed between 2 and 5 HTVCs each show slight differences in the number of reflections (-2 to -4) of the HTVC relative to the Top Tang horizon. This may reflect the lateral differences in deposition or erosion of sediments, or the feeder sill is actually a sill complex at depth where multiple sills intruded into the same area and it is not possible to differentiate between them – in addition, as noted by Manton (2015), there may be cases where two sills are feeding an HTVC.

Fig. 6.6 also shows the diameter of the HTVCs coloured so as to highlight the HTVCs that were reutilised (in blue) against those that were not (in red). HTVCs ranging in diameter from 354 – 3076 m are interpreted to have been reutilised; however, the majority of those reutilised have diameters greater than 700 m. This suggests that the larger HTVCs are more likely to be reutilised.

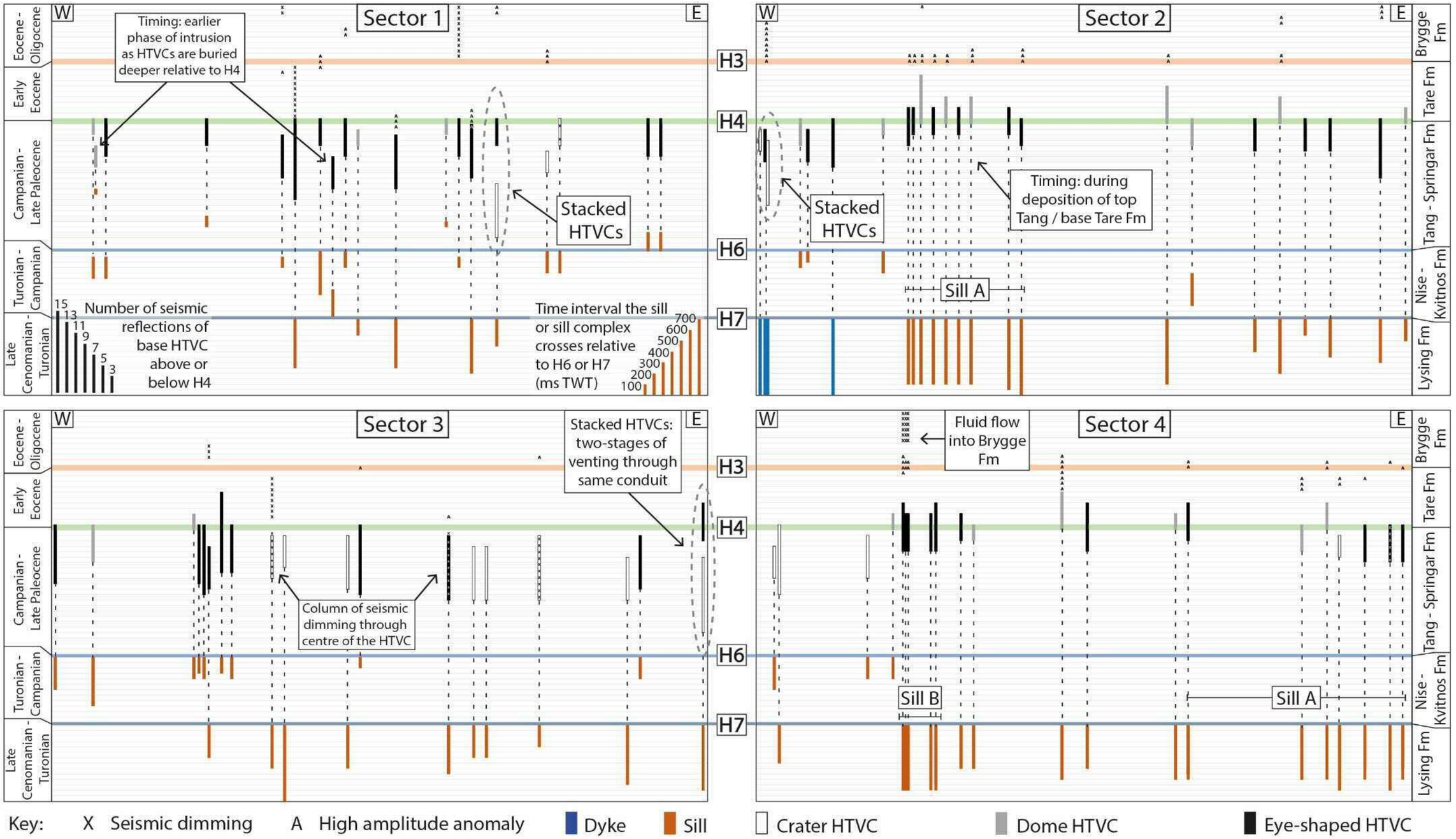

Fig. 6.9. Plots showing the relative timing of formation of HTVCs and associated high-amplitude anomalies (A), seismic dimming (X) and underlying source sills, in the four sectors of the study area. HTVCs are plotted from their base, in number of seismic reflections relative to horizon H4, whilst high-amplitude anomalies and seismic dimming are plotted relative to horizon H3. For sills, every horizontal interval represents 50 ms TWT thickness. Sector 2 contains three interpreted dykes that feed the HTVCs (blue). Reference horizons are labelled: H3 (Top Tare Formation); H4 (Top Tang Formation); H6 (Top Nise Formation) and H7 (Top Lysing Formation), with ages labelled on the left-hand side and stratigraphic units on the right-hand side of the figure. Dotted lines connect HTVCs to their corresponding feeder sills.

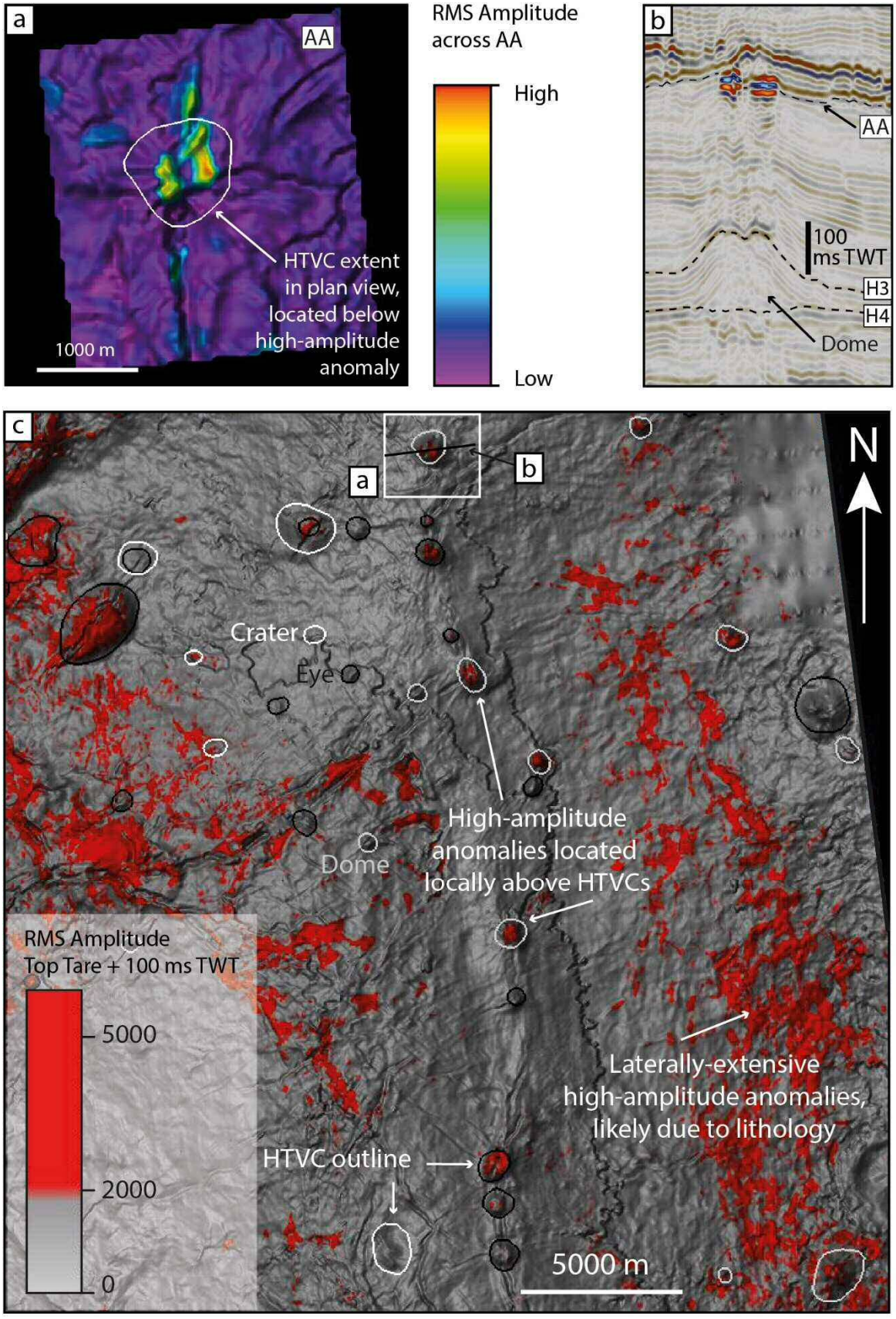

Fig. 6.10. a) Map view of the laterally-restricted high-amplitude anomaly overlying a dome HTVC; b) seismic section showing the HTVC and amplitude anomaly; c) Map view showing the location of a) and b), and the distribution of high-amplitude anomalies within 100 ms TWT above the Top Tare Formation (H3), this is shown in b). Some of the high-amplitude anomalies are local and located above HTVCs, whilst others are more extensive, likely due to lithological changes.

6.5.3 High-amplitude anomalies within faulted Upper Cretaceous strata

The Nise Formation is clearly faulted throughout the study area (Fig. 6.2, Fig. 6.11). The uppermost Nise Formation contains localised high-amplitude anomalies ('flags') indicating that magmatic material or fluids migrated along the faults and are trapped in this unit. High-amplitude anomalies are particularly prevalent in the south-eastern parts of the study area, where the concentration of HTVCs is low (Fig. 6.11b). These higher amplitudes may reflect local stratigraphic changes, such as the presence of sandstone stringers. However, there are instances of flags cross-cutting the faulted strata (Fig. 6.11c).

In most cases, saucer-shaped sills (and where present, HTVC conduits) cross-cut Upper Cretaceous faults, whilst in other cases sills appear to propagate along these faults indicating that these faults can either be bypassed or utilised as magmatic and fluid migration pathways (Fig. 6.11). Manton (2015) deduced that sills along fault planes have not been faulted, rather, some sills intruded along polygonal faults on the Modgunn Arch, although the majority of sills cross-cut the polygonal faults.

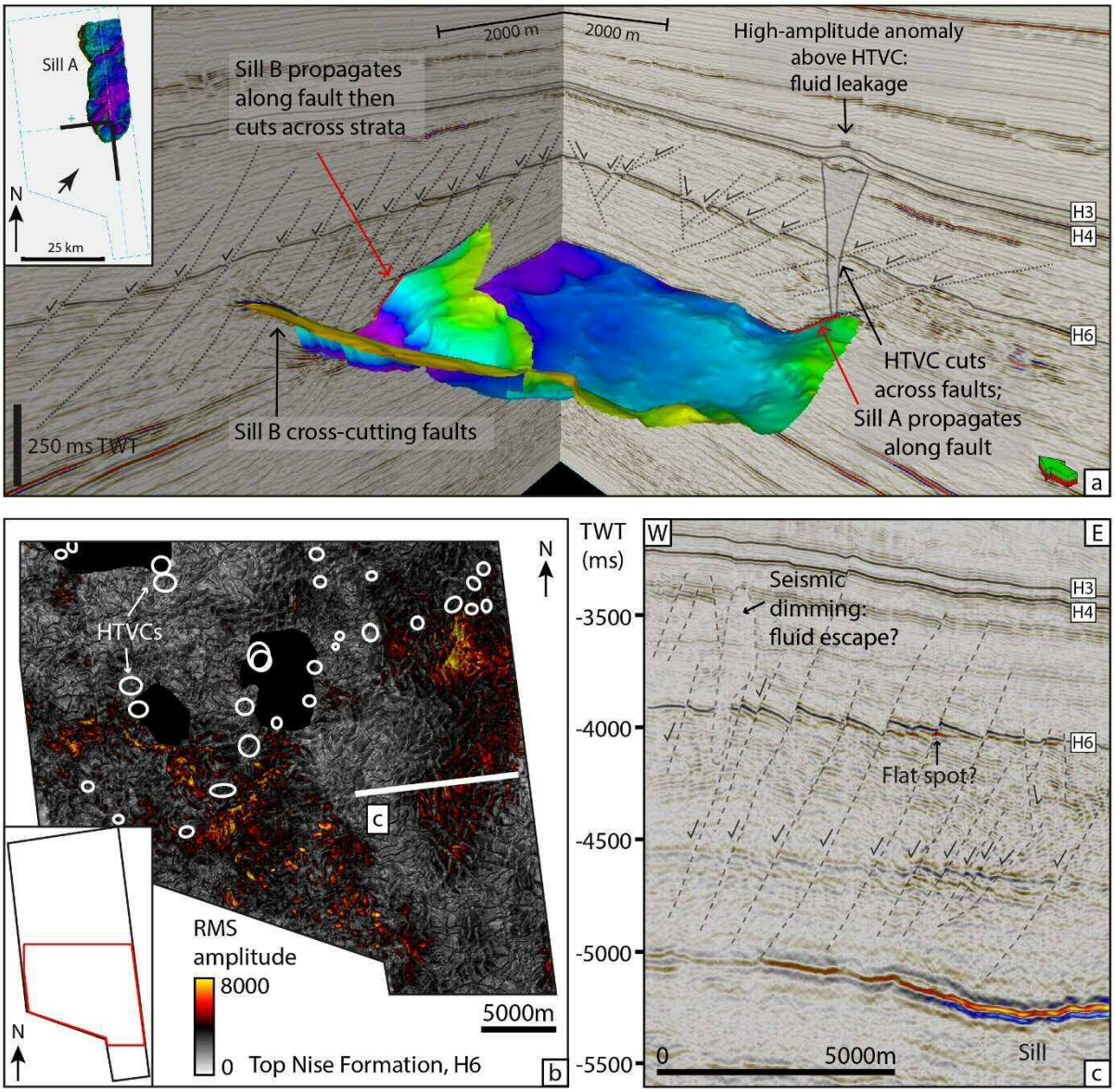

Fig. 6.11. a) 3D seismic representation of Sill A and B. Sill A cross-cuts faults and feeds a hydrothermal vent complex. Sill B cross-cuts faults to the southwestern limb and propagates along a fault on the north-eastern limb of the Modgunn Arch. b) Close-up map view of the RMS amplitude across the Top Nise Formation with location of seismic profile Fig. 6.11c indicated, where no hydrothermal vent complexes are interpreted. c) Seismic dimming associated with the faulted Nise Formation, and a possible flat spot, both features suggesting fluid migration along faults.

6.6 Discussion

6.6.1 Timing and distribution of intrusions and fluid flow features in the Modgunn Arch

Interpretation of a 3D seismic dataset from the Modgunn Arch has revealed a complex arrangement of intrusive sills, hydrothermal vent complexes and fluid flow anomalies. Extrusive basalts were also emplaced on the continental crust at this time, but are not discussed here. The timing of formation of HTVCs is considered to coincide with the timing of sill intrusions. The sills intruded into Cretaceous strata, during continental breakup, while oceanic crust formed west of the study area. The intrusions rapidly heated the surrounding rocks, resulting in boiling of pore water and, in places, rapid maturation of organic material in the sill aureole (Jamtveit et al., 2004). As pressure cannot be dissipated quickly enough, the zones around the sill tips became overpressured and fracture networks formed along which gas, water and magmatic material escaped to the palaeo-surface. Fluid overpressure may also be generated during metamorphic dehydration reactions when various gases such as CO_2 and SO_2 are produced (Aarnes et al., 2011). Generation of large quantities of gaseous hydrocarbons such as CH_4 can result in overpressures large enough to trigger catastrophic blowouts and the formation of HTVCs (Aarnes et al., 2012; Iyer et al., 2017). In some cases, HTVCs formed a crater where material was excavated, or a dome where material was intruded into shallow strata or extruded onto the palaeo-seafloor in a similar manner to a mud volcano. Eye-shaped HTVCs were also formed where some excavation and erosion of material occurred together with gas seepage into the sediments, inhibiting high levels of compaction and resulting in doming (Planke et al., 2005). Although it is still not well understood why these different HTVC structures form, it is clear that they are spatially correlatable with source sills below (Planke et al., 2005; Kjoberg et al., 2017; Schmiedel et al., 2017).

The intrusions of the North Atlantic Igneous Province, spanning eastern Greenland, parts of the United Kingdom, and Norway, are considered to have fed the methane and carbon dioxide gases that contributed to the temperature anomaly of the Paleocene-Eocene Thermal Maximum (PETM) (Svensen et al., 2004; Reynolds et al., 2017). The PETM is recorded between 55-55.8 Ma (Svensen et al., 2004), whilst this study reveals a more protracted intrusion of sills (and therefore expulsion of greenhouse gases) throughout the Paleocene to early Eocene. Planke et al. (2005) and Hansen (2006) showed in regional studies that there were two (2) to three (3) main episodes of igneous intrusion to form the North Atlantic Igneous Province. Whilst it is difficult to accurately distinguish between the timings of intrusion due to the limited

number of exploration wells crossing the Modgunn Arch, the inherent resolution limits of seismic data, and possible lateral differences in sedimentation rates, it is still apparent that several episodes of igneous intrusion occurred in the study area (Fig. 6.9). Where wells and detailed stratigraphic data are available on the Norwegian Margin, the timing of sill intrusion can be well constrained. For example, biostratigraphic data combined with well-tie correlations revealed that the sill related to the Tulipan Field in the Møre Basin was emplaced during the earliest Eocene and was active for some time after, evidenced by the 100 m-thick transition zone seen in well 6302/6-1 (Kjoberg et al., 2017; Schmiedel et al., 2017). Furthermore, field studies in the North Atlantic Igneous Province have revealed the detailed characteristics of vent breccias and the relative timings of magmatic activity, which can be related to offshore subsurface examples in seismic data (Angkasa et al., 2017). Due to the presence of: a) stacked HTVCs below the Top Tang Formation, b) HTVCs immediately below the Top Tang Formation, and c) dome HTVCs above the Top Tang Formation, at least four (4) intrusion episodes are interpreted, as illustrated schematically in Fig. 6.12. Hamilton and Minshell (2019) also presented at least four (4) phases of intrusions throughout the Paleocene and Early Eocene in the Faroe-Shetland Basin, which is part of the North Atlantic Igneous Province, to the south of the study area.

Three (3) examples of ‘stacked’ HTVCs have been interpreted in this study, where a crater formed during the early Paleocene, followed by an eye-shaped HTVC. These are examples of hydrothermal conduits that have been reutilised for the rapid escape of hydrothermal fluids, as opposed to low-flux fluid seepage after the main eruptive event. Fluid seepage is interpreted from the presence of high-amplitude anomalies and also described by Svensen et al. (2003). For stacked HTVCs to occur, another sill must have intruded into the existing sill complex to heat the host rock and produce fluids in the same manner as the first intrusion. The fluids subsequently migrated along the established hydrothermal conduit with an explosive force to form another HTVC. One of the ‘stacked’ HTVC pairs may have been fed by a vertical dyke (Fig. 6.8c), as no clear sills are imaged below, and although vertical dykes are also not imaged as bright reflections, they can subtly manifest as chaotic, low-amplitude seismic columns (Thomson, 2007). As seismic data resolution decreases with depth, particularly when imaging below basalt, an alternative explanation is that the HTVCs could have been fed directly from basement faults, or sills that are not seismically resolved. However, given how clearly other surrounding deep sills are imaged, it is interpreted that dykes are the source points for these HTVCs, which may be expected in such a setting. Skogseid et al. (1992) and Davies et al. (2002) also presented examples of dyke-fed volcanic vents or craters at the

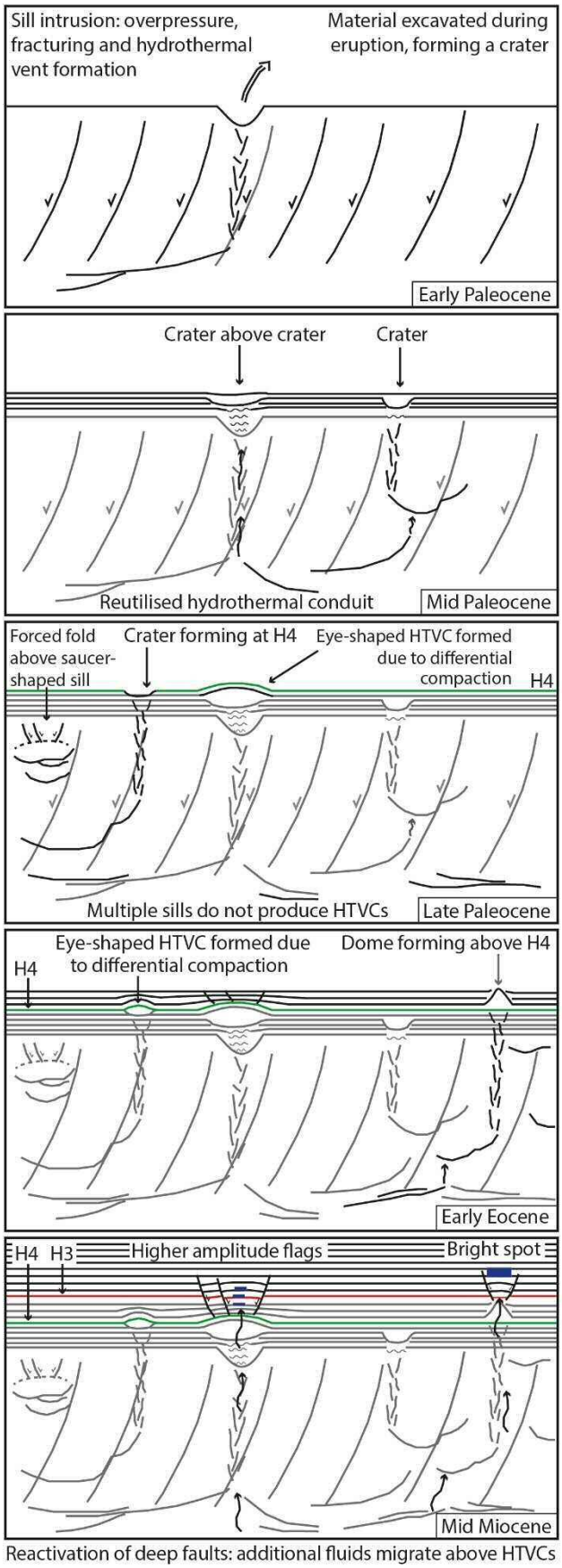

Fig. 6.12. Schematic summary showing the key phases of Paleocene sill intrusion in the study area, and subsequent reutilisation of hydrothermal vent conduits for fluid flow. At least four phases of magmatic activity are interpreted, with additional fluid flow in the mid-Miocene. Diagram is not to scale.

sea floor within the Vøring and Faroe-Shetland Basins respectively; therefore, this is also expected to be the case on the Modgunn Arch. High-amplitude anomalies and seismic dimming must always be interpreted with caution. Variations in cementation, pore fluid pressure, lithology, differential compaction, to name a few, can also cause a change in acoustic impedance contrast and result in amplitude anomalies (Harilal and Biswal, 2010). Seismic dimming may indicate that fluids have migrated along this pathway, possibly with patchy gas distributed in this zone, whilst high-amplitude anomalies may indicate the presence of a gas pocket at present time (Løseth, et al., 2009). High-amplitude anomalies are found across the study area, located above 39% of the HTVC conduits, that are mostly fed from deep sills, particularly on the eastern flank of the Modgunn Arch. Therefore, fluids fed primarily from deeper parts of the basin have migrated along sills and the HTVCs to overlying strata, at some point from the early Miocene, as amplitude anomalies are found across the Eocene to early Miocene-age strata. Other conduits that do not appear to be seeping may be sealed, or the seismic does not clearly show evidence of subsequent fluid flow (Fig. 6.7e).

6.6.2 Morphology and depth of sills sourcing HTVCs.

The diameters of source sills found in this study area range from 1 to 18 km on average, with one sill extending north-south for at least 50 km, likely continuing beyond the study area (Fig. 6.5). These are on-par with those found in field studies in the Karoo Basin, South Africa, where saucer-shaped sills in outcrop have diameters of up to 60 km (Polteau et al., 2008). There is no clear correlation between the size of the sills and the presence of HTVCs, yet a greater proportion of the larger HTVCs are reutilised when compared to the smaller HTVCs (Fig. 6.6). The larger the HTVC, the greater the amount of overpressure was required to form it; if the conduit is larger or more fractured, there may be a greater chance for later pulses of fluids to migrate along this pathway.

Only five (5) of the mapped HTVCs appear to be fed from shallower depth sills. Aarnes et al., (2012) modelled the reaction-induced fluid overpressure build-up – such as that occurring in the metamorphic aureole of a sill intrusion – to constrain the conditions necessary to hydraulically fracture the overburden for pipe formation and focused fluid escape. They determined that decreasing host rock permeability is required for fracturing to occur with increasing intrusion depth, as opposed to fluid escape through the pore network. When heated, high total organic content values in the sediment (e.g. TOC, 1-5%) will produce large volumes of methane gas that increase overpressure in such settings, although much higher TOC will decrease the tensile strength of the host rock and venting becomes less likely. Furthermore,

heating due to sill intrusions will boil water already present in the rocks, which will also increase pore fluid pressure. For instance, Manton (2015) recorded 98 small (100-300 m across) vents directly above a shallow-depth sill on the Modgunn Arch, confirming that vents can be fed from shallow sills but these have not been analysed in this study. Planke et al. (2005) and Reynolds et al. (2017) found that the larger HTVCs are fed from deeper sills. The deepest sills in the study area are found to feed the greatest number of HTVCs, in part owing to their size; the largest (50 km diameter) sill alone feeds 20 HTVCs (Fig. 6.5). The size of vents depends on the surrounding region or rock volume of overpressure accessed by the sill tip (Iyer et al., 2017). The medium-depth sills also feed HTVCs – although these sills are aerially smaller than the deeper sills or sill complexes, they are typically more saucer-shaped and cross-cut large volumes of rock strata. Saucer-shaped sills and transgressive sills with steep sides may channel fluids sub-vertically along the base sill-sediment interface to sill tips and fracture the overburden (Planke et al., 2005).

Deep, vertical dykes are interpreted to feed three (3) HTVC conduits in the north of the study area. Dykes are difficult to image in seismic data due to the vertical and narrow structure, in the same way as pipes, whilst sub-vertical or tilted dykes become more reflective (Thomson, 2007; Løseth et al., 2011).

6.6.3 Implications of reutilising magmatic migration pathways in continental margins

The main implications of reutilising magmatic migration pathways are: 1) the preferential focusing of fluids and potentially hydrocarbons in post-HTVC strata; 2) the generation of migration pathways along faults and sills during long ‘post-intrusion’ periods; and 3) the local addition of heat to promote diagenesis in parts of the basin, impacting on the porosity and permeability of the strata.

The first postulate above considers that magmatic features are increasingly shown to provide additional fluid-focusing pathways in sedimentary basins. For example, the fracture zone around sills and dykes can often be of heightened permeability compared to the surrounding host strata, focusing fluid flow to shallower units (Rateau et al., 2013; Senger et al., 2017). If forced folds are created above saucer-shaped sills, this creates a possible trapping mechanism as evidenced by the Tulipan well in the outer Møre Basin, where a small gas discovery was recorded in a dome above a saucer-shaped sill (Polteau et al., 2008; Holford et al., 2012; Kjoberg et al., 2017; Schmiedel et al., 2017). Schmiedel et al. (2017) also showed that the dome above the Tulipan sill was formed by a combination of syn-sill-emplacement

forced folding and post-emplacement differential compaction, the latter of which is an important mechanism for forming subtle traps for hydrocarbons (Ward et al., 2018). This work also shows that hydrothermal vent complexes play an important role in controlling the plumbing system of a volcanic sedimentary basin. Hydrothermal fluids and hydrocarbons can migrate along pre-existing HTVCs that cross-cut kilometres of host strata into much shallower and younger units. An example of this is illustrated by Svensen et al. (2003), who interpreted continued seep carbonate growth for ~50 million years within Eocene-Pliocene sediments above a HTVC linked to a Paleocene-age sill in the Vøring Basin. They showed that HTVCs can act as long-lasting fluid flow paths to shallower units or the sea floor, as the carbon isotopes from the carbonates are isotopically light and thought to have been fed from hydrocarbons migrating from the deep parts of the basin across the HTVC into overlying strata. In addition, Hamilton and Minshell (2019) documented high-amplitude anomalies above HTVCs in the Faroe-Shetland Basin. They were able to use AVO analysis to show an increase of negative amplitudes with increasing offset, characteristic of low-impedance gas sandstones. A range of near- to long-offset seismic data was not available for this study and could have been useful in further analyses of amplitude anomalies. However, Hamilton and Minshell (2019) also noted that the amplitude anomalies could be diagenetic or lithological, and direct sampling is often required to conclude their true nature.

The second aspect being discussed considers the presence of high amplitude ‘flags’ cross-cutting the Upper Cretaceous Nise Formation (Fig. 6.11) as well as relatively higher amplitudes along the fault planes. Their presence supports the postulate that Cretaceous faults acted as fluid migration pathways, with fluids or magmatic material being trapped in sand units within the uppermost Nise Formation, or migrating to form shallower sills or flows. Sills intruding into pre-existing faults such as those in the Nise Formation cause the faults to dilate and fracture further, contributing to form an additional fluid focusing pathway that may have not been viable prior to magma intrusion. In most cases, imaged HTVC conduits cross-cut these faults. However, the fact that some saucer-shaped sills propagate along these faults increases the importance of taking into account these faults as fluid and magmatic pathways, particularly if the faults form structural traps suitable for hydrocarbons to accumulate. An example of this is the nearest hydrocarbon discovery to the study area, the ‘Ellida’ discovery in the southernmost part of the Helland Hansen Arch (Factpage 6405/7-1, 2005). Well 6405/7-1 was drilled in 2003 by Statoil (now Equinor), ~80 km southeast of well 6403/6-1. The first level found with hydrocarbons was the Upper Cretaceous Nise Formation – the primary target of the well. The presence of oil stains in well 6403/6-1 suggests that hydrocarbons also migrated into the Nise Formation in the southern part of the Modgunn Arch, but have since been lost along

the existing fault pathways or during tectonic reactivation that formed the Modgunn Arch. Sills have not been interpreted in the southern Helland Hansen Arch, therefore it is possible that magmatic activity has hindered a potential petroleum system on the Modgunn Arch.

Amongst the two previous postulates, it should also be considered that if magma migrates along an existing fault and crystallises, the magma and additional diagenesis in the metamorphic aureole may 'plug' the fault zone, reducing its permeability and compartmentalising the basin further (Holford et al., 2012). The impact of magmatic features on hydrocarbons depends on the timing of magma intrusion; if hydrocarbons are already in place, magma intrusions can compartmentalise fields, form preferential fluid escape pathways, or, if the intrusions are stratigraphically below hydrocarbon accumulations, they may have no impact (Senger et al., 2017). In contrast, if hydrocarbons are yet to be produced or migrated, the intrusions will either form preferential migration pathways to shallower reservoirs or to the surface, hinder migration, or decrease the quality of potential reservoirs. Reservoir quality is reduced either by sills intruding into the reservoirs themselves, or by chemical diagenesis due to additional fluids migrating into the reservoirs or excessive heating, increasing the saturation of chemicals which precipitate as cement in the pore spaces (Aarnes et al., 2011). As an example, Manton (2015) demonstrated that the Nise Formation placed controls on the intrusion of sills around the Modgunn Arch due to its greater sand content. Therefore, several sills propagated immediately below, or into the sandier layers, which would have been detrimental to reservoir properties.

Finally, Brekke (2000) discusses the tectonic evolution of the Vøring Basin, noting the presence of a fossilized Opal A-CT boundary. The Opal A-CT transition occurs during early diagenesis, as silica converts from Opal-A to Opal-CT. Resulting strata containing recrystallised Opal-CT has a greater impedance contrast and results in a hard bottom simulating reflector in seismic data (Neagu et al., 2010). The Opal A-CT transition is temperature dependent (Roaldset and He, 1995) and although the reflection cross-cuts a significant thickness of strata on the Modgunn Arch, it does not follow the sea floor reflection. Therefore, it is considered to be a 'fossilized' Opal A-CT reflection, i.e. recording a higher-than-present geothermal gradient (Brekke, 2000). This timing coincides with the reactivation of the Jan Mayen Corridor, associated faulting, and the consequent formation of the Modgunn Arch (Brekke, 2000; Gómez and Vergés, 2005). It is possible to consider that this event instigated further fluid migration along basement faults, sills and HTVCs, which may explain the presence of high-amplitude anomalies in Eocene-Miocene strata (Fig. 6.12). These fluids will have added local heat to the upper crust to fossilize the Opal A-CT boundary along the Modgunn Arch. Nevertheless, Song et al. (2020) also observed that the fossilized Opal A-CT traces the

distribution of the deep, 50 km sill on the eastern flank of the Modgunn Arch and suggested a spatial correlation between the location of the intrusion and the Opal A-CT reflection. If renewed magmatic input was associated with the reactivation of the Jan Mayen Corridor, enhanced heat flow via conduction could have fossilised the Opal A-CT transition.

6.7 Chapter specific summary

Three-dimensional (3D) seismic data was used in this study to interpret the relative timing and spatial distribution of intrusions and associated hydrothermal vent complexes on the Modgunn Arch. As seismic resolution and imaging of magmatic features improves, the reliability of interpreting the presence and timing of formation of these fluid migration pathways improves. This is vital for assessing hydrocarbon plays or geothermal prospectivity in volcanic sedimentary basins. Therefore, the results of this chapter are summarised as follows:
a) At least four (4) phases of magmatic intrusions are interpreted by the diachroneity revealed by the hydrothermal vent complexes;
b) Three (3) instances of stacked hydrothermal vent complexes are presented for the first time on the southern part of the Modgunn Arch, indicating preferential high energy fluid expulsion along an established hydrothermal vent conduit;
c) Hydrothermal vent complexes are acting as preferential fluid focusing pathways since the main magmatic fluid expulsion event during the Paleocene-Eocene;
d) Specifically, three dykes are interpreted to feed hydrothermal vent complexes, including one stacked hydrothermal vent complex pair, therefore dykes are also reutilised migration pathways. Upper Cretaceous faults are both utilised and bypassed by magmatic intrusions and hydrothermal fluid flow;
e) Potential deep crustal faults may have been reactivated during the Middle Miocene to form the Modgunn Arch, which could have re-introduced fluids and heat into the upper crust.

Therefore, this study shows how understanding the timing and distribution of hydrothermal vent complexes and magmatic features is crucial for exploration and is applicable to magma-rich continental margins around the world.

CHAPTER SEVEN

Summary of findings and discussion of results

7 Discussion

7.1 Preamble

The results chapters in this thesis are focused on understanding fluid flow pathways in salt and magmatic basins and their impact on petroleum systems and exploration. The main findings of Chapters 4, 5 and 6 are summarised and presented schematically in Fig. 7.1. Fluid flow pathways are recorded within salt minibasins in relatively deep, Late Paleozoic-Triassic strata in the Central North Sea. Fluid flow pathways around salt diapirs occur in the most recent strata of the Gulf of Mexico, whilst the mid-Norwegian margin contains hydrothermal and magmatic migration pathways in mid-crustal levels.

This chapter aims to discuss the wider implications of the results in this thesis, examine the limitations of the research and propose themes for further investigation.

7.2 Summary of scientific results

7.2.1 Chapter 4: Buried pipes and fluid flow features across salt minibasins

The first data chapter in this thesis (Chapter 4) investigated the timing, distribution and formation mechanism of deeply buried pipe-like features, which terminate in depressions on the Jæren High, in the Norwegian Central North Sea. 3D Seismic data was calibrated to borehole (well) data to determine the ages and lithologies of the seismic units, interpret seismic horizons and to perform depth conversions. The depth-converted horizons were exported to ArcGIS where the Seabed Mapping Toolbox (created by the BGS) was used to semi-automatically map depressions on the horizons. The morphologies of the depressions were also extracted using the Toolbox and compared across the interpreted seismic horizons.

The interpretations in Chapter 4 have implications for assessing the risk of potential carbon capture and storage sites. By superimposing the mapped depressions and salt isopach maps, it was shown that the depressions were strictly located above salt welds and Triassic pods – this indicates that salt welds were the main seal-breach pathways from the Rotliegend Group at the time of the deposition of the Upper Jurassic Mandal Formation and Lower Cretaceous Cromer Knoll Group. The fact that depressions were found within shale units, while only ‘drape features’ were found in some parts of the Shetland Chalk Group, supported the interpretation

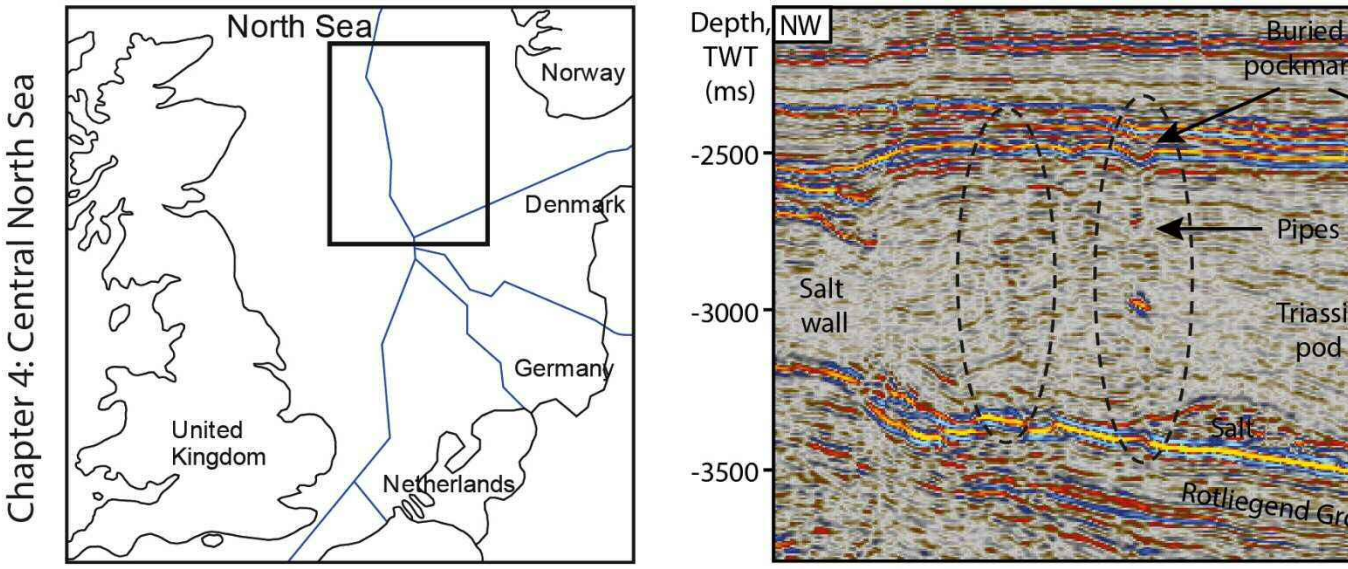
Chapter 4: Central North Sea
North Sea
Norway
Denmark
Germany
United Kingdom
Netherlands
Depth, TWT (ms)
-2500
-3000
-3500
NW
Buried pockmar
Pipes
Salt wall
Triassi pod
Salt
Rotliegend Gr

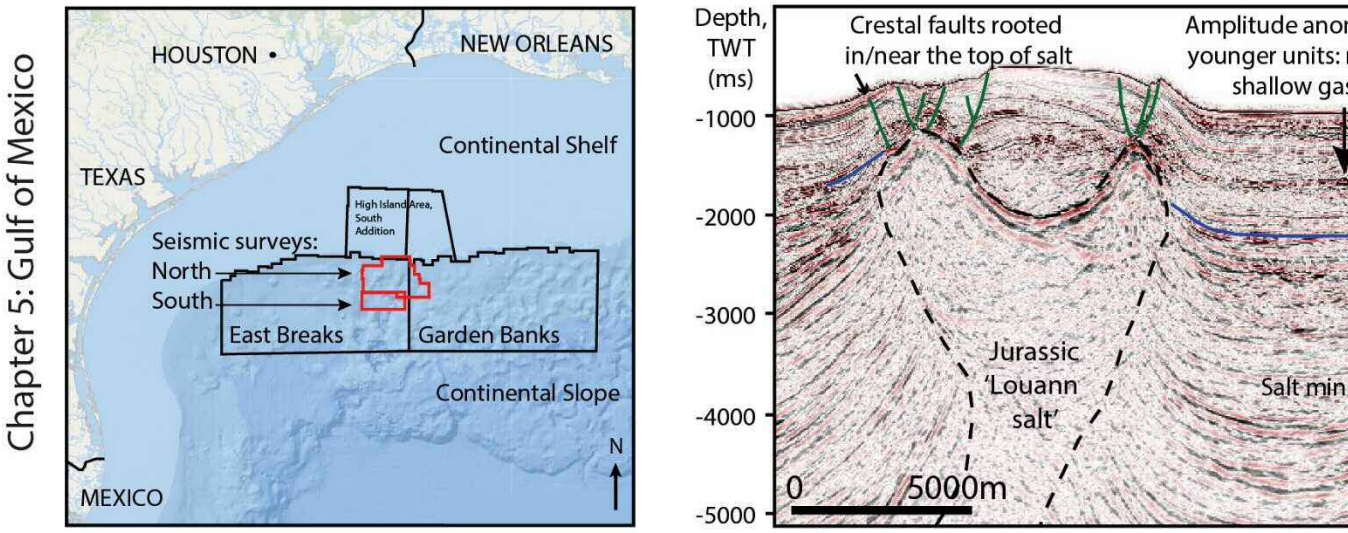
Chapter 5: Gulf of Mexico
HOUSTON
NEW ORLEANS
Continental Shelf
TEXAS
High Island Area, South Addition
Seismic surveys:
North
South
East Breaks
Garden Banks
Continental Slope
N
MEXICO
Depth, TWT (ms)
-1000
-2000
-3000
-4000
-5000
Crestal faults rooted in/near the top of salt
Amplitude anor younger units: shallow gas
Jurassic 'Louann salt'
Salt min
0
5000m

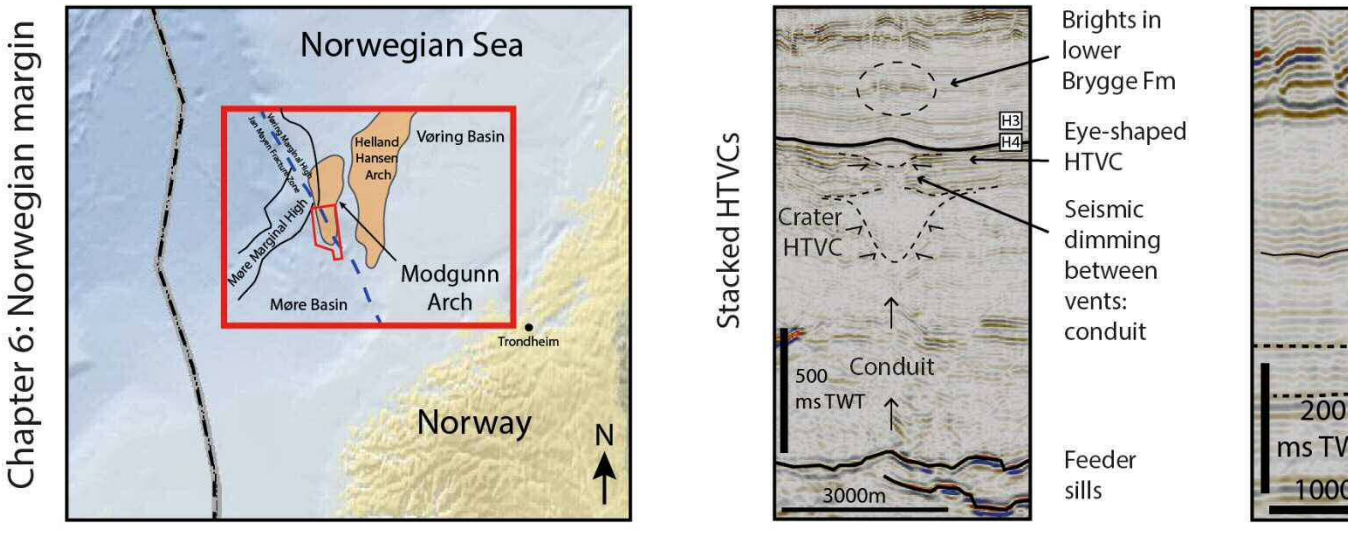
Chapter 6: Norwegian margin
Norwegian Sea
Helland Hansen Arch
Vøring Basin
Møre Marginal High
Modgunn Arch
Møre Basin
Trondheim
Norway
N
Stacked HTVCs
Brights in lower Brygge Fm
H3
H4
Eye-shaped HTVC
Crater HTVC
Seismic dimming between vents: conduit
Conduit
500 ms TWT
Feeder sills
3000m
200 ms TW
1000

of pockmarks as opposed to hypogenic karst features (Masoumi et al., 2014). The size of the pockmarks ranges between 225 – 842 m in width and 14 – 178 m in vertical relief.

At the end of Chapter 4, burial history modelling was undertaken using wells on the Jæren High and in the nearby East Central Graben and Cod Terrace, to assess the timing of maturation of potential source rocks. Results showed that, should Carboniferous coal be present, it would be in the gas generation window either within the East Central Graben or Cod Terrace by the mid Triassic, allowing gas to migrate up-dip onto the Jæren High. The Triassic pods were grounded on the Rotliegend strata as early as the Middle-Late Triassic (Smith et al., 1993) and, once sufficiently high overpressures were reached, gas pressure overcame overburden pressure to escape across the salt welds during the Late Jurassic and Early Cretaceous. High-amplitude anomalies laterally restricted to the pipes were also observed and interpreted to represent either cemented zones or possibly gas pockets. If the pipes are not fully sealed or are susceptible to reactivation, then the risk increases when considering the Rotliegend Group on the Jæren High as a target for carbon capture and storage.

7.2.2 Chapter 5: Structural controls on recent pockmarks above salt diapirs

After addressing the origin and distribution of buried pipes and fluid flow features in the Central North Sea, a dataset from the Gulf of Mexico was interpreted in Chapter 5 to characterise the distribution of fluid flow features near the sea floor, in contrast to the buried features in Chapter 4. As many as 720 pockmarks and 62 mud volcanoes were interpreted in the East Breaks area of the northern Gulf of Mexico using a combination of manual and semi-automated mapping methods, including the Seabed Mapping Toolbox. The mapped fluid flow features were also compared with data from the USGS to cross-check the interpretations in this thesis, from which it was clarified that they are indeed pockmarks and mud volcanoes. The features were correlated to underlying structures controlling their distribution, and the depth of source was estimated. Some of these features were actively leaking gas and fluids to the sea, and oil slicks were also apparent in close proximity to the mud volcanoes, indicating that the study area contains an active petroleum system. Half of the pockmarks were structurally controlled by crestal faults rooted in the tops of salt diapirs; pockmarks were located strictly within the fault scarps and 96% of the pockmarks were associated with salt diapirs. The pipes connecting the pockmarks to deeper strata either terminated at top salt level, in faults terminating in the top salt, or in the supra-salt stratigraphy. Therefore, focused fluid flow from along the flanks of salt structures is the main fluid migration pathway in the East Breaks area.

In parallel, diffusion across the minibasins is also an important fluid flow mechanism, as evidenced by the soft bright spots in shallow strata and the flat spots indicating the presence of a fluid contact, likely gas-on-water. The pockmarks range in size from 20 – 400 m width and 1 – 41 m vertical relief, whilst the mud volcanoes range between 135 – 725 m width and 2 – 55 m vertical relief.

Although no clear correlation was found between the size of the features and the depth of fluid sources, the shallow plumbing system was shown to be dominated by pockmark formation, whilst the deeper plumbing system influenced the formation of mud volcanoes. These features were more prominent in areas where minibasins were larger and had steeper dipping edges along salt structures, which was apparent to the south of the study area in deeper waters. Such features are important to map and consider when assessing the risk of shallow gas hazards and hydrocarbon leakage from deeper reservoirs.

7.2.3 Chapter 6: Reutilisation of hydrothermal vent complexes for fluid flow

One key aspect of magma-rich continental margins is that igneous sills play an important role in controlling fluid migration pathways, either by compartmentalising a basin or focusing fluids (Rateau et al., 2013). In contrast with fluid flow features buried up to 4 km and at the sea floor in the two salt basins in Chapters 4 and 5, Chapter 6 investigated the role of hydrothermal vent complexes in focusing fluid flow vertically across strata around 0.5 – 2 km depth, as well as the main fluid and magmatic migration pathways on the Modgunn Arch, mid-Norwegian margin. The Modgunn Arch contains abundant evidence of magmatic intrusions and hydrothermal vent formation from the tips of sills; hence, the stratigraphic level of the hydrothermal vent complexes was used as an indicator of the timing of sill intrusion. A total of 85 hydrothermal vent complexes were interpreted and the depth of their bases were plotted in number of seismic reflections relative to the Paleocene-age Top Tang Formation, revealing the diachronous formation of vents across the study area. At least four phases of magma intrusion were interpreted, in contrast to the regional study of the mid-Norwegian margin by Planke et al. (2005) which suggested two or three phases. Three examples of stacked hydrothermal vent complexes were also interpreted, indicating two phases of intrusion and eruption of hydrothermal fluids across an established vent. Hydrothermal vent complexes have diameters ranging from 300 – 3100 m and a vertical relief from 27-374 m, whilst the diameter of sills ranges from 0.5 – 50 km. Furthermore, high-amplitude flags above the hydrothermal vent complexes in Eocene – Early Miocene strata were considered as robust evidence for focused

fluid flow across the hydrothermal vent complexes from the deeper parts of the basin, most likely during mid-Miocene reactivation of basement faults. In addition, Cretaceous faults were found to be both utilised and bypassed by sill intrusions and fluid flow.

Chapter 6 thus highlights the complexity of interpreting fluid flow pathways in magma-rich continental margins, whilst the reutilisation of hydrothermal vent complexes has a positive impact on petroleum systems if hydrocarbons migrate along these pathways to shallower strata and accumulate in traps above the magmatic features.

7.3 Pipe formation on the Jæren High, Central North Sea: Evaluating the feasibility of a Carboniferous gas source

In Chapter 4, seismic interpretation revealed the presence of pipes which cross salt welds and Triassic pods, connecting Rotliegend strata to Upper Jurassic-Cretaceous units. The sources of fluid for pipe formation were unclear, thus burial history modelling was undertaken to determine whether the timing of maturation of a gas-prone source rock would occur in advance of pipe formation. The results showed that a coal-based source rock in Carboniferous strata present on the Cod Terrace (southeast of the Jæren High) would have been in the gas generation window from the Early Triassic (Fig. 4.12). The results led to the interpretation that gas migrated up-dip through the Rotliegend Group of the Jæren High and, once overpressures overcame the confining pressure at the salt welds, pipes formed across the Triassic pods. Therefore, although salt welds formed during the Triassic, the generation of fluid pipes was delayed until the Late Jurassic-Early Cretaceous. In addition, burial history modelling showed that the Carboniferous briefly entered the gas generation window on the Jæren High during the Jurassic – Early Cretaceous, which could have resulted in some gas production here also. Gas may also have been sourced from the adjacent East Central Graben, where the Carboniferous reached the gas generation window as early as the Triassic. Regional uplift and erosion during the Early Jurassic as a result of the North Sea Dome (Underhill and Partington, 1993) may have reduced the confining pressure and allowed for gas expansion, further increasing pore-fluid pressure in Rotliegend strata.

As very few wells penetrated the deeply buried Paleozoic strata in the Norwegian Central North Sea, it is nevertheless uncertain if there is even a source of gas (such as coal) in Carboniferous strata. For example, well 7/3-1, which is 30 km east of well 7/1-1 in the study area, penetrated Carboniferous strata at 4692 m depth just before reaching total depth of 4700 m, and found only dolomitic limestone in this interval (Table 4.5). In contrast, Carboniferous

strata in the Southern North Sea occur at much shallower depths due to uplift during Alpine reactivation and compression in the Miocene (Coward et al., 2003). Widespread gas fields in the Southern North Sea are sourced from significant coal measures in Westphalian strata – in most areas, the cumulative thickness of coals is several tens of meters (Pletsch et al., 2010). As the Central North Sea area and Mid North Sea High were uplifted and eroded during the Late Carboniferous – Early Permian (Zanella and Coward, 2003), Westphalian strata are expected to be largely absent and these coal measures are not typically expected to be present here. Milton-Worssell et al. (2010) presented the case for a potential Carboniferous petroleum system in the Central North Sea. They suggested that either long-distance migration from Westphalian coals occurred in the south of the study area or, instead, the Lower Carboniferous (Visean) 'Scremerston Coal Group' is present, as identified by well 39/7-1 in the UKCS (Fig. 7.2).

More recently, Monaghan et al. (2017) synthesised well and seismic data and models across UK Quadrants 25 – 44 from the '21st Century Exploration Roadmap Palaeozoic Project (2014-2016)', which contributed to increased exploration activity of the 'frontier' Mid North Sea High region. The presence of Visean-age coals in the Scremerston Group, and Visean-Namurian-age basinal shales in the Cleveland Group were confirmed in wells, particularly towards the southern part of the Mid North Sea High (Kearsey et al., 2015; Monaghan et al., 2017). One-dimensional burial history modelling also proved burial of these Lower Carboniferous strata to depths of gas maturation, and the discovery of the Breagh Field in UK blocks 42/12a and 42/13a proved a working petroleum system in the Visean-Namurian age strata (Monaghan et al., 2017). Although UK Quadrants 25 – 44 are to the south and west of the Jæren High and on the other side of the Central Graben, it is possible that these Lower Carboniferous play elements may extend to the Norwegian side of the basin also. In addition, Hay et al. (2005) mapped gas chimneys in the Mesozoic and Cenozoic strata in UK Quadrant 29, which overlie an interpreted Visean coal-measure basin and show widespread Zechstein seal breaching (Milton-Worssell et al., 2010). These observations support the interpretation of a Visean coal source in the Central North Sea. Moreover, the study by Strozyk et al. (2018) also supports the interpretation provided in Chapter 4, which proposes gas generation and migration across salt welds during the Lower Cretaceous, although their study area is in the Netherlands, i.e. a region where Westphalian coal presence is known. Strozyk et al. (2018) interpreted circular, 300 – 850 m-wide and 10 – 50 m-deep pockmarks at the top of the Lower Cretaceous unit in 3D seismic data, which are comparable to those in Chapter 4 of this thesis.

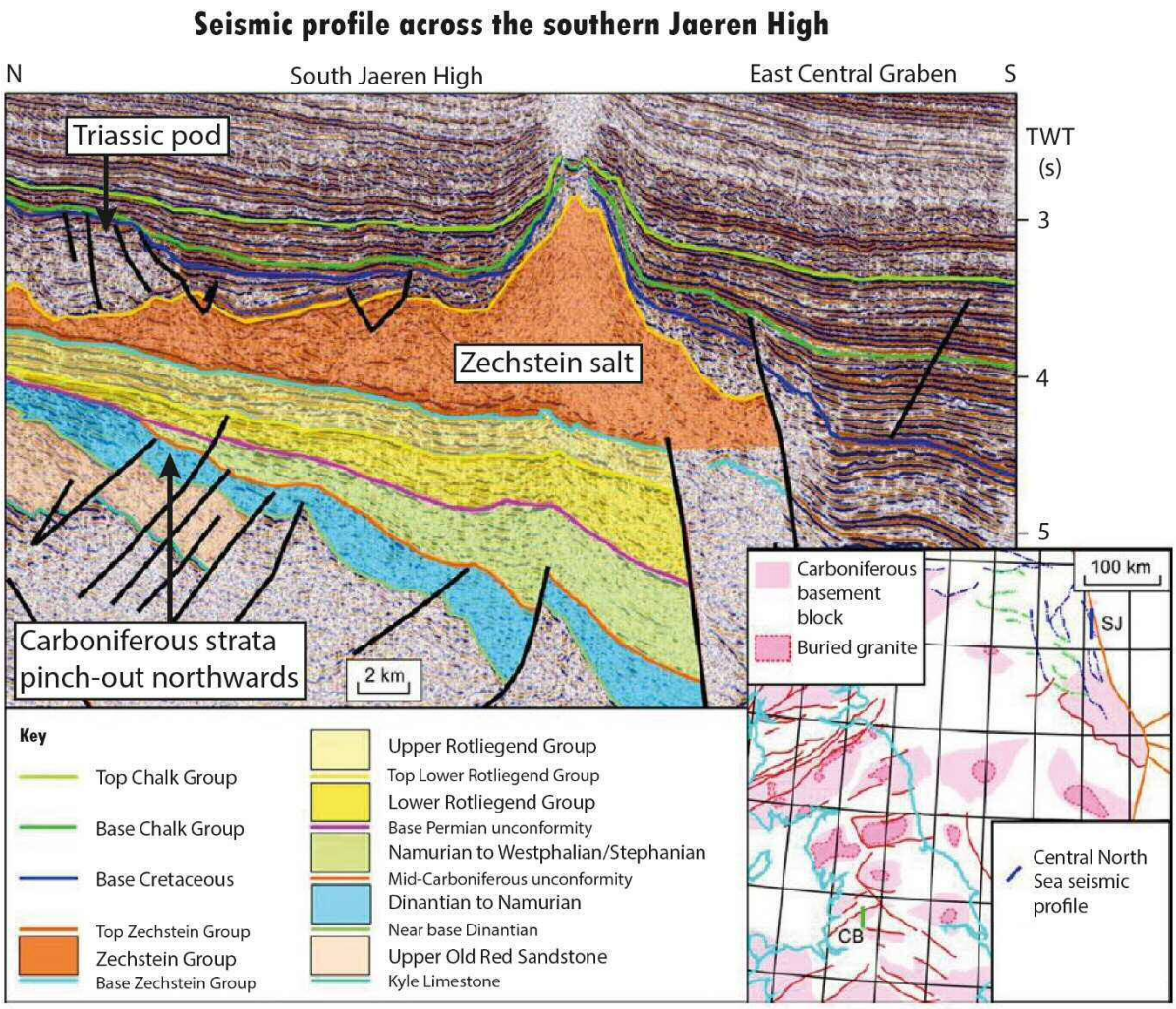

Fig. 7.2. Interpreted north-south seismic profile from the south Jæren High (SJ), showing the sedimentary basement structure and the result of erosion of Carboniferous strata towards the northern Jæren High. Profile is located a few kilometres southwest of the study area in Chapter 4. After Milton-Worssell et al., (2010).

If there is no gas source in the study area or neighbouring regions, the question remains: what would be the alternative mechanism to form these pipe features? Clark et al. (1999) described pipe-like structures called 'salt chimneys' on the West Central Shelf of the Central North Sea, a region with Triassic pod – salt wall geometries similar to the Jæren High. Clark et al. (1999) proposed that early Triassic salt karstification was succeeded by later influx of salt into the cavities, which subsequently dissolved during Upper Jurassic to Lower Cretaceous deposition of marine mudstones, forming collapse structures with circular faults. However, the depressions on the Jæren High are not associated with circular faults and only some of the pipes contain high-amplitude anomalies, which were interpreted as the tops of salt chimneys in the dataset by Clark et al. (1999).

The pipes in Chapter 4 are also not considered to be dewatering structures of the Smith Bank Formation. Dewatering structures such as pipes and polygonal faults typically occur due to rapid burial of thick, mudstone-dominated successions where overpressures build as pore-fluids are unable to escape the fine-grained strata (Berndt et al., 2003). On the Jæren High, Triassic pods were grounded onto Rotliegend strata and inverted into turtle anticlines in the mid-late Triassic, during which time fracturing may have occurred in the arch of the anticlines due to the effect of extensional stresses. Pore fluids from dewatering of mudstones could have escaped along these fractures. Dewatering might be expected to be synchronous during the Triassic, but fluid flow features affect Upper Jurassic and Lower Cretaceous strata where, in some cases, depressions are stacked suggesting multiple fluid escape events. Thus, the interpretation that the depressions in Chapter 4 are due to gas escape is preferred, baring similarities to the interpretation in Strozyk et al. (2018).

Overall, uncertainty remains about the presence of a gas-prone source rock in Carboniferous strata in the Jæren High and surrounding areas, which can only be proved by drilling deeper wells. If a petroleum system is proved in Carboniferous strata, there may be renewed exploration interest of the Central North Sea basin. Alternatively, if there is no gas or it has been expelled in the past, the Rotliegend Group may be explored as an aquifer for potential CCS sites. The effectiveness of storing CO_2 underground has already been proved in the Sleipner field (Michael et al., 2010). The North Sea is a mature basin with extensive subsurface knowledge – exploiting it further using existing infrastructure will be beneficial in the Energy Transition, as the world seeks solutions to lower carbon emissions.

Regardless of their genesis, the interpreted pipes are an important seal bypass mechanism (Cartwright et al., 2007) that should be considered when exploring salt basins. While some studies – including Chapter 5 in the Gulf of Mexico – show pipes and pockmarks above salt diapirs that indicate fluid migration along salt flanks, the pipes in Chapter 4 are

strictly located away from the salt walls, having formed across salt welds. This could be detrimental to sub-salt exploration, as hydrocarbons leak from potential reservoir targets such as the Rotliegend Group. Meanwhile, pipe formation across welds may benefit hydrocarbon exploration if hydrocarbons have migrated along these features and are trapped in shallower reservoirs instead. This would decrease the cost of drilling as wells are shallower, and de-risk exploration in the area.

7.4 How do the geometry and seismic character of fluid flow features change from the deepest to shallowest parts of a sedimentary basin?

7.4.1 Morphological changes of fluid flow features with depth

The datasets analysed in this thesis cover a range of fluid flow features and depths of a sedimentary basin. Chapter 4 investigated pockmarks and blowout pipes (Cartwright et al., 2007) from a sedimentary basement at a depth of 3-4 km. For comparison, Chapter 5 investigated pockmarks and mud volcanoes at the sea floor. Chapter 6 aimed to analyse a different type of blowout feature, hydrothermal vent complexes, at a medium-basin depth of 0.5-1 km below the sea floor, where magmatic material was sourced from deeper crustal levels. Results from three different depth zones allow for the comparison of geometry and seismic character of fluid flow features across the three datasets and with literature from other sedimentary basins.

Outputs from the Seabed Mapping Toolbox provided substantial morphological data which may offer crucial insights on how the depressions formed (Gafeira et al., 2018). The studies in this thesis also add to a database of morphological data. The density, width and vertical relief of pockmarks, mud volcanoes and hydrothermal vent complexes from this thesis and pockmarks from 20 other studies in the literature are summarised in Table 7.1, referencing the age of fluid flow features and resolution of the data. Andresen et al. (2008) summarised the width and vertical relief from literature up to 2006; the table presented here is an extension and update of their work. From Table 7.1, it is apparent that as the size of pockmarks increases, density decreases. Where there are metre-scale pockmarks the density can be as high as 800 / km^2 (Gafeira et al., 2018), whilst large pockmarks such as those in Chapter 4 of this thesis are sparse, as low as 1 or 2 per km^2. This is partly controlled by the size of the pockmarks and

partly by the 'pockmark drainage cell', i.e. the area supplying a pockmark or drained during the formation of a pockmark (Moss et al., 2012).

Fig. 7.3 summarises graphically the ranges of width and vertical relief of fluid flow features in Table 7.1, also distinguishing between those that are buried (dashed lines) and recent (solid lines). The plot shows a similar distribution to that of Pilcher and Argent (2007) which covers literature from before 2006 (Fig. 7.4), whilst Fig. 7.3 shows data from 2006 to the present day. The results from this thesis are represented in colour. From Fig. 7.3, it is apparent that features ranging in scale between three (3) orders of magnitude are mappable in a given study area, whilst pockmarks are recorded across four (4) orders of magnitude, from decimetre-scale to over 1 km in width. The pockmarks analysed in this thesis are comparable in size with the literature, whilst some pockmarks in Chapter 4 have sizes greater than what is recorded in the published literature, adding to the published morphological database of large pockmarks.
Many in-depth studies of pockmarks use multibeam echosounder data with resolutions of up to centimetre to decimetre scale to map the sea floor (e.g. Moss et al., 2012; Szpak et al., 2015). It is possible that, when buried, pockmarks (generally) smaller than 10 m cannot be resolved by seismic data, despite being present. As the quality and resolution of 3D seismic data improve, more recent and buried pockmark arrays are being discovered, showing important fluid leakage events in time.

Area and vertical relief are plotted for the different fluid flow features across the three datasets in Fig. 7.5. The logarithmic plot shows a slight overlap in the sizes of the buried versus recent pockmarks and mud volcanoes, whilst the buried HTVCs and buried pockmarks appear to overlap more. The similarity in sizes of these different features may be owing to the similarity in physical processes during their formation, as all three features result from a build-up of pore-fluid overpressure due to gas and, or fluid accumulation, resulting in breaching of the overburden and vertically-focused fluid escape. These physical processes will be discussed further in Section 7.5.

The morphological results from this thesis can also be compared to graphical representations in Gafeira et al. (2018) (Fig. 7.6). Overall, the size distribution of the features in the three studies combined resemble a trend similar to the North Sea dataset in Fig. 7.6a, where the range in vertical relief is small for a large range in area, and the dispersion of data increases with size. However, the data in Fig. 7.6a occur across such a small scale compared with this thesis, so Fig. 7.6c shows a close-up of Fig. 7.6b at the same scale as Fig. 7.6a.

Table 7.1. Table summarising the ranges of density, width and vertical relief of focused fluid flow features, mainly pockmarks of the first documented pockmarks by King and MacLean (1970), and from 2006 onwards, as older pockmarks are already represen (2007). Morphology of the features in this table are represented graphically in Fig. 7.3.

Number	Articles	Density /km^2	Width (m)	Vertical Relief (m)	Age	Data and Resolution
1	King and MacLean (1970)	45 - 200	15 – 45	5 – 10	Recent	Sidescan sonar. Horizontal resolution = 0.5 m Frequency = 48 kHz
2	Gay et al. (2006)	Uneven, linear clusters	100 – 300	few – 20	Recent	3D Seismic Bin spacing = 12.5 m
3	Pilcher and Argent (2007)	0.15 – 1.4	200 – 1500	20 – 150	Recent	3D Seismic Bin spacing = 12.5 m
4	Andresen et al. (2008)	n/a	Few 100's	7 – 70 Average = 30	Oligo-Miocene	3D Seismic Frequency 10 – 80 Hz, Dominant f = 45 Hz Bin spacing = 12.5 m Horizontal resolution 20 – 30 m Vertical resolution 10 – 15 m in Miocene
5	Hustoft et al. (2009)	n/a	200 – 600	Up to 10 m (Vogt et al., 1994)	Recent	Swath bathymetric data Bin size = 50 m

6	Moss and Cartwright (2010)	1 – 7, average = 2	50 – 600 (pipe width)	3 – 25	Neogene	3D Seismic Bin spacing = 25 m
7	Reiche et al. (2011)	n/a	80 - 1013	0.9 - 15	Recent	Multibeam Echosounder: Frequency 95 kHz Horizontal resolution = 15 x 15 m cell size
8	Andresen and Huuse (2011)	0.5 – 2	70 – 500	10 – 30	Plio-Pleistocene	3D Seismic Bin spacing = 12.5 m Horizontal resolution = 20 m Vertical resolution = 10 m
9	Betzler et al. (2011)	n/a Slope: 1-70°; 1-25; Up to 40-50; Up to 60-70	<30 – 3000	Up to 180 m	Recent	Multibeam Echosounder: Frequency 70 – 100 kHz Horizontal resolution = 5 m grid Vertical resolution = centimetre-decimetre scale Multichannel 2D Seismic Bin spacing = 12.5 m Frequency 100 – 120 Hz
10	Sun et al. (2011)	n/a	870 – 3210 Average = 1640	18.1 – 165.2 Average = 96.7	Recent	Multibeam Echosounder Grid size = 100 m Vertical resolution = 1 – 3.3 m

11	Gafeira et al. (2012)	2 – 30	20 – 500	3 – 17 Average = 1.82	Recent	Multibeam Echosounder, x18 datasets Average grid size = 2 m, Range from 1 – 10 m	Witch Ground Graben, UK North Sea	Shallow source, biogenic gas
12	Moss et al. (2012)	100 – 600	5 – 41 Average = 16	0.4 – 0.8 Average = 0.5	Recent	Multibeam Echosounder Frequency = 200 kHz Bin size = 3 m 2D High resolution Seismic Bin size = 6.25 m Vertical resolution < 5 m Chirp profiler Frequency 2- 10 kHz Vertical resolution 0.15 m	Rosetta Region, Eastern Slope, Western Nile Deep Sea Fan: Mediterranean	Dip slopes >6 degrees. Biogenic / thermogenic gas source
13	Anka et al. (2014)	n/a	200 – 1400 Pockmarks 750 – 1000 Volcanic mounds	15 – 150 Pockmarks 50 – 150 Volcanic mounds	Recent	2D Seismic and 8 wells Resolution unknown	Colorado Basin, offshore Argentina, South Atlantic margin	Pockmarks and mounds of volcanic origin are present. Thermogenic gas source
14	Masoumi et al. (2014)	n/a	50 – 580	Average = 10	Late Cretaceous	3D Seismic Bin spacing = 25 m Few meters detectability	Danish North Sea	Buried, elongated due to bottom currents. Biogenic / thermogenic source. Pockmarks are buried 1-1.5 km below the seabed
15	Rise, et al. (2014)	150 – 200	20 – 50	2 – 5	Recent	Sidescan sonar Frequencies of 50 kHz and 100 kHz	Southwest Barents Sea, north of Norway	Pockmarks from dissociated gas hydrates
16	Rise et al. (2014)	300 – 600	10 – 40	1.5 – 4	Recent	Multibeam Echosounder Gridding = 5 x 10 m	Finnmark Fjords, north of Norway	Pockmarks from dissociated gas hydrates

17	Brothers et al. (2014)	1 - 15	50 - 500	5 - 15	Recent	Multibeam Echosounder Gridding =10 m, 25 m, 50 m, 100 m depending on area	US East Coast Atlantic margin: Hudson Apron/southern New England	Dissociation of gas hydrates and compaction induced pore fluid overpressure release
18	Szpak et al. (2015)	n/a	5 – 17	0.2 – 0.8	Recent	Multibeam Echosounder Frequency = 240 kHz Gridding = 1 x 1 m	Dunmanus Bay, Ireland	Micropockmarks. Biogenic gas source
19	Gafeira et al. (2018)	300 – 800	25 - 220	0.5 – 7 Average = 2.2	Recent	Multibeam Echosounder Gridding = 5 x 5 m	Barents Sea, north of Norway	Pockmarks from dissociated gas hydrates
20	Gafeira et al. (2018)	n/a	50 – 785 Average = 124	0.2 – 5.5 Average = 0.36	Recent	Multibeam Echosounder Frequencies 93 – 98 kHz Gridding = 5 x 5 m Vertical Resolution 0.4 m	Malin Basin, Ireland	Biogenic gas source
21	Picard et al. (2018)	Up to > 700; Most common: 25 – 200	10 – 30	0.5 – 2	Recent	Multibeam Echosounder Horizontal resolution = 1 m	NW Australian Shelf	Biogenic gas source
22	Strozyk et al. (2018)	0 – 2	300 – 850	10 – 50	Early Cretaceous	3D Seismic Bin spacing = 25 m Vertical resolution = 15 – 20 m at the base Chalk horizon	Lower Saxony Basin, onshore Netherlands	Pipes cut across salt welds; sourced by thermogenic gases. Pockmarks occur 1-1.5 km below ground level
23	Tasianas et al. (2018)	n/a (elliptical pockmarks) 600 – 700 (unit pockmarks)	Up to 300 3 – 20	Up to 12 Up to 1	Recent	3D Seismic Frequency bandwidth 50 – 300 Hz Bin spacing = 6.25 m Vertical resolution = 1.5 m Multibeam Echosounder Frequency = 30 kHz Gridding = 5 x 5 m	Snøvit Area, Hammerfest Basin, southwest Barents Sea, north of Norway	Thermogenic and biogenic gas sources; dissociation of gas hydrates

24	Böttner et al. (2019)	1 - 25	26 - 140	0.9 – 3.1	Recent	2D Seismic Horizontal bins = 1.5625 m Vertical resolution = 6-7 m 3D Seismic Horizontal bins = 12.5 m Vertical resolution = 20 m Multibeam Echosounder Gridding = 5 x 5 m	Witch Ground Graben	Related to compaction and dewatering.
25	Chapter 4 of this thesis	0 – 2	225 – 842 Median = 452	14 – 178 Median = 50	Early Cretaceous	3D Seismic Bin spacing = 50 m Vertical resolution = 50 m at depth of interest	Jæren High, Norwegian Central North Sea	Buried pipes cut across salt welds; 2.5 – 3 km below the seabed
26	Chapter 5 of this thesis	0 – 15 Pockmarks	20 – 400 Pockmarks Median = 80	1 – 41 Pockmarks Median = 7.7	Recent	3D Seismic x2 datasets 1) Bin spacing 20 x 25 m Dominant Frequency = 50 Hz Vertical resolution = 8 m at the sea floor, limit of detectability = 1 m	East Breaks, northern Gulf of Mexico, USA	Pockmarks and mud volcanoes; thermogenic fluids
		0 – 2 Mud volcanoes	135 – 725 Mud volcanoes Median = 306	2 – 55 Mud volcanoes Median = 9.8		2) Bin spacing 100 x 100 ft (30.5 x 30.5 m) Dominant Frequency = 35 Hz Vertical resolution = 11 m at the sea floor, limit of detectability = 1.3 m		
27	Chapter 6 of this thesis	0 – 1.4	300 – 3100 Median = 706	30 – 428 Median = 134	Paleo-Eocene	3D Seismic Bin spacing = 12.5 m Vertical resolution = 17 m at depths of HTVCs, up to 36 m at depths of amplitude flags	Modgunn Arch, mid-Norwegian Margin	Hydrothermal vent complexes 0.5 – 1 km below the seabed

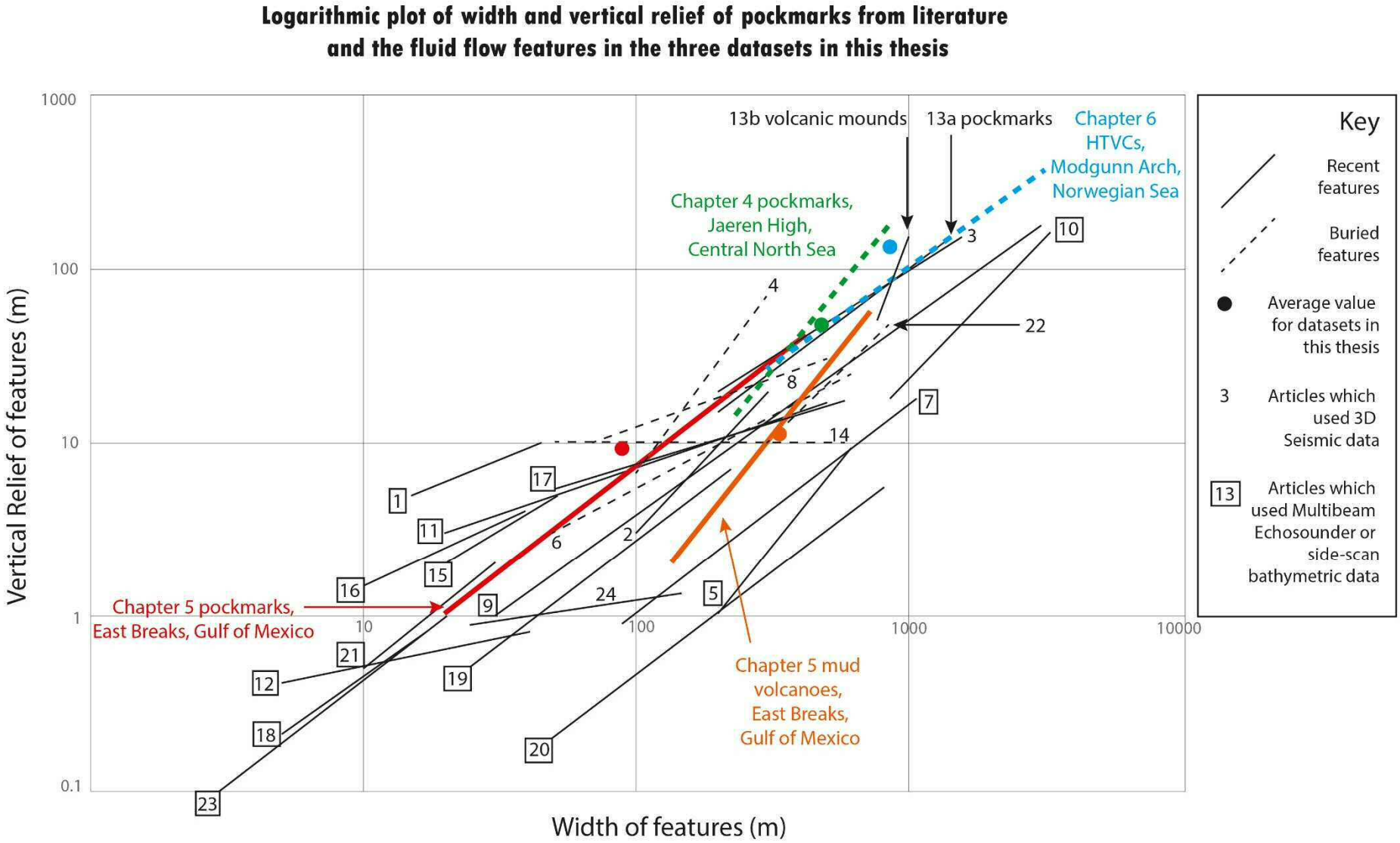

Fig. 7.3. Logarithmic plot showing the ranges of width vs. vertical relief of recent and buried pockmarks in the literature. The results from the datasets used in this thesis have been added in colour, with a point for the average values. Lines are labelled by paper in Table 7.1 and the lines drawn connect the minimum to maximum points for each paper. Paper numbers in boxes used multibeam echosounder or side-scan bathymetric data, whilst those not in boxes used 3D Seismic data. Dashed lines indicate buried features whilst solid lines are recent features. CNS = Central North Sea; GOM = Gulf of Mexico; HTVCs = Hydrothermal vent complexes.

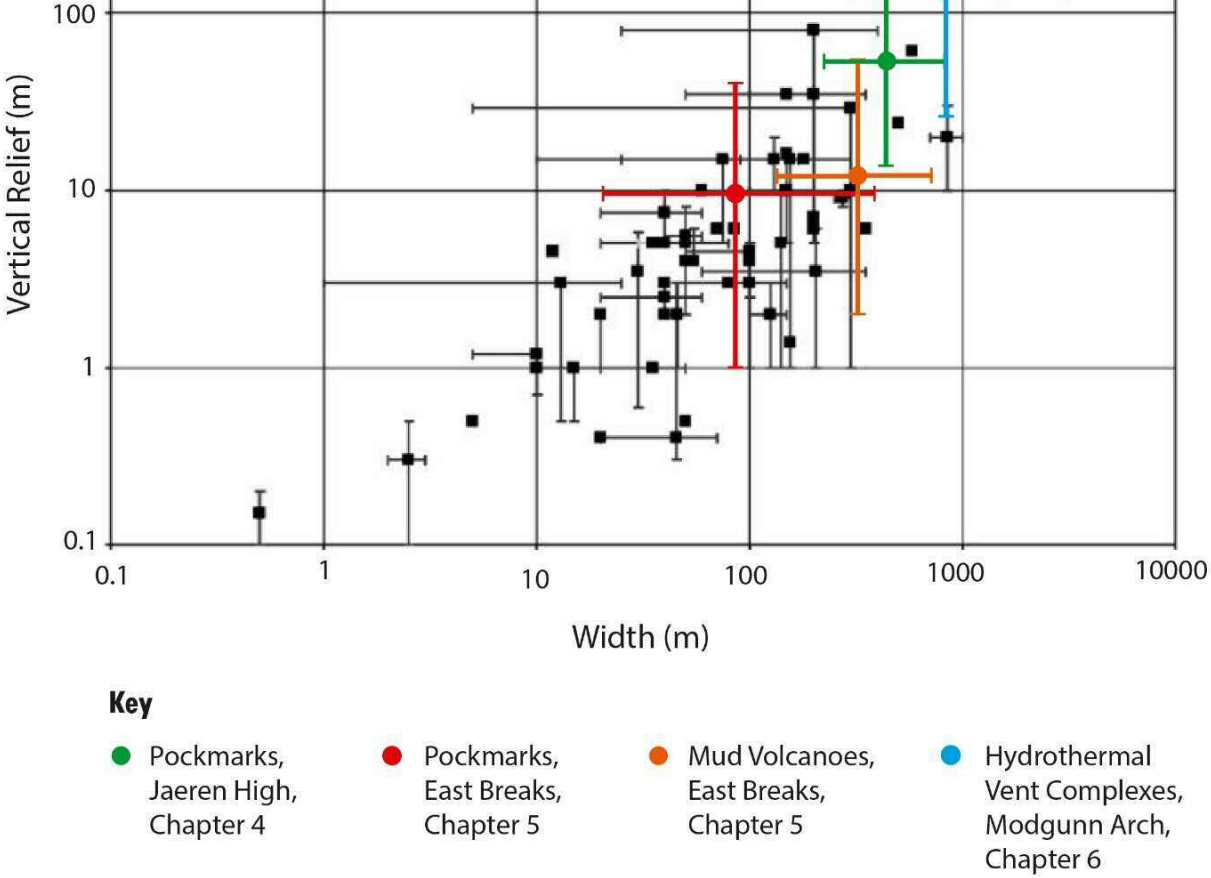

Fig. 7.4. Logarithmic graph displaying the ranges in size of 57 published occurrences of pockmarks from around the world, from 1982 to 2007. Single points represent single measurements or the average measurements, whilst error bars represent the ranges of sizes in a given pockmark field. Size ranges of the fluid flow features in this thesis are added in colour for comparison. Modified after Pilcher and Argent (2007).

is easily excavated in the fluid escape process. Subsequent pockmark venting will also act to sustain or even expand the size of the pockmark, whilst inactive pockmarks with unstable edges may experience erosion and side-wall collapse, increasing the area whilst decreasing the vertical relief of the pockmarks.

Another important detail is that the shapes of seafloor depressions are typically adjusted by bottom-water currents and scouring (Andresen et al., 2008; Picard et al., 2018), erosion and slumping of the sidewalls of the depressions and deposition (Betzler et al., 2011; Masoumi et al., 2014). It is apparent that pockmarks in the Gulf of Mexico found within fault scarps are elongated, with width to length ratios as low as 0.3, and a median value of 0.78 (Fig. 5.17). In contrast, the minimum width to length ratio of those pockmarks in the Central North Sea was 0.62 and their median value was 0.89, indicating these are more circular than elongate (Table 4.4). Seabed 'corridors' formed by fault scarps may funnel bottom-water currents, which erode and elongate the pockmarks in directions that are parallel to the strike of the fault. In contrast, those pockmarks which formed across salt welds in the Central North Sea have not exhibited this style of morphological adjustment.

Infill of pockmarks and compaction during burial is expected to decrease the slope angles of the pockmarks, which may explain the reduction in maximum slope from the seafloor pockmarks in the East Breaks dataset to the buried pockmarks in the Jæren High dataset (Fig. 7.7). Andresen et al. (2008) and Masoumi et al. (2014) analysed the morphological profile of pockmarks in terms of being more V- or U-shaped. They found that active or very recent pockmarks exhibited more V-shaped profiles, whilst inactive or older pockmarks that had experienced erosion, slumping and infill exhibited U-shaped profiles. In addition, 60% of the pockmarks interpreted by Masoumi et al. (2014) – buried at least 1 km below the seabed – were U-shaped. This suggests that buried pockmarks will appear more U-shaped than recent

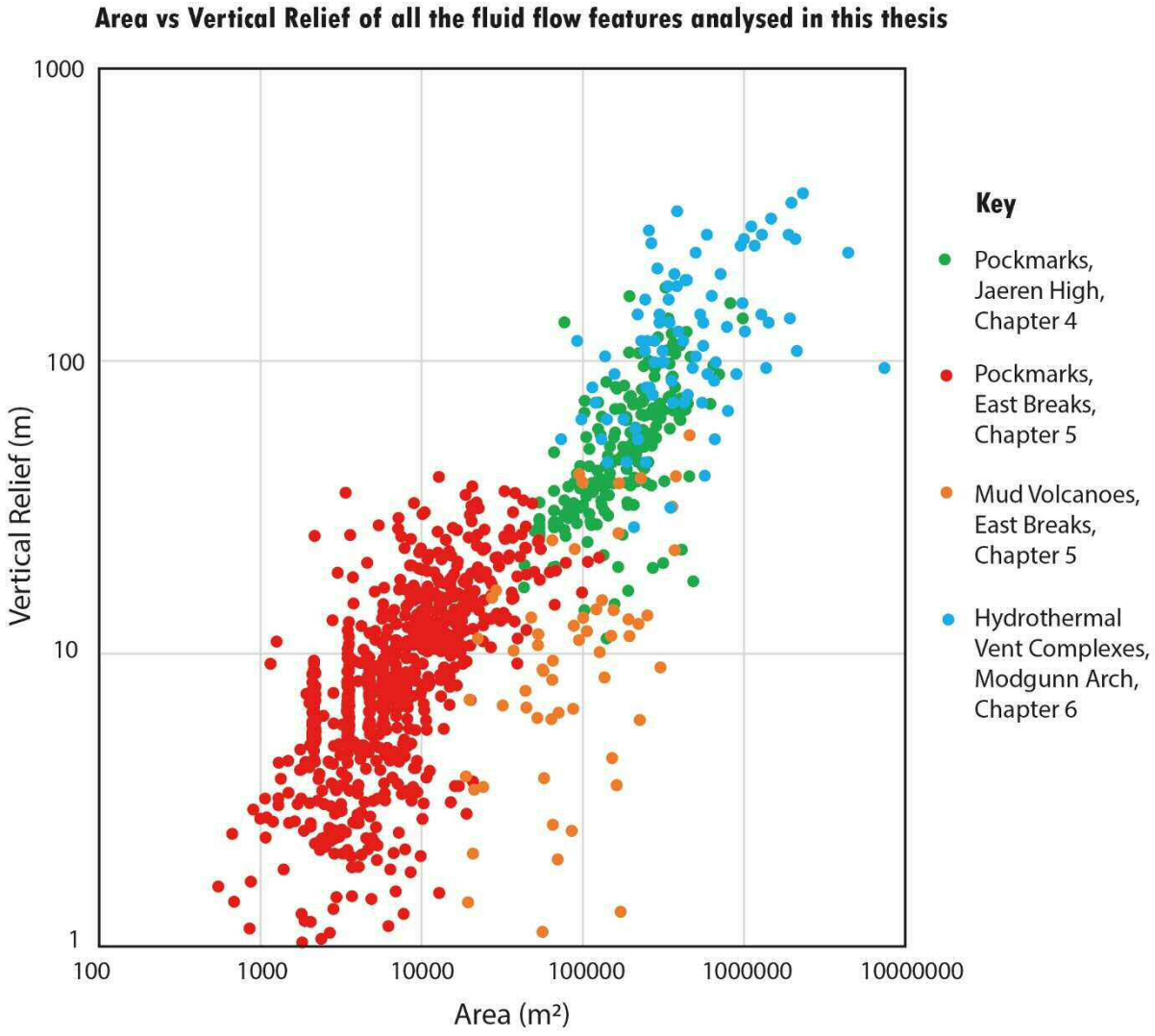

Fig. 7.5. Logarithmic cross-plot of the area (x) and vertical relief (y) of the fluid flow features in this thesis, colour-coded by dataset.

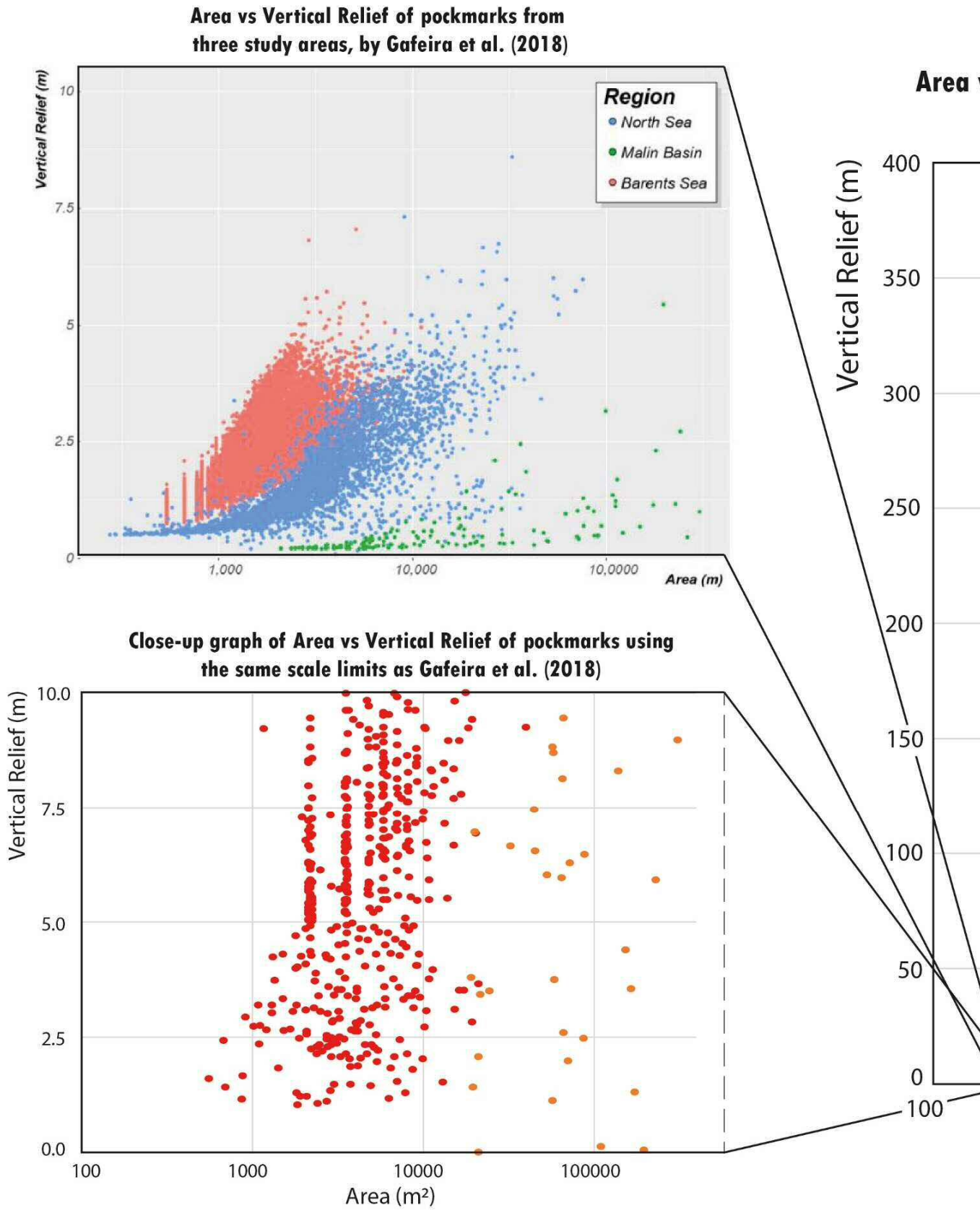

Fig. 7.6. Vertical relief as a function of area, comparing pockmarks mapped in: a) three study areas from Gafeira et al. (2018
al. (2018) were mapped from Multibeam Echosounder data, whilst the fluid flow features in this thesis were all extracted fro
The difference in scale of features is clear, whilst the trend is similar on a large scale, with area increasing logarithmically as

pockmarks, although the comparison between the pockmarks at East Breaks and the Jæren High appears to show the opposite (Fig. 7.8). The recent pockmarks have higher profile indicators and are therefore more U-shaped than the buried pockmarks. This may be a reflection of the elongation, erosion and slumping processes which have occurred at East Breaks, compared to the relatively undeformed buried features on the Jæren High.

The way that buried pockmarks and associated pipes appear in seismic data will also depend on the data resolution at their depths, and if there are seismic artefacts such as velocity pull-ups due to higher velocity methane-derived authigenic carbonates (MDAC) in the pockmarks, or velocity push-downs due to later-stage gas accumulations within sediment immediately above the pockmarks (Ho et al., 2012; Moss and Cartwright, 2010).

The style of the blow-out event and subsequent fluid flow will additionally impact the morphology of the fluid flow features as they are buried. A single blow-out event which removes sediment from the seabed, will leave a crater subject to erosion and infill, as described above. This was also seen in the crater-shaped hydrothermal vent complexes (HTVCs) in Chapter 6. If low level fluid flux occurs immediately after the main event or during burial, the pore-fluid pressure in the sediment infilling the crater may be raised, limiting compaction. This results in differential compaction across the feature to form eye-shaped HTVCs (Planke et al., 2005). Subsequent fluid flow may also sustain the pipe as an open fluid leakage pathway, or one that is prone to reactivation.

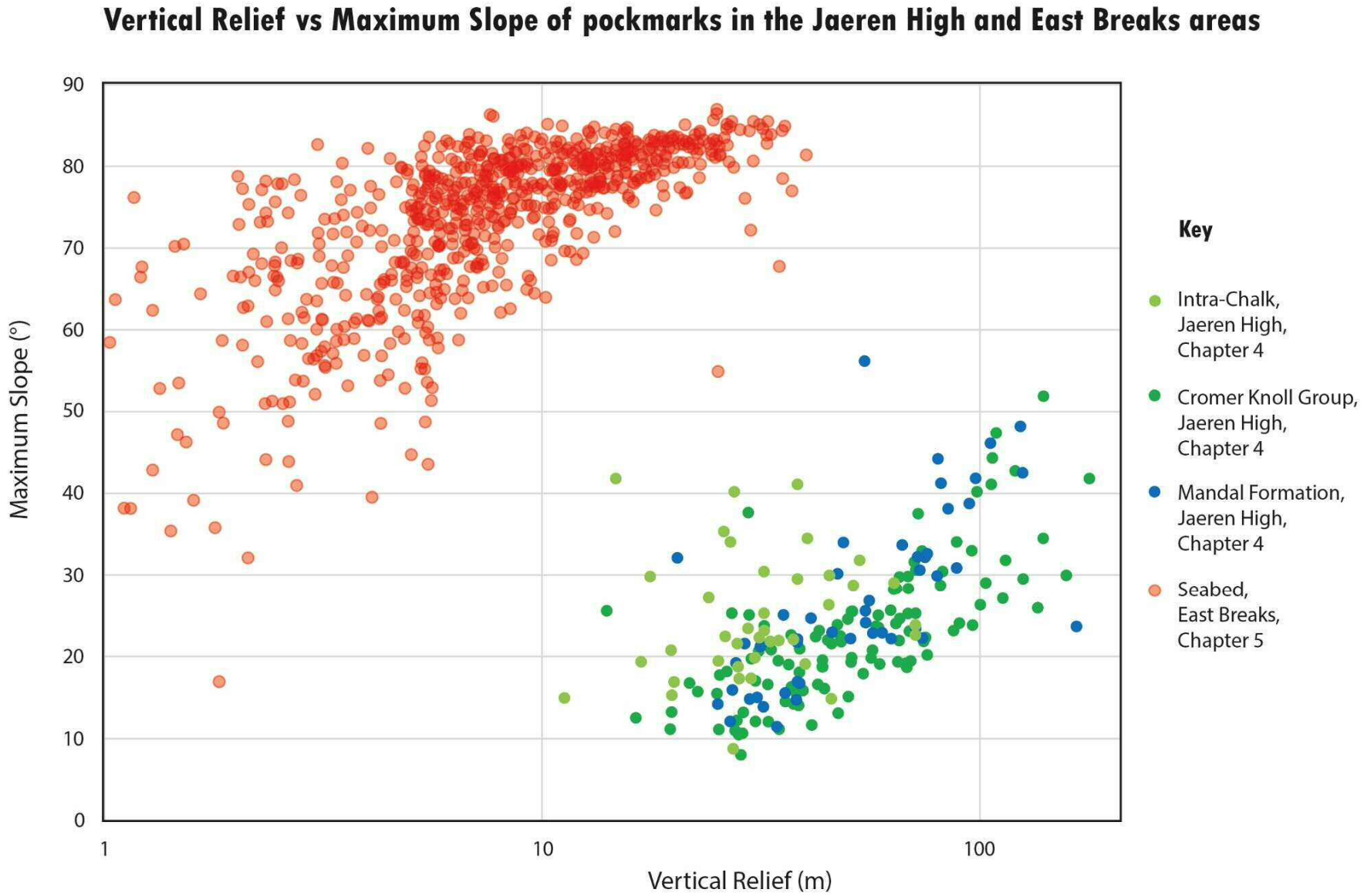

Fig. 7.7. Scatter plot of vertical relief (x) and maximum slope (y) of the buried pockmarks in Chapter 4, coloured by horizon, in the Central North Sea (CNS); and the recent pockmarks in Chapter 5, Gulf of Mexico (GOM). The datasets occupy two distinct clusters on the graph. The recent pockmarks have generally smaller vertical relief but greater maximum slope, whilst the buried pockmarks are generally larger in size but have smaller maximum slope.

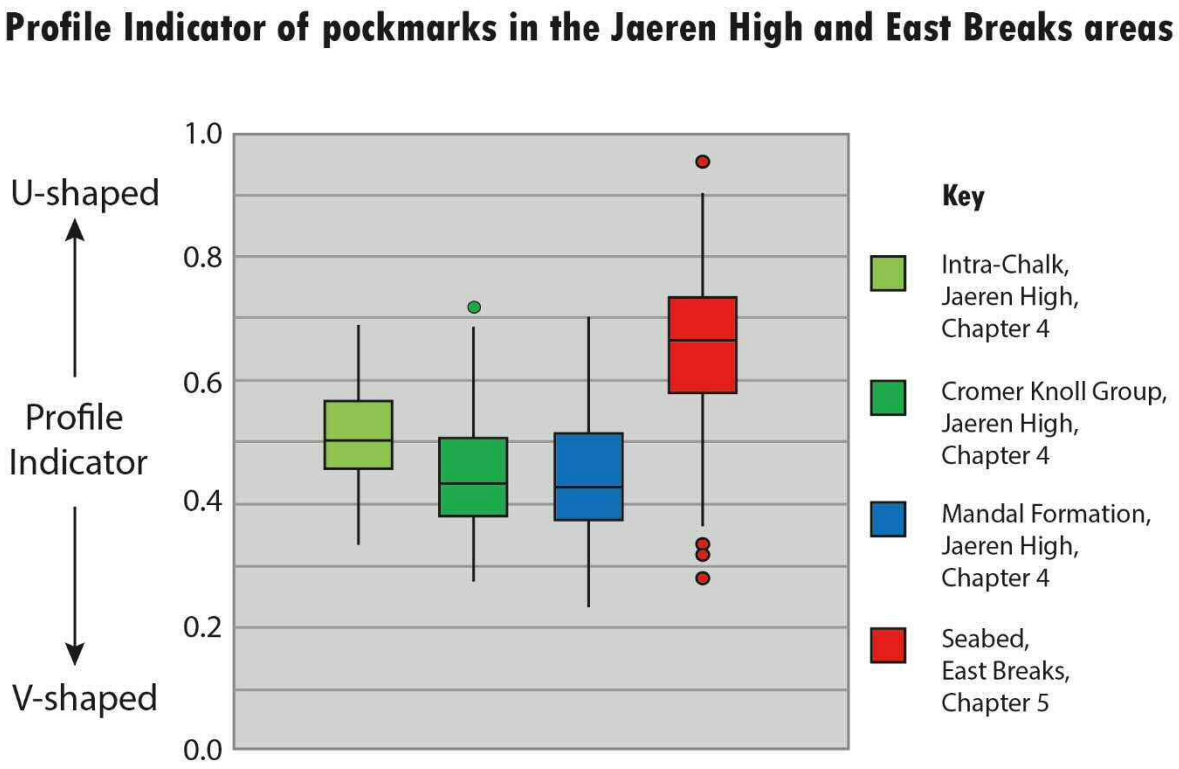

Fig. 7.8. Box plots showing the range of profile indicators for buried pockmarks in the three horizons on the Jæren High (Intra-Chalk, Cromer Knoll Group, Mandal Formation) and for recent pockmarks at East Breaks, Gulf of Mexico.

7.4.2 Seismic data parameters, resolution, and visualising fluid flow features at different depths of investigation

Visualisation of fluid flow features in seismic data is dependent on the parameters used during acquisition, processing and stacking of a seismic dataset.

During acquisition, the frequency of the input acoustic energy is set to resolve features at certain depth ranges. High-frequency waves have shorter wavelengths and shallow depth of penetration, whilst low frequency waves have longer wavelengths and deeper depth of penetration into the subsurface; therefore resolution decreases with depth (Kearey et al., 2002). When acquiring seismic for imaging deeper basin-crustal structures, lower frequency waves may be used and consequentially, smaller scale features both in the shallow and deep subsurface are not resolved. In addition, even if a large frequency spectrum is used during seismic-data acquisition, high frequencies may be filtered out during the processing sequence to improve the signal-to-noise (SN) ratio of the deeper subsurface, exasperating the problem further. If the area of interest is more likely to be shallow, higher frequencies are used. An extreme example of this is data from 'Pingers', where frequencies of 3-12 kHz are used and acoustic data is produced at vertical resolutions as high as 10-20 cm, but the depth of penetration is only a few tens of metres (Kearey et al., 2002). Pinger data are useful and important when assessing seafloor stability and shallow gas hazards for placing seabed infrastructure and drilling. For this reason, seabed surveys (side-scan sonar and multibeam echosounder data) play an important role in exploration and are often done separately, whilst larger scale 3D seismic surveys focus on deeper imaging.

As data resolution decreases with depth, the ability to image fluid flow features decreases. Schofield et al. (2017) discussed imaging sills in the Faroe-Shetland Basin and showed that 88% of the sills penetrated by 19 wells were under 40 m, the resolution limit of the seismic data in that study. It is therefore imaginable that a large proportion of pipes and pockmarks are commonly well below seismic resolution, which is an important consideration in hydrocarbon exploration and when assessing fluid leakage pathways. In practice, it is not possible to identify all the specific leakage locations, but predictions can still be made based on the presence of those fluid flow features that are imaged. Many studies of pockmarks and pipes are based on analyses of the upper 0-2 km of strata in sedimentary basins, where resolution can be close to or even below 10 m near the sea floor (e.g. Andresen et al., 2008; Andresen et al., 2011). Present day pockmarks can even be studied to a sub-metre scale with side-scan sonar and bathymetry maps (Dimitrov and Woodside, 2003), whereas in Chapter 4 the horizontal

resolution at 2.5 to 4 km depth on the Jæren High is 50 m - only features greater than 50 m width are imaged in the interpreted seismic volume. Notwithstanding these facts, the width of the smallest features mapped was 225 m and the majority had widths greater than 300 m, so it may be the case that only large-scale features occur in that study area.

In Chapter 5, it was apparent that a pockmark can be present without an underlying pipe being imaged in seismic data. The internal geometry of a pipe is typically made of seismic artefacts – these artefacts at the pipe boundary do not extend through the interior of the pipe if the width of the pipe is larger than the dominating seismic wavelength (Løseth et al., 2011). Therefore, when a pipe below a pockmark is barely imaged, it is likely that the pipe is very narrow. Alternatively, the pipe has 'healed' such that the fluid expulsion did not permanently affect the strata across which the fluid migrated (Andresen, 2012). Furthermore, in Chapter 4, it was shown that salt welds provide the 'windows' for fluids to escape across the Zechstein salt, and these are difficult to image. As well as resolving fluid flow features, salt welds are also difficult to image. Salt becomes immobile when the thickness decreases and boundary drag forces become too great, therefore the only way to remove the remaining salt is through dissolution (Wagner and Jackson, 2011). In Chapter 4, the vertical resolution limit is 50 m at the depth of the salt, and there may still be up to 50 m of salt at some of the 'welds'. Thin salt sequences can still act as seals, depending on the remnant salt thickness at the weld (Wagner and Jackson, 2011), thereby complicating matters further and should be taken into consideration when interpreting salt welds and their sealing capability.

Løseth et al. (2011) modelled the acoustic response of a 1000 m blow-out gas pipe of 50 m width, to postulate the seismic imaging of a pipe seen at outcrop in Rhodes, Greece (Fig. 7.9). The material inside the pipe was assumed to be structureless and varied with changing acoustic impedances relative to the strata outside of the pipe. This modelling showed that the pipe is imaged but only as a disruption of the surrounding layered sequence. When the width of the pipe is much less than the wavelength of the seismic waves, the diffraction points on each side of the pipe merge and appear as an apparent reflector within the pipe, such as Fig. 7.9f. In contrast, Fig. 7.9h does not show any apparent internal reflectors where the width of the pipe is greater than the seismic wavelength (Løseth et al., 2011). Furthermore, where the acoustic impedance contrast between the material inside and outside the pipe is small, there are no artefacts below the pipe, whereas where the contrast is large, there are high-amplitude anomalies (Fig. 7.9a,b). These anomalies may help to determine the source or 'root zone' of the pipe, the depth of which can be difficult to predict.

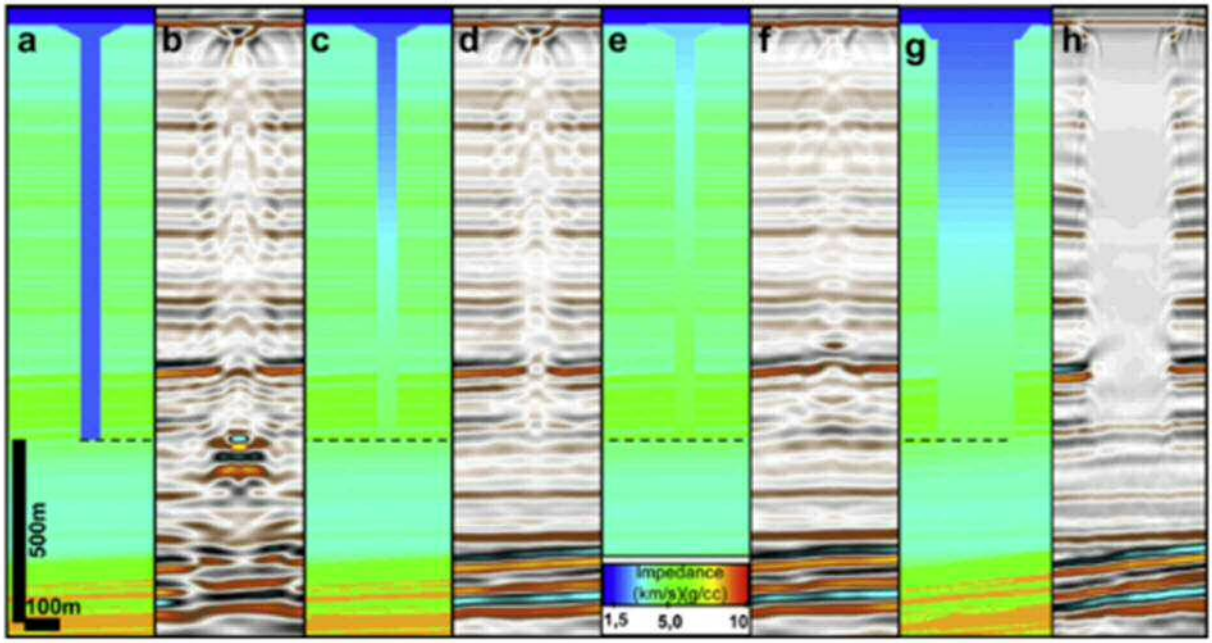

Fig. 7.9. Parts a), c) and e) show parts of a layered acoustic model from Johansen et al. (2007) with a 50 m wide (150 m at seafloor) and 1 km deep pipe comprising structureless material. The acoustic impedance in the material inside the pipe is constant in a), gradually increasing to depth in c), e), and g). Synthetic seismic data models a), c) and e) are shown in b), d) and f), respectively. The pipe is clearly visible as a disruption of the surrounding layered sequence on the seismic data in all models. There is a significant change in expression of the lower part of the intra-pipe reflections from d) and f) where the acoustic impedance is slightly lower and higher than the surrounding layered material. For g) and h), a 500 m wide pipe was modelled to show that the artefacts at the pipe boundary do not extend throughout the interior of the pipe if the width of the pipe is larger than the dominating seismic wavelength. Figure from Løseth et al. (2011).

Cartwright and Santamarina (2015) noted that the 'root zones' or base of pipes are often difficult to image or interpret, as scattering and attenuation of acoustic energy and poorly migrated diffraction 'tails' may reduce the signal to noise ratio. Furthermore, pipes may be sourced from or 'rooted' in a single horizon or structure, or from a wider zone comprising several seismic reflections and depths. Where clear underlying structures are present pipes are likely to be sourced from these, such as in the East Breaks data (Chapter 5) where 96% of the pockmarks are located above a structure such as faults and salt diapirs. In the same area, however, the depth of source for the mud volcanoes was less clear and a minimum value was interpreted. In parallel, seismic chimneys were only found to be present below the areas identified by the BOEM to actively be leaking gas, as well as below mud volcanoes. Scattering of acoustic energy typically occurs due to small gas saturations in largely impermeable strata such as shales which, when distributed over a large area, are imaged as seismic chimneys or gas clouds (Baristeas et al., 2012; Judd and Hovland, 2007).

With reference to the modelling by Løseth et al. (2011) and interpretations, the pipes in Chapter 4 may be akin to those in Fig. 7.9a, b, or Fig. 7.9c, d, whilst those in Chapter 5 are likely to be similar to those in Fig. 7.9e, f. Even though the pipes in Chapter 4 are expected to be greater in diameter than in Chapter 5, the seismic wavelength at the depth of the pipes in Chapter 4 is greater than the shallowest pipes considered in Chapter 5. In contrast, the hydrothermal vent complexes in Chapter 6 are one to two orders of magnitude greater in size than the pockmarks in Chapters 4 and 5. For this reason, the seismic characteristics of the infilling material within the eyes, domes or craters are well imaged and not considered to be artefacts, although the narrow, vertical conduits resemble the buried pipes seen in Chapter 4.

7.4.3 Imaging amplitude anomalies

Much of the interpretation in this thesis involved the detailed spatial analyses of high-amplitude anomalies and flags, which are typically attributed to fluid flow (Andresen et al., 2011; Cartwright, 2007). High-amplitude anomalies are a result of local changes in the acoustic properties of a unit, which may be due to changes in lithology, porosity, cementation, fluid type and presence of fluids (Harilal and Biswal, 2010). Lithological explanations for amplitude anomalies have been discussed in each of the results chapters. Additional considerations for interpreting amplitude anomalies are discussed below.

When a seismic dataset has been processed, the range of amplitudes present can be displayed on a histogram, which often shows a normal distribution. The lowest amplitudes are typically associated with noise whilst the highest amplitudes can be important hydrocarbon

indicators (Brown, 2011; Kidd, 2014). During the data loading process, the amplitudes are often binned, which reduces the dynamic range (the centre of the bell curve). If the dynamic range of the data of interest becomes too narrow, subtle changes are difficult to recognize, thus the lowest and highest amplitudes are clipped to increase the dynamic range and improve structural interpretation – although this reduces the accuracy of interpreting bright spots (Brown, 2011; Gao, 2009; Henry, 2004; Kidd, 2014). None of the datasets used in this thesis have been clipped, but this should be taken into account when interpreting amplitude anomalies.

Local high-amplitude anomalies can occur in seismic data due to tuning effects – when two reflections approach each other such as in the case of onlap or lateral thinning of strata, constructive or destructive interference of the wavelets of two seismic reflectors can occur, causing brightening or dimming of seismic amplitudes, respectively (Andresen et al., 2011; Henry, 2004). For example, Eide et al. (2018) illustrated in a model how the amplitude of a discontinuous reflector changes with wedge thickness, for a dolerite 'wedge' and a mudstone 'wedge' (Fig. 7.10). As the wedge narrows and tuning thickness is reached, the amplitude of the reflections increases due to constructive interference of the wavelets. The amplitude decreases as the wedge thins to the limit of detectability. These tuning effects may be misinterpreted as fluid flow features. Nevertheless, effects of tuning were taken into consideration when interpreting amplitude anomalies in the datasets used by critically analysing the seismic reflections either side of the amplitude anomaly.

The acoustic impedance of sedimentary rocks containing different fluid types will change with depth. The question that follows is can the polarity of amplitude anomalies be used to interpret fluids in depths of 2.5-4 km, as in Chapter 4, in the same way as one would interpret shallow gas anomalies within 1 km of the seabed in Chapter 5? Amplitude versus offset (AVO) analysis is used to interpret whether amplitude anomalies are true indicators of fluids, or due to changes in lithology. Near-stack data usually has higher resolution as is preferred for seismic interpretation, and Andresen et al. (2011) noted that high-amplitude anomalies that also appear in the far-stack volume tend to be stronger because of the higher elastic impedance contrast of gas- and oil-filled shallow sands. The acoustic response of a shale-on-sand boundary changes with depth from a positive to a negative (Fig. 7.11), so the acoustic response of fluids depends on the depth of interest of the features being interpreted.

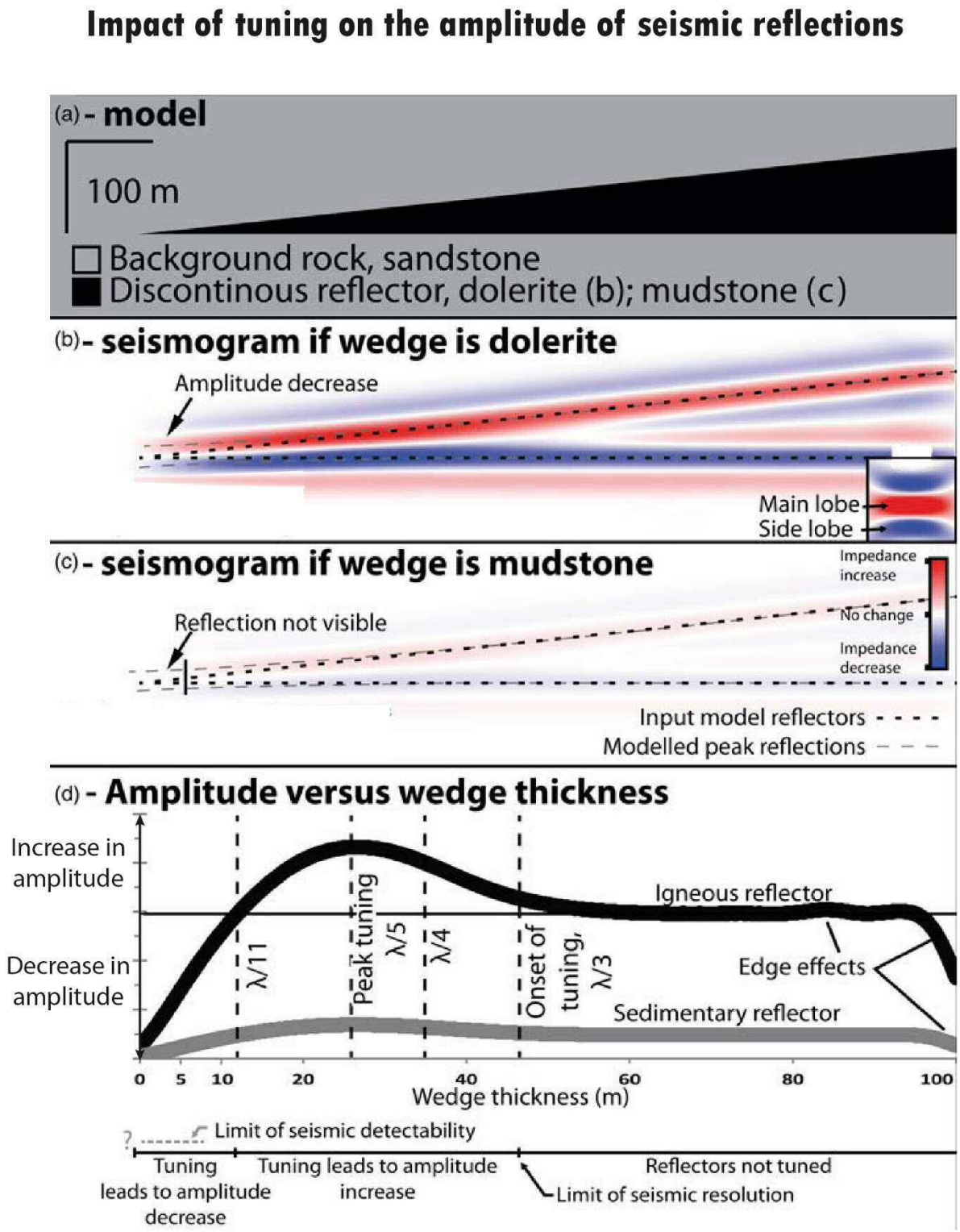

Fig. 7.10. Wedge model showing how the amplitude of seismic reflections change as a discontinuous reflector of dolerite (b) or mudstone (c) thins within background sandstone rock. d) Amplitude changing with wedge thickness, with tuning labelled. Modified after Eide et al. (2018).

As stated in Chapter 4, the high-amplitude anomalies are more likely to be related to cementation, but their abundant presence and variation in polarity was cause for investigation as evidence of palaeo-fluid flow. AVO analysis is only possible on pre-stack data, with separate near-, mid- and far-offset datasets, which was not available for this thesis. Therefore, amplitude anomalies were interpreted cautiously, with the understanding that some amplitude anomalies are likely to be spurious seismic artefacts or a result of other, lithological-based changes in the rock strata.

As discussed in Chapter 5, high-amplitude anomalies can arise from as little as 2% gas saturation; therefore shallow high-amplitude anomalies were not interpreted to indicate gas accumulations, but simply as a way to stress the presence of focused fluid flow in shallow strata (Conn and Arthur, 1990; Judd and Hovland, 1992). Finally, amplitude anomalies may represent fluid accumulation from long-distance migration, or localised changes such as the presence of a marked diagenetic boundary on the Modgunn Arch (Chapter 6). Care was taken not to assume that the high-amplitude anomalies in the Brygge Formation (Fig. 6.2) were due to fluid flow from the depth of the sills, or simply being due to the shallower phase-boundary of Opal A-CT. Therefore, higher amplitude flags were interpreted within 100 ms TWT above the Top Tare Formation as well as a few exceptions, below the level of the Opal A-CT boundary (Fig. 6.10).

To conclude, it is clear that there are several factors which influence the presence of amplitude anomalies in seismic data and these should be considered when interpreting amplitude anomalies. Detailed discussions beyond the scope of this study are provided by Henry (2004) and Harilal and Biswal (2010).

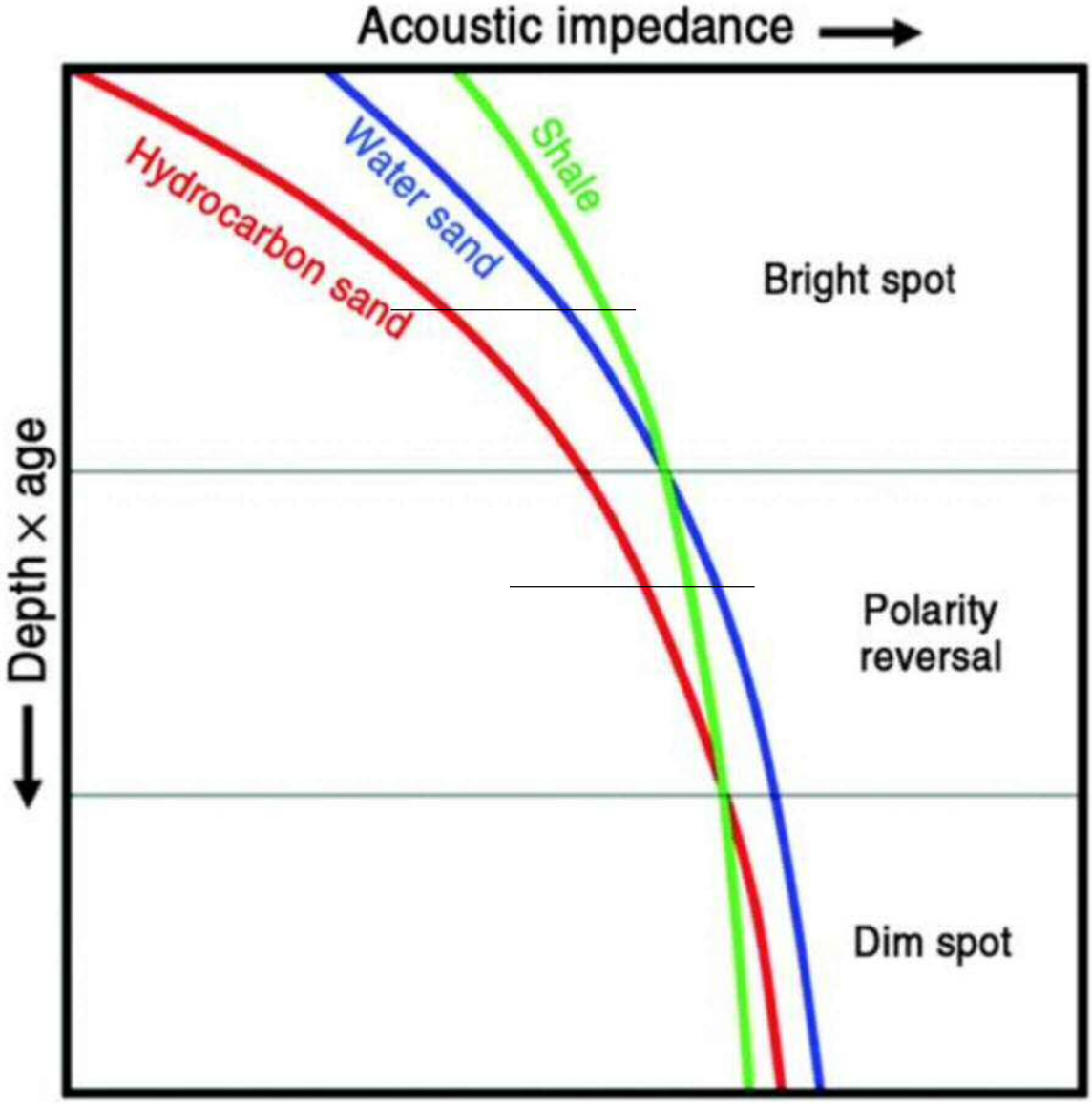

Fig. 7.11. Plot showing the change of acoustic impedance with depth of a shale, water-filled sand and gas-filled sand, and the change in seismic response between the three groups with depth from bright spot to polarity reversal to dim spot. Taken from Brown and Abriel (2014).

7.5 How do the stress states and conditions for overburden failure change after initial fluid pipe formation?

The formation of pipes across low-permeability rocks reduces or limits the degree of overpressure-build-up, especially when the pipe connects to the sea floor (Sibson, 2003). Once the initial pipe and pockmark are formed, low-flux fluid venting may occur along these pathways, as opposed to renewed overpressure build-up and rapid expulsion. This is apparent in the case of the East Breaks data, Gulf of Mexico, where oil and gas are actively leaking (Fig. 5.13). In contrast, examples of stacked palaeo-pockmarks are recorded in the Lower Congo Basin, where after initial formation, the pipes would have sealed sufficiently for pore-pressure in the source region to build-up and the pipes to be reutilised in similar, explosive fluid escape events (Andresen et al., 2011; Andresen and Huuse, 2011).

Two other examples of fluid flow after initial pockmark formation are given in Bertoni et al. (2017) and in Ho et al. (2018). Recent and buried fluid flow features including mud volcanoes, high-amplitude anomalies and pockmarks were identified in the Nile Delta region, ranging in age from ~6 Ma to Recent (Bertoni et al., 2017). Some of the fluids which formed these features crossed thick, Messinian evaporitic sequences, in stark contrast to Chapter 4 of this thesis on the Jæren High, where fluids migrated across salt welds. The range of depths and ages of these features are considered a result of pressure cycling due to changing sea level, as well as continued hydrocarbon migration and rapid loading and burial, leading to renewed overpressure generation through time (Bertoni et al., 2017). The presence of high-amplitude anomalies above pockmarks and close to the sea floor was attributed to generation of biogenic gas and a shallow plumbing system (Bertoni et al., 2017), similar to the high-amplitude anomalies in the salt minibasins of the Gulf of Mexico (Chapter 5). In contrast, the high-amplitude anomalies above HTVCs on the Modgunn Arch were interpreted to indicate fluid seepage across the pre-existing HTVCs (Chapter 6).

Ho et al. (2018) described stacked pockmarks spatially coincident with underlying turbiditic channels, in the Lower Congo Basin offshore Angola. They showed that these vertically stacked pockmarks are laterally shifted, likely due to bottom current activity, and that various intensities of episodic fluid escape followed by periods of quiescence and infill occurred (Ho et al., 2018). In contrast, the pockmarks in Chapter 4 in the Cromer Knoll Group directly overly pockmarks in the Mandal Formation (where present), and the eccentricity values of the pockmarks were low, which led to the interpretation that bottom-current erosion and morphological adaptation were not prevalent on the Jæren High.

Before discussing how blow-out pipes may be reutilised, it is worth reiterating how they are formed in the first place. Section 1.2.2 documents that pipes form when fluids accumulate beneath a seal interval where the overburden (lithostatic) stress is equal to the maximum stress. When the fluids are unable to escape to the surface through a connected pore-network, they are not in hydrostatic equilibrium and the pore-fluid pressure increases; hence, the rock strata of interest are said to be overpressured (Mann and Mackenzie, 1990). Once the pore fluid pressure reaches lithostatic pressure, or a pressure close to it, the overburden will fracture and fluid escapes vertically along a 'fracture-mesh' to the surface (Sibson, 2000; 2003) (Fig. 1.1, Fig. 1.12). Fracture meshes comprise faults interlinked with extensional-shear and extensional vein-fractures, generated by the permeation of pressurised fluids into a stressed heterogeneous rock with varying material properties (Sibson, 1996). Therefore, blow-out pipes and hydrothermal vent conduits are thought to consist of a network of vertical to sub-vertical fractures from the source or root region to the surface or palaeo-surface, as the upward flow of overpressured fluids hydraulically fractured the overburden (Cartwright et al., 2007). For this reason, the mechanics behind reutilisation of fluid flow pathways, namely that of pipes and hydrothermal vent conduits, can be thought of as being analogous to the reactivation of a fracture or fault, in the simplest terms.

Osborne and Swarbrick (1997) noted that the main mechanism building overpressure in subsurface intervals is the increase of compressive stress by high sedimentation rates and rapid burial of fine-grained sediments, such as hemipelagic mudstones. This is particularly seen in the Gulf of Mexico, where several kilometres of marine sediment have been deposited in salt minibasins in the relatively short space of a few million years. It is expected that high overpressures have been reached in these salt minibasins. On the Jæren High, overpressure likely built up from loading and pore fluid pressures that were increased further due to the migration of fluids into a structural trap, such as the tilted Rotliegend Formation that occurs below thick (sealing) mudstones and Zechstein salt. On the Modgunn Arch, although sedimentary loading of thick (>1 km) Cretaceous marls will have increased pore-fluid pressures, the overpressures thus attained to form hydrothermal vent complexes (HTVCs) were due to the intrusion of magma and rapid heating of the surrounding mudstones, producing large volumes of hydrothermal fluids and gases within a relatively confined space (Jamtveit et al., 2004).

Sibson (2003) noted that if pre-existing faults or fractures are in place, especially those suitably oriented for reactivation, lower overpressures are required to reactivate a fault compared with fracturing an undeformed rock. Therefore, the fractures or pipes will be reactivated before new ones are formed. Whilst the orientation of existing fractures is an

important factor for reactivation, Sibson (2017) stated that when the rate of pore-fluid pressure increase exceeds the rate of change in differential stress, fractures of any orientation can be reactivated, for example in regions of intense fluid release such as sills intruding into sediments, as seen on the Modgunn Arch.

The properties of the fault gauge also play a role in controlling whether faults or fractures will be reactivated, such that it was documented in western Texas that the degree of cement fill in natural fractures, rather than fracture orientation, governed fluid flow (Laubach et al., 2004). Several authors have concluded that the tensile strength and cohesion of quartz- and carbonate-cemented fractures in siliciclastic and carbonate host successions (respectively) is greater than the host rock (e.g. Dewhurst and Jones, 2003; Sibson, 1998; Tenthorey et al., 2003; Woodcock et al., 2007). Experiments which investigated the inter-seismic strength recovery of fault rocks at mid-crustal (5-10 km) depths showed that where hydrothermal cementation occurred, the fault rock increased in strength relative to the host rock (Sibson, 2017; Tenthorey et al., 2003). The pipes in the study areas in this thesis occur less than 5 km below the sea floor, but this principal may be applicable, particularly on the Modgunn Arch where hydrothermal venting occurred. In contrast, it is possible that cemented pipes are still weaker than the host rock.

Furness (2016) investigated siderite and calcite-filled fractures in a volcanogenic sandstone in the Otway Ranges, Australia. They interpreted several phases of reactivation: siderite cement veins were cross cut by calcite cement, which exhibited crack-seal textures, indicating repeated fracturing and healing of the fracture (Laubach et al., 2004). They suggested that the contacts between siderite, calcite and the host clastic rock could act as planes of weakness and be favourably reactivated (Laubach et al., 2010; Tassone, 2014). Solum, et al., (2010) also recorded that fault-related authigenic clay along the Moab fault occurs as thin coatings on slip surfaces, which lead to a reduction in the coefficient of friction – therefore the fault is more prone to reactivation. To summarise, if the pipes or fractures within the pipes are cemented, either a) the tensile strength of the pipes increases, particularly if the cement mineralogy is the same as the host rock or if hydrothermal cementation has occurred, or b) the contact boundary between the cement and the host rock may still be a plane of weakness, if there are heterogeneities in the fracture texture and especially if the cement mineralogy differs from the host rock.

Schematic Mohr circles and pressure-depth plots are henceforth used to consider and illustrate the impact of the different depths of basin and structural settings on the formation and reactivation of fluid escape pipes in each study area considered in Chapters 4, 5 and 6. Failure of the overburden due to stress state and pore-fluid pressure can be illustrated on a Mohr Circle

diagram, the basic principles of which are described in section 1.3. In the pressure-depth plots compiled for this thesis, the hydrostatic pressure gradient is considered to be 10 MPa/km and the lithostatic pressure gradient is 23 MPa/km, assuming an average rock density of 2.3 g/cm^3 (Ward et al., 2016; Zoback, 2010).

7.5.1 Reactivation of buried pipes on the Jæren High, Central North Sea

The effects of reintroducing excessive pore fluid pressures to reactivate pipes on the Jæren High is considered in this section. A simplified pressure-depth plot for the Jæren High is shown in Fig. 7.12a. The Cretaceous Chalk in the Central North Sea is known to have poor reservoir properties and act as a regional seal (Swarbrick et al., 2010), therefore formation pressure increases at a greater rate in and below this unit, although it is thinner in the study area compared to the neighbouring graben. Formation pressure continues to increase across the Triassic pods, with large overpressures immediately below, in the Rotliegend Group. Fig. 7.12b shows a simplified example of what the pressure profile could look like if, for example, CO_2 was injected into the Rotliegend Group and fluids were to breach the Triassic pods today and migrate vertically, transferring the overpressure to the Cretaceous Chalk Group. The Cretaceous Chalk is not of reservoir quality in the study area (*7_1_1_Completion_Report*, 1971), and is likely to act as a seal. The well report for well 7/1-1 states that stylolites were seen in the core, which form as a result of chemical compaction by pressure solution (Bjørlykke and Høeg, 1997). These features are cemented with a clay-like material and may be fractured if overpressures increase sufficiently in or below the Chalk, after which fluids may continue to migrate towards the surface. Alternatively, the CO_2 and brines could react with the calcium carbonate in the Chalk Group, dissolving the rock to form karst systems (Masoumi et al., 2014; Palmer, 1991).

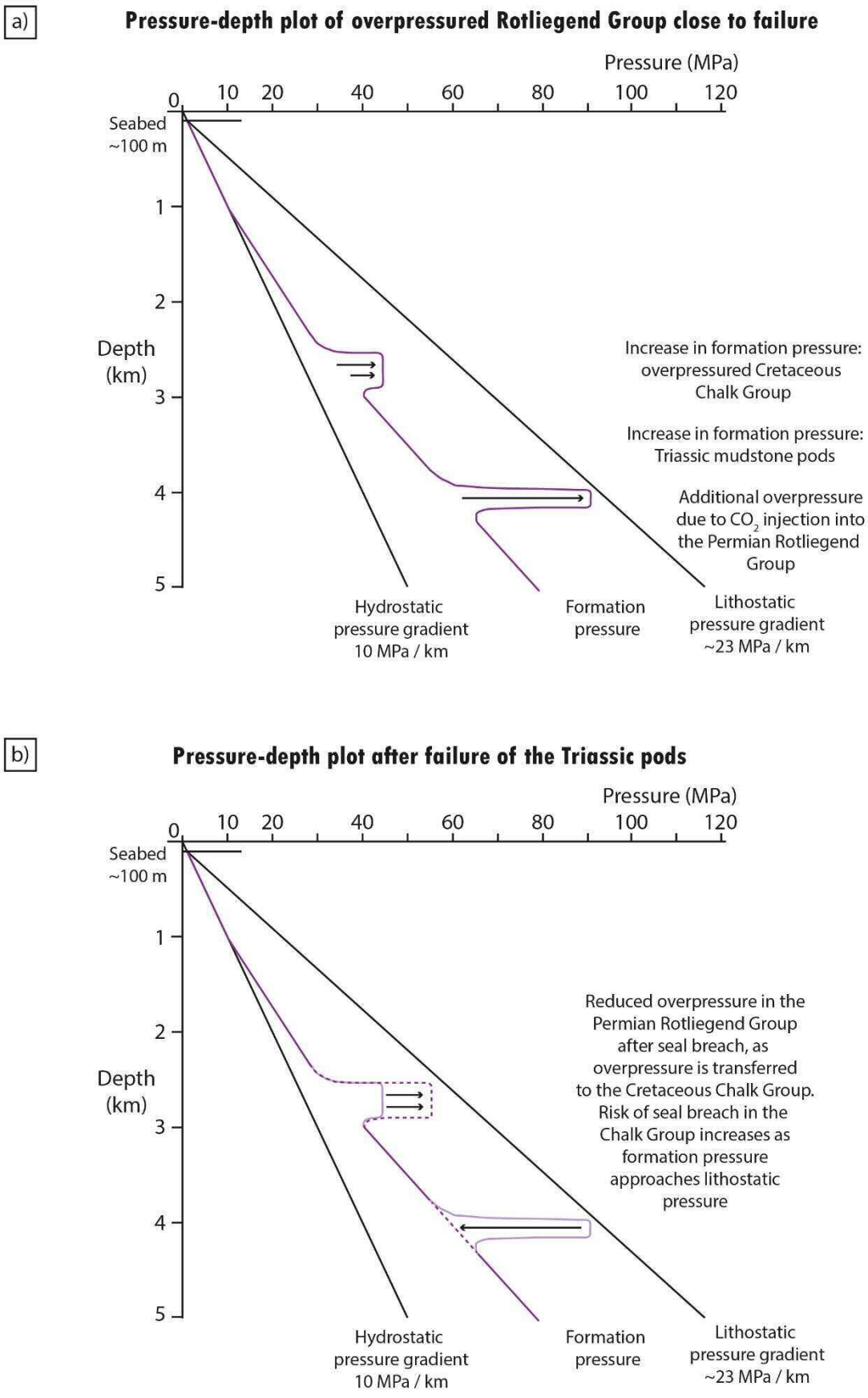

Fig. 7.12. Schematic pressure-depth plots representative of the Jæren High study area, showing a) increasing formation pressure with depth due to overpressure build-up, and change in pressure in the Rotliegend Group due to CO_2 injection, before overburden failure; b) reduced pressure in the Rotliegend Group after overburden failure, with overpressure transferred to the shallower Chalk Group.

Fig. 7.13 shows simplified Mohr Circles and corresponding failure envelopes for different seal breaching scenarios, some of which could happen at the present day. At the depth of the Rotliegend Group (~ 4 km) it is assumed that vertical stress is much greater than horizontal stress ($\sigma_v >> \sigma_H > \sigma_h$). When differential stress is greater than four times the tensile strength of the rock, $(\sigma_1 - \sigma_3) > 4T$, the rocks will experience compressional shear failure (Sibson, 2003). The state of stress without additional pore fluid pressure is shown by the black Mohr circle.

a) Scenario 1: the pipes are cemented, such that the strength of the pipe rock is the same as the host rock. Alternatively, seal breaching occurs where there are no pipes. The new pipes will form when enhanced pore fluid pressure reduces the effective stress, which shifts the Mohr Circle to the left in Fig. 7.13. It contacts the failure envelope for an undeformed rock and shear failure occurs along a fault with an angle 90-θ°, or in this case, a 'fracture mesh' (Sibson, 2000, 2003).
b) Scenario 2: the pipes are open or cemented but still weaker than the surrounding host rock, i.e. failure occurs by the reactivation of a 'cohesionless fault' with a failure envelope that crosses the y-axis at $\tau = 0$. Lower pore fluid pressure is required to reactivate the pipes than to form new ones.
c) Scenario 3: the tensile strength of the cemented pipes is greater than that of the host rock. Thus, a greater pore fluid pressure increase is required to reactivate these pipes. Fisher and Knipe (1998) found that reservoirs greater than 3 km depth in the North Sea exhibit enhanced pressure solution and quartz cementation in fault rocks relative to the host rock, and that burial to depths where temperatures are greater than 90°C is required for these processes to occur (Dewhurst and Jones, 2003; Walsh et al., 2018). Therefore, it is likely that cementation of the pipes has increased their strength and inhibits fluid flow.

If the pipes themselves are overpressured, then a further increase in overpressure due to fluid accumulation may cause the rock to re-fracture and, consequently, the pipes to be preferentially reactivated. Overall, the possibility of pipes being reactivated should be taken into account if the Rotliegendes on the Jæren High are to be chosen for a CO_2 storage site.

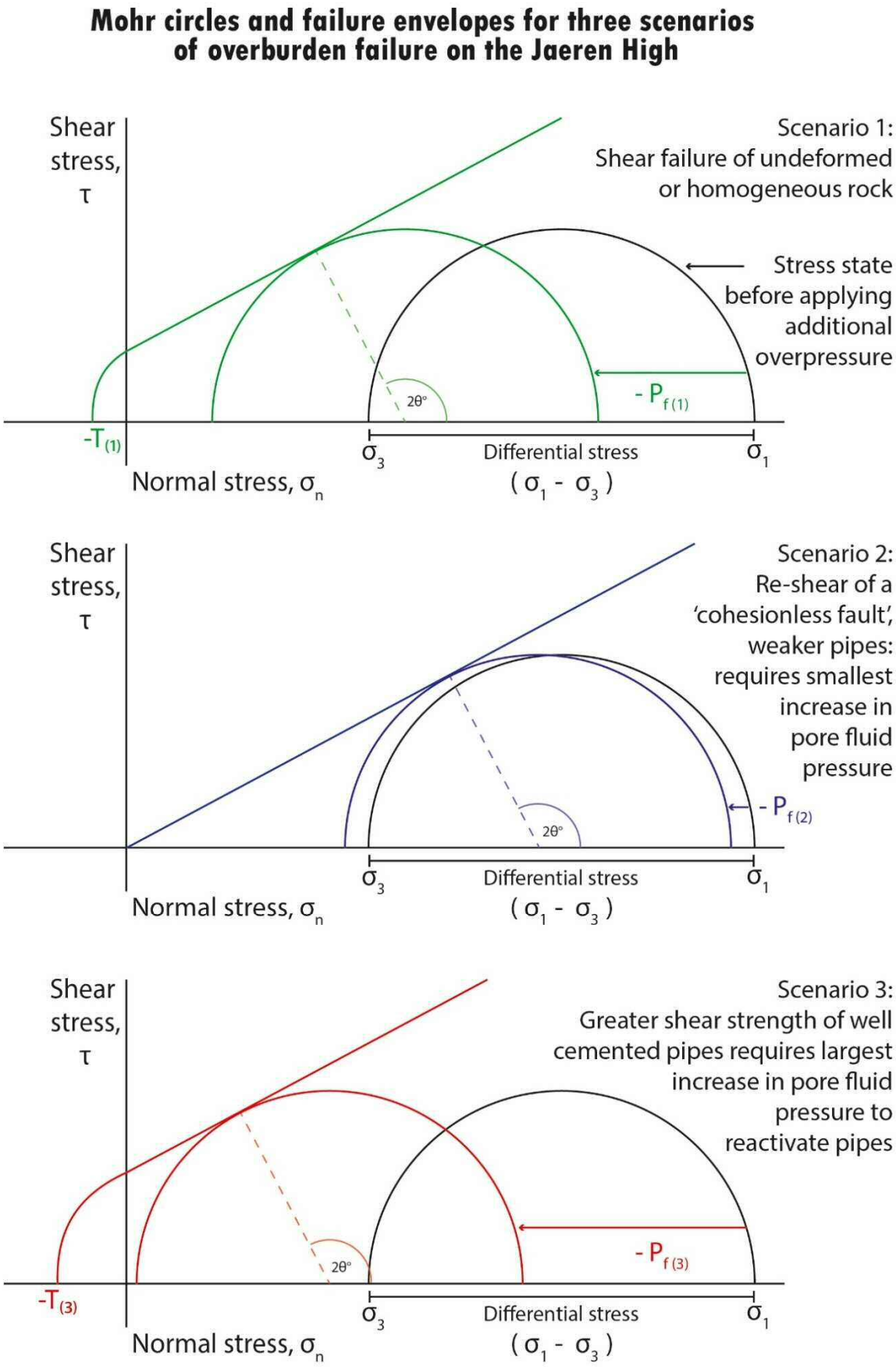

Fig. 7.13. Schematic Mohr circles and failure envelopes for the three scenarios of overburden failure on the Jæren High, explained in Section 7.5.1. Colours match the Mohr circle and pore fluid pressure to the relevent failure envelope: green = scenario 1, blue = scenario 2, red = scenario 3. T is the tensile strength of the rock. All three failure scenarios occur within the shear stress regime.

7.5.2 Reactivation of recent pipes in the East Breaks area, Gulf of Mexico

In contrast to the 4 km-deep Rotliegend Group of the Jæren High, the effect of reintroducing excessive pore fluid pressures on reactivation of recent pipes is now considered within a few hundred meters below the sea floor in the East Breaks area. A simplified pressure-depth plot for the East Breaks area is shown in Fig. 7.14.

In the East Breaks area, a value of 400 m was chosen as the representative water depth used in Fig. 7.14, as water depth ranges from 85 m to 1395 m in the study area (Fig. 5.1). As the depth of source of pockmarks ranges from 50 to 1750 ms TWT (Fig. 5.15), the median value for depth of source of pockmarks in the 'Top Salt' category is used here (650 ms TWT) as the base of the 'seal unit'. Assuming an approximate seismic velocity for shallow-buried hemipelagic mudstone of 1700 m/s, this depth is ~550 m.

The rapid burial of sediments in the Gulf of Mexico during the Plio-Pleistocene resulted in high pressures being generated in subsurface strata as sedimentation rate outpaced fluid escape through pore-networks. Gas plumes were recorded by the BOEM above a few pockmarks, which are presently active. These indicate gas seepage through open pipes, where overpressure does not build-up. Below the remainder of the pockmarks, formation pressure is expected to gradually increase above hydrostatic values with depth. However, as focused fluid escape has already occurred to form these pockmarks and the strata have not been buried further since, the overpressure is not expected to be significant. However, it can still be increased to a point of overburden failure if there is a rapid flow of fluids such as hydrocarbons migrating from below.

Fig. 7.15 shows simplified Mohr Circles and failure envelopes for different scenarios of seal breaching and reactivation in the East Breaks area. The upward movement of salt caused extension in the overburden and formation of crestal faults, reducing horizontal stress. At such shallow depths, (~ 550 m), vertical stress is greater than horizontal stress ($\sigma_v > \sigma_H > \sigma_h$), but the differential stress is small and extensional to extensional-shear-type failure is expected to occur (Sibson, 1998, 2003) (Fig. 1.11).

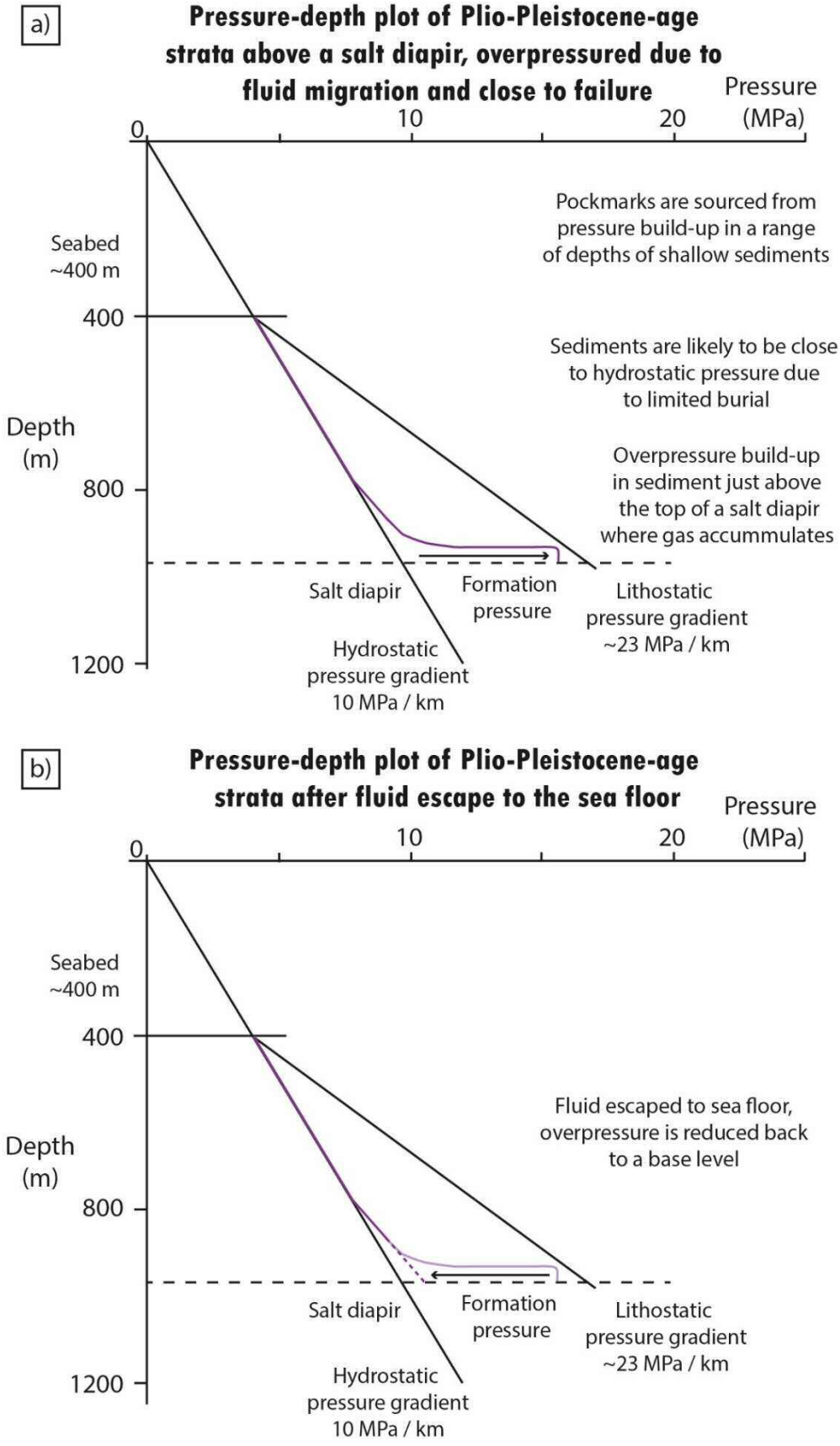

Fig. 7.14. Schematic pressure-depth plots representative of the Plio-Pleistocene-age sediments directly above a salt diapir. The sediments are close to hydrostatic pressure, but if there was a rapid input of fluids such as hydrocarbons (a), overpressure would increase towards lithostatic pressure and the overburden may be fractured as fluids escape to the sea floor, then overpressure reduces back to previous levels (b).

a) Scenario 1: when pore fluid pressures are increased, new pipes form, and assuming differential stress (σ_1 - σ_3) is less than or equal to four times the tensile strength of the overburden (4T), extensional and extensional-shear fractures will form.
b) Scenario 2: some of the pipes could be 'plugged' by mobilized muds, whilst others and faults resemble a 'cohesionless surface', such that low overpressure is required to reactivate these preferential fluid flow pathways. Faults which contain clay-rich gauges and are located at shallow depths in unlithified or weakly lithified sediments are likely to remain cohesionless, or have lower strengths than the host rock (Dewhurst and Jones, 2003). Thus, the pipes found in the East Breaks area are unlikely to be cemented. This scenario is represented by a 'cohesionless fault' failure envelope, which crosses the y-axis at $\tau = 0$.

The evidence of gas plumes and oil slicks identified by the BOEM indicates that some of the pipes are open and seepage is actively occurring.

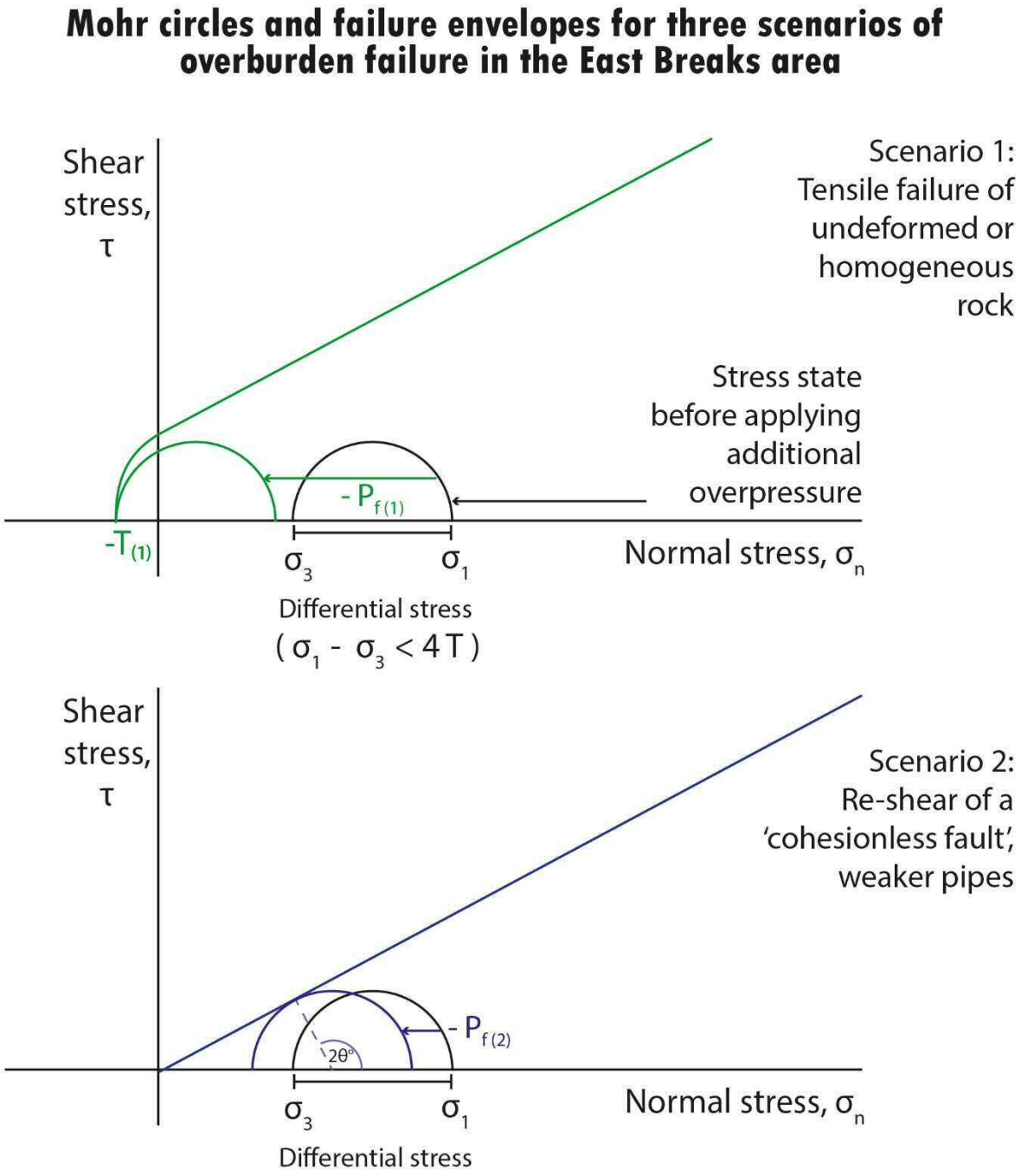

Fig. 7.15. Schematic Mohr circles and failure envelopes for the two scenarios of overburden failure in the East Breaks area, explained in Section 7.5.2. Colours match the Mohr circle and pore fluid pressure to the relevent failure envelope: green = scenario 1, blue = scenario 2. T is the tensile strength of the rock. Initial formation of pipes form in the extensional to extensional-shear regime. Reactivation of existing, weak pipes or faults requires the smallest increase in pore fluid pressure and involves compressional-shear of existing fractures.

7.5.3 Reactivation on the Modgunn Arch

Simplified pressure-depth plots are used to consider overpressure changes during reactivation of hydrothermal vent complexes on the Modgunn Arch at present (Fig. 7.16). The depths used on the pressure-depth plot are based on well 6403/6-1, which is located in the centre of the Modgunn Arch. The base of the seal interval of interest to this discussion is represented by the Top Lysing Formation; the stratigraphic level at which 43% of sills intruded from which HTVCs formed. In Fig. 7.16, formation pressure is shown to track close to hydrostatic pressure until the Top Tang Formation, below which it increases above hydrostatic pressure with depth. Polygonal faults cross the Cenozoic units down to the Tare Formation, showing evidence for dewatering during compaction. Furthermore, submarine landslide activity has redistributed shallow sediments and associated depressurisation may have allowed pulses of fluids from shallow units to escape during these events (Beget and Addison, 2007). Large faults cross-cut the hemipelagic-dominated Cretaceous units with small displacements – these could be polygonal faults and formed during the Cretaceous, before the sills intruded their host rock, as some sills cross-cut faults whilst others trace the fault path (Fig. 6.11a). Overpressure is expected to increase further with depth. If sufficiently high overpressures are achieved, the faults and/or hydrothermal vent conduits will be reactivated. Fluids may migrate to the sea floor, or, if energy is dissipated and a shallow reservoir is encountered, overpressure may be transferred to a shallower unit above the HTVCs (Fig. 7.16b).

Three (3) examples of stacked HTVCs were interpreted in the Modgunn Arch, implying that the same conduit was reutilised for hydrothermal fluid escape to the palaeo-sea floor during the Paleocene. If the HTVC conduits had not yet been cemented and sealed, then overpressures would not have built up and fluid seepage would have occurred along the conduit fracture network. Alternatively, the increase in pressure occurred so rapidly that fluid pressure could not be dissipated as would be expected in such a setting with pre-existing fractures, such that a secondary violent eruption of hydrothermal fluids occurred. This rapid overpressuring occurred due to the intrusion of sills and boiling of host rock in the metamorphic aureole, as explained in section 6.2. A snapshot of this overpressure change due to sill intrusion is shown in Fig. 7.17, illustrating the relative change in pore fluid pressure with time. If the conduits are cemented after the hydrothermal fluid venting, these may be less likely to be reactivated. Nevertheless, if the conduits remained open fluid migration pathways, then the conduits may not need to be ‘reactivated’ per se, and fluid seepage will occur – which is expected to have occurred, as evidenced by the high-amplitude flags above the HTVCs (Fig. 6.10). In this

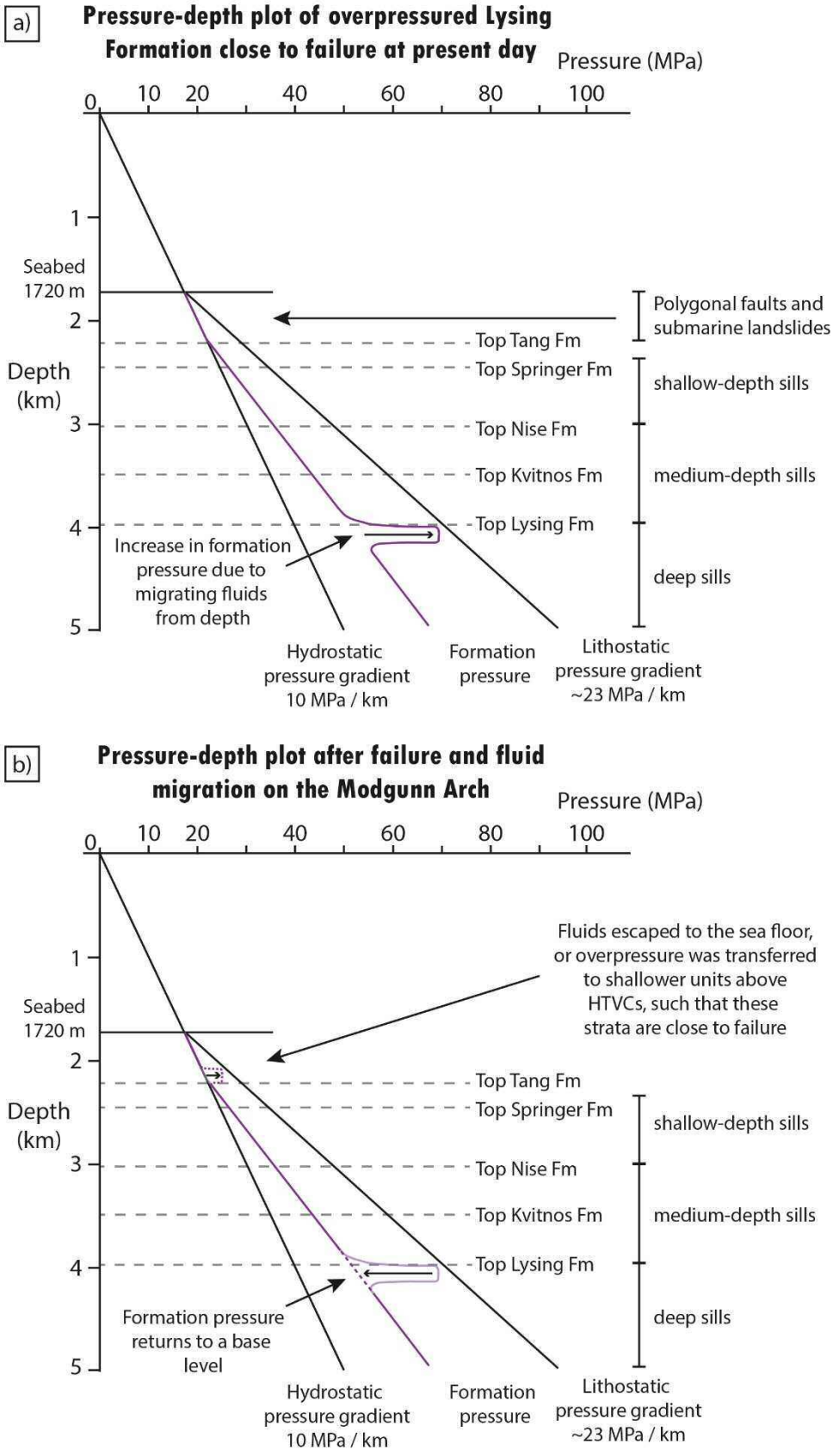

Fig. 7.16. Schematic pressure-depth plots representative of the southern area of the Modgunn Arch. The shallow sediments are close to hydrostatic pressure, increasing with depth through thick shale units. a) Hypothetical increase of pore pressure as fluids migrate to the Lysing Formation. b) Possible transfer of overpressure if fluids were to migrate across hydrothermal vent complexes and accumulate in shallow strata.

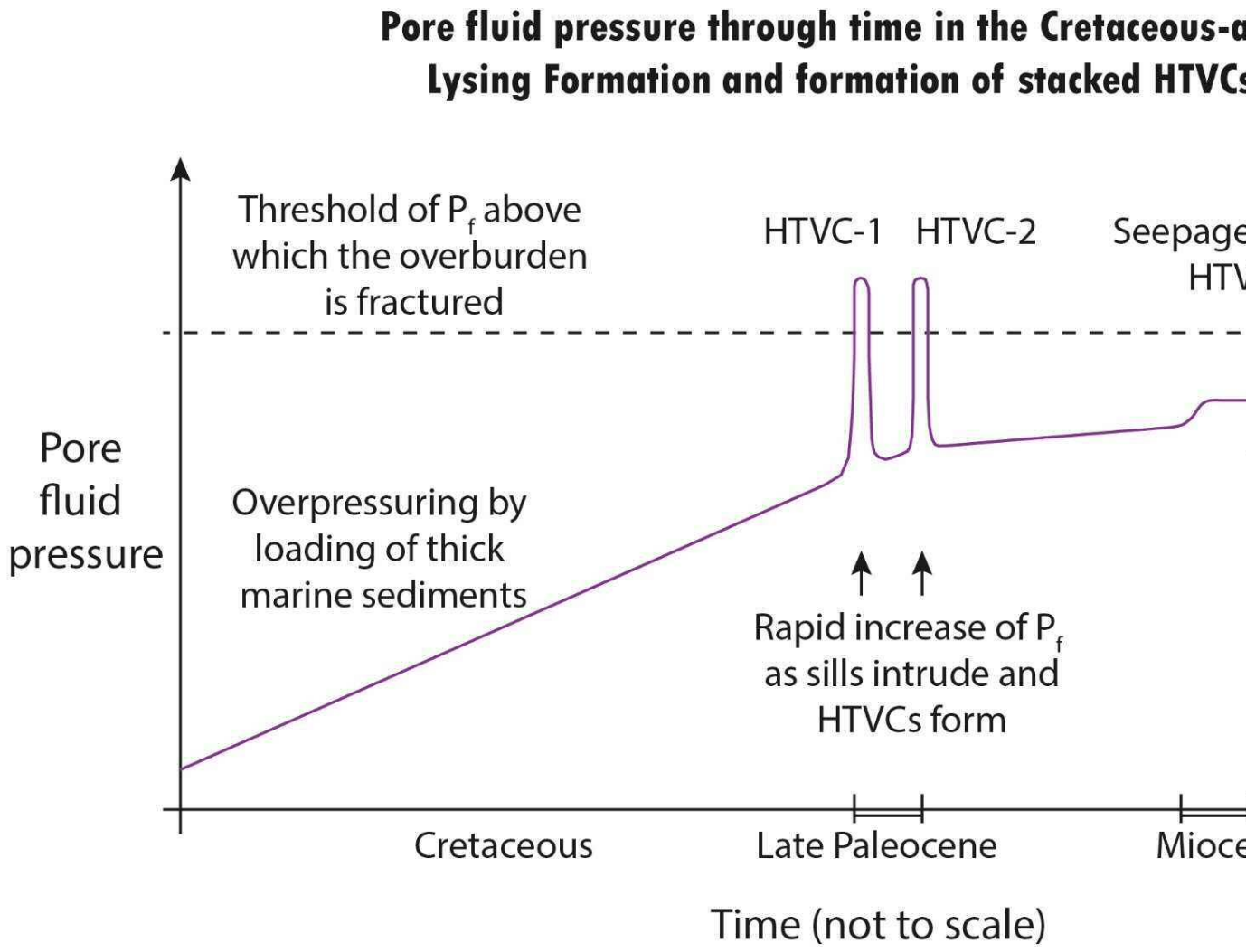

Fig. 7.17. Schematic plot of the increase of pore fluid pressure through time, in the Cretaceous-age Lysing Formation. Pore flu
sills intruded and hydrothermal vent complexes were formed. Figure is not to scale.

particular case, hydrothermal venting may include the transport of heavy minerals, and fractures in the conduits may be sealed by mineralisation, increasing the tensile strength of the overburden, such that it becomes much more difficult to reactivate and reutilise existing conduits (Sibson, 2017; Tenthorey et al., 2003).

Simplified Mohr Circles and failure envelopes for three (3) different scenarios of present-day seal breaching and reactivation of HTVCs on the Modgunn Arch are given in Fig. 7.18. During the Paleocene, the Modgunn Arch area was in a post-rift extensional setting, such that ($\sigma_v >> \sigma_H > \sigma_h$), therefore the differential stress would have been large but the style of rock failure was still compressional shear at the depth of interest (~1800 m). The Modgunn Arch formed due to reactivation of deep crustal faults and resulting compression (Brekke 2000; Gomez and Verges 2005), thus it is expected that σ_h increased and differential stress decreased slightly. Continued sedimentation and burial since the Modgunn Arch formed also caused vertical stress to increase. At the present-day depth of interest (~2250 m), the differential stress is still likely to be greater than four times the tensile strength ($\sigma_1 - \sigma_3 > 4T$), therefore compressional shear would be the dominant style of rock failure if seal breach occurred today.

a) Scenario 1: the faults and HTVCs are cemented and have the same tensile strength as the host rock, or seal breach occurs where there are no HTVCs or faults. New pipes will only form when a sufficiently high pore fluid pressure reduces the effective stress such that the Mohr Circle crosses the failure envelope for an undeformed rock, and shear failure occurs (similar to Scenario 1 on the Jæren High).
b) Scenario 2: the faults and HTVCs are cemented, but the strength of the cemented zones is less than the host rock, or contrasts between cement and host lithology provide planes of weakness, so these are the preferential leakage pathways. Reactivation is represented by the 'cohesionless fault' failure envelope, which crosses the y-axis at $\tau = 0$. Pore fluid pressures required for reactivation are lower than to form new pipes in Scenario 1.
c) Scenario 3: hydrothermal mineralisation occurred during cementation, thus increasing the tensile strength of the HTVCs and faults. Therefore, a greater increase in pore fluid pressure is required to reactivate the existing HTVCs and faults.

Overall, the pore fluid pressure required to breach the seal is greatest for cemented pipes that have a greater tensile rock strength than the host rock; intermediate for previously undeformed host rock or if sealed pipes have the same tensile strength as the host rock, and the least for reactivating weaker pipes or faults.

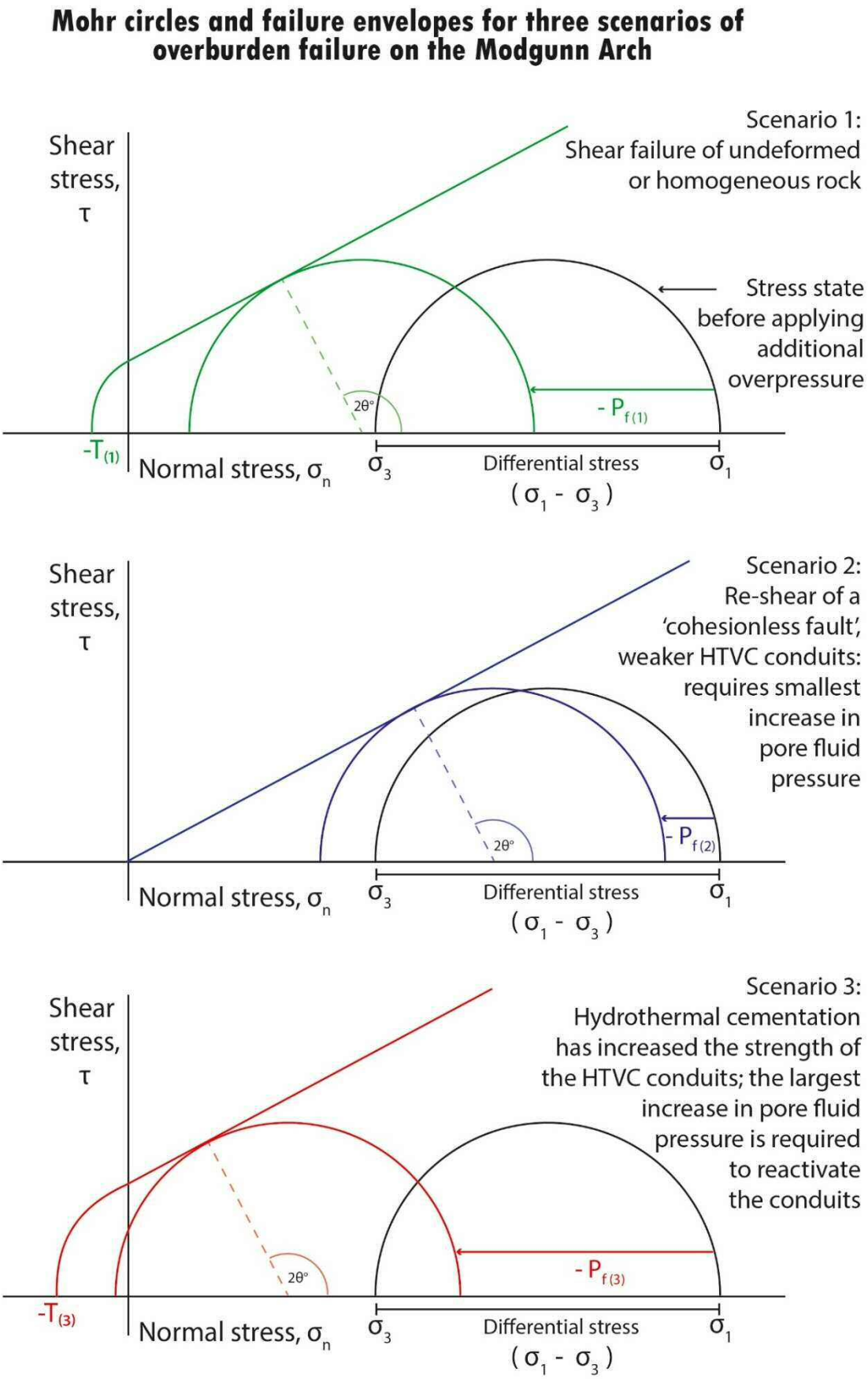

Fig. 7.18. Schematic Mohr circles and failure envelopes for the three scenarios of overburden failure on the Modgunn Arch, explained in Section 7.5.3. Colours match the Mohr circle and pore fluid pressure to the relevent failure envelope: green = scenario 1, blue = scenario 2, red = scenario 3. T is the tensile strength of the rock. All three failure scenarios occur within the shear stress regime.

7.5.4 Additional considerations for fluid migration pathways in the study areas

7.5.4.1 Fluid flow across anticline crests

A further consideration of stress state on the Jæren High is related to the inversion of Triassic pods into turtle-anticline structures in between the salt walls. The formation of anticlines results in strain variation across the units involved, as the upper layers are characterised by layer-parallel extension, whilst the lower and central layers of the fold experience layer-parallel shortening and increases in overpressures; these two zones are separated by a 'neutral line', on which the principal strains are zero (Carminati et al., 2010; Frehner, 2011; Ramsay, 1967). If stresses in the extensional regime of the fold overcome the tensile strength of the rock, layer-perpendicular fractures will form, particularly at the fold hinge – these fractures across the hinge could have focused fluid flow which aided in releasing overpressures within the (dominantly mudstone) Smith Bank Formation (Eckert et al., 2016; Frehner, 2011).

In contrast to the turtle-anticlines on the Jæren High, the Modgunn Arch is a much larger-scale anticline structure, which formed in the Miocene, more than 30 million years after the intrusion of sills and formation of hydrothermal vent complexes. Although the structure is not well imaged at depth due to the high absorption of seismic energy by the magmatic features, it is possible that the sills are located above the neutral line of the Arch, because during the reactivation of deep faults to form the Arch, fluids were focused along sills and faults towards the shallower, extensional regime and migrated across HTVCs, as evidenced by the high-amplitude flags above the HTVCs. The greater the degree of folding and shortening, the further the neutral line migrates towards the inner arc and therefore the larger the area of the fold undergoing extension (Frehner, 2011).

7.5.4.2 Fluid flow across salt minibasins

A comparison of the salt minibasins of the Jæren High (CNS) and East Breaks (GOM) shows how the timing of fluid escape versus structure formation and scale controls the preferred fluid migration pathway. The thickness of the salt diapirs and salt minibasins are far greater in the East Breaks area than on the Jæren High. On the Jæren High, grounding of Triassic sediment pods occurred around the mid-Triassic (Smith et al., 1993), which means the migration windows across the salt had formed almost 90 million years before the earliest pockmarks in

the Late Jurassic. The pore-fluid pressures had not increased enough to breach the overburden during the Triassic. Approximately 1 km of terrestrial mudstones with occasional interbedded siltstones and thin sandstone beds were deposited in the Early-Middle Triassic, i.e. ~15 million years. In contrast, approximately 6.0 s TWT of deep-marine, hemipelagic mud with occasional interbedded siltstones and submarine fans and turbidites were deposited in the East Breaks area of the Gulf of Mexico since the Pliocene, roughly ~5 million years. If we assume an average rock velocity of 2 km/s in the East Breaks salt minibasins, then 6.0 s TWT equates to 6 km of strata in salt minibasins. This gives an average deposition rate (6 km in 5 million years) of 1200 m per million years, which is two orders of magnitude greater than that during the Triassic on the Jæren High (1000 m in 15 million years), of 67 m per million years. The combination of a relatively lower sedimentation rate and fracturing of the arch of turtle anticlines may have allowed some pore fluids to escape the Triassic pods, limiting the amount of overpressure achieved. In contrast, the rapid sedimentation and burial of fine grained, hemipelagic mudstones in the Gulf of Mexico inhibited the hydrostatic connection of buried rocks, causing the minibasins strata to become highly overpressured and subject to overburden failure.

Furthermore, inversion of salt minibasins into turtle anticlines has not occurred in the East Breaks area. The seismic reflections are tilted upwards against the flanks of salt diapirs, often becoming near-vertical towards the salt-sediment interface and at depth. These tilted units provide more effective fluid migration pathways compared to the formation of vertical pipes across minibasins strata, which was the case on the Jæren High. By the time the hydrocarbons matured and migrated beneath the salt welds at the bases of the salt minibasins, the thickness of the salt minibasin strata was likely to be too great for pore fluid pressures to overcome the confining pressure in the centre of the salt minibasins and for pipes to form in the same way as on the Jæren High. However, hydrocarbons may have migrated across salt welds and subsequently, up-dip laterally towards the salt structures along the tilted minibasin strata, as shown schematically in Fig. 5.18.

In summary, where pore-fluids became sufficiently overpressured to breach the overburden, pipes formed straight across salt minibasins (Jæren High); whilst in the East Breaks area the minibasins are too thick and confining pressure is too great to form vertical pipes from the base of salt minibasins, such that alternative fluid migration pathways formed along the salt-sediment interface.

7.5.4.3 Fluid flow and diagenesis

The impact of diagenesis on fluid flow has already been discussed in terms of how cementation affects the strength of fault rocks and therefore the pipes in the study areas. A

further consideration when exploring in a magmatic sedimentary basin is assessing the impact of magmatic intrusions on diagenesis of the host sedimentary rocks. Intruding magma can have temperatures in the order of 1000°C, therefore the host rocks are rapidly heated, especially in the metamorphic aureole (Sydnes et al., 2019). The heating induces quartz cementation in the nearby host rocks, which reduces porosity and permeability, increases the shear and tensile strength of the rocks and causes these zones to be more brittle than the unaffected sedimentary rocks (Sydnes et al., 2019). Hence, although diagenesis reduces the quality of any nearby reservoirs, if fractured, high-permeability fluid flow pathways are created, which is seen in Chapter 6 on the Modgunn Arch, as HTVCs formed stratigraphically above sill tips.

Regional diagenesis also occurs or is enhanced due to heat from sill intrusions. Sydnes et al. (2019) modelled the impact of magmatic intrusion on diagenesis of Opal A-CT, Opal CT-quartz, and quartz cementation, using a 2D seismic section across the Vøring Basin. The effect of heating on quartz cementation was seen to be highest in the zones surrounding the intrusions, particularly where intrusions are thicker or clustered as a sill complex (Aarnes et al., 2011; Fjeldskaar et al., 2008; Sydnes et al., 2019; Sydnes et al., 2018). The heating effect was also shown to extend vertically on a regional scale, such that Opal A-CT and Opal CT-quartz transitions occurred at shallower depths in the basin than they normally would without the impact of intrusions (Sydnes et al., 2019). As mentioned in Chapter 6, a fossilized Opal A-CT transition is seen on the eastern flank of the Modgunn Arch within the Brygge Formation at a very shallow level compared to what is normally expected (Fig. 6.2). This phenomenon is apparent across the northeast Atlantic margin, as discovered by other authors (Brekke et al., 1999; Brekke, 2000; Davies and Cartwright, 2002; Neagu et al., 2010).

Davies and Cartwright (2002) found the fossilized Opal A-CT transition to currently be at a temperature of 24 °C in well 214/4-1 in the Faroe-Shetland Basin, and interpreted that during the Early Pliocene, the transition would have been at temperatures of 8-15 °C, if the geothermal gradient was the same as at present day. However, Hein et al. (1978) found that the modern Opal A-CT transition in the Bering Sea occurs at temperatures between 35-50 °C, which suggests that there was a considerably higher geothermal gradient in the past in the northeast Atlantic margin. The models by Sydnes et al. (2019) do imply that sill intrusions could have instigated Opal A-CT transition at very shallow depths, however, the magmatic activity in the Vøring Basin ceased in the Early Eocene, whilst the fossilized Opal A-CT transition is found in Oligo-Miocene-age strata and estimated to have fossilized sometime during the Pliocene (Brekke, 2000; Davies and Cartwright, 2002; Neagu et al., 2010), therefore, the timings do not match up.

The cause of this fossilization is unclear. Davies and Cartwright (2002) proposed several mechanisms for cooling in the Faroe-Shetland Basin, including: initiation of glaciation and onset of deepwater circulation, both of which caused bottom waters and the seabed to cool; and uplift and erosion. The latter is shown to have occurred during the formation of the Modgunn Arch, however, none of the reasons above – individually or combined – are sufficient to account for the change in temperature required to explain the fossilization event (Davies and Cartwright, 2002). Authors conclude that there may have been some unknown thermal event, and/or enhanced geothermal gradient in the past, after which significant cooling occurred (Brekke et al., 1999; Brekke, 2000; Davies and Cartwright, 2002; Neagu et al., 2010). It is suggested in this thesis that a thermal anomaly was associated with the formation of the Modgunn Arch and could have resulted in this shallow Opal A-CT transition, as well as heat from vertically migrating fluids – although this is entirely speculative.

Nevertheless, regional diagenesis and the conversion of Opal A to Opal CT results in a reduction in the porosity and permeability of the rocks – as much as 20% porosity reduction – which can increase tortuosity of migrating fluids, or inhibit flow entirely – forming seals (Roaldset and Wei, 1997; Sydnes et al., 2019). For example, two hydrocarbon accumulations were found to be sealed by mudstones containing the Opal CT-quartz boundary, due to its lower permeability – the Yurihara oil and gas field (Japan) and the Monterey Formation in California (USA) (Dralus, 2013; Sydnes et al., 2019; Tsuji et al., 2011). This could be applicable to the Modgunn Arch, where fluids have migrated from the deeper parts of the basin, across HTVCs and accumulated locally below the Opal A-CT boundary – that is, assuming the high-amplitude anomalies identified in Chapter 6 are due to fluid flow. Although, during the Opal A-CT conversion, water is produced, which increases the pore pressure of the mudstones and can cause fracturing – which may explain the polygonal faults seen, cross-cutting the Brygge Formation on the Modgunn Arch. Polygonal faults form in fine-grained sedimentary rocks during compaction (Cartwright and Dewhurst, 1998; Cartwright et al., 2007; Cartwright et al., 2003) and may form leakage pathways for fluids to the sea floor – for example, Berndt et al., (2003) found pockmarks and pipes spatially coincident with polygonal faults in the Vøring Basin, and concluded vertically focused fluid flow due to dewatering from the polygonal faults. Thus, all these factors are important when interpreting fluid migration pathways and seal breaching in these settings.

Another diagenetic boundary is the base of the gas hydrate stability zone (GHSZ). The GHSZ is shallow, within 100s of metres below the sea floor, but free gas may accumulate and be trapped below this zone, particularly if the gas hydrates are laterally extensive (Gay et al., 2006). Again, if sufficiently large volumes of free gas accumulate below the gas hydrates – or

if there are temperature or pressure changes causing dissociation of gas hydrates – the seal may be breached and fluids migrate to the sea floor (Gay et al., 2006). In the Gulf of Mexico basin, gas hydrates are known to be present (Boswell et al., 2012), but the shallowest limit of the GHSZ is thought to cross the southern part of the East Breaks study area in Chapter 5. Few pockmarks were seen in the southern part of the study area, and it is possible that gas hydrates are present and acting as a regional shallow seal, preventing fluid escape and pockmark formation in the way that is seen up-dip (Fig. 5.5).

The detailed mechanics and impact of these diagenetic boundaries on fluid flow are beyond the scope of this thesis, but in summary, diagenesis is an important factor to consider in basin modelling, which will influence fluid migration pathways and indicate thermal changes in the history of the basin.

7.6 Limitations; the Seabed Mapping Tool and final remarks

7.6.1 Limitations of the study

A key limitation of this study includes the quality of the seismic datasets and their resolution. This limited what fluid flow features could be resolved and interpreted, as well as the interpretation of amplitude anomalies, as described in Section 7.3. Crucially, the absence of well data for the East Breaks (Gulf of Mexico) and Modgunn Arch (Norwegian Sea) datasets, posed a major limiting factor for the analysis of these two datasets, for interpreting the lithologies, undertaking time-depth conversions and constraining ages and stratigraphy at high resolution. In addition, the boreholes on the Jæren High are not drilled into any pipes or as deep as the Permian or Carboniferous-age strata, and no core data was available from any wells, which would be useful in determining the nature of the pipes and properties of the rocks.

Should the Gulf of Mexico dataset be re-processed, the imaging of deeper structures and strata, particularly adjacent to salt bodies, may be improved, as well as data resolution. The Jæren High seismic dataset was of sufficient quality for the study undertaken. Although, the spatial extent of the recently re-processed ‘mega-merge survey plus’ 3D seismic data by PGS unfortunately terminates at the western edge of the Jæren High, which, if it had covered the study area, might have revealed the fluid flow features in greater detail. The resolution of the Modgunn Arch dataset is very good, although acoustic absorption and scattering by the igneous sills reduced the quality and amplitudes of underlying seismic reflections such that, for

example, the Nise Formation could not be interpreted with confidence over much of the study area (Fig. 6.2, Fig. 6.3c).

7.6.2 The Seabed Mapping Tool

The Seabed Mapping Tool was originally used on multibeam sonar bathymetric data (Gafeira et al., 2012) and proved to be a very effective semi-automated mapping method which helped to save time and improve accuracy and precision when mapping features in 3D seismic data. The higher the data quality and more homogeneous the surface, the greater the accuracy of mapping features. A systematic approach also reduces human error and subjectivity and aims to minimise systematic errors. In the case of complicated bathymetry such as that in Chapter 5, significant manual quality control was required to remove spurious results due to undulating bathymetry as a result of underlying faults and salt deforming the subsurface.

The Tool is used on data presented in meters depth, therefore depth conversion of seismic data was required. When the Tool is applied to deeply buried horizons (as opposed to bathymetry), the velocities used in depth conversion need to be accurate, otherwise errors or artefacts may arise in the mapping process. However, the manual quality control step of visualising the mapped features over the original dataset in two-way time ensured that artefacts were not misinterpreted. Higher quality and resolution of data is important to capture the greatest range of sizes of the features, however, the greater the size of the study area and data quality, the longer the processing time required in ArcGIS to run the Tool.

The Tool was not used to map hydrothermal vent complexes for Chapter 6, due to the range of morphologies of the HTVCs (domes, eyes and craters) as well as the range of depths that the features occurred at. It was decided that manual interpretation would be quicker and sufficient to capture the range of sizes and morphologies of these features, as well as to visualise their spatial distribution.

7.6.3 Future work

In this thesis, the morphology and distribution of focused fluid flow features have been investigated in three different study areas, which include a failed rift basin (Central North Sea), a passive margin setting (Gulf of Mexico), and a passive margin setting with deep crustal reactivation (mid-Norwegian margin). The first two study areas involved salt structures, whilst the latter contained magmatic sills, which controlled fluid migration pathways. It may prove useful in the future to acquire additional seismic datasets where fluid flow features are associated with different structures and different tectonic settings, particularly compressional

tectonics where the maximum compressive stress may not be vertical. These datasets could be used to further explore the impact of structure on fluid flow pathways, and to compare and contrast with the study areas in this thesis. Furthermore, it would be interesting to use the Seabed Mapping Tool to map and characterise more pockmark fields, in particular buried pockmarks, and compare the pockmark morphologies with the buried and recent pockmarks in Chapters 4 and 5 respectively, to increase the database of detailed pockmark morphology and investigate the controls on this.

In addition to obtaining further seismic datasets, it will be useful to be able to calibrate these with well data, especially if pressure and local stress data were available. Using these data to model slip tendency of faults and leakage risk (e.g. Mattos et al., 2016; Morris et al., 2016; Ward et al., 2016) would provide more robust results to interpret regarding the risk of creating or reactivating fluid flow pathways, compared to the discussion in Chapter 7 in which theoretical pressure-depth plots were drawn and hypothetical scenarios of overburden failure were presented.

As mentioned in Section 7.4.3, pre-stack seismic data was not available for any of the study areas. If this data were obtained, amplitude-versus-offset (AVO) analysis could be undertaken to determine whether the high-amplitude anomalies are lithological or due to fluids, which will aid the interpretation of fluid flow pathways.

7.6.4 Final remarks

In summary, pipes and hydrothermal vent conduits are shown to be key seal bypass mechanisms in the studies presented in this thesis. The presence of their upper terminations, be that pockmarks, mud volcanoes, amplitude anomalies or hydrothermal vent complexes, have allowed the timing of fluid escape to be deduced in relation to major tectonic events in the evolution of the Central North Sea basin, the northern Gulf of Mexico basin and the mid-Norwegian passive margin. It is important to interpret such fluid flow features, which are often subtle in seismic data, during basin analysis to assess if and where seal breaching has occurred. As many of the ‘easily identifiable’, large hydrocarbon fields have been discovered, exploration is becoming ever increasingly challenging, and these features are important indicators of active or previous petroleum systems. Careful assessment of the risk of reactivating existing pipes, conduits or faults, must also be undertaken when considering a carbon capture and storage site. Whilst focused fluid flow pathways can remain as open seal bypass systems or cemented and form a stronger seal, diagenesis on a regional scale is also an important factor to consider when assessing fluid migration and reservoir quality in sedimentary basins.

CHAPTER EIGHT

Conclusions of this thesis

8 Conclusions

This thesis provides a detailed analysis of focused fluid flow features and pathways in the shallow (Chapter 5), intermediate (Chapter 6) and deeper (Chapter 4) parts of sedimentary basins. A summary of the main conclusions of this work is provided below.

8.1 Conclusions of Chapter 4

- Fluid escape pipes were identified in 2.5-4 km deep strata on the Jæren High across the border of the UK and Norwegian Central North Sea. These pipes are rooted in the Permian Rotliegendes Group, cross-cut salt welds and Triassic minibasins. The pipes terminate as pockmarks in the Upper Jurassic Mandal Formation and Lower Cretaceous Cromer Knoll Group.
- Large pockmarks, up to 842 m width and 178 m vertical relief, indicate that very high overpressures developed for fluids to escape and form structures of this size. The overpressure was interpreted to be due to gas accumulation in the Rotliegendes, which could have been sourced from Visean coals in the East Central Graben and, or the Cod Terrace. If this is the case, an underexplored Carboniferous play may be present in the Central North Sea.
- A total of 295 high-amplitude anomalies were identified in the Triassic minibasins, of which 178 are not associated with pockmarks in the Jurassic or Cretaceous-age strata. These high-amplitude anomalies can represent cemented pipes or possible gas pockets.
- Cemented pipes may strengthen or weaken the pipes, putting these at risk of reactivation if pressures in the Rotliegendes were increased again at present day.

8.2 Conclusions of Chapter 5

- A total of 720 pockmarks and 62 mud volcanoes were mapped on the sea floor in the East Breaks area of the Gulf of Mexico, and 96% of the pockmarks are located above

the salt diapirs, whilst all of the mud volcanoes are located above the flanks of salt diapirs.

- The salt-sediment interface around salt diapirs, and crestal faults are the key fluid focusing pathways, bringing hydrocarbons to the sea floor at present day.
- Diffusive fluid flow occurred through the minibasins to shallower units, and intra-minibasin faults may also play a role in connecting deeper reservoirs to shallow strata, particularly sand-rich units such as turbidites, as evidenced by soft, high-amplitude anomalies.
- Pockmarks range in size between 20 – 400 m width and 1 – 41 m vertical relief. The size of pockmarks does not increase with depth of source, however the shallow plumbing system is indicated by the presence of pockmarks, whilst mud volcanoes reflect high overpressures reached in the deeper parts of the minibasins.
- The semi-automated mapping method increases accuracy and reduces time spent characterising shallow fluid-flow systems. Pockmarks as small as those with 1 m vertical relief were clearly visible and characterised by the Seabed Mapping Tool from seismic data, which have previously been mainly identified in multibeam and sonar data.

8.3 Conclusions of Chapter 6

- Hydrothermal vent complexes on the mid-Norwegian margin were diachronous in their formation, indicating that the associated greenhouse gas emissions attributed to the Paleocene-Eocene thermal maximum were emitted over a period of several million years, as opposed to one event at the Paleocene-Eocene boundary. At least four phases of magmatic intrusions are interpreted on the Modgunn Arch.
- The largest hydrothermal vent complexes tend to be fed by the deeper sills, but small hydrothermal vent complexes are not exclusively fed by shallow sills, therefore size of vent is not a direct indicator of depth of source.
- Three examples of stacked hydrothermal vent complexes are indicative of high-energy reactivation and hydrothermal fluid escape along established conduits.
- Amplitude anomalies located above hydrothermal vent complexes indicate that sills, dykes and hydrothermal vent complexes are important fluid focusing pathways, even long after their initial emplacement and formation.

Finally, fluid flow features may weaken or strengthen host strata and influence the amount of overpressure that can build up before the overburden is fractured – or refractured – and fluids migrate towards the surface. The Seabed Mapping Toolbox is an accurate and efficient way of identifying and characterising large pockmark fields, and can be used for other attributes such as amplitude. Buried fluid focusing features including pipes, pockmarks and hydrothermal vent complexes can act as fluid focusing structures for renewed, or later stages of fluid flow, both in the past and at present day.

References

6403/6-1. (2008). Retrieved January 27, 2020, from Factpages, Norwegian Petroleum Directorate website: https://factpages.npd.no/factpages/Default.aspx?culture=no

6405/7-1. (2005). Retrieved January 30, 2020, from Factpages, Norwegian Petroleum Directorate website: https://factpages.npd.no/factpages/Default.aspx?culture=no

7_1_1_Completion_Report. (1971). Oslo, Norway.

Aarnes, I., Podladchikov, Y., & Svensen, H. (2012). Devolatilization-induced pressure build-up: Implications for reaction front movement and breccia pipe formation. *Geofluids*, *12*(4), 265–279. https://doi.org/10.1111/j.1468-8123.2012.00368.x

Aarnes, Ingrid, Planke, S., Trulsvik, M., & Svensen, H. (2015). Contact metamorphism and thermogenic gas generation in the Vøring and Møre basins, offshore Norway, during the Paleocene–Eocene thermal maximum. *Journal of the Geological Society*, *172*(5), 588–598. https://doi.org/10.1144/jgs2014-098

Aarnes, Ingrid, Svensen, H., Polteau, S., & Planke, S. (2011). Contact metamorphic devolatilization of shales in the Karoo Basin, South Africa, and the effects of multiple sill intrusions. *Chemical Geology*, *281*(3–4), 181–194. https://doi.org/10.1016/j.chemgeo.2010.12.007

Agada, S., Jackson, S., Kolster, C., Dowell, N. Mac, Williams, G., Vosper, H., … Krevor, S. (2017). The impact of energy systems demands on pressure limited CO2 storage in the Bunter Sandstone of the UK Southern North Sea. *International Journal of Greenhouse Gas Control*, *65*(August), 128–136. https://doi.org/10.1016/j.ijggc.2017.08.014

Ahmadi, Z. M., Sawyers, M., Kenyon-Roberts, S., Stanworth, C. W., Kugler, K. A., Kristensen, J., & Fugelli, E. M. (2003). Paleocene. In *In: The Millennium Atlas: petroleum geology of the Central and Northern North Sea. Evans, D, Graham, C, Armour, A, and Bathurst, P (editors and co-ordinators). (London: The Geological Society of London).* (pp. 235–259).

Alves, T. M. (2012). Scale-relationships and geometry of normal faults reactivated during gravitational gliding of Albian rafts (Espírito Santo Basin, SE Brazil). *Earth and Planetary Science Letters*, *331–332*, 80–96. https://doi.org/10.1016/j.epsl.2012.03.014

Alves, T. M., & Elliott, C. (2014). Fluid flow during early compartmentalisation of rafts: A North Sea analogue for divergent continental margins. *Tectonophysics*. https://doi.org/10.1016/j.tecto.2014.07.015

Amado, L. (2013). Chapter 12: Field Case Evaluations. In *Reservoir Exploration and Appraisal* (pp. 53–156). https://doi.org/10.1016/b978-1-85617-853-2.00012-0

Anderson, E. M. (1905). The Dynamics of Faulting. *Geological Society, London, Special Publications, 8*(3), 387–402. https://doi.org/10.1144/SP367.16

Andresen, Katrine J., Huuse, M., & Clausen, O. R. (2008). Morphology and distribution of Oligocene and Miocene pockmarks in the Danish North Sea -implications for bottom current activity and fluid migration. *Basin Research*, *20*(3), 445–466. https://doi.org/10.1111/j.1365-2117.2008.00362.x

Andresen, Katrine J., Huuse, M., Schødt, N. H., Clausen, L. F., & Seidler, L. (2011). Hydrocarbon plumbing systems of salt minibasins offshore Angola revealed by three-dimensional seismic analysis. *AAPG Bulletin*, *95*(6), 1039–1065. https://doi.org/10.1306/12131010046

Andresen, Katrine Juul. (2012). Fluid flow features in hydrocarbon plumbing systems: What do they tell us about the basin evolution? *Marine Geology*, *332*, 89–108.

Andresen, Katrine Juul, & Huuse, M. (2011). "Bulls-eye" pockmarks and polygonal faulting in the Lower Congo Basin: Relative timing and implications for fluid expulsion during shallow burial. *Marine Geology*, *279*, 111–127. https://doi.org/10.1016/j.margeo.2010.10.016

Angkasa, S. S., Jerram, D. A., Millett, J. M., Svensen, H. H., Planke, S., Taylor, R. A., … Howell, J. (2017). Mafic intrusions, hydrothermal venting and the basalt-sediment transition: Linking onshore and offshore examples from the north atlantic igneous province. *Interpretation*, *5*(3), 83–101. https://doi.org/10.1190/int-2016-0162.1

Anka, Z., Loegering, M. ., di Primio, R., Marchal, D., Rodriquez, J. ., & Vallejo, E. (2014). Distribution and origin of natural gas leakage in the Colorado Basin , offshore Argentina Margin , South America : seismic interpretation and 3D basin modelling. *Geologica Acta*, *12*(4), 269–285. https://doi.org/10.1344/GeologicaActa2014.12.4.1

Archer, S., Ward, S., Menad, S., Shahim, I., Grant, N., Sloan, H., & Cole, A. (2009). The Jasmine Discovery, Central North Sea, UKCS. *Petroleum Geology: From Mature Basins to New Frontiers*, *7*, 1–19.

Armentrout, J. . (1999). Chapter 4: Sedimentary Basin Analysis. In *Treatise of Petroleum Geology/Handbook of Petroleum Geology: Exploring for Oil and Gas Traps* (pp. 4-1-4–123).

Arts, R. J., Vandeweijer, V. P., Hofstee, C., Pluymaekers, M. P. D., Loeve, D., Kopp, A., & Plug, W. J. (2012). The feasibility of CO2 storage in the depleted P18-4 gas field

offshore the Netherlands (the ROAD project). *International Journal of Greenhouse Gas Control*, *11*(SUPPL), 10–20. https://doi.org/10.1016/j.ijggc.2012.09.010

Bacon, M., Simm, R., & Redshaw, T. (2007). *3-D seismic interpretation*. Cambridge University Press.

Badley, M. E. (1985). *Practical seismic interpretation*. Boston, MA: United States: IHRDC Press.

Baristeas, N., Anka, Z., di Primio, R., Rodriguez, J. F., Marchal, D., & Dominguez, F. (2012). Distribution of hydrocarbon leakage indicators in the Malvinas Basin, offshore Argentine continental margin. *Marine Geology*, *332–334*, 56–74. https://doi.org/10.1016/j.margeo.2012.09.011

Barker, C. (1990). Calculated volume and pressure changes during the thermal cracking of oil to gas in reservoirs (1). *AAPG Bulletin*, *74*(8), 1254–1261.

Beaubouef, R. T., & Friedmann, S. J. (2000). High Resolution Seismic/Sequence Stratigraphic Framework for the Evolution of Pleistocene Intra Slope Basins, Western Gulf of Mexico: Depositional Models and Reservoir Analogs. *Deep-Water Reservoirs of the World: 20th Annual*, (September), 40–60. https://doi.org/10.5724/gcs.00.15.0040

Beget, J. E., & Addison, J. A. (2007). Methane gas release from the Storegga submarine landslide linked to early-Holocene climate change: A speculative hypothesis. *Holocene*, *17*(3), 291–295. https://doi.org/10.1177/0959683607076435

Berndt, C., Bünz, S., Clayton, T., Mienert, J., & Saunders, M. (2004). Seismic character of bottom simulating reflectors: Examples from the mid-Norwegian margin. *Marine and Petroleum Geology*, *21*(6), 723–733. https://doi.org/10.1016/j.marpetgeo.2004.02.003

Berndt, C., Bünz, S., & Mienert, J. (2003). Polygonal fault systems on the mid-Norwegian margin: a long-term source for fluid flow. *Subsurface Sediment Mobilisation, Geological Society, London, Special Publications*, *216*(1), 283–290. https://doi.org/10.1144/GSL.SP.2003.216.01.18

Bertoni, C., Kirkham, C., Cartwright, J., Hodgson, N., & Rodriguez, K. (2017). Seismic indicators of focused fluid flow and cross-evaporitic seepage in the Eastern Mediterranean. *Marine and Petroleum Geology*, *88*, 472–488.

Betzler, C., Lindhorst, S., Hübscher, C., Lüdmann, T., Fürstenau, J., & Reijmer, J. (2011). Giant pockmarks in a carbonate platform (Maldives, Indian Ocean). *Marine Geology*, *289*, 1–16. https://doi.org/10.1016/j.margeo.2011.09.004

Biondi, B. (2006). *3D Seismic Imaging*. Society of Exploration Geophysicists Tulsa.

Birch, P., & Haynes, J. (2003). The Pierce Field, Blocks 23/22a, 23/27, UK North Sea.

Geological Society, London, Memoirs, (20), 647–659.

Bird, D. E., Burke, K., Hall, S. A., & Casey, J. F. (2005). Gulf of Mexico tectonic history: Hotspot tracks, crustal boundaries, and early salt distribution. *AAPG Bulletin*, *89*(3), 311–328. https://doi.org/10.1306/10280404026

Bischoff, A., Nicol, A., Cole, J., & Gravley, D. (2019). Stratigraphy of Architectural Elements of a Buried Monogenetic Volcanic System. *Open Geosciences*, *11*(1), 581–616. https://doi.org/10.1515/geo-2019-0048

Bishop, D. J., Buchanan, P. G., & Bishop, C. J. (1995). Gravity-driven thin-skinned extension above Zechstein Group evaporites in the western central North Sea: an application of computer-aided section restoration techniques. *Marine and Petroleum Geology*, *12*(2), 115–135. https://doi.org/10.1016/0264-8172(95)92834-J

Bjørlykke, K., & Høeg, K. (1997). Effects of burial diagenesis on stresses, compaction and fluid flow in sedimentary basins. *Marine and Petroleum Geology*, *14*(3), 267–276. https://doi.org/10.1016/S0264-8172(96)00051-7

Boswell, R., Collett, T. S., Frye, M., Shedd, W., McConnell, D. R., & Shelander, D. (2012). Subsurface gas hydrates in the northern Gulf of Mexico. *Marine and Petroleum Geology*, *34*(1), 4–30. https://doi.org/10.1016/j.marpetgeo.2011.10.003

Bott, M. H. P. (1959). The Mechanics of Oblique Slip Faulting. *Geological Magazine*, *96*(02), 109. https://doi.org/10.1017/S0016756800059987

Böttner, C., Berndt, C., Reinardy, B. T. I., Geersen, J., Karstens, J., Bull, J. M., … Haeckel, M. (2019). Pockmarks in the Witch Ground Basin, Central North Sea. *Geochemistry, Geophysics, Geosystems*, *20*(4), 1698–1719. https://doi.org/10.1029/2018GC008068

Brekke, H., Dahlgren, S., Nyland, B., & Magnus, C. (1999). The prospectivity of the Vøring and Møre basins on the Norwegian Sea continental margin. *Petroleum Geology Conference Proceedings*, *5*(0), 261–274. https://doi.org/10.1144/0050261

Brekke, Harald. (2000). The tectonic evolution of the Norwegian Sea Continental Margin with emphasis on the Vøring and Møre Basins. In *Geological Society, London, Special Publications* (Vol. 167). https://doi.org/10.1144/gsl.sp.2000.167.01.13

Brothers, D. S., Ruppel, C., Kluesner, J. W., Ten Brink, U. S., Chaytor, J. D., Hill, J. C., … Flores, C. (2014). Seabed fluid expulsion along the upper slope and outer shelf of the U.S. Atlantic continental margin. *Geophysical Research Letters*, *41*(1), 96–101. https://doi.org/10.1002/2013GL058048

Brown, A. (2003). Capillary effects on fault-fill sealing. *AAPG Bulletin*, *87*(3), 381–395.

Brown, A. R., & Abriel, W. L. (2014). Detection of hydrocarbons using non-bright-spot

seismic techniques. *Interpretation SEG*, *2*(4), SP41–SP44.

Brown, A.R. (2004). *Interpretation of three-dimensional seismic data*. American Association of Petroleum Geologists, Tulsa.

Brown, Alistair R. (2011). *Interpretation of Three-Dimensional Seismic Data*. Society of Exploration Geophysicists and American Association of Petroleum Geologists.

Brown, M. (1990). The Nature and Hydrogeologic Significance of Mud Diapirs and Diatremes for Accretionary Systems. *Journal of Geophysical Research*, *95*, 8969–8982.

Bryan, S. E., & Ernst, R. E. (2008). Revised definition of Large Igneous Provinces (LIPs). *Earth-Science Reviews*, *86*(1–4), 175–202. https://doi.org/10.1016/j.earscirev.2007.08.008

Carminati, E., Scrocca, D., & Doglioni, C. (2010). Compaction-induced stress variations with depth in an active anticline: Northern Apennines, Italy. *Journal of Geophysical Research: Solid Earth*, *115*(2), 1–17. https://doi.org/10.1029/2009JB006395

Cartwright, J. (2007). The impact of 3D seismic data on the understanding of compaction, fluid flow and diagenesis in sedimentary basins. *Journal of the Geological Society*, *164*(5), 881–893. https://doi.org/10.1144/0016-76492006-143

Cartwright, J. (2011). Diagenetically induced shear failure of fine-grained sediments and the development of polygonal fault systems. *Marine and Petroleum Geology*, *28*(9), 1593–1610. https://doi.org/10.1016/j.marpetgeo.2011.06.004

Cartwright, J. A., & Dewhurst, D. N. (1998). Layer-bound compaction faults in fine-grained sediments. *Bulletin of the Geological Society of America*, *110*(10), 1242–1257. https://doi.org/10.1130/0016-7606(1998)110<1242:LBCFIF>2.3.CO;2

Cartwright, J., Huuse, M., & Aplin, A. (2007). Seal bypass systems. *AAPG Bulletin*, *91*(8), 1141–1166. https://doi.org/10.1306/04090705181

Cartwright, J., James, D., & Bolton, A. (2003). The genesis of polygonal fault systems: A review. *Geological Society Special Publication*, *216*, 223–234. https://doi.org/10.1144/GSL.SP.2003.216.01.15

Cartwright, J., & Santamarina, C. (2015). Seismic characteristics of fluid escape pipes in sedimentary basins: Implications for pipe genesis. *Marine and Petroleum Geology*, *65*, 126–140. https://doi.org/10.1016/j.marpetgeo.2015.03.023

Cathles, L. M., Su, Z., & Chen, D. (2010). The physics of gas chimney and pockmark formation, with implications for assessment of seafloor hazards and gas sequestration. *Marine and Petroleum Geology*, *27*(1), 82–91. https://doi.org/10.1016/j.marpetgeo.2009.09.010

Chaika, C., & Dvorkin, J. (2000). Porosity reduction during diagenesis of diatomaceous rocks. *AAPG Bulletin*, *84*(8), 1173–1184. https://doi.org/10.1306/a9673c70-1738-11d7-8645000102c1865d

Charles, R., & Ryzhikov, K. (2015). Merganser Field: managing subsurface uncertainty during the development of a salt diapir field in the UK Central North Sea. *Geological Society, London, Special Publications*, *403*.

Chen, J., Song, H., Guan, Y., Yang, S., Pinheiro, L. M., Bai, Y., … Geng, M. (2015). Morphologies, classification and genesis of pockmarks, mud volcanoes and associated fluid escape features in the northern Zhongjiannan Basin, South China Sea. *Deep-Sea Research Part II: Topical Studies in Oceanography*, *122*, 106–117. https://doi.org/10.1016/j.dsr2.2015.11.007

Clark, J. A., Cartwright, J. A., & Stewart, S. A. (1999). Mesozoic dissolution tectonics on the West Central Shelf, UK Central North Sea. *Marine and Petroleum Geology*, *16*(3), 283–300. https://doi.org/10.1016/S0264-8172(98)00040-3

Clark, P. J., & Evans, F. C. (1954). Distance to Nearest Neighbor as a Measure of Spatial Relationships in Populations Stable. *Ecology*, *35*(4), 445–453.

Cobbold, P. R., & Szatmari, P. (1991). Radial gravitational gliding on passive margins. *Tectonophysics*, *188*(3–4), 249–289. https://doi.org/10.1016/0040-1951(91)90459-6

Conn, P., & Arthur, J. (1990). *Safety in offshore drilling: the role of shallow gas surveys* (D. A. Ardus & C. D. Green, Eds.). Dordrecht: Kluwer Academic Publishers.

Copestake, P., Sims, A. P., Crittenden, S., Hamar, G. P., Ineson, J. R., Rose, P. T., & Tringham, M. E. (2003). Lower Cretaceous. In *In: The Millennium Atlas: petroleum geology of the Central and Northern North Sea. Evans, D, Graham, C, Armour, A, and Bathurst, P (editors and co-ordinators). (London: The Geological Society of London).* (pp. 191–211).

Coward, M. P., Dewey, J. F., Hempton, M., Holroyd, J., & Mange, M. A. (2003). Tectonic Evolution. In D. Evans, C. Graham, A. Armour, & P. Bathurst (Eds.), *The Millennium Atlas: petroleum geology of the central and northern North Sea.* (pp. 17–33). London: The Geological Society of London.

Dalland, A., Worsley, D., & Ofstas, K. (1988). *Bulletin 4 Mesozoic-Cenozoic Mid-Northern Norway.pdf*.

Davies, R., Bell, B. R., Cartwright, J. A., & Shoulders, S. (2002). Three-dimensional seismic imaging of Paleogene dike-fed submarine volcanoes from the northeast Atlantic margin. *Geology*, *30*(3), 223–226. https://doi.org/10.1130/0091-

7613(2002)030<0223:TDSIOP>2.0.CO;2

Davies, R. J., & Cartwright, J. (2002). A fossilized Opal A to Opal C/T transformation on the northeast Atlantic margin: Support for a significantly elevated palaeogeothermal gradient during the Neogene? *Basin Research*, *14*(4), 467–486. https://doi.org/10.1046/j.1365-2117.2002.00184.x

De Clippele, L. H., Gafeira, J., Robert, K., Hennige, S., Lavaleye, M. S., Duineveld, G. C. A., … Roberts, J. M. (2017). Using novel acoutic and visual mapping tools to predict the small-scale spatial distribution of live biogenic reef framework in cold-water coral habitats. *Springer*, *Coral Reef*(36), 255–268.

de Mahiques, M. M., Schattner, U., Lazar, M., Sumida, P. Y. G., & Souza, L. A. P. de. (2017). An extensive pockmark field on the upper Atlantic margin of Southeast Brazil: spatial analysis and its relationship with salt diapirism. *Heliyon*, (e00257), 1–21. https://doi.org/10.1016/j.heliyon.2017.e00257

Deegan, C. E., & Scull, B. J. (1977). A proposed standard lithostratigraphic nomenclature for the central and northern North Sea. *Report of the Institute of Geological Sciences*.

Demercian, S., Szatmari, P., & Cobbold, P. R. (1993). Style and pattern of salt diapirs due to thin-skinned gravitational gliding, Campos and Santos basins, offshore Brazil. *Tectonophysics*, *228*, 393–433. https://doi.org/10.1016/0040-1951(93)90351-J

Dewhurst, D. N., & Jones, R. M. (2003). Influence of physical and diagenetic processes on fault geomechanics and reactivation. *Journal of Geochemical Exploration*, *78–79*(03), 153–157. https://doi.org/10.1016/S0375-6742(03)00124-9

Dimitrov, L. I., & Dontcheva, V. (1994). Bulletin of the Geological Society of Denmark, Vol. 41/1 pp. 24-33. *Bulletin of the Geological Society of Denmark*, *41*, 24–33.

Dimitrov, L., & Woodside, J. (2003). Deep sea pockmark environments in the eastern Mediterranean. *Marine Geology*, *195*, 263–276. https://doi.org/10.1016/S0025-3227(02)00692-8

Doré, A. G., Lundin, E. R., Fichler, C., & Olesen, O. (1997). Patterns of basement structure and reactivation along the NE Atlantic margin. *Journal of the Geological Society, London*, *154*, 85–92.

Dow, W. G., Yukler, M. A., Senftle, J. T., Kennicutt, M. C., & Armentrout, J. . (1990). Miocene oil source beds in the East Breaks basin, Flex-Trend, offshore Texas. *Gulf Coast Section SEPM 9th Annual Research Conference*, 139–150.

Dralus, D. (2013). *Chemical Interactions between Silicates and Their Pore Fluids: How They Affect Rock Physics Properties from Atomic to Reservoir Scales*. Stanford University.

Duncan, L., Helland, D., & Dennehy, C. (2009). The Rosebank Discovery. A new play type in intra basalt reservoirs of the North Atlantic volcanic province. *Devex 2009*, (May).

Eckert, A., Liu, X., & Connolly, P. (2016). Pore pressure evolution and fluid flow during visco-elastic single-layer buckle folding. *Geofluids*, *16*(2), 231–248. https://doi.org/10.1111/gfl.12145

Eichhubl, P., Greene, H. G., Naehr, T., & Maher, N. (2000). Structural control of fluid flow: offshore fluid seepage in the Santa Barbara Basin, California. *Journal of Geochemical Exploration*, *69–70*, 545–549.

Eide, C. H., Schofield, N., Lecomte, I., Buckley, S. J., & Howell, J. A. (2018). Seismic interpretation of sill complexes in sedimentary basins: implications for the sub-sill imaging problem. *Journal of the Geological Society*, *175*(2), 193–209. https://doi.org/10.1144/jgs2017-096

Eiken, O., Ringrose, P., Hermanrud, C., Nazarian, B., Torp, T. A., & Høier, L. (2011). Lessons Learned from 14 years of CCS Operations: Sleipner, In Salah and Snohvit. *Energy Procedia*, *4*, 5541–5548. https://doi.org/10.1016/j.egypro.2011.02.541

Erratt, D., Thomas, G. ., & Wall, G. R. . (1999). The evolution of the Central North Sea Rift. *Petroleum Geology of Northwest Europe: Proceedings of the 5th Conference on Petroleum Geology of NW. Europe, at the Barbican Centre, London*, 63–82.

Evans, B. J. (1997). *A handbook for seismic data acquisition in exploration. Society of exploration geophysicists* (Geophysica).

Feng, J. (1995). *Post mid-Cretaceous seismic stratigraphy and depositional history, deep Gulf of Mexico* (p. 253). p. 253. University of Texas at Austin, Austin, Texas.

Ferrill, D. A., & Morris, A. P. (2003). Erratum to: "Dilational normal faults." *Journal of Structural Geology*, *25*(5), 827. https://doi.org/10.1016/s0191-8141(02)00196-7

Ferrill, D. A., Morris, A. P., McGinnis, R. N., Smart, K. J., Wigginton, S. S., & Hill, N. J. (2017). Mechanical stratigraphy and normal faulting. *Journal of Structural Geology*, *94*, 275–302. https://doi.org/10.1016/j.jsg.2016.11.010

Finkbeiner, T., Zoback, M., Flemings, P., & Stump, B. (2001). Stress, pore pressure, and dynamically constrained hydrocarbon columns in the South Eugene Island 330 field, northern Gulf of Mexico. *AAPG Bulletin*, *85*(6), 1007–1031.

Fisher, Q. J., & Knipe, R. J. (1998). Fault sealing processes in siliciclastic sediments. *Geological Society Special Publication*, *147*, 117–134. https://doi.org/10.1144/GSL.SP.1998.147.01.08

Fjeldskaar, W., Helset, H. M., Johansen, H., Grunnaleite, I., & Horstad, I. (2008). Thermal

modelling of magmatic intrusions in the Gjallar Ridge, Norwegian Sea: Implications for vitrinite reflectance and hydrocarbon maturation. *Basin Research*, *20*(1), 143–159. https://doi.org/10.1111/j.1365-2117.2007.00347.x

Fowler, S. R., Mildenhall, J., Zalova, S., Riley, G., Elsley, G., Desplanques, A., & Guliyev, F. (2000). Mud volcanoes and structural development on Shah Deniz. *Journal of Petroleum Science and Engineering*, *28*(4), 189–206. https://doi.org/10.1016/S0920-4105(00)00078-4

Franke, D. (2013). Rifting, lithosphere breakup and volcanism: Comparison of magma-poor and volcanic rifted margins. *Marine and Petroleum Geology*, *43*, 63–87. https://doi.org/10.1016/j.marpetgeo.2012.11.003

Fraser, S. I., Robinson, A. M., Johnson, H. D., Underhill, J. R., Kadolsky, D. G. A., Connell, R., … Ravnås, R. (2002). Upper Jurassic. In *In: The Millennium Atlas: petroleum geology of the Central and Northern North Sea. Evans, D, Graham, C, Armour, A, and Bathurst, P (editors and co-ordinators). (London: The Geological Society of London).* (pp. 157–189).

Frederiksen, S., Nielsen, S. B., & Balling, N. (2001). Post-Permian evolution of the Central North Sea: A numerical model. *Tectonophysics*, *343*(3–4), 185–203. https://doi.org/10.1016/S0040-1951(01)00224-4

Frehner, M. (2011). The neutral lines in buckle folds. *Journal of Structural Geology*, *33*(10), 1501–1508. https://doi.org/10.1016/j.jsg.2011.07.005

Furness, L. (2016). *Fractures of the Eumeralla Formation , Otway Ranges , Australia : Timing and Generation of Fluid Flow*. University of Adelaide.

Gafeira, J, Long, D., & Diaz-Doce, D. (2012). Semi-automated characterisation of seabed pockmarks in the Central North Sea. *Near Surface Geophysics*, *10*(4), 303–314.

Gafeira, Joana, Dolan, M., & Monteys, X. (2018). Geomorphometric Characterization of Pockmarks by Using a GIS-Based Semi-Automated Toolbox. *Geosciences*, *8*(5), 154. https://doi.org/10.3390/geosciences8050154

Galloway, W. E. (1989). Genetic stratigraphic sequences in basin analysis II: application to northwest Gulf of Mexico Cenozoic basin. *American Association of Petroleum Geologists Bulletin*, *73*(2), 143–154. https://doi.org/10.1306/703C9AFA-1707-11D7-8645000102C1865D

Galloway, W.E., Ganey-Curry, P. E., Li, X., & Buffler, R. T. (2000). Cenozoic depositional history of the Gulf of Mexico basin. *AAPG Bulletin*, *84*(11), 1743–1774.

Galloway, William E. (2008). Chapter 15 Depositional Evolution of the Gulf of Mexico

Sedimentary Basin. In *Sedimentary Basins of the World* (Vol. 5). https://doi.org/10.1016/S1874-5997(08)00015-4

Gao, D. (2009). 3D seismic volume visualization and interpretation: An integrated workflow with case studies. *Geophysics*, *74*(1), W1–W12. https://doi.org/10.1190/1.3002915

Gay, A., Lopez, M., Cochonat, P., Séranne, M., Levaché, D., & Sermondadaz, G. (2006). Isolated seafloor pockmarks linked to BSRs, fluid chimneys, polygonal faults and stacked Oligocene-Miocene turbiditic palaeochannels in the Lower Congo Basin. *Marine Geology*, *226*(1–2), 25–40. https://doi.org/10.1016/j.margeo.2005.09.018

Gay, A., Lopez, M., Cochonat, P., Sultan, N., Cauquil, E., & Brigaud, F. (2003). Sinuous pockmark belt as indicator of a shallow buried turbiditic channel on the lower slope of the Congo basin, West African margin. *Subsurface Sediment Mobilization*, *216*(1), 173–190. https://doi.org/10.1144/gsl.sp.2003.216.01.12

Gay, Aurélien, Lopez, M., Cochonat, P., & Sermondadaz, G. (2004). Polygonal faults-furrows system related to early stages of compaction - upper Miocene to recent sediments of the Lower Congo Basin. *Basin Research*, *16*(1), 101–116. https://doi.org/10.1111/j.1365-2117.2003.00224.x

Geldof, J.-B., Gafeira, J., Contet, J., & Marquet, S. (2014). GIS Analysis Of Pockmarks From 3D Seismic Exploration Surveys. *Offshore Technology Conference*, *25088*, 1–10.

Gibb, F. G. F., & Kanaris-Sotiriou, R. (1988). The geochemistry and origin of the Faeroe-Shetland sill complex. *Geological Society Special Publication*, *39*(39), 241–252. https://doi.org/10.1144/GSL.SP.1988.039.01.22

Glennie, K. ., & Underhill, J. . (1998). Origin, development and evolution of structural styles. In *Petroleum geology of the North Sea: Basic concepts and recent advances*. https://doi.org/10.1002/9781444313413.ch2

Glennie, K. W. (1998). Lower Permian - Rotliegend. In *Petroleum Geology of the North Sea: Basic Concepts and Recent Advances: Fourth Edition* (pp. 137–173). https://doi.org/10.1002/9781444313413.ch5

Gluyas, J., & Swarbrick, R. (2013). *Petroleum Geoscience*. John Wiley & Sons.

Goldsmith, P. J., Hudson, G., & Van Veen, P. (2003). *Goldsmith et al., 2003.pdf*.

Gómez, M., & Vergés, J. (2005). Quantifying the contribution of tectonics vs. differential compaction in the development of domes along the Mid-Norwegian Atlantic margin. *Basin Research*, *17*(2), 289–310. https://doi.org/10.1111/j.1365-2117.2005.00264.x

Griffith, A. E. (1924). Theory of rupture. In C. B. Biezeno & J. M. Burgers (Eds.), *Proceedings of the First International Congress on Applied Mechanics, Waltman, Delft*

(pp. 53–63).

Gross, O. P., Hood, K. C., Wenger, L. M., & Harrison, S. C. (1995). Seismic imaging and analysis of source and migration within an integrated hydrocarbon system study, northern Gulf of Mexico Basin. *1st Latin American Geophysical Conference*, 1–4.

Hackley, P. C., & Ewing, T. E. (2010). Assessment of undiscovered conventional oil and gas resources, onshore Claiborne Group, United Statespart of the northern Gulf of Mexico Basin. *AAPG Bulletin*, *94*(10), 1607–1636. https://doi.org/10.1306/04061009139

Hafeez, A., Planke, S., Jerram, D. A., Millett, J. M., Maharjan, D., & Prestvik, T. (2017). Upper paleocene ultramafic igneous rocks offshore mid-Norway: Re-interpretation of the vestbrona formation as a sill complex. *Interpretation*, *5*(3), 103–120. https://doi.org/10.1190/int-2016-0143.1

Hamilton, R. V., & Minshell, B. J. (2019). Hydrothermal vents and seismic anomalies: Implications for the petroleum system NE of Shetland. *Petroleum Geoscience*, *25*(1), 90–101. https://doi.org/10.1144/petgeo2017-072

Hancock, P. L. (1985). Brittle microtectonics: principles and practice. *Journal of Structural Geology*, *7*(3–4), 437–457. https://doi.org/10.1016/0191-8141(85)90048-3

Hansen, D. M. (2006). The morphology of intrusion-related vent structures and their implications for constraining the timing of intrusive events along the NE Atlantic margin. *Journal of the Geological Society*, *163*(5), 789–800. https://doi.org/10.1144/0016-76492004-167

Hansen, D. M., & Cartwright, J. (2006). Saucer-shaped sill with lobate morphology revealed by 3D seismic data: implications for resolving a shallow-level sill emplacement mechanism. *Journal of the Geological Society*, *163*(3), 509–523. https://doi.org/10.1144/0016-764905-073

Hansen, Dorthe Møller, & Cartwright, J. (2006). The three-dimensional geometry and growth of forced folds above saucer-shaped igneous sills. *Journal of Structural Geology*, *28*(8), 1520–1535. https://doi.org/10.1016/j.jsg.2006.04.004

Hansen, J. P. V, Cartwright, J. A., Huuse, M., & Clausen, O. R. (2005). 3D seismic expression of fluid migration and mud remobilization on the Gjallar Ridge, offshore mid-Norway. *Basin Research*, *17*(1), 123–139. https://doi.org/10.1111/j.1365-2117.2005.00257.x

Harilal, & Biswal, S. . (2010). Pitfalls in seismic amplitude interpretation: Lessons from Oligocene channel sandstones. *The Leading Edge, SEG*, *29*(4), 384–390.

Hart, B. S. (1999). Definition of subsurface stratigraphy, structure and rock properties from 3-

D seismic data. *Earth Science Reviews*, *47*(3–4), 189–218. https://doi.org/10.1016/S0012-8252(99)00029-X

Hasiotis, T., Papatheodorou, G., Kastanos, N., & Ferentinos, G. (1996). A pockmark field in the Patras Guld (Greece) and its activation during the 14/7/93 seismic event. *Marine Geology*, *130*, 333–344.

Hay, S., Jones, C. M., Barker, F., & He, Z. (2005). *Exploration of unproven plays; Mid North Sea High.* Retrieved from https://www.og.decc.gov.uk/UKpromote/posters/expl_unp_plays.htm

Hearon Iv, T. E., Rowan, M. G., Giles, K. A., & Hart, W. H. (2014). Halokinetic deformation adjacent to the deepwater Auger diapir , Garden Banks 470 , northern Gulf of Mexico : Testing the applicability of an outcrop- based model using subsurface data. *Interpretation*, (November). https://doi.org/10.1190/INT-2014-0053.1

Heggland, R. (1998). Gas seepage as an indicator of deeper prospective reservoirs. A study based on exploration 3D seismic data. *Marine and Petroleum Geology*, *15*(1), 1–9. https://doi.org/10.1016/S0264-8172(97)00060-3

Hein, J. R., Scholl, D. W., Barron, J. A., Jones, M. G., & Miller, J. (1978). Diagenesis of late Cenozoic diatomaceous deposits and formation of the bottom simulating reflector in the southern Bering Sea. *Sedimentology*, *25*(2), 155–181. https://doi.org/10.1111/j.1365-3091.1978.tb00307.x

Henry, S. (2004). Understanding Seismic Amplitudes. *Search and Discovery*, (40135), 1–7.

Hermansen, H., Landa, G. H., Sylte, J. E., & Thomas, L. K. (2000). Experiences after 10 years of waterflooding the Ekofisk Field, Norway. *Journal of Petroleum Science and Engineering*, *26*(1–4), 11–18. https://doi.org/10.1016/S0920-4105(00)00016-4

Hill, D. P. (1977). A model for earthquake swarms. *Journal of Geophysical Research*, *82*(8), 1347–1352.

Hill, P. J., & Wood, G. V. (1980). Geology of the Forties field, UK continental shelf, North Sea. *AAPG Special Volumes*, 81–93. Retrieved from http://archives.datapages.com/data/specpubs/fieldst2/data/a012/a012/0001/0050/0081.htm

Hjelstuen, B. O., Eldholm, O., & Skogseid, J. (1999). Cenozoic evolution of the northern Voring margin. *GSA Bulletin*, *111*(12), 1792–1807.

Ho, S., Cartwright, J. A., & Imbert, P. (2012). Vertical evolution of fluid venting structures in relation to gas flux, in the Neogene-Quaternary of the Lower Congo Basin, Offshore Angola. *Marine Geology*, *332–334*, 40–55. https://doi.org/10.1016/j.margeo.2012.08.011

Ho, Sutieng, Hovland, M., Blouet, J., Wetzel, A., & Imbert, P. (2018). Formation of linear planform chimneys controlled by preferential hydrocarbon leakage and anisotropic stresses in faulted fine-grained sediments , offshore Angola. *Solid Earth*, *9*, 1437–1468.

Hodgson, N. A., Farnsworth, J., & Fraser, A. J. (1992). Salt-related tectonics, sedimentation and hydrocarbon plays in the Central Graben, North Sea, UKCS. *Geological Society, London, Special Publications*, *67*(1), 31–63. https://doi.org/10.1144/GSL.SP.1992.067.01.03

Høiland, O., Kristensen, J., & Monsen, T. (1993). Mesozoic evolution of the Jaeren High area, Norwegian Central North Sea. *Petroleum Geology of Northwest Europe: Proceedings of the 4th Conference on Petroleum Geology of NW. Europe, at the Barbican Centre, London*, 1189–1195. https://doi.org/10.1144/0041189

Holford, S. P., Schofield, N., & Reynolds, P. (2017). Subsurface fluid flow focused by buried volcanoes in sedimentary basins: Evidence from 3D seismic data, Bass Basin, offshore southeastern Australia. *Interpretation*, *5*(3), SK39–SK50. https://doi.org/10.1190/int-2016-0205.1

Holford, S., Schofield, N., MacDonald, J., Duddy, I., & Green, P. (2012). Seismic analysis of igneous systems in sedimentary basins and their impacts on hydrocarbon prospectivity: examples from the southern Australian margin. *The APPEA Journal*, *52*(1), 229. https://doi.org/10.1071/aj11017

Hood, K. C., Wenger, L. M., Gross, O. P., & Harrison, S. C. (2002). Hydrocarbon systems analysis of the northern Gulf of Mexico: Delineation of hydrocarbon migration pathways using seeps and seismic imaging. *Surface Exploration Case Histories: Applications of Geochemistry, Magnetics, and Remote Sensing: AAPG Studies in Geology*, *48*(1), 25–40. Retrieved from http://www.oilfield.searchanddiscovery.com/documents/hood/%5Cnpapers2://publication/uuid/F7DF6868-6F13-46AE-A48A-9DAA76E04C02

Hovland, M., Gardner, J. V., & Judd, A. G. (2002). The significance of pockmarks to understanding fluid flow processes and geohazards. *Geofluids*, *2*(2), 127–136. https://doi.org/10.1046/j.1468-8123.2002.00028.x

Hovland, Martin, & Judd, a. G. (1988). *Seabed pockmarks and seepages — impact on geology, biology and the marine environment*. https://doi.org/10.1016/0264-8172(89)90010-X

Hovland, Martin, Svensen, H., Forsberg, C. F., Johansen, H., Fichler, C., Fosså, J. H., … Rueslåtten, H. (2005). Complex pockmarks with carbonate-ridges off mid-Norway:

Products of sediment degassing. *Marine Geology*, *218*(1–4), 191–206. https://doi.org/10.1016/j.margeo.2005.04.005

Howarth, V., & Alves, T. M. (2016). Fluid flow through carbonate platforms as evidence for deep-seated reservoirs in Northwest Australia. *Marine Geology*. https://doi.org/10.1016/j.margeo.2016.06.011

Hudec, M. R., & Jackson, M. P. A. (2007). Terra infirma: Understanding salt tectonics. *Earth-Science Reviews*, *82*(1–2), 1–28. https://doi.org/10.1016/j.earscirev.2007.01.001

Hudec, M. R., Jackson, M. P. A., & Peel, F. J. (2013). Influence of deep Louann structure on the evolution of the northern Gulf of Mexico. *AAPG Bulletin*, *97*(10), 1711–1735. https://doi.org/10.1306/04011312074

Hudec, M. R., Jackson, M. P. A., & Schultz-Ela, D. D. (2009). The paradox of minibasin subsidence into salt: Clues to the evolution of crustal basins. *Bulletin of the Geological Society of America*, *121*(1–2), 201–221. https://doi.org/10.1130/B26275.1

Hudec, M. R., Norton, I. O., Jackson, M. P. A., & Peel, F. J. (2013). Jurassic evolution of the Gulf of Mexico salt basin. *AAPG Bulletin*, *97*(10), 1683–1710. https://doi.org/10.1306/04011312073

Hustoft, S., Bünz, S., Mienert, J., & Chand, S. (2009). Gas hydrate reservoir and active methane-venting province in sediments on < 20 Ma young oceanic crust in the Fram Strait, offshore NW-Svalbard. *Earth and Planetary Science Letters*, *284*(1–2), 12–24. https://doi.org/10.1016/j.epsl.2009.03.038

Hutchinson, D., Ruppel, C., Roberts, H., Carney, R., & Smith, M. (2011). Gas hydrates in the Gulf of Mexico. In C. Holmes (Ed.), *Gulf of Mexico: Its Origin, Waters, and Biota* (pp. 247–275). Texas A&M University Press.

Huuse, M., Jackson, C. A. L., Van Rensbergen, P., Davies, R. J., Flemings, P. B., & Dixon, R. J. (2010). Subsurface sediment remobilization and fluid flow in sedimentary basins: An overview. *Basin Research*, (22), 342–360. https://doi.org/10.1111/j.1365-2117.2010.00488.x

Huuse, M., & Mickelson, M. (2004). Eocene sandstone intrusions in the Tampen Spur area (Norwegian North Sea Quad 34) imaged by 3D seismic data. *Marine and Petroleum Geology*, *21*(2), 141–155. https://doi.org/10.1016/j.marpetgeo.2003.11.018

Iyer, K., Schmid, D. W., Planke, S., & Millett, J. (2017). Modelling hydrothermal venting in volcanic sedimentary basins: Impact on hydrocarbon maturation and paleoclimate. *Earth and Planetary Science Letters*, *467*, 30–42. https://doi.org/10.1016/j.epsl.2017.03.023

Jackson, B. A. (2004). Seismic evidence for gas hydrates in the North Makassar Basin,

Indonesia. *Petroleum Geoscience*, *10*(3), 227–238. https://doi.org/10.1144/1354-079303-601

Jackson, J., & McKenzie, D. (1983). The geometrical evolution of normal fault systems. *Journal of Structural Geology*, *5*(5), 471–482. https://doi.org/10.1016/0191-8141(83)90053-6

Jackson, M. P. A., & Cramez, C. (1989). Seismic recognition of salt welds in salt tectonics regimes. *SEPM Gulf Coast Section Tenth Annual Research Conference Program and Abstracts*, 66–71.

Jackson, M. P A, & Talbot, C. J. (1986). External shapes, strain rates, and dynamics of salt structures. *Geological Society of America Bulletin*, *97*(3), 305–323. https://doi.org/10.1130/0016-7606(1986)97<305:ESSRAD>2.0.CO

Jackson, M P A, & Talbot, C. J. (1991). A glossary of salt tectonics. *Bureau of Economic Geology, University of Texas at Austin*.

Jackson, M P A, & Vendeville, B. C. (1994). Regional extension as a geologic trigger for diapirism. *Geological Society of America Bulletin*, *106*, 57–73.

Jackson, Martin P.A., & Hudec, M. R. (2017). *Salt Tectonics: Principles and Practice*. Cambridge University Press.

Jaeger, J. . (1958). *The solidification and cooling of intrusive sheets* (pp. 77–87). pp. 77–87. In Doletrites, a symposium. Tasmania Univ. Geol. Dept.

Jaeger, J. C., & Cook, N. G. W. (1979). *Fundamentals of rock mechanics.*

Jaeger, J. C., Cook, N. G. W., & Zimmerman, R. W. (2007). Fundamentals of Rock Mechanics. In *Practice of Intramedullary Locked Nails: New Developments in Techniques and Applications* (Fourth Edi). https://doi.org/10.1007/3-540-32345-7_3

Jamtveit, B., Svensen, H., Podladchikov, Y. Y., & Planke, S. (2004). Hydrothermal vent complexes associated with sill intrusions in sedimentary basins. *Geological Society, London, Special Publications*, *234*(1), 233–241. https://doi.org/10.1144/gsl.sp.2004.234.01.15

Jolly, R. J. H., & Lonergan, L. (2002). Mechanisms and controls on the formation of sand intrusions. *Journal of the Geological Society*, *159*(5), 605–617. https://doi.org/10.1144/0016-764902-025

Judd, A. G., & Hovland, M. (1992). The evidence of shallow gas in marine sediments. *Continental Shelf Research*, *12*(10), 1081–1095. https://doi.org/10.1016/0278-4343(92)90070-Z

Judd, A. G., & Hovland, M. (2007). Seabed fluid flow: The impact on geology, biology and

the marine environment. *New York, Campridge University Press*, 441. https://doi.org/10.1007/s00254-004-1086-0.

Judd, A., & Hovland, M. (2007). Seabed Fluid Flow. In *Seabed Fluid Flow: The Impact on Geology, Biology, and the Marine Environment*. https://doi.org/10.1017/CBO9780511535918

Kaiser, M. J. (2018). Review of Gulf of Mexico well activity highlights decline. *Offshore Magazine*, (9), 2017–2019.

Karlo, J. F., Buchem, F. S. P. Van, Moen, J., & Milroy, K. (2014). Salt tectonics and interpretation Triassic-age salt tectonics of the Central North Sea. *Interpretation*, *2*(4), 19–28.

Kearey, P., Brooks, M., & Hill, I. (2002). An Introduction to Geophysical Exploration. In *Blackwell Science Ltd*. https://doi.org/10.1029/EO067i011p00132-01

Kearey, P., Brooks, M., & Hill, I. (2013). *An introduction to geophysical exploration*. John Wiley & Sons.

Kearsey, T., Ellen, R., Millward, D., & Monaghan, A. A. (2015). *Devonian and Carboniferous stratigraphical correlation and interpretation in the Central North Sea, Quadrants 25 – 44*. British Geological Survey Commissioned Report, CR/15/117.

Kettermann, M., & Urai, J. L. (2015). Changes in structural style of normal faults due to failure mode transition: First results from excavated scale models. *Journal of Structural Geology*, *74*, 105–116. https://doi.org/10.1016/j.jsg.2015.02.013

Kidd, G. D. (2014). Fundamentals of 3-D seismic volume visualization. *Search and Discovery*, (120169), 1–4.

King, L. H., & MacLean, B. (1970). Pockmarks on the Scotian Shelf. *Bulletin of the Geological Society of America*, *81*, 3141–3148. https://doi.org/10.1130/0016-7606(1970)81[3141:POTSS]2.0.CO;2

Kjoberg, S., Schmiedel, T., Planke, S., Svensen, H. H., Millett, J. M., Jerram, D. A., … Helsem, A. (2017). 3D structure and formation of hydrothermal vent complexes at the Paleocene-Eocene transition, the Møre Basin, mid-Norwegian margin. *Interpretation*, *5*(3), SK65–SK81. https://doi.org/10.1190/INT-2016-0159.1

Koyi, H, Jenyon, M. K., & Petersen, K. (1993). The effect of basement faulting on diapirism. *Journal of Petroleum Geology*, *16*(3), 285–312. https://doi.org/10.1111/j.1747-5457.1993.tb00339.x

Koyi, Hemin. (1994). Estimation of salt thickness and restoration of cross-sections with diapiric structures: a few critical comments on two powerful methods. *Journal of*

Structural Geology, *16*(8), 1121–1128. https://doi.org/10.1016/0191-8141(94)90056-6

Kramer, K. V., & Shedd, W. W. (2017). *A 1.4-billion-pixel map of the Gulf of Mexico seafloor* (p. Eos, 98). p. Eos, 98. https://doi.org/https://doi.org/10.1029/2017EO073557

Krijgsman, W., Hilgen, F. J., Raffi, I., Sierro, F. J., & Wilson, D. S. (1999). Chronology , causes and progression of the Messinian salinity crisis. *Nature*, *400*(August), 652–655.

Kubala, M., Bastow, M., Thompson, S., Scotchman, I., & Oygard, K. (2003). Geothermal regime, petroleum generation and migration. *In Evans, D., Graham, C. Armour, A., and Bathurst, P., Eds., The Millenium Atlas: Petroleum Geology of the Central and Northern North Sea: The Geological Society, London*, 664–688.

Lasocki, J., Guemene, J.-M., Hedayati, A., Legorjus, C., & Page, W. M. (1999). The Elgin and Franklin fields: UK Blocks 22/30c, 22/30b and 29/5b. *Petroleum Geology of Northwest Europe: Proceedings of the 5th Conference on the Petroleum Geology of Northwest Europe*, *2*, 1007–1020.

Laubach, S. E., Eichhubl, P., Hilgers, C., & Lander, R. H. (2010). Structural diagenesis. *Journal of Structural Geology*, *32*(12), 1866–1872. https://doi.org/10.1016/j.jsg.2010.10.001

Laubach, S. E., Reed, R. M., Olson, J. E., Lander, R. H., & Bonnell, L. M. (2004). Coevolution of crack-seal texture and fracture porosity in sedimentary rocks: Cathodoluminescence observations of regional fractures. *Journal of Structural Geology*, *26*(5), 967–982. https://doi.org/10.1016/j.jsg.2003.08.019

Laubach, Stephen E., Olson, J. E., & Gale, J. F. W. (2004). Are open fractures necessarily aligned with maximum horizontal stress? *Earth and Planetary Science Letters*, *222*(1), 191–195. https://doi.org/10.1016/j.epsl.2004.02.019

Leeder, M. R., & Hardman, M. (1990). Carboniferous geology of the Southern North Sea Basin and controls on hydrocarbon prospectivity. *Geological Society, London, Special Publications*, *55*(1), 87–105. https://doi.org/10.1144/GSL.SP.1990.055.01.04

Li, B., Zhou, F., Li, H., Duguid, A., Que, L., Xue, Y., & Tan, Y. (2018). Prediction of CO 2 leakage risk for wells in carbon sequestration fields with an optimal artificial neural network. *International Journal of Greenhouse Gas Control*, *68*(18), 276–286. https://doi.org/10.1016/j.ijggc.2017.11.004

Lockett, G. (2018). Geothermal power: an alternate role for redundant North Sea platforms? Retrieved from Offshore Magazine website: https://www.offshore-mag.com/pipelines/article/16762144/geothermal-power-an-alternate-role-for-redundant-north-sea-platforms

Løseth, H, Gading, M., & Wensaas, L. (2009). Hydrocarbon leakage interpreted on seismic data. *Marine and Petroleum Geology*, *26*, 1304–1319. https://doi.org/10.1016/j.marpetgeo.2008.09.008

Løseth, Helge, Wensaas, L., Arntsen, B., Hanken, N. M., Basire, C., & Graue, K. (2011). 1000 M Long Gas Blow-Out Pipes. *Marine and Petroleum Geology*, *28*(5), 1040–1060. https://doi.org/10.1016/j.marpetgeo.2010.10.001

Lundin, E., & Doré, A. G. (2002). Mid-Cenozoic post-breakup deformation in the "passive" margins bordering the Norwegian-Greenland Sea. *Marine and Petroleum Geology*, *19*(1), 79–93. https://doi.org/10.1016/S0264-8172(01)00046-0

Magoon, L. B. (1989). The petroleum system - status of research and methods, 1990. *US Geological Survey Bulletin*, *1992*(88).

Magoon, L. B., & Dow, W. G. eds. (1994). The petroleum system - from source to trap. *AAPG Memoir*, *60*(655).

Maia, A. R., Cartwright, J., & Andersen, E. (2016). Shallow plumbing systems inferred from spatial analysis of pockmark arrays. *Marine and Petroleum Geology*, *77*, 865–881. https://doi.org/10.1016/j.marpetgeo.2016.07.029

Maia, A. R. D. (2017). *Controls on shallow plumbing systems inferred from the spatial analysis of pockmark arrays*. Cardiff University.

Mann, D. M., & Mackenzie, A. S. (1990). Prediction of pore fluid pressures in sedimentary basins. *Marine and Petroleum Geology*, *7*(1), 55–65. https://doi.org/10.1016/0264-8172(90)90056-M

Manton, B. M. (2015). *The Mechanics of Sill Propagation and Associated Venting, Investigated using 3D Seismic Data from Offshore Norway* (Cardiff University). Retrieved from https://www.researchgate.net/publication/339208100

Marfurt, K. J., & Alves, T. M. (2015). Pitfalls and limitations in seismic attribute interpretation of tectonic features. *Interpretation*, *3*(1), 5–15.

Marshak, S. (2016). Brittle Structures: Joints and Veins. Retrieved July 6, 2020, from Learning Geology website: http://geologylearn.blogspot.com/2016/03/brittle-structures.html

Masoumi, S., Reuning, L., Back, S., Sandrin, A., & Kukla, P. A. (2014). Buried pockmarks on the Top Chalk surface of the Danish North Sea and their potential significance for interpreting palaeocirculation patterns. *International Journal of Earth Sciences*, *103*(2), 563–578. https://doi.org/10.1007/s00531-013-0977-2

Mattos, N. H., & Alves, T. M. (2018). Corridors of crestal and radial faults linking salt diapirs

in the Espírito Santo Basin, SE Brazil. *Tectonophysics*, *728–729*(February), 55–74. https://doi.org/10.1016/j.tecto.2017.12.025

Mattos, N. H., Alves, T. M., & Omosanya, K. O. (2016). Crestal fault geometries reveal late halokinesis and collapse of the Samson Dome, Northern Norway: Implications for petroleum systems in the Barents Sea. *Tectonophysics*, *690*, 76–96. https://doi.org/10.1016/j.tecto.2016.04.043

Mazzini, A. (2009). Mud volcanism : Processes and implications. *Marine and Petroleum Geology*, *26*(9), 1677–1680. https://doi.org/10.1016/j.marpetgeo.2009.05.003

McBride, B. C., Rowan, M. G., & Weimer, P. (1998). The evolution of allochthonous salt systems, northern Green Canyon and Ewing Bank (offshore Louisiana), northern Gulf of Mexico. *AAPG Bulletin*, *82*(5 B), 1013–1036. https://doi.org/10.1306/1D9BC9FD-172D-11D7-8645000102C1865D

Mello, U. T., & Karner, G. D. (1996). Development of sediment overpressure and its effect on thermal maturation: Application to the Gulf of Mexico basin. *AAPG Bulletin*, *80*(9), 1367–1396. https://doi.org/10.1306/64ED9A42-1724-11D7-8645000102C1865D

Michael, K., Golab, A., Shulakova, V., Ennis-King, J., Allinson, G., Sharma, S., & Aiken, T. (2010). Geological storage of CO2 in saline aquifers-A review of the experience from existing storage operations. *International Journal of Greenhouse Gas Control*, *4*(4), 659–667. https://doi.org/10.1016/j.ijggc.2009.12.011

Miles, A., & Cartwright, J. (2010). Hybrid flow sills: A new mode of igneous sheet intrusion. *Geology*, *38*(4), 343–346. https://doi.org/10.1130/G30414.1

Milkov, A. V. (2000). *Worldwide distribution of submarine mud volcanoes and associated gas hydrates*. *167*, 29–42.

Milton-Worssell, R., Smith, K., McGrandle, A., Watson, J., & Cameron, D. (2010). The search for a Carboniferous petroleum system beneath the Central North Sea. *Petroleum Geology: From Mature Basins to New Frontiers—Proceedings of the 7th Petroleum Geology Conference*, *7*, 57–75. https://doi.org/10.1144/0070057

Mitchell, A. (2005). *The ESRI Guide to GIS Analysis*. ESRI Press.

Monaghan, A. A., Arsenikos, S., Quinn, M. F., Johnson, K. R., Vincent, C. J., Vane, C. H., … Williamson, J. P. (2017). Carboniferous petroleum systems around the Mid North Sea High, UK. *Marine and Petroleum Geology*, *88*, 282–302. https://doi.org/10.1016/j.marpetgeo.2017.08.019

Morley, C. K., King, R., Hillis, R., Tingay, M., & Backe, G. (2011). Deepwater fold and thrust belt classification, tectonics, structure and hydrocarbon prospectivity: A review.

Earth-Science Reviews, Elsevier, *104*, 41–91. https://doi.org/10.1130/GES00148.1

Morris, A. P., Ferrill, D. A., & McGinnis, R. N. (2016). Using fault displacement and slip tendency to estimate stress states. *Journal of Structural Geology*, *83*, 60–72. https://doi.org/10.1016/j.jsg.2015.11.010

Moss, J. L., & Cartwright, J. (2010). 3D seismic expression of km-scale fluid escape pipes from offshore Namibia. *Basin Research*, *22*(4), 481–501. https://doi.org/10.1111/j.1365-2117.2010.00461.x

Moss, J. L., Cartwright, J., Cartwright, A., & Moore, R. (2012). The spatial pattern and drainage cell characteristics of a pockmark field, Nile Deep Sea Fan. *Marine and Petroleum Geology*, *35*(1), 321–336. https://doi.org/10.1016/j.marpetgeo.2012.02.019

Neagu, R. C., Cartwright, J., Davies, R., & Jensen, L. (2010). Fossilisation of a silica diagenesis reaction front on the mid-Norwegian margin. *Marine and Petroleum Geology*, *27*(10), 2141–2155. https://doi.org/10.1016/j.marpetgeo.2010.09.003

Omosanya, Kamaldeen O., & Alves, T. M. (2013). A 3-dimensional seismic method to assess the provenance of Mass-Transport Deposits (MTDs) on salt-rich continental slopes (Espírito Santo Basin, SE Brazil). *Marine and Petroleum Geology*, *44*, 223–239. https://doi.org/10.1016/j.marpetgeo.2013.02.006

Omosanya, Kamaldeen O., Eruteya, O. E., Siregar, E. S. A., Zieba, K. J., Johansen, S. E., Alves, T. M., & Waldmann, N. D. (2018). Three-dimensional (3-D) seismic imaging of conduits and radial faults associated with hydrothermal vent complexes (Vøring Basin, Offshore Norway). *Marine Geology*, *399*(2017), 115–134. https://doi.org/10.1016/j.margeo.2018.02.007

Omosanya, Kamaldeen Olakunle, Maia, A. R., & Eruteya, O. E. (2020). Seismic, morphologic and scale variabilities of subsurface pipes and vent complexes in a magma-rich margin. *Bulletin of Volcanology*, *82*(6). https://doi.org/10.1007/s00445-020-01379-3

Osborne, M. J., & Swarbrick, R. E. (1997). Mechanisms for generating overpressure in sedimentary basins: a reevaluation: reply. *American Association of Petroleum Geologists Bulletin*, *82*(12), 2270–2271.

Palmer, A. N. (1991). Geological Society of America Bulletin Origin and morphology of limestone caves. *Geological Society Of America Bulletin*, *7606*(1), 1–21. https://doi.org/10.1130/0016-7606(1991)103<0001

Peel, F. J. (2014). How do salt withdrawal minibasins form? Insights from forward modelling, and implications for hydrocarbon migration. *Tectonophysics*, *630*(C), 222–235. https://doi.org/10.1016/j.tecto.2014.05.027

Penge, J., Munns, J. ., Taylor, B., & Windle, T. M. . (1999). Rift-raft tectonics: examples of gravitational tectonics from the Zechstein basins of northwest Europe. *Petroleum Geology of Northwest Europe: Proceedings of the 5th Conference*, 201–213.

Penge, J., Taylor, B., Huckerby, J. ., & Munns, J. . (1993). Extension and salt tectonics in the East Central Graben. *Petroleum Geology of Northwest Europe: Proceedings of the 4th Conference*, 1197–1209. https://doi.org/10.1007/BF00171455

Pepper, A. S., & Corvit, P. J. (1995). *Simple Kinetic Models of Petroleum Formation. Part I : oil and gas generation from kerogen*. *12*(3), 291–319.

Perry Jr, E. A., & Hower, J. (1972). Late-stage dehydration in deeply buried pelitic sediments. *AAPG Bulletin*, *56*(10), 2013–2021.

Pettingill, H. S., & Weimer, P. (2002). World-Wide Deepwater Exploration and Production: Past, Present and Future. *Proceedings of the Annual Offshore Technology Conference*, 371–376. https://doi.org/10.5724/gcs.01.21.0001

Picard, K., Radke, L., Williams, D., Nicholas, W., Siwabessy, P., Howard, F., … Nichol, S. (2018). Origin of High Density Seabed Pockmark Fields and Their Use in Inferring Bottom Currents. *Geosciences*, *8*(6), 195. https://doi.org/10.3390/geosciences8060195

Pietzsch, R., Oliveira, D. M., Tedeschi, L. R., Neto, J. V. Q., Figueiredo, M. F., Vazquez, J. C., & Schi, R. (2018). Palaeohydrology of the Lower Cretaceous pre-salt lacustrine system , from rift to post-rift phase , Santos Basin , Brazil. *Palaeogeography, Palaeoclimatology, Palaeoecology*, *507*(June), 60–80. https://doi.org/10.1016/j.palaeo.2018.06.043

Pilcher, R., & Argent, J. (2007). Mega-pockmarks and linear pockmark trains on the West African continental margin. *Marine Geology*, *244*, 15–32. https://doi.org/10.1016/j.margeo.2007.05.002

Planke, S., Rasmussen, T., Rey, S. S., & Myklebust, R. (2005). Seismic characteristics and distribution of volcanic intrusions and hydrothermal vent complexes in the Vøring and Møre basins. *In: Doré, A.G. & Vining, B.A. (Eds) Petroleum Geology: North-West Europe and Global Perspectives - Proceedings of the 6th Petroluem Geology Conference.*, 833–844.

Planke, S., Svensen, H., Myklebust, R., Bannister, S., Manton, B., & Lorenz, L. (2015). Geophysics and Remote Sensing. In Physical geology of shallow magmatic systems. *Springer.*, 131–146. https://doi.org/10.1007/11157

Pletsch, T., Appel, J., Botor, D., Clayton, C. J., Duin, E. J. T., Faber, E., … Van Bergen, F. (2010). Petroleum generation and migration. In J. C. Doornenbal & A. G. Stevenson

(Eds.), *Petroleum Geological Atlas of the Southern Permian Basin Area* (pp. 225–253). EAGE Publications b.v. (Houten).

Polteau, S., Mazzini, A., Galland, O., Planke, S., & Malthe-Sørenssen, A. (2008). Saucer-shaped intrusions: Occurrences, emplacement and implications. *Earth and Planetary Science Letters*, *266*(1–2), 195–204. https://doi.org/10.1016/j.epsl.2007.11.015

Prather, B. E., Booth, J. R., Steffens, G. S., & Craig, P. A. (1998). Classification, lithologic calibration, and stratigraphic succession of seismic facies of intraslope basins, deep-water Gulf of Mexico. *AAPG Bulletin*, *82*(5 A), 701–728. https://doi.org/10.1306/1D9BC5D9-172D-11D7-8645000102C1865D

Ramsay, J. . (1967). *Folding and fracturing of rocks*. Mc Graw Hill Book Company.

Rateau, R., Schofield, N., & Smith, M. (2013). The potential role of igneous intrusions on hydrocarbon migration, West of Shetland. *Petroleum Geoscience*, *19*(3), 259–272. https://doi.org/10.1144/petgeo2012-035

Rattey, R. P., & Hayward, A. B. (1993). Sequence stratigraphy of a failed rift system: the Middle Jurassic to Early Cretaceous basin evolution of the Central and Northern North Sea. *Petroleum Geology of Northwest Europe: Proceedings of the 4th Conference on Petroleum Geology of NW. Europe, at the Barbican Centre, London*, *1*, 215–249.

Reiche, S., Hjelstuen, B. O., & Haflidason, H. (2011). High-resolution seismic stratigraphy, sedimentary processes and the origin of seabed cracks and pockmarks at Nyegga, mid-Norwegian margin. *Marine Geology*, *284*(1–4), 28–39. https://doi.org/10.1016/j.margeo.2011.03.006

Reynolds, P., Planke, S., Millett, J. M., Jerram, D. A., Trulsvik, M., Schofield, N., & Myklebust, R. (2017). Hydrothermal vent complexes offshore Northeast Greenland: A potential role in driving the PETM. *Earth and Planetary Science Letters*, *467*, 72–78. https://doi.org/10.1016/j.epsl.2017.03.031

Rhys, G. H. (1974). A proposed standard lithostratigraphic nomenclature for the southern North Sea and an outline structural nomenclature for the whole of the (UK) North Sea. *Institute of Geological Sciences*, *74*(8), 14.

Rise, L., Bellec, V. K., Ch, S., & Bøe, R. (2014). Pockmarks in the southwestern Barents Sea and Finnmark fjords. *Norsk Geologisk Tidsskrift*, *94*(4), 263–282.

Roaldset, E., & He, W. (1995). *Silica-phase transformation of opal-A to opal-CT to quartz - an experimental approach.* Trondheim.

Roaldset, E., & Wei, H. (1997). Silica-phase transformation of opal-A to opal-CT to quartz, Part 2: Changes of physical properties. *Prepared for Submittal to AAPG*.

Rohrman, M. (2007). Prospectivity of volcanic basins: Trap delineation and acreage de-risking. *AAPG Bulletin*, *91*(6), 915–939. https://doi.org/10.1306/12150606017

Rollet, N., Logan, G. A., Ryan, G., Judd, A. G., Totterdell, J. M., Glenn, K., … Earl, K. L. (2009). Shallow gas and fluid migration in the northern Arafura Sea (offshore Northern Australia). *Marine and Petroleum Geology*, *26*(1), 129–147. https://doi.org/10.1016/j.marpetgeo.2007.07.010

Rowan, M. (2002). Do Salt Welds Seal? *Salt-Sediment Interactions and Hydrocarbon Prospectivity: Concepts, Applications, and Case Studies for the 21st Century*, 229–236.

Rowan, M G, Jackson, M. P. A., & Trudgill, B. D. (1999). Salt related fault families and falt welds in the northern Gulf of Mexico. *AAPG Bulletin*, *83*(9), 1454–1484. https://doi.org/10.1306/E4FD41E3-1732-11D7-8645000102C1865D

Rowan, Mark G., & Weimer, P. (1998). Salt-sediment interaction, northern Green Canyon and Ewing Bank (offshore Louisiana), northern Gulf of Mexico. *AAPG Bulletin*, *82*(5 B), 1055–1082. https://doi.org/10.1306/1d9bc9f3-172d-11d7-8645000102c1865d

Salisbury, R. S. K. (1990). Shallow Gas Reservoirs and Migration Paths Over a Central North Sea Diapir. In D. A. Ardus & C. D. Green (Eds.), *Safety in Offshore Drilling: The Role of Shallow Gas Surveys, Proceedings of an International Conference (Safety in Offshore Drilling) organized by the Society for Underwater Technology and held in London, U.K., April 25 {&} 26, 1990* (pp. 167–180). https://doi.org/10.1007/978-94-009-0669-3_8

Salvador, A. (1987). Late Triassic-Jurassic Paleogeography and Origin of Gulf of Mexico. *AAPG Bulletin*, *71*(4), 419–451. https://doi.org/10.1306/2F917F19-16CE-11D7-8645000102C1865D

Schmiedel, T., Kjoberg, S., Planke, S., Magee, C., Galland, O., Schofield, N., & Jackson, C. (2017). Mechanisms of overburden deformation associated with the emplacment of the Tulipan sill, mid-Norwegian margin. *Interpretation*, *5*(3), SK23–SK38.

Schmuck, E. A., & Paull, C. K. (1993). Evidence for gas accumulation associated with diapirism and gas hydrates at the head of the Cape Fear Slide. *Geo-Marine Letters*, *13*(3), 145–152. https://doi.org/10.1007/BF01593187

Schofield, N., Holford, S., Millett, J., Brown, D., Jolley, D., Passey, S. R., … Stevenson, C. (2017). Regional magma plumbing and emplacement mechanisms of the Faroe-Shetland Sill Complex: implications for magma transport and petroleum systems within sedimentary basins. *Basin Research*, *29*(1), 41–63. https://doi.org/10.1111/bre.12164

Senger, K., Millett, J., Planke, S., Ogata, K., Eide, C. H., Festøy, M., … Jerram, D. A. (2017). Effects of igneous intrusions on the petroleum system: a review. *First Break*, *35*, 1–10.

Sheriff, R. ., & Geldart, L. . (1995). *Exploration seismology*. Cambridge University Press.

Sibson, R. H. (1985). A note on fault reactivation. *Journal of Structural Geology*, *7*(6), 751–754. https://doi.org/10.1016/0191-8141(85)90150-6

Sibson, R. H. (1996). Structural permeability of fluid-driven fault-fracture meshes. *Journal of Structural Geology*, *18*(8), 1031–1042. https://doi.org/10.1016/0191-8141(96)00032-6

Sibson, R. H. (1998). Brittle failure mode plots for compressional and extensional tectonic regimes. *Journal of Structural Geology*, *20*(5), 655–660. https://doi.org/10.1016/S0191-8141(98)00116-3

Sibson, R. H. (2000). A brittle failure mode plot defining conditions for high-flux flow. *Economic Geology*, *95*(1), 41–47. https://doi.org/10.2113/gsecongeo.95.1.41

Sibson, R. H. (2003). Brittle-failure controls on maximum sustainable overpressure in different tectonic regimes. *American Association of Petroleum Geologists Bulletin*, *87*(6), 901–908. https://doi.org/10.1306/01290300181

Sibson, R. H. (2017). The edge of failure: Critical stress overpressure states in different tectonic regimes. *Geological Society Special Publication*, *458*(1), 131–141. https://doi.org/10.1144/SP458.5

Skogseid, J., Pedersen, T., Eldholm, O., & Larsen, B. T. (1992). Tectonism and magmatism during NE Atlantic continental break-up: the Vøring Margin. *Geological Society, London, Special Publications*, *68*(1), 305–320. https://doi.org/10.1144/gsl.sp.1992.068.01.19

Smallwood, J. R., & Maresh, J. (2002). The properties, morphology and distribution of igneous sills: Modelling, borehole data and 3D seismic from the Faroe-Shetland area. *Geological Society Special Publication*, *197*, 271–306. https://doi.org/10.1144/GSL.SP.2002.197.01.11

Smith, R. I., Hodgson, N., & Fulton, M. (1993). Salt Control on Triassic Reservoir Distribution, UKCS Central North Sea. *Petroleum Geology of Northwest Europe: Proceedings of the 4th Conference*, 547–557.

Solum, J. G., Davatzes, N. C., & Lockner, D. A. (2010). Fault-related clay authigenesis along the Moab Fault: Implications for calculations of fault rock composition and mechanical and hydrologic fault zone properties. *Journal of Structural Geology*, *32*(12), 1899–1911. https://doi.org/10.1016/j.jsg.2010.07.009

Song, J., Alves, T., Omosanya, K., & Ze, T. (2020). Tectonic evolution of strike-slip zones on continental margins and their impact on the development of submarine landslides (Storegga Slide, Northeast Atlantic). *GSA Bulletin*.

Speight, J. G. (2011). Chapter 2: Sources of Hydrocarbons. In *Handbook of Industrial Hydrocarbon Processes* (pp. 43–83). https://doi.org/10.1016/B978-0-7506-8632-7.10002-7

Stagpoole, V., & Funnell, R. (2001). Arc magmatism and hydrocarbon generation in the Northern Taranaki Basin, New Zealand. *Petroleum Geoscience*, *7*(3), 255–267. https://doi.org/10.1144/petgeo.7.3.255

Stewart, I. J. (1993). Structural controls on the Late Jurassic age shelf system , Ula Trend , Norwegian North Sea. *Petroleum Geology of Northwest Europe: Proceedings of the 4th Conference (Edited by J. R. Parker)*, 469–483.

Stewart, S. A. (2006). Implications of passive salt diapir kinematics for reservoir segmentation by radial and concentric faults. *Marine and Petroleum Geology*, *23*(8), 843–853. https://doi.org/10.1016/j.marpetgeo.2006.04.001

Stewart, S. a., Ruffell, A. H., & Harvey, M. J. (1997). Relationship between basement-linked and gravity-driven fault systems in the UKCS salt basins. *Marine and Petroleum Geology*, *14*(5), 581–604. https://doi.org/10.1016/S0264-8172(97)00008-1

Stewart, S A. (1999a). Geometry of thin-skinned tectonic systems in relation to detachment layer thickness in sedimentary basins. *Tectonics*, *18*(4), 719–732. https://doi.org/10.1029/1999TC900018

Stewart, S A. (1999b). Seismic interpretation of circular geological structures. *Petroleum Geoscience*, *5*(3), 273–285. https://doi.org/10.1144/petgeo.5.3.273

Stewart, S A. (2007). Salt tectonics in the North Sea Basin: a structural style template for seismic interpreters. *Special Publication of the Geological Society of London*, *272*, 361.

Stewart, S A, & Clark, J. A. (1999). Impact of salt on the structure of the Central North Sea hydrocarbon fairways. *Petroleum Geology of Northwest Europe: Proceedings of the 5th Conference on the Petroleum Geology of Northwest Europe*, *1*, 179–200. https://doi.org/10.1144/0050179

Stewart, Simon A., & Coward, M. P. (1995). Synthesis of salt tectonics in the southern North Sea, UK. *Marine and Petroleum Geology*, *12*(5), 457–475. https://doi.org/10.1016/0264-8172(95)91502-G

Stimac, J., Goff, F., & Goff, C. J. (2015). Intrusion-Related Geothermal Systems. In *The Encyclopedia of Volcanoes* (Second Edi, pp. 799–822). https://doi.org/10.1016/b978-0-12-385938-9.00046-8

Streit, J. E., & Hillis, R. R. (2004). Estimating fault stability and sustainable fluid pressures for underground storage of CO2 in porous rock. *Energy*, *29*(9–10), 1445–1456.

https://doi.org/10.1016/j.energy.2004.03.078

Strozyk, F., Reuning, L., Back, S., & Kukla, P. (2018). Giant pockmark formation from Cretaceous hydrocarbon expulsion in the western Lower Saxony Basin , The Netherlands. *From: Kilhams, B., Kukla, P.A., Mazur, S., McKie, T., Mijnlieff, H. F. & van Ojik, K. (Eds) Mesozoic Resource Potential in the Southern Permian Basin. Geological Society, London, Special Publications*, *469*.

Struijk, A. P., & Green, R. T. (1991). The Brent Field, Block 211/29, UK North Sea. *Geological Society Memoir*, (14), 63–72.

Sulak, R. . (1991). Ekofisk Field: The First 20 Years. *OnePetro*, *43*(10).

Svensen, H., Jamtveit, B., Planke, S., & Chevallier, L. (2006). Structure and evolution of hydrothermal vent complexes in the Karoo Basin, South Africa. *Journal of the Geological Society*, *163*(4), 671–682. https://doi.org/10.1144/1144-764905-037

Svensen, H., Planke, S., & Corfu, F. (2010). Zircon dating ties NE Atlantic sill emplacement to initial Eocene global warming. *Journal of the Geological Society*, *167*(3), 433–436. https://doi.org/10.1144/0016-76492009-125

Svensen, H., Planke, S., Jamtveit, B., & Pedersen, T. (2003). Seep carbonate formation controlled by hydrothermal vent complexes: A case study from the Vøring Basin, the Norwegian Sea. *Geo-Marine Letters*, *23*(3–4), 351–358. https://doi.org/10.1007/s00367-003-0141-2

Svensen, H., Planke, S., Maithe-Sørensen, A., Jamtveit, B., Myklebust, R., Eidem, T. R., & Rey, S. S. (2004). Release of methane from a volcanic basin as a mechanism for initial Eocene global warming. *Nature*, *429*(6991), 542–545. https://doi.org/10.1038/nature02566

Swarbrick, R. E., Lahann, R. W., O'Connor, S. a., & Mallon, a. J. (2010). Role of the Chalk in development of deep overpressure in the Central North Sea. *Petroleum Geology Conference Series*, *7*, 493–507. https://doi.org/10.1144/0070493

Swarbrick, R. E., & Osborne, M. J. (1998). Chapter 2: Mechanisms that Generate Abnormal Pressures: an Overview. *AAPG Memoirs*, *70*, 13–34.

Swarbrick, R. E., Seldona, B., & Mallon, N. J. (2005). Modelling the Central North Sea pressure history. *Petroleum Geology of Northwest Europe: Proceedings of the 6th Petroleum Geology Conference*, 1237–1245.

Sydnes, M., Fjeldskaar, W., Grunnaleite, I., Mjelde, R., & Løtveit, I. F. (2019). The influence of magmatic intrusions on diagenetic processes and stress accumulation. *Geosciences (Switzerland)*, *9*(11), 1–28. https://doi.org/10.3390/geosciences9110477

Sydnes, M., Fjeldskaar, W., Løtveit, I. F., Grunnaleite, I., & Cardozo, N. (2018). The importance of sill thickness and timing of sill emplacement on hydrocarbon maturation. *Marine and Petroleum Geology*, *89*(4068), 500–514. https://doi.org/10.1016/j.marpetgeo.2017.10.017

Szpak, M. T., Monteys, X., Reilly, S. S. O., Lilley, M. K. S., Scott, G. A., Hart, K. M., … Kelleher, B. P. (2015). Occurrence , characteristics and formation mechanisms of methane generated micro-pockmarks in Dunmanus Bay , Ireland. *Continental Shelf Research*, *103*, 45–59. https://doi.org/10.1016/j.csr.2015.04.023

Talbot, C. J. (1993). Spreading of salt structures in the Gulf of Mexico. *Tectonophysics*, *228*, 151–166.

Tasianas, A., Bünz, S., Bellwald, B., Hammer, Ø., Planke, S., Lebedeva-Ivanova, N., & Krassakis, P. (2018). High-resolution 3D seismic study of pockmarks and shallow fluid flow systems at the Snøhvit hydrocarbon field in the SW Barents Sea. *Marine Geology*, *403*(June), 247–261. https://doi.org/10.1016/j.margeo.2018.06.012

Tassone, D. R. (2014). *COMPRESSIONAL DEFORMATION AND EXHUMATION IN SEDIMENTARY BASINS AT ' PASSIVE ' CONTINENTAL MARGINS , WITH IMPLICATIONS FOR HYDROCARBON EXPLORATION AND DEVELOPMENT*.

Taylor, M. H., Dillon, W. P., & Pecher, I. A. (2000). Trapping and migration of methane associated with the gas hydrate stability zone at the Blake Ridge Diapir: New insights from seismic data. *Marine Geology*. https://doi.org/10.1016/S0025-3227(99)00128-0

Tenthorey, E., Cox, S. F., & Todd, H. F. (2003). Evolution of strength recovery and permeability during fluid-rock reaction in experimental fault zones. *Earth and Planetary Science Letters*, *206*(1–2), 161–172. https://doi.org/10.1016/S0012-821X(02)01082-8

The 2014 NPD lithostratigraphic charts. (2014). Retrieved from Norwegian Petroleum Directorate website: https://www.npd.no/en/facts/geology/lithostratigraphy/

The Oil & Gas Authority. (2018). *Wells Insight Report*. 56.

Thomas, S. (2008). Enhanced oil recovery - an overview. *Oil & Gas Science and Technology-Revue …*, *63*(1), 9–19. https://doi.org/10.2516/ogst

Thompson, K. F. ., Kennicutt, M. ., & Brooks II, J. . (1990). Classification of offshore Gulf of Mexico oils and gas condensates. *AAPG Bulletin*, *74*, 187–198.

Thomson, K. (2007). Determining magma flow in sills, dykes and laccoliths and their implications for sill emplacement mechanisms. *Bulletin of Volcanology*, *70*(2), 183–201. https://doi.org/10.1007/s00445-007-0131-8

Tingay, M. R. P., Hillis, R. R., Swarbrick, R. E., Morley, C. K., & Damit, A. R. (2007).

"Vertically transferred" overpressures in Brunei: Evidence for a new mechanism for the formation of high-magnitude overpressure. *Geology*, *35*(11), 1023–1026. https://doi.org/10.1130/G23906A.1

Tsuji, T., Masui, Y., & Yokoi, S. (2011). New hydrocarbon trap models for the diagenetic transformation of Opal CT to quartz in Neogene siliceaous rocks. *AAPG Bulletin*, *95*(3), 449–477.

Underhill, J. . (1998). Jurassic. In *Petroleum Geology of the North Sea: Basic Concepts and Recent Advances, Fourth Edition* (pp. 245–293).

Underhill, J. R. (2003). The tectonic and stratigraphic framework of the United Kingdom's oil and gas fields. *Geological Society, London, Memoirs*, *20*(1), 17–59.

Underhill, J. R., & Partington, M. a. (1993). Jurassic thermal doming and deflation in the North Sea: implications of the sequence stratigraphic evidence. *Petroleum Geology of Northwest Europe: Proceedings of the 4th Conference on Petroleum Geology of NW. Europe, at the Barbican Centre, London*, *1*, 337–345.

Varela, C. L., & Mohriak, W. U. (2013). Halokinetic rotating faults, salt intrusions, and seismic pitfalls in the petroleum exploration of divergent margins. *AAPG Bulletin*, *97*(9), 1421–1446. https://doi.org/10.1306/02261312164

Veeken, P. C. . (2006). *Seismic Stratigraphy, Basin Analysis and Reservoir Characterisation* (K. Helbig & S. Treitel, Eds.). Elsevier.

Vendeville, B. C., & Jackson, M. P. A. (1992). The rise of diapirs during thin-skinned extension. *Marine and Petroleum Geology*, *9*, 331–353. https://doi.org/10.1016/0264-8172(92)90047-I

Vogt, P. R., Crane, K., Sundvor, E., Max, M. D., & Pfirman, S. L. (1994). Methane-generated(?) pockmarks on young, thickly sedimented oceanic crust in the Arctic: Vestnesa Ridge, Fram Strait. *Geology*, *22*(3), 255–258. https://doi.org/10.1130/0091-7613(1994)022<0255:MGPOYT>2.3.CO;2

Wagner, B. H., & Jackson, M. P. A. (2011). Viscous flow during salt welding. *Tectonophysics*, *510*(3–4), 309–326. https://doi.org/10.1016/j.tecto.2011.07.012

Walsh, J. J., Torremans, K., Güven, J., Kyne, R., Conneally, J., & Bonson, C. (2018). Fault-Controlled Fluid Flow Within Extensional Basins and Its Implications for Sedimentary Rock-Hosted Mineral Deposits. *SEG Special Publications*, (21), 237–269. https://doi.org/10.5382/sp.21.11

Ward, N. I. P., Alves, T. M., & Blenkinsop, T. G. (2016). Reservoir leakage along concentric faults in the Southern North Sea: Implications for the deployment of CCS and EOR

techniques. *Tectonophysics*, *690*, 97–116. https://doi.org/10.1016/j.tecto.2016.07.027

Ward, N. I. P., Alves, T. M., & Blenkinsop, T. G. (2018). Differential compaction over Late Miocene submarine channels in SE Brazil: Implications for trap formation. *Bulletin of the Geological Society of America*, *130*(1–2), 208–221. https://doi.org/10.1130/B31659.1

Watts, A. B. (1982). Tectonic subsidence, flexure and global changes of sea level. *Nature*, *297*(5866), 469–474. https://doi.org/10.1038/297469a0

Weijermars, R., Jackson, M. P. A., & Dooley, T. P. (2014). Quantifying drag on wellbore casings in moving salt sheets. *Geophysical Journal International*, *198*(2), 965–977. https://doi.org/10.1093/gji/ggu174

Weimer, P., Bouroullec, R., Adson, J., & Cossey, S. P. J. (2017). An overview of the petroleum systems of the northern deep-water Gulf of Mexico. *AAPG Bulletin*, *101*(7), 941–993. https://doi.org/10.1306/09011608136

White, R., & McKenzie, D. (1989). Magmatism at rift zones: the generation of volcanic continental margins and flood basalts. *Journal of Geophysical Research*, *94*(B6), 7685–7729. https://doi.org/10.1029/JB094iB06p07685

Wilkinson, M., Haszeldine, R. S., Mackay, E., Smith, K., & Sargeant, S. (2013). A new stratigraphic trap for CO2 in the UK North Sea: Appraisal using legacy information. *International Journal of Greenhouse Gas Control*, *12*, 310–322. https://doi.org/10.1016/j.ijggc.2012.09.013

Williams, J. D. O., Jin, M., Bentham, M., Pickup, G. E., Hannis, S. D., & Mackay, E. J. (2013). Modelling carbon dioxide storage within closed structures in the UK Bunter Sandstone Formation. *International Journal of Greenhouse Gas Control*, *18*, 38–50. https://doi.org/10.1016/j.ijggc.2013.06.015

Woodcock, N. H., Dickson, J. A. D., & Tarasewics, J. P. T. (2007). Transient permeability and reseal hardening in fault zones: Evidence from dilation breccia textures. *Geological Society Special Publication*, *270*, 43–53. https://doi.org/10.1144/GSL.SP.2007.270.01.03

Worrall, D. M., & Snelson, S. (1989). Evolution of the northern Gulf of Mexico, with emphasis on Cenozoic growth faulting and the role of salt. In *The Geology of North America—An Overview* (pp. 97–138). https://doi.org/10.1130/dnag-gna-a.97

Wu, S., Bally, A. W., & Cramez, C. (1990). Allochthonous salt, structure and stratigraphy of the north-eastern Gulf of Mexico. Part II: Structure. *Marine and Petroleum Geology*, *7*(4). https://doi.org/10.1016/0264-8172(90)90014-8

Xia, C., & Wilkinson, M. (2017). The geological risks of exploring for a CO 2 storage reservoir. *International Journal of Greenhouse Gas Control*, *63*(July), 272–280.

https://doi.org/10.1016/j.ijggc.2017.05.016

Yardley, G. S., & Swarbrick, R. E. (2000). Lateral transfer: A source of additional overpressure? *Marine and Petroleum Geology*, *17*(4), 523–537. https://doi.org/10.1016/S0264-8172(00)00007-6

Yilmaz, O. (2001). *Seismic data analysis*. Society of Exploration Geophysicists Tulsa.

Zanella, E., & Coward, M. P. (2003). Structural Framework. *In Evans, D., Graham, C. Armour, A., and Bathurst, P., Eds., The Millenium Atlas: Petroleum Geology of the Central and Northern North Sea: The Geological Society, London*, 45–59.

Ziegler, P. . (1992). North sea rift system. *Tectonophysics*, *208*, 55–75.

Ziegler, P. A. (1990). Geological Atlas of Western and Central Europe (2nd Edition). *Bath: Geological Society for Shell Internationale Petroleum Maatschappij B.V., The Hague*.

Zoback, M. D. (2010). *Reservoir Mechanics*. Cambridge University Press.

Appendix A: Maturation Models Parameters, Jæren High

Palaeo-water depth values were estimated based on: a) the typical water depths for the lithologies encountered in wells, b) geological well reports from the Norwegian Petroleum Directorate, and c) data in Frederiksen et al. (2001) and Haq et al. (1988). The sea water temperature was calculated by an algorithm embedded in Petromod®, which takes into account palaeo-water depth and latitude through time. Heat flow (thermal history) was also obtained from Frederiksen et al. (2001).

Age (Ma)	Palaeo-Water Depth (m)	Seawater Temperature (°C)	Heat Flow (mW/m^2)
0	82	5.0	55
5	100	5.8	56
12	120	8.8	57
20	180	15.6	58
25	200	17.0	58
30	250	16.0	59
40	280	16.2	60
60	300	17.3	62
64	300	13.4	63
70	287	17.7	64
88	227	20.8	67
102	160	22.2	68
106	78	23.3	69
113	21	24.3	76
122	0	n/a	80
138	0	n/a	86
157	0	n/a	89
161	0	n/a	76
170	0	n/a	72
174	0	n/a	70
177	0	n/a	67
180	19	18.3	67
184	34	18.7	65
187	52	17.8	65
190	74	17.8	62
194	71	17.9	61
195	63	18.0	61
197	34	19.0	60
200	0	n/a	60
250	0	n/a	69
252	32	24.2	64
255	50	24.0	60
260	28	23.3	59
262	0	23.7	59
280	0	n/a	65
290	0	n/a	75
295	0	n/a	81
305	0	n/a	72
310	0	n/a	65
320	0	n/a	60
333	0	n/a	58

Appendix B: Morphological attributes of pockmarks on the Jæren Sea

Horizon	FID	Area	Perimeter	MBG Width	MBG Length	MBG W:L Ratio	Vrelief	Min WD	Max WD	Mean
Intra Chalk	0	53942	828	250	251	1	25	-2688	-2709	-270
Intra Chalk	1	53942	828	250	251	1	26	-2527	-2559	-254
Intra Chalk	2	53942	828	250	251	1	27	-2532	-2567	-254
Intra Chalk	3	88889	1079	318	344	0.93	38	-2447	-2508	-247
Intra Chalk	4	66480	928	251	301	0.83	27	-2609	-2630	-261
Intra Chalk	5	66480	928	251	301	0.83	28	-2627	-2692	-267
Intra Chalk	6	87814	1073	300	351	0.86	30	-2573	-2601	-258
Intra Chalk	7	89619	1097	301	352	0.86	31	-2520	-2550	-253
Intra Chalk	8	100352	1169	301	403	0.75	32	-2542	-2576	-255
Intra Chalk	9	113285	1238	334	424	0.79	27	-2501	-2526	-251
Intra Chalk	10	112014	1228	304	401	0.76	28	-2682	-2704	-269
Intra Chalk	11	109854	1201	351	353	1	30	-2575	-2608	-259

Intra Chalk	12	130521	1370	302	501	0.6	33	-2721	-2760	-274
Intra Chalk	13	136682	1382	400	451	0.89	31	-2483	-2512	-250
Intra Chalk	14	131744	1318	377	447	0.84	32	-2558	-2591	-257
Intra Chalk	15	142276	1397	352	452	0.78	38	-2434	-2495	-246
Intra Chalk	16	138688	1346	401	403	1	35	-2495	-2550	-252
Intra Chalk	17	189790	1668	416	573	0.73	32	-2380	-2415	-240
Intra Chalk	18	198568	1628	483	518	0.93	38	-2588	-2628	-260
Intra Chalk	19	209107	1707	483	554	0.87	40	-2389	-2422	-240
Intra Chalk	20	207026	1682	500	532	0.94	53	-2594	-2657	-262
Intra Chalk	21	217647	1748	468	580	0.81	46	-2376	-2436	-240
Intra Chalk	22	217666	1754	477	616	0.77	45	-2514	-2555	-253
Intra Chalk	23	255755	1925	452	653	0.69	45	-2539	-2582	-255
Intra Chalk	24	299863	2054	554	702	0.79	71	-2827	-2921	-286
Intra Chalk	25	303794	2024	602	603	1	64	-2551	-2615	-257
Intra Chalk	26	458187	2561	670	893	0.75	40	-2500	-2538	-252

Intra Chalk	27	618882	3070	804	955	0.84	71	-2580	-2686	-2638	0.55	23.8	11.8
Intra Chalk	28	485654	2510	749	839	0.89	18	-2498	-2576	-2552	0.69	29.8	5.9
Intra Chalk	29	157926	1428	427	453	0.94	15	-2483	-2533	-2506	0.46	41.8	7.4
Intra Chalk	30	43665	766	225	269	0.83	20	-2505	-2529	-2519	0.59	16.9	4.8
Intra Chalk	31	107233	1190	341	403	0.85	24	-2493	-2520	-2506	0.48	27.2	3.8
Intra Chalk	32	50325	817	225	296	0.76	26	-2463	-2482	-2470	0.37	22.4	3.8
Intra Chalk	33	65749	929	272	306	0.89	20	-2539	-2561	-2551	0.56	20.7	4.1
Intra Chalk	34	68074	954	255	323	0.79	20	-2606	-2620	-2615	0.6	15.3	2.5
Intra Chalk	35	43288	754	225	251	0.89	17	-2684	-2705	-2696	0.59	19.4	3.6
CKG	0	53942	828	250	251	1	25	-2670	-2697	-2688	0.69	15.5	5.7
CKG	1	53942	828	250	251	1	25	-2683	-2700	-2693	0.59	11.1	4.2
CKG	2	53942	828	250	251	1	27	-2839	-2898	-2867	0.47	25.2	12.2
CKG	3	53942	828	250	251	1	28	-2814	-2832	-2822	0.42	8.0	3.5
CKG	4	53942	828	250	251	1	29	-2631	-2655	-2640	0.36	10.7	4.9
CKG	5	53942	828	250	251	1	29	-2596	-2626	-2613	0.59	13.2	5.9
CKG	6	53942	828	250	251	1	33	-2606	-2650	-2628	0.5	16.6	7.4
CKG	7	144107	1446	342	505	0.68	30	-2902	-2992	-2952	0.56	37.6	16.1
CKG	8	66480	928	251	301	0.83	28	-2613	-2630	-2620	0.4	10.5	4.1
CKG	9	66541	928	252	300	0.84	31	-2620	-2646	-2629	0.35	12.1	5.7
CKG	10	66541	928	252	300	0.84	31	-2664	-2702	-2682	0.47	17.0	7.9
CKG	11	77169	1001	300	302	1	26	-2692	-2722	-2711	0.65	18.2	5.6
CKG	12	77186	1001	301	302	1	33	-2606	-2651	-2634	0.62	20.8	6.9

CKG	13	77169	1001	300	302	1	136	-2758	-2811	-2777	0.36	25.9	8.3
CKG	14	81578	1028	301	302	1	30	-2776	-2819	-2804	0.64	25.0	7.8
CKG	15	81578	1028	301	302	1	30	-2815	-2858	-2841	0.61	19.7	8.3
CKG	16	81578	1028	301	302	1	31	-2710	-2743	-2725	0.45	20.6	8.1
CKG	17	81578	1028	301	302	1	37	-2870	-2909	-2885	0.38	16.3	8.7
CKG	18	87847	1073	301	351	0.86	33	-3069	-3112	-3089	0.47	21.3	10.1
CKG	19	92303	1101	302	351	0.86	28	-2637	-2661	-2648	0.46	12.2	5.8
CKG	20	96645	1128	301	352	0.86	37	-2729	-2778	-2750	0.43	19.0	10.6
CKG	21	96645	1128	301	352	0.86	44	-2634	-2694	-2659	0.42	19.5	11.3
CKG	22	105448	1173	351	352	1	35	-2614	-2661	-2640	0.55	19.5	8.3
CKG	23	122606	1340	351	451	0.78	28	-2664	-2685	-2676	0.58	11.0	4.5
CKG	24	109854	1201	351	353	0.99	44	-2663	-2716	-2682	0.37	18.7	10.2
CKG	25	109874	1201	351	353	1	50	-2621	-2687	-2648	0.42	24.5	12.9
CKG	26	114149	1218	351	401	0.87	36	-2855	-2890	-2871	0.44	14.5	7.6
CKG	27	124682	1287	377	412	0.91	59	-2660	-2732	-2689	0.4	25.0	9.9
CKG	28	122980	1273	351	402	0.87	39	-2628	-2671	-2649	0.48	20.9	8.5
CKG	29	122980	1273	351	402	0.87	42	-2835	-2893	-2862	0.47	22.4	11.7
CKG	30	128991	1311	379	424	0.89	39	-2751	-2791	-2767	0.39	15.9	7.8
CKG	31	133395	1338	400	402	1	37	-2978	-3030	-3005	0.51	22.6	10.0
CKG	32	131591	1314	401	402	1	65	-2652	-2729	-2675	0.3	28.3	12.8
CKG	33	138708	1346	401	403	1	44	-2709	-2762	-2731	0.41	18.7	10.5
CKG	34	145366	1401	355	451	0.79	35	-2701	-2731	-2716	0.53	11.2	4.3
CKG	35	143149	1373	401	403	0.99	38	-2596	-2638	-2618	0.52	15.4	8.0
CKG	36	143144	1373	401	403	0.99	39	-2662	-2696	-2676	0.41	14.1	7.7
CKG	37	147653	1401	401	404	0.99	41	-2739	-2773	-2752	0.38	11.7	6.2
CKG	38	147653	1401	401	404	0.99	51	-2605	-2657	-2625	0.39	19.9	10.2
CKG	39	151850	1418	401	452	0.89	45	-2811	-2870	-2839	0.46	22.0	11.4
CKG	40	158926	1446	404	452	0.89	68	-2611	-2689	-2639	0.35	25.2	12.8
CKG	41	167423	1487	446	491	0.91	46	-2884	-2939	-2908	0.43	21.6	12.2
CKG	42	176806	1575	452	501	0.9	47	-2620	-2663	-2637	0.4	13.1	6.3
CKG	43	172027	1530	402	454	0.88	69	-2684	-2761	-2705	0.28	28.3	13.5

CKG	44	207552	1754	451	551	0.82	32	-2775	-2828	-2813	0.72	23.7	6.8
CKG	45	177936	1555	452	501	0.9	51	-2590	-2654	-2617	0.43	25.5	12.5
CKG	46	189722	1658	468	513	0.91	33	-2720	-2752	-2737	0.55	12.0	5.5
CKG	47	194459	1614	452	503	0.9	107	-2690	-2818	-2728	0.3	44.3	20.1
CKG	48	180965	1569	405	501	0.81	82	-2676	-2767	-2703	0.3	30.4	13.3
CKG	49	186373	1609	452	502	0.9	38	-2663	-2705	-2685	0.53	16.2	7.1
CKG	50	186627	1607	446	535	0.83	64	-2638	-2708	-2662	0.35	24.0	11.7
CKG	51	187470	1587	451	503	0.9	43	-2604	-2648	-2625	0.47	16.6	8.0
CKG	52	189026	1613	437	548	0.8	48	-2763	-2834	-2801	0.53	22.5	11.6
CKG	53	187256	1583	451	501	0.9	63	-2602	-2668	-2626	0.36	25.6	12.9
CKG	54	194135	1611	452	502	0.9	51	-2722	-2795	-2759	0.5	25.5	13.0
CKG	55	197488	1644	468	535	0.87	57	-2595	-2672	-2633	0.49	20.7	11.0
CKG	56	206815	1711	451	553	0.81	47	-2766	-2836	-2803	0.54	23.8	11.8
CKG	57	216781	1779	497	581	0.86	39	-3172	-3219	-3198	0.55	18.1	7.2
CKG	58	205975	1669	452	504	0.9	71	-2614	-2697	-2645	0.38	31.6	14.3
CKG	59	216001	1730	453	602	0.75	48	-2593	-2656	-2624	0.48	21.8	12.0
CKG	60	212520	1683	501	503	1	50	-2656	-2702	-2673	0.37	15.1	8.4
CKG	61	212779	1687	501	504	0.99	59	-2857	-2927	-2887	0.43	19.1	11.3
CKG	62	223466	1769	456	551	0.83	106	-2595	-2728	-2639	0.33	41.1	18.6
CKG	63	230895	1823	503	602	0.84	65	-2578	-2660	-2612	0.42	29.8	12.2
CKG	64	241790	1904	502	601	0.83	43	-2592	-2648	-2621	0.52	23.1	9.6
CKG	65	231875	1788	501	552	0.91	44	-2718	-2760	-2739	0.49	16.1	5.6
CKG	66	239954	1840	483	624	0.77	51	-2678	-2738	-2707	0.48	19.3	9.0
CKG	67	235088	1779	504	552	0.91	72	-2639	-2773	-2717	0.58	37.5	17.1
CKG	68	239273	1810	505	551	0.92	96	-2865	-2982	-2908	0.37	33.0	16.6
CKG	69	237574	1789	504	551	0.91	58	-2756	-2835	-2797	0.52	23.7	11.5
CKG	70	242162	1804	551	553	1	65	-2750	-2817	-2776	0.39	19.4	10.0
CKG	71	293360	2038	554	701	0.79	120	-2630	-2769	-2675	0.33	42.7	19.2
CKG	72	256123	1856	505	601	0.84	100	-2664	-2771	-2695	0.28	26.3	13.1
CKG	73	257114	1878	551	553	1	54	-2640	-2699	-2665	0.43	17.9	9.4
CKG	74	255461	1858	548	611	0.9	66	-2618	-2685	-2643	0.38	24.6	11.8

CKG	75	267000	1950	527	624	0.84	38	-2713	-2750	-2733	0.53	14.2	6.5
CKG	76	327191	2097	602	654	0.92	178	-2621	-2820	-2678	0.29	41.8	22.6
CKG	77	305839	2145	579	690	0.84	98	-2583	-2690	-2623	0.37	40.2	15.0
CKG	78	265324	1883	552	554	1	56	-2600	-2659	-2625	0.43	19.8	9.9
CKG	79	274593	1959	457	701	0.65	65	-2736	-2810	-2767	0.42	21.9	13.2
CKG	80	274386	1954	552	602	0.92	69	-2596	-2665	-2620	0.35	23.1	10.2
CKG	81	339483	2171	643	659	0.98	140	-2676	-2869	-2755	0.41	51.9	24.2
CKG	82	338901	2327	501	803	0.62	109	-2588	-2761	-2667	0.46	47.4	21.2
CKG	83	302263	2004	602	604	1	71	-2673	-2762	-2713	0.45	25.2	13.4
CKG	84	316702	2095	579	722	0.8	68	-2703	-2776	-2732	0.4	19.2	11.2
CKG	85	341295	2194	603	701	0.86	75	-2749	-2843	-2792	0.46	22.3	13.3
CKG	86	352251	2242	595	769	0.77	76	-2789	-2870	-2820	0.39	20.2	11.1
CKG	87	347652	2172	651	654	1	59	-2644	-2711	-2676	0.47	23.5	11.2
CKG	88	355838	2232	603	707	0.85	87	-2594	-2683	-2624	0.33	23.1	13.1
CKG	89	364661	2280	652	701	0.93	68	-2600	-2673	-2632	0.43	19.1	9.4
CKG	90	373973	2291	653	751	0.87	81	-3045	-3150	-3094	0.46	28.7	12.7
CKG	91	448364	2859	670	871	0.77	71	-2704	-2806	-2755	0.5	30.6	11.0
CKG	92	379835	2269	654	701	0.93	69	-2816	-2913	-2869	0.54	29.8	12.4
CKG	93	402567	2393	664	757	0.88	113	-2771	-2898	-2813	0.33	27.1	14.3
CKG	94	399780	2389	654	754	0.87	64	-2589	-2660	-2622	0.47	28.2	10.2
CKG	95	392870	2300	653	705	0.93	70	-2747	-2823	-2779	0.43	19.4	10.7
CKG	96	441116	2476	690	817	0.85	126	-2588	-2726	-2632	0.32	29.5	14.7
CKG	97	406209	2341	702	704	1	74	-2789	-2872	-2825	0.43	21.8	12.0
CKG	98	443629	2677	589	1048	0.56	74	-2791	-2899	-2846	0.51	32.9	15.0
CKG	99	466920	2516	705	803	0.88	103	-2614	-2721	-2651	0.35	29.0	14.4
CKG	100	435370	2424	658	753	0.87	68	-2659	-2738	-2697	0.48	18.7	9.5
CKG	101	364878	2222	633	759	0.83	114	-2694	-2828	-2745	0.38	31.8	17.1
CKG	102	647568	3007	843	1000	0.84	96	-2704	-2820	-2760	0.48	23.8	13.4
CKG	103	826007	3487	902	1203	0.75	158	-2650	-2832	-2718	0.37	30.0	16.3
CKG	104	701970	3131	905	952	0.95	90	-2737	-2842	-2787	0.47	24.0	10.2
CKG	105	986565	3813	960	1318	0.73	140	-2672	-2838	-2742	0.42	34.5	16.6

CKG	106	192013	1580	462	536	0.86	16	-2702	-2746	-2726	0.54	12.5	5.3
CKG	107	102907	1176	344	384	0.9	14	-2634	-2717	-2678	0.53	25.6	11.9
CKG	108	411974	2383	683	791	0.86	23	-2587	-2640	-2609	0.42	15.7	5.7
CKG	109	272234	1877	534	616	0.87	20	-2590	-2627	-2605	0.4	11.2	5.5
CKG	110	166233	1474	409	525	0.78	20	-2667	-2699	-2681	0.45	13.2	6.0
CKG	111	176599	1514	416	526	0.79	25	-2998	-3044	-3022	0.52	17.7	8.1
CKG	112	134798	1310	395	429	0.92	22	-2854	-2895	-2873	0.45	16.8	7.6
Mandal Fm	0	78465	1013	286	353	0.81	25	-2853	-2872	-2864	0.55	14.2	4.5
Mandal Fm	1	53942	828	250	251	1	27	-2817	-2843	-2830	0.52	12.1	6.0
Mandal Fm	2	66541	928	252	300	0.84	27	-2809	-2833	-2821	0.49	15.9	6.1
Mandal Fm	3	66480	928	251	301	0.83	28	-2819	-2853	-2838	0.55	19.2	8.0
Mandal Fm	4	66480	928	251	301	0.83	36	-2857	-2895	-2867	0.27	15.6	7.5
Mandal Fm	5	66541	928	252	300	0.84	49	-2809	-2906	-2846	0.38	34.0	14.5
Mandal Fm	6	77169	1001	300	302	1	30	-2820	-2852	-2833	0.42	14.8	7.6
Mandal Fm	7	81578	1028	301	302	1	29	-2877	-2919	-2899	0.53	21.6	9.6
Mandal Fm	8	81578	1028	301	302	1	31	-2789	-2821	-2801	0.38	15.0	7.5
Mandal Fm	9	92320	1101	302	351	0.86	32	-2838	-2868	-2851	0.45	13.9	6.0
Mandal Fm	10	92303	1101	302	351	0.86	41	-2818	-2881	-2846	0.43	24.6	12.9
Mandal Fm	11	96645	1128	301	352	0.86	32	-2883	-2922	-2905	0.58	21.2	7.4
Mandal Fm	12	102756	1169	334	401	0.83	66	-2777	-2856	-2798	0.27	33.7	13.6

Mandal Fm	13	103045	1173	303	401	0.75	73	-2906	-2994	-2927	0.23	30.6	12.8
Mandal Fm	14	105446	1173	351	352	1	34	-2849	-2881	-2864	0.45	11.5	6.6
Mandal Fm	15	105413	1173	341	412	0.83	55	-2795	-2853	-2812	0.3	24.1	10.1
Mandal Fm	16	115918	1242	350	402	0.87	36	-2844	-2895	-2873	0.57	25.1	8.7
Mandal Fm	17	114211	1218	352	400	0.88	38	-2820	-2873	-2849	0.54	21.7	10.3
Mandal Fm	18	124934	1297	354	402	0.88	72	-2808	-2892	-2832	0.28	32.2	14.9
Mandal Fm	19	128970	1310	400	401	1	56	-2799	-2882	-2837	0.45	26.8	13.1
Mandal Fm	20	140606	1373	352	452	0.78	85	-2796	-2904	-2832	0.33	38.1	18.5
Mandal Fm	21	143149	1373	401	403	0.99	47	-2887	-2953	-2914	0.42	30.2	14.7
Mandal Fm	22	152171	1428	402	404	0.99	38	-2822	-2875	-2847	0.47	22.1	12.2
Mandal Fm	23	154417	1418	403	451	0.89	38	-2834	-2871	-2849	0.42	14.7	8.5
Mandal Fm	24	156213	1442	403	452	0.89	55	-2823	-2891	-2849	0.38	25.6	13.7
Mandal Fm	25	165826	1541	401	503	0.8	46	-2795	-2856	-2823	0.47	22.9	11.1
Mandal Fm	26	158906	1446	404	452	0.89	57	-2815	-2877	-2837	0.35	22.8	11.5
Mandal Fm	27	160631	1469	402	452	0.89	82	-2881	-2999	-2928	0.4	41.2	19.1
Mandal Fm	28	163452	1473	404	451	0.9	80	-2896	-3026	-2955	0.46	44.2	21.6
Mandal Fm	29	183739	1573	405	502	0.81	51	-2811	-2875	-2843	0.5	22.2	11.5

Mandal Fm	30	194497	1614	453	503	0.9	75	-2838	-2926	-2868	0.34	32.2	15.9
Mandal Fm	31	199750	1618	454	501	0.91	76	-2810	-2894	-2837	0.32	32.6	15.8
Mandal Fm	32	356204	2161	654	664	0.99	124	-2851	-2998	-2913	0.42	48.2	23.0
Mandal Fm	33	219430	1711	501	504	1	71	-2778	-2860	-2809	0.38	23.4	14.2
Mandal Fm	34	233265	1759	502	553	0.91	80	-2832	-2907	-2855	0.3	29.9	12.5
Mandal Fm	35	240743	1826	501	601	0.83	74	-2848	-2930	-2878	0.37	22.2	13.2
Mandal Fm	36	247996	1858	500	659	0.76	38	-2782	-2823	-2803	0.51	16.9	8.3
Mandal Fm	37	280732	1952	554	602	0.92	95	-2948	-3096	-3024	0.51	38.8	20.1
Mandal Fm	38	285971	2165	426	837	0.51	55	-2778	-2942	-2894	0.7	56.2	21.3
Mandal Fm	39	321805	2451	608	825	0.74	39	-2797	-2839	-2820	0.55	16.7	5.9
Mandal Fm	40	279221	1928	555	601	0.92	88	-2805	-2906	-2845	0.39	30.8	15.2
Mandal Fm	41	346815	2235	602	752	0.8	98	-2816	-2925	-2857	0.37	41.8	16.7
Mandal Fm	42	286058	1955	555	601	0.92	60	-2977	-3042	-3004	0.41	22.9	11.4
Mandal Fm	43	430944	2448	695	766	0.91	125	-2762	-2909	-2819	0.39	42.5	19.4
Mandal Fm	44	404643	2467	692	737	0.94	63	-2805	-2880	-2842	0.49	22.2	10.4
Mandal Fm	45	375117	2240	576	794	0.73	106	-2839	-2966	-2906	0.53	46.1	11.6
Mandal Fm	46	195257	1598	456	527	0.87	167	-2928	-2993	-2959	0.47	23.6	11.8

Summary of high-amplitude anomalies

FID	Area	Perimeter	BPI	MBG_Width	MBG_Length	w_l_ratio	My_ID	Stacked or single anomaly
0	9786	431	12470	113	114	0.99	146	single
1	9786	431	13016	113	114	0.99	147	stacked
2	9786	431	13843	113	114	0.99	148	single
3	9786	431	14081	113	114	0.99	149	single
4	9786	431	20088	113	114	0.99	77	single
5	11227	404	22626	113	114	0.99	150	single
6	12646	432	13303	114	114	1.00	40	single
7	56232	988	17535	215	379	0.57	151	stacked
8	39261	886	16349	171	276	0.62	152	single
9	18323	736	14027	113	265	0.43	153	single
10	49128	946	13757	189	342	0.55	154	single
11	20930	631	21508	164	164	1.00	155	single
12	23453	580	27051	164	164	1.00	156	single
13	26979	685	22378	166	216	0.77	157	single
14	24500	731	27073	118	264	0.45	158	single
15	28976	673	15645	165	214	0.77	159	single
16	27573	732	21943	119	263	0.45	160	single
17	23347	879	13960	176	234	0.75	161	single
18	40963	763	21978	215	216	1.00	60	single
19	95756	1419	17606	247	529	0.47	162	single
20	42800	822	24145	216	269	0.80	129	stacked
21	48687	951	23663	217	315	0.69	58	single
22	55949	1044	20666	260	317	0.82	163	single
23	66388	1036	17919	267	302	0.89	164	single
24	71210	1223	32160	310	405	0.77	165	stacked
25	99373	1931	31717	266	674	0.39	73	stacked

26	143253	1645	27233	383	484	0.79	166	single
27	90073	1261	25739	267	468	0.57	167	single
28	64897	972	31620	252	346	0.73	168	single
29	71617	1385	23160	213	466	0.46	169	stacked
30	152101	1654	31500	394	620	0.64	170	stacked
31	58492	945	20232	232	329	0.71	171	stacked
32	13979	454	19245	109	161	0.68	172	single
33	294543	4139	38248	323	1789	0.18	173	stacked
34	85616	1225	28891	267	484	0.55	174	single
35	52957	923	16696	177	378	0.47	175	single
36	21133	587	17304	123	213	0.58	176	single
37	65216	1086	18287	216	412	0.52	177	stacked
38	55360	968	19126	175	400	0.44	178	single
39	17043	487	19222	134	156	0.86	179	single
40	1156931	5245	26952	1173	1517	0.77	180	single
41	122129	1666	19802	317	660	0.48	132	single
42	32071	674	30082	189	219	0.86	181	single
43	325502	4085	31571	517	1169	0.44	182	stacked
44	56019	899	34683	246	316	0.78	183	stacked
45	48827	874	17679	180	336	0.54	78	single
46	16694	474	20070	140	150	0.93	184	single
47	123367	1440	27886	365	504	0.72	38	stacked
48	18065	504	18335	126	175	0.72	185	single
49	44275	1215	14680	134	515	0.26	186	stacked
50	120873	1299	23924	356	409	0.87	130	stacked
51	75510	1344	30951	199	584	0.34	187	single
52	55391	942	23307	203	378	0.54	188	single
53	18901	530	14590	126	198	0.63	189	single
54	44234	820	20691	179	301	0.59	190	stacked
55	246749	1979	26475	548	695	0.79	191	single
56	256613	2099	23113	430	835	0.52	192	stacked

57	71994	1094	22749	218	440	0.50	193	stacked
58	49381	922	19166	189	354	0.54	194	stacked
59	54562	977	20517	203	387	0.53	195	single
60	111801	1449	18109	226	608	0.37	196	stacked
61	51915	912	16839	224	314	0.71	197	stacked
62	108443	1308	37914	327	424	0.77	198	stacked
63	351472	2911	29786	379	1236	0.31	199	stacked
64	146046	2025	17446	266	836	0.32	200	single
65	24614	598	18375	164	202	0.81	201	single
66	281484	2929	22216	440	1134	0.39	202	stacked
67	268638	4039	19087	428	1338	0.32	203	stacked
68	95347	1544	21646	308	561	0.55	204	stacked
69	243209	2329	24945	567	717	0.79	205	stacked
70	38279	722	19401	201	237	0.85	206	single
71	33238	697	18253	169	263	0.64	207	single
72	189521	1919	24739	363	754	0.48	208	single
73	132319	1562	32984	325	653	0.50	209	single
74	72493	1166	28265	233	468	0.50	210	stacked
75	17832	511	17185	150	167	0.90	211	stacked
76	61734	933	28794	243	325	0.75	212	stacked
77	30094	667	21412	191	225	0.85	213	single
78	90222	1155	22083	265	418	0.63	214	single
79	34330	722	26111	196	235	0.83	215	single
80	37705	759	24548	215	225	0.96	216	single
81	29440	651	25608	165	230	0.72	217	single
82	70486	1193	23718	212	476	0.44	218	single
83	134640	1573	19492	420	433	0.97	219	single
84	70880	981	25065	277	332	0.83	220	single
85	98129	1191	29219	322	425	0.76	221	single
86	66721	1017	27557	232	377	0.62	222	single
87	123709	1440	27691	339	533	0.64	75	single

88	186755	1650	25794	442	534	0.83	74	stacked
89	58191	899	22084	232	318	0.73	223	single
90	68058	993	24536	223	369	0.60	224	single
91	18442	509	19747	152	160	0.95	125	stacked
92	44847	798	31296	218	279	0.78	225	single
93	259805	1915	35367	535	645	0.83	72	single
94	49835	871	18479	206	318	0.65	226	single
95	92628	1139	43611	283	424	0.67	71	stacked
96	29360	657	27234	173	221	0.78	70	single
97	27879	630	27941	177	213	0.83	227	single
98	44708	772	36144	209	258	0.81	69	single
99	61923	945	24179	260	311	0.83	228	single
100	35416	721	21099	208	240	0.87	229	stacked
101	48261	868	18716	211	327	0.65	230	stacked
102	5617	298	15828	59	117	0.51	231	single
103	40346	733	25122	214	237	0.90	232	single
104	266941	2046	36609	427	814	0.52	68	single
105	48017	834	19840	219	293	0.75	20	stacked
106	136613	1447	31215	392	512	0.77	18	stacked
107	24670	597	17443	148	223	0.66	233	single
108	57908	956	15897	187	381	0.49	234	single
109	65972	1156	18644	214	473	0.45	235	stacked
110	95981	1417	29608	327	472	0.69	66	single
111	88488	1166	32357	322	388	0.83	65	single
112	78387	1050	43931	308	357	0.86	236	single
113	23569	604	18657	137	221	0.62	64	single
114	59456	922	31580	226	341	0.66	237	single
115	17016	496	15964	121	182	0.66	238	stacked
116	42984	786	20136	218	244	0.89	63	single
117	41093	752	17265	202	269	0.75	239	stacked
118	135613	1346	36034	378	433	0.87	62	single

119	33056	737	20896	150	301	0.50	9	single
120	12029	460	12540	123	124	0.99	240	single
121	12029	460	13193	123	124	0.99	241	single
122	12029	460	13521	123	124	0.99	99	single
123	12029	460	13572	123	124	0.99	242	single
124	23920	651	13642	152	253	0.60	243	single
125	12029	460	13968	123	124	0.99	19	single
126	12029	460	14037	123	124	0.99	244	single
127	12029	460	14285	123	124	0.99	245	single
128	16406	476	14342	123	158	0.78	246	single
129	12029	460	14962	123	124	0.99	247	single
130	93298	2282	15562	299	945	0.32	248	single
131	12029	460	16507	123	124	0.99	54	single
132	12029	460	16848	123	124	0.99	249	single
133	12029	460	16981	123	124	0.99	250	stacked
134	12029	460	17316	123	124	0.99	251	single
135	26825	730	18164	123	287	0.43	57	single
136	12029	460	19511	123	124	0.99	252	single
137	12029	460	20430	123	124	0.99	253	single
138	14875	463	15882	124	124	1.00	93	single
139	41595	860	16433	194	303	0.64	90	single
140	14875	463	18286	124	124	1.00	254	single
141	15468	558	13343	124	172	0.72	53	single
142	16669	514	13818	122	199	0.61	255	single
143	24473	778	13897	151	274	0.55	256	single
144	17433	529	14190	123	176	0.70	116	single
145	65751	1365	14501	225	494	0.46	14	single
146	14937	500	22522	124	165	0.75	43	single
147	22315	587	24323	123	214	0.57	45	single
148	19418	545	25123	123	175	0.70	87	single
149	18314	561	14339	125	173	0.72	257	stacked

150	18314	561	14604	125	173	0.72	258	single
151	18314	561	16888	125	173	0.72	259	single
152	29625	658	16946	164	224	0.73	91	single
153	18314	561	17836	125	173	0.72	260	single
154	18314	561	18243	125	173	0.72	48	single
155	21425	568	18260	125	208	0.60	261	single
156	18314	561	30967	125	173	0.72	67	single
157	21168	625	15979	125	222	0.56	262	single
158	18753	660	16148	123	225	0.55	263	single
159	21050	605	17124	123	225	0.55	25	single
160	25862	649	20071	172	204	0.85	264	single
161	24072	612	21866	123	225	0.55	42	single
162	21183	660	16598	154	221	0.70	13	single
163	23133	635	19278	126	222	0.57	265	single
164	50586	1169	21450	177	431	0.41	105	stacked
165	21267	655	29845	161	197	0.82	16	single
166	20820	764	15750	146	241	0.61	266	single
167	74409	1114	16912	283	377	0.75	107	single
168	24183	658	15250	174	174	1.00	100	stacked
169	25923	608	16241	161	232	0.70	47	single
170	95909	1603	16998	351	518	0.68	33	single
171	24113	658	20062	161	232	0.70	56	single
172	25650	663	14965	144	256	0.56	98	single
173	24552	758	15292	154	266	0.58	267	single
174	26839	727	16598	175	222	0.79	268	single
175	24745	760	16800	161	267	0.60	269	single
176	25923	665	18078	155	243	0.64	270	single
177	26488	632	21926	175	176	1.00	12	single
178	27728	663	28876	129	224	0.57	131	single
179	27052	758	25075	173	225	0.77	271	single
180	46170	927	14322	224	307	0.73	272	single

181	77524	1512	19582	263	579	0.45	273	stacked
182	44343	1030	20385	165	423	0.39	109	single
183	72722	1354	23989	286	413	0.69	22	single
184	72068	1405	22390	227	484	0.47	11	stacked
185	34156	778	23645	166	305	0.54	274	single
186	29605	864	30223	176	288	0.61	4	single
187	33038	758	21624	176	224	0.79	97	single
188	35614	781	15918	197	267	0.74	275	stacked
189	37141	820	23901	215	248	0.86	276	single
190	39705	816	22436	173	273	0.63	277	single
191	36950	858	19489	176	226	0.78	117	single
192	40219	805	26288	175	274	0.64	278	single
193	35991	852	36242	224	224	1.00	114	single
194	37911	895	18272	149	380	0.39	10	single
195	85493	1746	16902	259	560	0.46	279	stacked
196	48456	1103	17924	220	393	0.56	113	single
197	136242	1822	18126	421	569	0.74	27	single
198	76739	1113	18754	300	372	0.81	89	single
199	39093	962	26148	197	338	0.58	280	single
200	45436	904	17990	233	274	0.85	281	stacked
201	51331	1194	20146	244	367	0.66	101	stacked
202	59863	931	32371	255	276	0.93	95	single
203	91861	1276	32813	273	495	0.55	3	single
204	40223	837	34604	164	340	0.48	21	single
205	49763	1124	22140	222	378	0.59	103	stacked
206	44395	858	28799	226	226	1.00	282	single
207	50055	853	30774	226	276	0.82	283	single
208	101420	1597	21427	288	519	0.55	127	single
209	45394	949	29102	224	275	0.81	284	single
210	51638	1053	26470	214	347	0.62	285	stacked
211	53196	1164	27028	223	369	0.60	49	single

212	50237	1058	42517	201	382	0.53	44	single
213	92381	1576	23650	311	471	0.66	28	stacked
214	47100	1056	18639	228	339	0.67	128	single
215	49640	1063	20696	221	355	0.62	286	single
216	52188	1059	24273	224	325	0.69	287	single
217	54759	1014	19101	175	374	0.47	288	single
218	150150	2327	19135	300	933	0.32	5	stacked
219	57635	1030	19876	257	355	0.72	289	single
220	77884	1195	23020	303	370	0.82	290	stacked
221	57386	890	24894	249	286	0.87	291	single
222	68277	1328	15053	279	410	0.68	292	single
223	65395	1446	18113	277	360	0.77	293	single
224	56372	960	36982	214	381	0.56	76	stacked
225	54345	1102	20674	266	333	0.80	294	single
226	124259	1757	26561	378	533	0.71	104	single
227	119817	1478	22427	360	484	0.74	29	stacked
228	60546	1018	21249	264	372	0.71	295	single
229	137636	1912	20244	371	649	0.57	296	stacked
230	317285	3138	23611	476	1015	0.47	32	single
231	79518	1347	19681	332	440	0.76	15	stacked
232	64787	1068	20013	228	357	0.64	96	single
233	56297	1168	20041	223	375	0.59	111	single
234	61567	1090	34922	228	376	0.61	55	single
235	53507	899	31875	230	308	0.75	94	single
236	66181	1101	33431	276	325	0.85	297	single
237	68569	1063	43481	273	328	0.83	122	single
238	89846	1238	26701	304	421	0.72	124	single
239	91471	1348	27391	284	473	0.60	106	single
240	75850	1465	28845	218	561	0.39	298	single
241	65820	1102	28857	219	393	0.56	110	single
242	71445	1316	24675	226	456	0.50	299	single

243	89726	1219	25456	286	437	0.66	1	single
244	72705	1212	34310	239	444	0.54	300	single
245	115349	2024	27293	320	747	0.43	24	stacked
246	82459	1338	26720	310	424	0.73	301	single
247	154132	2056	24926	424	665	0.64	302	single
248	69685	1204	31518	230	492	0.47	303	single
249	83358	1431	26284	274	474	0.58	304	stacked
250	164345	2424	19135	473	660	0.72	30	single
251	96891	1336	24024	288	511	0.56	305	stacked
252	105037	1387	21176	320	479	0.67	306	single
253	96995	1385	27289	367	408	0.90	115	stacked
254	90670	1449	31747	338	409	0.83	119	single
255	121714	1775	21350	373	518	0.72	23	stacked
256	91856	1133	29006	328	331	0.99	31	stacked
257	64671	1067	24171	234	319	0.73	307	single
258	192113	1962	20229	464	647	0.72	112	single
259	112568	1672	32826	355	535	0.66	308	single
260	112096	1612	28374	373	482	0.77	121	stacked
261	102283	1371	33731	353	450	0.78	309	stacked
262	111594	1765	38015	326	573	0.57	310	single
263	108869	1356	24435	354	418	0.85	8	stacked
264	109170	1420	34736	329	462	0.71	102	single
265	134740	1993	29258	301	742	0.41	2	stacked
266	144349	1763	32512	425	431	0.99	6	single
267	127320	2205	35649	400	605	0.66	36	single
268	136792	2156	31619	409	515	0.79	311	single
269	173486	2157	22434	402	677	0.59	35	single
270	172461	2534	29951	405	820	0.49	120	single
271	282257	3158	45459	522	930	0.56	126	stacked
272	147421	1779	31961	454	486	0.93	312	single
273	198703	2526	28630	530	628	0.84	313	stacked

274	194701	2116	37933	457	671	0.68	314	single
275	135806	1782	28003	327	622	0.53	315	single
276	207111	2145	25183	476	626	0.76	123	single
277	268981	3051	30536	423	1029	0.41	92	single
278	274650	2817	38109	561	826	0.68	39	stacked
279	320868	4311	31682	556	1072	0.52	34	single
280	14477	523	15594	92	217	0.42	88	single
281	11490	554	14521	82	225	0.36	316	single
282	9180	424	13468	76	171	0.45	317	single
283	19879	519	10679	137	186	0.73	118	stacked
284	76858	1126	16003	282	416	0.68	26	stacked
285	27729	663	15695	176	247	0.71	318	stacked
286	34880	705	19931	202	215	0.94	319	stacked
287	8910	362	12122	98	138	0.71	52	single
288	41894	957	13167	194	353	0.55	51	single
289	8149	368	12312	95	134	0.71	50	single
290	9822	423	15985	69	174	0.40	320	single
291	10662	395	21821	108	146	0.74	321	single
292	9228	365	17447	97	135	0.72	322	single
293	30398	712	12823	157	271	0.58	108	single
294	50039	960	19773	197	353	0.56	61	single

2843	194	1.34	50	71	14	0.71	-288	-292	-290	0.64	52.81
689	94	1.42	29	30	26	0.96	-546	-547	-547	0.70	35.38
4896	258	1.45	62	95	89	0.65	-547	-555	-553	0.70	70.20
2970	194	1.47	59	62	22	0.95	-263	-265	-264	0.63	47.17
3712	224	1.48	56	84	5	0.66	-262	-264	-263	0.49	53.48
12890	425	1.52	100	167	45	0.60	-566	-572	-569	0.53	70.47
6949	302	1.54	81	109	126	0.75	-308	-312	-311	0.68	46.26
551	84	1.60	25	27	160	0.92	-461	-463	-463	0.96	39.16
875	105	1.66	32	34	77	0.92	-491	-495	-493	0.54	64.39
8574	341	1.79	83	130	91	0.64	-263	-265	-264	0.56	35.80
1399	136	1.83	37	48	115	0.77	-310	-313	-313	0.89	49.94
6409	286	1.83	85	94	34	0.90	-266	-268	-267	0.56	16.91
3718	223	1.86	58	82	177	0.70	-309	-313	-311	0.62	58.70
4084	229	1.87	69	77	59	0.89	-249	-252	-251	0.54	48.60
5302	269	1.97	66	105	3	0.63	-319	-326	-324	0.71	66.57
3689	217	2.02	66	73	136	0.90	-441	-455	-451	0.70	78.76
9889	354	2.03	108	115	23	0.94	-471	-483	-479	0.63	72.88
4244	233	2.05	67	81	57	0.83	-294	-299	-297	0.52	66.44
2883	193	2.07	57	64	167	0.89	-363	-371	-369	0.79	77.24
3256	205	2.07	58	73	20	0.79	-461	-465	-463	0.51	58.13
6722	295	2.08	80	103	69	0.78	-512	-518	-515	0.55	62.72
3484	211	2.13	61	72	14	0.84	-468	-475	-472	0.52	62.91
2354	175	2.13	50	60	60	0.83	-564	-566	-565	0.39	32.09
4669	249	2.14	64	92	143	0.69	-576	-582	-580	0.66	67.04
7949	325	2.14	84	123	15	0.68	-569	-584	-580	0.73	75.33
2545	182	2.19	52	65	91	0.80	-391	-398	-394	0.50	69.26
5354	265	2.21	69	97	52	0.71	-356	-362	-359	0.53	66.01
2191	171	2.24	43	64	66	0.67	-495	-499	-498	0.60	56.10
5123	256	2.27	73	88	14	0.83	-355	-363	-361	0.70	73.17
2743	187	2.29	56	63	89	0.89	-417	-423	-420	0.52	68.09
2350	174	2.29	48	61	94	0.79	-570	-581	-576	0.60	77.12
2868	191	2.33	57	63	41	0.91	-413	-416	-415	0.65	50.97
2435	177	2.34	49	63	137	0.79	-312	-314	-313	0.42	44.10
4544	240	2.34	74	77	104	0.96	-392	-400	-398	0.76	74.29
4941	253	2.34	73	82	94	0.90	-499	-515	-509	0.65	78.20
1081	122	2.35	29	47	93	0.61	-560	-564	-562	0.53	61.02

2060	163	2.56	46	57	13	0.81	-266	-269	-268	0.60	50.96
2054	162	2.63	49	55	157	0.89	-496	-499	-498	0.78	48.81
4090	229	2.63	66	78	180	0.85	-412	-416	-415	0.69	61.34
3932	225	2.63	64	77	115	0.84	-326	-334	-332	0.72	74.29
1512	139	2.64	42	46	162	0.91	-325	-327	-326	0.53	43.89
3778	220	2.65	65	74	178	0.89	-332	-335	-334	0.77	51.16
1202	124	2.66	37	41	92	0.89	-323	-326	-324	0.52	58.70
1645	149	2.67	37	56	83	0.66	-206	-211	-208	0.41	68.47
10141	358	2.72	110	115	112	0.95	-558	-568	-564	0.54	78.35
1003	113	2.73	34	37	173	0.92	-499	-502	-502	0.82	53.87
1095	118	2.75	35	41	93	0.85	-488	-490	-490	0.77	40.96
4065	228	2.76	66	80	163	0.82	-283	-288	-286	0.67	68.15
4820	255	2.77	63	97	145	0.65	-333	-339	-337	0.67	68.61
4019	232	2.81	57	87	52	0.66	-448	-459	-457	0.81	76.45
19088	495	2.83	147	169	6	0.87	-330	-337	-333	0.49	58.30
2914	197	2.83	51	74	125	0.69	-302	-308	-306	0.68	62.15
2940	194	2.85	58	61	1	0.95	-348	-351	-350	0.67	53.73
4235	233	2.86	66	81	73	0.81	-499	-503	-501	0.46	61.48
3203	208	2.90	52	79	115	0.65	-297	-302	-301	0.75	63.74
906	108	2.93	31	38	9	0.84	-546	-549	-548	0.70	56.49
2738	193	3.01	47	73	90	0.65	-560	-563	-561	0.28	56.40
1296	129	3.03	37	43	96	0.86	-495	-498	-497	0.81	52.10
2490	178	3.06	54	57	102	0.95	-330	-333	-332	0.62	56.83
1706	148	3.06	42	51	32	0.82	-360	-365	-364	0.70	63.52
3179	201	3.06	60	66	15	0.91	-337	-342	-340	0.66	60.07
10334	393	3.07	82	158	32	0.52	-590	-607	-600	0.63	82.67
2029	161	3.08	49	53	117	0.92	-408	-414	-412	0.75	71.85
15208	439	3.10	133	145	42	0.92	-674	-684	-680	0.61	70.49
4448	238	3.10	71	79	107	0.90	-417	-423	-421	0.65	69.00
5009	255	3.13	70	90	25	0.77	-543	-549	-545	0.32	57.39
8696	338	3.14	92	122	153	0.76	-425	-433	-431	0.65	65.68
2271	173	3.14	47	62	112	0.75	-304	-309	-307	0.63	61.31
5962	276	3.15	80	95	47	0.84	-528	-533	-530	0.45	61.20
5337	266	3.19	71	98	8	0.72	-305	-312	-310	0.70	73.53
1799	151	3.19	47	48	174	0.98	-519	-522	-521	0.69	55.62
1075	118	3.19	32	42	80	0.77	-555	-558	-556	0.51	57.91
1297	129	3.20	36	44	102	0.83	-546	-550	-549	0.65	55.39

7567	310	3.31	96	102	11	0.94	-507	-514	-511	0.63	67.86	5.19	550	STRATIGRAPHY
4025	228	3.33	62	79	90	0.79	-558	-567	-564	0.59	71.70	6.61	800	FAULT
5925	275	3.33	81	95	175	0.85	-306	-309	-308	0.71	57.11	3.77	500	FAULT
1497	140	3.34	37	50	88	0.74	-552	-560	-556	0.47	65.81	7.50	550	STRATIGRAPHY
9437	380	3.36	75	155	176	0.48	-539	-548	-544	0.60	73.59	5.16	750	TOP_SALT
8468	327	3.39	102	106	101	0.96	-345	-349	-347	0.57	58.59	4.12	350	STRATIGRAPHY
8078	321	3.39	93	110	123	0.85	-261	-266	-263	0.52	55.90	3.74	1000	TOP_SALT
2428	179	3.40	47	66	56	0.72	-542	-552	-548	0.58	78.11	5.85	350	STRATIGRAPHY
3588	214	3.40	61	73	93	0.83	-352	-357	-356	0.77	60.08	4.66	700	FAULT
2963	195	3.41	57	64	170	0.90	-330	-336	-334	0.67	65.70	6.05	250	COMBO
4053	230	3.48	62	85	170	0.74	-293	-305	-302	0.74	75.91	4.48	700	FAULT
8881	336	3.50	101	110	108	0.91	-383	-395	-392	0.73	80.37	5.00	500	COMBO
16149	457	3.52	125	162	93	0.77	-347	-353	-350	0.60	67.62	3.79	150	STRATIGRAPHY
17088	489	3.52	113	193	67	0.58	-639	-649	-643	0.43	74.02	4.43	1150	TOP_SALT
3133	201	3.53	55	71	143	0.78	-300	-304	-303	0.62	58.78	3.90	800	FAULT
3292	204	3.54	64	65	79	0.99	-284	-288	-287	0.67	60.41	5.10	200	FAULT
4075	227	3.56	70	74	45	0.95	-331	-336	-335	0.78	64.24	3.39	750	COMBO
7149	317	3.58	71	121	127	0.59	-331	-338	-336	0.61	71.97	4.79	600	FAULT
5873	274	3.60	77	95	90	0.81	-590	-594	-592	0.48	53.15	3.64	350	MINIBASIN
2780	190	3.60	51	69	98	0.75	-457	-463	-460	0.48	69.06	5.60	850	TOP_SALT
20847	525	3.65	138	190	102	0.72	-311	-322	-317	0.55	77.08	5.18	350	TOP_SALT
2304	172	3.72	51	55	93	0.93	-302	-306	-305	0.72	58.93	4.38	500	COMBO
1346	131	3.73	40	43	58	0.95	-489	-494	-493	0.73	60.86	5.13	550	STRATIGRAPHY
6606	296	3.77	79	110	39	0.72	-484	-492	-488	0.51	70.73	5.83	450	FAULT
10759	380	3.77	95	143	72	0.67	-267	-273	-271	0.53	61.35	4.09	500	FAULT
3450	212	3.78	57	77	59	0.75	-436	-450	-445	0.65	74.36	7.88	700	TOP_SALT
2338	173	3.88	51	57	174	0.90	-350	-357	-354	0.62	72.70	5.94	450	COMBO
3215	202	3.92	61	65	97	0.94	-311	-315	-314	0.71	56.87	4.64	450	COMBO
11289	379	3.97	111	128	112	0.87	-280	-288	-284	0.54	64.34	4.28	400	STRATIGRAPHY
5564	265	4.00	81	87	102	0.93	-451	-465	-461	0.68	82.20	8.05	550	FAULT
1769	150	4.00	45	49	80	0.91	-337	-341	-340	0.74	61.16	3.74	650	FAULT
1812	152	4.03	44	50	180	0.88	-354	-358	-358	0.85	61.07	2.58	750	FAULT
4531	241	4.04	75	78	144	0.95	-458	-465	-461	0.37	72.14	5.06	450	FAULT
9018	363	4.06	81	147	43	0.55	-512	-520	-517	0.59	74.92	4.53	50	MINIBASIN
9185	342	4.06	104	110	17	0.94	-560	-576	-569	0.57	77.57	7.02	400	STRATIGRAPHY
2025	161	4.09	46	55	95	0.83	-496	-498	-497	0.34	39.52	2.34	600	STRATIGRAPHY
2832	200	4.20	45	79	126	0.57	-310	-316	-314	0.73	63.76	4.40	500	FAULT
2716	187	4.23	52	66	69	0.78	-507	-512	-511	0.75	64.02	4.59	550	STRATIGRAPHY
1303	129	4.24	40	41	57	0.96	-423	-429	-426	0.50	62.33	5.06	450	COMBO
3489	216	4.24	54	78	91	0.69	-223	-233	-230	0.72	76.56	8.21	700	FAULT
1915	157	4.26	45	52	72	0.87	-507	-513	-511	0.65	61.33	5.86	500	STRATIGRAPHY
2186	169	4.27	47	61	4	0.78	-580	-585	-584	0.85	65.56	4.35	300	MINIBASIN
7264	307	4.27	87	110	38	0.79	-267	-272	-270	0.68	53.79	2.57	550	STRATIGRAPHY
2660	186	4.28	51	65	103	0.79	-497	-500	-498	0.57	48.53	3.50	450	STRATIGRAPHY
1493	139	4.30	40	47	167	0.85	-549	-553	-551	0.56	56.81	4.81	650	TOP_SALT
9383	345	4.30	106	110	88	0.97	-327	-331	-329	0.64	61.54	3.26	600	STRATIGRAPHY
5263	263	4.30	69	94	95	0.73	-299	-306	-304	0.59	70.18	5.13	650	STRATIGRAPHY
6393	287	4.31	81	102	82	0.80	-499	-507	-504	0.65	72.14	5.28	800	TOP_SALT
2162	167	4.36	47	57	26	0.83	-357	-362	-360	0.69	66.13	4.71	650	TOP_SALT

4200	247	4.36	54	99	151	0.54	-296	-301	-299	0.58	65.85	4.82	800	FAULT
7886	322	4.45	88	114	52	0.77	-270	-275	-273	0.56	54.50	3.57	400	STRATIGRAPHY
3151	200	4.50	61	65	142	0.95	-363	-367	-366	0.77	58.31	4.31	500	COMBO
5956	279	4.50	77	100	72	0.77	-308	-320	-319	0.87	80.96	4.36	600	MINIBASIN
7520	309	4.53	92	103	102	0.89	-375	-380	-379	0.73	66.77	3.43	550	MINIBASIN
3473	216	4.53	54	78	3	0.69	-218	-223	-222	0.78	66.05	5.38	850	FAULT
4714	248	4.60	69	88	137	0.79	-222	-229	-228	0.84	70.95	5.79	800	FAULT
6777	293	4.62	91	92	85	0.99	-463	-470	-467	0.56	68.25	5.18	550	FAULT
4130	230	4.64	67	76	99	0.88	-322	-326	-325	0.65	63.72	4.82	600	FAULT
2159	166	4.65	51	52	4	0.98	-126	-138	-135	0.71	78.09	10.15	350	STRATIGRAPHY
1777	151	4.70	44	51	112	0.87	-364	-369	-367	0.58	59.78	5.64	300	COMBO
3550	218	4.76	55	79	3	0.70	-281	-296	-294	0.83	79.92	7.81	600	FAULT
6130	284	4.76	74	106	50	0.70	-285	-292	-288	0.49	68.25	4.98	1050	TOP_SALT
5453	288	4.78	57	118	121	0.49	-450	-462	-458	0.67	79.82	7.12	800	STRATIGRAPHY
2881	191	4.83	58	61	4	0.95	-397	-402	-401	0.82	68.11	2.91	500	COMBO
8202	325	4.83	94	107	63	0.88	-289	-296	-294	0.72	68.31	4.10	900	FAULT
4251	232	4.85	70	76	164	0.92	-604	-608	-606	0.48	58.93	4.64	300	MINIBASIN
4379	237	4.85	68	82	49	0.82	-266	-270	-268	0.43	62.38	4.22	450	STRATIGRAPHY
2038	162	4.86	46	55	57	0.84	-505	-508	-507	0.67	52.84	3.60	550	STRATIGRAPHY
5115	261	4.88	72	92	15	0.78	-279	-289	-287	0.81	74.98	3.49	800	FAULT
3090	198	4.90	61	64	28	0.95	-268	-274	-272	0.62	65.28	5.70	1200	TOP_SALT
7687	313	4.91	91	106	132	0.86	-350	-355	-353	0.59	66.01	3.41	350	STRATIGRAPHY
2160	166	4.91	51	52	91	0.98	-228	-233	-232	0.69	66.69	7.10	800	FAULT
8657	347	4.92	81	136	25	0.59	-598	-613	-607	0.64	79.10	6.52	1100	TOP_SALT
3550	218	4.93	55	79	3	0.70	-224	-235	-233	0.77	79.55	7.15	800	FAULT
3803	224	4.98	60	84	151	0.72	-352	-362	-358	0.60	70.96	7.30	400	COMBO
2159	166	5.02	51	52	4	0.98	-406	-414	-411	0.69	75.24	7.95	300	COMBO
2206	168	5.02	51	52	91	0.99	-497	-503	-502	0.78	69.67	6.73	450	STRATIGRAPHY
2160	166	5.03	51	52	91	0.98	-496	-499	-498	0.74	44.71	4.46	450	STRATIGRAPHY
2160	166	5.03	51	52	91	0.98	-279	-284	-283	0.67	67.60	7.26	1050	TOP_SALT
2115	164	5.04	50	51	91	0.99	-513	-521	-518	0.67	74.55	4.86	550	STRATIGRAPHY
2115	164	5.05	50	51	91	0.99	-569	-580	-578	0.78	77.07	9.48	600	STRATIGRAPHY
2206	168	5.08	51	52	91	0.99	-569	-575	-573	0.72	69.38	7.14	400	STRATIGRAPHY
7821	332	5.08	75	130	100	0.57	-347	-361	-357	0.74	77.75	7.19	700	FAULT
2206	168	5.09	51	52	91	0.99	-334	-342	-340	0.78	71.94	7.72	1100	FAULT
2206	168	5.10	51	52	91	0.99	-431	-440	-438	0.77	73.31	8.49	750	FAULT
2206	168	5.15	51	52	91	0.99	-513	-520	-518	0.67	74.10	8.44	550	STRATIGRAPHY
2160	166	5.16	51	52	91	0.98	-842	-849	-847	0.74	69.11	7.34	1000	TOP_SALT
2115	164	5.17	50	51	91	0.99	-415	-424	-422	0.75	74.89	8.78	400	FAULT
2160	166	5.18	51	52	91	0.98	-491	-498	-496	0.72	70.86	7.78	450	STRATIGRAPHY
3550	218	5.18	55	79	3	0.70	-215	-220	-219	0.71	66.36	6.24	800	FAULT
2160	166	5.19	51	52	91	0.98	-377	-383	-381	0.69	66.94	8.83	350	FAULT
2159	166	5.20	51	52	4	0.98	-262	-270	-268	0.73	73.65	8.21	1000	TOP_SALT
5047	254	5.20	74	84	5	0.88	-336	-341	-339	0.61	61.75	3.89	450	COMBO
2115	164	5.21	50	51	91	0.99	-273	-277	-276	0.84	60.86	4.39	450	STRATIGRAPHY
3473	216	5.21	54	78	3	0.69	-492	-500	-498	0.76	74.99	7.11	550	STRATIGRAPHY
2159	166	5.22	51	52	4	0.98	-423	-432	-430	0.80	73.50	7.68	350	FAULT
3473	216	5.24	54	78	3	0.69	-508	-519	-517	0.80	76.35	6.97	400	TOP_SALT
2115	164	5.25	50	51	91	0.99	-417	-421	-420	0.78	64.15	6.01	700	FAULT

2206	168	5.27	51	52	91	0.99	-519	-527	-525	0.70	73.57	8.13	500	STRATIGRAPHY
2159	166	5.28	51	52	4	0.98	-625	-633	-631	0.76	75.46	6.91	850	FAULT
5459	263	5.29	80	86	33	0.93	-672	-677	-676	0.69	55.25	3.69	300	STRATIGRAPHY
2160	166	5.30	51	52	91	0.98	-550	-566	-563	0.77	81.15	9.41	500	FAULT
4790	246	5.30	74	82	65	0.90	-528	-537	-534	0.67	76.67	6.67	550	STRATIGRAPHY
2115	164	5.31	50	51	91	0.99	-284	-290	-288	0.66	67.63	8.01	450	STRATIGRAPHY
2160	166	5.32	51	52	91	0.98	-273	-285	-281	0.70	80.08	9.68	700	FAULT
2115	164	5.32	50	51	91	0.99	-314	-318	-317	0.80	55.96	4.91	900	FAULT
2206	168	5.39	51	52	91	0.99	-331	-346	-340	0.65	82.50	10.78	300	COMBO
3473	216	5.39	54	78	3	0.69	-461	-466	-465	0.80	61.79	5.14	1100	TOP_SALT
2115	164	5.40	50	51	91	0.99	-435	-438	-437	0.75	55.20	5.12	450	FAULT
2160	166	5.41	51	52	91	0.98	-505	-517	-513	0.70	78.81	9.98	500	STRATIGRAPHY
2206	168	5.41	51	52	91	0.99	-348	-351	-350	0.71	48.73	5.50	650	TOP_SALT
2115	164	5.41	50	51	91	0.99	-339	-351	-347	0.67	79.06	11.03	700	FAULT
2160	166	5.42	51	52	91	0.98	-482	-491	-489	0.75	77.05	7.95	550	FAULT
2159	166	5.42	51	52	4	0.98	-343	-347	-346	0.70	59.62	6.63	650	MINIBASIN
3550	218	5.43	55	79	3	0.70	-673	-680	-679	0.73	72.91	6.65	500	FAULT
2206	168	5.46	51	52	91	0.99	-333	-341	-339	0.73	74.74	7.92	400	STRATIGRAPHY
9191	355	5.47	86	132	9	0.65	-291	-293	-293	0.78	53.57	2.55	850	FAULT
3473	216	5.48	54	78	3	0.69	-402	-409	-407	0.80	69.26	5.71	500	MINIBASIN
5809	272	5.48	83	84	89	0.99	-496	-499	-498	0.75	60.33	3.98	500	STRATIGRAPHY
6067	311	5.49	58	131	179	0.44	-572	-574	-574	0.68	43.53	3.02	250	STRATIGRAPHY
10786	377	5.49	106	141	144	0.75	-326	-336	-332	0.62	72.84	6.17	400	COMBO
3550	218	5.49	55	79	3	0.70	-501	-509	-507	0.73	73.27	7.69	500	STRATIGRAPHY
2160	166	5.49	51	52	91	0.98	-497	-507	-505	0.80	77.46	6.59	650	STRATIGRAPHY
2160	166	5.51	51	52	91	0.98	-411	-421	-420	0.88	77.90	6.72	700	FAULT
2159	166	5.52	51	52	4	0.98	-269	-273	-272	0.67	58.77	5.82	400	STRATIGRAPHY
2159	166	5.52	51	52	4	0.98	-344	-365	-359	0.73	83.55	10.91	450	TOP_SALT
13791	419	5.52	127	133	24	0.96	-288	-305	-301	0.75	78.82	5.87	950	FAULT
2206	168	5.53	51	52	91	0.99	-389	-402	-398	0.71	79.45	10.24	500	COMBO
8387	329	5.54	92	109	7	0.84	-495	-512	-506	0.62	78.41	7.16	400	STRATIGRAPHY
2160	166	5.54	51	52	91	0.98	-536	-541	-539	0.70	64.49	7.24	500	TOP_SALT
7083	323	5.58	70	126	154	0.55	-570	-574	-573	0.81	66.72	3.85	300	STRATIGRAPHY
4814	265	5.59	56	106	0	0.53	-564	-567	-566	0.60	51.34	4.66	400	STRATIGRAPHY
4683	249	5.61	71	88	45	0.81	-374	-383	-380	0.71	75.74	8.07	250	TOP_SALT
2160	166	5.61	51	52	91	0.98	-321	-324	-323	0.68	52.91	6.06	600	MINIBASIN
3567	218	5.64	55	78	89	0.70	-543	-552	-550	0.85	74.36	6.55	350	STRATIGRAPHY
2115	164	5.67	50	51	91	0.99	-590	-603	-600	0.75	78.94	9.55	450	STRATIGRAPHY
3550	218	5.67	55	79	3	0.70	-363	-371	-369	0.71	73.96	7.90	500	FAULT
5679	268	5.69	84	84	65	0.99	-485	-494	-489	0.52	70.77	6.26	450	STRATIGRAPHY
5942	280	5.69	79	99	180	0.79	-774	-784	-782	0.83	78.31	4.68	750	TOP_SALT
4714	248	5.71	69	88	137	0.79	-314	-325	-324	0.84	76.32	6.42	450	TOP_SALT
2115	164	5.72	50	51	91	0.99	-390	-400	-396	0.61	76.05	10.25	550	COMBO
3227	202	5.72	63	64	26	0.99	-560	-565	-564	0.78	65.54	4.26	800	FAULT
2160	166	5.74	51	52	91	0.98	-558	-563	-561	0.65	64.59	7.09	350	MINIBASIN
2159	166	5.74	51	52	4	0.98	-581	-586	-584	0.63	63.16	7.65	850	TOP_SALT
3550	218	5.76	55	79	3	0.70	-493	-503	-501	0.75	78.71	7.19	400	FAULT
2115	164	5.77	50	51	91	0.99	-495	-502	-499	0.59	72.78	8.56	300	TOP_SALT
2865	198	5.77	47	76	96	0.62	-265	-269	-268	0.87	59.01	1.88	400	STRATIGRAPHY

3550	218	5.77	55	79	3	0.70	-558	-569	-566	0.79	76.70	7.53	400	TOP_SALT
3473	216	5.79	54	78	3	0.69	-278	-282	-280	0.64	57.77	6.23	400	STRATIGRAPHY
2160	166	5.79	51	52	91	0.98	-490	-496	-494	0.67	70.34	8.28	550	STRATIGRAPHY
3445	214	5.80	54	77	89	0.70	-317	-325	-323	0.80	70.24	6.77	400	COMBO
4786	251	5.80	72	88	42	0.81	-212	-226	-224	0.83	81.07	7.73	800	FAULT
2160	166	5.83	51	52	91	0.98	-376	-382	-380	0.72	70.25	8.04	500	FAULT
2160	166	5.83	51	52	91	0.98	-487	-493	-491	0.66	66.59	7.22	500	FAULT
4795	250	5.84	70	87	45	0.81	-545	-552	-551	0.86	71.80	4.52	300	FAULT
2115	164	5.85	50	51	91	0.99	-315	-321	-319	0.68	70.47	8.48	800	FAULT
4786	251	5.86	72	88	132	0.81	-282	-290	-287	0.68	67.31	7.36	200	MINIBASIN
2206	168	5.86	51	52	91	0.99	-592	-600	-598	0.78	72.97	7.81	1000	FAULT
2206	168	5.87	51	52	91	0.99	-415	-419	-418	0.71	63.86	6.29	1200	FAULT
2160	166	5.90	51	52	91	0.98	-263	-281	-276	0.73	82.47	10.84	450	COMBO
2159	166	5.91	51	52	4	0.98	-480	-490	-486	0.64	78.51	9.96	150	MINIBASIN
10692	425	5.91	72	180	160	0.40	-550	-560	-559	0.90	77.29	3.17	450	FAULT
3550	218	5.93	55	79	3	0.70	-577	-585	-583	0.78	74.40	6.83	450	FAULT
5809	272	5.96	83	84	89	0.99	-333	-339	-337	0.74	67.34	5.62	200	TOP_SALT
8184	339	5.98	80	126	153	0.63	-276	-281	-280	0.80	64.94	3.14	400	FAULT
3567	218	6.02	55	78	89	0.70	-263	-271	-270	0.79	75.35	7.00	400	STRATIGRAPHY
3550	218	6.05	55	79	3	0.70	-544	-563	-560	0.86	83.15	7.28	300	STRATIGRAPHY
3550	218	6.06	55	79	3	0.70	-285	-291	-289	0.69	66.86	7.07	1050	TOP_SALT
3550	218	6.08	55	79	3	0.70	-524	-533	-531	0.73	75.77	7.98	550	STRATIGRAPHY
3550	218	6.09	55	79	3	0.70	-293	-306	-303	0.81	77.73	7.79	950	FAULT
6971	303	6.11	82	109	101	0.75	-540	-550	-549	0.87	78.27	4.87	450	FAULT
2472	177	6.13	55	56	7	0.99	-336	-342	-342	0.89	72.44	3.70	450	COMBO
2160	166	6.15	51	52	91	0.98	-370	-387	-382	0.68	82.80	11.10	300	FAULT
2159	166	6.21	51	52	4	0.98	-540	-553	-548	0.65	80.88	9.68	400	TOP_SALT
2160	166	6.22	51	52	91	0.98	-500	-509	-507	0.77	72.37	9.02	500	FAULT
3550	218	6.24	55	79	3	0.70	-280	-288	-287	0.77	70.48	6.83	500	FAULT
3506	216	6.25	55	78	4	0.71	-344	-352	-350	0.75	71.45	7.34	600	STRATIGRAPHY
2115	164	6.27	50	51	91	0.99	-345	-354	-351	0.69	76.42	9.48	550	STRATIGRAPHY
2180	167	6.27	51	55	174	0.93	-504	-510	-509	0.75	68.77	5.91	550	STRATIGRAPHY
4775	249	6.28	70	88	137	0.80	-455	-466	-464	0.79	75.93	7.51	1100	TOP_SALT
3473	216	6.29	54	78	3	0.69	-579	-590	-587	0.70	75.17	8.56	900	TOP_SALT
2115	164	6.30	50	51	91	0.99	-582	-591	-588	0.64	77.06	10.14	550	TOP_SALT
4729	260	6.33	56	103	91	0.54	-668	-672	-670	0.57	63.78	5.95	1100	TOP_SALT
3445	214	6.36	54	77	89	0.70	-258	-265	-262	0.67	73.05	7.93	400	FAULT
4786	251	6.36	72	88	42	0.81	-213	-224	-221	0.73	80.53	8.60	700	TOP_SALT
5950	289	6.36	70	109	119	0.65	-340	-354	-352	0.84	79.29	6.09	900	FAULT
4775	249	6.37	70	88	137	0.80	-357	-367	-365	0.80	74.06	6.91	650	TOP_SALT
10448	375	6.39	97	136	34	0.71	-333	-343	-339	0.63	77.43	5.48	400	COMBO
5809	272	6.41	83	84	89	0.99	-502	-510	-508	0.78	74.88	6.53	500	STRATIGRAPHY
7001	304	6.42	82	107	172	0.77	-366	-383	-381	0.88	82.44	5.70	200	FAULT
5733	270	6.43	82	84	89	0.98	-496	-503	-501	0.72	68.81	5.53	550	STRATIGRAPHY
7031	304	6.45	83	108	86	0.77	-397	-402	-400	0.72	58.77	4.62	300	FAULT
4873	266	6.50	57	105	0	0.54	-485	-492	-490	0.72	74.76	5.66	500	FAULT
5917	283	6.52	71	104	38	0.68	-585	-592	-590	0.74	62.01	5.21	200	STRATIGRAPHY
3473	216	6.53	54	78	3	0.69	-378	-390	-386	0.68	79.82	9.13	250	TOP_SALT
8241	323	6.55	98	104	12	0.95	-494	-504	-500	0.61	77.93	5.93	450	TOP_SALT

5809	272	6.56	83	84	89	0.99	-258	-267	-265	0.75	75.75	6.62	600	FAULT
5809	272	6.57	83	84	89	0.99	-547	-553	-551	0.73	64.82	5.10	300	FAULT
2160	166	6.58	51	52	91	0.98	-370	-378	-376	0.69	74.54	9.10	500	FAULT
7924	356	6.62	71	150	7	0.47	-571	-575	-574	0.67	65.96	3.51	300	STRATIGRAPHY
3567	218	6.62	55	78	89	0.70	-500	-508	-506	0.75	75.39	7.59	500	STRATIGRAPHY
5493	264	6.64	81	86	40	0.94	-407	-415	-413	0.75	69.56	4.45	400	STRATIGRAPHY
3473	216	6.64	54	78	3	0.69	-222	-237	-234	0.77	79.91	9.17	1000	FAULT
2115	164	6.66	50	51	91	0.99	-602	-613	-609	0.64	77.99	10.22	100	STRATIGRAPHY
7877	336	6.67	75	130	84	0.57	-339	-346	-344	0.78	72.78	4.21	100	MINIBASIN
3550	218	6.67	55	79	3	0.70	-447	-454	-451	0.59	72.15	8.26	450	FAULT
14978	435	6.67	132	144	33	0.92	-541	-562	-556	0.69	82.28	6.28	550	COMBO
3550	218	6.68	55	79	3	0.70	-493	-501	-498	0.70	70.93	7.35	450	STRATIGRAPHY
10337	371	6.72	104	129	169	0.81	-464	-472	-470	0.80	73.48	4.47	400	STRATIGRAPHY
3473	216	6.73	54	78	3	0.69	-310	-317	-315	0.67	72.82	7.92	700	MINIBASIN
8171	335	6.75	82	130	80	0.63	-594	-605	-603	0.84	76.41	4.64	400	STRATIGRAPHY
8139	332	6.76	84	125	1	0.67	-366	-384	-381	0.83	82.95	5.27	200	FAULT
2025	160	6.77	48	54	59	0.89	-371	-380	-375	0.44	70.34	6.12	250	COMBO
3550	218	6.78	55	79	3	0.70	-570	-576	-574	0.78	63.89	5.94	300	STRATIGRAPHY
5924	290	6.82	69	107	154	0.65	-650	-668	-664	0.80	83.91	7.00	400	FAULT
5809	272	6.82	83	84	89	0.99	-523	-537	-534	0.74	81.50	7.63	450	STRATIGRAPHY
4794	263	6.82	56	102	90	0.55	-568	-587	-582	0.75	82.98	9.09	600	TOP_SALT
2159	166	6.85	51	52	4	0.98	-512	-521	-518	0.62	75.99	10.74	550	STRATIGRAPHY
6239	315	6.85	59	132	179	0.45	-327	-333	-331	0.61	67.71	6.67	800	FAULT
3473	216	6.87	54	78	3	0.69	-441	-455	-451	0.71	79.90	9.86	400	TOP_SALT
2206	168	6.90	51	52	91	0.99	-541	-547	-544	0.63	70.57	8.74	350	STRATIGRAPHY
3550	218	6.91	55	79	3	0.70	-501	-511	-508	0.75	77.98	7.95	550	STRATIGRAPHY
2160	166	6.91	51	52	91	0.98	-612	-627	-622	0.68	80.85	11.40	1100	FAULT
20182	535	6.93	135	208	69	0.65	-520	-527	-525	0.76	70.66	3.57	450	FAULT
6996	304	6.99	82	107	172	0.77	-270	-277	-275	0.73	70.00	5.47	500	FAULT
2115	164	6.99	50	51	91	0.99	-403	-411	-409	0.73	71.71	8.44	800	TOP_SALT
5809	272	7.00	83	84	89	0.99	-549	-558	-556	0.75	77.10	6.18	350	STRATIGRAPHY
8014	323	7.00	87	110	89	0.79	-513	-522	-519	0.74	76.20	5.99	550	STRATIGRAPHY
6811	313	7.04	66	119	28	0.55	-566	-575	-573	0.78	76.61	6.12	500	STRATIGRAPHY
2159	166	7.07	51	52	4	0.98	-273	-280	-278	0.72	67.76	8.59	400	FAULT
4757	250	7.09	71	88	41	0.81	-368	-377	-374	0.75	74.49	7.65	500	FAULT
3550	218	7.10	55	79	3	0.70	-364	-374	-371	0.72	76.88	8.68	450	FAULT
7931	323	7.10	93	108	27	0.86	-161	-169	-166	0.67	69.79	5.39	700	FAULT
3489	216	7.11	54	78	91	0.69	-266	-272	-270	0.68	67.61	6.51	400	STRATIGRAPHY
4795	250	7.13	70	87	45	0.81	-494	-501	-499	0.75	68.10	6.03	400	FAULT
13216	421	7.14	109	154	84	0.71	-489	-501	-499	0.82	79.57	4.93	500	FAULT
6994	303	7.14	83	107	86	0.77	-546	-556	-553	0.74	73.52	6.14	700	STRATIGRAPHY
6996	304	7.14	82	107	172	0.77	-790	-808	-804	0.82	83.52	6.64	850	FAULT
8885	340	7.15	92	123	138	0.75	-267	-276	-274	0.77	75.08	5.71	400	FAULT
3489	216	7.19	54	78	91	0.69	-376	-384	-382	0.75	72.96	7.68	350	FAULT
5809	272	7.20	83	84	89	0.99	-517	-533	-530	0.82	81.42	7.04	450	STRATIGRAPHY
4742	249	7.21	69	88	136	0.79	-589	-603	-599	0.73	81.32	8.65	650	TOP_SALT
2115	164	7.21	50	51	91	0.99	-426	-436	-433	0.71	75.60	10.01	750	FAULT
9852	385	7.23	79	153	45	0.52	-499	-510	-507	0.79	78.89	5.56	500	FAULT
7899	327	7.25	84	122	48	0.68	-424	-434	-432	0.78	77.62	5.81	350	FAULT

2206	168	7.25	51	52	91	0.99	-312	-325	-322	0.73	81.83	10.06	600	FAULT
1934	157	7.28	45	54	91	0.84	-408	-415	-413	0.70	68.54	5.13	550	COMBO
3550	218	7.28	55	79	3	0.70	-287	-304	-301	0.86	81.79	7.64	350	STRATIGRAPHY
2849	193	7.33	53	67	106	0.79	-353	-360	-357	0.60	68.00	5.67	350	FAULT
5063	257	7.34	69	94	123	0.73	-261	-266	-264	0.66	65.20	4.49	400	FAULT
4763	250	7.34	69	87	44	0.80	-750	-760	-757	0.70	76.40	7.85	600	TOP_SALT
6953	320	7.36	68	126	152	0.54	-345	-355	-353	0.77	78.25	6.00	600	FAULT
5809	272	7.38	83	84	89	0.99	-245	-254	-251	0.69	72.88	7.28	750	TOP_SALT
9988	387	7.41	79	152	36	0.52	-324	-332	-330	0.75	71.47	5.12	500	FAULT
5768	274	7.43	77	96	112	0.80	-392	-405	-398	0.48	78.96	7.53	450	COMBO
3550	218	7.46	55	79	3	0.70	-515	-534	-529	0.74	83.13	8.89	400	FAULT
3550	218	7.46	55	79	3	0.70	-445	-457	-454	0.75	78.09	8.94	400	TOP_SALT
2115	164	7.48	50	51	91	0.99	-290	-304	-301	0.79	79.94	10.01	400	FAULT
6119	311	7.48	58	127	90	0.45	-519	-528	-525	0.69	77.04	6.52	500	STRATIGRAPHY
2115	164	7.49	50	51	91	0.99	-418	-431	-427	0.74	78.72	9.97	150	STRATIGRAPHY
3567	218	7.51	55	78	89	0.70	-513	-527	-523	0.74	80.09	9.34	400	FAULT
4761	250	7.53	69	87	46	0.80	-294	-304	-301	0.71	74.30	7.52	900	FAULT
6239	315	7.56	59	132	179	0.45	-220	-231	-227	0.65	79.62	6.84	750	FAULT
8025	349	7.61	71	133	0	0.54	-604	-636	-632	0.87	86.33	6.50	1000	TOP_SALT
8086	325	7.62	87	111	89	0.78	-356	-363	-361	0.69	75.14	6.17	350	FAULT
4837	265	7.68	56	103	90	0.55	-534	-543	-540	0.70	73.89	6.51	500	TOP_SALT
15011	440	7.69	126	154	41	0.82	-515	-522	-520	0.75	65.38	3.88	400	TOP_SALT
3550	218	7.69	55	79	3	0.70	-546	-559	-555	0.68	81.60	9.42	750	TOP_SALT
7406	310	7.70	91	104	80	0.87	-591	-604	-598	0.53	76.08	6.61	500	STRATIGRAPHY
2206	168	7.71	51	52	91	0.99	-496	-507	-504	0.67	78.77	10.70	350	FAULT
4873	266	7.72	57	105	0	0.54	-379	-388	-385	0.67	77.50	8.17	550	FAULT
5733	270	7.74	83	83	2	0.99	-297	-307	-305	0.79	77.15	6.42	500	FAULT
3473	216	7.74	54	78	3	0.69	-203	-236	-230	0.81	86.13	7.96	750	TOP_SALT
5809	272	7.75	83	84	89	0.99	-284	-295	-293	0.76	76.32	7.14	500	FAULT
11069	384	7.76	100	139	34	0.72	-454	-476	-472	0.79	80.91	6.35	700	TOP_SALT
4682	248	7.78	71	88	131	0.81	-461	-475	-473	0.81	80.95	8.41	350	FAULT
16565	474	7.78	130	172	177	0.76	-345	-353	-350	0.67	71.16	4.31	450	FAULT
5809	272	7.78	83	84	89	0.99	-482	-490	-488	0.74	73.78	6.93	500	FAULT
7022	305	7.78	82	108	11	0.76	-355	-366	-363	0.77	76.77	6.63	750	FAULT
10090	359	7.81	106	121	167	0.88	-234	-243	-239	0.63	70.10	5.86	200	MINIBASIN
8127	345	7.85	80	134	17	0.60	-597	-607	-604	0.71	75.96	6.46	450	FAULT
5809	272	7.93	83	84	89	0.99	-376	-384	-381	0.66	75.52	6.53	500	FAULT
6989	304	7.93	83	110	11	0.76	-336	-345	-343	0.70	72.73	6.46	700	FAULT
3473	216	7.95	54	78	3	0.69	-254	-262	-259	0.59	72.45	8.71	150	STRATIGRAPHY
8086	325	7.96	87	111	89	0.78	-328	-334	-332	0.65	67.04	5.81	600	STRATIGRAPHY
11336	390	7.96	106	139	19	0.76	-549	-557	-555	0.70	74.76	4.86	700	TOP_SALT
2115	164	7.97	50	51	91	0.99	-363	-374	-370	0.66	77.17	10.47	500	COMBO
5809	272	7.98	83	84	89	0.99	-314	-329	-326	0.80	80.56	7.38	350	FAULT
4814	265	7.98	56	106	0	0.53	-487	-499	-496	0.70	76.80	8.32	550	STRATIGRAPHY
5733	270	8.00	82	84	89	0.98	-347	-361	-358	0.77	79.31	7.69	450	MINIBASIN
4066	241	8.04	55	94	83	0.58	-346	-350	-349	0.69	62.12	3.52	200	TOP_SALT
3473	216	8.04	54	78	3	0.69	-488	-504	-500	0.75	80.17	9.16	750	TOP_SALT
3550	218	8.06	55	79	3	0.70	-460	-474	-471	0.72	80.76	9.13	600	STRATIGRAPHY
9191	355	8.06	86	132	99	0.65	-363	-373	-370	0.73	76.83	6.15	650	FAULT

13210	412	8.10	129	131	100	0.99	-544	-550	-548	0.67	68.74	4.57	900	TOP_SALT
3550	218	8.12	55	79	3	0.70	-277	-290	-286	0.69	80.73	9.29	600	FAULT
6952	301	8.13	83	106	164	0.78	-274	-282	-279	0.67	76.37	6.14	400	FAULT
6091	283	8.18	78	99	87	0.79	-337	-345	-341	0.54	73.23	7.25	900	FAULT
5809	272	8.25	83	84	89	0.99	-336	-344	-341	0.64	73.39	7.47	600	MINIBASIN
8126	332	8.27	84	125	1	0.67	-321	-332	-329	0.71	79.57	6.24	800	FAULT
11081	403	8.29	90	158	150	0.57	-353	-359	-356	0.57	65.46	4.53	350	STRATIGRAPHY
11045	376	8.32	108	130	75	0.83	-825	-834	-832	0.75	77.87	5.25	800	STRATIGRAPHY
15014	439	8.34	129	150	179	0.86	-322	-329	-327	0.70	70.34	4.25	450	TOP_SALT
4644	247	8.36	71	87	41	0.81	-798	-813	-810	0.76	82.14	7.87	650	FAULT
4786	251	8.37	72	88	132	0.81	-429	-446	-442	0.80	83.25	7.55	450	TOP_SALT
5809	272	8.39	83	84	89	0.99	-308	-320	-316	0.67	79.33	8.22	650	FAULT
9005	339	8.40	105	109	79	0.97	-246	-259	-256	0.80	80.97	6.31	550	STRATIGRAPHY
5733	270	8.45	83	83	2	0.99	-279	-295	-291	0.76	81.04	8.01	950	FAULT
6874	298	8.46	86	97	87	0.88	-456	-465	-463	0.73	62.58	3.75	450	FAULT
13086	480	8.46	79	209	150	0.38	-677	-689	-686	0.77	79.48	5.59	400	FAULT
9041	376	8.46	73	151	51	0.48	-498	-506	-503	0.61	74.33	6.06	500	FAULT
2115	164	8.47	50	51	91	0.99	-368	-377	-374	0.66	74.25	9.90	600	MINIBASIN
5905	282	8.47	72	106	133	0.68	-327	-343	-340	0.79	79.34	8.11	650	FAULT
6952	303	8.49	82	107	101	0.77	-497	-512	-508	0.73	82.82	7.23	550	STRATIGRAPHY
6958	302	8.52	83	107	164	0.78	-376	-386	-383	0.70	74.78	7.16	550	FAULT
2115	164	8.53	50	51	91	0.99	-644	-656	-652	0.69	79.90	10.31	650	MINIBASIN
2206	168	8.57	51	52	91	0.99	-368	-381	-377	0.63	79.64	10.42	500	COMBO
5809	272	8.58	83	84	89	0.99	-485	-496	-493	0.73	76.00	7.56	450	FAULT
9158	349	8.59	91	128	34	0.71	-222	-234	-231	0.71	78.83	6.15	600	FAULT
8022	320	8.63	92	108	138	0.85	-309	-321	-319	0.81	76.16	6.25	1000	FAULT
3489	216	8.68	54	78	91	0.69	-348	-360	-356	0.69	77.69	9.31	650	FAULT
3473	216	8.68	54	78	3	0.69	-582	-596	-592	0.68	81.78	9.39	1000	TOP_SALT
5809	272	8.70	83	84	89	0.99	-286	-297	-293	0.64	78.05	7.36	900	FAULT
3550	218	8.73	55	79	3	0.70	-287	-305	-301	0.78	81.68	9.27	700	FAULT
9056	346	8.79	95	118	61	0.80	-505	-520	-515	0.71	80.22	7.30	500	FAULT
5277	259	8.81	80	82	69	0.97	-345	-354	-351	0.69	73.17	5.38	250	COMBO
4761	250	8.81	69	87	46	0.80	-396	-409	-405	0.74	79.10	8.36	450	COMBO
2160	166	8.82	51	52	91	0.98	-456	-469	-465	0.65	79.97	10.75	600	TOP_SALT
6952	303	8.86	82	107	101	0.77	-502	-514	-510	0.68	79.99	7.50	450	STRATIGRAPHY
5809	272	8.93	83	84	89	0.99	-440	-463	-457	0.76	83.81	8.30	400	TOP_SALT
13859	422	8.96	120	144	151	0.83	-377	-387	-384	0.69	75.21	5.64	400	FAULT
16023	462	8.96	125	172	175	0.73	-252	-268	-259	0.44	80.28	5.80	500	FAULT
4722	250	8.99	71	89	135	0.80	-367	-379	-375	0.69	76.86	8.02	550	FAULT
5243	276	9.04	60	108	88	0.56	-261	-280	-272	0.56	83.10	7.99	750	FAULT
5809	272	9.08	83	84	89	0.99	-356	-369	-365	0.69	77.72	8.36	150	TOP_SALT
3567	218	9.11	55	78	89	0.70	-425	-448	-443	0.78	82.11	10.36	1000	FAULT
6951	302	9.15	83	109	11	0.77	-281	-292	-289	0.70	79.93	7.30	900	FAULT
4786	251	9.20	72	88	132	0.81	-261	-272	-268	0.67	76.45	8.14	400	STRATIGRAPHY
2159	166	9.22	51	52	4	0.98	-482	-506	-499	0.71	84.06	11.63	400	FAULT
10222	412	9.22	78	176	79	0.44	-368	-384	-380	0.75	82.00	6.68	500	FAULT
1161	122	9.22	36	43	128	0.85	-420	-429	-424	0.48	64.94	6.64	750	FAULT
18111	632	9.23	85	290	17	0.29	-460	-472	-469	0.72	80.54	4.95	400	FAULT
5809	272	9.24	83	84	89	0.99	-464	-476	-472	0.67	80.28	7.93	1000	TOP_SALT

10100	369	9.25	92	137	140	0.67	-312	-323	-319	0.65	77.25	6.26	1100	FAULT
39369	754	9.25	176	285	165	0.62	-679	-690	-687	0.78	75.23	4.15	1200	TOP_SALT
4196	232	9.29	66	81	92	0.81	-266	-272	-271	0.75	66.54	2.91	450	STRATIGRAPHY
3845	223	9.41	63	79	90	0.80	-416	-425	-422	0.62	75.23	7.86	650	FAULT
19083	517	9.41	119	194	166	0.62	-398	-405	-402	0.52	66.04	4.02	900	FAULT
2159	166	9.44	51	52	4	0.98	-476	-488	-483	0.56	79.71	10.44	550	TOP_SALT
5809	272	9.50	83	84	89	0.99	-286	-297	-293	0.65	77.97	7.56	1100	FAULT
6275	292	9.52	71	108	32	0.66	-270	-279	-276	0.70	73.66	5.49	450	FAULT
5809	272	9.57	83	84	89	0.99	-318	-331	-327	0.67	77.60	7.70	850	FAULT
8933	337	9.61	104	109	86	0.96	-271	-280	-276	0.57	73.82	6.33	550	FAULT
3647	223	9.61	55	85	152	0.65	-324	-328	-327	0.63	64.45	4.63	900	FAULT
3489	216	9.62	54	78	91	0.69	-407	-427	-421	0.72	83.60	10.43	350	COMBO
8086	325	9.63	87	111	89	0.78	-225	-234	-231	0.61	75.13	6.89	700	FAULT
4763	250	9.71	69	87	44	0.80	-526	-539	-533	0.57	81.24	8.53	500	STRATIGRAPHY
8075	325	9.78	87	111	1	0.78	-421	-433	-430	0.74	77.33	7.11	200	FAULT
15223	459	9.81	118	167	74	0.71	-208	-219	-215	0.65	80.16	5.28	900	TOP_SALT
4619	242	9.83	72	79	94	0.91	-579	-589	-585	0.55	71.66	6.50	550	TOP_SALT
6951	302	9.90	83	109	11	0.77	-373	-390	-386	0.74	82.82	7.75	500	COMBO
6684	293	9.98	82	102	60	0.80	-407	-419	-413	0.46	77.75	7.38	700	FAULT
3489	216	9.99	54	78	91	0.69	-303	-317	-312	0.65	77.87	9.66	700	TOP_SALT
17463	473	10.00	133	164	65	0.81	-558	-579	-571	0.63	83.33	7.05	600	MINIBASIN
14911	441	10.11	136	137	111	0.99	-247	-259	-255	0.66	74.94	5.97	900	FAULT
10906	382	10.15	96	142	61	0.67	-499	-513	-509	0.74	81.62	6.39	500	FAULT
13240	413	10.18	116	141	88	0.82	-495	-504	-500	0.56	70.81	5.69	450	STRATIGRAPHY
6081	279	10.20	82	93	131	0.88	-280	-291	-287	0.64	63.95	4.46	900	FAULT
14375	431	10.26	120	143	2	0.84	-431	-443	-439	0.67	77.05	6.41	500	FAULT
4383	236	10.30	72	76	23	0.95	-538	-561	-551	0.59	85.14	9.34	600	TOP_SALT
10240	373	10.35	89	136	87	0.66	-263	-273	-269	0.62	74.80	6.75	400	STRATIGRAPHY
12050	403	10.36	101	152	99	0.67	-271	-282	-278	0.63	73.18	5.98	400	STRATIGRAPHY
3489	216	10.38	54	78	91	0.69	-223	-239	-232	0.58	80.95	10.38	800	FAULT
10182	366	10.41	103	130	11	0.80	-351	-363	-358	0.61	79.52	6.12	550	MINIBASIN
26976	592	10.50	165	209	172	0.79	-545	-552	-549	0.48	68.53	3.85	900	TOP_SALT
7194	305	10.51	85	109	15	0.78	-580	-591	-587	0.60	70.90	7.04	1000	TOP_SALT
8124	332	10.52	84	125	1	0.67	-310	-321	-317	0.58	74.90	7.13	1000	FAULT
12686	430	10.53	98	173	18	0.57	-317	-336	-331	0.74	82.28	5.63	600	TOP_SALT
18220	490	10.56	141	175	35	0.81	-334	-344	-340	0.59	71.41	5.79	250	TOP_SALT
15938	472	10.57	118	179	82	0.66	-491	-507	-503	0.75	79.51	6.23	500	STRATIGRAPHY
7959	319	10.58	92	109	42	0.85	-288	-301	-296	0.60	76.23	6.36	900	FAULT
15068	454	10.61	113	177	8	0.64	-348	-358	-354	0.58	71.92	5.93	350	FAULT
6991	302	10.61	83	107	164	0.78	-587	-600	-595	0.60	77.88	6.99	400	STRATIGRAPHY
20078	539	10.64	119	212	3	0.56	-513	-525	-521	0.69	79.55	5.44	250	TOP_SALT
6965	303	10.68	82	106	172	0.77	-442	-457	-451	0.63	79.70	8.51	350	FAULT
8984	342	10.69	92	124	138	0.74	-320	-331	-327	0.64	75.37	7.04	750	MINIBASIN
3550	218	10.74	55	79	3	0.70	-336	-349	-343	0.56	79.54	10.10	450	FAULT
9692	355	10.75	100	129	9	0.78	-480	-498	-488	0.47	83.06	8.15	550	FAULT
5733	270	10.80	83	83	2	0.99	-478	-491	-486	0.61	78.29	8.71	300	TOP_SALT
14061	436	10.82	111	158	174	0.70	-395	-410	-405	0.69	82.34	5.94	600	TOP_SALT
11289	383	10.83	102	134	155	0.76	-313	-330	-324	0.63	80.41	7.35	400	COMBO
8086	325	10.97	87	111	89	0.78	-264	-274	-270	0.60	77.99	7.17	600	FAULT

1266	129	10.98	36	46	130	0.78	-587	-598	-593	0.53	77.21	8.49	400	MINIBASIN
8152	336	11.01	82	131	16	0.62	-300	-317	-313	0.72	82.99	7.54	500	FAULT
24059	572	11.02	147	217	35	0.68	-536	-549	-546	0.72	77.66	4.99	350	FAULT
13733	420	11.03	120	142	60	0.85	-250	-261	-257	0.61	77.62	6.41	550	STRATIGRAPHY
13180	412	11.07	117	140	170	0.83	-329	-344	-340	0.72	79.71	6.95	400	FAULT
7018	304	11.10	83	110	10	0.76	-499	-516	-512	0.72	81.53	7.82	300	TOP_SALT
5175	260	11.12	70	95	177	0.74	-280	-297	-290	0.59	77.85	6.96	700	TOP_SALT
12065	394	11.12	114	135	3	0.85	-572	-595	-590	0.79	84.94	7.19	800	TOP_SALT
6958	302	11.12	83	107	164	0.78	-300	-313	-307	0.55	79.96	7.97	1100	FAULT
16784	469	11.20	131	170	148	0.77	-287	-302	-298	0.71	81.56	5.70	450	TOP_SALT
39604	759	11.26	171	309	19	0.55	-387	-397	-393	0.58	69.62	4.06	1100	COMBO
10065	358	11.32	107	120	167	0.89	-331	-343	-338	0.59	75.89	7.23	650	STRATIGRAPHY
3550	218	11.41	55	79	3	0.70	-415	-429	-424	0.62	82.02	9.53	650	TOP_SALT
6029	283	11.50	78	99	179	0.79	-466	-484	-477	0.62	82.27	9.47	450	FAULT
14980	452	11.55	115	161	63	0.72	-549	-561	-556	0.54	73.26	5.64	700	TOP_SALT
13210	417	11.57	114	153	7	0.75	-304	-318	-313	0.67	78.23	6.63	1150	FAULT
8993	338	11.60	105	108	168	0.98	-352	-364	-359	0.55	73.49	6.99	500	MINIBASIN
11179	403	11.60	87	159	61	0.55	-418	-428	-423	0.51	69.57	5.44	750	FAULT
4786	251	11.74	72	88	132	0.81	-412	-429	-423	0.69	81.61	9.45	500	COMBO
17752	494	11.79	118	186	153	0.64	-382	-397	-392	0.69	80.69	5.87	550	COMBO
11981	398	11.80	104	147	37	0.71	-327	-339	-333	0.51	75.50	5.52	100	MINIBASIN
10994	382	11.89	104	137	44	0.76	-321	-333	-328	0.57	77.65	7.15	900	FAULT
11232	434	11.92	76	182	107	0.42	-354	-368	-362	0.61	80.34	5.83	850	FAULT
5190	265	11.95	66	100	135	0.66	-319	-331	-326	0.64	76.22	7.33	900	FAULT
18631	495	11.96	131	174	113	0.75	-509	-525	-521	0.72	81.92	5.91	500	FAULT
3498	211	11.99	64	70	57	0.91	-501	-506	-504	0.55	68.60	6.19	450	STRATIGRAPHY
11188	383	12.00	112	127	176	0.88	-236	-261	-255	0.76	83.37	7.43	850	FAULT
17000	467	12.01	139	159	176	0.88	-558	-568	-563	0.52	71.78	6.15	500	FAULT
44823	879	12.02	152	374	31	0.41	-543	-558	-554	0.71	78.47	4.84	400	FAULT
13722	420	12.05	119	145	30	0.82	-332	-349	-344	0.68	80.12	7.09	600	FAULT
6192	280	12.10	88	92	164	0.96	-264	-275	-270	0.57	75.28	6.54	550	STRATIGRAPHY
20858	563	12.16	118	234	18	0.50	-261	-274	-269	0.65	76.73	6.18	50	STRATIGRAPHY
16900	571	12.22	82	254	73	0.32	-312	-328	-323	0.66	82.31	6.69	700	FAULT
8216	336	12.30	83	125	178	0.67	-301	-315	-308	0.53	77.74	7.65	500	FAULT
10120	364	12.32	103	126	179	0.81	-353	-367	-361	0.60	81.00	7.01	850	TOP_SALT
4249	235	12.41	64	84	77	0.76	-422	-428	-425	0.54	69.37	5.52	700	FAULT
12093	399	12.42	108	143	60	0.76	-500	-514	-509	0.63	79.61	7.73	600	STRATIGRAPHY
8966	337	12.47	105	108	86	0.97	-340	-354	-348	0.59	80.43	7.64	650	FAULT
24246	587	12.48	127	227	109	0.56	-280	-296	-291	0.70	81.25	6.05	450	FAULT
11209	378	12.54	115	117	87	0.99	-551	-571	-565	0.73	82.64	7.65	600	FAULT
6952	301	12.61	83	106	164	0.78	-269	-284	-277	0.53	79.63	8.77	900	FAULT
7023	299	12.63	92	92	141	0.99	-283	-296	-291	0.60	76.82	7.77	900	FAULT
12729	407	12.65	108	145	60	0.75	-337	-349	-344	0.59	77.54	6.70	700	FAULT
16141	457	12.67	133	152	19	0.87	-240	-256	-250	0.62	80.07	7.29	500	FAULT
12043	395	12.70	108	141	155	0.76	-373	-389	-383	0.64	81.53	7.82	500	COMBO
16792	466	12.73	137	153	159	0.89	-349	-366	-361	0.68	81.06	6.69	700	FAULT
11012	378	12.75	112	127	1	0.88	-498	-514	-508	0.65	80.69	7.37	600	STRATIGRAPHY
12949	411	12.76	109	143	152	0.76	-461	-485	-478	0.72	84.30	7.78	450	FAULT
3550	218	12.79	55	79	3	0.70	-348	-368	-361	0.65	81.02	10.35	250	FAULT

13147	413	12.81	115	141	173	0.81	-342	-362	-356	0.70	84.10	7.68	700	FAULT
37810	712	12.85	178	262	52	0.68	-434	-446	-441	0.61	74.67	5.10	400	FAULT
11276	388	12.86	108	137	167	0.79	-356	-368	-363	0.58	77.67	6.82	200	FAULT
17864	700	12.92	82	324	4	0.25	-464	-475	-470	0.55	77.00	5.50	500	FAULT
30937	631	12.93	183	225	151	0.81	-351	-363	-358	0.58	78.48	4.25	850	FAULT
11162	391	12.94	103	149	0	0.69	-523	-539	-532	0.58	79.92	7.61	300	MINIBASIN
2808	190	12.98	56	63	168	0.88	-304	-317	-312	0.59	79.96	9.45	750	FAULT
14848	434	12.99	132	144	146	0.91	-483	-499	-494	0.68	79.87	7.42	600	FAULT
9175	352	12.99	87	132	176	0.66	-339	-357	-351	0.66	83.49	7.66	1100	FAULT
16052	456	13.01	129	161	77	0.80	-308	-326	-319	0.60	78.03	5.24	950	FAULT
5702	271	13.13	76	97	2	0.78	-578	-591	-584	0.42	71.30	6.01	650	TOP_SALT
27284	629	13.14	140	246	51	0.57	-351	-368	-363	0.70	80.35	5.89	550	FAULT
26891	665	13.15	119	270	83	0.44	-318	-334	-329	0.68	77.91	5.84	700	FAULT
10120	360	13.15	107	122	148	0.88	-413	-439	-433	0.78	84.82	8.45	750	FAULT
24601	635	13.21	114	274	29	0.42	-466	-482	-477	0.66	77.50	5.96	350	FAULT
33694	654	13.29	193	216	63	0.89	-690	-709	-698	0.41	81.52	5.64	600	MINIBASIN
5809	272	13.32	83	84	89	0.99	-363	-377	-372	0.63	81.63	8.72	700	FAULT
6501	289	13.38	83	99	60	0.84	-356	-369	-364	0.61	74.87	5.60	800	STRATIGRAPHY
14194	478	13.49	98	203	19	0.48	-344	-359	-352	0.52	77.57	6.49	1100	FAULT
7925	316	13.51	98	102	14	0.96	-275	-290	-282	0.47	78.05	6.33	550	STRATIGRAPHY
16121	453	13.52	138	155	174	0.90	-310	-326	-320	0.59	78.58	5.65	950	FAULT
31607	715	13.54	127	297	73	0.43	-490	-505	-500	0.68	80.15	6.01	500	FAULT
10076	359	13.55	107	122	42	0.88	-305	-323	-317	0.69	82.10	8.03	900	FAULT
9457	346	13.58	107	112	105	0.96	-259	-273	-265	0.44	78.49	5.06	550	FAULT
15741	487	13.61	105	198	0	0.53	-299	-313	-307	0.55	78.14	6.85	550	FAULT
29426	618	13.70	175	215	77	0.82	-376	-391	-386	0.67	80.75	5.87	400	FAULT
32311	663	13.77	164	248	143	0.66	-245	-263	-257	0.66	77.33	6.08	500	FAULT
17377	471	13.87	142	149	135	0.95	-292	-305	-299	0.54	77.36	6.27	450	FAULT
18674	536	13.88	118	203	21	0.58	-685	-699	-692	0.46	79.76	4.05	500	TOP_SALT
5809	272	13.89	83	84	89	0.99	-604	-630	-620	0.64	84.12	9.41	900	FAULT
12286	397	13.96	115	138	9	0.83	-264	-278	-270	0.40	80.20	6.50	600	STRATIGRAPHY
10052	358	13.98	107	122	148	0.88	-349	-364	-356	0.50	81.77	8.58	800	TOP_SALT
22778	573	14.06	126	223	83	0.57	-331	-348	-342	0.65	82.34	6.52	400	TOP_SALT
6797	294	14.08	90	94	14	0.95	-372	-382	-378	0.62	74.24	5.24	500	FAULT
16012	488	14.15	105	201	35	0.52	-792	-812	-804	0.62	80.04	6.30	300	STRATIGRAPHY
10989	388	14.17	92	147	79	0.63	-266	-286	-277	0.59	81.03	6.97	700	FAULT
10849	381	14.19	94	140	28	0.67	-437	-452	-444	0.50	79.15	7.07	350	FAULT
13280	415	14.37	116	141	173	0.82	-299	-318	-310	0.60	81.03	8.54	900	FAULT
8075	325	14.45	87	111	1	0.78	-380	-399	-392	0.65	83.78	8.92	500	COMBO
20339	569	14.49	110	231	173	0.48	-242	-258	-249	0.45	77.42	5.90	600	FAULT
18109	492	14.60	129	174	135	0.74	-265	-281	-275	0.59	77.70	7.05	350	STRATIGRAPHY
18454	491	14.68	132	179	99	0.74	-359	-371	-367	0.72	72.02	5.28	650	FAULT
67206	1058	14.69	195	442	155	0.44	-538	-559	-553	0.72	81.98	4.94	650	FAULT
8259	324	14.72	96	105	3	0.91	-260	-273	-268	0.63	80.00	6.86	400	FAULT
5809	272	14.76	83	84	89	0.99	-456	-485	-476	0.69	84.55	9.68	700	MINIBASIN
12938	415	14.78	107	151	124	0.71	-292	-311	-304	0.62	81.26	7.91	750	FAULT
22387	554	14.82	136	207	172	0.66	-299	-313	-307	0.58	78.29	6.46	600	FAULT
3787	220	14.83	66	73	22	0.91	-367	-384	-380	0.76	82.59	8.27	800	FAULT
10806	376	14.87	104	132	16	0.79	-466	-480	-473	0.52	78.80	7.24	400	FAULT

9004	338	15.19	105	109	86	0.96	-434	-452	-443	0.51	81.41	8.52	700	FAULT
24523	561	15.23	166	188	104	0.88	-386	-401	-394	0.54	80.79	5.46	1100	COMBO
14524	428	15.29	133	138	60	0.96	-301	-315	-309	0.55	77.35	6.42	600	FAULT
8943	342	15.34	94	119	119	0.79	-319	-343	-336	0.69	84.00	8.29	650	FAULT
36531	771	15.36	147	334	8	0.44	-547	-567	-560	0.66	82.71	6.28	350	FAULT
9147	352	15.39	87	132	179	0.66	-577	-590	-583	0.47	81.32	7.71	400	STRATIGRAPHY
8933	337	15.44	104	109	86	0.96	-393	-413	-406	0.63	84.49	8.14	500	FAULT
9683	380	15.46	79	149	69	0.53	-368	-387	-379	0.58	82.67	7.38	150	TOP_SALT
37418	764	15.49	142	302	169	0.47	-350	-365	-359	0.59	79.15	5.64	550	FAULT
14164	452	15.49	104	182	178	0.57	-337	-359	-353	0.72	82.78	6.51	550	FAULT
20654	540	15.50	128	213	99	0.60	-330	-350	-342	0.60	80.58	6.69	600	STRATIGRAPHY
18420	487	15.51	136	170	80	0.80	-427	-444	-437	0.58	80.10	6.40	350	FAULT
11132	380	15.57	112	126	178	0.89	-397	-414	-407	0.58	81.47	7.90	550	TOP_SALT
9057	341	15.59	106	107	177	0.99	-564	-582	-574	0.53	79.23	8.95	500	STRATIGRAPHY
12945	406	15.65	121	133	122	0.91	-290	-307	-298	0.46	82.19	7.44	500	FAULT
10826	377	15.65	102	136	82	0.75	-349	-370	-363	0.70	84.16	7.16	650	TOP_SALT
15976	452	15.66	133	153	130	0.87	-385	-416	-409	0.77	84.75	7.57	350	FAULT
19866	532	15.69	118	210	93	0.56	-301	-319	-311	0.58	81.74	6.90	850	FAULT
8587	332	15.74	96	115	39	0.83	-379	-395	-388	0.56	76.16	5.62	800	STRATIGRAPHY
12059	392	15.76	114	132	4	0.86	-230	-248	-240	0.54	83.36	8.12	650	FAULT
27234	664	15.77	124	272	53	0.46	-303	-320	-314	0.67	76.46	5.57	950	FAULT
12025	392	15.84	120	121	64	0.99	-339	-360	-352	0.61	81.79	7.42	900	FAULT
16940	467	16.03	132	164	63	0.80	-282	-299	-291	0.50	81.15	6.36	450	STRATIGRAPHY
9986	361	16.08	102	130	80	0.79	-319	-335	-327	0.50	81.92	7.67	450	STRATIGRAPHY
12038	401	16.13	107	142	167	0.75	-338	-354	-346	0.49	80.84	7.54	700	FAULT
36449	696	16.14	193	256	20	0.75	-335	-352	-345	0.61	78.04	5.95	150	TOP_SALT
99121	1254	16.15	281	490	112	0.57	-674	-692	-683	0.53	75.68	4.33	400	TOP_SALT
5134	263	16.26	67	99	12	0.67	-293	-307	-303	0.68	77.90	7.84	800	FAULT
19922	510	16.33	142	174	170	0.81	-225	-242	-233	0.48	78.79	7.22	600	FAULT
21455	521	16.34	160	167	72	0.96	-382	-408	-401	0.72	83.04	7.03	200	TOP_SALT
7280	319	16.54	76	119	7	0.64	-345	-359	-352	0.50	78.31	6.35	150	TOP_SALT
8014	323	16.54	87	110	89	0.79	-287	-305	-297	0.56	82.57	8.99	750	STRATIGRAPHY
9115	351	16.58	87	132	174	0.66	-269	-287	-278	0.52	82.77	8.03	700	STRATIGRAPHY
15182	440	16.78	131	144	161	0.91	-281	-298	-290	0.54	81.40	7.44	350	STRATIGRAPHY
5870	273	16.78	80	92	126	0.87	-318	-335	-329	0.65	78.56	7.18	850	FAULT
10948	373	16.94	113	123	132	0.92	-348	-363	-357	0.63	81.12	7.21	550	FAULT
8966	337	17.08	105	108	86	0.97	-417	-436	-427	0.51	80.24	7.78	400	FAULT
27322	616	17.23	147	242	8	0.61	-372	-389	-381	0.53	79.60	6.85	650	MINIBASIN
13919	419	17.34	129	137	46	0.94	-498	-511	-506	0.61	78.60	6.26	450	FAULT
12913	419	17.51	103	160	92	0.64	-328	-345	-336	0.49	81.99	7.14	750	FAULT
15174	453	17.56	120	161	57	0.75	-491	-511	-501	0.49	83.25	7.07	450	FAULT
18354	484	17.57	148	148	89	1.00	-274	-291	-282	0.46	78.75	6.99	800	STRATIGRAPHY
19272	534	17.62	116	211	89	0.55	-548	-567	-557	0.48	82.15	6.45	600	FAULT
26726	589	17.68	168	199	152	0.85	-362	-384	-376	0.65	83.03	6.85	150	TOP_SALT
14922	435	17.76	132	145	49	0.91	-279	-301	-291	0.53	80.66	8.01	450	FAULT
7391	307	17.86	90	104	138	0.86	-361	-374	-370	0.71	79.59	5.89	650	FAULT
54310	1134	17.86	136	527	1	0.26	-385	-407	-399	0.66	82.29	5.53	650	MINIBASIN
18823	490	18.02	141	166	11	0.85	-411	-432	-424	0.61	83.82	7.99	650	FAULT
12610	406	18.06	108	146	157	0.74	-301	-318	-311	0.58	82.95	7.20	500	FAULT

15338	440	18.12	135	146	28	0.93	-481	-499	-494	0.69	79.01	5.69	800	TOP_SALT
3766	263	18.21	41	115	11	0.36	-304	-311	-307	0.42	74.63	5.63	1000	FAULT
23088	554	18.22	143	205	66	0.70	-494	-512	-505	0.62	80.88	6.41	450	FAULT
39395	990	18.32	119	434	95	0.27	-273	-291	-284	0.65	80.69	6.09	850	STRATIGRAPHY
44858	969	18.62	126	426	83	0.30	-272	-290	-282	0.54	81.89	6.13	500	FAULT
24123	561	18.64	150	203	135	0.74	-440	-465	-456	0.68	83.42	7.17	250	FAULT
15986	463	18.70	123	176	28	0.70	-267	-288	-282	0.69	82.60	6.82	400	FAULT
20314	524	18.76	130	198	113	0.66	-263	-284	-275	0.55	83.63	7.11	400	FAULT
3024	203	18.88	50	74	31	0.67	-301	-312	-306	0.41	77.58	5.31	450	FAULT
12059	392	18.94	114	132	4	0.86	-343	-365	-357	0.61	83.07	8.07	700	TOP_SALT
25144	570	18.97	159	202	119	0.79	-364	-387	-378	0.61	80.30	6.72	350	TOP_SALT
62745	922	18.97	231	352	100	0.66	-581	-599	-589	0.48	76.41	4.95	850	TOP_SALT
50088	842	19.01	195	333	72	0.58	-316	-336	-326	0.50	79.46	5.41	550	FAULT
10826	374	19.13	107	133	17	0.80	-295	-310	-303	0.54	81.36	7.17	900	FAULT
68363	1036	19.20	211	429	65	0.49	-497	-518	-508	0.56	81.15	5.52	350	FAULT
10168	372	19.32	89	136	89	0.66	-415	-435	-425	0.51	82.99	8.06	700	TOP_SALT
9653	356	19.51	93	130	98	0.72	-258	-278	-271	0.66	82.26	7.72	400	FAULT
22381	537	19.72	152	176	2	0.86	-314	-338	-329	0.60	83.57	7.62	900	FAULT
30353	641	19.84	165	243	95	0.68	-383	-408	-398	0.61	83.18	6.64	200	TOP_SALT
16662	469	19.95	130	170	147	0.76	-270	-290	-281	0.57	83.74	7.63	650	STRATIGRAPHY
8519	330	19.98	99	108	23	0.92	-264	-283	-276	0.63	82.22	8.12	400	STRATIGRAPHY
8744	352	19.98	79	139	118	0.57	-300	-315	-311	0.74	79.85	5.71	850	FAULT
78775	1300	20.42	165	597	52	0.28	-246	-272	-262	0.61	83.58	7.50	450	FAULT
4619	243	20.43	72	81	109	0.90	-375	-390	-386	0.75	80.48	7.57	800	FAULT
107745	1366	20.59	232	580	84	0.40	-459	-485	-476	0.67	82.68	5.65	1100	COMBO
16782	471	20.63	127	157	92	0.81	-264	-276	-270	0.56	77.38	5.35	750	TOP_SALT
13348	414	20.95	120	147	24	0.81	-297	-321	-311	0.61	80.46	7.33	650	FAULT
10954	384	20.98	101	144	129	0.70	-510	-535	-528	0.69	83.20	7.07	350	TOP_SALT
34567	666	21.07	192	219	149	0.88	-424	-449	-438	0.58	82.68	5.97	300	FAULT
28846	642	21.21	142	247	31	0.57	-535	-571	-559	0.68	85.07	7.37	550	FAULT
126512	1376	21.25	296	546	3	0.54	-445	-466	-454	0.43	76.70	4.17	450	FAULT
29726	640	21.34	151	241	75	0.63	-334	-356	-343	0.42	83.01	5.92	500	TOP_SALT
40963	744	21.42	185	261	5	0.71	-430	-449	-440	0.50	76.83	5.15	300	FAULT
15251	450	21.63	118	159	174	0.74	-369	-393	-382	0.53	82.37	8.62	650	FAULT
35140	707	21.64	157	273	39	0.57	-398	-428	-416	0.61	82.80	7.18	450	FAULT
11250	392	21.71	101	146	7	0.69	-269	-293	-282	0.52	80.43	7.54	700	FAULT
12704	431	22.08	93	173	20	0.54	-304	-322	-317	0.72	83.21	6.53	750	FAULT
9697	370	22.14	87	145	89	0.60	-420	-438	-427	0.41	82.15	7.31	700	FAULT
14905	436	22.36	132	144	120	0.92	-331	-353	-341	0.46	83.85	8.06	850	FAULT
24148	556	22.56	159	190	104	0.84	-337	-364	-353	0.57	81.66	6.90	650	FAULT
55025	858	22.72	212	319	132	0.67	-233	-263	-253	0.65	82.85	7.13	500	FAULT
9934	362	22.86	98	131	80	0.75	-340	-357	-346	0.35	78.60	6.60	300	STRATIGRAPHY
44584	947	22.91	131	418	147	0.31	-608	-639	-625	0.54	84.03	7.06	400	FAULT
7866	321	22.93	92	108	27	0.86	-464	-490	-477	0.49	84.31	8.98	350	FAULT
24981	568	22.93	159	200	39	0.80	-291	-314	-302	0.47	82.08	7.04	700	FAULT
44096	776	23.00	185	291	25	0.63	-301	-327	-316	0.58	80.26	6.84	850	FAULT
22093	542	23.36	137	201	120	0.68	-330	-356	-343	0.49	83.22	7.56	750	FAULT
52824	847	24.10	225	298	20	0.75	-326	-355	-344	0.61	82.79	6.15	300	FAULT
53639	859	24.41	209	329	32	0.64	-335	-367	-354	0.61	81.86	6.85	400	FAULT

14181	424	24.41	129	137	121	0.94	-340	-366	-354	0.53	81.40	7.80	600	FAULT
8632	331	24.60	100	106	5	0.94	-263	-287	-281	0.73	83.29	7.93	550	STRATIGRAPHY
33063	661	24.61	174	232	84	0.75	-230	-259	-248	0.61	85.64	7.10	600	FAULT
36866	705	24.83	181	253	45	0.72	-429	-458	-448	0.67	82.75	6.69	400	FAULT
19620	500	24.88	150	165	27	0.90	-330	-357	-348	0.66	81.09	6.57	250	TOP_SALT
35143	670	25.05	194	231	84	0.84	-266	-303	-291	0.68	86.44	7.74	550	FAULT
7500	309	25.06	93	100	22	0.93	-376	-394	-387	0.59	83.17	7.72	700	FAULT
32610	695	25.09	153	286	76	0.54	-547	-585	-569	0.58	86.95	6.62	600	FAULT
2179	167	25.22	50	56	71	0.89	-514	-519	-516	0.52	54.89	4.10	450	FAULT
3615	215	25.39	62	74	105	0.84	-584	-600	-594	0.59	82.44	8.09	400	STRATIGRAPHY
22305	532	25.44	163	179	21	0.91	-288	-310	-303	0.66	81.33	6.43	650	FAULT
41910	756	25.53	193	285	145	0.68	-354	-380	-364	0.40	81.44	6.87	650	FAULT
12625	402	26.09	115	139	129	0.82	-409	-442	-430	0.63	83.50	8.35	700	FAULT
16632	468	26.40	123	172	144	0.72	-597	-623	-611	0.53	84.58	7.38	350	FAULT
35081	788	26.43	125	336	27	0.37	-540	-573	-558	0.53	85.14	7.98	600	FAULT
24601	609	26.52	123	240	30	0.51	-301	-322	-314	0.63	82.60	6.05	750	FAULT
7184	309	26.73	81	116	169	0.69	-303	-320	-315	0.75	80.54	7.06	500	FAULT
15694	463	26.88	116	173	7	0.67	-415	-444	-427	0.40	84.88	7.79	450	COMBO
44519	823	27.14	164	336	120	0.49	-256	-287	-272	0.51	85.47	6.79	700	FAULT
5435	271	27.39	67	102	69	0.66	-391	-402	-399	0.73	79.87	5.90	400	FAULT
20560	560	28.31	111	231	50	0.48	-416	-444	-436	0.72	84.46	7.84	700	FAULT
7203	304	29.06	90	101	88	0.89	-391	-404	-397	0.47	76.08	6.07	400	FAULT
19998	549	29.75	114	226	50	0.50	-413	-446	-432	0.58	84.33	8.25	650	FAULT
10165	359	29.97	110	117	111	0.94	-387	-398	-394	0.60	72.18	5.63	650	FAULT
10461	368	30.35	101	133	6	0.76	-301	-323	-315	0.62	80.64	7.44	500	FAULT
37064	692	30.42	195	240	145	0.81	-247	-276	-259	0.40	85.48	7.03	500	FAULT
22690	553	31.37	140	203	101	0.69	-258	-291	-276	0.55	85.11	8.28	800	FAULT
20399	509	31.94	154	168	131	0.91	-294	-325	-313	0.61	84.60	7.59	500	FAULT
48910	800	32.57	220	281	110	0.78	-288	-322	-302	0.43	83.81	7.20	900	FAULT
9013	340	32.64	96	117	116	0.82	-347	-367	-359	0.59	82.78	7.99	300	TOP_SALT
21993	533	32.80	151	183	175	0.82	-573	-599	-582	0.34	85.48	6.86	300	STRATIGRAPHY
42833	738	33.34	222	251	57	0.89	-263	-299	-280	0.49	83.90	8.32	600	STRATIGRAPHY
18819	492	34.85	151	154	95	0.98	-394	-403	-400	0.69	67.77	4.07	450	TOP_SALT
38116	729	35.33	173	287	157	0.60	-344	-377	-360	0.49	84.38	7.15	650	FAULT
3383	211	35.42	55	77	39	0.71	-398	-410	-408	0.82	78.49	5.21	400	FAULT
32742	647	35.86	187	225	61	0.83	-232	-270	-250	0.47	84.92	8.25	600	FAULT
20696	530	37.23	130	199	54	0.65	-395	-414	-406	0.56	76.99	6.70	450	FAULT
12826	433	40.12	90	175	48	0.52	-395	-417	-407	0.57	81.38	6.28	550	FAULT

Appendix D: Morphological attributes of mud volcanoes in the East Breaks area, northern Gulf of Mexico

Area	Perimeter	VRelief	MBG_Width	MBG_Length	MBG_W_L Ratio	MinWD	MaxWD	MeanWD	Source depth
48091	797	13.27	232	254	0.91	-181	-199	-190	1400
251781	1799	13.48	541	600	0.90	-268	-304	-281	1300
379556	2301	40.31	572	854	0.67	-232	-287	-263	2100
57241	870	8.70	255	300	0.85	-409	-431	-416	1000
88080	1183	12.45	315	398	0.79	-659	-685	-667	1400
95015	1142	11.12	335	377	0.89	-389	-411	-397	1200
121690	1312	14.16	324	467	0.69	-350	-385	-367	800
106526	1212	11.92	321	455	0.71	-551	-580	-563	900
71033	986	6.28	263	346	0.76	-567	-594	-581	900
27507	608	15.51	160	213	0.75	-588	-628	-609	900
137040	1421	8.29	382	534	0.71	-563	-595	-574	1300
20841	522	2.07	157	169	0.93	-553	-565	-558	600
108935	1199	0.13	334	407	0.82	-562	-606	-584	1000
63907	914	5.96	278	300	0.93	-564	-575	-570	1000
304155	2301	8.97	468	926	0.51	-446	-479	-460	2100
194313	1608	0.04	428	590	0.73	-347	-402	-363	800
44194	761	7.45	225	245	0.92	-529	-543	-533	2600
19455	506	1.41	155	165	0.94	-552	-569	-556	1100
101013	1199	13.23	332	398	0.83	-346	-402	-366	900
195427	1599	11.46	462	533	0.87	-318	-349	-331	1000
168767	1483	38.15	442	476	0.93	-294	-348	-318	1200
230166	1785	39.77	494	613	0.81	-870	-939	-900	2300
52488	846	6.02	214	323	0.66	-285	-309	-293	700

65523	922	2.60	272	304	0.89	-412	-437	-417	1000
85746	1057	2.48	302	358	0.84	-388	-426	-397	900
20953	523	0.00	156	170	0.92	-368	-395	-378	1000
172219	1487	1.31	438	485	0.90	-495	-525	-508	1500
24179	567	3.50	154	203	0.76	-453	-465	-458	900
70105	965	1.98	269	341	0.79	-449	-479	-459	900
18930	505	3.80	137	180	0.76	-491	-507	-494	600
152251	1453	4.39	424	475	0.89	-667	-702	-677	1000
57582	883	3.75	232	304	0.76	-728	-744	-733	500
89393	1090	22.72	309	362	0.85	-702	-745	-722	700
132170	1316	15.23	380	445	0.86	-844	-909	-872	700
53115	837	11.64	242	269	0.90	-730	-750	-741	800
95245	1113	40.99	335	363	0.92	-690	-741	-722	1000
64802	971	24.36	267	354	0.75	-648	-685	-667	1100
65258	971	9.44	229	365	0.63	-703	-727	-713	1100
19883	511	6.95	145	177	0.82	-711	-728	-718	1200
127840	1383	10.10	308	526	0.59	-708	-733	-718	1200
155698	1412	14.07	433	447	0.97	-710	-732	-722	1100
37428	698	10.22	210	233	0.90	-685	-705	-695	900
52864	828	10.67	253	271	0.93	-434	-452	-443	400
166874	1483	25.75	409	506	0.81	-633	-674	-648	2000
56496	865	8.82	245	298	0.82	-461	-484	-470	700
226558	1730	5.92	453	628	0.72	-545	-598	-559	2300
150727	1428	11.50	370	519	0.71	-506	-542	-522	1000
31966	650	6.65	178	231	0.77	-399	-418	-406	700
44802	768	6.54	215	271	0.79	-460	-481	-467	400
29037	646	16.42	148	238	0.62	-399	-424	-410	700
193035	1640	13.08	478	536	0.89	-404	-440	-416	1200
64702	961	8.12	282	319	0.88	-315	-333	-324	1600
21272	535	3.42	141	192	0.73	-276	-296	-282	1100
162319	1453	3.55	432	481	0.90	-741	-765	-750	1000

359962	2157	31.73	646	703	0.92	-834	-900	-857	2100
461698	2477	55.69	725	827	0.88	-749	-876	-814	1600
100194	1150	38.46	345	380	0.91	-876	-925	-908	1300
372993	2232	22.52	631	716	0.88	-857	-933	-883	2000
222676	1726	12.63	494	545	0.91	-930	-1012	-958	1800
87445	1083	6.47	305	384	0.80	-728	-749	-737	900
56441	863	1.12	252	289	0.87	-779	-801	-788	800
22428	538	11.26	158	173	0.91	-749	-774	-760	700

4	crater	320	288	1111871	1190	deep	y	3
5	eye	360	324	386482	702	deep	y	3
6	crater	150	135	1424773	1347	deep	n	3
7	crater	150	135	346229	664	medium	n	3
8	crater	210	189	434626	744	medium	n	4
9	eye	290	261	1002598	1130	medium	n	3
10	eye	175	157.5	981993	1118	medium	y	3
11	crater	300	270	1296407	1285	deep	n	3
12	dome	45	40.5	571813	853	medium	n	4
13	eye	105	94.5	1378096	1325	deep	y	3
14	crater	290	261	2090817	1632	deep	y	3
15	eye	60	54	130745	408	shallow	n	4
16	dome	30	27	208142	515	shallow	n	4
17	dome	100	90	899211	1070	deep	y	4
18	eye	105	94.5	481845	783	deep	y	4
19	dome	75	67.5	796169	1007	deep	y	4
20	crater	140	126	391805	706	shallow	y	4
21	eye	130	117	420227	732	shallow	y	4
22	eye	100	90	595284	871	deep	y	4
23	eye	125	112.5	561280	846	deep	y	4
24	eye	150	135	299324	617	deep	n	4
25	eye	85	76.5	448336	756	deep	n	4
26a	crater	275	247.5	1166518	1219	deep	n	3
26b	crater	160	144	1282905	1278	deep	n	3
27	eye	150	135	559703	844	deep	n	4
28	dome	385	346.5	1972446	1585	deep	y	4
29	dome	50	45	142779	426	deep	n	4
30	eye	110	99	668754	923	deep	y	4
31	crater	340	306	1476927	1372	deep	n	4
32	eye	185	166.5	633684	898	deep	y	4
33	eye	220	198	716193	955	medium	y	4
34	dome	80	72	365224	682	medium	n	3
35	eye	200	180	337431	656	medium	n	3
36	eye	180	162	341662	660	medium	n	3
37	eye	180	162	244184	558	medium	n	3
38	dome	35	31.5	349950	668	medium	n	3

52	eye	220	198	370817	687	medium	y	2
53	dome	80	72	425420	736	deep	n	2
54	eye	415	373.5	2329895	1723	deep	y	2
55	crater	160	144	300390	619	medium	y	1
56	dome	80	72	119811	391	shallow	n	1
57	eye	300	270	1894898	1554	deep	y	1
58	dome	50	45	247203	561	medium	n	2
59	eye	90	81	249324	564	medium	n	1
60	eye	130	117	231350	543	medium	n	2
61	dome	80	72	550434	837	shallow	y	2
62	eye	70	63	141401	424	deep	y	2
63	crater	130	117	279591	597	medium	n	2
64	eye	260	234	4449062	2381	deep	y	1
65	eye	105	94.5	7427003	3076	medium	y	1
66	eye	120	108	243014	556	shallow	y	1
67	crater	275	247.5	956264	1104	deep	y	1
68	eye	115	103.5	505145	802	deep	y	1
69	eye	155	139.5	1932978	1569	deep	y	1
70	dome	60	54	73434	306	deep	n	1
71	eye	115	103.5	137774	419	medium	y	1
72	eye	160	144	537542	828	deep	y	2
73	eye	200	180	384533	700	deep	n	2
74	eye	70	63	98222	354	deep	y	2
75	dome	145	130.5	784972	1000	deep	y	2
76	dome	95	85.5	357419	675	medium	n	2
77	eye	120	108	313564	632	deep	n	2
78	eye	110	99	280126	597	deep	n	2
79	eye	130	117	250879	565	deep	n	2
80	dome	140	126	1013911	1136	deep	y	2
81	crater	120	108	2131669	1648	deep	y	2
82	eye	310	279	258163	573	deep	y	2
83	crater	70	63	179263	478	medium	y	1
84	dome	95	85.5	654771	913	deep	y	2

Sector 1 data for Figure 6.9.

Inline	HTVC number	HTVC structure	Number of reflections the HTVC crosses (bar thickness)	Number of reflections of the top of the HTVC above or below Tang Fm (bar level)	Sill number that is feeding HTVC	Sill area, m2	Minimum sill diameter, m. Sills on edge of study area are in italics	Feeder sill thickness, ms TWT	Sill depth: shallow, medium or deep	Amplitude anomalies between sill and HTVC?	Amplitude anomalies above HTVC?	Number of reflections of AAs relative to Tare Fm	Comments
4665													
4640													
4615													
4590	43	dome	2	base= -2 below tang	38	10716649	4000	200	medium	n	n		
4585	56	dome	4	base = -8 below tang	9	15299342	6100	80	shallow	n	n		
4565	40	eye	6	-2	123	4297048	*2600*	200	medium	n	n		
4540													
4515													
4490													
4465													
4440													
4415													
4390													
4365	42	eye	4	0, below	51	20843544	4250	100	shallow	n	n		
4340													
4315													
4290													
4265													
4240													
4215	65	eye	8 (4 and 4)	-6	37	32064180	960	120	medium	n	y	-2	Seismic dimming in Brygge Fm
4190	57	eye	14 (4 up and 10 down)	-4	96	8245227	5700	450	deep	n	n		Seismic dimming in Tare Fm
4165													
4140	44	eye	4	0, below	10	16347542	3200	500	medium	n	y	-1, 0, +1	
4115	71	eye	6 (2 up 4 below)	-8	36	11414938	4575	270	medium	n	n		
4090	66	eye	6 (2 up 4 below)	-2	7	5681795	2850	180	medium	n	y	+5, +6	
4065	70	dome	2	-4	97	14114238	4800	160	deep	n	n		
4040													
4015													
3990	69	eye	10 (2 above, 8 below)	-4	97	14114238	4800	450	deep	n	y	Tang: -1, +1	
3965													
3940													
3915													
3890	45	dome	2	-2	83	2237582	2000	80	shallow	n	n		
3865	50	eye	6 (2 up, 4 below)	-2	125	2214068	2300	130	medium	n	n		Seismic dimming above Tare Fm
3840	64	eye	10 (2 up, 8 below)	-2	37	32064180	960	500	deep	n	y	Tang: -1, +1, +2	
3815													
3790													

3765												
3740	67	crater	10	-12	97	14114238	4800	260	deep	n	n	
3740	68	eye	4 (2 up 2 down)	-2	97	14114238	4800	260	deep	n	n	
3715												
3690												
3665												
3640	83	crater	4	-6	6	17798779	7000	200	medium	n	y	0, +1, +2
3615	55	crater	4	0	13	16265501	4000	200	medium	n	n	Seismic dimming through HTVC
3590												
3565												
3540												
3515												
3490												
3465												
3440	59	eye	6 (2 above, 4 below)	-2	13	16265501	4000	180	medium	n	n	
3415	49	eye	6 (2 above, 4 below)	-2	13	16265501	4000	180	medium	n	n	
3390												
3365												
3340												
3315												

Sector 2 data for Figure 6.9.

Inline	HTVC number	HTVC structure	Number of reflections the HTVC crosses (bar thickness)	Number of reflections of the top of the HTVC above or below Tang Fm (bar level)	Sill number that is feeding HTVC	Sill area, m2	Minimum sill diameter, m. Sills on edge of study area are in italics	Feeder sill thickness, ms TWT	Sill depth: shallow, medium or deep	Amplitude anomalies between sill and HTVC?	Amplitude anomalies above HTVC?	Number of reflections of AAs relative to Tare Fm	Comments
3340	63	crater	4	-2	DYKE?				deep	n	n		
3330	81	crater	12; upper 4 are incised by eye_82	-4	DYKE?				deep	n	y	0 to +8	
3330	82	eye	2 above, 4 below. Bottom 4 incise into top of crater_81	-4	DYKE?				deep	n	y	0 to +8	
3305													
3280													
3265	48	dome	4	-4	5	20461454	5480	150	medium	n	n		
3250	60	eye	6	-2	6	17798779	7000	120	medium	n	n		
3225													
3200	73	eye	8 (2 above, 6 below)	-2	DYKE?				deep	n	n		
3175													
3150													
3125													
3100	58	dome	2	-2	5	20461454	5480	200	medium	n	n		

3075													
3050	72	eye	2 above, 4 below	0, across	2	423116100	*3650*	600	deep	n	y	0, +1	
3040	74	eye	2 above, 2 below	0, across	2	423116100	*3650*	600	deep	n	y	0, +1	
3025	75	dome	8	0, above	2	423116100	*3650*	600	deep	n	y	0, +1, +10	Very bright spot in Brygge Fm
3000	62	eye	2 above, 2 below	0, across	2	423116100	*3650*	600	deep	n	y	0, +1	
2975	84	dome	4	0, above	2	423116100	*3650*	600	deep	n	y	0, +1	
2950	46	eye	2 above, 2 below	0, across	2	423116100	*3650*	600	deep	n	y?		
2925	47	dome	4	0, above	2	423116100	*3650*	600	deep	n	y	0, +1, +2	
2900													
2875													
2850	51	eye	2 above, 2 below	0, across	2	423116100	*3650*	650	deep	n	n		
2825	52	eye	4	0, below	2	423116100	*3650*	720	deep	n	y	0, +1, +2	
2800													
2775													
2750													
2725													
2700													
2675													
2650													
2625													
2600													
2575													
2550													
2525	80	dome	6	0, above	124	39679975	9950	600	deep	n	y	-1, 0, +1	
2500													
2475	76	dome	4	.-4, below	124	39679975	9950	380	medium	n	n		
2450													
2425													
2400													
2375													
2350	77	eye	2 above, 2 below	-4	124	39679975	9950	340	deep	n	n		
2325													
2300	61	dome	4	0, above	2	423116100	*3650*	540	deep	n	y	0, +1, +7, +8	
2275													
2250	78	eye	2 above, 2 below	-4	124	39679975	9950	150	deep	n	n		
2225													
2200	79	eye	2 above, 2 below	-4	124	39679975	9950	350	deep	n	n		
2175													
2150													
2125													
2100	54	eye	10	0, below	2	423116100	*3650*	400	deep	n	y	+13,+14,+15	
2075													
2050	53	dome	2	0, above	2	423116100	*3650*	240	deep	n	n		
2025													
2000													

Sector 3 data for Figure 6.9.

Inline	HTVC number	HTVC structure	Number of reflections the HTVC crosses (bar thickness)	Number of reflections of the top of the HTVC above or below Tang Fm (bar level)	Sill number that is feeding HTVC	Sill area, m2	Minimum sill diameter, m. Sills on edge of study area are in italics	Feeder sill thickness, ms TWT	Sill depth: shallow, medium or deep	Amplitude anomalies between sill and HTVC?	Amplitude anomalies above HTVC?	Number of reflections of AAs relative to Tare Fm	Comments
4665	37	eye	10	0, below tang	15	33145790	*8200*	330	medium	n	n		
4640													
4615													
4590	34	dome	6	0, below tang	15	33145790	*8200*	450	medium	n	n		
4565													
4540													
4515													
4490													
4465													
4440													
4415													
4390	38	dome	2	0, above tang	1	28909955	6650	200	medium	n	n		
4380	41	eye	10	0, below tang	1	28909955	6650	170	medium	n	n		
4370	35	eye	12	0, below tang	15	33145790	*8200*	220	medium	n	n		
4360	5	eye	8	-4	42	58749484	8000	300	deep	n	n		Seismic dimming column through HTVC
4335	39	eye	6 above, 8 below	across tang	1	28909955	6650	150	medium	n	n		
4315	36	eye	8	0, below tang	15	33145790	*8200*	240	medium	n	n		
4275													
4235	3	crater	8	-2	122	10779644	6000	440	deep	n	dimming	-2	Seismic dimming column through HTVC, up to 2 reflections below Tare Fm
4210	1	crater	6	-2	122	10779644	6000	700	deep	n	n		
4185													
4160													
4135													
4110													
4085	11	crater	10	-2	121	87686262	18013	440	deep	n	n		
4060	10	eye	12	0, below tang	21	11053117	3900	130	medium	n	y	0	
4010													
3960													
3910													
3885	2	eye	12	-2	42	58749484	8000	450	deep	y	y	2 above Tang Fm	Flags in underlying faulted region near Nise Fm.
3835	26a	crater	10	-4	62	113095240	10750	310	deep	n	n		
3810	26b	crater	10	-4	62	113095240	10750	310	deep	n	n		

3760													
3710													
3685	4	crater	12	-2	42	58749484	8000	240	deep	n	y	+2	
3635													
3585													
3535													
3510	6	crater	8	-6	42	58749484	8000	550	deep	n	n		Flags in underlying fault region
3485	9	eye	10	-2	19	16854339	5050	220	medium	n	n		
3435													
3385													
3360	13	eye	4 above, 2 below	across Tang Fm	121	87686262	18013	600	deep	n	n		Stacked
3360	14	crater	14	-6	121	87686262	18013	70	deep	n	n		Stacked
3310	7	crater	6	-4	19	16854339	5050	300	medium	n	n		

Sector 4 data for Figure 6.9.

Inline	HTVC number	HTVC structure	Number of reflections the HTVC crosses (bar thickness)	Number of reflections of the top of the HTVC above or below Tang Fm (bar level)	Sill number that is feeding HTVC	Sill area, m2	Minimum sill diameter, m. Sills on edge of study area are in itallics	Feeder sill thickness, ms TWT	Sill depth: shallow, medium or deep	Amplitude anomalies between sill and HTVC?	Amplitude anomalies above HTVC?	Number of reflections of AAs relative to Tare Fm	Comments
3300	31	crater	12	0	104	103795450	14900	350	deep	n	n		
3275													
3250													
3225													
3200													
3175													
3150													
3125	8	crater	8	-2	19	16854339	5050	200	medium	n	n		
3100													
3075	12	dome	2	0, above	19	16854339	5050	200	medium	n	n		
3055	33	eye	4 above, 4 below	0, across	3	51993429	10100	600	deep	n	y	-1, 0, +1, +2	High amplitudes in Brygge Fm disrupted, dimming cuts across
3050	32	eye	2 above, 4 below	0, across	3	51993429	10100	600	deep	n	y	0, +1, +2, +12	High amplitudes in Brygge Fm disrupted, dimming cuts across
3045	30	eye	2 above, 4 below	0, across	3	51993429	10100	600	deep	n	y	0, +1	Seismic dimming in Brygge
3000	27	eye	2 above, 4 below	0, across	3	51993429	10100	650	deep	n	n		
2990	25	eye	4 above, 4 below	0, across	3	51993429	10100	550	deep	n	n		
2965													

2940	15	eye	2 above, 2 below	0, across	121	87686262	18013	440, sill complex	deep	n	n		
2915	16	dome	2	0, below	121	87686262	18013	440, sill complex	deep	n	n		
2890													
2865													
2840													
2815													
2790													
2765													
2740	17	dome	6	0, above	2	423116100	*3650*	520	deep	n	y	+2 to -4	
2715													
2690	24	eye	4 above, 4 below	0, across	3	51993429	10100	450	deep	n	n		
2665													
2640													
2615													
2590													
2565													
2540													
2515	29	dome	2	0, above	3	51993429	10100	500	deep	n	n		
2490	18	eye	4 above, 2 below	0, across	2	423116100	*3650*	500	deep	flags in nearby faults	y	0, +1	High amplitude flags in faulted Springer-Nise Fm
2465													
2440													
2415													
2390													
2365													
2340													
2315													
2290													
2265	19	dome	4, below	0, below	2	423116100	*3650*	500	deep	flags in column and in faults below	y	-2,-3,-4	High amplitude flags in faulted Springer-Nise Fm
2240													
2215	28	dome	4 above	0, above	2	423116100	*3650*	500	deep	n	y	0, +1	
2190	20	crater	4	-2	2	423116100	*3650*	600	deep, same as 23	flags in column	y	-2, -3	High amplitude flags in faulted Springer-Nise Fm
2165													
2140	22	eye	6	0, below	2	423116100	*3650*	500	deep, same as 21	flag in column	y	-2	High amplitude flags in faulted Springer-Nise Fm
2115													
2090	21	eye	6	0, below	2	423116100	*3650*	600	deep, same as 22	n	y	+1	High amplitude flags in faulted Springer-Nise Fm. Seismic dimming in HTVC
2065	23	eye	6	0, below	2	423116100	*3650*	500	deep, same as 20	flag in column	y	0	High amplitude flags in faulted Springer-Nise Fm